Observational Astrophysics

Lecture notes parts 1 and 2

JOHAN BLEEKER
SRON Netherlands Institute for Space Research
Astronomical Institute Utrecht

Observational Astrophysics

Lecture notes part 1

Contents

Chapter 1

Discovery Space

(Reproduced from Harwit, 1984)

1.1 Historical remarks

Traditional astronomy was concerned with studying the light, i.e. optical radiation,from objects in space. The range of light is in fact surprisingly limited, it includes only radiation with wavelenghts 30 percent shorter to 30 percent longer than the wavelength to which the human eye is most sensitive. Present day astronomy covers the full electromagnetic spectrum covering wavelenghts less than one thousand-millionth as long (gamma-rays), to over a hundred million times the wavelength of light for the longest radio waves. To make an analog with sound, traditional astronomy was an effort to understand the symphony of the universe with ears which could hear only middle C and the two notes immediately adjacent.
The accidental discovery in 1931 by Karl Jansky, a radio engineer at Bell Telephone Laboratory, of radio waves beyond the Earth showed that there was non-optical radiations from space. The rapid growth of astronomy over the recent decades basically arises from overcoming two major barriers.

The first is a natural barrier, the earth's atmosphere, which absorbs most radiations from space,consequently space-based instruments and platforms are required to cross this barrier. This "space age" started in the 1950s and has been absolutely seminal for the development of modern astrophysics.

The second barrier was technological: new types of telescopes had to be built to gather other kinds of electromagnetic radiation than optical or radio waves, this also included techniques for collecting cosmic-ray particles and neutrinos. Also, a host of new sensor techniques to detect and record the images and spectra gathered by these telecopes needed to be developed, including their suitability to be launched by rockets and carried on satellite platforms operated in space. As a consequence, many cosmic phenomena have only come to be recognized in the past forty-five years, largely through the introduction into astronomy of radio, X-ray, infrared, and gamma-ray techniques. None of the new phenomena had been anticipated before World War II, and it is natural to wonder how many more remain unrecognized even today, how rich and complex the universe might be. Further, if technological advances already have helped us uncover so many new cosmic features, how many more innovations of similar kinds could we put to use in future cosmic searches?

Astronomy is largely an observational science, and for at least the next century our technology will be insuffIciently advanced to permit exploration of the universe beyond the solar system. Because astronomy is so dependent on observations, it is relatively simple to assess

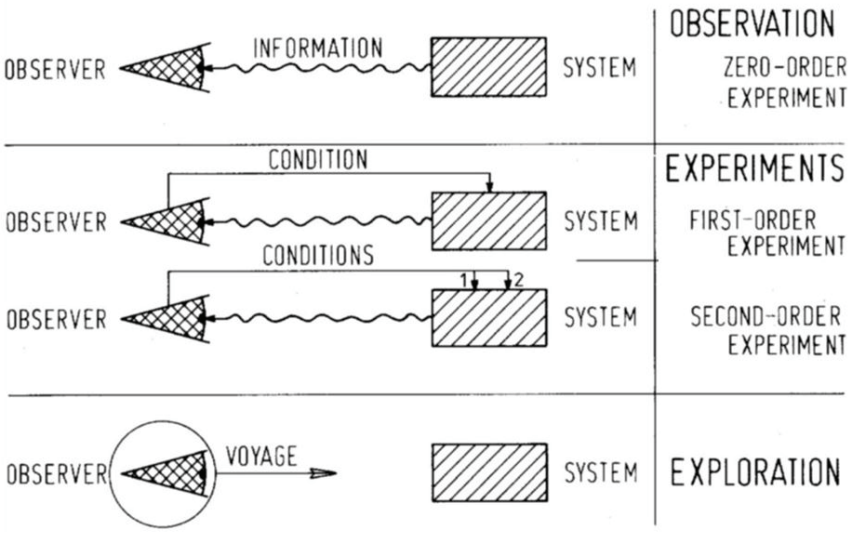

Figure 1.1: *Observation, experiments, and exploration. Observation is the most passive means for gathering data. The observer receives and analyzes information transmitted naturally by the system he is studying. The experimenter, in contrast, stimulates the system under controlled conditions to evoke responses in some observable fashion. Exploration is an attempt to gather increasing amounts of information by means of a voyage which brings the experimenter or observer closer to the system to be studied. Credit Harwit (1984).*

the impact that further technological advances are likely to make. In the experimental sciences such an assessment would be far more complex. The experimentalist studies a system by imposing constraints and observing the system's response to a controlled stimulus. The variety of these constraints and of stimuli may be extended at will, and experiments can become arbitrarily complex as indicated in figure 1.1.

Astronomy is different. The observer has only two choices. He can seek to detect and analyze signals incident from the sky, or he may choose to ignore them. But he has no way of stimulating a cosmic source to alter its emission. He can only observe what is offered. He is entirely dependent on the carriers of information that transmit to him all he may learn about the universe.

1.2 Discovery and rediscovery

Though there is no unique definition of a cosmic phenomenon, most astronomers would compile a list much like the one shown in figure 1.2 if asked to name the principal phenomena characterizing the universe.

The 43 phenomena named are given prominence in most astronomical texts and standard reference works. Conferences and symposia concern themselves with individual phenomena on the list, and books or review articles frequently focus on one or another of these entries. The discovery dates for the phenomena shown in the top curve cannot always be precisely pinpointed because the realization of a discovery sometimes dawns slowly. At times a discovery involves the recognition that a previously known phenomenon actually comprises two quite distinct sources or classes of events — giant and main sequence stars, novae and supernovae, galaxies that contain gas — while others do not. Such discoveries are indicated by a slash (/)

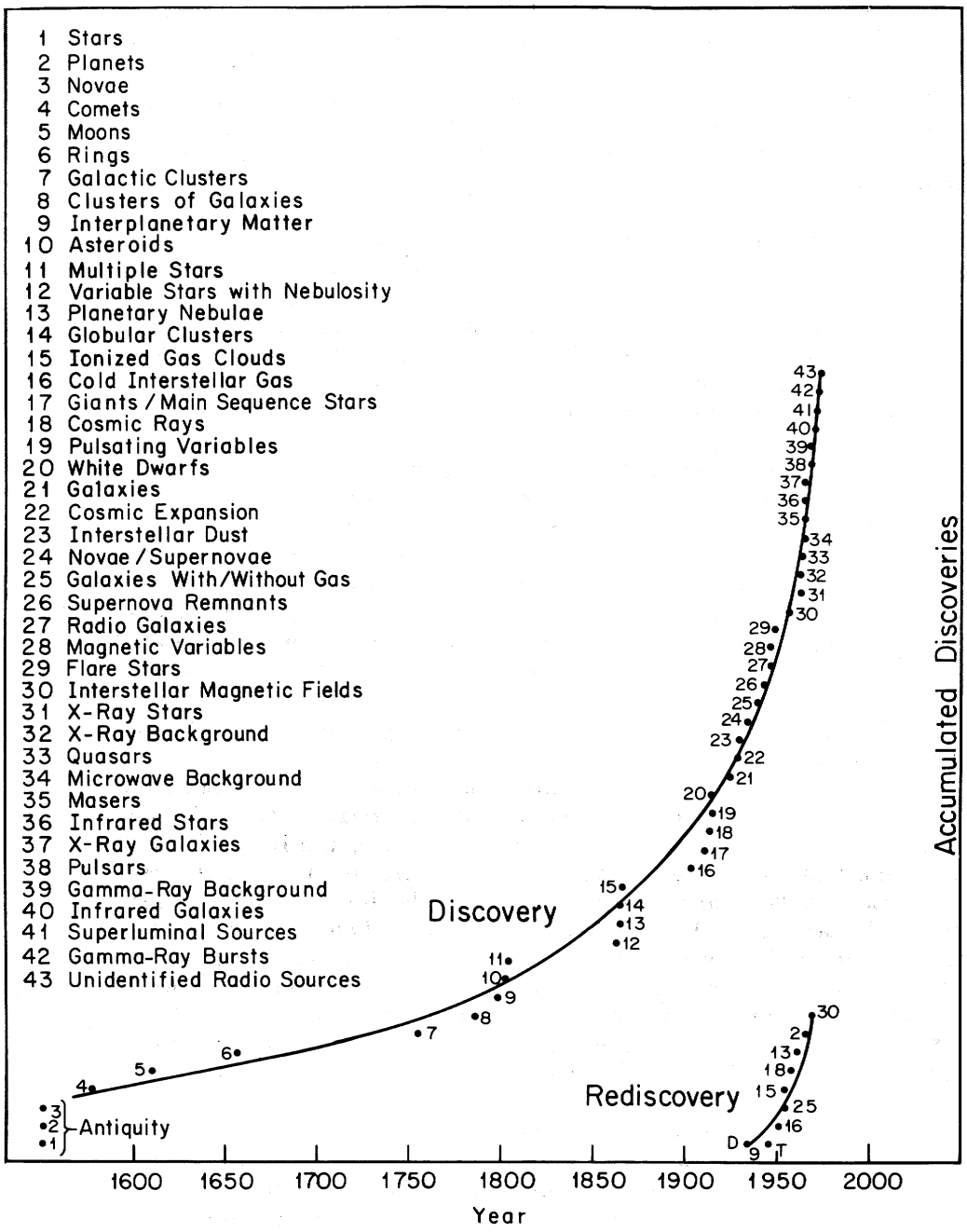

Figure 1.2: *Major astronomical discoveries and rediscoveries. Credit Harwit (1984).*

in the designation of the two phenomena that become resolved. The lower curve shows phenomena that are redundantly recognized through two totally independent techniques. Thus, the existence of planets in the solar system would by now have been discovered even if optical telescopes had never been invented. An astronomer on an ever-cloudy body, such as Venus, would by now also have discovered the system of planets by virtue of planetary radio emission alone. One phenomenon, interplanetary matter, is known not only in doubly (D) but in triply (T) independent ways. We see the faint zodiacal light in the night sky; we observe meteors and meteorites burning as they enter the atmosphere and can collect meteorites that hit the

ground; finally, we obtain radar reflections from fine dust grains that burn on entering the upper atmosphere.
The most striking aspect of the two curves is the increasingly accelerated rate of discovery shown by the rapid rise in the top curve. Simultaneously with this rise comes an increasing recognition of previously known phenomena, now rediscovered by means of radio telescopes.

1.3 The search

The search for cosmic phenomena is one of mankind's greatest adventures and one of the most ambitious enterprises of modern science. To understand its conduct we will need to discern the nature of the phenomena, identify the people caught up in the search, describe the skills these scientists possess, analyze the plans they follow to their goals, and identify the tools required for their quest. We will need to know how the most significant discoveries are being made, whether past successes can guide us to further discoveries, whether there are ways to gauge the future scope of the search — of deciding whether our inventory of cosmic phenomena is nearly complete, whether we are close to being the last generation of astronomers needed to unravel the complexities of the universe, or whether there will be an endless cadre of cosmic researchers stretching into an uncertain future. There is only one way to approach this study: we must look at the conduct of past searches in order to discern trends that can lead to assessments of the future. Seven traits common to many discoveries are these:

1. **The most important observational discoveries result from substantial technological innovation in observational astronomy.**
   Galileo's spyglass enabled him to resolve features on the moon considerably finer than any that can be distinguished with the unaided eye. He could also see stars several magnitudes fainter. Viktor Hess's discovery of cosmic rays led to an increasing awareness that electromagnetic radiation is not the only carrier of astronomical information reaching Earth; there also exist energetic subatomic particles that inform us about catastrophic events far away in the cosmos. Karl Jansky looked out into the universe and saw signals from our galaxy at wavelengths 20 million times longer than anything the eye can see; the scientists at the Naval Research Laboratory and at the American Science and Engineering Corporation were able to detect signals at wavelengths 1,000 times shorter than visible light, and these techniques led to the discovery of X-ray stars and galaxies. The Vela military satellites could detect brief bursts of gamma-rays and found just such bursts arriving from unknown parts in the sky; and short pulses detected at radio wavelengths similarly had led Anthony Hewish and Jocelyn Bell to the discovery of pulsars in 1968. Technological innovations that led to discovery have usually involved completely new wavelength ranges never used in astronomy before, or have made use of instruments with unprecedented precision for resolving sources to exhibit structural features, time variations or spectral features never seen before.

2. **Once a powerful new technique is applied in astronomy, the most profound discoveries follow with little delay.**
   Many discoveries are made within weeks or months of the introduction of new observing equipment. In the past twenty-five years there have been no discoveries that could have been made with instruments available a quarter-century earlier. Occasionally a discovery is verified by an observer who can point to records he had obtained some two or three years before; on these the new phenomenon may already be discerned, though not perhaps convincingly enough to stand out.

3. **A novel instrument soon exhausts its capacity for discovery.**
   This corollary to the speed with which new discoveries follow technical innovations does not imply that new apparatus quickly becomes useless. It just means that the instrument's function changes. It joins an existing array of tools available to the astronomer for analytical work, rather than for discovery, and continues useful service in that capacity. To revitalize a technique for further searches for new phenomena, its sensitivity or resolving power must be substantially increased, often by as much as several factors of 10. Thus the discovery of *quasars* became possible only after radio-astronomical techniques had advanced to a stage at which sources subtending angles no larger than 1 second of arc could be identified and accurately located in the sky. The radio equipment available earlier to Jansky could simply not have coped with such observations.

4. **New cosmic phenomena frequently are discovered by physicists and engineers or by other researchers originally trained outside astronomy.**
   In a wide-ranging study of the emergence of radio astronomy in Great Britain, the sociologists David Edge and Michael Mulkay have noted that all of the early British radio astronomers were physicists or electrical engineers and that radio astronomy, worldwide, was originally staffled largely by workers trained in physics or electrical engineering. The same trait can be discerned all across modern astronomy. We speak of "cosmic-ray physicists", and, in fact, cosmic-ray research is largely carried out in the physics departments of universities. Similarly, the early X-ray or gamma-ray astronomers had been trained as physicists. This trend is not just confined to modern times. We need only think of the work of Galileo, William Herschel and Joseph Fraunhofer, who brought new methods and techniques to astronomy after working in other fields. Many of these pioneers initially worked at what professional astronomers would have considered the outskirts of astronomy.

5. **Many of the discoveries of new phenomena involved use of equipment originally designed for military use.**
   The rapid development of radio astronomy after World War II was made possible by existing radar equipment developed for the war effort. Even before the war's end, however, James Stanley Hey, at the time employed by the British radar network, had noted occasional strong radio emission from the Sun and had discovered radar reflections from meteor trails. Subsequently both solar radio astronomy and radar meteor observations developed into subdisciplines with their own practitioners. In 1946, shortly after the end of the war, Hey and his collaborators, still using war-time equipment available to them, also discovered a curiously undulating cosmic radio signal that proved to be the first extragalactic radio source, Cygnus A. In the United States the earliest post-war solar X-ray and far-ultraviolet observations were carried out with German V-2 rockets. Advances in infrared astronomy were similarly based on progress in the construction of military detectors, but the most sensitive far-infrared detectors were not developed until some time after the war and did not become available for astronomical work until the late 1950s and early 1960s. This relationship between the tools of surveillance in war and in astronomy is not new: Galileo had pointed out the military value of the spyglass to the Venetian senate. His gift of the spyglass so pleased the senators that they at once doubled his salary and made his professorship at the University of Padua a lifetime appointment.

6. **The instruments used in the discovery of new phenomena often have been constructed by the observer and used exclusively by him.**

The instruments used by Galileo, Hess, Jansky, and the early X-ray astronomers were built by them and were under their sole control. The Los Alamos group that discovered gamma-ray bursts had access to all the data gathered by the passive Vela satellites. Men like Christian Huygens, James Bradley, William Herschel, Friedrich Wilhelm Bessel, William Huggins, and William Parsons, third earl of Rosse, responsible for prime discoveries in the seventeenth, eighteenth and nineteenth centuries, also had instruments that they alone might use: When faced with a surprising result, they could check their apparatus at leisure, repeat the observations, and cross-check their results until they were certain that a finding was genuine and not due to some instrumental artifact. More than half of the phenomena discovered in historical times were made with instruments under exclusive control of the astronomers responsible for the discovery.

7. **Observational discoveries of new phenomena frequently occur by chance — they combine a measure of luck with the will to pursue and understand an unexpected finding.**
   Before Viktor Hess set out to make his balloon observations, the slow discharge that always takes place in electroscopes had generally been attributed to radioactivity in the earth. If that were true, Hess argued, absorption of the radiation in 5 kilometers of air should shield his instruments and cause them to discharge more slowly. Instead, Hess noted an increased discharging rate at higher altitudes and concluded that the rays were cosmic. Karl Jansky, in 1931, was concerned with the mundane problem of finding ways to lower interference in radio telephone transmission. Instead he is now remembered for finding radio emission from the Milky Way. The Los Alamos gamma-ray physicists were searching for surreptitious nuclear bomb tests and found cosmic gamma-ray bursts instead. The first X-ray star was discovered through a search for lunar X-ray fluorescence. The cosmic microwave background radiation was found when Arno Penzias and Robert Wilson at Bell Laboratories found they could not reduce below a certain level the noise registered by a new sensitive radiometer they had developed. Pulsars forced attention upon themselves when Anthony Hewish and Jocelyn Bell were actually set to measure scintillation — twinkling — of radio sources. About half the cosmic phenomena now known were chance discoveries. The number of these surprises is a measure of how little we know our universe.

In addition to providing new discoveries, novel astronomical techniques have also provided another, almost equally important datum, the rediscovery of phenomena recognized from earlier observations. Frequently even this rediscovery occurs unexpectedly. The detection of strong radio emission from Jupiter in 1955 represented the first, unexpected measure of radio emission from a planet. Previously, planets had been considered to be undetectable with available radiotelescopes because their theoretically predicted flux was too low to permit detection.We say that a phenomenon is recognized in two completely independent ways if it could be discovered equally well with separate instruments that differ by at least a factor of a 1000 in one of their observing capacities. Spiral galaxies, for example, can be recognized equally well through radio observations and through optical studies at wavelengths a million times shorter. This independent recognition of phenomena through widely differing channels of information provides a statistical key to the total number of observational discoveries we might ultimately hope to make. A simple example illustrates the idea: consider a collection of baseball or football cards. At the beginning of each season when the collection is still small, all the cards differ from each other. But as the collection grows, an increasingly large fraction of the cards becomes duplicated. Assume that all individual pictures are equally represented

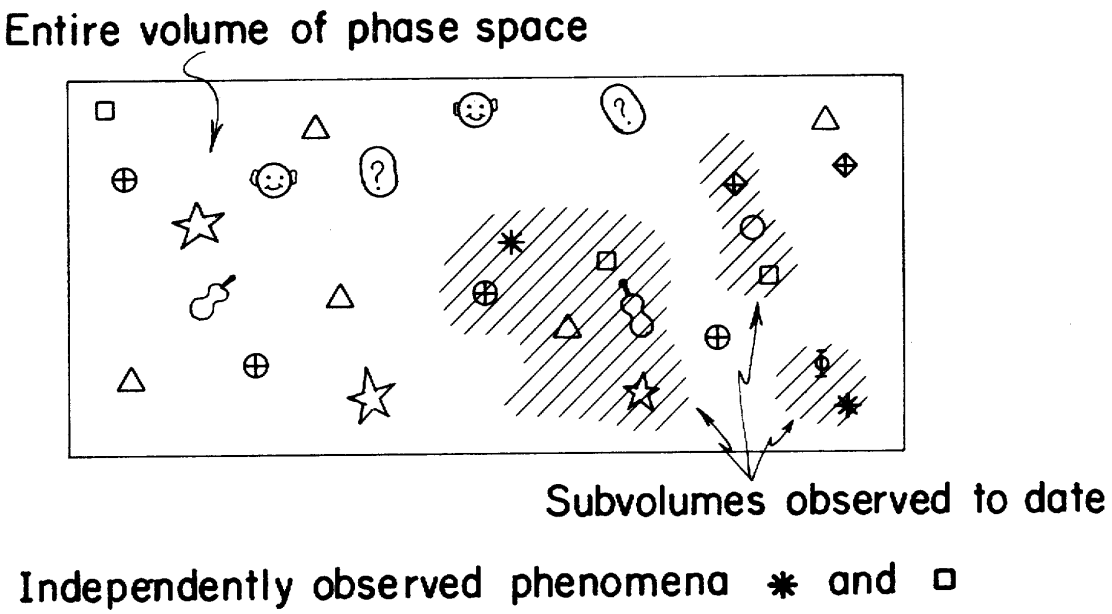

Figure 1.3: *Phase space of discoveries. Credit Harwit (1984).*

and assume further that the cards are obtained in some statistically random order. Then the very first duplicate obtained tells us an important characteristic of the set — namely, *that it is finite.* In a collection containing an infinite number of different cards randomly distributed, no duplicates would ever be found unless an infinite number of cards were examined. As the collection of cards grows and the number of duplicates increases, the relationship between the number of single cards in the collection and the number of duplicates can yield an increasingly accurate estimate of the total number of different cards in a complete set. The statistics governing our search for cosmic phenomena through different channels of observation is similar to the statistics of baseball cards. Each newly opened channel corresponds to a newly opened package of cards. Initially, as our technical expertise grows and the number of available channels increases, we discover an increasing number of new phenomena. But as the number of our discoveries grows, a survey carried out through a completely new channel will mainly uncover an increasing number of duplicates, i.e. phenomena already known from earlier discovery through previously established channels. We currently recognize already quite a number of duplicates, the rediscoveries of figure 1.2, such as the planets and the spiral, gas-containing galaxies. *Thus the number of cosmic phenomena is finite and can be estimated!*

1.4 The phase space of observations

The phase space of observations is a multidimensional space, each point of which corresponds to a different basic observing capability. The rectangular bordershown in figure 1.3 encompasses the space containing all conceivable astronomical observations that can be carried out in our universe. The region of this space in which a given phenomenon appears, are determined by its observable traits and not by its position in the sky. The phenomenon's location in the phase space will therefore not change appreciably from one phase in the evolution of our galaxy to the next, though the constellations of stars seen in the sky would change appreciably during that time. If we consider the case of electromagnetic observations, as an example, five

orthogonal axes can be defined, i.e. the spectral frequency or wavelength of the observation, the angular resolution, the time resolution and the polarization of the received light. The parameters define *a five-dimensional space* and any point contained in this space corresponds to a particular observation one can carry out. Conversely, any observation one might possibly conceive corresponds to one or more points that can be unambiguously located in the volume. This five-dimensional space constitutes therefore the phase space for electromagnetic observations (sometimes a sixth dimension, the intensity, is also added to EM-phase space).

The framed portion of figure 1.3 represents the entire accessible multidimensional space. The shaded portions are regions in which observations have already been undertaken. The cosmic phenomena are represented by a variety of symbols. Some of these symbols appear in several portions of the space. Violins appear both in a region to which we already have access and in a portion of the space in which we currently lack the instrumental capabilities to observe. Some phenomena, such as the one represented by the Greek letter Φ appear only once. Some, like the question marks or the little men — which might represent life in theuniverse — appear outside current instrumental reach. These phenomena remain to be discovered. Others, still, have been observed in two widely separated shaded regions. These are exemplified by the asterisks and open squares and represent phenomena independently observed in two different ways.

1.5 Estimating the total number of cosmic phenomena

To estimate how many more phenomena might be discovered in further cosmic searches, one must assume that past discoveries have been characteristic for those expected in the future. If we take a total (finite) volume V for the phase space and consider a small portion v of this volume to represent all the observations that have already been made, a cosmic phenomenon with multiplicity m in V will have an average value mv/V if we pick randomly small compartments out of V until they make up a total subvolume v. The multiplicity m refers to m points (or rather small compartments) in phase space at locations that would lead to an independent recognition of the specific cosmic phenomenon. Let us take, for example, the supernova phenomenon. Apart from detecting this as a bright optical flash, it can independently be detected as a pulse of neutrinos (SN1987A) and, possibly, as a pulse of gravitational waves. The multiplicity m would have to be set at either 2 or 3 or higher. The probability of finding k independent recognitions of a particular cosmic phenomenon with a multiplicity m in a subvolume v is given by the binomial distribution:

$$P(k) = \left(\begin{array}{c} m \\ k \end{array} \right) \; p^k \; (1-p)^{m-k} \tag{1.1}$$

with $p = v/V$ and the binomial coefficient

$$\left(\begin{array}{c} m \\ k \end{array} \right) = \frac{m!}{k! \; (m-k)!} \tag{1.2}$$

The average $\bar{k}$ of this distribution equals $mp = mv/V$ as we noted earlier. Suppose now that apart from the cosmic phenomenon under consideration (e.g. the supernova phenomenon) n other phenomena do exist. Let us also assume, since we have no other clue, that the multiplicities of these n phenomena are all the same, i.e. equal to m. The number of singly (k=1) detected phenomena in the subvolume v are then given by:

$$X = n \, P(1) = n \; m \; p \; (1-p)^{m-1} \tag{1.3}$$

Cosmic phenomena	Year of Tally		
	1959	1969	1979
Total discovered $(A + B + C)$	30	39	43
Singly recognized (A)	25	31	35
Doubly recognized (B)	4	7	7
Triply recognized (C)	1	1	1
Best estimate for total in universe (n)	103	99	123
Recognized fraction of total	0.29	0.39	0.35

Table 1.1: *The number of phenomena estimated in different years.*

We also have for doubly and triply detected phenomena:

$$Y = n\,P(2) \;=\; \frac{n\;m\;(m-1)}{2}\;p^2\;(1-p)^{m-2} \tag{1.4}$$

$$Z = n\,P(3) \;=\; \frac{n\;m\;(m-1)\;(m-2)}{6}\;p^3\;(1-p)^{m-3} \tag{1.5}$$

If we assume m to be rather large and p to be small, we get an estimate of the total number of phenomena n:

$$n \approx \frac{X}{2Y}\,(X+2Y) \tag{1.6}$$

provided that n is large compared to X and Y. The number of still unknown phenomena follows from $n-(X+Y)$. Although this estimate gives no clue what so ever as to the nature of these phenomena, it nevertheless provides a sense of complexity of the cosmos, i.e. a measure of the scope of work lying ahead. When we tally the number of simply and doubly recognized phenomena from figure 1.2, we get X=35 and Y=7. Using the above formula for n, we can then estimate the total number of cosmic phenomena we may ultimately recognize to be $n \approx 125$, i.e. only one-third are known today. To verify the plausibility of the above approach, one can perform the following tests.The number n is a property of the universe, and our estimate of n should therefore be constant, independent of the epoch in which the estimate is made. With the data shown in figure 1.2, we can obtain estimates for n, based on values for the number of singly and doubly recognized phenomena known in 1959, 1969, and 1979. Using the equation relating n to X and Y then permits us to calculate the best estimate for n that we would have obtained in each of these years. Table 1.1 shows that these estimates only differ by about 20 percent. With the limited available data we can expect no greater constancy than that.

1.6 Unimodal and Multimodal Phenomena

The estimate just made of the wealth of cosmic phenomena, n, was based on the assumption that each of the phenomena could potentially be found in several different locations in the volume represented by figure 1.3. However, we have no assurance that this assumption is valid. A substantial number of phenomena could exist that revealed themselves only through a unique astronomical observing mode and were otherwise beyond reach of observational discovery. How many of these unimodal phenomena does the universe contain? Are they more numerous than the multimodal phenomena we estimate to number n $\approx$ 125? How can we tell? We can estimate the maximum number of unimodal phenomena in this way: we examine all the phenomena X that have thus far been singly recognized. Among these there will be a subgroup numbering X', for which we cannot be certain whether a redundant recognition is bound to be possible. For the remaining $(X - X')$phenomena, astrophysical theory will permit the prediction of an alternate mode of observation, based on our more intimate understanding of these phenomena. At present there may be as many as four phenomena for which we are not certain about the possibility of redundant recognition, and we can therefore set $X' = 4$ for the current epoch of astronomy. We may divide X', by a factor p, representing current competence for making observations. That competence is just the fraction of the observing space that technical developments have permitted us to search — the shaded fraction of the plot in figure 1.3. The ratio X'/p then provides an upper limit to the number of phenomena that ultimately would remain singly recognized. It can be made plausible that $p \approx 0.01$ at present, and therefore $X'/p \approx$ 400. We therefore expect a maximum number of about 400 unimodal phenomena. These may quadruple the total number of phenomena ultimately to be found, making a total number of approximately 500. At our present stage of development in astronomy, this is a satisfactorily close estimate which should continually improve as we learn more about the phenomena we uncover.

We can see at least that we are not dealing with a list of phenomena numbering in the thousands or the millions, an estimate that could have been quite conceivable without the approach developed here. If this way of viewing the universe as a system of finite variety seems slightly improbable right now, one should remember that geography, too, was once an unimaginably variegated field. During the fifteenth and sixteenth centuries, discovery followed great discovery. But then it all came to an end. Today there are few surface features on Earth that remain unknown. The probability of discovering a new ocean or finding a mountain higher than Mount Everest is nil. Uncharted features on the earth's surface are now measured in meters, not kilometers or miles. In a similar way we may expect the undiscovered cosmic phenomena to shrivel in number until only minor features remain unnoticed.

1.7 The End of the Search

The history of most efforts at discovery follows a common pattern, whether we consider the discovery of varieties of insects, the exploration of the oceans for continents and islands, or the search for oil reserves in the ground. There is an initial accelerating rise in the discovery rate as increasing numbers of explorers become attracted. New ideas and new tools are brought to bear on the search, and the pace of discovery quickens. Soon, however, the number of discoveries remaining to be made dwindles, and the rate of discovery declines despite the high efficiency of the methods developed. The search is approaching an end. An occasional, previously overlooked, feature can be found or a particularly rare species encountered; but the rate of discovery begins to decline quickly and then diminishes to a trickle. Interest drops,

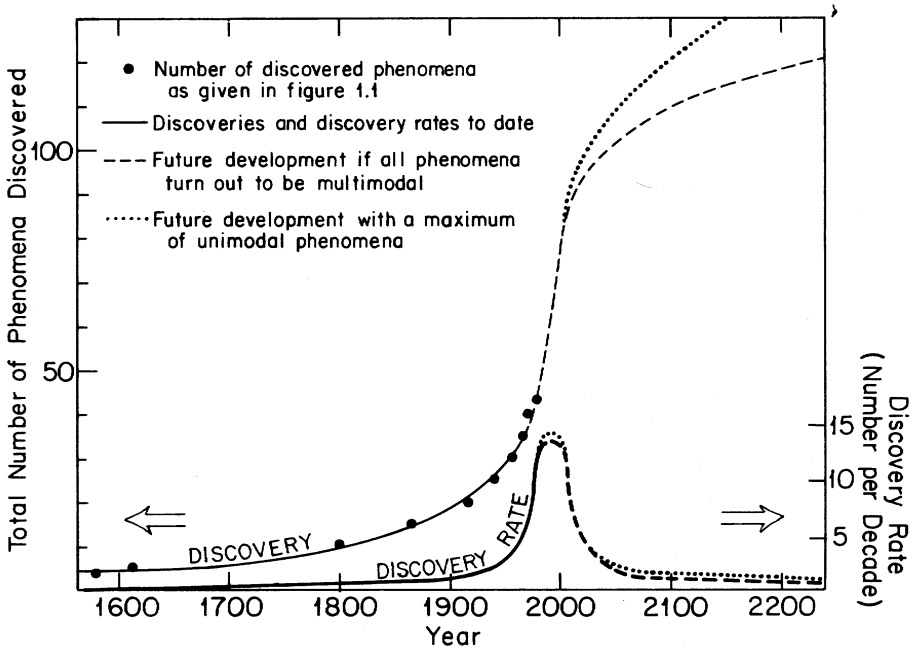

Figure 1.4: *Discovery and discovery rate projected into the future. Credit Harwit (1984).*

researchers leave the field, and there is virtually no further activity. The discovery rate in this course of events follows a bell-shaped curve, roughly as drawn in figure 1.4.
Correspondingly, there also is a steep S-shaped curve which represents the accumulation of discoveries. The discovery rate for cosmic phenomena, averaged over early decades when discoveries were sparse, is shown in the bottom, bell-shaped curve. The dashed portion is an extension into the future, based on the rates measured in the past. It is computed for a total wealth of multimodal phenomena estimated at 125, as explained in the text. The tall S-shaped curve clearly exhibits the accelerating rate of discovery in recent decades and represents data shown in figure 1.2. The dashed and dotted lines extend the curve into the future, taking into account the general rise and fall of discovery rates seen in other ventures, as well as the total estimated number of phenomena still awaiting discovery. The dashed line assumes that there are no unimodal phenomena and levels off at $n \approx$ 125 phenomena. The dotted curve assumes a maximum number of unimodal phenomena and can reach a level as high as 500. Projections into the future are based on two factors, a belief that a smooth bell-shaped curve, symmetric about its peak, well represents the rate of discovery throughout the search and a belief that the total number of multimodal phenomena to be found will equal our best estimate of roughly 125. If this curve accurately corresponds to future developments, we should have found some 90 percent of all the multimodal phenomena by the year 2200. Thereafter,however, it might take several millennia to find the remaining few percent. Just as astronomical discovery started a few thousand years ago with an awareness of planets that regularly move through the starry sky, so too, the search may continue thousands of years into the future. This is particularly true if many cosmic phenomena are unimodal. Discoveries will then take place as long as new observational techniques can be introduced into astronomy, i.e. as long as any portions of the volume drawn in figure 1.3 remain unshaded.
The phenomena to be discovered last might be those that occur with great rarity and emit too little energy to be found at great distances across the universe. Alternatively, the last

few phenomena might be those that emit carriers for which observing apparatus is developed very late in the history of technological progress. The rate of discovery in that case would be delayed by technical factors rather than by limitations intrinsic to the nature of the undisclosed phenomena.

Chapter 2

Information Carriers

An information carrier is defined here as a physical phenomenon which can be "sensed" and processed by a detection system. In this way information can be extracted about the (physical) state and characteristics of the information source, i.e. in this case a cosmic source.

In astronomy there are four important information carriers:

1. Electromagnetic radiation / Photons
2. Neutrinos
3. Cosmic-rays
4. Gravitational radiation / Gravitons

These will be discussed in the following sections. Other carriers also exist (such as meteorites, moon rocks, space plasma) but these are beyond the scope of this course and will not be discussed.

2.1 Electromagnetic radiation

2.1.1 Characterisation

Detection of electromagnetic radiation is the most commonly used way of doing astronomical observations. An electromagnetic wave can be described by its wavelength λ, frequency ν, energy ϵ or characteristic temperature T. These quantities are mutually related and are commonly given in the following units[1]:

wavelength	λ				in Å, nm, μm, mm, cm, m
frequency	ν	$= \frac{c}{\lambda}$			in MHz, GHz, THz
energy	ϵ	$= \frac{hc}{\lambda}$	$= h\nu$		in eV, keV, MeV, GeV (1 eV = $1.6 \cdot 10^{-19}$ J)
char. temperature	T	$= \frac{hc}{\lambda k}$	$= \frac{h\nu}{k}$	$= \frac{\epsilon}{k}$	in K

with c the velocity of light, h Planck's constant and k Boltzmann's constant.

The entire electromagnetic spectrum is divided into several classes, like gamma-rays and radio waves. Most (groups of) classes have their own detection methods which will be treated in the next chapters. Each class has its own convention of describing the waves: in X-ray

[1] In these lecture notes SI units will be used, unless stated otherwise

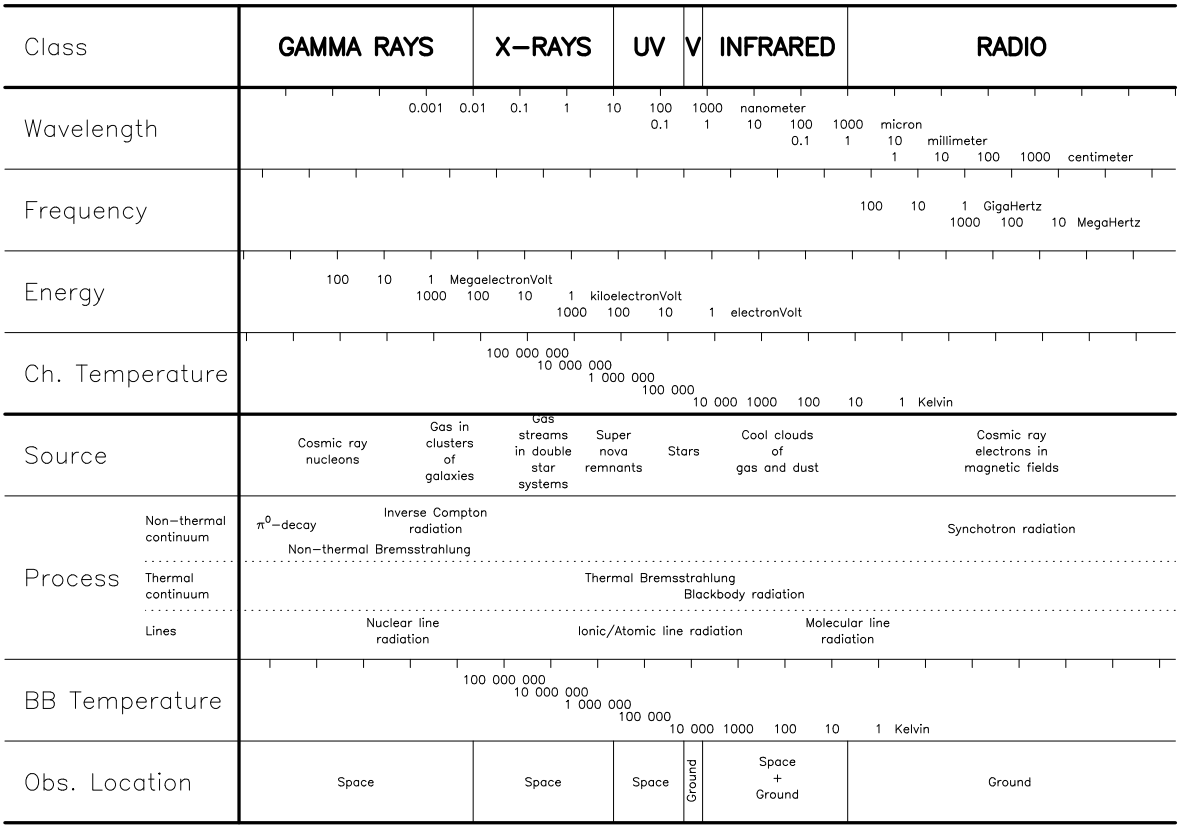

Figure 2.1: *The electromagnetic spectrum. The observable part covers about twenty decades. Waves with wavelengths above 10 km are absorbed by the interstellar medium.*

astronomy observers use photon energy ϵ, in the infrared one commonly uses wavelength. An overview of the electromagnetic spectrum is given in figure 2.1. We shall now briefly review the basic principles of the most important physical processes that give rise to cosmic sources of EM-radiation.

2.1.2 Thermal radiation

There are two basic sources of thermal radiation:

- An optically thick radiator producing blackbody radiation governed by Planck's law.
- An optically thin radiator producing a superposition of Bremsstrahlung, recombination and line radiation.

Blackbody radiation

The energy density radiated by a blackbody at temperature T in a narrow frequency band from ν to $\nu + \Delta\nu$ is given by Planck's law:

$$\rho(\nu)d\nu = \frac{8\pi h}{c^3}\frac{\nu^3}{\exp\left(\frac{h\nu}{kT}\right) - 1}d\nu \tag{2.1}$$

This equation can be rewritten as a function of the energy density $\rho(\epsilon)$ between ϵ and $\epsilon + d\epsilon$

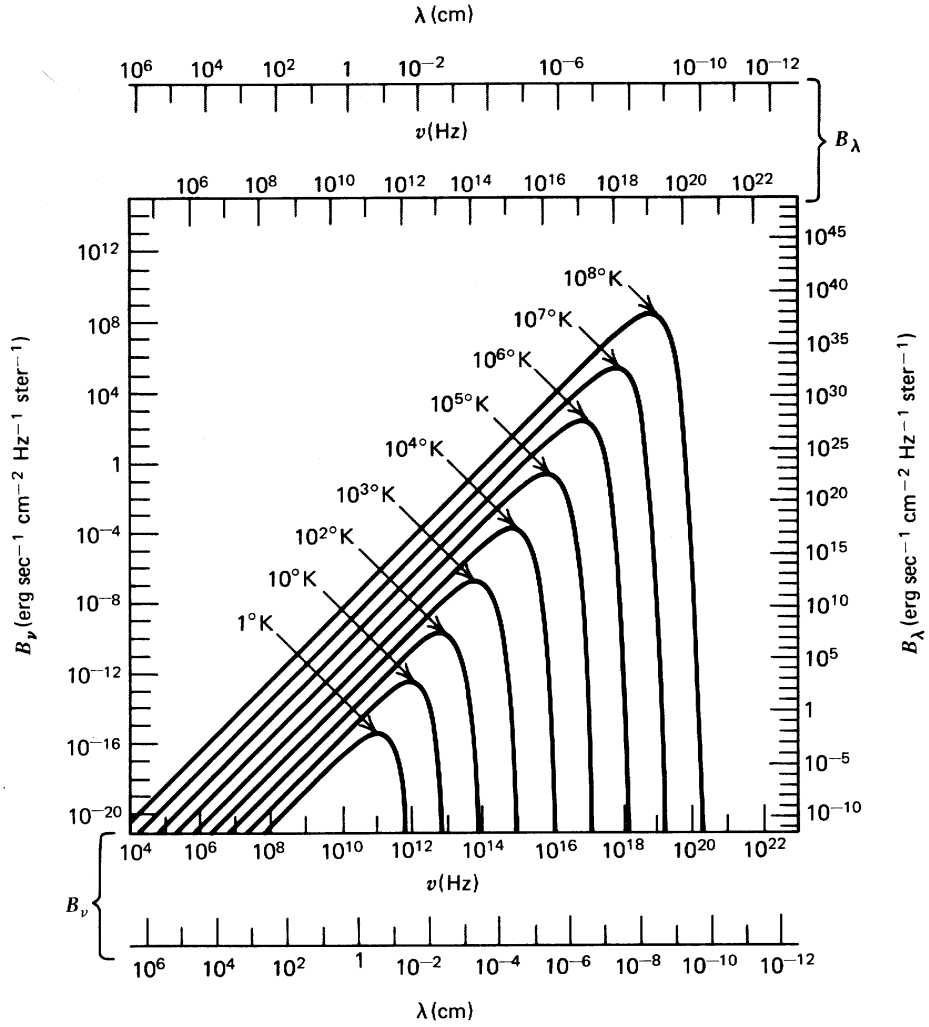

Figure 2.2: *Intensity spectra of blackbody radiation at various temperatures.* $B_\nu d\nu = \frac{c}{4\pi}\rho_\nu d\nu$. *Note the difference between the horizontal axis for* B_ν *and* B_λ. *Credit Kraus (1966).*

or $\rho(\lambda)$ between λ and $\lambda + d\lambda$ using $\rho(\nu)\,|\,d\nu\,| = \rho(\epsilon)\,|\,d\epsilon\,| = \rho(\lambda)\,|\,d\lambda\,|$:

$$\rho(\epsilon)d\epsilon = \frac{8\pi}{(hc)^3}\frac{\epsilon^3}{\exp\left(\frac{\epsilon}{kT}\right)-1}d\epsilon \tag{2.2}$$

$$\rho(\lambda)d\lambda = \frac{8\pi hc}{\lambda^5}\frac{1}{\exp\left(\frac{hc}{\lambda kT}\right)-1}d\lambda \tag{2.3}$$

The energy for which the energy density function is at maximum can be found by

$$0 = \frac{d\rho(\nu)}{d\nu} \;\Rightarrow\; \frac{h\nu_{max}}{kT} = 3\left[1-\exp\left(-\frac{h\nu_{max}}{kT}\right)\right]$$

$$\nu_{max} \approx 2.82\frac{kT}{h} \tag{2.4}$$

Similarly one obtains $\epsilon_{max} \approx 2.82kT$ and $\lambda_{max} \approx hc/4.97kT$ (see also equation 2.40). Note that this wavelength does not correspond to the frequency ν_{max}.

Spectral densities in X-rays and γ-rays are usually given as a photon number density instead of an energy density:

$$n(\epsilon)d\epsilon = \frac{\rho(\epsilon)}{\epsilon}\, d\epsilon = \frac{8\pi}{(hc)^3}\, \frac{\epsilon^2}{\exp\left(\frac{\epsilon}{kT}\right) - 1}\, d\epsilon \tag{2.5}$$

Question 1: Show that the energy where the photon number is at maximum

$$(\epsilon_{max})_n \approx 1.59kT \tag{2.6}$$

◁

The mean photon energy for a blackbody with temperature T is given by

$$\begin{aligned} \bar{\epsilon} &= \frac{\int_0^\infty \epsilon n_\epsilon d\epsilon}{\int_0^\infty n_\epsilon d\epsilon} \\ &\approx 2.7\ kT \end{aligned} \tag{2.7}$$

Note that this energy is larger than the energy where the photon number is at its maximum.

The calculation of this integral is non-trivial. Consider the general form,

$$I = \int_0^\infty \frac{x^n}{e^x - 1}\, dx = \Gamma(n+1)\, \zeta(n+1) \tag{2.8}$$

with $\Gamma(n)$ the gamma function that has the properties

$$\Gamma(n+1) = n \cdot \Gamma(n) \quad ; \quad \Gamma(0) = 1 \quad \Rightarrow \quad \Gamma(n) = (n-1)! \qquad [n > 1] \tag{2.9}$$

and $\zeta(n)$ the Riemann ζ function defined as:

$$\zeta(n) \;=\; \sum_{k=1}^{\infty} \frac{1}{k^n} \;=\; 1 + \frac{1}{2^n} + \frac{1}{3^n} + \frac{1}{4^n} + \cdots \qquad [n > 1]. \tag{2.10}$$

Calculating these integrals results in

$n = 1$	I	$= \frac{\pi^2}{6}$	$= 1.645$
$n = 2$	I		$= 2.402$
$n = 3$	I	$= \frac{\pi^4}{15}$	$= 6.494$
$n = 4$	I		$= 24.886$
$n = 5$	I	$= \frac{8\pi^6}{63}$	$= 122.081$

Thermal Bremsstrahlung

If an electron moves through an electric field, such as the Coulomb field of an ion (density N_{ion}, charge Z), it is accelerated and thus, it emits radiation. The electron loses kinetic energy. If the electrons and ions are in local thermal equilibrium, the emission is thermal. The emission coefficient is equal to:

$$j(\nu) = 5.4 \cdot 10^{-39} Z^2 N_e N_{ion} T_e^{-\frac{1}{2}} e^{-h\nu/kT_e} \bar{g}_{ff} \quad \mathsf{erg\ cm^{-3}\ s^{-1}\ sr^{-1}\ Hz^{-1}} \tag{2.11}$$

with $\bar{g}_{ff}$ the average Gaunt factor (of order unity) and T_e the electron temperature.

Thermal line radiation

A molecule, atom or ion can decay spontaneously from a higher state u to a lower state l emitting a photon. If the energy difference between the two states is $\Delta\epsilon = h\nu_0$, the frequency of the emitted photon should be close to ν_0 (not exactly because of the quantum uncertainty principle $\Delta\epsilon \cdot \Delta t = h$). The frequency distribution function around ν_0 is given by a Lorentzprofile:

$$\psi(\nu - \nu_0) = \frac{\Gamma_u/4\pi^2}{(\nu - \nu_0)^2 + (\Gamma_u/4\pi)^2} \tag{2.12}$$

with

$$\Gamma_u = \sum_l A_{ul} \tag{2.13}$$

the sum over all transition probabilities A_{ul} per second per particle from state u to all possible lower states l (Einstein A coefficient). The life time in the state u is $\Delta t = \Gamma_u^{-1}$. If there is local thermal equilibrium the emission coefficient is

$$j(\nu)_{spont} = \frac{1}{4\pi}\, h\nu\, n_u\, A_{ul}\, \psi(\nu - \nu_0) \tag{2.14}$$

with n_u the population density of the upper state.

2.1.3 Non-thermal radiation[2]

Radiation is not always emitted by a thermal source, but can also be the result of non-thermal interaction between two particles.

The most important non-thermal interactions comprise:

- π^0 decay
- Electron with photon
  - low energy photon: *Thomson scattering*
  - high energy photon: *Compton scattering*
  - high energy electron: *Inverse-Compton radiation*
- Electron in an $\vec{E}$-field
  - *Non-thermal Bremsstrahlung*
- Electron in a $\vec{B}$-field
  - Non-relativistic electron: *cyclotron radiation*
  - Relativistic electron: *synchroton radiation*

π^0 decay

A π^0 (pi naught meson or pion) is a particle comprising an up and an anti-down quark (or vice versa, see section 2.2.1). It can be formed during a high energy collision of two baryonic particles. It is instable and has a mean life time of $8.4 \cdot 10^{-17}$ seconds and it decays into two gamma-ray photons:

$$\pi^0 \longrightarrow \gamma + \gamma \tag{2.15}$$

The rest mass energy of a π^0 is 135 MeV, so both photons have energies of about 70 MeV in the rest frame of the pion.

[2]Only the most important equations are given here.

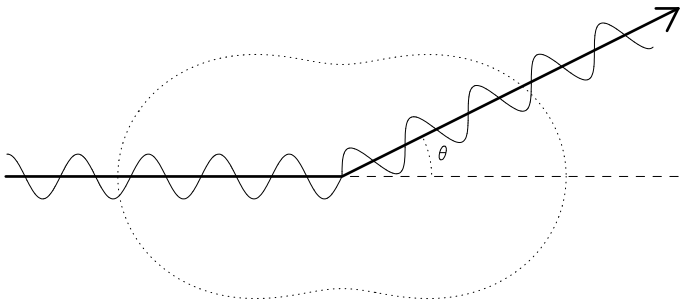

Figure 2.3: *Radiation geometry (dotted line) of Thomson scattering for an unpolarised photon beam.*

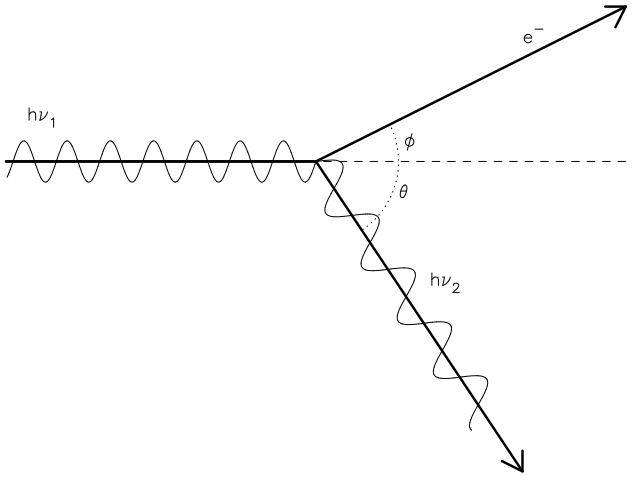

Figure 2.4: *Compton scattering event.*

Thomson scattering

Photons can be scattered on free electrons. If the photon energy $h\nu$ is much less than the rest mass energy of the electrons $m_e c^2$, the frequency of the incoming photon is not changed, only its direction: elastic scattering. Consequently, thermal radiation will remain thermal after scattering.

The probability of scattering is given by the electron density and the Thomson cross-section for electrons

$$\sigma_T \equiv \frac{8\pi}{3} r_e^2 = 6.65 \cdot 10^{-29} \ \ \mathsf{m}^2 \tag{2.16}$$

with r_e the classical electron radius $e^2/m_e c^2$. The scattering is not equally strong in all directions, the radiation geometry for unpolarised radiation has a typical dipole structure. The derivative of the Thomson cross-section to the solid angle Ω is

$$\left[\frac{d\sigma_T}{d\Omega}\right]_{unpol} = \frac{r_e^2}{2}(1 + \cos^2\theta) \tag{2.17}$$

with θ the angle between the incoming and scattered radiation (see figure 2.3).

Compton scattering

If the photon energy is of the order of the rest mass energy of the electrons, the scattering becomes inelastic and energy and impulse is transferred from the photon to the electron. The

wavelength change is given by

$$\lambda_2 - \lambda_1 = \lambda_c(1 - \cos\theta) \tag{2.18}$$

with λ_c the Compton wavelength:

$$\lambda_c \equiv \frac{h}{m_e c} = 2.4 \cdot 10^{-3} \text{ nm} \tag{2.19}$$

This energy loss is only important if $\lambda_1 \approx \lambda_c$, so for gamma-ray photons. In other cases the photon is Thomson scattered.

The cross-section for this process is given by the Klein-Nishina equation:

$$\sigma_c(\epsilon_1, \epsilon_2) = \frac{r_e^2}{2} \int_\Omega \left(\frac{\epsilon_2}{\epsilon_1}\right)^2 \left(\frac{\epsilon_1}{\epsilon_2} + \frac{\epsilon_2}{\epsilon_1} - \sin^2\theta\right) d\Omega \tag{2.20}$$

Question 2: Show that this equation is equal to the Thomson cross-section σ_T if $\epsilon_2 = \epsilon_1$.

Inverse-Compton radiation

The process described above can also be reversed: very energetic electrons transfer energy and momentum to (low energy) photons. This process can occur if the Lorentz factor γ of the electrons is (much) larger than 1, $\gamma \gg 1$. If the frequency of the incoming photon is ν_1, with its direction of propagation making an angle θ with the velocity vector of the electron, the electron 'sees' a frequency ν_1' in its inertial system:

$$\nu_1' = \gamma(1 - \frac{v}{c}\cos\theta)\nu_1 \tag{2.21}$$

If the photons are not too energetic (i.e. $\gamma h\nu_1 \ll m_e c^2$) normal Thomson scattering will take place in the rest frame of the electrons: $\nu_2' = \nu_1'$. After transforming back to the observer's system, the frequency of the scattered photon becomes:

$$\begin{aligned} \nu_{ic} = \nu_2 &= \nu_1\gamma^2(1 + \frac{v}{c}\cos\theta')(1 - \frac{v}{c}\cos\theta) \\ &\approx \frac{4}{3}\gamma^2\nu_1 \qquad \text{averaged over an isotropic radiation field} \qquad (2.22) \\ &\approx 4\gamma^2\nu_1 \qquad \text{head} - \text{on collision} \qquad (2.23) \end{aligned}$$

Consequently the electrons will slow down and the photons will gain energy rapidly. The average power radiated by the electron in an isotropic photon field equals:

$$\bar{P} = \frac{4}{3}\,\sigma_T\,\gamma^2\,U_{ph}\,\frac{v^2}{c} \tag{2.24}$$

with U_{ph} the energy density of the photon field.

In the observer's inertial system the emitted radiation will be strongly beamed in the forward direction, see figure 2.5. The beam width of the scattered photons is approximately proportional to γ^{-1}. This effect is called relativistic beaming.

For a blackbody photon field

$$U_{ph} = \int \epsilon n_{BB}(\epsilon)\, d\epsilon = n_{ph}\bar{\epsilon} \tag{2.25}$$

with n_{ph} the number density of the photon field and $\bar{\epsilon} = h\bar{\nu} = 2.7kT$ (see equation 2.7). The average power $\bar{P}$ of equation 2.24 for relativisistic electrons ($v \approx c$) can be rewritten as

$$\bar{P} = c\sigma_T n_{ph}\bar{\epsilon}_{ic} \tag{2.26}$$

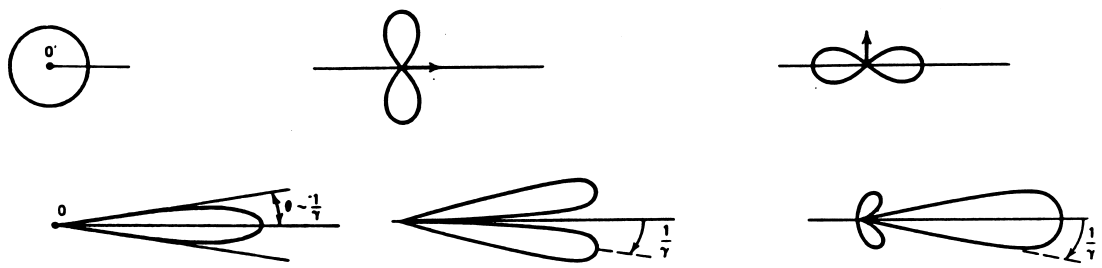

Figure 2.5: *Radiation geometry of inverse-Compton radiation. The upper plots show the radiation geometry in the rest frame of the electron, the arrows indicate the direction of acceleration. The lower plots show the radiation geometry in the rest frame of the observer, the electron velocity is along the horizontal axis.*

which is self-explanatory if the cross-section for this process equals σ_T in the electron rest frame.

Suppose that the energy distribution of the electrons is a power law in total energy[3]:

$$n(\varepsilon_{tot})d\varepsilon_{tot} \sim \varepsilon_{tot}^{-\alpha} d\varepsilon_{tot} \quad \Leftrightarrow \quad n(\gamma)d\gamma \sim \gamma^{-\alpha} d\gamma \tag{2.27}$$

since $\varepsilon = \gamma m_e c^2$. The shape of the associated number spectrum of inverse-Compton scattered photons can be easily derived from the relation

$$n(\epsilon_{ic}) = n_{ph} K_e \int \sigma(\epsilon_{ic}, \bar{\epsilon}, \gamma)\, \gamma^{-\alpha}\, d\gamma \tag{2.28}$$

with K_e the normalisation constant for the electron energy distribution and $\sigma(\epsilon_{ic}, \bar{\epsilon}, \gamma)$ the cross-section for producing a photon with energy ϵ_{ic} from the scattering of an electron with Lorentz factor γ on a blackbody photon with average energy $\bar{\epsilon}$. In this case we have

$$\sigma(\epsilon_{ic}, \bar{\epsilon}, \gamma) = \sigma_T\, \delta\left(\epsilon_{ic} - \frac{4}{3}\bar{\epsilon}\gamma^2\right) \tag{2.29}$$

Question 3: Show that substitution of this cross-section yields:

$$n(\epsilon_{ic}) \quad \sim \quad \bar{\epsilon}^{(\alpha-1)/2}\, \epsilon_{ic}^{-(\alpha+1)/2} \tag{2.30}$$

$$\text{or} \quad n(\nu_{ic}) \quad \sim \quad \bar{\nu}^{(\alpha-1)/2}\, \nu_{ic}^{-(\alpha+1)/2} \tag{2.31}$$

◁

Multiplication with $h\nu_{ic}$ yields the shape of the energy density of the scattered photons:

$$\rho(\nu_{ic}) \sim \bar{\nu}^{(\alpha-1)/2}\, \nu_{ic}^{-(\alpha-1)/2} \tag{2.32}$$

Non-thermal Bremsstrahlung

When a non-thermal electron is accelerated in an electric field, it will always emit Bremsstrahlung. If the electron distribution is non-Maxwellian (out of thermal equilibrium), equation 2.11 is not valid. The emission coefficient will not depend on the temperature T_e, but will depend on the energy distribution of the electron beam. If the kinetic energy distribution of the electrons is a power law in electron kinetic energy:

$$N(\varepsilon_{kin})d\varepsilon_{kin} \sim \varepsilon_{kin}^{-\alpha} d\varepsilon_{kin} \tag{2.33}$$

[3]Note that ϵ is used for a photon energy and ε is used for an electron energy

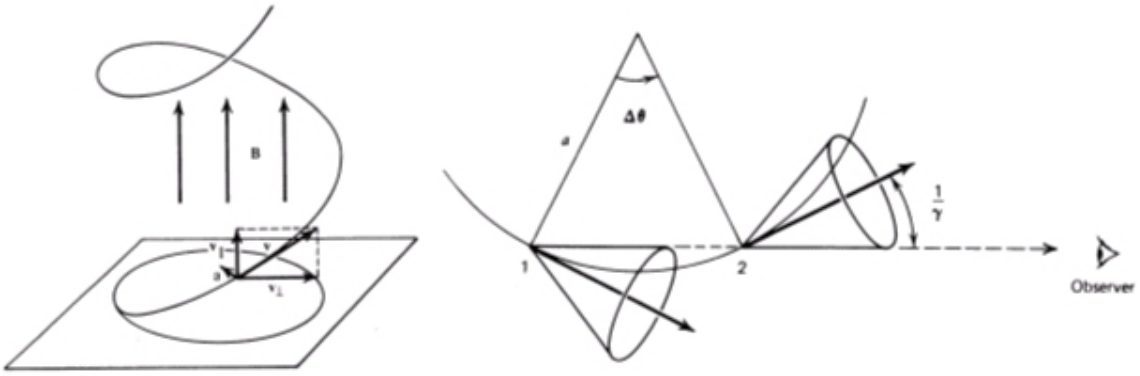

Figure 2.6: *Left: electron spirals around a magnetic field line. Right: emission cones for relativistic gyrating electrons. Credit Rybicky and Lightman (1979).*

two cases for the emerging non-thermal Bremsstrahlung distribution can be distinguished:

- the electrons are non-relativistic. The Bremsstrahlung spectrum will be a power law with photon number index $-(\alpha + 1)$.
- the electrons are ultra-relativistic ($\varepsilon_{tot} \approx \varepsilon_{kin}$). The Bremsstrahlung distribution will be a power law with photon number index $-\alpha$.

Cyclotron and synchrotron radiation

When an electron with charge q moves through a $\vec{B}$-field, it will spiral around a magnetic field line. Because the electron is accelerated it will emit radiation with a frequency

$$\nu_c = \frac{qB}{2\pi m_e} \tag{2.34}$$

the so-called Larmor or cyclotron frequency. This is the frequency at which the electron completes one rotation around the field line. The radius of this helix is dependent on the angle α between $\vec{v}$ and $\vec{B}$. The power emitted by the electron is also dependent on this angle (see figure 2.6):

$$P = \sigma_T \, \frac{B^2}{\mu_0} \, \frac{v^2}{c} \sin^2 \alpha = 2\sigma_T \, U_{mag} \, \frac{v^2}{c} \sin^2 \alpha \tag{2.35}$$

with $U_{mag} = \frac{B^2}{2\mu_0}$ the energy density of the magnetic field.

For a random distribution of the magnetic field lines, equation 2.35 can be averaged over all possible angles:

$$\bar{P} = \frac{4}{3} \, \sigma_T \, U_{mag} \, \frac{v^2}{c} \tag{2.36}$$

Normally the magnetic field will not be uniform and the radiation will not be monochromatic. However, in the spectra of X-ray pulsars cyclotron lines have been observed.

> *Consider non-relativistic electrons ($\gamma \approx 1$) near the surface of a neutron star with $B \approx 10^8$ T. According to equation 2.34 they will emit 11.6 keV photons, i.e. X-ray radiation!*

The frequency of the radiation emitted by fast electrons in a magnetic field is lower than that of slow electrons due their relativistic mass increase. The rotation frequency (or gyro-frequency) is given by:

$$\nu_g = \frac{\nu_c}{\gamma} = \frac{qB}{2\pi\gamma m_e} \tag{2.37}$$

and the averaged power has increased with a factor γ^2:

$$\bar{P} = \frac{4}{3}\,\sigma_T\,\gamma^2\,U_{mag}\,\frac{v^2}{c} \tag{2.38}$$

As in the inverse-Compton process, this radiation power is again strongly beamed. The observer will not see the radiation continously, but he will only see a short pulse whenever the electron is moving in his direction. The principal frequency of these pulses is called the synchrotron frequency ν_s:

$$\nu_s = \frac{3}{2}\gamma^3\nu_g \sin\alpha \tag{2.39}$$

and is (much) larger than the gyro-frequency if $\gamma \gg 1$. These are very short pulses (γ^{-3} of a rotation period). This pulse spectum will be broad and consists of many discrete components, i.e. the Fourier components of a sharp radiation pulse. This will blend into a real continuum, when the electrons have a velocity distribution, or when the magnetic field is not uniform, which is the practical case.

Since $\nu_s \sim \gamma^2$, similar to the inverse-Compton process, the photon distribution function is again a power law with spectral index $(\alpha+1)/2$ provided that the electrons have a power law energy distribution with index α.

2.1.4 Astrophysical relevance

Radiation of black bodies is typically emitted in a broad band around the maximum wavelength

$$\lambda_{max} = \frac{0.00290}{T}\ \mathsf{m} \tag{2.40}$$

For temperatures between 1 and 10^6 Kelvin, this radiation will thus fall between the near-radio (microwaves) and the extreme-ultraviolet (EUV). Cold objects (around 10 - 100 K), such as cool clouds of gas and dust, emit infrared waves. Normal stars are best observable in the visible regime. Very hot objects (white dwarfs, neutron stars, supernova remnants) are predominantly shining in the ultraviolet and soft X-ray regime. Large velocities are involved for the emission of harder X-rays.

Not only accreting neutron stars and black holes produce hard X-rays, also heavy stars with extended hot atmospheres, and hot diffuse gas in clusters of galaxies are good X-ray emitters.

Gamma-rays can not be formed in this way, much higher energy particles are needed, such as cosmic-rays. When these particles interact with any atom, gamma-rays will be emitted. The main source of these photons are nebulae, dark molecular clouds and central parts of galaxies.

The inverse-Compton effect produces high energy photons. Their energy can be estimated from equation 2.22 and 2.7

$$\left(\frac{\epsilon_{ic}}{1\ \mathsf{eV}}\right) \approx 1200\,T_z\left(\frac{\epsilon_e}{1\ \mathsf{GeV}}\right)^2 \tag{2.41}$$

with $\epsilon_e = \gamma m_e c^2$. If the cosmic background radiation ($T_z = 2.7$ K) is used as the incoming radiation field, an electron of 550 MeV will boost the photon to 1 keV (X-rays). An electron of 550 GeV will produce a hard gamma-ray photon of 1 GeV.

Consider a proton (with mass m_p) falling from infinity onto the surface of a compact star (mass M_*, radius R_*). Its potential energy is converted into kinetic energy through:

$$\frac{1}{2} m_p v^2 = \frac{GM_*}{R_*} m_p \Longrightarrow v = \left(\frac{2GM_*}{R_*} \right)^{1/2} \tag{2.42}$$

For a neutron star ($M_* = 1\ M_\odot, R_* = 10\ km$), $v \approx 0.5c$! If all this kinetic energy would be converted into thermal energy, an estimate of the maximum temperature T_{max} follows from

$$kT_{max} = \frac{GM_*}{R_*} m_p \Longrightarrow T_{max} \approx 10^{12}\ K \tag{2.43}$$

for a neutron star. For a white dwarf ($M_* = 1\ M_\odot, R_* = 10^4\ km$) T_{max} amounts to $\approx 10^9\ K$.
Consider next "bulk-mass" accretion flow onto the compact star with a rate $\dot{M} = \frac{dM}{dt}$. The radiation luminosity arising from this bulk-mass infall into the gravitational potential well of the compact star is given by

$$L = \frac{GM_*}{R_*} \dot{M} \tag{2.44}$$

An estimate of the effective *temperature T_e can now be obtained by employing Stefan-Boltzmann's law for a black body radiator with the total surface area of the compact star, i.e.*

$$L = \frac{GM_*}{R_*} \dot{M} = 4\pi {R_*}^2 \sigma_{SB} {T_e}^4 \tag{2.45}$$

with σ_{SB} the Stefan-Boltzmann constant ($= 5.67 \cdot 10^{-8}\ W\ m^{-2}\ K^{-4}$). For an accretion rate $\dot{M} = 10^{-9}\ M_\odot\ yr^{-1}$ this yields an effective temperature $T_e \approx 10^7\ K$ ($L = 10^{30}\ W$) for a neutron star and $T_e \approx 6 \cdot 10^4\ K$ ($L = 10^{27}\ W$) for a white dwarf. Such temperatures make these accreting objects shine in the ultraviolet, extreme-ultraviolet (EUV) and X-ray wavelength regimes.

The energy range in which synchrotron photons are emitted, depends on the magnetic field strength and the typical electron energy $\epsilon_e = \gamma m_e c^2$. From equation 2.39 we find:

$$\left(\frac{\epsilon_s}{1\ \mathrm{eV}} \right) \approx 0.07 \left(\frac{B_\perp}{1\mathrm{G}} \right) \left(\frac{\epsilon_e}{1\ \mathrm{GeV}} \right)^2 \tag{2.46}$$

So galaxies ($B = 1\ \mu$G, $\epsilon_e = 1$ GeV) are observable at radio frequencies.

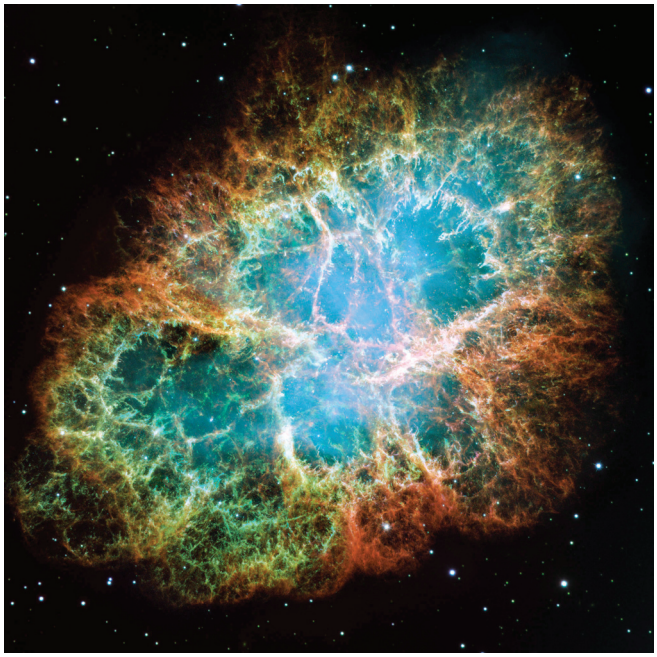

A substantial part of the electromagnetic radiation of the Crab nebula is synchrotron emission. Picture credit NASA/ESA Hubble, Allison Loll/Jef Hester (2005). This radiation is observed over a very broad frequency band, from radio to gamma-ray waves. The typical magnetic field strength in this nebula is $B \approx 5 \cdot 10^{-4}$ G, so the electrons which are involved should range from

Radio emission	$\epsilon_s \approx 10^{-7}$ *eV (24 MHz)*	$\Rightarrow$	$\varepsilon_{tot} \approx 50$ *MeV* $(\gamma \approx 10^2)$
Gamma emission	$\epsilon_s \approx 1$ *GeV*	$\Rightarrow$	$\varepsilon_{tot} \approx 5$ *PeV* $(\gamma \approx 10^{10})$

2.1.5 Multispectral correlations

To understand the source of radiation (the information source) better it is often enlightening to look for multispectral correlations in the observed radiation fluxes. For instance: if an observer wants to trace a dark (molecular) cloud, he can study the H, H_2, CO or OH lines in the radio and infrared. But the cloud is potentially also visible in gamma-rays: primary cosmic-ray protons and heavy nuclei (see section 2.3.1) can interact with cloud gas, producing π^0-mesons which decay in γ-rays.

Synchrotron and inverse-Compton radiation are coupled through their generating electron beams. This can already be seen from the similarities in the equations for the average power (2.24) and (2.38). When an electron beam travels through interstellar space, which has a very low magnetic field (approximately 5 μG), both synchrotron radiation and inverse-Compton radiation (from the cosmic background photons) are produced, but in a completely different wavelength range: the synchrotron radiation will be emitted as radio waves and the inverse-Compton effect produces X-ray or gamma-ray photons. The energy ratio of the two waves is (using equations 2.41 and 2.46):

$$\frac{\epsilon_{ic}}{\epsilon_s} = 2 \cdot 10^4 \, T_z \, \left(\frac{B_\perp}{1 \, \mathsf{G}} \right)^{-1} \tag{2.47}$$

If a magnetic field $B_\perp = 5\ \mu$G and $T_z = 2.7$ K are substituted, a ratio $\epsilon_{ic}/\epsilon_s = 10^{10}$ is obtained.

This equation can also be derived if the synchrotron process is described as a change of the electron energy as a result of the magnetic field. This change is proportional to the magnetic field strength and the proportionality constant is the Bohr magneton:

$$\mu_B = \frac{\hbar q}{2m_e} \tag{2.48}$$

The ratio (2.47) can then be calculated as

$$\frac{\epsilon_{ic}}{\epsilon_s} = \frac{2.7kT_z}{\mu_B B} = 4 \cdot 10^4\ T_z\ \left(\frac{B_\perp}{1\ \mathsf{G}}\right)^{-1} \tag{2.49}$$

The difference of about a factor of 2 in the numerical coefficient arises from the fact that the inverse-Compton and synchrotron spectra produced by a monochromatic electron beam are not δ-functions but show a rather wide distribution. This has not been taken into account in these 'order of magnitude' calculations.

2.1.6 Observing locations

There are two distinct ways of observation:

- In-situ, such as the
  - *geosphere, e.g. the magnetic field of the Earth*
  - *sun, e.g. solar wind composition and velocity observations by a space probe (e.g. Ulysses, SOHO)*
  - *planets, e.g. magnetic fields, atmosphere and rock composition (Viking, Pionier, Voyager, Mars Sojourner, Spirit, Opportunity)*
- **Remote sensing (or teledetection)**

Remote sensing is the dominant technique for astronomical observations. During the past several decades a very large number of observing facilities have been built which detect electromagnetic waves from space.
One major division between observing locations is ground-based and space-based. Both have advantages. Ground telescopes can in principle be

- larger ($\gg$ 10 m diameter of the primary mirror)
- cheaper (80 – 100 M$, typically a factor 10 less than space telescopes)
- long lasting ($\geq$ 50 year)
- easily accessible (changing instruments and refurbishment are 'routine')
- upgraded (install new, bigger and more complex detectors)

In contrast, space telescopes are more sensitive because they do not suffer from the atmosphere and the telescopes can more easily work at lower temperatures. Ground telescopes can only observe in the radio and optical band. Only at some locations also observations in the infrared can be done. Moreover, ground telescopes have only access to a limited part of the sky.

The main influence from the atmosphere is due to

- absorption
- emission
  - *black body radiation of atmosphere itself (infrared above 2 μm)*
  - *variable OH emission lines (1 – 2 μm, 30 – 40 % variations within a few seconds)*

> *This absorption and BB-emission is mainly caused by H_2O in the atmosphere, but the H_2O-content (and so the pressure $P(z)$) is a strong function of altitude.*
>
> $$P(z) = P(z=0) \cdot e^{-\frac{z}{H}} \tag{2.50}$$
>
> *with H the scaleheight, which is different for air and water:*
>
> $$\begin{aligned} H_{air} &= 8000\ m \\ H_{water} &= 3000\ m \end{aligned}$$
>
> *Observation at high altitudes (mountains, airplanes) gives large improvements in the thermal IR windows, but it does not reduce the OH emission which is formed at about 90 km height.*

- scattering due to dust
- scintillation and seeing
  When a plane coherent wave front travels through the Earth's atmosphere, it encounters density variations due to turbulence and temperature differences. These inhomogeneities form cells with different indices of refraction, so that the wave front is distorted. These cells have typical diameters of 10 cm and change with temporal frequencies between 1 and 1000 Hz. So a 1 meter telescope sees about 100 of these cells changing potentially every 1 to 10 milliseconds. Micro turbulence (even smaller scales) causes seeing. All this results in a high frequency jitter of the image: *a twinkling star!*

Conditions for a good observing site are

- a stable atmosphere
- as high as possible
- on a island (water vapour is kept in a low inversion layer above the ocean)
- no pollution (dirt)
- no light pollution

Good sites are La Palma (Canary Islands, Spain), Hawaii (USA), La Silla and Paranal (Chili) and Kitt Peak (USA).

Space telescopes have two possible orbits, a high (or deep) and a low (near-earth) orbit. Low orbits are within the Van Allen radiation belts. It is relatively easy to put a high mass telescope in such an orbit which can be serviced by the Space Shuttle (e.g. the Hubble Space Telescope). But the orbit degrades and eventually the spacecraft will re-enter the atmosphere.

Moreover, it cannot observe a source for a long uninterupted time interval, because its low orbit around the earth gives rise to extended eclipses during each, typically 90 minute, orbital period.

High orbit satelites suffer from extra noise due to solar flares and its detectors should be radiation shielded. But it can observe a source for a long uninterupted period (24 – 100 consecutive hours) and it has a real-time data link with a single ground station during almost its complete orbit (Example: ESA's Infrared Space Observatory (ISO)).

2.2 Neutrinos

2.2.1 Characterisation

In particle physics all particles are divided in two groups: quarks and leptons. Moreover anti-particles of these types do also exist. All these particles have spin 1/2, they follow Fermi-Dirac statistics and are called fermions.

Single quarks have never been observed, but they constitute the building blocks of larger particles, *the hadrons*. Several types of quarks are known and they are characterised by a flavour and a colour. Six flavours exist: up(u), down(d), strange(s), charm(c), bottom(b) and top(t), and there are three colours, red(r), green(g) and blue(b).

	d	u	s	c	b	t
Mass (GeV)	0.004 - 0.008	0.002 - 0.004	0.08 - 0.12	1.15 - 1.35	4.1 - 4.4	170 - 190
Charge (q)	-1/3	+2/3	-1/3	+2/3	-1/3	+2/3
Spin $\vec{J}$	1/2	1/2	1/2	1/2	1/2	1/2
Baryon number	1/3	1/3	1/3	1/3	1/3	1/3

Table 2.1: *Mass and quantum numbers of quarks.*

Particles consisting of three quarks are called baryons, such as the proton (u-u-d, each a different color) and the neutron (u-d-d). Mesons are made up of two quarks, such as the pion (π meson) which consists of an up and an anti-down quark (or vice versa).

There are six types of leptons and anti-leptons. The lepton family consists of the electron (e^-), muon (μ^-), tau (τ^-), electron-neutrino (ν_e), muon-neutrino (ν_μ) and the tau-neutrino (ν_τ). The anti-lepton family consists of e^+ (positron), μ^+, τ^+ and the anti-neutrinos $\bar{\nu}_e$, $\bar{\nu}_\mu$ and $\bar{\nu}_\tau$. Leptons do not have a color and they do not possess an electric or magnetic moment. They do not stick together to form other particles.

	e	ν_e	μ	ν_μ	τ	ν_τ
Mass (MeV)	0.511	$\leq$ 10 eV	105.66	$\leq$ 0.17	1784.1	$\leq$ 24
Charge (q)	-1	0	-1	0	-1	0
Decay time (s)	$> 10^{29}$		$2.2 \cdot 10^{-6}$		$3 \cdot 10^{-13}$	
Spin	1/2	1/2	1/2	1/2	1/2	1/2

Table 2.2: *Mass, decay time and quantum numbers of leptons.*

It is still not clear whether or not the neutrinos have a mass, although rather recently (1998) evidence was found that neutrinos should have at least some mass. Their existence

was derived because energy and impulse should be conserved in β-decay reactions, such as:

$$^{14}_{6}\mathrm{C} \longrightarrow {}^{14}_{7}\mathrm{N} + \mathrm{e}^- + \ldots \tag{2.51}$$

If this were a two body process, conservation of energy and impulse would require that the electron would always get a fixed velocity (two particles with two unknown velocities and two conservation laws give a unique solution). But it was observed that there was a distribution of electron velocities. So a third particle needed to be invoked, *the neutrino*. Basically a neutron in the unstable core of the atom decays into a proton, an electron and an anti-neutrino:

$$\mathrm{n} \longrightarrow \mathrm{p}^+ + \mathrm{e}^- + \bar{\nu_\mathrm{e}} \tag{2.52}$$

A muon-neutrino is formed during the decay of a muon or a pion:

$$\mu^\pm \longrightarrow \mathrm{e}^\pm + \nu_\mathrm{e} + \bar{\nu_\mu} \tag{2.53}$$

$$\pi^\pm \longrightarrow \mu^\pm + \nu_\mu \tag{2.54}$$

Neutrino radiation is always characterised by its energy in electronVolts (eV).

2.2.2 Astrophysical relevance

Neutrinos from only two cosmic sources have been detected. Practically all detected neutrinos are produced in nuclear reactions in the core of the sun, such as:

$$\mathrm{p}^+ + \mathrm{p}^+ \longrightarrow {}^{2}_{1}\mathrm{H} + \mathrm{e}^+ + \nu_\mathrm{e} \tag{2.55}$$

$$^{13}_{7}\mathrm{N} \longrightarrow {}^{13}_{6}\mathrm{C} + \mathrm{e}^+ + \nu_\mathrm{e} \tag{2.56}$$

This last reaction is an example of β-decay which produces a positron.

Another neutrino source was the supernova 1987A from which a pulse containing about 10 neutrinos was detected. These neutrinos are formed in the inverse β-decay process during the collapse of the core of the star:

$$\mathrm{p}^+ + \mathrm{e}^- \longrightarrow \mathrm{n} + \nu_\mathrm{e} \tag{2.57}$$

2.2.3 Observing locations

Neutrinos interact rarely with other particles and are consequently very difficult to detect. Large tanks of a suitable absorbing material are necessary. These should be located deeply underground (e.g. mines or mountains) to shield the neutrino telescope maximally against noise signals.

The first detector was built in 1968, comprising a large tank of tetracloroethene ($\mathrm{C_2Cl_4}$), a cheap cleaning agent. About 20 years later two watertanks, originally constructed to observe possible proton decay, turned out to be good neutrino detectors. These are the Kamiokande detector in Japan and the Irvine-Michigan-Brookhaven (IMB) detector in the USA. A gallium based detector was recently completed in the Gran Sasso tunnel (Appenine mountains) in Italy.

2.3 Cosmic-rays

2.3.1 Characterisation

Cosmic-rays (also energetic particles from the sun are sometimes included in cosmic radiation) consist mainly of atomic nuclei at very high velocities. Most particles are protons (84 %) and

helium nuclei (14 %), the rest are heavier nuclei, positrons and electrons. These have Lorentz factors ranging from 2 to 10^{11}. Cosmic-ray particles are always characterised by their energy (in electronVolts). For a particle which is more massive than a proton, its kinetic energy is usually given in *energy per nucleon.*

Electrons have a rest mass energy of 511 keV, protons have 938 MeV. The total energy of larger particles with charge Z and mass $M = Am_p$ is

$$E_{cr} = \gamma Mc^2 = E_{cr}^{rest} + E_{cr}^{kin} \tag{2.58}$$

So the kinetic energy per nucleon of such a particle is given by

$$\frac{E_{cr}^{kin}}{A} = (\gamma - 1)m_p c^2 \tag{2.59}$$

A particle becomes relativistic when $\gamma \geq 2$; an electron becomes relativistic, if its kinetic energy is above 0.5 MeV, a proton if its energy exceeds 1 GeV. Most cosmic-ray particles incident on the Earth's atmosphere have energies around 10^9 eV and a velocity of 0.9c. These so-called *primary cosmic-rays* have a flux of 10^4 particles per square meter per second. The energy spectra of cosmic-ray particles above 1 GeV show a typical power law dependence. This is shown in figure 2.7 for four species: H, He, C and Fe nuclei.

2.3.2 Astrophysical relevance

Cosmic-rays are presumably produced in supernovae and near the surface of pulsars. They can be accelerated in shocks (circumstellar and interstellar) and in pulsar magnetospheres. Their composition (including isotopic composition) near the Earth gives us important clues to cosmic acceleration and propagation phenomena and to the composition of interstellar clouds.

2.3.3 Observing locations

Primary particles cannot reach sea level and need to be observed from high-altitude-balloons and space platforms. If such a primary cosmic-ray particle enters the earth's atmosphere it will collide with an air particle (predominantly N and O) at an average height of 30 to 60 kilometer. This interaction produces a large number of different particles such as protons, neutrons, electrons, positrons, gamma photons, neutrinos, pions and muons. If the incoming particle is sufficiently energtic (TeV (10^{12}) to PeV (10^{15}) energies), these secondary particles will have sufficient energy to interact in turn with other particles, so a particle shower will reach the surface of the earth. These particles are called *secondary cosmic-rays.*

Also muons are detected as secondary particles which may seem puzzling, since their mean travel distance before they decay is about 660 meters according to Newtonian mechanics. They are formed at heights above 30 kilometer, but due to relativistic time dilatation it is possible for them to reach the ground before they decay.

The study of very-high-energy cosmic-rays by means of air shower production can therefore be done from the ground with the aid of a so-called *coincidence technique* between several radiation detector arrays.

2.4 Gravitational radiation

2.4.1 Characterisation

A mass m which is accelerated in a gravitational field due to a mass M emits gravitational waves. But since action = – reaction, both masses move in opposite directions, so the dipole

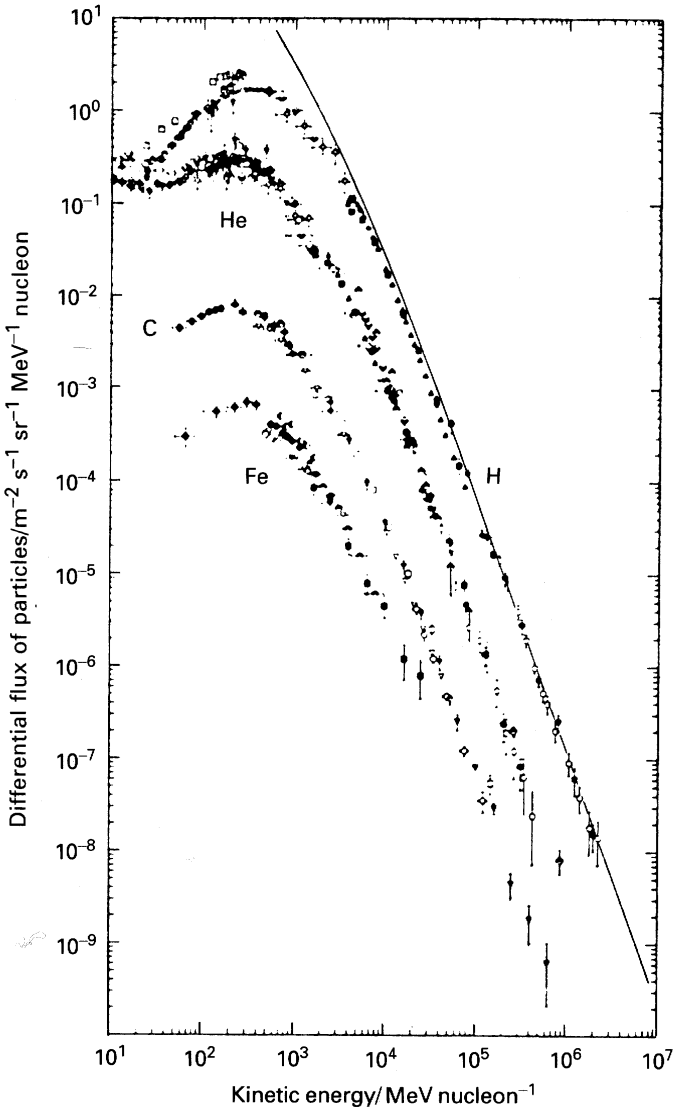

Figure 2.7: *The differential energy spectra of cosmic-rays as measured from observations made from above the Earth's atmosphere. The spectra for hydrogen, helium, carbon and iron are shown. The solid line shows the unmodulated spectrum for hydrogen, i.e. the effects of propagation through the interplanetary medium upon the energy spectra of the particles have been eliminated using a model for the modulation process. The flux of the helium nuclei below about 60 MeV nucleon^{-1} is due to an additional flux of these particles which is known as the anomalous ^{4}He component. Credit Longair (1992).*

part of the radiation cancels and the lowest order term becomes the quadrupole radiation.

Except for the indirect measurement of gravitational waves from the binary pulsar PSR B1913+16, for which Russell Hulse and Joseph Taylor shared the Nobel price in 1993, no direct detection of gravitational radiation has yet been made. PSR B1913+16 comprises two orbiting neutron stars with a period of 7.8 hours, one of the neutron stars is observable as a radio pulsar, with a period of 37.9 milliseconds. The shift in the times of periastron passage measured over 20 years with respect to a constant orbital period is shown in figure 2.8. The general theory of relativity predicts the curved solid line

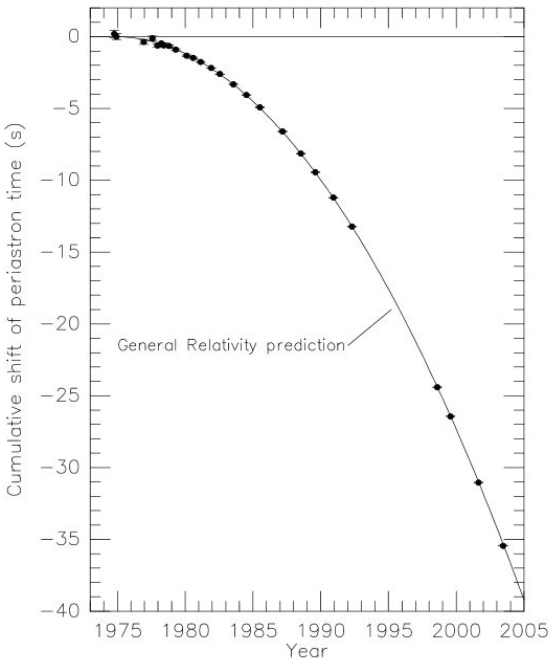

Figure 2.8: *Emission of gravitational radiation by PSR B1913+16 leads to an increasing deviation in the time of the periastron passage compared with a hypothetical system whose orbital period remains constant. Solid curve corresponds to the deviation predicted by the general theory of relativity. Dots represent the measured deviation. The data provide the strongest evidence now available for the existence of gravitational radiation. Credit Weisberg & Taylor (2005).*

2.4.2 Astrophysical relevance

According to the general theory of relativity, detectable gravitational waves should be emitted by a number of nearby, very close double star systems. Since the frequency of the signal is known, detection of the periodic signal should be greatly facilitated, it is to be expected at relatively low frequencies (10^{-4} – 1 Hz), corresponding to wavelengths in the range $3 \cdot 10^8$ – $3 \cdot 10^{12}$ m (the latter value being 20 times the distance from the Sun to the Earth!).

2.4.3 Observing locations

Ground-based detectors will search for signals from supernovae, compact binary coalescence and pulsars at frequencies well above 1 Hz. The low-frequency range (below 1 Hz) will never be accessible from the ground because it is masked by Earth-based gravitational noise. Moreover, there are several intrinsic uncertainties about the strength and distribution of all sources emitting higher frequencies.

Space-based observatories are required for frequencies below 1 Hz, moreover local close binaries emitting at these low frequencies, are potentially assured sources. Supermassive black holes, residing in the cores of active galaxies, do not radiate above 10^{-2} Hz and consequently also require space-based detectors. Currently a space-based gravitational wave antenna (the Laser Interferometer Space Antenna LISA) is under development as a joint project between the US(NASA) and Europe(ESA) for an anticipated launch in 2013.

Chapter 3

Stochastic Character of Radiation Fields

3.1 Radiometric units

The *spectral radiance* or *monochromatic intensity* is the basic quantity to describe a radiation field. It is defined as the amount of radiant energy per unit time, per unit area perpendicular to the beam, per unit solid angle, per unit wavelength (or frequency, energy). The relevant geometry is displayed in figure 3.1, the spectral radiance is expressed as:

$$I(\lambda, \vec{\Omega}, t) = \frac{dE}{\vec{n} \cdot \vec{\Omega}\, d\Omega\, dt\, d\lambda\, dA} \tag{3.1}$$

The *monochromatic radiation flux density* or *spectral irradiance* $F(\lambda, t)$ is derived by integrating $I(\lambda, \vec{\Omega}, t)$ over the solid angle:

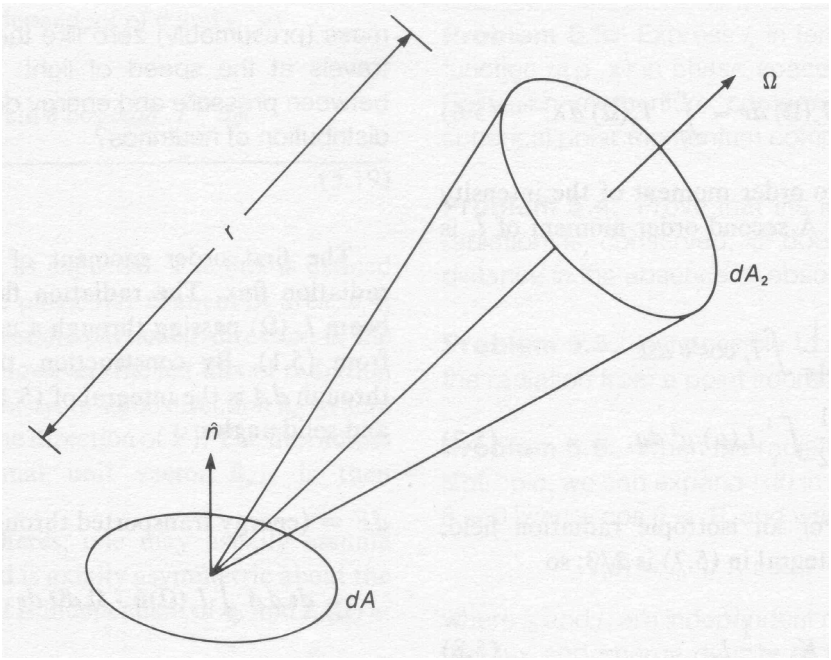

Figure 3.1: *geometry for defining intensity(radiance). Credit Bowers and Deeming (1984).*

$$F(\lambda,t) = \frac{dE}{dt\ dA\ d\lambda} = \int\limits_{\Omega} I(\lambda,\vec{\Omega},t)\ \vec{n}\cdot\vec{\Omega}\ d\Omega$$
$$= \int\limits_{0}^{2\pi}\int\limits_{0}^{\pi} I(\lambda,\theta,\phi,t)\ \cos\theta\ \sin\theta\ d\theta\ d\phi \tag{3.2}$$

The *total irradiance* $F(t)$ is subsequently obtained by integrating over all wavelengths.
The *spectral(monochromatic) radiant flux* is the total amount of monochromatic radiant energy that is transported through a given area per unit time interval:

$$\Phi(\lambda,t) = \frac{dE}{dt\ d\lambda} = \int\limits_{\Omega}\int\limits_{A} I(\lambda,\vec{\Omega},t)\ \vec{n}\cdot\vec{\Omega}\ d\Omega\ dA \tag{3.3}$$

Finally, the *radiant flux* represents the total amount of radiant energy that is transported through a given area, integrated over all wavelengths, per unit time:

$$\Phi(t) = \frac{dE}{dt} = \int\limits_{\Omega}\int\limits_{A}\int\limits_{\lambda} I_\lambda(\vec{\Omega},t)\ \vec{n}\cdot\vec{\Omega}\ d\Omega\ dA\ d\lambda \tag{3.4}$$

For an isotropic radiation field from the upper hemisphere, e.g. an isotropically distributed sky background, the following relation holds:

$$F(\lambda,t) = \pi I(\lambda,\vec{\Omega},t) \tag{3.5}$$

and for a point source at position $\vec{\Omega}_0$ with spectral radiance $S_p(\lambda,t)$ the spectral irradiance is:

$$F(\lambda,t) = \int\limits_{\Omega} S_p(\lambda,t)\ \delta(\vec{\Omega}-\vec{\Omega}_0)\ \vec{n}\cdot\vec{\Omega}\ d\Omega$$
$$= S_p(\lambda,t)\ \vec{n}\cdot\vec{\Omega}_0 = S_p(\lambda,t)\ \cos\theta_0 \tag{3.6}$$
$$= S_p(\lambda,t) \qquad \text{for normal incidence} \tag{3.7}$$

The spectral radiance I, which characterizes the radiation beam, has intrinsic statistical fluctuations. As a consequence, an astronomical measurement has to be treated as a stochastic process.
In the following paragraph, some basic statistical notions will first be reiterated, like the definition of random variables and the properties of frequently encountered probability distributions. Next, the concept of a stochastic variable is introduced and some basic properties are discussed. These will be used later for describing the astronomical measuring process.

3.2 Random phenomena and variables

3.2.1 Parent population

A *random phenomenon* is characterized by the fact that the outcome, in terms of a numerical value, is not predictable in a deterministic sense, but exhibits a more or less smooth distribution of outcomes if repeated many times. Associated with this notion is the *random*

variable (RV), which value constitutes a numerical outcome of a certain random phenomenon. The probability density distribution of a random variable gives the possible values and the probabilities assigned to these values.
Random variables can be subdivided in two categories:

- *Discrete* random variables, comprising a finite number of possible values.
- *Continuous* random variables, comprising all values in a certain number interval, i.e. an infinite number of possible values.

If an infinite number of measurements could be taken, the result would give the way in which the observed data points are distributed, i.e. the *true* probability distribution. This distribution is called the *parent distribution*, practical measurements can be hypothesized as samples of an infinite number of possible measurements which are distributed according to the parent population. In other words the parent population parameters can be perceived to become equal to the experimental parameters *in the limit of an infinite number of measurements*:

$$(\text{Parent parameter}) = \lim_{N\to\infty} (\text{experimental parameter}) \tag{3.8}$$

If N measurements are made of a quantity x, labeled $x_1, x_2, ..., x_N$, the *mean* μ of the parent population can be defined as:

$$\mu \equiv \lim_{N\to\infty} \left(\frac{1}{N} \sum_i x_i \right) \tag{3.9}$$

The mean is therefore equivalent to the *centroid* or *average value* of the quantity x.

The *median value* $\mu_{1/2}$ of the parent distribution is that value at which there are equal numbers of values higher and lower than $\mu_{1/2}$. Expressed differently, the probability that an arbitrarily selected value is higher than the median is 50%, and the probability that an arbitrarily selected value is lower is 50% also:

$$P(x_i > \mu_{1/2}) \equiv P(x_i < \mu_{1/2}) \equiv 0.5 \tag{3.10}$$

Finally, the *most probable value* $\mu_{\max}$ of the parent distribution is the value at which the distribution peaks:

$$P(\mu_{\max}) \geq P(x_i \neq \mu_{\max}) \tag{3.11}$$

For symmetric distributions, like the Gauss function, the average, median and most probable value are all the same. The differences are only visible in asymmetric functions, as in Figure 3.2.

An appropriate measure of the dispersion of observations is the *standard deviation* σ. The *variance* σ^2 is defined as the limit of the average of squares of the deviations from the mean μ:

$$\sigma^2 \equiv \lim_{N\to\infty} \left[\frac{1}{N} \sum_i (x_i - \mu)^2 \right] = \lim_{N\to\infty} \left(\frac{1}{N} \sum_i x_i^2 \right) - \mu^2 \tag{3.12}$$

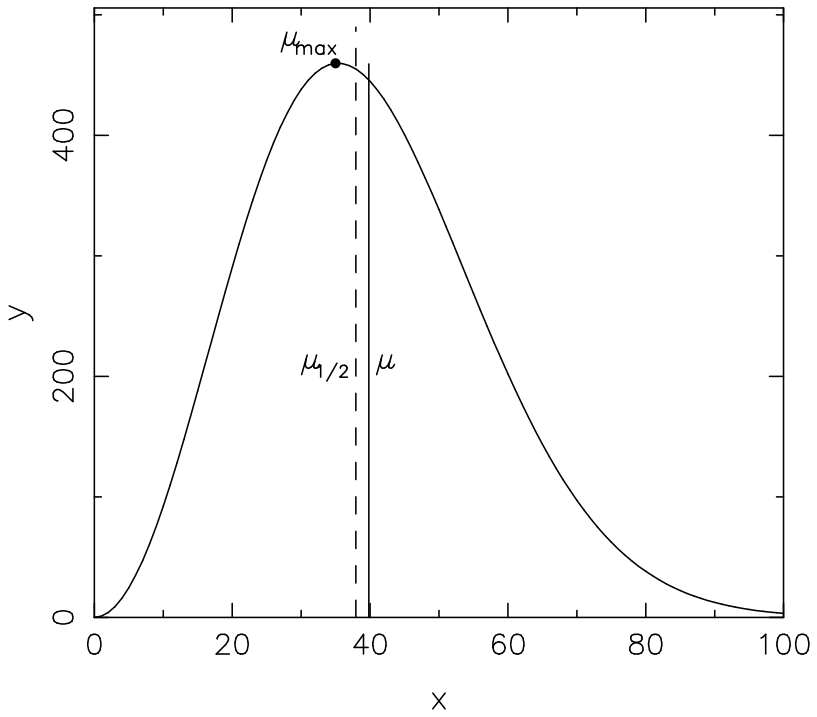

Figure 3.2: *Illustration of the various definitions of "average", illustrated for the Maxwellian distribution function* $f(x) = x^2 G(x, 0, 25)$ *where* $G(x, \mu, \sigma)$ *is the Gauss-function of equation 3.27.*

3.2.2 Discrete and continuous distributions: expectation values

If there are n different observable values of a discrete random variable x, expression (3.9) can be replaced by:

$$\mu = \sum_{j=1}^{n} x_j P(x_j) \tag{3.13}$$

where $P(x_j)$ is the probability to obtain the discrete value x_j and no two values of x_j are equal. Similarly, the definition of the variance can be redefined in terms of the probability function $P(x_j)$:

$$\sigma^2 = \sum_{j=1}^{n} \Big[(x_j - \mu)^2 P(x_j)\Big] = \sum_{j=1}^{n} \Big[x_j^2 P(x_j)\Big] - \mu^2 \tag{3.14}$$

The mean μ is the expectation value $\mathbf{E}\{x\}$ of x, and the variance σ^2 is the expectation value $\mathbf{E}\{(x-\mu)^2\}$ of the square of the deviations of x from μ.
The expectation value of any function $f(x)$ of x is given by

$$\mathbf{E}\{f(x)\} = \sum_{j=1}^{n} [f(x_j) P(x_j)] \tag{3.15}$$

If the parent distribution is considered as a continuous, smoothly varying function $p(x)$, the mean μ and the variance σ^2 are given by the following integral expressions:

$$\mu = \int_{-\infty}^{+\infty} x P(x) dx \quad \text{and} \quad \sigma^2 = \int_{-\infty}^{+\infty} x^2 P(x) dx - \mu^2 \tag{3.16}$$

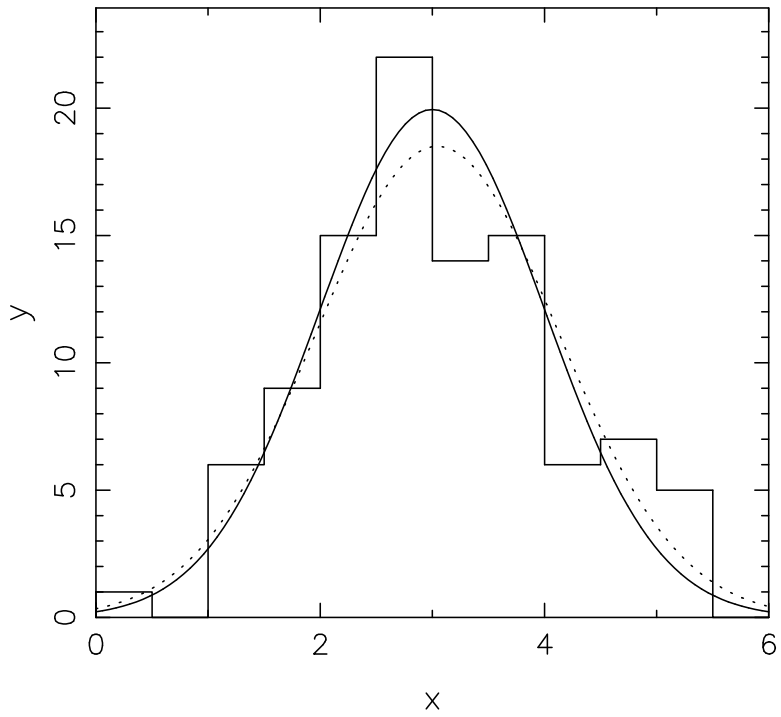

Figure 3.3: *Illustration of the difference between the parent distribution and the distribution derived from a finite number of measurements, in this case 100 trials displayed with the histogram. The solid curve is the actual parent distribution, a Gaussian distribution with average* $\mu = 3.000$ *and standard deviation* $\sigma = 1.000$*. The dashed curve is the estimated parent distribution derived from the histogram with parameters* $\overline{x} = 3.045$ *and* $s = 1.078$*.*

The expectation value of any function $f(x)$ of x follows from:

$$\mathbf{E}\{f(x)\} = \int_{-\infty}^{+\infty} f(x)P(x)dx \tag{3.17}$$

3.2.3 Sample parameters

In practical experiments, only a finite number of observations will be made. Consequently, the experimental data only allow an *estimate* of the parameters of the parent distribution. For a series of N observations, the most probable estimate of the mean μ is the average $\overline{x}$ of the observations (see a later paragraph on *the method of maximum likelihood*). Hence:

$$\mu \approx \overline{x} \equiv \frac{1}{N}\sum_i x_i = \frac{1}{N}\sum_{j=1}^{n} f_j x_j \tag{3.18}$$

with f_j the number of times each value of x_j is observed, no two values of x_j being alike. This average $\overline{x}$ is called the *sample mean* and is distinctly different from the *parent mean* μ.
The best estimate of the *parent variance* σ^2 is given by the experimental or *sample variance* s^2, according to:

$$\sigma^2 \approx s^2 \equiv \frac{1}{N-1}\sum_i (x_i - \overline{x})^2 = \frac{1}{N-1}\sum_{j=1}^{n} f_j (x_j - \overline{x})^2 \tag{3.19}$$

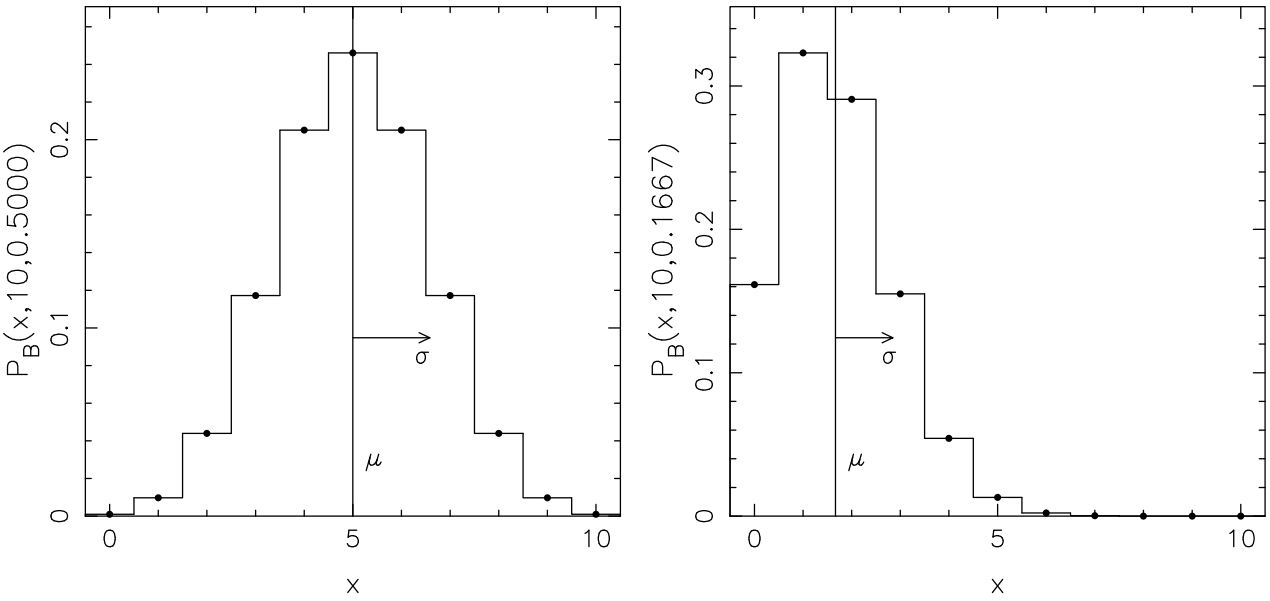

Figure 3.4: *(Left) Binomial distribution function for flipping a coin (10x)* $P_B(k,n,p)$*:* $n = 10$ *and* $p = 1/2$*;* $\mu = 5$ *and* $\sigma = 1.6$*. (Right) Binomial distribution function for throwing 10 dice* $P_B(k,n,p)$*:* $n = 10$ *and* $p = 1/6$*;* $\mu = 1.67$ *and* $\sigma = 1.2$*.*

where the factor $N - 1$ in the denominator is the number of degrees of freedom left for assessing s^2 *after determining the value of* $\overline{x}$ *from* N *observations*. Again, the value of the sample variance s^2 is distinctly different from the parent variance σ^2 unless $N \to \infty$.

Figure 3.3 shows the deviations between parent mean and sample mean, parent standard deviation and sample standard deviation respectivily, for a sample of 100 measurements. The magnitude of the errors in sample mean and variance is obviously dependent on the size of the sample. A quantitative estimate of these errors will be discussed later in this chapter.

3.3 Probability density distributions

In this section the probability density distributions are reviewed that often occur, or are postulated to occur, in measurement series.

3.3.1 The binomial and Poisson distributions

An observer tries to detect photons during a certain time interval. The expected number of photons to arrive in this interval is μ. How many photons will the observer detect? To address this question, the measurement interval is subdivided in n equal sub-intervals. In each sub-interval the probability that a photon arrives is therefore $p = \mu/n$ (a correction to this statement follows below!), the probability that no photon arrives is $1 - p$. The measurement of the observer can thus be considered as a series of n trials to find a photon, each trial having probability p of succeeding. The probability that k photons will be detected is then given by the binomial function:

$$P_B(k,n,p) = \left(\begin{array}{c} n \\ k \end{array} \right) p^k (1-p)^{n-k} \tag{3.20}$$

The binomial function also describes processes like flipping a coin, or throwing dice. For example, when a coin is flipped the probability of getting head is $p = 1/2$, and the probability

of getting k times head when the coin is flipped 10 times is given by $P_B(k, 10, 0.5)$, this illustrated at the left in figure 3.4. When we throw 10 dice, the probability of getting k times a 1 is given by $P_B(k, 10, 1/6)$, illustrated at the right in figure 3.4.
The mean μ of a binomial distribution can be evaluated by combining the definition of μ as the first moment of the distribution function and expression (3.20):

$$\mu = \sum_{k=0}^{n} \left[k \frac{n!}{k!(n-k)!} p^k (1-p)^{n-k} \right] = np \tag{3.21}$$

Likewise, the variance σ^2 of a binomial distribution is computed by considering the expectation value of $(k-\mu)^2$:

$$\sigma^2 = \sum_{k=0}^{n} \left[(k-n)^2 \frac{n!}{k!(n-k)!} p^k (1-p)^{n-k} \right] = np(1-p) \tag{3.22}$$

Note: evaluate these sums yourself!
The results for the mean μ and the variance σ are remarkably simple. If the probability for a single success p is equal to the probability for failure $p{=}1-p{=}\frac{1}{2}$, the distribution is symmetric about the mean μ, and the median $\mu_{\frac{1}{2}}$ and the most probable value are both equal to the mean. In this case the variance σ^2 is equal to half the mean: $\sigma^2{=}\mu/2$. If p and $q{=}1-p$ are not equal, the distribution is asymmetric with a smaller variance.
Return now to the experimenter measuring the arrival of photons. If the sub-interval is large, there is a finite probability that more than 1 photon will arrive in this particular interval, which is not taken into account in the above argument. To suppress this probability, the limit is taken of letting the number of trials n go to infinity, keeping the product $np \equiv \mu$ constant. In this limit the binomial distribution changes into the Poisson distribution, in which the probability of obtaining k photons is given by

$$P_P(k, \mu) = \frac{\mu^k}{k!} e^{-\mu} \tag{3.23}$$

The derivation of this expression follows from:

$$\begin{aligned} P(k) &= \binom{n}{k} p^k (1-p)^{n-k} = \frac{n!}{k!(n-k)!} \left(\frac{\mu}{n}\right)^k \left(1 - \frac{\mu}{n}\right)^{n-k} \\ &= \frac{\mu^k}{k!} \frac{n(n-1)(n-2)..(n-k+1)}{n^k} \frac{(1-\mu/n)^n}{(1-\mu/n)^k} = \frac{\mu^k}{k!} 1 \frac{e^{-\mu}}{1} = \frac{\mu^k}{k!} e^{-\mu} \end{aligned} \tag{3.24}$$

The exponent makes sure that the sum $\sum P_P(k, \mu)$ over all probabilities from $k = 0$ to $k = \infty$ is 1 (remember $e^x = 1 + x + x^2/2! + x^3/3! \ldots$.).

Suppose the observer carries out an infinite number of observations (this is obviously a thought experiment), and should then on average detect μ photons: $\overline{k} = \mu$. The variance $\sigma^2 \equiv \overline{(k-\mu)^2}$ also equals μ.
The derivations of these results follow from:

$$\begin{aligned} \overline{k} &= \sum_{k=0}^{\infty} k \frac{\mu^k}{k!} e^{-\mu} = e^{-\mu}(0 + \mu + 2\frac{\mu^2}{2!} + \ldots) = e^{-\mu}(\mu + \frac{\mu^2}{1!} + \frac{\mu^3}{2!} \ldots) \\ &= e^{-\mu}\mu(1 + \frac{\mu}{1!} + \frac{\mu^2}{2!} + \ldots) = e^{-\mu}\mu e^{\mu} = \mu \end{aligned} \tag{3.25}$$

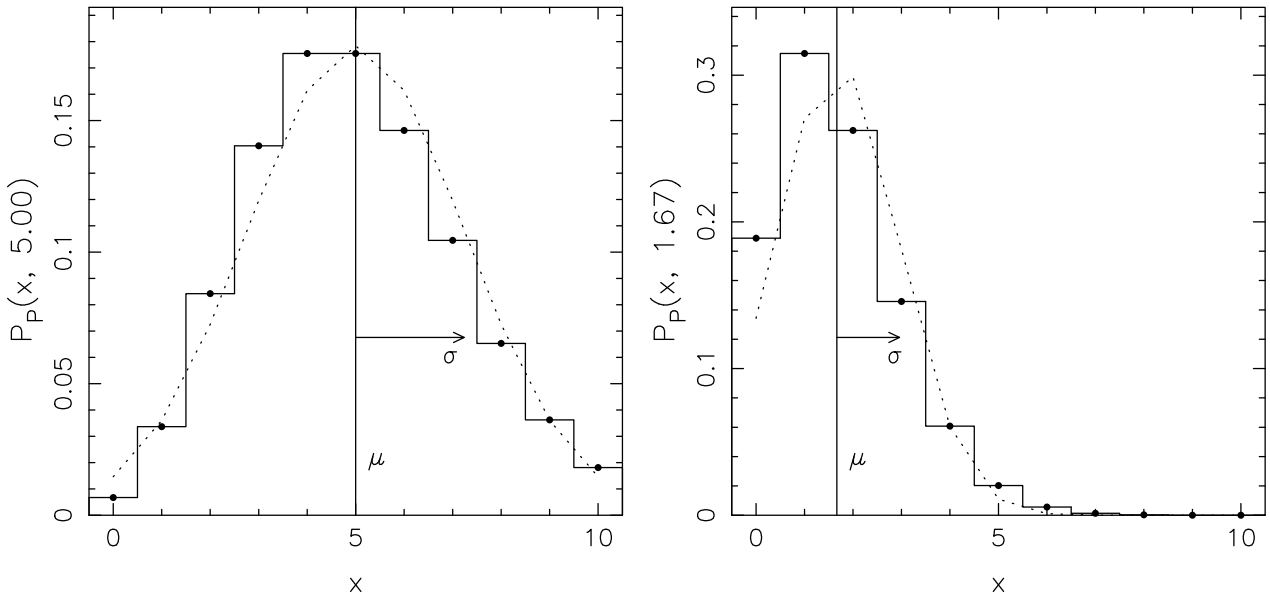

Figure 3.5: *(Left) Poisson distribution function $P_P(k,\mu)$ for $\mu = 5$. (Right) Poisson distribution function $P_P(k,\mu)$ for $\mu = 1.67$. The dotted lines show Gaussian approximations to the Poisson function.*

$$\begin{aligned}
\sum_{k=0}^{\infty} k^2 \frac{\mu^k}{k!} &= 0 + \mu + 2\mu^2 + 3\frac{\mu^3}{2!}.. = \mu(1 + \frac{\mu}{1!} + 3\frac{\mu^2}{2!}..) = \mu(1 + \frac{\mu}{1!} + \frac{\mu^2}{2!} + ..\frac{\mu}{1!} + 2\frac{\mu^2}{2!} + ..) \\
&= \mu(e^\mu + \mu[1 + \frac{\mu}{1!} + \frac{\mu^2}{2!} + ..]) = \mu e^\mu + \mu^2 e^\mu \qquad (3.26) \\
&\text{hence} \\
\sigma^2 &\equiv \overline{(k-\mu)^2} = \sum_{k=0}^{\infty} k^2 P(k) - \mu^2 = e^{-\mu} \sum_{k=0}^{\infty} k^2 \frac{\mu^k}{k!} - \mu^2 = \mu + \mu^2 - \mu^2 = \mu
\end{aligned}$$

Two examples of the Poisson distribution are given in figure 3.5. The dotted lines indicate Gaussian approximations to the Poisson function. It is clear from these examples that especially for low values of the mean μ, the Gaussian approximations underestimate the probability of large deviations!

3.3.2 The Normal or Gaussian distribution

If μ is large, the Poisson distribution is well approximated by the normal distribution, also called the Gaussian distribution:

$$P_G(x,\mu,\sigma) = \frac{1}{\sigma\sqrt{2\pi}} \exp\left[-\frac{1}{2}\left(\frac{x-\mu}{\sigma}\right)^2\right] \qquad (3.27)$$

for the special case where $\sigma = \sqrt{\mu}$. The Gauss function has the computational advantage over both the binomial and the Poission distribution that it is easy to compute; it does not contain such expensive calculations as the factorials. It also describes (or is assumed to describe) the distribution of measurements in many physical experiments.
The shape of the distribution is illustrated in figure 3.6. It is a bell-shaped curve symmetric about the mean μ. The width of the distribution is characterized by the *full-width at half-maximum*, which is generally called the *half-width* Γ. This is defined as the range of x between

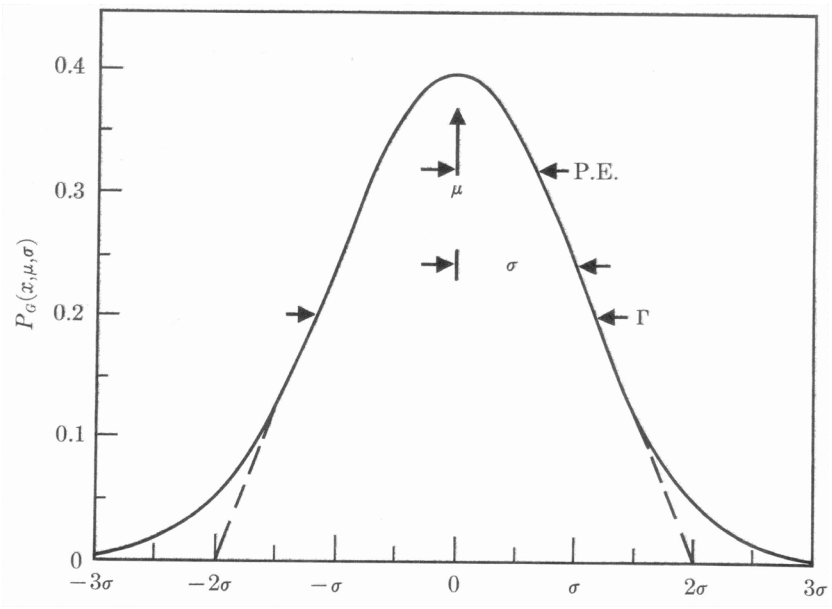

Figure 3.6: *Gaussian probability distribution* $P_G(x, \mu, \sigma)$ *versus* $x - \mu$*;* $\Gamma = 2.354\sigma$ *and P.E.* $= 0.6745\sigma$*. Credit Bevington (1969).*

the values at which the probability $P_G(x, \mu, \sigma)$ is half its maximum value:

$$P_G(x \pm \frac{1}{2}\Gamma, \mu, \sigma) = \frac{1}{2}P_G(\mu, \mu, \sigma) \qquad \Gamma = 2.354\sigma \tag{3.28}$$

A tangent drawn along the portion of steepest descent of the curve intersects the curve at the $e^{-\frac{1}{2}}$ points $x{=}\mu \pm \sigma$ and intersects the x-axis at the points $x{=}\mu \pm 2\sigma$:

$$P_G(\mu \pm \sigma, \mu, \sigma) = e^{-\frac{1}{2}}P_G(\mu, \mu, \sigma) \tag{3.29}$$

The mean and standard deviation of the Gaussian distribution are equal to the parameters μ and σ given explicitly in the probability density equation (3.27). This equivalence can be verified by using the definitions of μ and σ as the expectation values of x and $(x - \mu)^2$ for continuous distributions, as discussed in the previous paragraph.
The *probable error P.E.* is defined to be the absolute value of the deviation $|x - \mu|$ such that the probability for the deviation of any random observation $|x_i - \mu|$ to be less is equal to $\frac{1}{2}$. In other words, half the observations of an experiment are expected to fall within the boundaries denoted by $\mu \pm P.E.$. The relation between the *P.E.* and the standard deviation σ is found by evaluating the point at which the integral probability curve yields a probability of $\frac{1}{2}$ of being exceeded.

3.3.3 The Lorentzian distribution

The Lorentzian distribution is frequently encountered in spectroscopic data reduction, since it describes the resonance behaviour associated with atomic and nuclear transitions. The probability density function is displayed in figure 3.7 and defined as:

$$P_L(x, \mu, \Gamma) = \frac{1}{\pi}\frac{\Gamma/2}{(x - \mu)^2 + (\Gamma/2)^2} \tag{3.30}$$

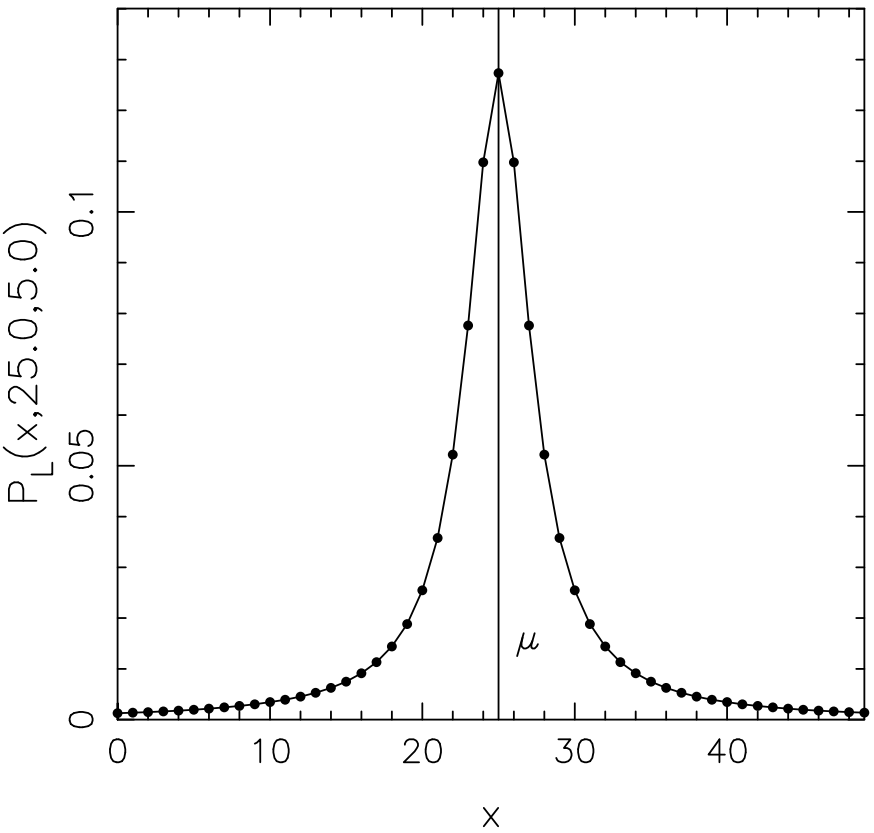

Figure 3.7: *The Lorentzian probability distribution for* $\mu = 25$ *and* $\Gamma = 5$.

The distribution is symmetric about its mean μ, with a half-width Γ. The most noticable difference with the Gaussian distribution is the fact that it does not diminish to zero so rapidly, for large deviations it only decreases proportional to the square of the deviation.
The mean μ is one of the free parameters, it is also equal to the median and the most probable value, like in the case of the Gaussian distribution. However, the *standard deviation is not defined for a Lorentzian distribution* as a consequence of its slowly decreasing behaviour for large deviations, i.e. the integral defining the expectation value for the square of the deviations is *unbounded*. The width of a Lorentzian distribution is characterized by the half-width parameter Γ, defined such that when the deviation from the mean $x - \mu = \Gamma/2$, the probability density $P_L(x, \mu, \Gamma)$ is half its value at the maximum. **Note:** verify this yourself!

Figure 3.8 shows a comparison of the Gaussian and Lorentzian distributions with equal values for their means μ and half-widths Γ.

3.4 Method of maximum likelihood

3.4.1 Calculation of the mean

Consider an observation that comprises a set of N data points, and is presumed to be a random selection from a Gaussian parent distribution $P_G(x_i, \mu, \sigma)$. How does one arrive at an estimate μ' from the data, giving the maximum likelihood that the parent distribution had a mean equal to μ, and what is the error in the estimate μ'?
If we hypothesize a trial parent distribution $P_G(x_i, \mu', \sigma)$, the probability of observing a par-

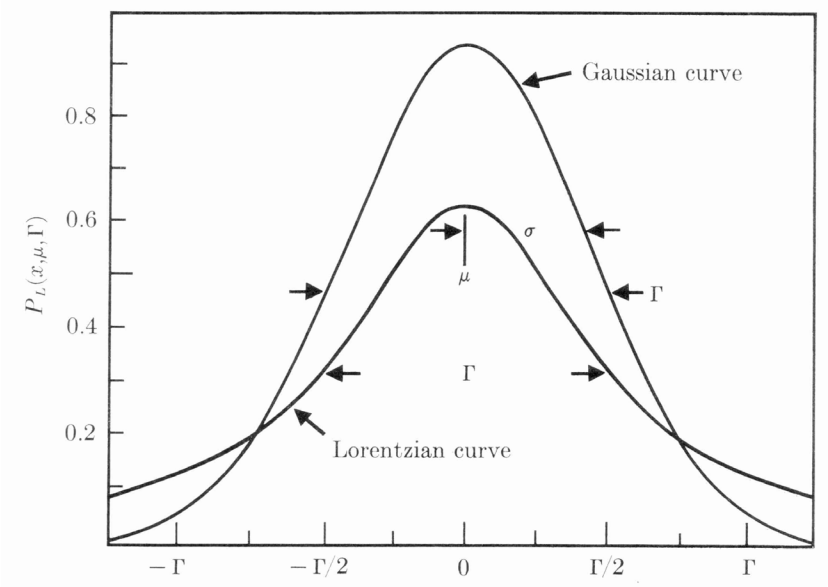

Figure 3.8: *Lorentzian probability distribution $P_L(x, \mu, \Gamma)$ versus $x-\mu$, compared to a Gaussian distribution with the same mean and half-width. Credit Bevington (1969).*

ticular value x_i for one of the data points is given by

$$P_G(x_i, \mu', \sigma) = \frac{1}{\sigma\sqrt{2\pi}} exp\left[-\frac{1}{2}\left(\frac{x_i - \mu'}{\sigma}\right)^2\right] \tag{3.31}$$

Considering now the entire set of N observational values, the probability for observing that particular set is given by

$$P(\mu', \sigma) = \prod_{i=1}^{N} P_G(x_i, \mu', \sigma) = \left(\frac{1}{\sigma\sqrt{2\pi}}\right)^N exp\left[-\frac{1}{2}\sum_i \left(\frac{x_i - \mu'}{\sigma}\right)^2\right] \tag{3.32}$$

According to the *method of maximum likelihood*, when comparing $P(\mu', \sigma)$ for several values of μ', the most likely parent population from which such a set of data might have come, i.e. when $P(\mu', \sigma)$ is at the maximum value, is assumed to be the correct one.
The value $P(\mu', \sigma)$ in equation (3.32) is maximum if the exponential term is minimized, hence:

$$-\frac{1}{2}\frac{d}{d\mu'}\sum_i \left(\frac{x_i - \mu'}{\sigma}\right)^2 = 0 \Longrightarrow \mu' = \overline{x} \equiv \frac{1}{N}\sum_i x_i \tag{3.33}$$

In practise, some data points might be measured with better or worse precision than others, this can be accomodated by assigning to each data point x_i its own standard deviation σ_i, representing the precision with which that particular data point was measured, hence:

$$-\frac{1}{2}\frac{d}{d\mu'}\sum_i \left(\frac{x_i - \mu'}{\sigma_i}\right)^2 = 0 \Longrightarrow \mu' = \frac{\sum_i (x_i/\sigma_i^2)}{\sum_i (1/\sigma_i^2)} \tag{3.34}$$

The most probable value for the mean is therfore the weighted average of the data points, each data point being weighted inversely by its own variance.

3.4.2 Estimated error of the mean

What uncertainty σ_μ is associated with the estimate of the mean μ' in equation 3.34?
Each individual variance σ_i^2 contributes some uncertainty; assuming uncorrelated measurement points x_i the accumulated variance σ_μ^2 of the estimated mean μ' follows from:

$$\sigma_\mu^2 = \sum_i \left[\sigma_i^2 \left(\frac{\partial \mu'}{\partial x_i} \right)^2 \right] \tag{3.35}$$

if higher-order terms in the expansion of σ_μ^2 are neglected. The values of the partial differential quotients $\partial\mu'/\partial x_i$ can be derived from expression 3.34:

$$\frac{\partial \mu'}{\partial x_i} = \frac{1/\sigma_i^2}{\sum_i (1/\sigma_i^2)} \Longrightarrow \sigma_\mu^2 = \frac{1}{\sum_i (1/\sigma_i^2)} \tag{3.36}$$

If the uncertainties in the data points are all equal, i.e. if $\sigma_i = \sigma$, the error of the mean reduces to the simple expression:

$$\sigma_\mu^2 = \frac{\sigma^2}{N} \tag{3.37}$$

Example: Consider the sample displayed in figure 3.3 of a previous paragraph, that comprises 100 measurements. The mean was estimated to be $\mu \approx \mu' = \overline{x}$=3.045, the standard deviation was estimated to be $\sigma \approx s$=1.078. Since all the uncertainties σ in the individual data points are equal, the uncertainty in the determination of the mean equals $\sigma_\mu \approx s/\sqrt{N}$=0.108. This is already substantially larger than the actual error of 0.045.
Important notion: If the discrete values of x in figure 3.3, i.e. the centres of the vertical bins at 0.25, 0.75, 1.25,....., 5.75, are not the exact trial values but merely reflect the lumping of trial values in bin widths of 0.5 straddling these centre values, the exact numerical results on the sample mean $\overline{x}$ and the sample standard deviation s will depend on the selected bin widths (0.5 in this case)and the bin grid (centre values of x). The choice of the appropriate bin widths in data acquisition and handling is the subject of optimal sampling, which will be discussed in Chapter 5.

3.5 Stochastic processes

3.5.1 Distribution functions

A stochastic process is defined as an infinite series of stochastic variables, one for each value of the time t. For a specific value of t, the *stochastic variable* $X(t)$ possesses a certain probability density distribution. The numerical value of the stochastic variable $X(t)$ at time t corresponds to a particular draw (outcome) from this probability distribution at time t. The time series of draws represents a single time function and is commonly referred to as a *realisation* of the stochastic process. The full set of all realisations is called the *ensemble of time functions* (see Fig. 8.1).
At each time t, the stochastic variable $X(t)$ describing the stochastic process, is distributed by a *momentary* cumulative distribution, called the first-order distribution:

$$F(x;t) = \mathbf{P}\{X(t) \leq x\}, \tag{3.38}$$

which gives the probability that the outcome at time t will not exceed the numerical value x. The probability density function, or first-order density, of $X(t)$ follows from the derivative of

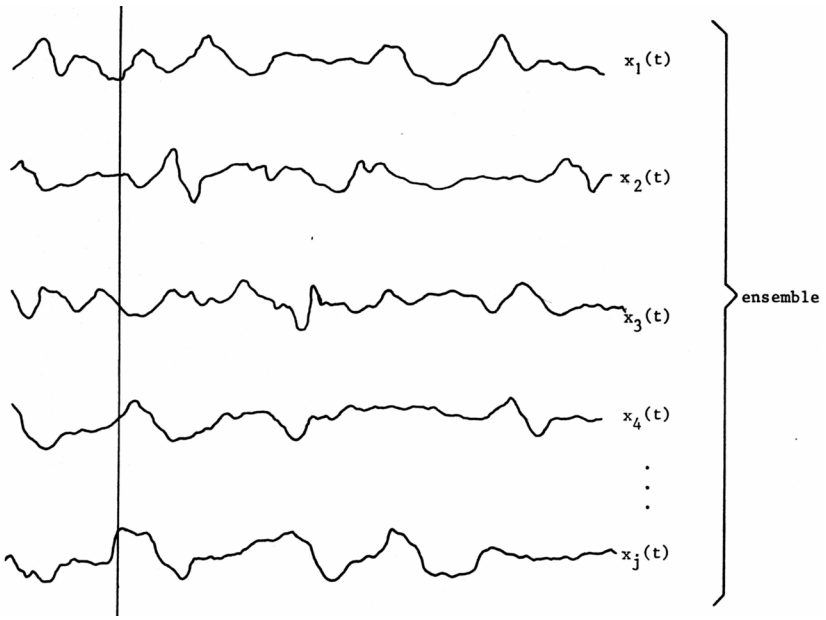

Figure 3.9: *The ensemble of time functions of a stochastic process.*

$F(x;t)$,

$$f(x;t) \equiv \frac{\partial F(x;t)}{\partial x}. \tag{3.39}$$

This probability function may be a binomial, Poisson or normal (Gaussian) distribution.

3.5.2 Mean and variance

For the determination of the statistical properties of a stochastic process it suffices in many applications to consider only certain averages, in particular the expected values of $X(t)$ and of $X^2(t)$.

The *mean* or *average* $\mu(t)$ of $X(t)$ is the expected value of $X(t)$ and is defined as

$$\mu(t) = \mathbf{E}\{X(t)\} = \int_{-\infty}^{+\infty} x\, f(x;t)\, dx. \tag{3.40}$$

The variance of $X(t)$ is the expected value of the square of the difference of $X(t)$ and $\mu(t)$ and is, by definition, equal to the square of the standard deviation:

$$\sigma^2(t) = \mathbf{E}\{(X(t) - \mu(t))^2\} = \mathbf{E}\{X^2(t)\} - \mu^2(t) \tag{3.41}$$

(in case of real functions $X(t)$ and $\mu(t)$).

3.6 Intrinsic stochastic nature of a radiation beam

3.6.1 Bose-Einstein statistics

Irrespective of the type of information carrier, e.g. electromagnetic or particle radiation, the incoming radiation beam in astronomical measurements is subject to fluctuations which derive from the incoherent nature of the emission process in the information (=radiation) source. For

a particle beam this is immediately obvious from the corpuscular character of the radiation, however for electromagnetic radiation the magnitude of the fluctuations depends on whether the wave character or the quantum character (i.e. photons) dominates. By employing Bose-Einstein statistics, the magnitude of these intrinsic fluctuations can be computed for the specific case of a blackbody radiation source, which is incoherent or "chaotic" with respect to time.
In this course we shall not embark on a detailed treatment of these fluctuations, this is a subject that will be elaborated in the more advanced course Observational Astrophysics 2 (OAF2). It suffices here to give the outcome of applying Bose-Einstein statistics to a blackbody radiation field:

- For a photon energy $h\nu \ll kT$, the statistical fluctuations in the radiation beam are dominated by the wave character of the radiation. If the average radiation power per unit frequency interval is given by $\overline{P}(\nu)$ (e.g. in Watt Hz^{-1}), the variance in this power is given by:

$$\overline{\Delta P^2}(\nu) = \overline{P}^2(\nu) \tag{3.42}$$

$$\text{and} \qquad \overline{P}(\nu) = kT \tag{3.43}$$

  The value of $\overline{P}(\nu)$ *applies to one degree of polarisation*!
  This case is called the thermal limit for an electromagnetic radiation beam.

- In the other extreme case that $h\nu \gg kT$, photon statistics prevails and the statistical fluctuations in the signal can be expressed as Poissonian noise:

$$\overline{\Delta n^2}(\nu) = \overline{n}(\nu) \tag{3.44}$$

  in which $\overline{n}(\nu)$ represents the number of photons in the observation sample. This condition is called the quantum limit of the fluctuations and it represents the minimum value of intrinsic noise present in any radiation beam. Obviously, this always holds for corpuscular radiation (cosmic-rays) and neutrinos, since the wave character is not an issue.

Figure 8.5 shows the subdivision between thermal and quantum noise as a function of temperature. The transition between noise in the quantum limit to the thermal limit occurs at $h\nu \approx kT$. At room temperature, $T \approx 300$ K, this corresponds to a frequency $\nu \approx 6$ THz, or a wavelength $\lambda \approx 50$ μm. The relation $\nu = kT/h$ as a function of temperature T is displayed in figure 8.5. It is clear from this diagram that radio observations are always dominated by the wave character of the incoming beam and are therefore performed in the thermal limit. As a result, the treatment of noise in radio observations differs drastically from that of measurements at shorter wavelengths. Specifically at submillimetric and infrared wavelengths quantum limited observation is vigorously pursued but this remains still difficult.

The fluctuations in average power $\overline{P}(\nu)$, given in equation 8.54 for the thermal limit can be interpreted in such a way that whenever wave packet interference becomes important, the interference will cause the fluctuations to become of the same magnitude as the signal. The low frequency fluctuations can be thought of as caused by the random phase differences and beats of the wavefields, as described in the following paragraph.
Note: The above expression for the fluctuations in a blackbody photon gas applies only to the interior of a blackbody in which the receiving element is submerged, i.e. a blackbody cavity

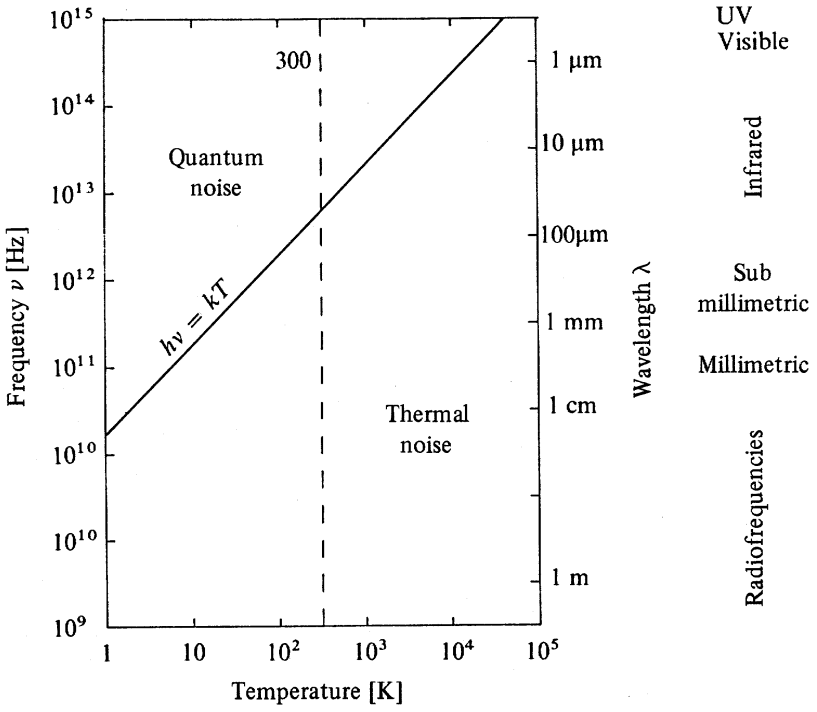

Figure 3.10: *Frequency as a function of temperature: division between thermal and quantum noise. Credit Lena et al (1998).*

or a thermal bath. This requires that the condition $\lambda^2 = c^2/\nu^2 = A_e\Omega$ is satisfied, in which A_e represents the effective collecting area of the telescope and Ω the solid angle subtented by the radiation source. The expression $A_e\Omega$ is called the *throughput or "etendue" of coherence.* (The derivation of this relation and the subject of coherent detection will be treated in detail later in OAF2). If this condition is not fulfilled, then even in the limit $h\nu \ll kT$ quantum noise may dominate. For example, if a star, whose spectrum resembles a blackbody at temperature T, is observed at frequency ν, such that $h\nu \ll kT$, thermal noise ought to dominate. The star may however be so distant that the radiation is effectively unidirectional and hence, $A_e\Omega \ll \lambda^2$. The photons will consequently arrive well separated in time and quantum noise evidently dominates.

3.6.2 Electromagnetic radiation in the thermal limit

In astrophysics, many sources of electromagnetic (EM) radiation have a thermal origin. This implies that the incoming wave-signal has been built up by the superposition of many individual wavepackets, which were all generated by a myriad of independent radiative atomic transitions at the radiation source. Each wavepacket has a limited duration that depends on the characteristic time scale of the particular atomic transition. The intrinsic spread in the frequency of the emitted wavepacket derives from the uncertainty relation of Heisenberg $\Delta\epsilon\Delta t = h$ with spread in frequency $\Delta\nu = 1/\Delta t$. The characteristic time length of such a wavepacket $\Delta t \equiv \tau_c = 1/\Delta\nu$ is called the *coherence time*, it represents the typical time scale over which the phase of the EM-wave can be predicted with reasonable accuracy at a given location in space. Figure 8.7 shows the stochastic signal comprising a random superposition of individual wavepackets. This wave signal fluctuates both in amplitude and in frequency,

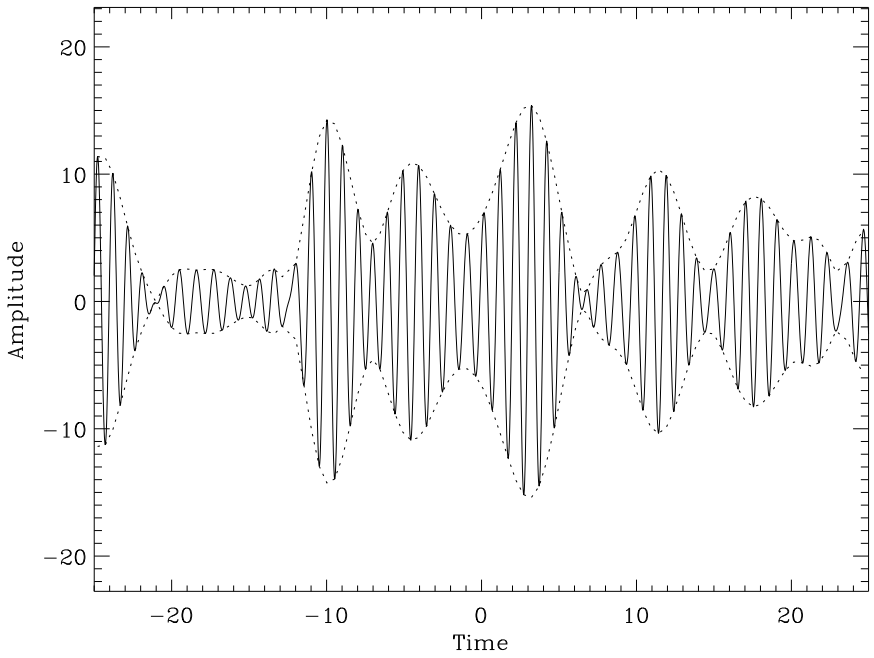

Figure 3.11: *A quasi-monochromatic wave.*

the latter characterised by a typical bandwidth $\Delta\nu$ around an average frequency $\bar{\nu}$. Such a signal represents a quasi-monochromatic wave with a frequency stability $\bar{\nu}/\Delta\nu$.

The frequency bandwidth $\Delta\nu$ can be accommodated by introducing a complex wave amplitude[1] $\tilde{E}_0(t) =\mid \tilde{E}_0(t) \mid \cdot e^{i\phi(t)}$, which involves a time dependent phase angle $\phi(t)$. The electromagnetic wave can then generally be expressed as follows:

$$\tilde{E}(t) = \tilde{E}_0(t) \cdot e^{i2\pi\bar{\nu}t} =\mid \tilde{E}_0(t) \mid \cdot e^{i(2\pi\bar{\nu}t+\phi(t))} \tag{3.45}$$

Taking the real part for one direction of polarisation, this equation becomes

$$E(t) = E_0(t)\cos(2\pi\bar{\nu}t + \phi(t)) \tag{3.46}$$

The stochastic variable describing the radiation field in the thermal limit is thus represented by the time variable electric field vector $E(t)$, i.e. $X(t) = E(t)$. A full treatment of the stochastic properties of a thermal radiation field is given in OAF2.
The time dependent behaviour of $E(t)$ is depicted in figure 8.7 representing one polarisation component of a quasi-monochromatic wave. Points on the EM-wave shown in this figure separated by more than τ_c in time are related to different wavepackets and show therefore no correlation in phase.

At optical wavelengths, a typical atomic transition takes $\tau_c \approx 10^{-9}$ s, this comprises about one million oscillations at a typical carrier frequency of 10^{15} Hz, i.e. the fluctuation frequencies of $\mid \tilde{E}_0(t) \mid$ and $\phi(t)$ for quasi-monochromatic radiation are much slower than $\bar{\nu}$.

[1] A tilde is put over quantities that are explicitly used as complex variables to avoid confusion

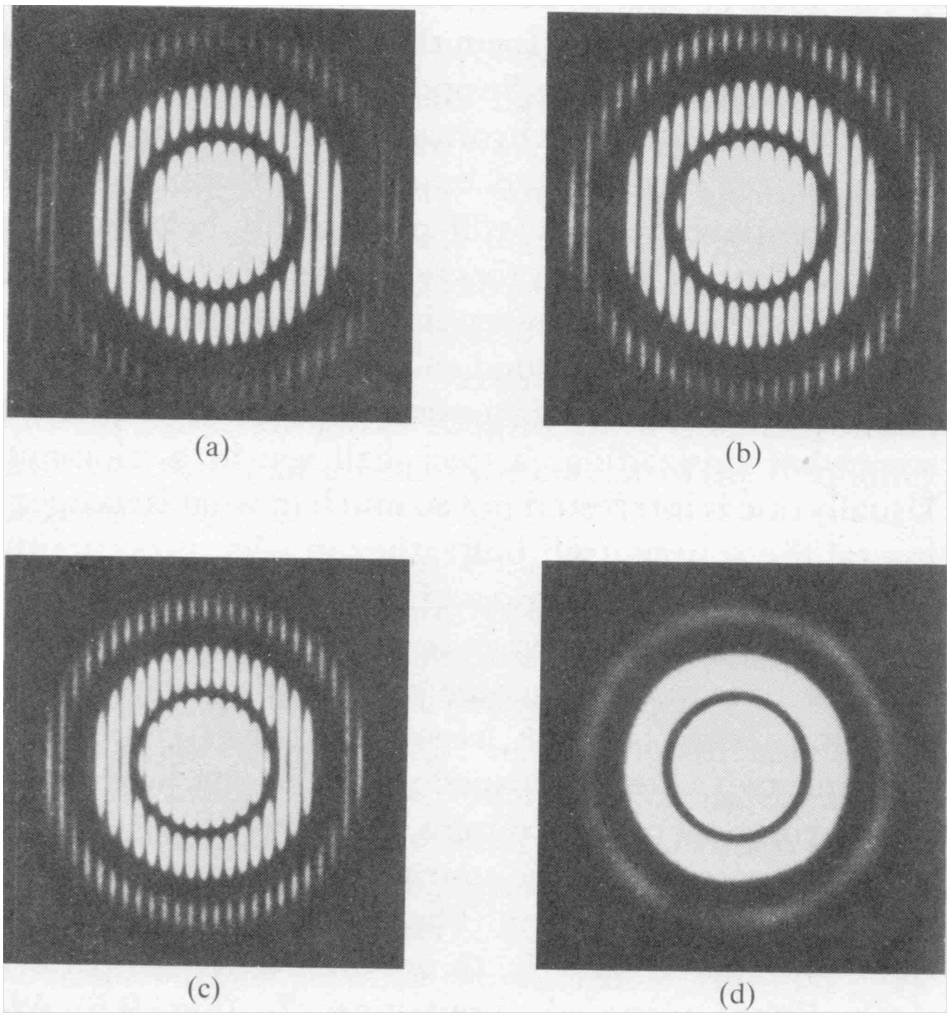

Figure 3.12: *Double-beam interference from a pair of circular apertures. (a) He-Ne laserlight (b) idem, but a 0.5 mm glass plate covers one hole (c) idem as (a) but with a Hg-discharge lamp (d) idem as (b) with the Hg-discharge lamp. Credit Hecht (1987).*

> *Gas discharge lamps possess a large bandwidth, the coherence length l_c is only a few millimeters. In contrast, white light has a frequency bandwidth $\Delta\nu \approx 300$ THz (from 4.5 to 7.5·10^{14} Hz), the coherence length only covers a few oscillations. Low-pressure isotope lamps, e.g. ^{198}Hg at 546 nanometers and ^{86}Kr at 605 nanometers, have a $\Delta\nu \approx 1$ GHz; the frequency stability is $\bar{\nu}/\Delta\nu \approx 10^6$ and the coherence length amounts to about one meter. These light sources can therefore be designated as quasi-monochromatic. Lasers possess a very high degree of coherence, i.e. $\Delta\nu \approx 20$ Hz with a frequency stability of about 10^{13}.*

The effect of the limited coherence length associated with light sources possessing a finite frequency bandwidth is demonstrated in figure 3.12. Panel (a) shows the interference fringes when two small circular apertures are illuminated by a He-Ne laser source. Panel (b) shows

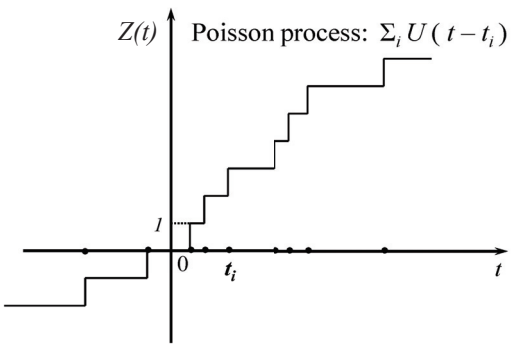

Figure 3.13: *Staircase function.*

the fringe patters when one of the apertures is covered with an optically flat piece of glas with a thickness of 0.5 mm. No change in the form of the pattern, other than a shift in its location, is evident because the coherence length of the laser light far exceeds the optical path-length difference introduced by the glass plate. On the other hand, when the same experiment is repeated using the light of a collimated Hg-discharge lamp, the fringes disappear (compare panel (c) and (d)). In this case the coherence length of the beam is appreciably shorter than the optical path difference introduced by the glass plate. Hence, the wavepackets emanating from the two apertures are uncorrelated and no fringe pattern is formed.

3.6.3 Electromagnetic radiation in the quantum limit

In the quantum limit no coherence effects occur and the radiation field fluctuations can be described by photon statistics only. Consider an incident radiation beam with an average flux of $\bar{n}_b$ photons (or particles or neutrinos) per second. The generation of photons at random times t_i can be described by a stochastic variable $X(t)$, which consists of a family of increasing staircase functions, with discontinuities at the the points t_i, see figure 8.11:

$$X(t) = \sum_i U(t - t_i) \tag{3.47}$$

with $U(t)$ the unit-step function

$$U(t) = \begin{cases} 1 & \text{for } t \geq 0 \\ 0 & \text{for } t < 0. \end{cases} \tag{3.48}$$

The derivative of the stochastic variable $X(t)$:

$$Y(t) = \frac{dX(t)}{dt} = \sum_i \delta(t - t_i) \tag{3.49}$$

represents a train of Dirac impulses at random time positions t_i. The number of photons $X_{\Delta T}$ registered during a measurement period ΔT (which is a (small) part of the total measurement time T), follows from

$$X_{\Delta T} = \int_t^{t+\Delta T} \sum_i \delta(t - t_i)\, dt = k \tag{3.50}$$

The *random variable* $X_{\Delta T}$ is distributed according to a Poisson distribution. The probability to detect k photons, if the mean value is μ, is:

$$p_P(k,\mu) = \frac{\mu^k}{k!}\, e^{-\mu} \tag{3.51}$$

with k an integer value. The (continuous) probability density function for Poissonian statistics can now be expressed as:

$$p(x,\mu) = \sum_{k=0}^{\infty} p_P(k,\mu)\ \delta(x-k) \tag{3.52}$$

So, the average value of $X_{\Delta T}$ is:

$$\mathbf{E}\{X_{\Delta T}\} = \int_{-\infty}^{+\infty} x\ p(x,\mu)\ dx = \mu = \bar{n}_b\ \Delta T \tag{3.53}$$

The variance σ^2 of a Poisson distribution equals the average μ, i.e. $\bar{n}_b\ \Delta T$, the standard deviation σ is $\sqrt{\bar{n}_b\ \Delta T}$. The signal to noise ratio (S/N) can be defined as $\mu/\sigma = \sqrt{\bar{n}_b\ \Delta T}$. Given an average flux of $\bar{n}_b$, the value of S/N thus improves with the measurement period ΔT proportional to $(\Delta T)^{\frac{1}{2}}$. In an analogous fashion the S/N of the stochastic variable $Y(t)$ improves with $\overline{n}_b^{\frac{1}{2}}$.

Chapter 4

Physical principles of radiation detection

4.1 Types of detection

Detection of a radiation field can generally be subdivided in two categories: amplitude detection and power detection.

4.1.1 Amplitude detection

This type of detection involves the measurement of the instantaneous amplitude of an electromagnetic wave with average frequency $\bar{\nu}$ and varying amplitude and phase. Considering one component of polarisation, the signal $S(t)$ varies as

$$S(t) = E_0(t)\cos(2\pi\bar{\nu}t + \phi(t)) \tag{4.1}$$

and is obtained by conversion of the electromagnetic field into a current by a receiving antenna. The relation between the signal and the amplitude of the wave can be regarded as linear, moreover the phase information $\phi(t)$ remains available. This detection process is therefore referred to as *coherent detection*.

4.1.2 Power (or intensity) detection

In this case the detection process involves the measurement of the average power of an electromagnetic wave, a particle or a neutrino beam, in which the averaging takes place over a certain time interval ΔT, i.e. the detection yields a running average over ΔT. For electromagnetic waves this integration interval ΔT is large compared to the period of the wave $c/\bar{\nu}$, the signal $S(t)$ follows from:

$$S(t) = \frac{1}{\Delta T}\int_{t}^{t+\Delta T} \tilde{E}(t')\cdot\tilde{E}^*(t')\,dt' = \frac{1}{\Delta T}\,\Pi\left(\frac{t}{\Delta T}\right) * |\,\tilde{E}(t)\,|^2 \tag{4.2}$$

If the electromagnetic wave is regarded as a photon beam, the equivalent expression is:

$$S(t) = \frac{1}{\Delta T}\int_{t}^{t+\Delta T} n(t')\,dt' \tag{4.3}$$

in which $n(t')$ represents the photon flux. This relation also applies to corpuscular radiation (cosmic rays) and neutrinos. As discussed in Chapter 3, $n(t')$ relates to a Poisson process. If the time interval ΔT is taken sufficiently small, equation 4.3 reduces to single photon (particle) counting.

In this course no detailed treatment of the mechanism of amplitude detection will be given, however in the following paragraphs the physical principles of photon, particle and neutrino detection will be briefly reviewed, since they underly the working principles of a large variety of radiation sensors.

4.2 Detection of electromagnetic radiation

4.2.1 Opacity, cross-section, Kirchhoff's law

Consider a beam of electromagnetic radiation with monochromatic intensity $I(\epsilon, 0)$ at normal incidence on a layer of absorbing material (e.g. a detection element). The absorption in an infinitesimal layer ds within the absorber at depth s can be derived from the relation:

$$I(\epsilon, s + ds) - I(\epsilon, s) = -dI(\epsilon, s) = I(\epsilon, s)\ k(\epsilon, s)\ ds \tag{4.4}$$

The parameter $k(\epsilon, s)$ represents the probability per unit path-length that a photon is either absorbed or scattered. In general $k(\epsilon, s)$ is a function of the position s, but for a uniform homogeneous absorber $k(\epsilon, s) = k(\epsilon)$, independent of s. $k(\epsilon, s)$ is commonly referred to as the (volume) opacity or total absorption (extinction) coefficient of the relevant medium. Also $k(\epsilon, s) = [l(\epsilon, s)]^{-1}$, in which $l(\epsilon, s)$ represents the mean free path of a photon with energy ϵ. In practice a related quantity

$$\kappa(\epsilon, s) = k(\epsilon, s)/\rho \tag{4.5}$$

is often used, where ρ is the specific mass. $\kappa(\epsilon, s)$ is called the mass absorption coefficient in units of surface area per unit mass (e.g. $\mathrm{m^2 kg^{-1}}$). The absorption coefficient per atom for a uniform absorber follows from:

$$\sigma(\epsilon) = \frac{\kappa(\epsilon)\ A_m}{N_A} \tag{4.6}$$

where A_m represents the atomic mass and N_A Avogadro's number. The quantity $\sigma(\epsilon)$ (or $\sigma(\lambda)$, or $\sigma(\nu)$) is called the absorption (scattering) cross-section and needs to be used when describing the microscopic properties of an absorbing medium. The volume opacities $k(\epsilon), k(\lambda), k(\nu)$ are usually applied when treating radiation transport phenomena on a macroscopic level, such as stellar atmospheres.

Integration of equation 4.4, taking a total absorption length s_0, yields the attenuated beam intensity $I(\epsilon, s_0)$ after passing through s_0:

$$I(\epsilon, s_0) = I(\epsilon, 0)\ \exp\left(-\int_0^{s_0} k(\epsilon, s)\ ds\right) = I(\epsilon, 0)\ \exp(-\tau(\epsilon, s_0)) \tag{4.7}$$

in which

$$\tau(\epsilon, s) = \int_0^{s} k(\epsilon, s')\ ds' \tag{4.8}$$

represents the *optical depth*.

In order to understand the absorption potential and properties of various materials, it is necessary to treat the nature of the physical interaction processes which give rise to this

absorption effect. In addition, the associated interaction products need to be assessed, since they comprise the conversion products which make up the physical signal at the detector output.

Basically the detection mechanisms for electromagnetic radiation can be divided into two major subclasses: *photo-electric devices* and *thermal devices*.

Photo-electric devices detect radiation by direct interaction of the individual photons with the atomic structure of the material (or with the free atoms in a gas). This can be quantitatively described with the aid of the linear absorption coefficient $k(\epsilon, \lambda, \nu)$ or the cross-section $\sigma(\epsilon, \lambda, \nu)$ as discussed in this section. This interaction of radiation with matter produces parameter changes that can be detected by associated circuitry or interfaces. Physical parameters that can change in these devices due to irradiation comprise resistance, inductance (due to charge generation), voltage and current.

Thermal devices respond to the "heating" effect of the incident radiation field by changing their temperature. This process requires two steps: the radiation field changes the temperature of the absorber and subsequently this temperature change causes or induces some measurable parameter change. The absorption characteristic of a thermal device is normally expressed by the so-called absorptance $\alpha(\lambda)$. Kirchhoff's law for electromagnetic radiation states that in thermodynamic equilibrium the amount of energy absorbed is equal to the amount of energy emitted. Therefore, for all surfaces:

$$\alpha(\lambda) = \mathcal{E}(\lambda) \tag{4.9}$$

with $\mathcal{E}$ the spectral emissivity and $\alpha(\lambda)$ the ratio of the amount of radiation absorbed to the amount of radiation incident monochromatically:

$$\alpha(\lambda) = \frac{(I(\lambda))_{abs}}{(I(\lambda))_{incid}} \tag{4.10}$$

A blackbody has a spectral emissivity $\mathcal{E}(\lambda) = 1$ and therefore absorbs all incident radiation, it can reflect no light and, hence, appears black.

In the following paragraphs the physical processes underlying thermal and photo-electric detection are briefly discussed.

4.2.2 Thermal detection

Thermal sensors are devices where the energy absorbed depends often on the *surface properties* of the material involved. The spectral response is determined by the spectral dependence of the surface absorptance:

$$\alpha(\lambda, T) = \mathcal{E}(\lambda, T) = \frac{I(\lambda, T)_{material}}{I(\lambda, T)_{blackbody}} \tag{4.11}$$

The energy transfer process can be regarded as a conversion of the radiation energy into mechanical energy of lattice vibrations in the target material, i.e. conversion into phonons:

$$\epsilon = h\nu_{rad} \quad \longrightarrow \quad \sum_i (h\nu_s)_i \tag{4.12}$$

in which $h\nu_s$ represents the characteristic phonon energy ($\simeq kT_{material}$). Values of "thermal mass" (= specific heat $\times$ mass) and thermal conductance are basic parameters for a thermal device and determine its response time. Thermal detectors are typically slower responding

devices than photo-electric sensors since their thermal mass must experience a rise and fall of temperature. A large temperature change per unit radiation power requires a small thermal mass or a well-isolated detector. Consequently the heat injection due to the radiation field will not dissipate very fast and the decay time becomes relatively long.

In addition the spectral response for a thermal device is much broader than a typical photo-electric sensor and extends into the far-infrared (up to several hundred micron). Some examples of a thermal sensor that produce a change in electrical parameter are:

Device:		*Physical parameter change*
Bolometer	$\longrightarrow$	resistance
Thermocouple	$\longrightarrow$	voltage
Pyroelectric	$\longrightarrow$	capacitance in ferro-electric material
Super-conductor	$\longrightarrow$	resistance

4.2.3 Photo-electric detection

The photo-electric effect

Consider first photo-electric absorption by free atoms (e.g. gases). The absorption of the photon up to energies of 10 to 100 keV (depending on the Z of the target atoms) takes place through the so-called photo-electric effect. This entails a destructive process in which the incident photon releases an electron from the parent atom:

$$\epsilon = W_e + \frac{1}{2}mv^2 \tag{4.13}$$

with W_e the required ionisation energy. The surplus energy of the photon is converted into kinetic energy of the so-called photo-electron. The atomic cross-section $\sigma_{pe}(\epsilon)$ for this process displays a number of characteristic features (*the absorption edges*) which correspond to the binding energies of the target atom, see figure 4.1, showing the atomic cross-sections for the noble gasses Argon and Xenon and displaying the absorption edges at the L- and K-shell ionisation energies. These absorption features show that the photo-electric effect is, classically speaking, a resonance process. For energies above the K-edge, up to $\epsilon \approx mc^2$, $\sigma_{pe}(\epsilon)$ can be obtained from the Born-approximation:

$$\sigma_{pe}(\epsilon) = 4\sqrt{2}\ \sigma_T\ Z^5\ \alpha^4\ \left(\frac{m_e c^2}{\epsilon}\right)^{7/2} \tag{4.14}$$

in which σ_T is the Thomson cross-section (see equation 2.16), Z is the atomic number of the target material and α is the fine structure constant ($\alpha = 1/137$). The process is strongly dependent on Z ($\sim Z^5$) and on the photon energy ϵ ($\sim \epsilon^{-7/2}$). The Born-approximation is not valid near the absorption edges.

In practise, most detection elements are solids and, apart from the innermost energy levels, the collective properties of the lattice structure has to be taken into account.

Figure 4.2 shows the orbital and energy-level diagram of a single atom in a highly schematic fashion. Figure 4.3c shows the energy-level diagram for a crystal containing several atoms. The innermost levels are so energetic that they normally do not interact. However, the outer levels interact and form a so-called band structure, figure 4.3a,b shows the subdivision of various energy levels as a function of lattice spacing for a hypothetical substance. Two important band structures emerge: the valence band and (directly above it) the conduction

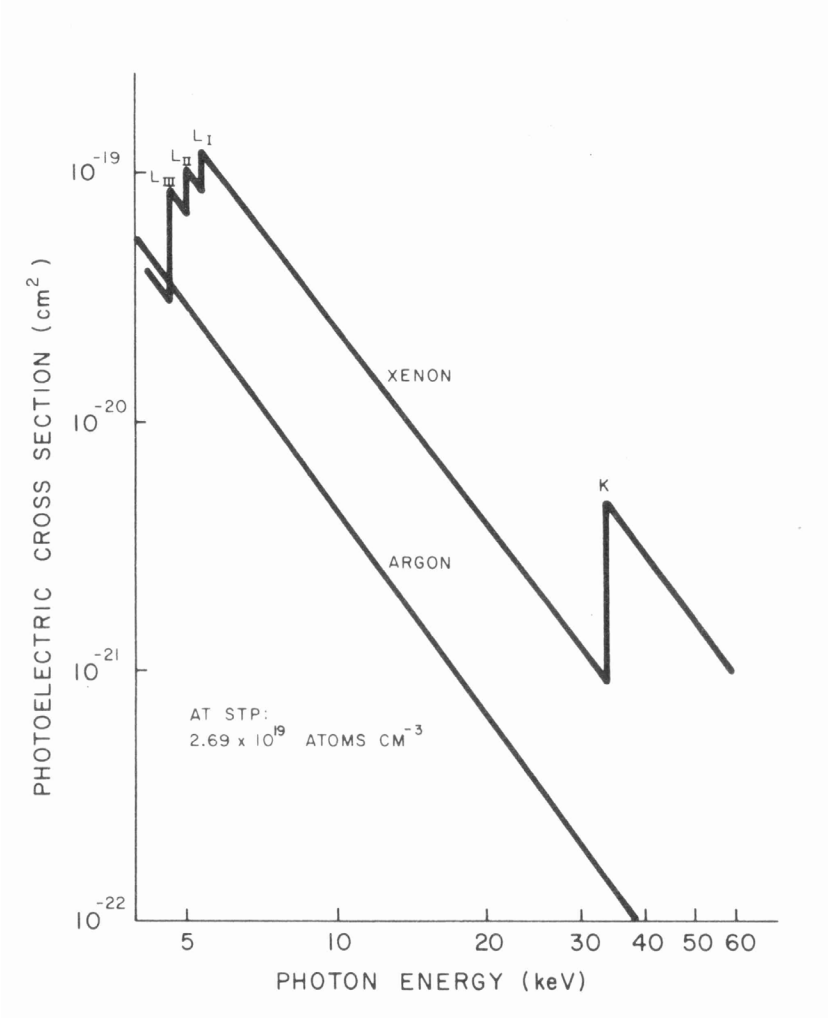

Figure 4.1: *Cross section $\sigma_{pe}(\epsilon)$ as a function of energy.*

band. The valence band represents the group of states containing the valence electrons of the atomic solid and determines the chemical properties. Both bands together determine the electrical properties of the solid. The valence and conduction band may be separated by a forbidden energy band $\Delta E = E_g$, because electrons can not exist in the crystal with these energies.

Metals do not possess an energy gap, semiconductors have energy gaps of the order of 1 eV and insulators of the order of 10 eV. Photons of sufficient energy incident on a semiconductor material may therefore excite electrons from the valence band into the conduction band. In this way free charge carriers are added to the conduction band which raises the materials conductivity proportional to the incident radiation flux (see figure 4.5). The linear absorption coefficient $k(\epsilon)$ for three well-known semiconductor materials, Si, Ge and GaAs, are displayed in figure 4.4, some more of these so-called *intrinsic semiconductors*, including infrared sensitive materials, are listed in table 4.1.

It is clear from the energetics of this process that photons with energies below the bandgap

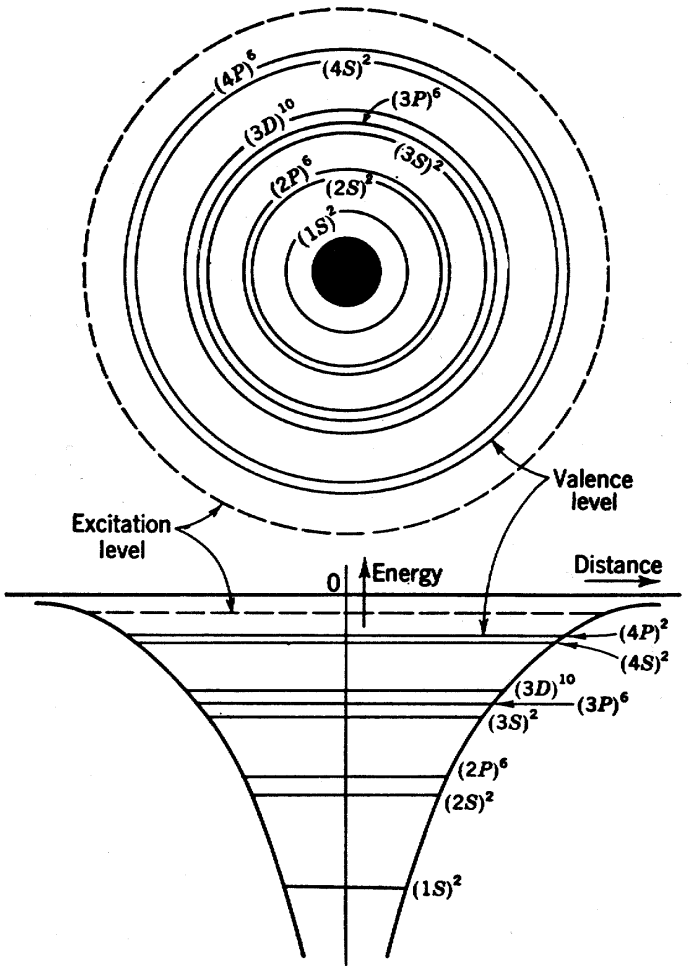

Figure 4.2: *Orbital and energy level diagram of an atom. Only relative positions and energies are shown. Credit Greiner (1961).*

cannot be detected, this manifests itself as a long-wavelength cut-off λ_c in wavelength response:

$$\lambda_c = \frac{1.24}{E_g(\text{in eV})} \quad \mu\text{m} \tag{4.15}$$

To get a longer wavelength response towards the infrared region, a smaller energy gap is needed. By doping the intrinsic semi-conductor material with alien atoms, donor- or acceptor-levels can be introduces in the energy level diagram of the band-structure (see figure 4.6). A donor-level is located just below the conduction band, so photons in the mid- and far-infrared wavelength range can introduce extra electrons in the conduction band. This material is called a *n-type semiconductor*. An acceptor-level corresponds to an energy just above the valence band and can accept an excited electron, leaving a hole in the lower band. This hole acts like a positive charge carrier, just like an electron in the conduction band. This material is called a *p-type semiconductor*. Together these doped materials are called *extrinsic semiconductors* and they need to be cooled to prevent ionisation by thermal excitation due to the ambient temperature field; see table 4.1 for some examples.

The photo-electric effect in solids just described, influences the conductivity (and hence, the resistance) of the material concerned, which can be employed to generate an electrical

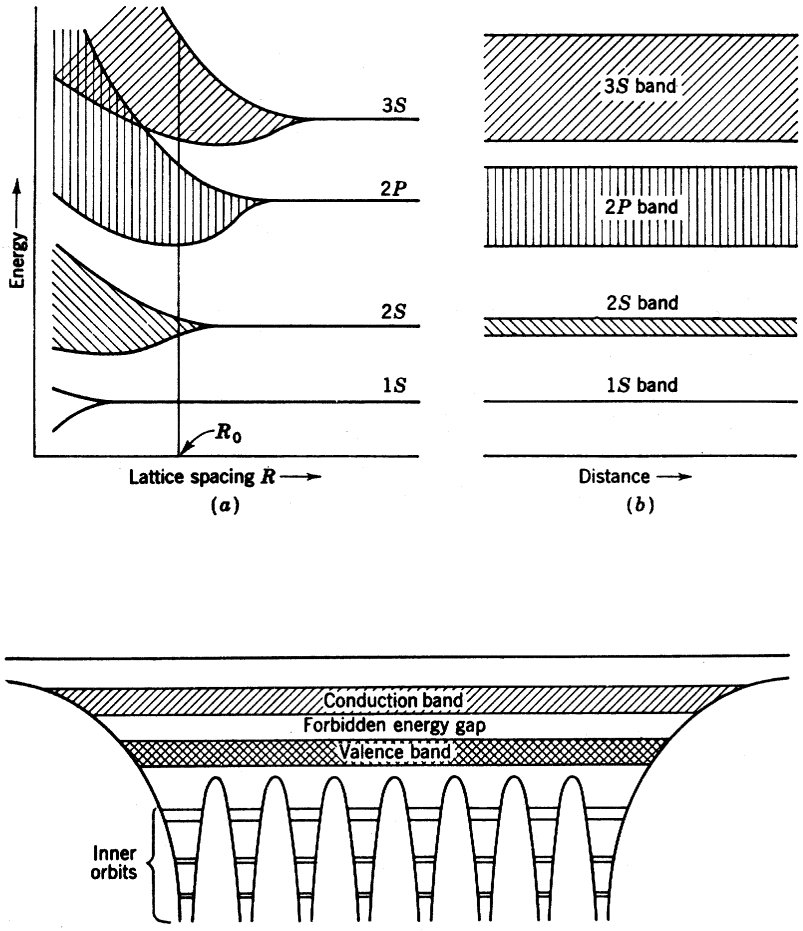

Figure 4.3: *Energy level diagram for a crystal containing several atoms. (a) levels as a function of lattice spacing R. (b) levels for a particular level spacing R_0. (c) (lower plot) conduction and valence band in this crystal. Credit Greiner (1961).*

signal, since the generated charge carriers do not leave the solid. This interaction process is referred to as the *internal* photo-electric effect. emission.

Complementing this interaction process is the *external* photo-electric effect. In this case the radiation-excited electron in the conduction band (metal or semiconductor) physically leaves the detecting material and moves in free space. This is illustrated in figure 4.7, where a so-called photo-cathode is the absorbing medium. The photon is absorbed in the photo-cathode material that has been deposited on an optically transparent substrate. The photo-electric interaction can produce an energetic electron that has sufficient energy to overcome the work-function of the cathode material. The electric potential represented by the work-function is the difference between the electric potential of the conduction band and the outside (=vacuum) electric potential. If the electron is released from the surface it can be captured in an electric field and adds to a current signal. The photo-cathode material should preferably have a high $k(\epsilon)$ combined with a long mean free path for the photo-electron to leave the material (helped, of course, by a low value of the work-function). Table 4.1 lists several photo-cathode materials that are sensitive for optical and near-infrared radiation.

In the case of very energetic radiation, like X-ray and gamma-ray photons, the atomic

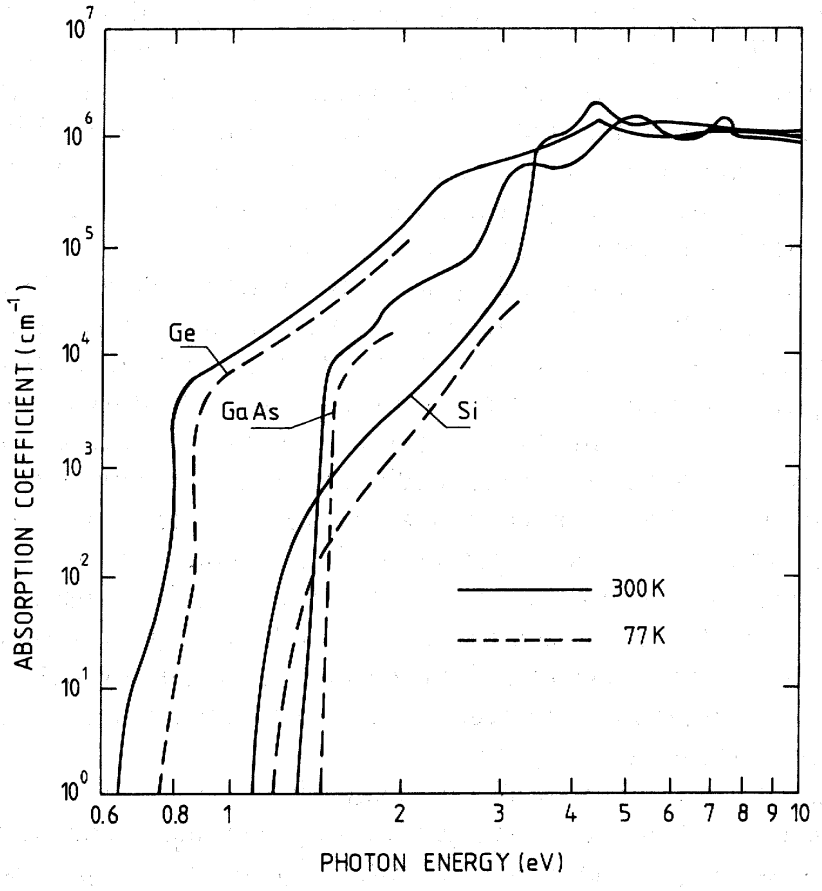

Figure 4.4: *Measured absorption coefficient for three semiconductors: Si, Ge and GaAs, as a function of incident photon energy. Credit Middelhoek & Audet (1989).*

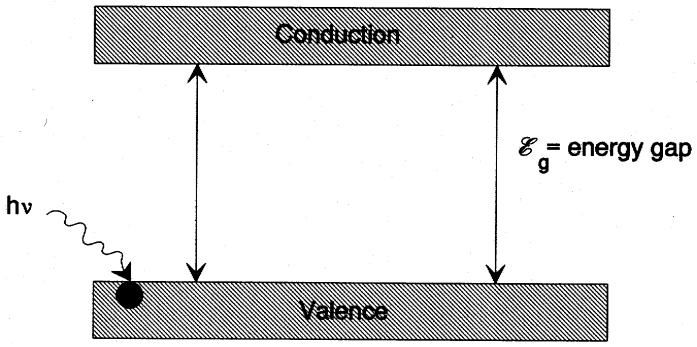

Figure 4.5: *Intrinsic semiconductor energy level diagram. Credit Dereniak & Boreman (1996).*

cross-section is still applicable for solids since the photo-electrons are emitted from the innermost orbits, which are hardly influenced by the atomic lattice structure. Figure 4.8 shows some values of $k(\epsilon)$ for these photon energies, starting from 10 keV, and it also shows that at higher photon energies other interaction mechanisms start to become dominant, i.e. Compton scattering and pair production. These will be shortly discussed in the next sections.

Not all photo-electric interactions need to result in free charge carriers. One alternative is that the photo-electron energy may be quickly thermalised through interaction with the

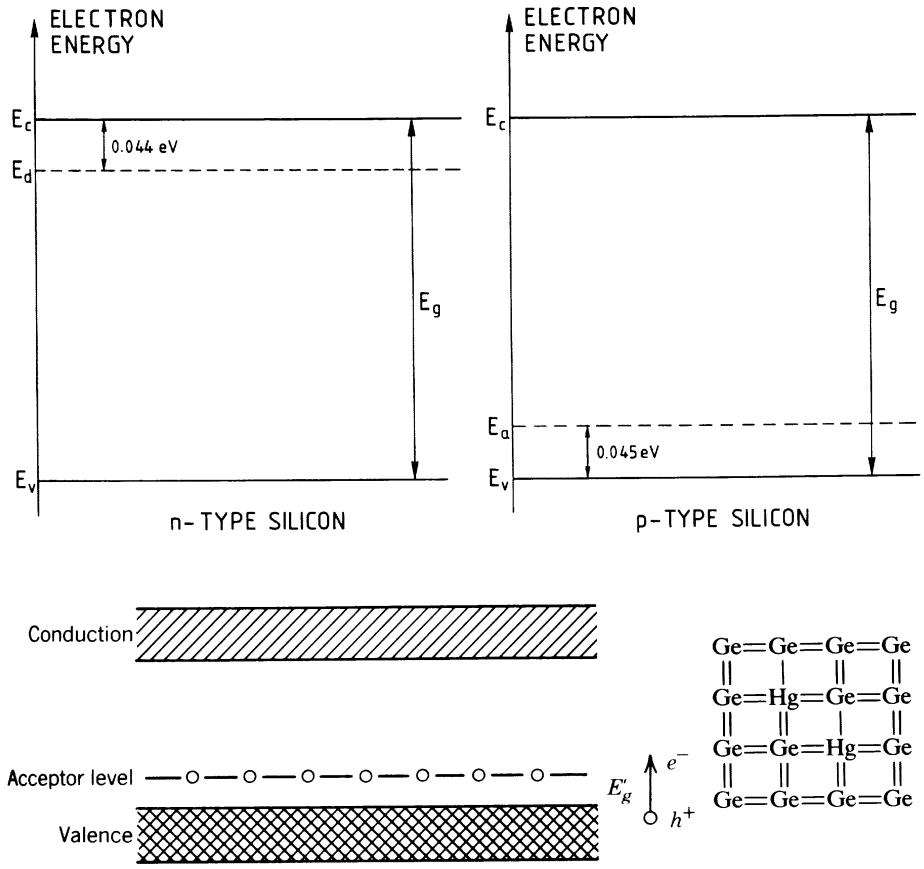

Figure 4.6: *(Above:) Schematic energy level diagram of a n- and p-type silicon semiconductor. Figure taken from Middelhoek & Audet (1989). (Below:) Energy level diagram of a p-type semiconductor with an example of an Ge(Hg) lattice. Credit Dereniak & Crowe (1984).*

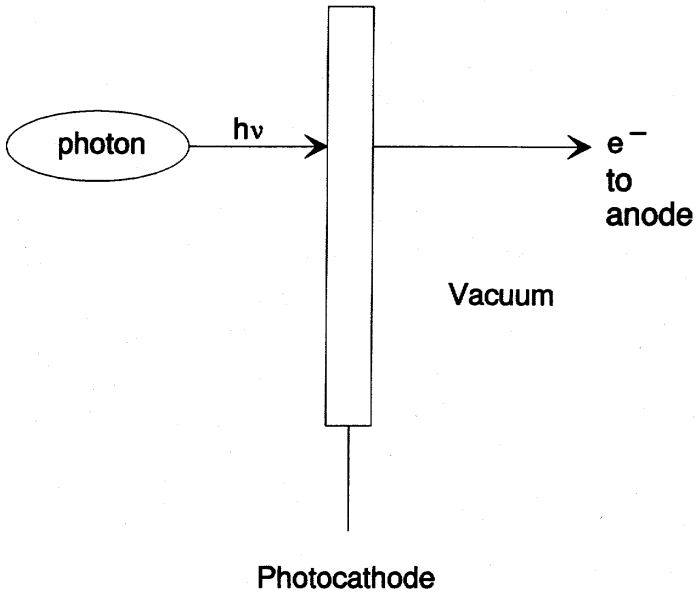

Figure 4.7: *External photo-electric process. Credit Dereniak & Boreman (1996).*

	Material	*Typical efficiency*	λ_c *(μm)*	*Nominal temp. (K)*
Intrinsic semiconductor	CdS	0.50	0.52	300
	CdSe	0.50	0.69	300
	Si	0.50	1.1	300
	Ge	0.50	1.9	300
	PbS	0.50	3.0	300
	PbSe	0.50	5.4	300
	HgCdTe	0.60	25	77
Extrinsic semiconductor	Na_2KSb	0.21	0.36	
	Cs_3Sb	0.16	0.38	
	Na_2KSb-Cs	0.22	0.38	
	K_2CsSb	0.27	0.38	
	Cs_3Sb-O	0.19	0.39	
	CsSb-O	0.23	0.41	
	BiAgO-Cs	0.068	0.42	
	AgOCs	0.004	0.8	
	Si-In	0.40	8	45
	Ge-Hg	0.30	14	4
	Si-Ga	0.40	19	18
	Si-As	0.40	24	4
	Ge-Cu	0.30	27	4
	Si-P	0.40	29	12
	Ge-In	0.30	120	4
Photo-cathode (IR-sensitive)	GaAsP	0.30	0.9	
	Cs-Na-K-Sb	0.20	0.9	
	Ag-O-Cs	0.01	1.1	

Table 4.1: *Cut-off wavelength of some semiconductor and photo-cathode materials.*

crystal lattice, resulting in vibrations and sound waves in the lattice. These waves act like particles and are called phonons and can again be measured as a thermal signal.

Another alternative is the creation of so-called activation centers in inorganic crystals by adding certain impurities that give rise to a number of intermediate energy levels in the forbidden energy gap between the valence and conduction band. De-excitation of electron-hole pairs created by an energetic photo-electron through these intermediate activator levels results in photon production at much lower energies than the original incoming photon. These low energy photons can be in the visible range if the impurities are properly chosen. This optical

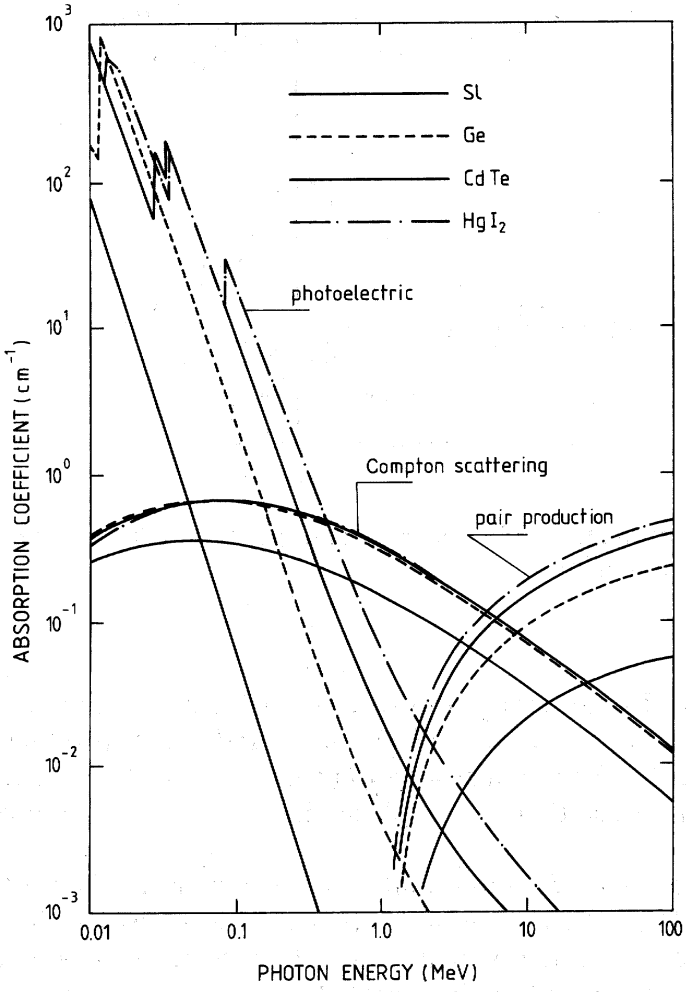

Figure 4.8: *Absorption coefficients as a function of the photon energy for materials used for X-ray and gamma-ray absorption. Compare figure 4.1 and 4.4. Credit Middelhoek & Audet (1989).*

photon emission during de-excitation is called scintillation. If the main solid is transparent for this scintillation light, the light can be detected by a photo-cathode and converted into an electric signal. This is the principle of scintillation sensors. The total energy yielded in the low-energy scintillation light is a measure of the incoming X- or gamma-ray photon energy. Examples of some inorganic scintillators are given in table 4.2, the activating impurities are given in parenthesis.

Compton scattering

This process has already been discussed in Chapter 2. The cross-section $\sigma_c(\epsilon)$ in the extreme relativistic limit ($\epsilon \gg mc^2$) follows from the Klein-Nishina formula (2.20):

$$\sigma_c(\epsilon) = \frac{3}{8}\,\sigma_T\,\frac{mc^2}{\epsilon}\,\left(\ln\frac{2\epsilon}{mc^2} + \frac{1}{2}\right) \tag{4.16}$$

Material	*Wavelength of maximum emission* λ_{max} *(nm)*	*Decay constant* (μs)	*Index of refraction at* λ_{max}
NaI(Tl)	410	0.23	1.85
CsI(Na)	420	0.63	1.84
CsI(Tl)	565	1.0	1.84
^{6}LiI(Eu)	470 – 485	1.4	1.96
ZnS(Ag)	450	0.20	2.36
CaF_2(Eu)	435	0.9	1.44

Table 4.2: *Properties of some inorganic scintillators.*

in which the atomic electrons are considered to be essentially free (W_e negligible). The atomic cross-section for a target material with atomic mass A_m follows simply from:

$$\sigma_c^{A_m}(\epsilon) = \sigma_c(\epsilon) Z \tag{4.17}$$

with Z the atomic number. This process is therefore proportional to Z (compare $\sim Z^5$ for the photo-electric effect). Moreover, since this process is a scattering process, the full detection of the photon-energy requires an interaction cascade: the primary photon is successively down-scattered in energy until it is sufficiently reddened to be captured by the photo-electric effect. Figure 4.8 shows $k(\epsilon)$ for a few commonly used detection materials.

Pair production

Pair production is a typical quantum theoretical process. It can be envisaged as a photo-electric effect with an electron of negative energy in the Dirac-electron sea (virtual electron). The result of this interaction causes the disappearance of the photon (destructive) resulting in an electron-positron pair (charge conservation), both having a positive energy.

The materialisation process can only be initiated in the strong electric field of an atomic nucleus, the latter takes care of the momentum balance, but gains negligible energy. The energy balance can therefore be written as:

$$\epsilon = 2mc^2 + (E_{kin})_{e^+} + (E_{kin})_{e^-} \tag{4.18}$$

The theoretical threshold energy is $\epsilon = 2mc^2 = 1.02$ MeV, in practise this turns out to be considerably higher before any measurable efficiency becomes apparent. For energetic gamma-rays (≥ 70 MeV in hydrogen and ≥ 24 MeV in Fe) the cross-section for this process reduces to

$$\sigma_p(\epsilon) = \frac{4}{137}\, Z\,(Z+1)\, r_0^2\, \left(\frac{7}{9} \ln \frac{183}{Z^{1/3}}\right) \tag{4.19}$$

with r_0 the classical electron radius. For the higher Z elements pair production is thus proportional to Z^2 and independent of the incident photon energy ϵ. In practise the mass-

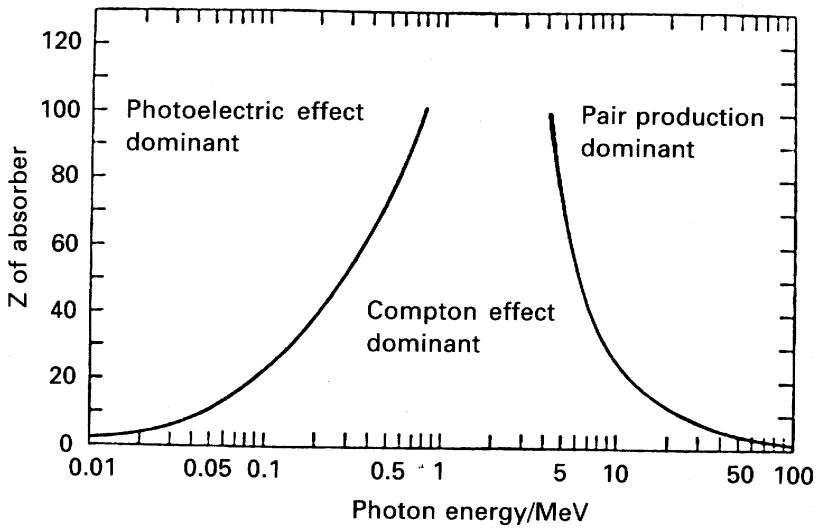

Figure 4.9: *The relative importance of different forms of energy loss mechanisms for γ-rays as a function of photon energy and atomic number. Credit Longair (1992).*

absorption coefficient is always used:

$$\kappa_p(\epsilon) = \frac{N_A}{A_m}\,(\sigma_p(\epsilon) = \frac{7}{9}\,X_0^{-1} \tag{4.20}$$

with

$$X_0 = \left(\frac{4}{137}\,\frac{N_A}{A_m}\,Z\,(Z+1)\,r_0^2\,\ln\frac{183}{Z^{1/3}}\right)^{-1} \tag{4.21}$$

As can be seen from this equation, X_0 only depends on the material properties under consideration and not on the photon energy ϵ. X_0 is called the *radiation length* in units of kg·m^{-2}, and is a standard parameter in high-energy γ-ray astrophysics. It really is a mass absorption coefficient with the same units as a surface density, but after multiplication with the density it becomes a length scale.

The radiation length is then used to characterise the absorbing medium: the attenuation is given by:

$$I(x) = I(0)\exp\left(-\frac{7}{9}\,\frac{x}{X_0}\right) \tag{4.22}$$

Numerical values for largely different Z are

$X_0 \simeq 6$ g·cm^{-2}	$\longrightarrow$	5.3 mm	for a lead slab
$X_0 \simeq 62$ g·cm^{-2}	$\longrightarrow$	7 km	for hydrogen at 1 bar

Figure 4.9 summarizes the relative importance of the three major types of photo-electric radiation absorption. The solid lines show the values of Z and ϵ for which the two neighboring effects are just equal.

Reflection and refraction

In the previous sections the physical principles of thermal and photo-electric absorption have been described. If a radiation beam arrives at the interface between two media with refractive

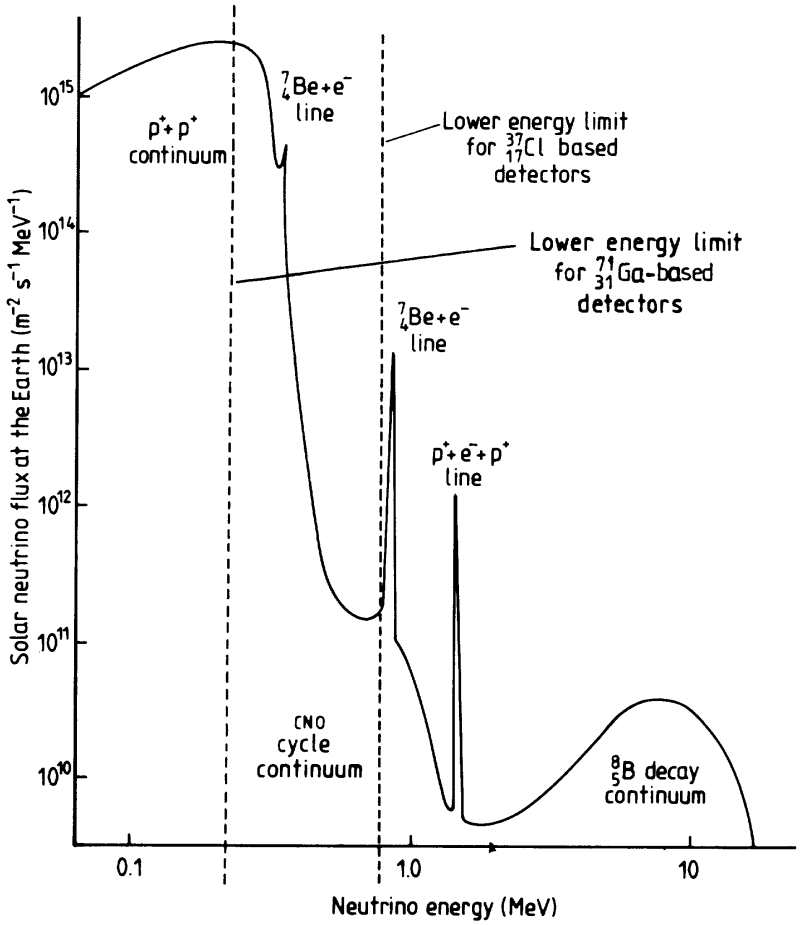

Figure 4.10: *Theoretical solar neutrino spectrum. Credit Kitchin (1998).*

indices n_i and n_t, Fresnel's laws apply giving the relation between the intensity of the incident, the reflected and the transmitted (=refracted) beam. This is relevant for low energy photons and plays an important role in the overall efficiency of the detection process since reflection losses at the interface may be substantial. Since Fresnel's laws are extensively treated in any standard textbook on optics, this subject will not be elaborated in this course.

4.3 Neutrino detection

The mean free path for neutrino detection

$$\lambda(\epsilon_\nu) = \frac{1}{\sigma(\epsilon_\nu)N} \tag{4.23}$$

is extremely long due to the exceedingly small value of the nuclear cross-section $\sigma(\epsilon_\nu)$ for the interaction process. For the highest electron-neutrino energies, $\sigma(\epsilon_{\nu_e})$ for capture in chlorine amounts to $\approx 10^{-46}$ m^2, yielding a $\lambda \approx 1$ parsec in pure $^{37}_{17}$Cl.

The neutrino capture reaction in chlorine can be written as:

$$\nu_e \; + \; {}^{37}_{17}\mathrm{Cl} \quad \longrightarrow \quad {}^{37}_{18}\mathrm{Ar} \; + \; e^- \tag{4.24}$$

The threshold energy for this reaction to occur is $\epsilon_{\nu_e} = 0.814$ MeV. This is greater than the maximum energy of the electron neutrinos generated in the main p-p chain in stellar interiors, but smaller than that of those produced in the decay of ^{8}B, see figure 4.10.

In the deep mine of the Home-state Gold Mining Company (South Dakota), the radioactive ^{37}Ar is generated in about 600 tons of perchloro-ethylene C_2Cl_4. The incoming electron neutrinos release the ^{37}Ar from the molecule and they can be flushed out of the fluid by passing He through the volume. The ^{37}Ar decays with a half life of 34.8 days by capturing one of the inner orbital electrons (electron capture, EC). The photon which is released by this process is used to expel one of the outer electrons and ionise the atom. This free electron is called the Auger electron and has a fixed energy of 2.82 keV:

$$^{37}_{18}\mathrm{Ar} \;+\; \mathrm{EC} \;\longrightarrow\; ^{37}_{17}\mathrm{Cl}^{+} \;+\; \mathrm{e}^{-}\;(2.82\mathrm{keV}) \tag{4.25}$$

This low-energy electron is detected in a sensitive gas proportional counter.

The Kamiokande experiment (Mitsui Mining Company in Japan) uses an active volume of 3000 tons of very pure water. The neutrino produces an energetic electron by scattering:

$$\nu_{\mathrm{x}} \;+\; \mathrm{e} \;\longrightarrow\; \nu'_{\mathrm{x}} \;+\; \mathrm{e}' \tag{4.26}$$

This electron will move with a speed greater than the local speed of light. Due to the abrupt change of the electric field the surrounding atoms will emit radiation. This so-called Čerenkov radiation can be detected and also provides some directionality information due to the forward beaming of the cone of Čerenkov emission. As indicated with ν_x, this technique has also some sensitivity for the detection of ν_μ and ν_τ. The scattering probabilities are:

$$p_s(\nu_\mu) \approx p_s(\nu_\tau) \approx \frac{1}{7}\, p_s(\nu_e) \tag{4.27}$$

Two other large neutrino experiments entail the SAGE (Soviet-American Gallium Experiment) and the GALLEX (Gallium Experiment) located in the Gran Sasso Underground Laboratory in the Italian Appennino Mountains, which comprises a collaboration between Europe, the United States and Israel. These experiments make use of the reaction:

$$\nu_{\mathrm{e}} \;+\; ^{71}_{31}\mathrm{Ga} \;\longrightarrow\; ^{71}_{32}\mathrm{Ge} \;+\; \mathrm{e}^{-} \tag{4.28}$$

The threshold energy for this reaction is approximately 0.233 MeV which allows the large flux of low energy neutrinos emitted in the p-p process to be detected.

GALLEX employs 30 tonnes of gallium used in an aqueous solution of gallium chloride and hydrochloric acid. The ^{71}Ge decays with a half lifetime of 11.4 days by electron capture:

$$^{71}_{32}\mathrm{Ge} \;+\; \mathrm{EC} \;\longrightarrow\; ^{71}_{31}\mathrm{Ga}^{+} \;+\; \mathrm{e}^{-}\;(10.37\ \mathrm{keV}) \tag{4.29}$$

The Auger electron is again measured in a sensitive gas-filled radiation sensor.

SAGE uses 60 tonnes of solid gallium, located in the Caucasus mountains (Baksan Valley). Heating melts the gallium and flushing with hydrochloric acid brings out the volatile $GeCl_4$. No firm results are yet available.

Both the Kamiokande experiment in Japan and the IMB detector in the United States have seen a neutrino pulse from the supernova explosion in the Large Magellanic Cloud SN1987A on February 23th, 1987. During the collapse of the core of the progenitor star, about 10^{58} neutrinos were emitted. Of these neutrinos 20 were detected in the water detectors mentioned above, see figure below. Precisely on that day there were problems with the Japanese electricity net, due to which the clocks were not completely synchronised with Universal Time. Hence, the arrival times of the neutrinos detected with Kamiokande have an uncertainty of about 60 seconds.
The IMB detected the first neutrinos at 07:35:41. At 09:22 Jones did not observe any new star, at 10:38 the first optical picture of the supernova was made by Garrad and McNaught, but they did not develop their film immediately. Only in the following night Shelton and Duhalde were the first to see a supernova in 383 years with their naked eye.

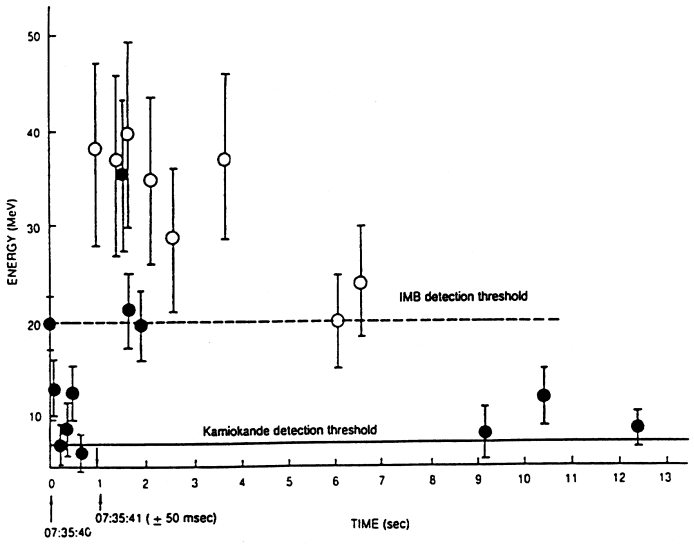

An important recent development has been the completion and operation of the Sudbury Neutrino Observatory (SNO)in Ontario, Canada. This neutrino detector has been built two kilometers underground, the detection principle is based on neutrino interaction with the Deuterium nucleus in heavy water. Three reactions are possible:

$$\nu_e + {}^2_1H \longrightarrow p + p + e^- \tag{4.30}$$

$$\nu_x + {}^2_1H \longrightarrow p + n + \nu_x \tag{4.31}$$

$$\nu_x + e^- \longrightarrow \nu_x + e^- \tag{4.32}$$

The neutrino absorption in the first reaction only applies to electron-neutrino's, the other reactions, i.e. the deuteron break-up and energetic electron scatter respectivily, apply to any type of neutrino (ν_x). In the deuteron break-up reaction, the nucleus splits into its constituent components, i.e. a proton and a neutron, the neutron eventually recombines with another

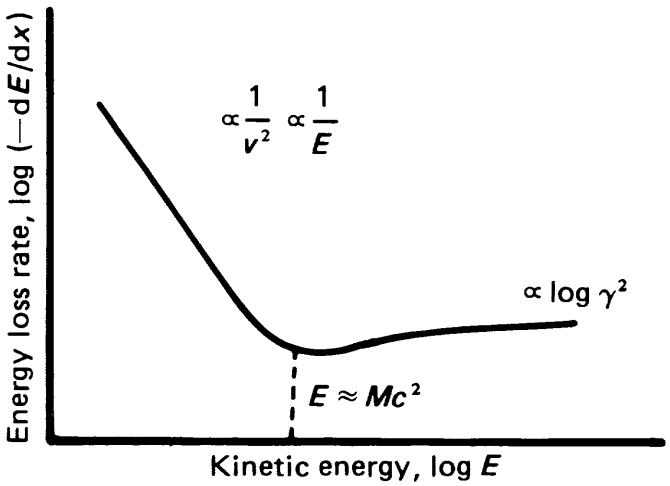

Figure 4.11: *Energy loss rate due to ionisation losses for cosmic-ray particles. Credit Longair (1992).*

deuteron, releasing a gamma-ray photon that , in turn, knocks-on an energetic electron. The energetic electrons are all detected by the emission of Čerenkov light. The deuteron break-up reaction measures the total flux of all neutrino flavours above a threshold energy of ≈ 2.2 MeV, consequently the detector is sensitive to the ^{8}B solar neutrino flux (see figure 4.10). The detector comprises a volume of 1000 tons of heavy water, viewed by more than 9500 photomultiplier tubes, held on an 18-meter geodesic sphere, that measure the emitted Čerenkov light cones. The different reactions can be separated by the different energy distributions and emission geometries of the energetic electrons. Recently, 2 kilotons of NaCl (salt) was added to enhance the efficiency of neutron-capture after the deuteron break-up reaction.
The most recent results of this instrument have convincingly demonstrated that solar neutrino's indeed change "flavour" on there journey from the solar interior to the earth, i.e. that phase transitions occur between ν_e, ν_μ and ν_τ neutrino's. This is not in agreement with "the standard model" in physics, and implies that neutrino's have at least some mass. This result also solves the almost 30 years standing problem of the so-called *deficit* in the solar neutrino flux, namely that the number of electron neutrino's observed appeared to be only one-third to one-half of the flux computed on the basis of standard stellar nuclear fusion models.
The estimated flux density of electron neutrino's is $(1.59 \pm 0.08)\,10^6$ cm^{-2}s^{-1}, the total neutrino flux density amounts to $(5.21 \pm 0.27)\,10^6$ cm^{-2}s^{-1}. The latter value is very close to the flux density derived from current models of stellar evolution.

4.4 Cosmic-ray detection

Cosmic-ray particles lose energy by ionisation when traversing matter. The ionisation loss per unit path-length is given by relativistic quantum theory and is known as the Bethe-Bloch formula:

$$-\frac{dE}{dx} = -\frac{dE_{kin}}{dx} = \frac{Z^2 q^4 n Z_0}{4\pi\epsilon_0^2 m_e v^2}\left[\ln\left(\frac{2\gamma^2 m_e v^2}{\bar{I}}\right) - \frac{v^2}{c^2}\right] = Z^2 n Z_0 f(v) \qquad (4.33)$$

with Zq the charge of the cosmic-ray particle under consideration, n the atomic density of the target material, Z_0 its atomic number, $\bar{I}$ the average ionisation potential and v the particle

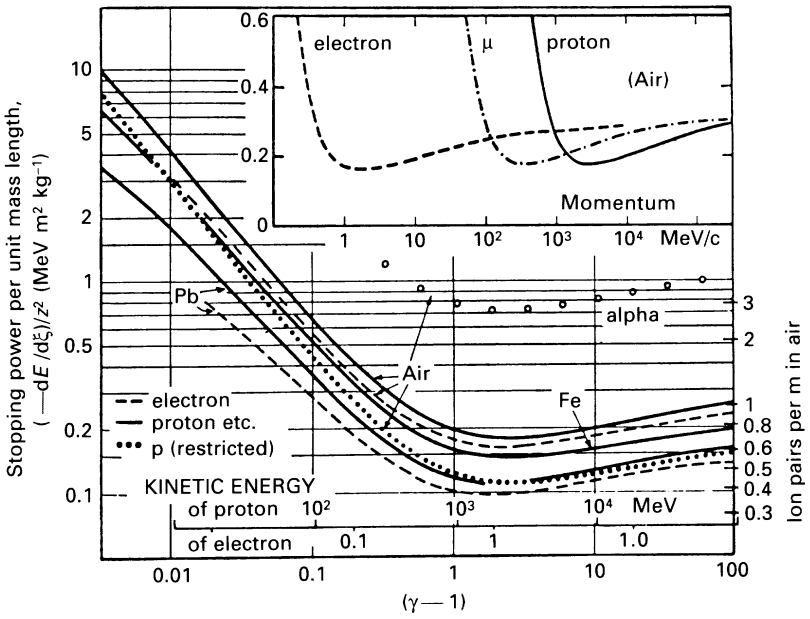

Figure 4.12: *Stopping power per unit mass length in various materials as a function of the Lorentz factor γ, kinetic energy and momentum (inset). Credit Longair (1992).*

velocity. The formula indicates that the energy loss depends only on the velocity of the particle and on its charge, given a medium characterised by nZ_0. The velocity (or energy) dependence is shown in figure 4.11. Up to velocity $v \approx c$ or kinetic energy $E_{kin} \approx A_m m_p c^2$ the ionisation loss decreases as v^{-2} or E_{kin}^{-1}. For energies around $A_m m_p c^2$ there is a minimum in the ionisation loss: a particle with this kinetic energy is designated as a *minimum ionising* particle. At higher energies the ionisation loss slowly increases again proportional to $\ln(\gamma^2)$.

The quantity dE/dx is often referred to as the *stopping power* of the material. This power can also be expressed in terms of the mass per unit area traversed by the cosmic-ray particle (equivalent to the mass-absorption coefficient for electromagnetic radiation $\kappa(\epsilon)$. With $\xi = \rho x$ (in kg m^{-2}):

$$-\frac{dE_{kin}}{d\xi} = -\frac{dE_{kin}}{dx}\,\frac{dx}{d\xi} = \frac{1}{nA_0 m_p}\,Z^2 nZ_0 f(v) = Z^2 f(v)\frac{Z_0}{A_0 m_p} \tag{4.34}$$

The ratio $Z_0/A_0 m_p$ is rather insensitive to Z for all stable elements, it varies from $1/(2m_p)$ for light elements to $1/(2.4m_p)$ for uranium. Thus, the only variation of the energy loss from element to element is the variation in $\bar{I}$. Figure 4.12 shows $-dE/d\xi$ as a function of kinetic energy per nucleon (expressed in terms of $\gamma - 1$, see equation 2.59) for singly charged (protons and electrons) and doubly charged (He-nuclei) particles for several target materials. Despite the wide range of values of $\bar{I}$ for those materials, it can be seen that the curves lie remarkably close together for singly charged particles, this is due to the logarithmic dependence on $\bar{I}$. This means that the quantity $(dE_{kin}/d\xi)/Z^2$ is almost constant and if the energy loss $dE_{kin}/d\xi$ is measured as a function of the kinetic energy E_{kin} of the particle, the charge Z (the only variable left) can be measured. Moreover, the minimum ionisation loss occurs at a Lorentz-factor $\gamma \approx 2$ and can be well approximated for any species by $0.2Z^2$ MeV (kg m^{-2})$^{-1}$. If this energy loss is measured the relativistic movement of the particle is ascertained.

In the astrophysics of the origin and propagation of cosmic-rays, the *isotopic abundances* are of fundamental importance. The differences between isotopes of the same species only

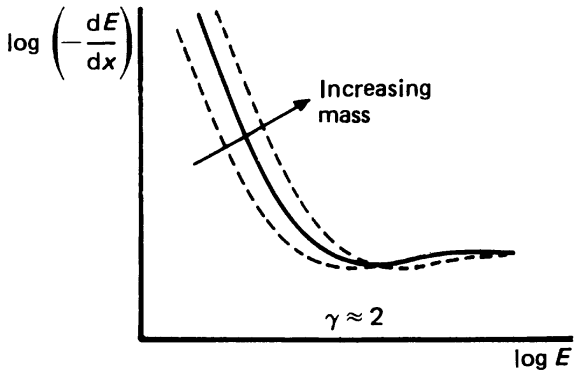

Figure 4.13: *Energy loss rate as a function of kinetic energy and isotope mass. Credit Longair (1992).*

becomes apparent if the *total* kinetic energy of the particles is measured. The ionisation loss $-dE/d\xi$ is independent of the total particle mass $A_m m_p$, but the total kinetic energy $E_{kin} = (\gamma - 1)A_m m_p c^2$ depends linearly on A_m. Isotopes of the same element can therefore be distinguished in the $dE/d\xi$ versus E_{kin} diagram by a slight displacement of the curves for ionisation loss relative to one another. This is schematically shown in figure 4.13.

Chapter 5

Characterization of instrumental response

5.1 Characteristic parameters

Characterization of the performance and response of a physical measurement system can be achieved by considering a multidimensional parameter space, in which each coordinate axis relates to a specific instrument parameter that has a major influence on the quality of the measurement. For astrophysical observations these parameters comprise, among others, bandwidth, field of view, precision and resolution, limiting sensitivity.

In the following paragraphs a brief description of these parameters is given. It should be kept in mind, however, that a certain "bandwidth" in the definitions of these parameters is inevitable and due account must be taken of their exact meaning in a particular observational context.

5.1.1 Bandwidth (symbol: $\lambda\lambda$, $\nu\nu$, or $\epsilon\epsilon$)

The *bandwidth*, or rather *spectral bandwidth*, is defined as the wavelength (or frequency, or energy) interval over which the instrument has adequate detection efficiency, i.e. over which it is observationally employed. The long and short wavelength cut-offs are derived from the wavelength dependent detection efficiency, which is governed by the physical interaction process (see chapter 4). The precise criteria for choosing the cut-off values are mostly rather arbitrary, e.g. cut-off is defined at 50 % or 10 % of the value of maximum efficiency in the bandpass.

5.1.2 Field of view (FOV, symbol: Ω_{FOV})

The *field of view* is defined as the solid angle subtended on the sky by the selected telescope configuration. If the effective area of the telescope is a continuously declining function of the off-axis (optical axis) angle, the choice of the effective FOV is somewhat arbitrary (like in the case of spectral bandwidth), e.g. decline to half the maximum sensitive area (FOV at Full Width at Half Maximum (FWHM)) or to zero sensitive area (FOV at Full Width at Zero Response (FWZR)). The effective FOV is also dependent on the angular resolution which is required for an observation: due to the potential decline of the image quality with off-axis angle not the whole field of view may qualify for a particular observation.

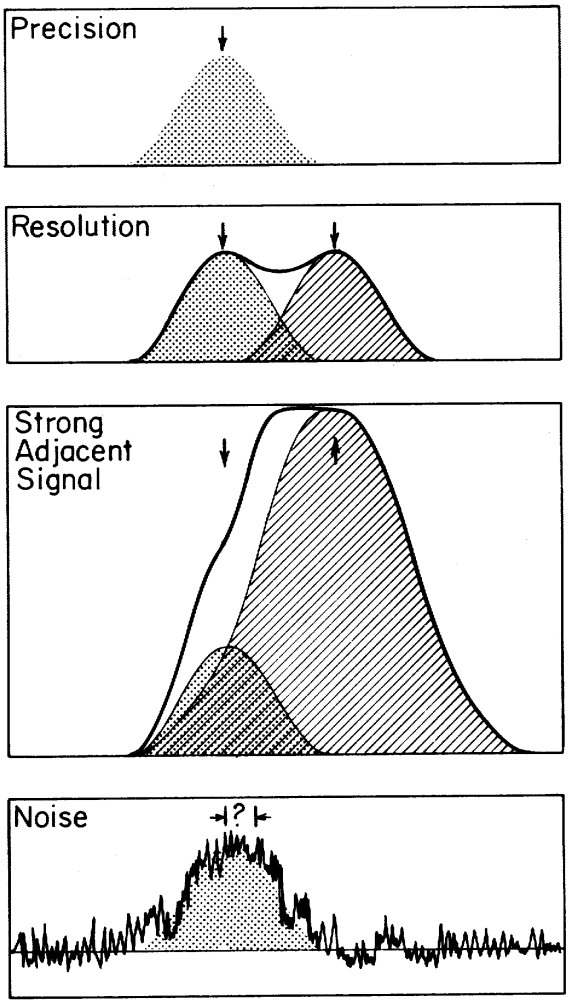

Figure 5.1: *Precision and resolution. The top panel shows that precision is the accuracy with which the centroid of a point (line) spread function can be determined. The panel below shows that the resolution is the interval which two signals of equal strength should be apart to be recognised separately. It is harder to resolve a weak signal adjacent to a strong one (panel below). The bottom panel shows the deterioration of precision in the presence of noise. Credit Harwitt (1984).*

5.1.3 Precision and resolution

First of all, it is important to make a proper distinction between precision and resolution.

Precision

Precision represents the accuracy with which the exact value of a certain quantity can be established. In astrometry precision reflects the ability to accurately measure the position of a star, in spectroscopy precision reflects the ability to accurately pin down the exact wavelength (or frequency, or energy) of a spectral line. The precision of which an instrument is capable may substantially exceed its resolution.

For example: a point source of radiation. The image is blurred by the finite angular

resolution of the telescope, however if this blur is more or less symmetical in shape, the centre of the image can be determined with substantially higher precision than the spot size (see figure 5.1). The ultimate positional accuracy will be governed by the brightness of the spot with respect to the sky background, by instrumental noise sources and by a potential off-set between the measured position and the true position as a result of systematic errors. An example of such a systematic error is the misalignment between the telescope axis and the attitude reference system in a space-based astronomical observatory. The optical axis of the star sensors provide the attitude information and consequently the pointing position on the sky and may be slightly misaligned with the main telescope axis due to thermal gradients in the spacecraft. Of course, this can be calibrated on celestial sources visible in both the main telescope and the optical reference sensors, but presumably not always. Consequently, for high absolute position accuracies, this "bias" error may be non-negligible compared to the statistical spread in the centroid determination of the point source image. The final accuracy to which a position can be derived is sometimes referred to as *position resolution*, not to be confused with angular resolution (see later).

Suppose that the measurements of the stochastic variable X are normally distributed about the true value μ with width parameter σ_X. N independent measurements of X are done and the average is calculated:

$$\bar{X} = \frac{X_1 + \cdots + X_N}{N} \tag{5.1}$$

The standard deviation in the mean is:

$$\begin{aligned} \sigma_{\bar{X}} &= \sqrt{\left(\frac{\partial \bar{X}}{\partial X_1}\,\sigma_{X_1}\right)^2 + \cdots + \left(\frac{\partial \bar{X}}{\partial X_N}\,\sigma_{X_N}\right)^2} \\ &= \sqrt{\left(\frac{1}{N}\,\sigma_X\right)^2 + \cdots + \left(\frac{1}{N}\,\sigma_X\right)^2} \\ &= \frac{\sigma_X}{\sqrt{N}} \end{aligned} \tag{5.2}$$

So the width of the Gaussian curve will reduce by the square root of the number of measurements, which is shown in the following figure for the case of $N = 10$ (Credit Taylor (1982)):

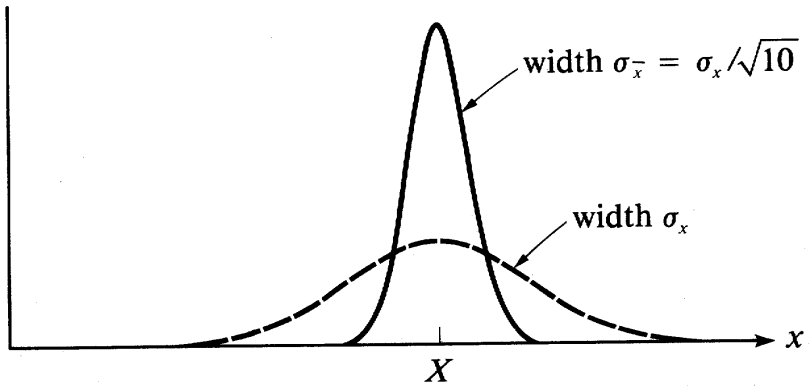

Another example is the timing precision (symbol: $\Delta t_{abs} = t_{abs} - t_{observatory}$), which equals the difference between the measured time and true time. The absolute timing accuracy is particularly important for synchronisation of periodic phenomena over time series with repeated interupts (satellite data) or over different observations. For example in pulsar observations, the period of a pulsar (and other parameters like period derivative or orbital period and orbital period derivative in case of a binary) can be determined to a much higher precision, when two observations at different times are synchronised: i.e. the exact number of pulse periods between the two observations should be known. From the time of arrival of the pulse at the first observation and the predicted period (and period derivative etc.) a prediction is made of the time of arrival of the pulses in the second observation. From the deviation of the measured time of arrival a better value of the period (and period derivative etc.) can be determined. (The absolute time of an observation is usually determined by comparing the observatory maser clock with a GPS system (Global Positioning System) which is locked to Univeral Time (UT) determined by the world's best atomic clocks.)

Resolution

Resolution (or *resolving power*) represents the capability of measuring the separation between two closely spaced features, e.g. two spectral lines or two point like radiation sources. The following resolutions are commonly used in astrophysical data:

- *Angular resolution* (symbol: $\Delta\theta$)
  This is defined as the minimum angular separation needed between two equally bright point sources to ensure that they can be individually just separated ("resolved").

  If an angle of $\Delta\theta$ radians can just be resolved, the angular resolving power is

$$R_\theta = \frac{1}{\Delta\theta} \tag{5.3}$$

- *Spectral resolution* (symbol: $\Delta\lambda, \Delta\nu$ or $\Delta\epsilon$)
  This is defined as the separation in wavelength (or frequency, or energy) between two spectral lines of equal intensity, that is just large enough to resolve the lines individually.

  The spectral resolving power is the ratio of the wavelength λ at which the observation is carried out, to the wavelength difference $\Delta\lambda$ which can just be resolved:

$$R_S = \frac{\lambda}{\Delta\lambda} = \frac{\nu}{\Delta\nu} = \frac{\epsilon}{\Delta\epsilon} \tag{5.4}$$

- *Charge and mass resolution* (symbol: ΔZ and ΔA)
  These characteristic parameters are relevant for the measurement of the composition of a particle beam (e.g. cosmic-rays). It is defined as the fractional charge and mass which can just be separated by a particle telescope.

  The charge and mass resolving power is the ratio of the charge Z, mass A, which is being measured, to the charge difference ΔZ, mass difference ΔA, which can be just resolved:

$$R_Z = \frac{Z}{\Delta Z} \tag{5.5}$$

$$R_A = \frac{A}{\Delta A} \tag{5.6}$$

- *Temporal resolution* (symbol: Δt)
  This parameter can be defined as representing the minimum time interval between two consecutive samples of a realisation of a stochastic process for which these samples can be regarded as uncorrelated (independent) at the output of the measuring device.

It is important to realise that the characteristic resolution parameters defined above, apply to closely spaced features of comparable strength. If, for instance, a faint star lies very close to a brighter companion, or a faint spectral line lies near a far brighter spectral feature, the two may not be separable with a given resolution, even though a pair of equally bright stars or spectral lines would be easily resolved at the same separation.

5.1.4 Limiting sensitivity [symbol: $(F(\lambda, \nu, \epsilon)_{min}$]

The limiting sensitivity achievable with a specific observation facility is defined as the minimum value of the monochromatic flux density arising from a celestial point source, that can be detected significantly over a certain measuring period T in a predefined wavelength (frequency, energy) interval.

This parameter is a function of the effective telescope area A_{eff}, integration time T and angular resolution $\Delta\theta$, moreover it may strongly depend on sky position (background light) and instrumental noise (potentially variable). If the nature of the radiation source is truely diffuse in origin, like a cosmic-ray beam incident on a particle telescope, the collecting power of the instrument is normally related to the so-called *geometry factor* or *grasp*. This parameter is defined as the telescope effective area integrated over the FOV of the telescope:

$$GF = \int_{\Omega_{FOV}} A_{eff}\ d\Omega \tag{5.7}$$

Derivation of expressions for the limiting sensitivity will be discussed in some detail in chapter 6.

5.1.5 Polarisation sensitivity (symbol: Π_{min})

The information carried by the polarisation of electromagnetic radiation is important, since it characterizes the physical conditions of the emission region. The polarisation is defined by using four so-called *Stokes parameters*. The detection system may only be sensitive to one polarisation component (such as a radio dipole antenna) and the telescope (optics, waveguides) may potentially alter it. The polarisation sensitivity is therefore defined as the accuracy to which the Stokes parameters can be measured.

Consider a monochromatic wave. This wave is always fully elliptically polarised and can be seen as a superposition of two orthogonal linearly polarised waves. In the following figure (taken from Rohlfs (1986)) the electric vector is drawn. ξ and η are the major and the minor axes of the ellipse, x and y are the directions of the dipole receivers.

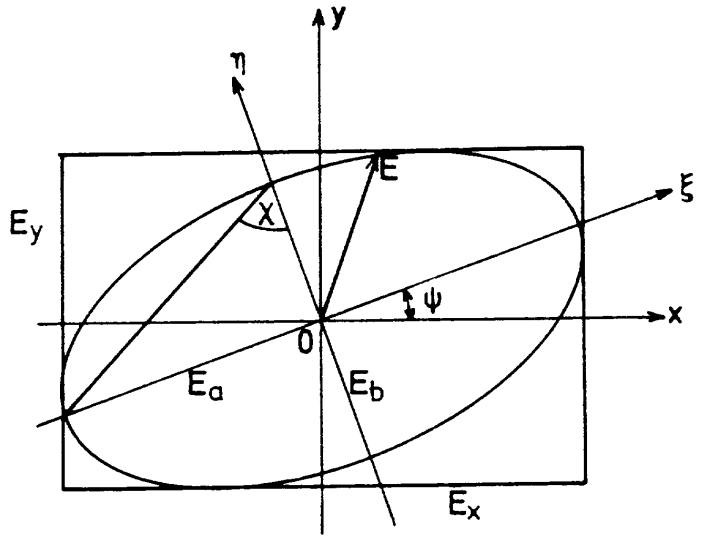

E_x and E_y are the observables. They are oscillating with the same frequency ν but with a phase difference δ. If $\delta > 0$ we call the wave right-handed polarised.
But in general the major axis ξ and the minor axes η of the ellipse do not coincide with the x- and y-dipoles of the receiver. The relation between the two coordinate systems is given by a simple linear rotation

$$\begin{aligned} E_\xi = E_a \cos(\tau + \delta) &= E_x \cos\psi + E_y \sin\psi \\ E_\eta = E_b \sin(\tau + \delta) &= -E_x \sin\psi + E_y \cos\psi \qquad (0 \le \psi \le \pi) \end{aligned} \tag{5.8}$$

in which ψ is the angle over which the ξ-axis is rotated with respect to the x-axis. Another angle χ can now be defined:

$$\tan\chi = \frac{E_a}{E_b} \qquad (0 \le \chi \le \frac{1}{2}\pi) \tag{5.9}$$

In 1892 Poincaré showed that there exists a one-to-one relation between polarisation states of a wave and points on a sphere with radius $E_a^2 + E_b^2$. The angles 2ψ and 2χ can be seen as the longitude and the lattitude of the sphere. The three coordinates of each point are the Stokes parameters Q, U and V, see the following figure (taken from Rohlfs (1986)).

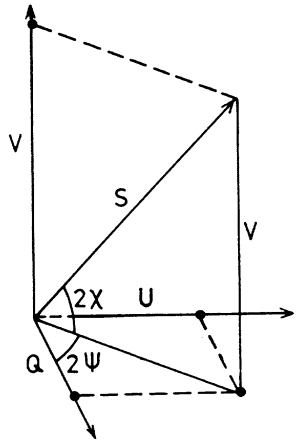

Points on the equator represents linear polarised waves ($V = 0$), the north pole represents a right-circular polarised wave and the south pole a left-circular. The Stokes parameters are defined as

$$I = E_a^2 + E_b^2 \tag{5.10}$$
$$Q = I \cos 2\psi \cos 2\chi \tag{5.11}$$
$$U = I \sin 2\psi \cos 2\chi \tag{5.12}$$
$$V = I \sin 2\chi \tag{5.13}$$

By definition a monochromatic wave is fully polarised:

$$I^2 = Q^2 + U^2 + V^2 \tag{5.14}$$

Now the Stokes parameters can be expressed in the observable parameters E_1, E_2 and δ:

$$I = E_1^2 + E_2^2 \tag{5.15}$$
$$Q = E_1^2 - E_2^2 \tag{5.16}$$
$$U = 2\,E_1\,E_2 \cos\delta \tag{5.17}$$
$$V = 2\,E_1\,E_2 \sin\delta \tag{5.18}$$

5.2 Convolutions

5.2.1 General

In the preceeding paragraph several characteristic parameters have been defined which relate to the resolution of the astrophysical instrumentation in use. Although this gives a handle on capability and potential performance, for quantitative handling of the data full account needs

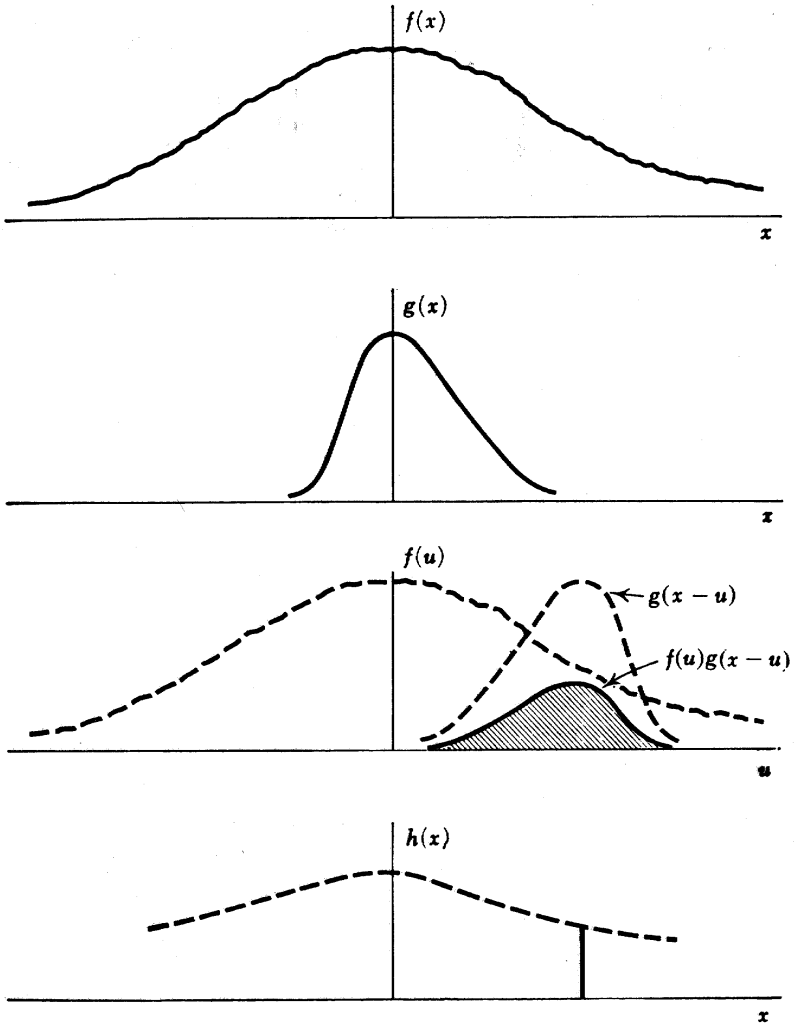

Figure 5.2: *The convolution h at point x (lower panel) of two functions f and g is equal to the integral of $f(u)$ and $g(x-u)$. Note that $g(x-u)$ is mirrored with respect to $g(x)$. Credit Bracewell (1986).*

to be taken of the influence of the instrument response on the incoming information carriers. This process can be described with the aid of convolutions: the measurement result can be described by a convolution of the measurand under study and the response function of the measurement device.

The convolution $h(x)$ of two functions $f(x)$ and $g(x)$ is:

$$h(x) = f(x) * g(x) = \int_{-\infty}^{+\infty} f(u) \cdot g(x-u)\, du \tag{5.19}$$

In words: a convolution describes the impact of a measuring device, described by $g(x)$, when it takes a weighted mean of some physical quantity $f(x)$ over a narrow range of the variable x, see figure 5.2. The simplest form of $g(x)$ is the window function $\frac{1}{\Delta x_0}\Pi\left(\frac{x}{\Delta x_0}\right)$, for which

the convolution integral reduces to the expression for the so-called *running average*:

$$\frac{1}{\Delta x_0}\int_{-\infty}^{+\infty} f(u)\Pi\left(\frac{x-u}{\Delta x_0}\right)du \;=\; \frac{1}{\Delta x_0}\int_{x-\frac{1}{2}x_0}^{x+\frac{1}{2}x_0} f(u)du \tag{5.20}$$

Convolutions are commutative, associative and distributive, i.e.:

$$f(x)*g(x) \;=\; g(x)*f(x) \tag{5.21}$$
$$f(x)*(g(x)*h(x)) \;=\; (f(x)*g(x))*h(x) \tag{5.22}$$
$$f(x)*(g(x)+h(x)) \;=\; f(x)*g(x)+f(x)*h(x) \tag{5.23}$$

5.2.2 Fourier transforms

Convolutions can be easily and elegantly handled by employing the Fourier transform technique. The Fourier transform of a function $g(x)$ exists if it satisfies the following conditions:

1. The integral of $|g(x)|$ exists, i.e. $\int_{-\infty}^{\infty}|g(x)|\,dx$ is convergent.
2. Discontinuities in $g(x)$ are finite.

The Fourier transform $\mathcal{F}(g(x))$ of $g(x)$ is called G and is a function of the Fourier domain variable s:

$$\mathcal{F}(g(x)) = G(s) = \int_{-\infty}^{+\infty} g(x)\,e^{-2\pi isx}\,dx \tag{5.24}$$

The inverse transform is given by

$$g(x) = \int_{-\infty}^{+\infty} G(s)\,e^{2\pi isx}\,ds \tag{5.25}$$

For a function $h(t)$ depending on time, its Fourier transform will depend on the frequency variable f:

$$H(f) = \int_{-\infty}^{+\infty} h(t)\,e^{-2\pi ift}\,dt \tag{5.26}$$

Sometimes the frequency variable f is replaced by the angular frequency $\omega = 2\pi f$, yielding

$$H(\omega) \;=\; \int_{-\infty}^{+\infty} h(t)\,e^{-i\omega t}\,dt \tag{5.27}$$

$$h(t) \;=\; \frac{1}{2\pi}\int_{-\infty}^{+\infty} H(\omega)\,e^{i\omega t}\,d\omega \tag{5.28}$$

which lacks the symmetry of the expressions in f.

A Fourier transform pair is often indicated in a symbolic way by a double arrow: $g(x) \Leftrightarrow G(s)$ or $h(t) \Leftrightarrow H(f)$.

A particular useful theorem from Fourier theory states that the Fourier transform of the convolution of two functions equals the product of the Fourier transforms of the individual functions

$$\mathcal{F}(f * g) = \mathcal{F}(f) \cdot \mathcal{F}(g) \qquad \text{or, in shorthand :} \quad f * g \Leftrightarrow F(s) \cdot G(s) \tag{5.29}$$

This is called the *convolution theorem*. Other useful and frequently applied theorems are

$$f(ax) \quad \Leftrightarrow \quad \frac{1}{|a|} F\left(\frac{s}{a}\right) \tag{5.30}$$

$$f(x) + g(x) \quad \Leftrightarrow \quad F(s) + G(s) \tag{5.31}$$

$$f(x - a) \quad \Leftrightarrow \quad e^{-2\pi i a s} F(s) \quad \textit{Shift theorem} \tag{5.32}$$

$$f(x)\ \cos \omega x \quad \Leftrightarrow \quad \frac{1}{2} F\left(s - \frac{\omega}{2\pi}\right) + \frac{1}{2} F\left(s + \frac{\omega}{2\pi}\right) \tag{5.33}$$

$$f(x) * f^*(-x) \quad \Leftrightarrow \quad |F(s)|^2 \tag{5.34}$$

$$f'(x) \quad \Leftrightarrow \quad 2\pi i s\ F(s) \tag{5.35}$$

$$\frac{d}{dx}(f(x) * g(x)) \quad = \quad f'(x) * g(x) \ = \ f(x) * g'(x) \tag{5.36}$$

$$\int_{-\infty}^{+\infty} |f(x)|^2\ dx \quad = \quad \int_{-\infty}^{+\infty} |F(s)|^2\ ds \quad \textit{Parseval's theorem} \tag{5.37}$$

$$\int_{-\infty}^{+\infty} f(x) g^*(x)\ dx \quad = \quad \int_{-\infty}^{+\infty} F(s) G^*(s)\ ds \tag{5.38}$$

$$f \text{ and } g \text{ real} \quad \int_{-\infty}^{+\infty} f(x) g(-x)\ dx \quad = \quad \int_{-\infty}^{+\infty} F(s) G(s)\ ds \tag{5.39}$$

5.3 Instrument response and data sampling

5.3.1 Response fuctions

In observational astrophysics it is often necessary to have a full and quantitative knowlegde of the angular and spectral reponse functions in order to perform a proper *deconvolution* of the measurement data to extract optimally the characteristics of the information source.

Consider the example of a spectrometer which possesses a response function $R(\lambda, \lambda')$. In many cases, the *smearing* effect (or *blurring*) of the spectrometer is solely a function of the wavelength difference $\lambda' - \lambda$, i.e. $R(\lambda, \lambda') = R(\lambda' - \lambda)$. If the information source emits a spectrum $S(\lambda)$, the source function, the measured distribution $M(\lambda)$ at the output of the spectrometer is given by the convolution:

$$M(\lambda) = \int_{-\infty}^{+\infty} S(\lambda') R(\lambda - \lambda')\ d\lambda' = \int_{0}^{\infty} S(\lambda') R(\lambda - \lambda')\ d\lambda' \tag{5.40}$$

since $S(\lambda) = 0$ for $\lambda \leq 0$. Applying the convolution theorem, with $S(\lambda) \Leftrightarrow S(s)$, $R(\lambda) \Leftrightarrow R(s)$ and $M(\lambda) \Leftrightarrow M(s)$

$$S(s) = \frac{M(s)}{R(s)} \tag{5.41}$$

The spectrum of the source can be reconstructed by deconvolution of the measured spectrum. This is accomplished through the inverse Fourier transform:

$$S(\lambda) = \mathcal{F}^{-1}\left[\frac{M(s)}{R(s)}\right] \tag{5.42}$$

To illustrate the notions just described, consider a spectrometer with a Gaussian response function:

$$R(\lambda) = \frac{1}{\sqrt{2\pi}\sigma}\, e^{-\frac{\lambda^2}{2\sigma^2}} \tag{5.43}$$

Suppose an infinitely narrow spectral line at wavelength λ_0 is measured: $S(\lambda) = S_0 \cdot \delta(\lambda - \lambda_0)$. The convolution of $S(\lambda)$ and $R(\lambda)$ gives the measured result, which is (of course) a Gaussian distributed profile around λ_0:

$$M(\lambda) = \frac{S_0}{\sqrt{2\pi}\sigma}\, e^{-\frac{(\lambda-\lambda_0)^2}{2\sigma^2}} \tag{5.44}$$

Suppose an observer has measured $M(\lambda)$ and $R(\lambda)$ is known. He can now reconstruct $S(\lambda)$. First the Fourier transform of $M(\lambda)$ is taken:

$$\begin{aligned}
M(s) &= \int_{-\infty}^{+\infty} M(\lambda)\, e^{-2\pi i s\lambda}\, d\lambda \\
&= \int_{-\infty}^{+\infty} \frac{S_0}{\sqrt{2\pi}\sigma}\, e^{-\frac{(\lambda-\lambda_0)^2}{2\sigma^2}}\, e^{-2\pi i s\lambda}\, d\lambda \\
&= \frac{S_0}{\sqrt{2\pi}\sigma}\, e^{-2\pi i s\lambda_0 - 2\pi^2 s^2\sigma^2} \int_{-\infty}^{+\infty} e^{-\frac{(\lambda-\lambda_0)^2}{2\sigma^2} - 2\pi i s(\lambda-\lambda_0) + 2\pi^2\sigma^2 s^2}\, d\lambda \\
&= \frac{S_0}{\sqrt{2\pi}\sigma}\, e^{-2\pi i s\lambda_0 - 2\pi^2 s^2\sigma^2} \int_{-\infty}^{+\infty} e^{-\pi\lambda'^2} \sqrt{2\pi}\sigma\, d\lambda' \\
&= S_0\, e^{-2\pi i s\lambda_0 - 2\pi^2 s^2\sigma^2}
\end{aligned} \tag{5.45}$$

where $\lambda' = \frac{\lambda-\lambda_0}{\sqrt{2\pi}\sigma} + i\sqrt{2\pi}\sigma s$. Analogously

$$R(s) = e^{-2\pi^2 s^2\sigma^2} \tag{5.46}$$

(Note that the Fourier transform of a Gaussian function is again Gaussian.) Applying equation 5.42 gives

$$S(\lambda) = \mathcal{F}^{-1}[S_0\, e^{-2\pi i s\lambda_0}] = S_0 \cdot \delta(\lambda - \lambda_0) \tag{5.47}$$

i.e. the observer has recovered the exact form of the spectral source function.

Consider now a spectrometer with a Gaussian response function with width σ. If σ is large, i.e. the line spread function is wide, the Fourier domain only contains low frequencies as can be seen from equation 5.46 and figure 5.3. By decreasing σ, the range of frequencies in the Fourier domain increases and consequently the range of *spectral frequencies* over which the measurement provides information. The $\ln R(s)$ is a parabola, which tends to a δ-function for the limit $\sigma \to \infty$ (no spectral resolution) and becomes flat for $\sigma \downarrow 0$ (perfect transmission at all frequencies).
Obtaining $S(\lambda)$ by this method is, in practise, complicated by two factors: *data sampling* and *noise*. This will be adressed in the following paragraphs.

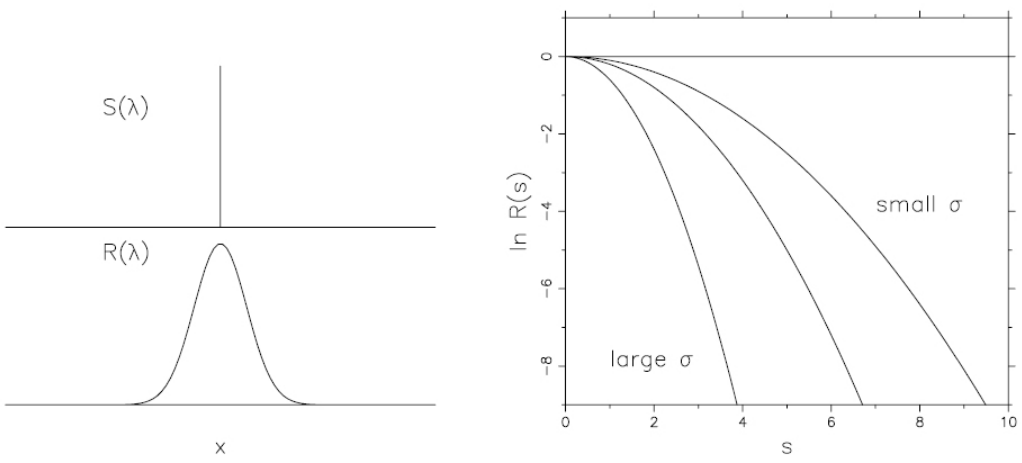

Figure 5.3: *The line $S(\lambda)$ is widened by the response function $R(\lambda)$. For a broad (narrow) response the Fourier transform of the measured function $M(s)$ contains information over a narrow (broad) range of frequencies.*

5.3.2 Discrete measurement intervals, the Nyquist criterion

First of all the measurement distribution $M(\lambda)$ is not a continuous function as assumed in equation 5.40, but is always sampled in discrete intervals or bins and is also not available over the whole interval from $-\infty$ to ∞.
The problem of discrete intervals can be overcome by using the discrete version of the Fourier transform.
Suppose there are N consecutive sampled values $g(x_k)$ with $x_k = k\tau$ $(k = 0, 1, 2, ..., N-1)$, the sampling interval is τ. With N *input numbers*, evidently no more than N independent *output numbers* can be produced. Estimates of the Fourier transform $G(s)$ can now be sought at discrete frequency values $s_n = \frac{n}{N\tau}$ $(n = -N/2, ..., N/2)$. The extreme values of n correspond in this case to the lower and upper limits of the Nyquist critical frequency (see later in this paragraph). Notice that in this case n takes $N+1$ rather than N values, this is because the two extreme values of n are not independent (i.e. they are equal), this reduces the count of independent numbers to N.

$$G(s_n) = \int_{-\infty}^{+\infty} g(x)\, e^{-2\pi i s_n x} dx \approx \sum_{k=0}^{N-1} g(x_k)\, e^{-2\pi i s_n x_k}\, \tau = G_D(s_n) \tag{5.48}$$

Substitution of x_k and s_n yields:

$$G_D(s_n) = \tau \sum_{k=0}^{N-1} g(x_k)\, e^{-2\pi i k n/N} \tag{5.49}$$

where $G_D(s_n)$ is the n^{th} value of the discrete transform of $g(x)$.
The inverse Fourier tranform, which recovers the set of sampled $g(x_k)$ values exactly from $G_D(s_n)$ is given by:

$$g(x_k) = \frac{1}{N} \sum_{n=0}^{N-1} G_D(s_n)\, e^{2\pi i k n/N} \tag{5.50}$$

N.B. Outside the measurement range the function values are set to zero.
Using discrete Fourier transforms instead of continuous transforms does not lead to loss of information, provided the interval between sampling points or the bin width τ satisfies the *Nyquist criterion* for optimum sampling. This can be qualitativily understood in the following way. Any physical measurement system has a finite frequency response, therefore the measured distribution $M(x)$, constituting some function of a parameter x, is contained in bandwidth, i.e. the Fourier transform $M(s) \Leftrightarrow M(x)$ is a bandlimited function, characterized by a maximum cut-off frequency s_{max}, also called the critical s_{cr} or Nyquist frequency. In the case of 'Gaussian' response for instance: the frequencies will never be distributed purely Gaussian since no physical system transmits the tail frequencies up to ∞.
Nyquist (and Shannon) established a theorem for optimum sampling of bandlimited observations. This theorem states that no information is lost if sampling occurs at intervals (or in bins) $\tau = \frac{1}{2s_{cr}}$. The formal derivation of this theorem will not be given here, it is treated in the follow-on course OAF2. Thus, the use of the discrete Fourier transform causes no loss of information, provided that the sampling frequency $\frac{1}{\tau}$ is twice the highest frequency in the continuous input function (i.e. the source function convolved with the response function). The maximum frequency s_{max} that can be determined for a given sampling interval equals therefore $\frac{1}{2\tau}$. If the input signal is sampled too slowly, i.e. if the signal contains frequencies higher than $\frac{1}{2\tau}$, then these cannot be determined after the sampling process and the finer details will be lost. More seriously however, the higher frequencies which are not resolved will beat with the measured frequencies and produce spurious components in the frequency domain below the Nyquist frequency. This effect is known as *aliasing* and may give rise to major problems and uncertainties in the determination of the source function.

Example: *Consider again the above spectrometer with the Gaussian response function. What is the proper sampling interval for the measured function $M(\lambda)$?*
As stated before: no physical system transmits the tail frequencies up to ∞. Suppose that the frequencies of the Gaussian shaped Fourier transform $R(s) = e^{-2\pi^2\sigma^2 s^2}$ are covered out to three standard deviations in the s domain, i.e. the exponent $2\pi^2\sigma^2 s_{cr}^2$ equals $\frac{9}{2}$ so that $s_{cr} \approx \frac{1}{2\sigma}$. As is clear from the right panel in the figure in section 5.3.1, the power in the Fourier domain above this value of s_{cr} can be neglected. The Nyquist frequency $s_{cr} = \frac{1}{2\sigma}$ can be considered as appropriate and since $s_{cr} = \frac{1}{2\tau}$ the proper sampling interval τ (or bin width) for $M(\lambda)$ in case of a Gaussian line spread function with width σ is:

$$\tau = \sigma \tag{5.51}$$

If sampling (binning) is performed at a higher frequency the information in $M(\lambda)$ is oversampled, at lower frequencies undersampled. It is important to note that although oversampling ensures the transfer of all information, it also leads to statistical dependence between adjacent points (bins). This implies that standard statistical tests, like the χ^2-test or other likelihood tests, do not apply anymore since they assume statistically independent samples.

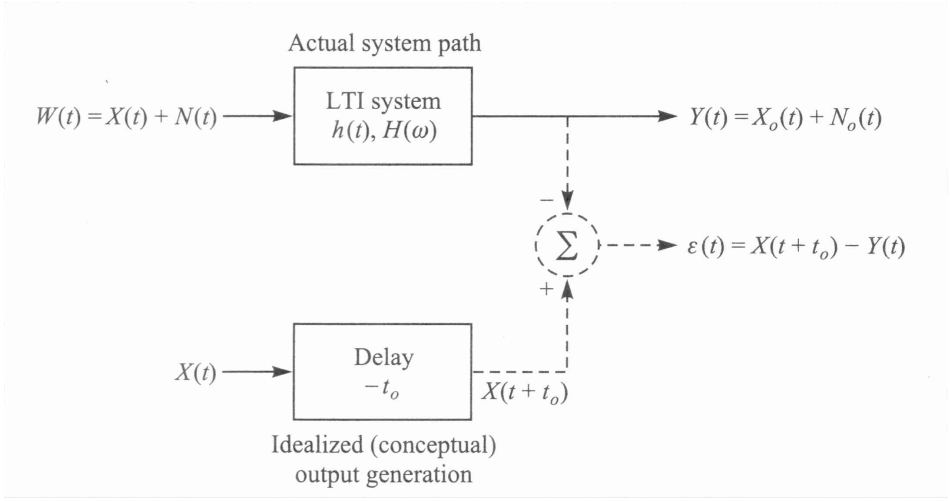

Figure 5.4: *Operation that defines the Wiener filter problem. Credit Peebles (2001).*

5.3.3 Noise

Secondly the presence of noise (both intrinsic to the signal and background noise) and disturbances will produce ambiguities in the values derived for $S(\lambda)$. Handling the errors and their propagation is a major subject in deconvolution processing to arrive at reliable confidence intervals for the physical parameters estimated for the radiation source. Sophisticated filter algorithms have been developed to optimally reduce the influence of noise. Random noise can be most efficiently reduced by employing so-called optimal or *Wiener* filters. If applied to a stochastic process, the Wiener filter is the optimum result if the filter is designed such that its output is a good estimate of either the past, the present or the future value of the input signal. The basic problem to be addressed is depicted in figure 5.4. The input signal $W(t)$ is a stochastic process comprising the sum of a signal component $X(t)$ and a noise component $N(t)$:

$$W(t) \;=\; X(t) \;+\; N(t) \tag{5.52}$$

The system is assumed to be linear with a tranfer function $H(f)$, being the Fourier transform of the impulse response function $h(t)$. The output of the system is denoted $Y(t)$.
In general , $H(f)$ is selected such that $Y(t)$ is the best possible estimate of the input signal $X(t)$ at the time $t + t_0$, that is the best estimate of $X(t + t_0)$. If $t_0 > 0$, $Y(t)$ is an estimate of a *future* value of $X(t)$ corresponding to a *prediction filter*. If $t_0 < 0$, $Y(t)$ is an estimate of the *past* value of $X(t)$, corresponding to a *smoothing filter*. If $t = 0$, $Y(t)$ is an estimate of the current value of $X(t)$.
If $Y(t)$ differs from the desired true value of $X(t + t_0)$, the error is:

$$\epsilon(t) \;=\; X(t + t_0) - Y(t) \tag{5.53}$$

This error is illustrated conceptually in figure 5.4 by dashed lines. The optimum filter will be chosen so as to minimize the mean-squared value of $\epsilon(t)$:

$$\text{minimize} \quad \mathbf{E}\left\{\epsilon^2(t)\right\} \;=\; \mathbf{E}\left\{[X(t + t_0) - Y(t)]^2\right\} \tag{5.54}$$

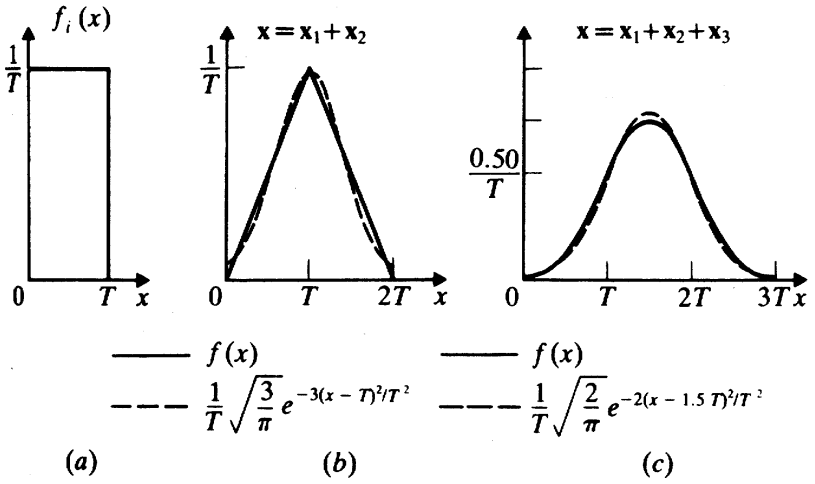

Figure 5.5: *Example of central limit theorem: window function and two consecutive selfconvolutions. The last one already resembles closely a Gaussian function. Credit Papoulis (1991).*

We shall not give the derivation of the expression for the optimum filter transfer function, but only give the result for the case of an uncorrelated input signal $X(t)$ and noise $N(t)$:

$$H_{opt}(f) \;=\; \frac{S_X(f)}{S_X(f) \;+\; S_N(f)}\; e^{2\pi i f t_0} \tag{5.55}$$

in which $S_X(f) = |X(f)|^2$ and $S_N(f) = |N(f)|^2$ represent the so-called *power spectral densities* of the input signal $X(t)$ and the noise $N(t)$ respectively.
Note: Let us check the value of $H_{opt}(f)$ for a noise free input, i.e. $S_N(f) = 0$. Equation (5.55) then reduces to:

$$H_{opt}(f) \;=\; e^{2\pi i f t_0} \tag{5.56}$$

This expression corresponds to an ideal delay line with delay $-t_0$ (recall the *shift theorem*!). If $t_0 > 0$, corresponding to prediction, we require an unrealizable negative delay line. If $t_0 < 0$, corresponding to a smoothing filter, the required delay is positive and realizable. $H_{opt}(f) = 1$ follows for $t_0 = 0$, this result is intuitively obvious.

5.4 The Central Limit Theorem

If a large number of functions are convolved together, the resultant function becomes increasingly smooth. Consider now n independent random variables X_i, each distributed according to a stationary probability density function $p_{X_i}(x)$. The sum X of these variables, i.e. $X = \sum_n X_i$ has a mean $\mu = \sum_n \mu_i$ and a variance $\sigma^2 = \sum_n \sigma_i^2$. Moreover, the probability density function of the sum X follows from the convolution of the individual probability densities:

$$p_X(x) = p_{X_1}(x) * p_{X_2}(x) * \;\cdots\; * p_{X_n}(x) \tag{5.57}$$

The central limit theorem (CLT) in its general form states that under applicable conditions the convolution of n functions (not necessarily the same) is a Gaussian function whose mean value is μ and whose variance is σ^2 plus a remainder which vanishes as $n \to \infty$:

$$\lim_{n\to\infty} p_X(x) = \frac{1}{\sqrt{2\pi}\sigma}\; e^{-\frac{1}{2}\left(\frac{(x-\mu)}{\sigma}\right)^2} \tag{5.58}$$

The central limit theorem is basically a property of convolutions: the convolution of a large number of positive functions is approximately Gaussian. An example is given in figure 5.5, which shows that two self-convolutions of the window function $\frac{1}{T}\Pi\left(\frac{x-\frac{1}{2}T}{T}\right)$ already produces a function which closely approximates a Gaussian density distribution. A starting condition for the CLT to hold in the case of repeated self-convolution is the requirement that the probability density function $p(x)$ or its Fourier transform can be approximated by a parabolic function in a small region around its maximum value.

Most physical measurement systems comprise a chain of elements, each contributing noise and changing response through it particular response function. The central limit theorem shows that in many cases these successive convolutions lead to an integral response, which can be approximated by a Gaussian function.

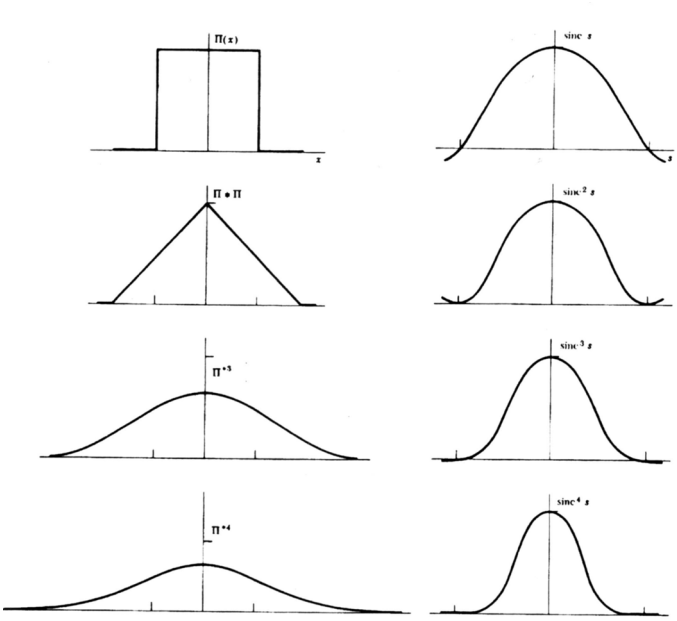

This figure shows the window function and three successive selfconvolutions and the associated Fourier transforms. The window function $\Pi(x)$ *forms a Fourier pair with the function* $sinc(x)$.
Successive self-convolutions of $\Pi(x)$ *yield successive self-multiplications of* $sinc(s)$ *(application of the convolution theorem, i.e.* $\Pi^{*n} \Leftrightarrow sinc^n(s)$*). In a small range* Δs *around* $s = 0$ *(maximum)* $sinc(s)$ *can be approximated by the parabolic curve* $(1 - as^2)$*, the* n^{th} *power of* $sinc(s)$ *is then approximated by* $(1 - as^2)^n$*. Taylor expansion of this function yields*

$$sinc^n(s) \approx (1 - as^2)^n = e^{-nas^2} + \text{rest term} \tag{5.59}$$

Keeping s *fixed and letting* $n \to \infty$ *causes the Gaussian (exponential) term to get continually narrower, its width goes as* $n^{-1/2}$*, and the rest term tends to zero. The Gaussian term in the* s*-domain has a Gaussian Fourier transform, i.e.* $\sqrt{\frac{\pi}{na}} \cdot e^{-\frac{\pi^2 x^2}{na}}$*, which continually becomes wider, a property that variances add under convolution. The interesting phenomenon that emerges from this illustration is the tendency towards Gaussian form under successive self-convolution and, also, under successive self-multiplication. Credit Bracewell (1986).*

Chapter 6

Signal to Noise Ratio

6.1 General

The feasibility of detecting a signal from a cosmic source depends on the level of noise (and disturbance) in which the signal is embedded during the measurement. Contributions to the noise signal potentially comprise other sources of radiation in the field of view of the observing instrument (sky-noise), background radiation from the operational environment of the telescope (e.g. atmosphere, radiation belts, earth) and noise arising from the constituting elements of the measurement chain (transducers, transmission lines, wave tubes, amplifiers, mixers, digitisers, etc.).

Consequently, the quality of a particular observation is determined by the magnitude of the so-called signal-to-noise ratio (*SNR*). This *SNR* is generally a function of integration time (T_{obs}) of the observation and depends on the bandwidth ($\lambda\lambda$, $\nu\nu$, $\epsilon\epsilon$) of the measurement. From this a limiting sensitivity can be derived, i.e. the weakest source signal that can still be detected significantly.

For electromagnetic radiation three types of noise characterisations dependent on wavelength, are in use.

1. In the radio-band coherent detection is employed, i.e. the phase information is preserved, with $h\nu \ll kT$. Noise and *SNR* are normally represented by *characteristic temperatures* and *temperature ratios*.

2. In the (far) infrared band ($h\nu \approx kT$) incoherent detection is used. A transducer (Latin: *transducere*) converts the radiation field into a voltage or current and noise is commonly expressed in terms of an *equivalent radiation power* (*power characterisation*).

3. At shorter wavelengths (Optical, UV, X-rays, γ-rays), the incoming photons can be registered individually: so-called single photon counting. The signal and noise contributions can then be evaluated by a statistical treatment of the accumulated quanta, i.e. *quantum characterisation*. The latter treatment of noise and *SNR* applies by definition for corpuscular radiation and neutrinos.

The three notions introduced above are discussed in some detail in the following sections and the parameters which are commonly used for *SNR* characterisation in these cases will be shortly reviewed.

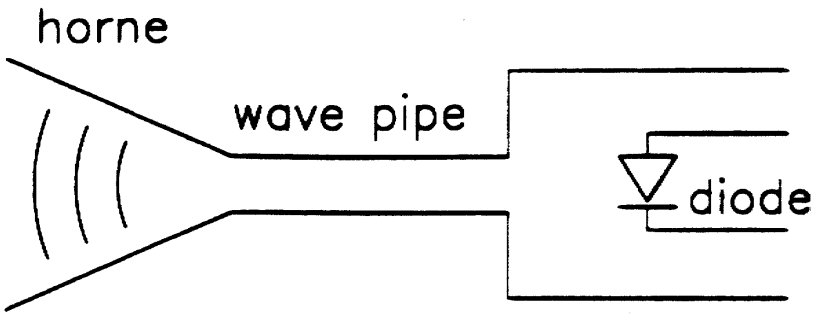

Figure 6.1: *Schematic view of a radio telescope, with the receiving horne, the wave tube and the detector diode.*

6.2 Temperature characterisation

6.2.1 Brightness and antenna temperature

Consider a thermal signal source radiating at radio wavelengths. If this source is optically thick, the specific intensity $B(\nu)$ is given by the Rayleigh-Jeans approximation ($h\nu \ll kT$) of a blackbody radiator:

$$B(\nu) = \frac{c}{4\pi}\rho(\nu) = \frac{2kT_b\nu^2}{c^2} = \frac{2kT_b}{\lambda^2} \tag{6.1}$$

in which T_b is the *brightness temperature*. (Note that although the last expression contains λ, the units remain however per unit frequency, e.g. Watt$\cdot$m$^{-2}\cdot$sr$^{-1}\cdot$Hz^{-1}. The convenience of using λ becomes apparent when integration over the beamsize is performed, see below.) In this way a radio brightness distribution $B(\nu, \vec{\Omega})$ on the sky can be described by an equivalent brightness temperature distribution $T_b(\vec{\Omega})$.

Radio waves arriving at the focus of a telescope enter the receiver input by a horn (or "feed") which matches the impedance of the vacuum to that of a wave-tube, that selects one degree of polarisation. The wave is subsequently guided through the wave-tube into a resonance cavity, which defines by its selectivity a bandwidth $\Delta\nu$ centered around a frequency ν_0 of the incoming radiation. A (always) non-linear detection element (transducer) in this resonance cavity converts the wave field (i.e. the electric vector) into a current. This is the simplest detection configuration for a radio telescope, nevertheless it suffices to describe the essential characteristics of the measurement process, see figure 6.1. The power reaching the non-linear element is in good approximation given by:

$$P(\nu) = \frac{1}{2}\,\eta(\nu)\,A(\nu)\,\frac{2k}{\lambda^2}\int\limits_{\Omega_{beam}} T_b(\vec{\Omega})\,d\vec{\Omega} \equiv \eta(\nu)kT_{ant} \tag{6.2}$$

in which the factor $\frac{1}{2}$ refers to a single polarisation component, $A(\nu)$ represents the telescope effective area at frequency ν, Ω_{beam} is the diffraction limited beamsize and $\eta(\nu)$ takes account of the frequency dependent transmission losses prior to detection by the non-linear element. $P(\nu)$ is given in units of Watt$\cdot$Hz^{-1}. Expression 6.2 can be set equal to the product of the transmission losses $\eta(\nu)$ and a thermal power kT_{ant} (per unit frequency) available at the receiver input. T_{ant} is called the *antenna temperature* and is therefore independent of the transmission in the receiver system. It should be noted that T_{ant} is only equal to the physical temperature T_b of the radio source if the following conditions are met:

- The source is optically thick at the frequency considered.

- The source is sufficiently extended to fill the diffraction limited beamsize Ω_{beam} of the telescope, i.e. Ω_{beam} satisfies $A(\nu)\ \Omega_{beam} = \lambda^2$, the 'etendue' of coherence introduced in Chapter 3.

If the radiation source is not a blackbody but has an arbitrary spectrum (e.g. an optically thin thermal source or a non-thermal source), the antenna temperature T_{ant} becomes frequency dependent and does not relate to a physical temperature. The power received at the detection element is now expressed as

$$P(\nu) = \eta(\nu) k T_{ant}(\nu) \tag{6.3}$$

in which $T_{ant}(\nu)$ is the antenna temperature at the specific frequency ν.

In this picture the antenna may be thought to be replaced by its characteristic resistance R_a at a fictitious temperature $T_{ant}(\nu)$ producing a thermal noise power $kT_{ant}(\nu)$ per unit frequency at frequency ν or kT_{ant} if the power received is white (frequency independent) over the bandwidth $\Delta\nu$ considered. In turn, this replacement is equivalent to a fictitious noise free resistor R_a in series with a voltage source which generates a power spectral density, in units of $\mathrm{Volt}^2 \cdot \mathrm{Hz}^{-1}$:

$$S_V(\nu) = 4 k T_{ant}(\nu) R_a \tag{6.4}$$

It is important to realize that $T_{ant}(\nu)$ has generally nothing to do with the physical temperature of the resistor R_a. To demonstrate this, consider an amplifier (bandwidth $\Delta\nu$ = 1 MHz), with an output impedance R = 50 Ω, generating a rms-white noise voltage σ_V = 1 mV. The available power per Hz at the output of this amplifier follows from

$$P = \frac{\sigma_V^2}{4\ R\ \Delta\nu} = 5 \cdot 10^{-15}\ \ Watt \cdot Hz^{-1} \tag{6.5}$$

The corresponding noise temperature is

$$T_{ant} = \frac{P}{k} \approx 3.5 \cdot 10^{8}\ \ K \tag{6.6}$$

whereas the physical temperature is about 300 Kelvin.
Only in the case of passive elements (i.e. which do not need energy), like wave guides, resistor networks and transmission cables embedded in the earth, the noise temperature and the physical temperature are about equal.

6.2.2 Noise sources at radio wavelengths

In practise, if the radio antenna is pointed at a sky region devoid of sources, a non-zero output will be measured at the output of the receiver. This arises from various noise sources:

- Residual thermal emission from the atmosphere and from the telescope itself. A simple approximation is available when the atmosphere is optically thin, i.e. if the optical depth $\tau(\nu)$ along the zenith is small compared to unity. In this case, the specific intensity $I(\nu) \approx \tau(\nu) B(\nu, \bar{T}_{atm})$, with $B(\nu, \bar{T}_{atm})$ the blackbody function at the average temperature $\bar{T}_{atm}$ of the atmosphere. Since $\tau(\nu)$ is a strong function of wavelength, the contribution of the atmospheric thermal emission to the noise is also a strong function

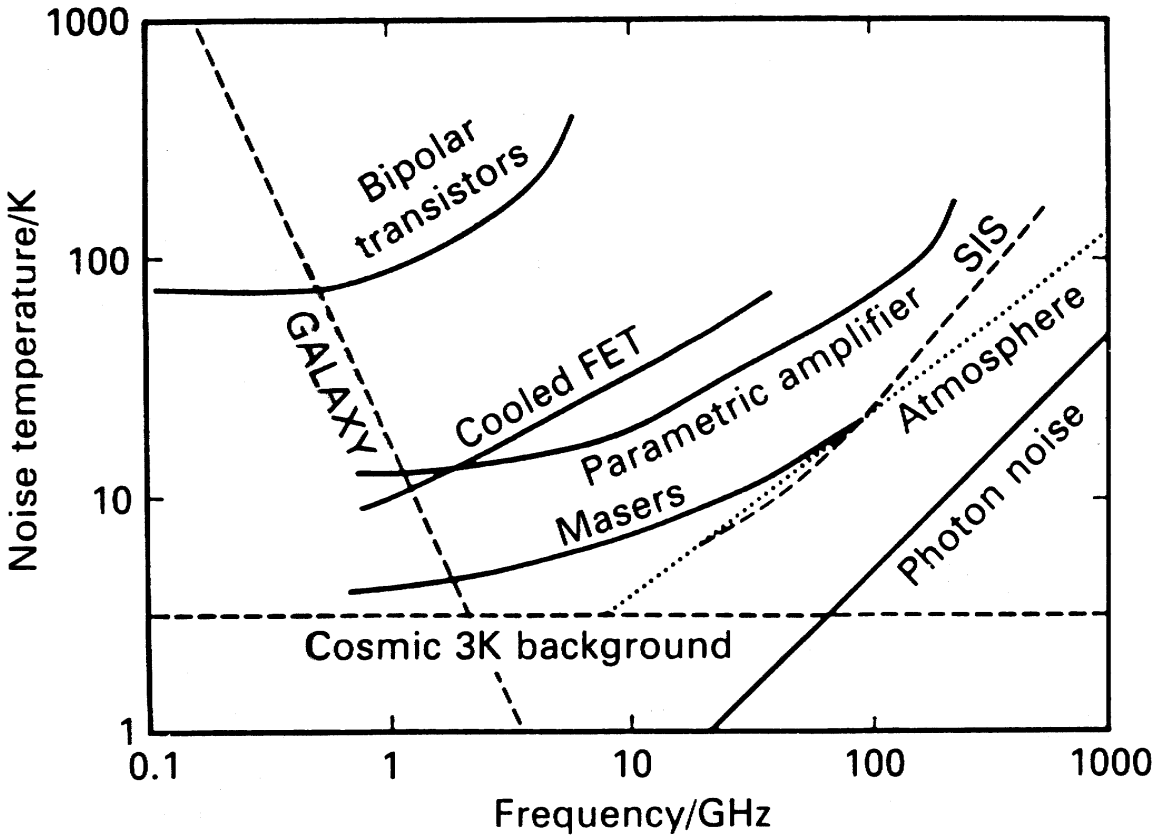

Figure 6.2: *Frequency dependence of the noise temperature for several sources of background radiation and receiver components. Credit Longair (1992).*

of wavelength and so is the associated noise temperature $T_{atm}(\nu)$. For example at ν = 100 GHz ($\lambda \approx 3$ mm), $\tau(\nu) \approx 0.2$, i.e. the atmospheric emission corresponds to an antenna temperature of about 50 Kelvin. Figure 6.2 shows, among others, the frequency dependence of the noise temperature associated with atmospheric emission.

- Thermal emission from the telescope environment and the earth surface, detected in the side lobes of the diffraction pattern of the telescope's angular response function (diffraction limit). This contribution to the antenna temperature is very site dependent. Symbol: $T_{lobe}(\nu)$.

- Thermal noise from the Galaxy and the microwave background. The Galactic contribution is again strongly frequency dependent, the microwave background is white. Both components are also indicated in figure 6.2. Symbol: $T_{Gal}(\nu)$ and T_{cb}.

- Contributions from the receiver chain, i.e. feed, wave guides, detection element, amplifiers, etc. This contribution to the total noise is normally expressed as an *effective noise temperature* $T_{eff}(\nu)$. The value of $T_{eff}(\nu)$ is derived in the following way. Suppose that the total noise power available at the antenna $P_{ant}(\nu)$, is subject to a power amplification $G(\nu)$ in the receiver chain. At the output stage of the receiver, the total power

$P_{out}(\nu)$ is then given by

$$P_{out}(\nu) = G(\nu) \cdot P_{ant}(\nu) + P_{rec}(\nu) = G(\nu) \cdot \left[P_{ant}(\nu) + \frac{P_{rec}(\nu)}{G(\nu)} \right] \tag{6.7}$$

in which $P_{rec}(\nu)$ represents the noise power introduced by the receiver chain. Division by Boltzmann's constant k yields:

$$T_{out}(\nu) = G(\nu) \cdot [T_{ant}(\nu) + T_{eff}(\nu)] = G(\nu) \cdot T_{op}(\nu) \tag{6.8}$$

$T_{out}(\nu)$ equals the noise temperature at the output of the whole telescope system (antenna + receiver chain), $T_{eff}(\nu)$ is the effective noise temperature introduced above. $T_{eff}(\nu)$ can be regarded as the temperature which has to be assigned to the characteristic resistance R_a of the antenna in order to have a fictitious *noise-free* system produce the same noise temperature as the noisy system for $T_{ant} = 0$ Kelvin. $T_{op}(\nu)$ represents in a similar way the temperature to be assigned to R_a to have a noise free system produce the same noise temperature as the noisy system at the actual value of the antenna temperature T_{ant}:

$$T_{op}(\nu) = T_{ant}(\nu) + T_{eff}(\nu) \tag{6.9}$$

$T_{op}(\nu)$ is the so-called *operational temperature* of the telescope system. This relation effectively contains all essential noise contributions: $T_{ant}(\nu)$ includes all components due to radiation noise, $T_{eff}(\nu)$ includes all components referring to the receiver chain. Figure 6.2 shows some typical values of $T_{eff}(\nu)$ for masers, cooled field-effect transistors (FET) used in the first amplifier stage, parametric amplifiers and superconducting mixer elements (SIS) which are employed in case of a heterodyne detection chain.

Note 1: If the receiver chain consists of a series of n noisy elements, each with a power gain $G_i(\nu)$ and an associated effective temperature $T_{eff_i}(\nu)$, the operational temperature $T_{op}(\nu)$ derives from:

$$T_{op}(\nu) = T_{ant}(\nu) \; + \; T_{eff_1}(\nu) \; + \; \frac{T_{eff_2}(\nu)}{G_1(\nu)} \; + \; \cdots \; + \; \frac{T_{eff_n}(\nu)}{\prod_{i=1}^{n-1} G_i(\nu)} \tag{6.10}$$

This is the cascade rule according to Friis (verify yourself). Expression 6.10 shows that the first stages in the receiver chain are mainly determining the noise behavior of the system, once the amplification is sufficiently high, the noise contributions of additional stages become small. In particular the input-stage is crucial with respect to the achievable noise performance.

Note 2: The power gains $G_i(\nu)$ may partly be smaller than unity, this represents transmission losses in passive components like wave tubes, transmission lines and resistor networks: $G_i(\nu) = \eta_i(\nu)$. These losses can seriously degrade the noise characteristics of the system since the physical temperature of the attenuating components enters the determination of $T_{op}(\nu)$. According to Kirchhoff's *reciprocity law*, in equilibrium the *absorbed power* by the passive components equals the *radiated power*. Hence, the contribution of a single loss-element at physical temperature T_L to the noise can be expressed as $(1 - \eta(\nu))T_L$ or $\frac{1}{L(\nu)}[L(\nu) - 1]T_L$, with $L(\nu) = \eta^{-1}(\nu)$ the frequency dependent loss-factor (by definition larger than unity). Employing this single loss-element behind an antenna yields a system output noise given by the expression:

$$T_{out}(\nu) = \frac{1}{L(\nu)} \; (T_{ant}(\nu) + [L(\nu) - 1]T_L) \tag{6.11}$$

i.e. $T_{eff}(\nu) = [L(\nu) - 1]\, T_L$, and

$$T_{op}(\nu) = T_{ant}(\nu) + [L(\nu) - 1]T_L \tag{6.12}$$

To show that this potentially strongly influences the value of $T_{op}(\nu)$, consider the following example.
Suppose the telescope is pointed at a cloudless sky region devoid of sources with $T_{ant}(\nu)$ = 20 K. If a small piece of wave tube between the antenna and the input of the amplifier introduces a loss of 10 %, i.e. $L(\nu) = 1.1$, and this wave tube is at room temperature ($T \approx 290$ K), the operational temperature becomes $T_{op}(\nu) = 20 + 0.1 \cdot 290 \approx 50$ K; a deterioration of a factor 2.5. If the wave tube is cooled with liquid Nitrogen ($T \approx 70$ K), $T_{op}(\nu)$ becomes about 27 K (35 % deterioration) and at liquid Helium temperature ($T \approx 4$ K), $T_{op}(\nu) = 20$ K, i.e. practically no deterioration. The importance of cooling of passive components at the receiver chain front-end is therefore amply demonstrated.

6.2.3 The *SNR*-degradation factor

With the above assessment of the various noise contributions, the total operational noise temperature is expressed as:

$$T_{op}(\nu) = T_{Gal}(\nu) + T_{cb} + T_{atm}(\nu) + T_{lobes}(\nu) + T_{eff}(\nu) \tag{6.13}$$

This represents the background power against which a potential source signal will have to be detected. If the signal power (i.e. radiation flux) is given by $\Phi_s(\nu) = kT_s(\nu)$, the *momentaneous SNR* at the input of the receiver chain is given by the ratio between the available source power and the power contained in the background radiation fields:

$$SNR_{in}(\nu) = \frac{T_s(\nu)}{T_{Gal}(\nu) + T_{cb} + T_{atm(\nu)} + T_{lobes}(\nu)} \tag{6.14}$$

The noise generated by the receiver chain degrades the *SNR* at the output to:

$$SNR_{out}(\nu) = \frac{G(\nu) \cdot T_s(\nu)}{G(\nu) \cdot [T_{Gal}(\nu) + T_{cb} + T_{atm}(\nu) + T_{lobes}(\nu) + T_{eff}(\nu)]} \tag{6.15}$$

The *SNR*-degradation factor $D(\nu)$ (≥ 1) is now simply expressed as

$$D(\nu) = \frac{SNR_{in}(\nu)}{SNR_{out}(\nu)} = \frac{T_{op}(\nu)}{T_{ant}(\nu)} \tag{6.16}$$

Referring to the example in Note 2 in the previous subsection, the deterioration of the *SNR* due to the loss in the wave tube would be specified by $D(\nu) \approx 2.5$ (room temperature), $D(\nu) \approx$ 1.35 (liquid Nitrogen) and $D(\nu) \approx 1$ (liquid Helium).

The *momentaneous SNR* $= \frac{T_s(\nu)}{T_{op}(\nu)}$ refers to the value obtained considering the radiation energy during one second (e.g. Watt) and in a bandwidth of 1 Hz. In reality this is of course greatly improved by integration over the selected bandwidth $\Delta\nu$ and over an exposure period T_{obs}. A full derivation of the resulting *SNR* is given in the more advanced course OAF2, here only the result is given:

$$SNR = \frac{T_s(\nu)}{T_{op}(\nu)} \sqrt{T_{obs}\ \Delta\nu} \tag{6.17}$$

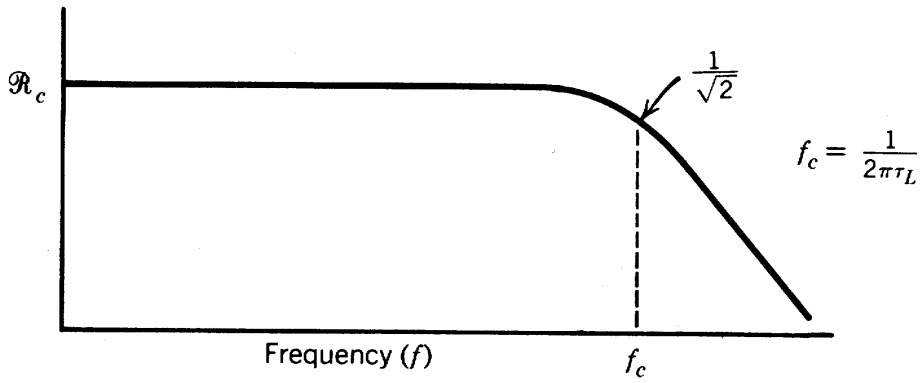

Figure 6.3: *Frequency spectrum of the noise of a transducer. Noise power is along the vertical axis. Credit Dereniak & Crowe (1984).*

i.e. the *SNR* improves with the square root of the product of the radio channel bandwidth and the observation time T_{obs}. The minimum detectable source power for a $SNR = 1$ is then given by

$$P_{s_{min}}(\nu) = \frac{2\ k\ T_{op}(\nu)}{\sqrt{T_{obs}\ \Delta\nu}} \tag{6.18}$$

Note: The value of $T_{op}(\nu)$ is measured for two values of the antenna temperature by looking alternatively at the source and at a neighboring (source-less) sky point. The $T_{op}(\nu)$ values in equations 6.17 and 6.18 refer to an antenna temperature excluding the signal source contribution.

6.3 Power characterisation

6.3.1 Typical set-up of observation

Consider the case of incoherent detection of a radiation field by a transducer which converts the incident radiant power into an electrical output (usually a current or a voltage). Two types of flux will be used to characterise the radiation source:

- Monochromatic flux $\Phi(\lambda_0)$ at a particular wavelength λ_0, defined as:

$$\Phi(\lambda_0) = \int_0^\infty \Phi(\lambda) \cdot \delta(\lambda - \lambda_0)\ d\lambda \tag{6.19}$$

- Blackbody flux $\Phi(T)$, which is the specific flux integrated over a blackbody profile:

$$\Phi(T) = \int_0^\infty \Phi_{bb}(\lambda, T)\ d\lambda \tag{6.20}$$

The incoming signal is modulated (e.g. by a chopper) with a fixed frequency f_{chop}. This signal is now the input for the transducer. This transducer has a spectral bandwidth $\lambda\lambda$ over which its integrates the incoming flux. It produces a time-dependent output voltage V_{out} or current I_{out}, which also contains the noise of the transducer. If thermal noise (so-called Johnson noise)

dominates, this noise is "white" in the temporal frequency domain: kT Watt·Hz^{-1} up to a cut-off frequency f_c, see figure 6.3. The *frequency bandwidth* of the transducer is in this case $\Delta f = f_c$. Since the source signal is periodic with known period $T = \frac{1}{f_{chop}}$, the outcoming signal can be folded *modulo* this period. In this process all transducer noise at other temporal frequencies can be filtered out.

$$\boxed{\text{Source}} \overset{\Phi}{\Longrightarrow} \boxed{\text{Chopper}} \Longrightarrow \boxed{\text{Transducer}}$$

6.3.2 Responsivity

For the case of incoherent detection a basic figure of merit is *responsivity*. This is the ratio of the electrical output (in Amperes or Volts) to the radiant input, i.e. total radiation flux (in Watts).

The *spectral voltage responsivity* of a detection system at a particular output wavelength λ_0 is the measured voltage output $V_{out}(f)$ divided by the monochromatic radiation flux $\Phi(\lambda_0, f)$ incident on the transducer:

$$R_V(\lambda_0, f) = \frac{V_{out}(f)}{\Phi(\lambda_0, f)} \qquad (\text{in Volt} \cdot \text{Watt}^{-1}) \tag{6.21}$$

Since the transducer generally has a limited frequency response or time resolving power (in figure 6.3 it is flat up to a cut-off frequency f_c) the output V_{out} will depend on the temporal behaviour of $\Phi(\lambda_0)$, which can be modulated with a chopping frequency f. For instance, if $f \gg f_c$, the response of the transducer will be zero. Simularly, the *spectral current responsivity* is defined as:

$$R_I(\lambda_0, f) = \frac{I_{out}(f)}{\Phi(\lambda_0, f)} \qquad (\text{in Ampere} \cdot \text{Watt}^{-1}) \tag{6.22}$$

Alternatively, a *blackbody responsivity* $R(T, f)$ can be defined, which represents the detector output signal divided by the incident radiation flux from a blackbody source $\Phi(T)$ modulated by frequency f:

$$R_V(T, f) = \frac{V_{out}(f)}{\Phi(T, f)} \tag{6.23}$$

The relation of $R_V(T, f)$ with $R_V(\lambda_0, f)$ can be easily seen by computing the voltage at the output of the transducer through integration of the spectral responsivity over a blackbody spectrum:

$$V_{out} = \int_0^\infty R_V(\lambda_0, f)\ \Phi_{bb}(\lambda_0, T)\ d\lambda_0 \equiv R_V(T, f)\ \int_0^\infty \Phi_{bb}(\lambda_0, T)\ d\lambda_0 \tag{6.24}$$

hence,

$$R_V(T, f) = \frac{\int_0^\infty R_V(\lambda_0, f)\ \Phi_{bb}(\lambda_0, T)\ d\lambda_0}{\int_0^\infty \Phi_{bb}(\lambda_0, T)\ d\lambda_0} = \overline{R_V(\lambda_0, f)} \tag{6.25}$$

which shows that $R_V(T, f)$ is obtained by averaging $R_V(\lambda_0, f)$ over a blackbody spectral distribution. Note that the blackbody responsivity is a measure of the detector response to incident radiation integrated over all wavelengths even though the transducer is only sensitive to a finite wavelength interval.

Example: consider a steady blackbody source with area A_s irradiating a sensor (transducer) area A_{tr}, both areas are normal to the optical axis connecting them. The power emitted by the blackbody source per unit solid angle equals $A_s\sigma_{SB}T^4/\pi$ (in Watt·sr^{-1}) with $\sigma_{SB} = 5.67{\cdot}10^{-8}$ Watt·m^{-2}·K^{-4} Stefan-Boltzmann's constant. The transducer area A_{tr} subtends a solid angle as seen by the blackbody source of A_{tr}/R^2 if the source is at a distance R. Hence, the blackbody voltage responsivity follows from:

$$R_V(T) = \frac{\pi R^2 V_{out}}{A_s A_{tr} \sigma_{SB} T^4} \qquad (\textit{in Volt}\cdot\ \textit{Watt}^{-1}) \tag{6.26}$$

This equation also holds if the transducer is preceded by a loss-less optical system that images all of the blackbody source area onto the detector area, since the ratio V_{out}/A_{tr} remains constant.

6.3.3 The Noise Equivalent Power (*NEP*)

The noise equivalent power (*NEP*) of a detector is the required power incident on the detector to produce a signal output equal to the rms-noise voltage at the output. Stating this in a different way, the *NEP* is the signal power that is required to produce a *SNR* equal to one. This signal power is given by

$$V_{out} = R_V \cdot \Phi \tag{6.27}$$

This yields a *SNR* of

$$SNR = \frac{R_V \cdot \Phi}{\sqrt{\overline{V_{noise}^2}}} = \frac{R_I \cdot \Phi}{\sqrt{\overline{I_{noise}^2}}} \tag{6.28}$$

and consequently for a $SNR = 1$:

$$\Phi \equiv NEP = \frac{\sqrt{\overline{V_{noise}^2}}}{R_V} = \frac{\sqrt{\overline{I_{noise}^2}}}{R_I} \tag{6.29}$$

Either the spectral responsivity $R(\lambda_0, f)$ or the blackbody responsivity $R(T, f)$ may be inserted in equation 6.29 to define two different noise equivalent powers. The spectral $NEP(\lambda_0, f)$ is the monochromatic radiant flux $\Phi(\lambda_0)$ required to produce a *SNR* of one at a frequency f. The blackbody $NEP(T, f)$ represents the blackbody radiant flux required to produce a *SNR* of one.

The noise equivalent power is useful for comparing similar detectors that operate under identical conditions. It should however not be used as a general measure of detector performance for comparing dissimilar detectors. Firstly, the larger the temporal frequency bandwidth Δf the larger the noise that is present. Also, increasing the detector area A_{tr} will in general decrease the responsivity if all other factors are held constant.

A more useful figure of merit is therefore the normalized noise equivalent power, either per unit bandwidth:

$$NEP^{\star} = \frac{NEP}{\sqrt{\Delta f}} \qquad (\text{in Watt} \cdot \text{Hz}^{-\frac{1}{2}}) \tag{6.30}$$

or per unit bandwidth and per unit area:

$$NEP^* = \frac{NEP}{\sqrt{A_{tr}\ \Delta f}} \qquad (\text{in Watt} \cdot \text{Hz}^{-\frac{1}{2}} \cdot \text{m}^{-1}) \tag{6.31}$$

Normalisation entails proportionality to the square root of bandwidth and collecting area A_{tr}.

The reciprocal values of the *NEP* and the *NEP** are the so-called *Detectivities*, D and D^*, and are often used, i.e.:

$$D = \frac{1}{NEP} \tag{6.32}$$

$$D^* = \frac{1}{NEP^*} = D \cdot \sqrt{A_{tr}\ \Delta f} \tag{6.33}$$

$$\tag{6.34}$$

implying the notion that *"larger is better"*. Again, either the spectral or blackbody *NEP* may be used to define spectral or blackbody detectivity, $D^*(\lambda_0, f)$ and $D^*(T, f)$ respectively.

An alternative equivalent expression for D^* is:

$$D^* = \frac{\sqrt{A_{tr}\ \Delta f}}{\Phi} \cdot SNR \tag{6.35}$$

with Φ the radiant power incident on the detector. Expression 6.35 can be interpreted as D^* to be equal to the *SNR* at the output of the transducer when 1 Watt of radiant power is incident on a detector area of 1 m^2 with a bandwidth of 1 Hz. This is of course only meant as a mental concept because most transducers are much smaller than 1 m^2 and they reach their limiting sensitivity output well below 1 Watt of incident power.

The figure of merit D^* may be used to compare directly the merit of transducers (sensors, detectors) of different physical size, whose performance was measured using different bandwidths.

6.4 Quantum characterisation

In observations where the individual information carriers are registered (photons, cosmic-ray particles or neutrinos), the signal to noise ratio considerations are based on a statistical treatment of the data. This leads to expressions for the limiting sensitivity for source detection depending on collecting area, exposure time and noise level. In what follows, statistical independence is assumed between subsequent events; the process possesses no internal coherence and the stochastic nature of the data can therefore be described by Poissonian statistics.

Consider a radiation beam, originating from a distant point source, with a photon flux density n_s (e.g. photons$\cdot\text{m}^{-2}\cdot\text{s}^{-1}$). Suppose this point source is embedded in uniformly distributed background radiation noise with a photon intensity n_{bg} (photons$\cdot\text{m}^{-2}\cdot\text{s}^{-1}\cdot\text{sr}^{-1}$). Furthermore, the quantum noise of the detector is given by n_{det} counts per unit detector area per unit time. If the telescope effective area equals $\bar{A}_{eff}$, where the energy dependent collecting area has been averaged over the energy bandwidth of the observation, the number of registered counts over an integration period T_{obs} in one image pixel equals:

$$N_1 = ((n_s + n_{bg}\Delta\Omega)\bar{A}_{eff} + n_{det}A_{pix})T_{obs} = (n_s + n_{bg}\Delta\Omega + n_{det}\delta)\bar{A}_{eff}T_{obs} \tag{6.36}$$

in which $\Delta\Omega$ represents the solid angle subtended on the sky by the angular resolution of the telescope and δ the ratio between the area of a single pixel on the face of the image detector

A_{pix} and $\bar{A}_{eff}$. An adjacent pixel without the point source accumulates in the same observing time:

$$N_2 = (n_{bg}\Delta\Omega + n_{det}\delta)\bar{A}_{eff}T_{obs} \tag{6.37}$$

According to Poissonian statistics the fluctuations in N_1 and N_2 equal $\sqrt{N_1}$ and $\sqrt{N_2}$ respectively. The *SNR* can now be defined as

$$SNR = \frac{N_1 - N_2}{\sqrt{N_1 + N_2}} \tag{6.38}$$

in which the signal strength is evaluated in terms of the magnitude of the statistical fluctuation in the noise component (beware: **not** in relation to the *absolute* magnitude of the noise component).

Consider two extreme cases:

- *The source signal strongly dominates the noise, i.e.* $N_2 \ll N_1$.

  In this case the *SNR* equals

  $$SNR = \sqrt{N_1} = \sqrt{n_s\bar{A}_{eff}T_{obs}} \tag{6.39}$$

  In terms of the limiting sensitivity, a minimum number of photons N_{min} is required in order to be able to speak of a detection, for example 10 or 25. In those cases the *SNR* equals 3 or 5.

  The limiting sensitivity follows from

  $$n_{s_{min}} = \frac{N_{min}}{\bar{A}_{eff}T_{obs}} \sim (\bar{A}_{eff}T_{obs})^{-1} \tag{6.40}$$

  This is the best possible case. The detection is so-called *signal-photon-noise limited*. The limiting sensitivity improves linearly with the effective collecting area and the integration time.

- *The source signal is drowned in the noise, i.e.* $N_1 \approx N_2 = N$.

  The criterium for source detection can be formulated on the basis of a certain level of confidence (minimal *SNR*) k. The limiting sensitivity now follows from

  $$n_{s_{min}} = k\frac{\sqrt{2N}}{\bar{A}_{eff}T_{obs}} \tag{6.41}$$

  Substituting $N = (n_s + n_{bg}\Delta\Omega + n_{det}\delta)\bar{A}_{eff}T_{obs}$:

  $$n_{s_{min}} = k\sqrt{\frac{2(n_{bg}\Delta\Omega + n_{det}\delta)}{\bar{A}_{eff}T_{obs}}} \sim (\bar{A}_{eff}T_{obs})^{-\frac{1}{2}} \tag{6.42}$$

  In this case the limiting sensitivity only improves with the square root of the telescope collecting area and the integration time.

  In the case $n_{det}\delta \ll n_{bg}\Delta\Omega$ (detector noise negligible), the detection is said to be *background-photon-noise limited*.

Note: implicitly the bandwidth of the observation also comes in when evaluating the *SNR*. The values n_s, n_{bg} and n_{det} were defined as integral values over a certain predetermined energy bandwidth. For example, if an energy bandwidth $\epsilon_2 - \epsilon_1 = \Delta\epsilon$ is considered, $n_s = \int\limits_{\Delta\epsilon} n_s(\epsilon)\, d\epsilon = \bar{n}_s(\epsilon)\Delta\epsilon$. Similarly, $n_{bg} = \bar{n}_{bg}(\epsilon)\Delta\epsilon$ and $n_{det} = \bar{n}_{det}(\epsilon)\Delta\epsilon$. Now the following relations hold:

- signal-photon-noise limited: $n_{s_{min}}(\epsilon) \sim (\bar{A}_{eff}T_{obs}\Delta\epsilon)^{-1}$
- background-photon-noise limited: $n_{s_{min}}(\epsilon) \sim (\bar{A}_{eff}T_{obs}\Delta\epsilon)^{-\frac{1}{2}}$

Different observatories are not only sensitive in different energy ranges, but have also different limiting sensitivities. The following figure shows the spectra of four objects (Crab nebula, 3C273 (a quasar at $z = 0.158$), NGC 1068 (an active Seyfert galaxy at 11 Mpc distance) and 3C273 if it were displaced at $z = 4$. It also shows in thick lines the limiting sensitivities of several observing facilities.

- *Radio: Westerbork (pre-upgrade), Very Large Array (New Mexico), Effelsberg 100 meter dish (near Bonn).*
- *Infrared: Aircraft balloon experiment, Infrared Space Observatory.*
- *Optical: eye, 200-inch telescope (5 meter) at Mount Palomar (California), Faint Object Camera in the Hubble Space Telescope.*
- *Ultraviolet + X-rays: UHURU-satellite, EXOSAT, Einstein Observatory and the Chandra X-ray Observatory (AXAF).*
- *γ-rays: COS-B.*

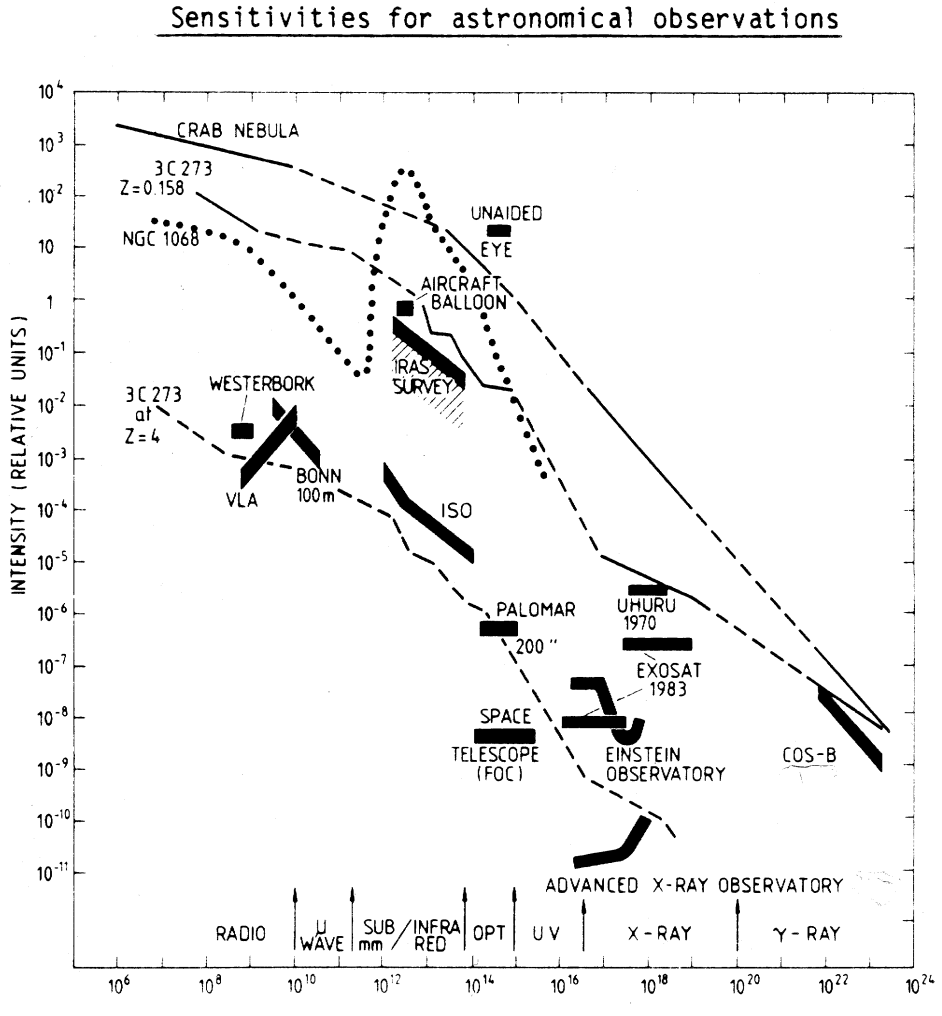

Chapter 7

Imaging in Astronomy

As introduced in Chapter 3, each position in the sky specified by a unit direction vector $\vec{\Omega}$ is associated with a *monochromatic intensity (spectral radiance)* $I(\vec{\Omega}, \lambda, t)$, received by an observer. This distribution is the monochromatic image or map of the sky (or source). The observation process inevitably degrades this image in at least three different ways:

- *Through* the finite exposure length, which leads to a finite number of photons incident during the measurement time. Consequently we always deal with a *sample* of the parent distribution representing the true image. This introduces measurement noise and leads to an imperfect restitution of $I(\vec{\Omega}, \lambda, t)$, releative to a measurement with infinite signal-to-noise ratio. We have treated the issue of signal-to-noise in some depth in Chapter 6. We shall also return to this subject in more quantitative detail in the master course Observational Astrophysics 2 (OAF2).

- *Through* the finite size of the telesope or antenna apertures, that imposes a fundamental restriction on the attainable image quality due to diffraction. In addition, the focussing properties and the imperfections in the realisation of the optical surfaces lead to geometrical aberrations that may become dominant over the fundamental restrictions imposed by diffraction.

- In the case of ground-based optical observatories, *through* the consequence of the radiation beam crossing the Earth's heterogeneous and turbulent atmosphere. In modern telescope systems this can partly be compensated for by employing adaptive optics.

In the following sections we shall treat in some detail the effects on image formation arising from diffraction, geometrical aberration and atmospheric "seeing".
At wavelengths shorter than ~ 0.1 nanometer, the application of focussing optics becomes untenable due to extremely low reflection efficiencies of the optical surfaces. Imaging can still be accomplished by employing beam modulation techniques (e.g. coded mask telescopes) and, at gamma-ray wavelengths, by exploiting the directionality properties of the photon interaction processes. In the latter case, the optical element and the detection system have become one and the same device. A discussion of these techniques is presented in the latter part of this chapter and is elaborated with reference to recently operated and planned space observatories.

7.1 Diffraction

7.1.1 The Huygens-Fresnel principle

Consider a point source S at great distance compared to the size of the aperture of an observing telescope, a condition that is mostly satisfied in observational astrophysics. The EM-wave incident on the telescope aperture can hence be described by a plane wave. Propagation of this plane wave beyond the aperture opening is then governed by the Huygens-Fresnel principle. This principle states that *every unobstructed point of a wavefront, at a given instant in time, serves as a source of secondary wavelets with the same frequency as that of the primary wave. The amplitude of the radiation field at any point* ***beyond****, is the superposition of all these wavelets considering their amplitudes and relative phases.*

7.1.2 Fresnel and Fraunhofer diffraction

Now imagine the aperture of the telescope as an opening in an opaque screen and consider a plane of observation very close behind this aperture. Under these conditions a clear and sharp image of the aperture is recognizable, despite some light fringing around its periphery (keep in mind that the idealized *geometric* aperture image corresponds to $\lambda \to 0$). If the plane of observation is moved further away from the aperture, the radiation starts to diverge and the image of the aperture becomes increasingly more structured as fringes become more prominent. This is known as **Fresnel** or **near field** diffraction. If the plane of observation is gradually moved out further, the fringes continually change, the projected pattern is now spread out considerably and bears almost no resemblance anymore to the actual aperture. Still further out, only the size of the pattern changes and not its shape. The radiation now propagates in spherical expansion. If R is the distance from the aperture, the wave amplitudes decrease proportional to R and the radiation power with R^2, in contrast to the plane wave incident on the aperture opening. In this region we have the **Fraunhofer** or **far field** limit for diffraction, which holds for the great majority of observations in astronomy. Putting it differently: taking a point source S and a point of observation P, both very far from the aperture opening, Fraunhofer diffraction applies as long as the incoming and outgoing (in a conical fashion) wavefronts approach being planar (i.e. differing therefrom by a small fraction of a wavelength over the extent of the diffracting aperture or obstacle).

Figure 7.1 shows the planar wave situation applicable to Fraunhofer diffraction, two lenses (L_1, L_2) have been inserted to reposition the radiation source S and the observation position P from infinity to a finite and physically feasible location.

A more quantitative way to appreciate this is that in the superposition of all wavelets at the observation point P (application of the Huygens-Fresnel principle defined above) the *phase* of each contributing wavelet at P, due to the differences in path traversed, is crucial to the determination of the resultant field amplitude in P. Now if the wavefronts impinging on and emerging from the aperture are planar, these path differences will be describable by a *linear function* of the two geometric aperture variables, say a 2-dimensional position vector $\vec{r}$. This *linearity in the aperture variables of the wavelet's phase differences* is the explicit mathematical criterion for the prevalence of Fraunhofer diffraction!

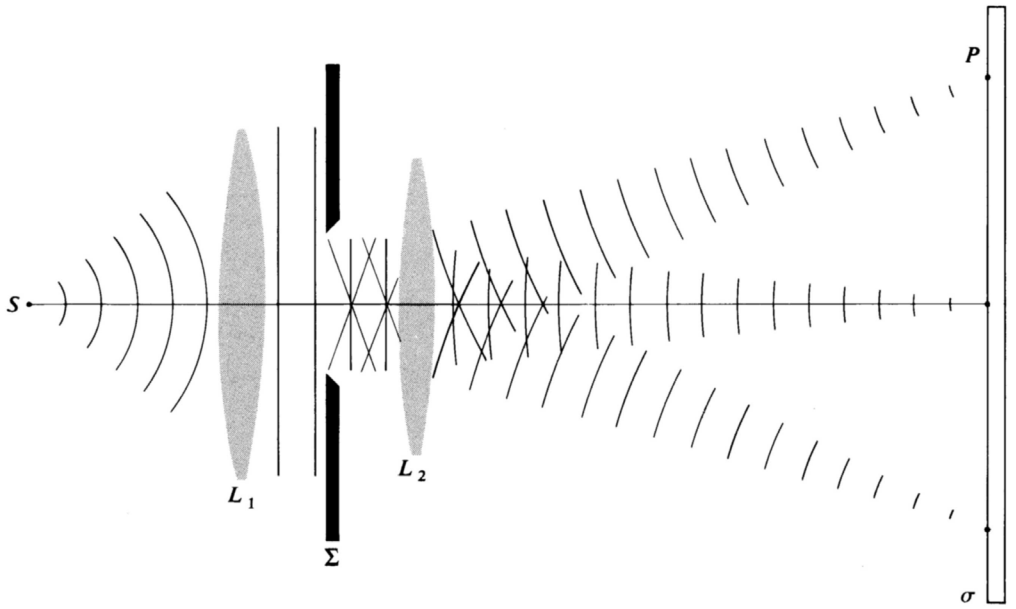

Figure 7.1: *Fraunhofer diffraction. Credit Hecht (1987).*

7.1.3 Point Spread Function (PSF) and Optical Transfer Function (OTF) in the Fraunhofer limit

Consider the primary mirror, lens or radio dish of a telescope viewing the sky. The plane through the rim of the primary mirror (dish) is defined as the *aperture* or *pupil plane*. A position in this pupil plane can be specified by a 2-dimensional position vector $\vec{r}$. The position of a celestial source in the sky field being observed can be specified by a unit direction vector $\vec{\Omega}(\Omega_x, \Omega_y, \Omega_z)$, its components represent the direction cosines relative to a Cartesian coordinate system with its origin at the centre of the mirror. The x-axis is chosen perpendicular to the pupil plane and the y and z axes are located in the pupil plane, see figure 7.2. Obviously $\Omega_x^2+\Omega_y^2+\Omega_z^2 = 1$ should hold, so if Ω_y and Ω_z are given Ω_x is fixed apart from its sign. However the radiation is incident from the upper hemisphere, hence we have $\Omega_x \geq 0$. Consequently a source position in the sky can be described by a 2-dimensional rather than a 3-dimensional vector $\vec{\Omega}(\theta_y, \theta_z)$. The angular components θ_y and θ_z refer to two orthogonal angular coordinate axes across the sky field under observation, they are related to the direction cosines of $\vec{\Omega}$ through $\sin\theta_y = \Omega_y/(1-\Omega_z^2)^{\frac{1}{2}}$ and $\sin\theta_z = \Omega_z/(1-\Omega_y^2)^{\frac{1}{2}}$. In observational astronomy a particular sky field under observation is practically always strictly limited in angular size ($\leq$ square degree). Therefore, in good approximation, we can assume that $\theta_y \approx \sin\theta_y \approx \Omega_y$ and $\theta_z \approx \sin\theta_z \approx \Omega_z$.

To stipulate the essence of Fraunhofer diffraction, we reduce the telescope primary mirror to a single pupil in the yz-plane. If we consider the image plane to be spherical at a very large distance $R \to \infty$ from the pupil plane, a celestial point source at sky coordinates $\vec{\Omega}_0(\theta_{y0}, \theta_{z0})$ will produce a geometrical image located at $-\vec{\Omega}_0(\theta'_{y0}, \theta'_{z0}) = -\vec{\Omega}_0(-\theta_{y0}, -\theta_{z0})$ in the image plane. *In this approach the telescope has been reduced to a Camera Obscura.* This has fundamentally no impact on our analysis, since in reality the *actual telescope mirror only serves to retrieve the point source image* at $R = \infty$ to a practical distance: the focal length of the telescope. As a consequence of the diffraction by the pupil, the image of the celestial point source will not be limited to the direction $\vec{\Omega}_0$ of the geometrical image, but will also

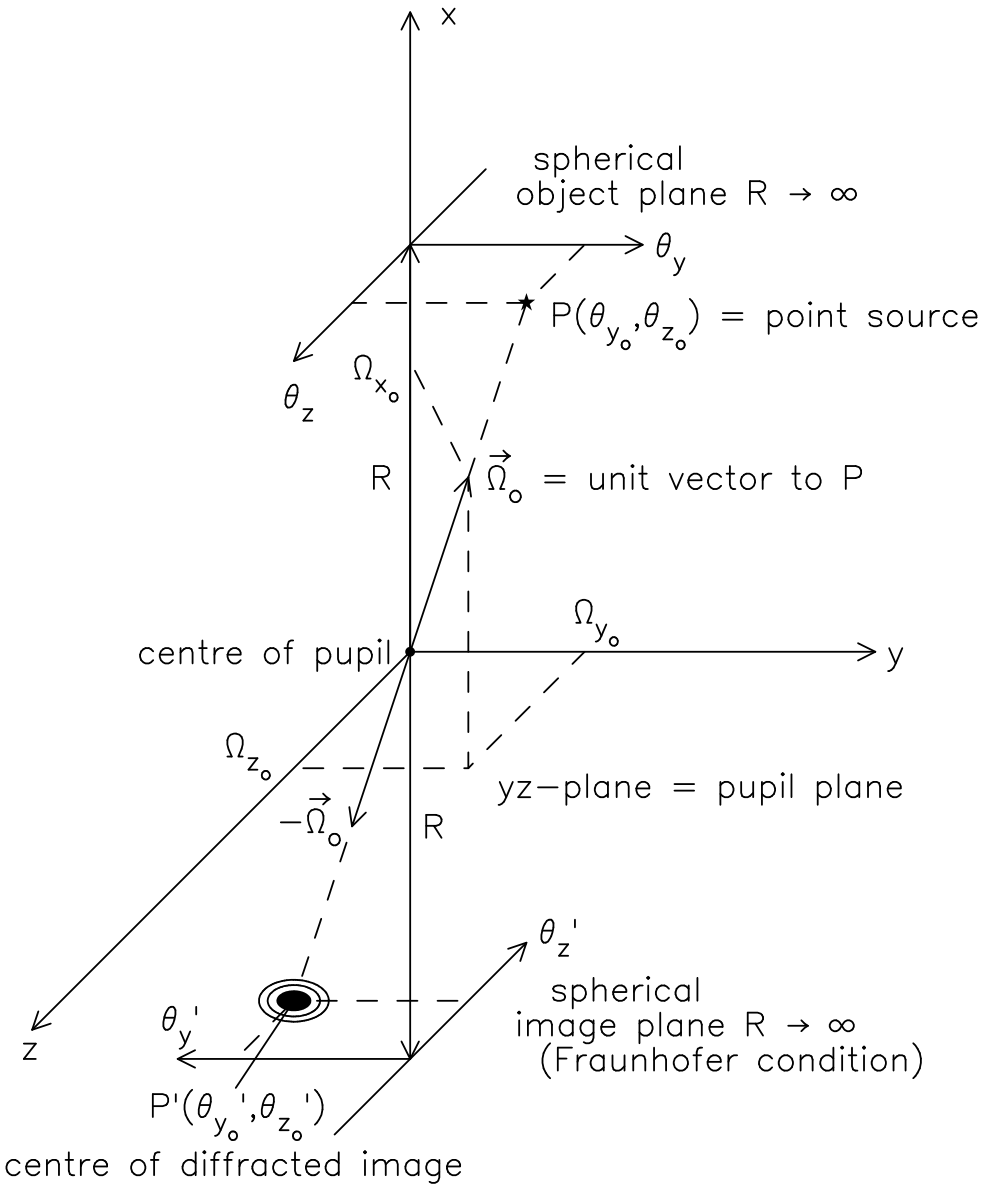

Figure 7.2: *Camera Obscura: sky and image coordinates in the Fraunhofer limit.*

be blurred around this direction. (*Interalia:* we can omit the minus sign by simply reversing the pointing direction of $\vec{\Omega}_0$, i.e. now pointing towards the image plane in the anti-source direction). Hence, if we have a celestial point source of *unit intensity* at a sky position $\vec{\Omega}_0$, the intensity of the diffraction image need to be described by a function $h(\vec{\Omega} - \vec{\Omega}_0)$: the Point Spread Function (PSF) of the diffraction-limited telescope. The Fourier transform of $h(\vec{\Omega} - \vec{\Omega}_0)$ is designated the Optical Tranfer Function (OTF), i.e. we have PSF $\Leftrightarrow$ OTF.
For the derivation, in the Fraunhofer limit, of the relation between the radiation field in the pupil plane and the emerging diffraction pattern described by the telescope's PSF consider the geometry in figure 7.3. A quasi-monochromatic celestial point source is located at the origin of the angular sky coordinates, i.e. along the direction of the x-axis ($\theta_y = 0, \theta_z = 0$). This source, at very large distance from the telescope aperture, produces a flat wavefront in the pupil plane. Taking the centre of the pupil as the origin, we have at every position $\vec{r}$ of the pupil the same electric field signal, i.e. a fully coherent field distribution across the pupil,

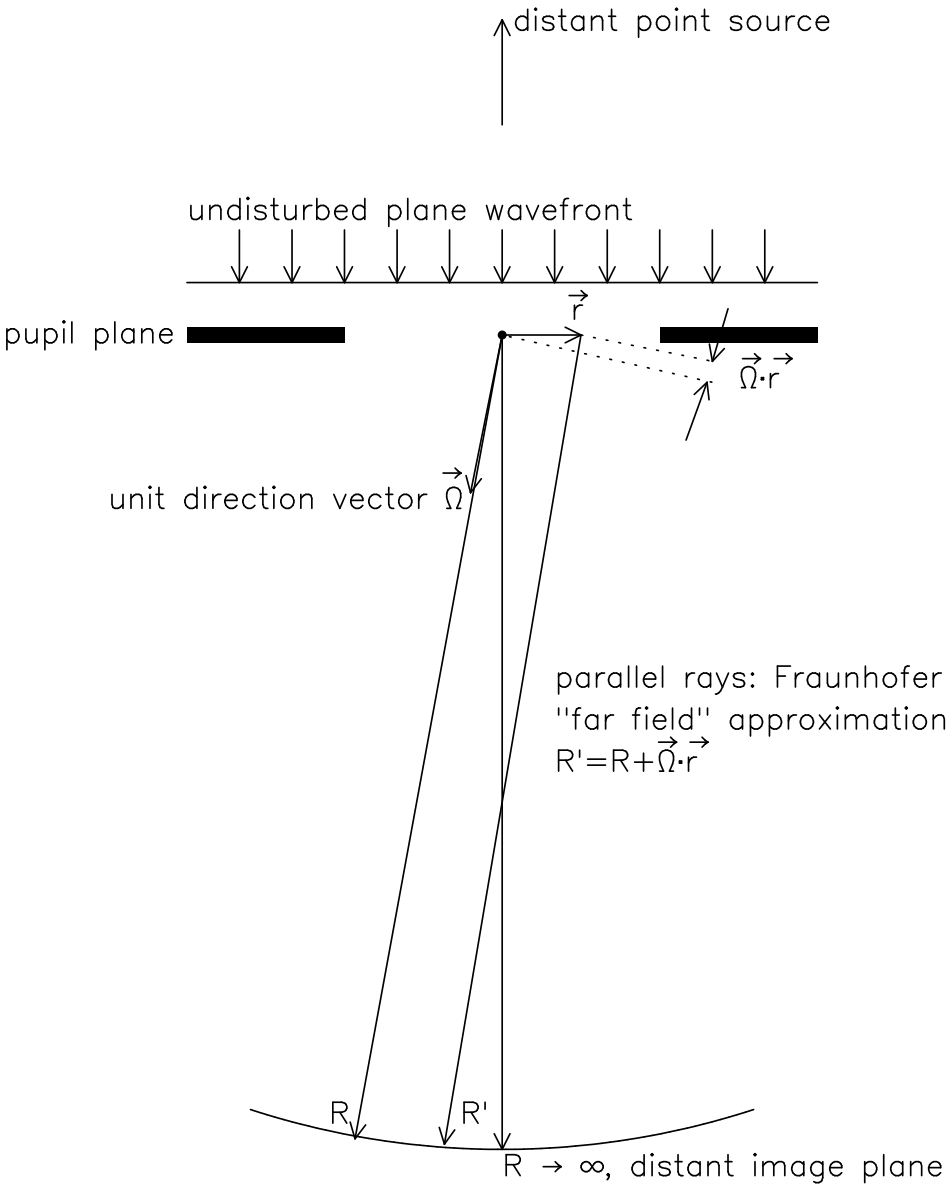

Figure 7.3: *Geometry for diffraction by the telescope pupil in the Fraunhofer limit.*

analytically expressed (see Chapter 3) as:

$$\tilde{E}(t) = \tilde{E}_0(t) \cdot e^{i2\pi\bar{\nu}t} \quad \text{with the amplitude "phasor"} \quad \tilde{E}_0(t) = |\tilde{E}_0(t)| \cdot e^{i\phi(t)} \tag{7.1}$$

According to *Huygens-Fresnel*, the resulting field $\tilde{E}(\vec{\Omega}, t)$ in a direction $\vec{\Omega}$ on a distant image sphere with radius R is the superposition of the contributions from all positions within the pupil, each contribution with its own specific phase delay due to the difference in path length:

$$\tilde{E}(\vec{\Omega}, t) \;=\; \frac{C}{R} \int\int_{\text{pupil}} \tilde{E}_0 \left(t - \frac{R'(\vec{\Omega}, \vec{r})}{c} \right) e^{i2\pi\bar{\nu}\left(t - \frac{R'(\vec{\Omega}, \vec{r})}{c}\right)} d\vec{r} \tag{7.2}$$

with $R'(\vec{\Omega}, \vec{r})$ the distance between the pupil position $\vec{r}$ and the image position in the direction $\vec{\Omega}$ (see figure 7.3), $d\vec{r} = dydz$, $1/R$ the amplitude damping factor due to the spherical expansion of the wavefield and C a proportionality constant. To evaluate the integral in equation (7.2) in the Fraunhofer limit, we make two important assumptions:

- The coherence length $l_c = c\tau_c$, see Chapter 3, is presumed large compared to the maximum path difference between the waves originating at different positions within the pupil (i.e. large compared to the pupil diameter). This imposes a requirement on the maximum allowable frequency bandwidth of the quasi-monochromatic source. With this condition fulfilled, the complex amplitude of the image in the direction $\vec{\Omega}$, $\tilde{E}_0\left(t - R'(\vec{\Omega}, \vec{r})/c\right)$, is independent of the pupil coordinate $\vec{r}$. Hence, the complex amplitude term in equation (7.2) can be placed in front of the integral.

- The far field approximation holds, i.e. the distance between position $\vec{r}$ in the pupil and the image position in the direction $\vec{\Omega}$ is linearily dependent on the pupil coordinate $\vec{r}$:

$$R'(\vec{\Omega}, \vec{r}) \;=\; R \;+\; \vec{\Omega} \cdot \vec{r} \tag{7.3}$$

  with $\vec{\Omega} \cdot \vec{r} = \Omega_y y + \Omega_z z = \theta_y y + \theta_z z$ the scalar product between the unit image-direction vector $\vec{\Omega}$ and $\vec{r}$ (by definition 2-dimensional, since $\vec{r}$ has no x-coordinate).

Implementing these assumption, we can rewrite equation (7.2) as:

$$\begin{aligned} \tilde{E}(\vec{\Omega}, t) \;&=\; \left(\frac{C}{R}\int\int_{\text{pupil}} e^{\frac{-2\pi i \vec{\Omega}\cdot\vec{r}}{\lambda}} d\vec{r}\right)\left[\tilde{E}_0(t - \frac{R}{c})\, e^{2\pi i \bar{\nu}(t - \frac{R}{c})}\right] \\ &=\; \left(\frac{C}{R}\int\int_{\text{pupil plane}} P(\vec{r})\, e^{\frac{-2\pi i \vec{\Omega}\cdot\vec{r}}{\lambda}} d\vec{r}\right)\tilde{E}(t - \frac{R}{c}) \end{aligned} \tag{7.4}$$

where we have introduced the pupil function $P(\vec{r})$, with $P(\vec{r}) = 1$ inside the pupil and $P(\vec{r}) = 0$ everywhere else.
Note: The notion of the pupil function can actually be implemented in a more general fashion and makes it a versatile tool for describing the influence of an aperture on the incident radiation field, like transmission, reflection, absorption and/or phase shifts. For example, the pupil may act as a phase mask that introduces position dependent phase changes $\phi(\vec{r})$, these can be represented by putting $P(\vec{r}) = e^{i\phi(\vec{r})}$, rather than $P(\vec{r}) = 1$ inside the pupil boundary.
Equation (7.4) is now expressed in the form of a Fourier integral, however the integral implies a *scaled* Fourier transform of the pupil function $P(\vec{r})$ with conjugate variables $\vec{\Omega}$ and $\vec{r}/\lambda$.
Next, the proportionality constant C can be determined by using the fact that the total energy flux (= radiant flux, see Chapter 3) $\Phi(t)$ through the pupil needs to be conserved in the diffraction image, i.e.:

$$\int\int_{\text{image plane}} |\tilde{E}(\vec{\Omega}, t)|^2 R^2 d\vec{\Omega} \;=\; \Phi(t) \;\;\Rightarrow\;\; \int\int_{\text{image plane}} |\tilde{E}(\vec{\Omega}, t)|^2 d\vec{\Omega} \;=\; \frac{\Phi(t)}{R^2} \tag{7.5}$$

Applying Parseval's theorem to the scaled Fourier transform given in equation (7.4) we also have:

$$\frac{1}{\lambda^2}\int\int_{\text{image plane}} |\tilde{E}(\vec{\Omega}, t)|^2 d\vec{\Omega} \;=\; \int\int_{\text{pupil plane}} \frac{C^2}{R^2} |P(\vec{r})\; \tilde{E}(t - \frac{R}{c})|^2 \frac{d\vec{r}}{\lambda^2} \;=\; C^2 \frac{\Phi(t)}{R^2} \tag{7.6}$$

Combining equations (7.5) and (7.6), we obtain $C = 1/\lambda$.
Substituting C in equation 7.4 and writing the Fourier integral as a "true" (i.e. *non-scaled*) Fourier transform in the conjugate variables $\vec{\Omega}$ and $\vec{\zeta} \equiv \vec{r}/\lambda$ (beware: $d\vec{\zeta} \equiv d\vec{r}/\lambda^2$), results in:

$$\tilde{E}(\vec{\Omega}, t) \;=\; \left[\left(\frac{\lambda}{R}\right)\int\int_{\text{pupil plane}} P(\vec{\zeta})\, e^{-2\pi i \vec{\Omega}\cdot\vec{\zeta}}\, d\vec{\zeta}\right]\tilde{E}(t - \frac{R}{c}) \;=\; \tilde{a}(\vec{\Omega})\tilde{E}(t - \frac{R}{c}) \tag{7.7}$$

The 2-dimensional conjugate vector variable $\vec{\zeta}$ has the dimension $radian^{-1}$ and represents a specific ***spatial frequency on the sky*** expressed in periods/radian. The **dimensionless function** $\tilde{a}(\vec{\Omega})$ is called the amplitude diffraction pattern:

$$\tilde{a}(\vec{\Omega}) \;=\; \left(\frac{\lambda}{R}\right) \int\int_{\text{pupil plane}} P(\vec{\zeta}\,)\, e^{-2\pi i \vec{\Omega}\cdot\,\vec{\zeta}}\, d\vec{\zeta} \quad \text{with} \quad a(\vec{\Omega}\,[0,0]\,) = \left(\frac{\lambda}{R}\right)\left(\frac{\textit{pupil area}}{\lambda^2}\right) \tag{7.8}$$

The **dimensionless quantity** $a(\vec{\Omega}\,[0,0]$ entails the product of the amplitude damping term $1/R$, *scaled to* λ, and the geometrical pupil area, *scaled to* λ^2.
Equation (7.8) shows a most important result regarding the diffraction phenomenon: in the Fraunhofer limit the amplitude diffraction pattern, with the proper normalisation factor at $\vec{\Omega}\,[0,0]$, can be obtained by taking the Fourier transform of the pupil function, i.e.:

$$\tilde{a}(\vec{\Omega}) \quad \Leftrightarrow \quad \left(\frac{\lambda}{R}\right) P(\vec{r}/\lambda) \tag{7.9}$$

This Fourier pair shows that the diffraction image depends on the size of the pupil, expressed in the number of wavelengths λ.
The derivation of the amplitude diffraction image $\tilde{a}(\vec{\Omega})$ was done for a quasi-monochromatic point source at the origin of the angular sky coordinates along the direction of the x-axis. A similar point source at an arbitrary position $\vec{\Omega}_0$ on the sky yields a diffraction image $\tilde{a}(\vec{\Omega}-\vec{\Omega}_0)$, i.e. the same diffraction image but displaced to the geometrical image position $\vec{\Omega}_0$. This is an obvious result, and straightforward to derive.

Equation (7.8) expresses the distribution of the amplitude diffraction pattern. Taking the square of the absolute value of this expression yields the intensity diffraction pattern, defined as the telescope's Point Spread Function (PSF).

Intermezzo: Power flux density transported by an EM-wave

The energy streaming through space in the form of an electromagnetic wave is shared between the constituent electric and magnetic fields.
The energy density of an electrostatic field (e.g. between plates of a capacitor) $\rho_{\vec{E}} = \epsilon_r \epsilon_0 |\vec{E}|^2/2$ (dimension Joule/m^3), with $|\vec{E}|$ the magnitude of the electric vector (dimension V/m) and ϵ_0 the vacuum permittivity ($8.8543 \cdot 10^{-12}$ Asec/Vm). Similarly, the energy density of a magnetic field (e.g. within a toroid) equals $\rho_{\vec{B}} = |\vec{B}|^2/(2\mu_r\mu_0)$ (dimension Joule/m^3), with $|\vec{B}|$ the magnitude of the magnetic vector (dimension Tesla = Vsec/m^2) and μ_0 the vacuum permeability ($4\pi \cdot 10^{-7}$ Vsec/Am).
The wave equation for a **plane electromagnetic wave** traveling along the x-direction in vacuum is given by:

$$\frac{\partial^2 E(x,t)}{\partial x^2} \;=\; \frac{1}{c^2}\frac{\partial^2 E(x,t)}{\partial t^2} \quad \text{and} \quad \frac{\partial^2 B(x,t)}{\partial x^2} \;=\; \frac{1}{c^2}\frac{\partial^2 B(x,t)}{\partial t^2} \tag{7.10}$$

for the electric field wave and the magnetic field wave respectively. The magnetic field wave travels in a plane perpendicular to the electric field, both the electric field and the magnetic field directions are perpendicular to the direction of propagation (x). The plane wave solution can be expressed by a harmonic function, using a complex scalar representation:

$$\tilde{E}(x,t) \;=\; E_0 e^{i\cdot 2\pi(\nu t - x/\lambda)} \quad \text{and} \quad \tilde{B}(x,t) \;=\; B_0 e^{i\cdot 2\pi(\nu t - x/\lambda)} \tag{7.11}$$

Consistency with Maxwell's equations requires that for the EM-wave holds $\rho_{\vec{E}} = \rho_{\vec{B}}$. Hence, from the above, we have $B_0 \;=\; E_0/c$.

The flow of electromagnetic energy through space associated with the traveling EM-wave is represented by the Poynting vector $\vec{S} = (1/\mu_0)\vec{E}\,\mathbf{x}\,\vec{B}$, a vector product that symbolizes the direction and magnitude of the energy transport per unit time across a unit area (e.g. in units Watt m^{-2}). The vector magnitude $|\vec{S}| = |\tilde{E}||\tilde{B}|(\sin\phi)/\mu_0$ equals $|\tilde{E}||\tilde{B}|/\mu_0$, since the magnetic field is perpendicular to the electric field ($\phi = \pi/2$). Representing the *actual* wave signal by taking the real part of expressions (8.75) we get:

$$|\vec{S}| = E_0 B_0 \cos^2 2\pi(\nu t - x/\lambda) = \epsilon_0 c E_0^2 \cos^2 2\pi(\nu t - x/\lambda) = (\epsilon_0/\mu_0)^{\frac{1}{2}} E_0^2 \cos^2 2\pi(\nu t - x/\lambda) \tag{7.12}$$

The *average* power flux density for an *ideal monochromatic* plane wave, $\overline{I(t)}$ equals $\overline{|\vec{S}(t)|}$:

$$\overline{I(t)} = (\epsilon_0/\mu_0)^{\frac{1}{2}} E_0^2 \overline{\cos^2 2\pi(\nu t - x/\lambda)} = (\epsilon_0/\mu_0)^{\frac{1}{2}} \frac{E_0^2}{2} = 2.6544 \cdot 10^{-3} \frac{E_0^2}{2} \tag{7.13}$$

expressed in Watt/m^2 for E_0 in Volts/meter.
An idealised monochromatic plane wave is represented in the time domain by an infinitely long wave train and is by definition *fully polarised*. As has already been discussed, an *unpolarised, quasi-monochromatic*, radiation field from a thermal source can be described by a complex expression for the electric field $\tilde{E}(t)$, comprising a harmonic oscillation at an average frequency $\bar{\nu}$ modulated by a slowly varying envelope, accomodated by the phasor $\tilde{E}_0(t)$, i.e. $\tilde{E}(t) = \tilde{E}_0(t) \cdot e^{i(2\pi\bar{\nu}t)}$. The average power flux density for this wave then follows from the expectation value of the product $\tilde{E}(t)\tilde{E}^*(t)$:

$$\overline{I(t)} = (\epsilon_0/\mu_0)^{\frac{1}{2}} \mathbf{E}\left\{\tilde{E}(t)\tilde{E}^*(t)\right\} = 2.6544 \cdot 10^{-3}\, \mathbf{E}\left\{|\tilde{E}_0(t)|^2\right\} \tag{7.14}$$

Since we are primarily concerned with *relative power flux densities generated by these traveling waves within the same medium*, we can disregard in what follows multiplication with the numerical constant in expression (8.78), since this (deterministic) quantity is only of relevance for assessing the *absolute numerical value* of the power flux density and bears no influence on the description of the stochastic nature of the signals. In practical computations, this constant should of course be applied!

End intermezzo: Power flux density transported by an EM-wave

The brightness distribution, $s_\lambda(\vec{\Omega}, t)$, of the cosmic source under observation is convolved with this PSF to obtain the diffraction-limited source image $d_\lambda(\vec{\Omega}, t)$. Similarly, the Fourier transform of the source brightness distribution, $S_\lambda(\vec{\zeta}, t)$, is multiplied with the Optical Transfer Function (OTF) of the telescope to obtain the spatial frequency spectrum of the diffraction-limited source image $D_\lambda(\vec{\zeta}, t)$. Hence we have:

$$\begin{aligned} d_\lambda(\vec{\Omega}, t) &= \int\int_{\text{source}} h_\lambda(\vec{\Omega} - \vec{\Omega}')\, s_\lambda(\vec{\Omega}', t)\, d\vec{\Omega}' \quad \text{and} \\ D_\lambda(\vec{\zeta}, t) &= H_\lambda(\vec{\zeta}) \cdot S_\lambda(\vec{\zeta}, t) \end{aligned} \tag{7.15}$$

In the above relations we have added an index λ to stipulate the wavelength dependence of the PSF and the OTF.
Multiplying (7.8) with its complex conjugate yields the mathematical expression for the PSF $h_\lambda(\vec{\Omega})$:

$$\text{PSF} = h_\lambda(\vec{\Omega}) = \tilde{a}(\vec{\Omega}) \cdot \tilde{a}^*(\vec{\Omega}) = \left|\, \tilde{a}(\vec{\Omega}) \,\right|^2 = \left| \left(\frac{\lambda}{R}\right) \int\int_{\text{pupil plane}} P(\vec{\zeta})\, e^{-2\pi i \vec{\Omega}\cdot\vec{\zeta}}\, d\vec{\zeta} \right|^2 \tag{7.16}$$

To obtain an expression for the OTF $H_\lambda(\vec{\zeta})$, taking the general case of a complex pupil function, we can use the following relations (verify this yourself!):

$$\tilde{a}(\vec{\Omega}) \;\Leftrightarrow\; \left(\frac{\lambda}{R}\right) P(\vec{\zeta}) \quad \text{and} \quad \tilde{a}^*(\vec{\Omega}) \;\Leftrightarrow\; \left(\frac{\lambda}{R}\right) P^*(-\vec{\zeta}) \tag{7.17}$$

Hence, by applying the convolution theorem, we get:

$$\tilde{a}(\vec{\Omega}) \cdot \tilde{a}^*(\vec{\Omega}) \;\Leftrightarrow\; \left(\frac{\lambda}{R}\right)^2 \left[P(\vec{\zeta}) \;*\; P^*(-\vec{\zeta})\right] \tag{7.18}$$

In the common case of a *centrally symmetric pupil*, the autoconvolution of equation (7.18) is just the autocorrelation, and so we can write:

$$\text{OTF} \;=\; H_\lambda(\vec{\zeta}) \;=\; \frac{1}{R^2} \int\int_{\text{pupil plane}} P(\vec{r})^*\, P(\vec{r} - \lambda\vec{\zeta})\, d\vec{r} \tag{7.19}$$

with the vector variable of the integral rescaled to the pupil coordinate $\vec{r}$. (The complex conjugate of the pupil function in equation (7.19) has of course no meaning in case the pupil function is real)
Equation (7.19) characterizes the response function of a low pass filter for spatial frequencies: the transmission continually decreases with increasing spatial frequency, at a certain value $\lambda\vec{\zeta}_{max}$, the mutually displaced pupil functions in (7.19) will no longer overlap and higher spatial frequencies will not be transmitted.
Important notion: *a finite pupil acts as a low pass filter for the spatial frequencies in the brightness distribution of the celestial object observed. Given a fixed size of the pupil: the longer the wavelength the lower the cut-off frequency ($\lambda|\vec{\zeta}\,| = constant$).*
Moreover it is worth noting that, although non-circular pupils are rarely encountered in astronomy, expressions (7.16) and (7.19) are applicable for *arbitrary* pupil geometries.

7.1.4 Circular pupils

Circular pupils play a central role in astronomy, so this warrants a special description. Given the circular symmetry, the pupil function can be expressed as a function of a scalar variable ρ with the aid of the 2-dimensional *circular* box function $\Pi(\rho)$, where $\Pi(\rho) \equiv 1$ for $|\rho| < 1/2$ and $\Pi(\rho) \equiv 0$ for $|\rho| \geq 1/2$. The Fourier transform of this function involves the first order Bessel function $J_1(x)$:

$$\Pi(\rho) \;\Leftrightarrow\; \frac{1}{2}\left[\frac{J_1(\pi\theta)}{\theta}\right] \tag{7.20}$$

in which the scalar variable θ, replacing the angular direction vector $\vec{\Omega}$, represents the circular symmetric diffraction angle. Taking a telescope diameter D and applying the scaling law for Fourier transforms, we have:

$$\Pi\left(\frac{\rho}{D}\right) \;\Leftrightarrow\; \frac{1}{2}\left[\frac{DJ_1(\pi\theta D)}{\theta}\right] \tag{7.21}$$

Substituting for ρ the spatial frequency variable (now also a scalar) $p = \rho/\lambda$, the amplitude of the diffracted field follows from equation (7.9):

$$a(\theta) \;\Leftrightarrow\; \left(\frac{\lambda}{R}\right) \Pi\left(\frac{\lambda p}{D}\right) \;\Rightarrow\; \left(\frac{\lambda}{R}\right)\left[\frac{1}{4}\pi(D/\lambda)^2\right]\left[\frac{2J_1(\pi\theta D/\lambda)}{\pi\theta D/\lambda}\right] \tag{7.22}$$

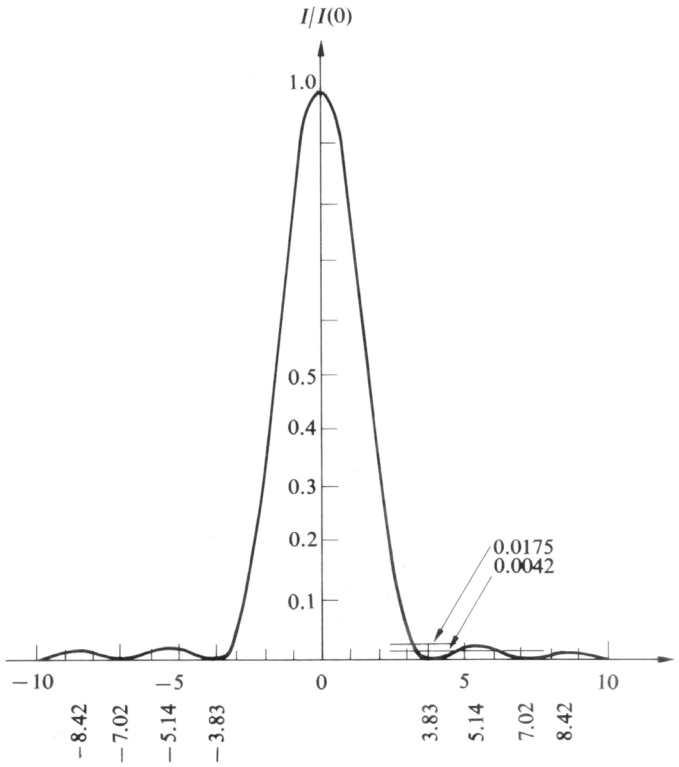

Figure 7.4: *The Airy brightness function normalised to unit intensity at* $\theta = 0$. *Credit Hecht (1987).*

Hence, introducing the reduced variable $u = \pi\theta D/\lambda$, we arrive at the expression for the *diffraction-limited* PSF for a circular telescope:

$$PSF \;=\; |a(\theta)|^2 \;=\; \left(\frac{\lambda}{R}\right)^2 \left(\frac{1}{4}\pi(D/\lambda)^2\right)^2 \left[\frac{2J_1(u)}{u}\right]^2 \tag{7.23}$$

The first term in the expression at the right-hand side is the normalisation of the PSF for undiffracted light, i.e. for $\theta = 0$. It involves the **dimensionless** quantity that accomodates the attenuation factor (*scaled to* λ) of the radiation energy due to the spherical expansion of the wavefield in the Fraunhofer limit and the geometrical area of the circular aperture, *scaled to* λ^2. The second term is often called the *Airy brightness function* and has a ring-like structure. We can designate this term as $h_\lambda(\theta)$, the point source response function normalised to unit intensity at $\theta = 0$, i.e.:

$$h_\lambda(\theta) \;=\; \left[\frac{2J_1(u)}{u}\right]^2 \;\equiv\; \left[\frac{2J_1(\pi\theta D/\lambda)}{\pi\theta D/\lambda}\right]^2 \tag{7.24}$$

The OTF can be derived from the autocorrelation of $\Pi(\lambda p/D)$:

$$\begin{aligned} OTF \;&=\; \left(\frac{\lambda}{R}\right)^2 \left[\Pi\left(\frac{\lambda p}{D}\right) * \Pi\left(\frac{\lambda p}{D}\right)\right] \\ &=\; \frac{1}{2}\left(\frac{D}{R}\right)^2 \left[\arccos\left(\frac{\lambda p}{D}\right) - \left(\frac{\lambda p}{D}\right)\left(1 - \left(\frac{\lambda p}{D}\right)^2\right)^{\frac{1}{2}}\right] \Pi\left(\frac{\lambda p}{2D}\right) \end{aligned} \tag{7.25}$$

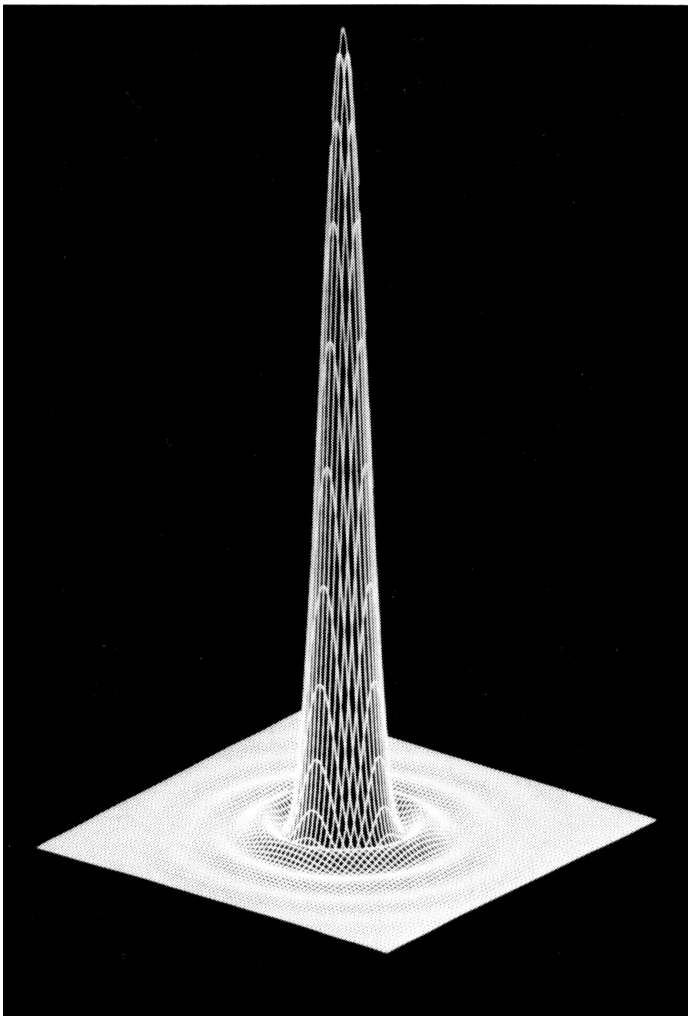

Figure 7.5: *The 2-dimensional Airy brightness function for the diffracted intensity. Credit Hecht (1987).*

Normalization to unity response for zero frequency ($p = 0$), by *dividing* with the telescope area and *disregarding* the $1/R^2$ attenuation factor resulting from spherical expansion of the diffracted field in the Fraunhofer limit, yields the spatial frequency response function $H_\lambda(p)$ of the telescope:

$$H_\lambda(p) = \frac{2}{\pi}\left[\arccos\left(\frac{\lambda p}{D}\right) - \left(\frac{\lambda p}{D}\right)\left(1 - \left(\frac{\lambda p}{D}\right)^2\right)^{\frac{1}{2}}\right]\Pi\left(\frac{\lambda p}{2D}\right) \tag{7.26}$$

Figure 7.4 and figure 7.5 show the Airy diffraction patterns in 1- and 2-dimensional display. The FWHM of the central peak is roughly equal to λ/D *radians*, around this main peak ring shaped secondary maxima are present that decrease monotonously in strength. Figure 7.6 shows the OTF resulting from self-convolution of the circular pupil function: the shape is referred to as the "Chinese hat", the transmission of spatial frequencies decreases almost linearly up to the cut-off frequency D/λ, beyond this frequency the transmission of the telescope equals zero.

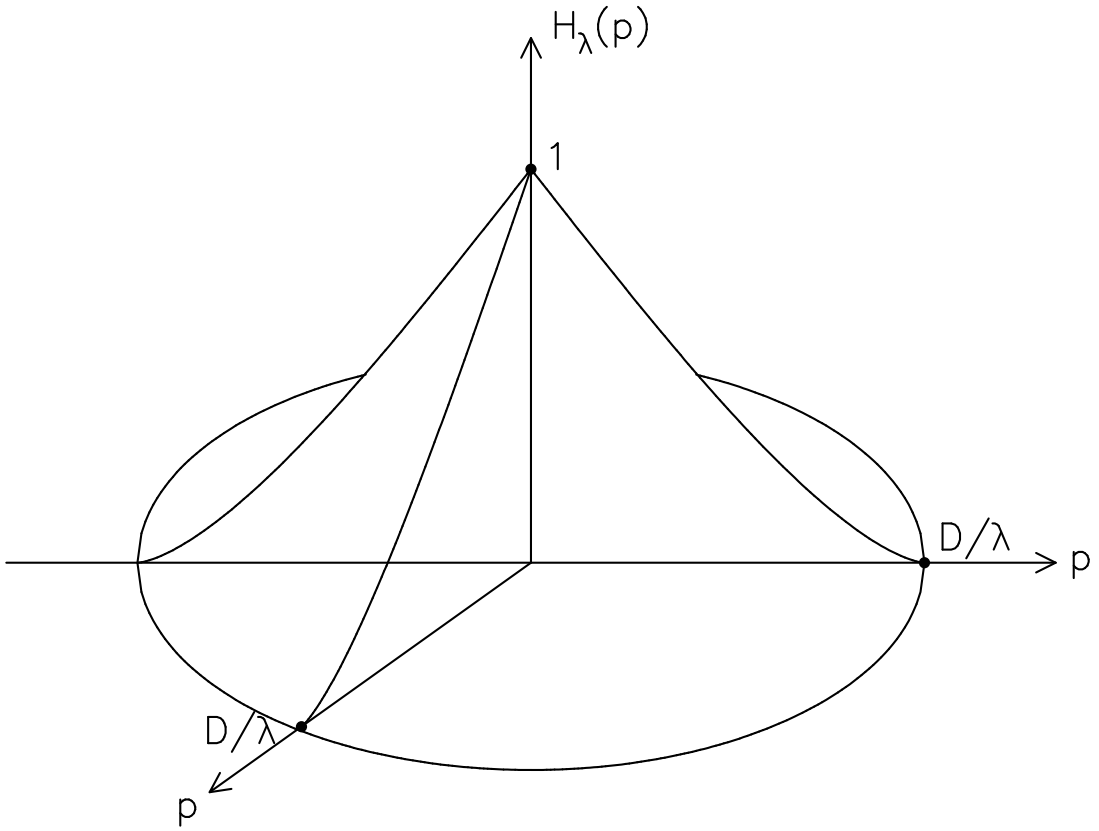

Figure 7.6: *The Optical Tranfer Function (OTF) for a circular aperture with diameter D. The 3d-shape is sometimes referred to as the Chinese Hat function.*

7.1.5 Rayleigh Resolution Criterion

The image of two, equally bright, point sources with an angular separation θ is the incoherent superposition of two identical Airy functions. The limiting angle at which the two sources can be separated has been fixed at the value where the maximum of the one Airy function coincides with the first zero of the other Airy function. The first zero of $J_1(u)$ occurs at a value of the reduced variable $u = u_0 = 3.832$, this relates to an angle $\theta = \theta_0 = 1.22\lambda/D$. This angular value is often used to specify the *angular resolving power* or discriminating power of the telescope pupil and is commonly referred to as the *Rayleigh criterion*. This criterion is only approximate and much less quantitative than the PSF $h_\lambda(\theta)$ for a circular pupil. Moreover, in certain cases it is possible to resolve two point sources closer than θ_0, for example in the case of the two components of a double star, if the measurement of the image is made with excellent signal to noise ratio (larger than a few hundred). In such a case the diffracted image profile $I(\theta)$ can significantly differ from the profile of a single point source $h_\lambda(\theta)$ even if the angular separation of the two components is less than θ_0. On the other hand, if the signal to noise ratio is poor, or if the two sources have greatly different brightness, the value of θ_0 might be largely insufficient to reliably extract separate source contributions. The latter case is certainly applicable to crowded source fields with high brightness contrasts between the observed field sources. In that case the value of θ_0 can be severely compromised and the actual resolving power will be significantly reduced in a case specific fashion!

7.1.6 Complex pupils

In expression (7.4) the pupil function was introduced in its simplest form, i.e. $P(\vec{r}) = 1$ inside the pupil and $P(\vec{r}) = 0$ everywhere else. We already noted at that point that the concept of the pupil function is much more general, we shall elaborate shortly on this here. $P(\vec{r}) = 1$ implies that all points within the pupil emit the same field amplitude $\tilde{E}(t) = \tilde{E}_0(t) \cdot e^{i2\pi\bar{\nu}t}$. If we now more generally introduce within the pupil a complex pupil function $\tilde{P}(\vec{r})$, the same treatment of the Fraumhofer diffraction holds as before. However, each pupil point now emits its own specific field amplitude and phase determined by the complex pupil function:

$$\tilde{E}(\vec{r}, t) \;=\; \tilde{P}(\vec{r})\tilde{E}_0(t) \cdot e^{i2\pi\bar{\nu}t} \tag{7.27}$$

The derivation of the amplitude diffraction pattern remains unchanged (verify this youself) and we have (see also equation(7.8)):

$$\tilde{a}(\vec{\Omega}) \;=\; \left(\frac{\lambda}{R}\right) \int\int_{\text{pupil plane}} \tilde{P}(\vec{\zeta}\,)\, e^{-2\pi i \vec{\Omega}\cdot\vec{\zeta}}\, d\vec{\zeta} \tag{7.28}$$

Complex pupil functions can be generated in several different ways, we give here two examples.

- *An optical mask inserted in the aperture.*
  Consider a plane wave incident on the pupil plane. Cover the aperture with a foil with a position dependent transparency (determines the amplitude of $\tilde{P}(\vec{r})$) and a position dependent thickness or refractive index, which determines the phase of $\tilde{P}(\vec{r})$.

- *Microwave phased-array antenna's.*
  Antenna's for radar waves and microwave communication often comprise a flat plane, filled with a large number of radiators, like waveguide exits, dipoles etcetera. They radiate according to expression (7.27). The radiation field emitted from the pupil $\tilde{P}(\vec{r})$ can be regulated electronically, in particular its phase. The radiation beam generated by the collection of individual radiators is defined by the distribution of radiation power over the sky direction vector $\vec{\Omega}$. If we have $\tilde{P}(\vec{r}) = 1$ this distribution is given by the Airy function centered around $\vec{\Omega} = 0$, i.e. perpendicular to the radiator plane. If we select a pupil function with a linear phase dependence, $\vec{\Omega} = e^{-2\pi i\vec{\Omega}_0 \cdot \vec{r}/\lambda}$, the radiation beam rotates towards sky direction $\vec{\Omega}_0$, commensurate with the Fourier *shift theorem*. In this way the direction of the radiation beam can be very rapidly controlled electronically in two angular dimensions without any mechanical rotation devices!

7.2 Other limits to image quality

7.2.1 Optical aberrations

A common and severe aberration of both lenses and mirrors is *spherical aberration*. This aberration arises from the fact that lens or mirror annuli with different radii have different focal lengths. In the case of a spherical mirror this aberration can be completely eliminated for rays parallel to the optical axis by deepening the spherical mirror surface to a paraboloidal surface. However a paraboloidal mirror suffers from another aberration called *coma*. Coma causes the images for objects that are not located on the optical axis to consist of a series of circles which correspond to the various annular zones of the mirror surface, these circles are progressivily shifted towards or away from the optical axis giving rise to a characteristic pear-shaped image blur (see figure 7.7). The figure also shows the condition that needs to be

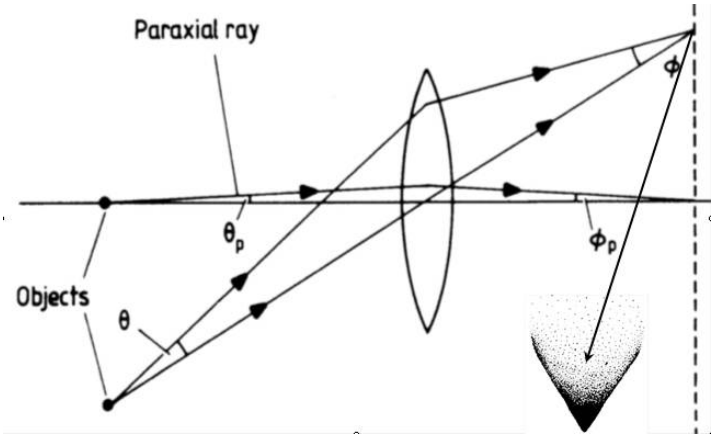

Figure 7.7: *Coma error for an off-axis object. The characteristic "pear-shaped" ray distribution near the off-axis geometrical image point is indicated in the lower right-hand corner. Credit Kitchin (1987).*

obeyed to reduce coma to zero in an optical system, the *Abbe sine condition*:

$$\frac{\sin\theta}{\sin\phi} = \frac{\theta_{parax}}{\phi_{parax}} = \text{constant} \tag{7.29}$$

where the angles are defined in figure 7.7.
The severity of the coma aberration at a given angular distance from the optical axis is inversely proportional to the square of the focal ratio of the telescope. Therefore, the effect of comatic aberration can be significantly reduced by employing as large a focal ratio as possible. Examples of optical designs with large focal ratios comprise the Cassegrain and Ritchey-Chretien systems, we shall dwell on these shortly in the following paragraph since they constitute the most common format for large telescopes in astronomy.
The configuration of the Cassegrain system is sketched in figure 7.8. It is based on a paraboloidal primary mirror and a convex hyperboloidal secondary mirror, the near focus of the secondary hyperboloid coincides with the the focus of the primary paraboloid. The Cassegrain focus is the distant focus of the secondary mirror. The major advantage of the Cassegrain system is its *telelens* characteristic: the secondary hyperboloid expands the beam from the primary mirror so that the focal length of the Cassegrain system becomes several times that of the primary mirror. The coma aberration is consequently substantially reduced to that of a single parabolic mirror with a focal length equal to the effective focal length of the Cassegrain. The beam expanding effect of the secondary mirror makes that Cassegrain telescopes normally work with focal ratios between $f12$ to $f30$, although the primary mirror is only $f3$ or $f4$! Figure 7.8 shows the images for a 25 cm primary in a $f4/f16$ configuration. Displayed are the theoretical on-axis geometrical image point, the on-axis Airy disk arising from diffraction by the 25 cm primary mirror, and the coma-dominated pear-shaped image blur at an off-axis angle of 0.5 degrees (the angular scale of 5 arcseconds is given for reference to the actual angular sizes of these images).
A large improvement in image quality can be obtained if the Cassegrain is modified to a Ritchey-Chretien design. The optical design is the same as for the Cassegrain configuration with the exception that the primary mirror is hyperboloidal rather than paraboloidal and a stronger hyperboloid is used for the secondary. With this design both spherical aberration and coma can be corrected, resulting in an aplanatic system. The improvement in the im-

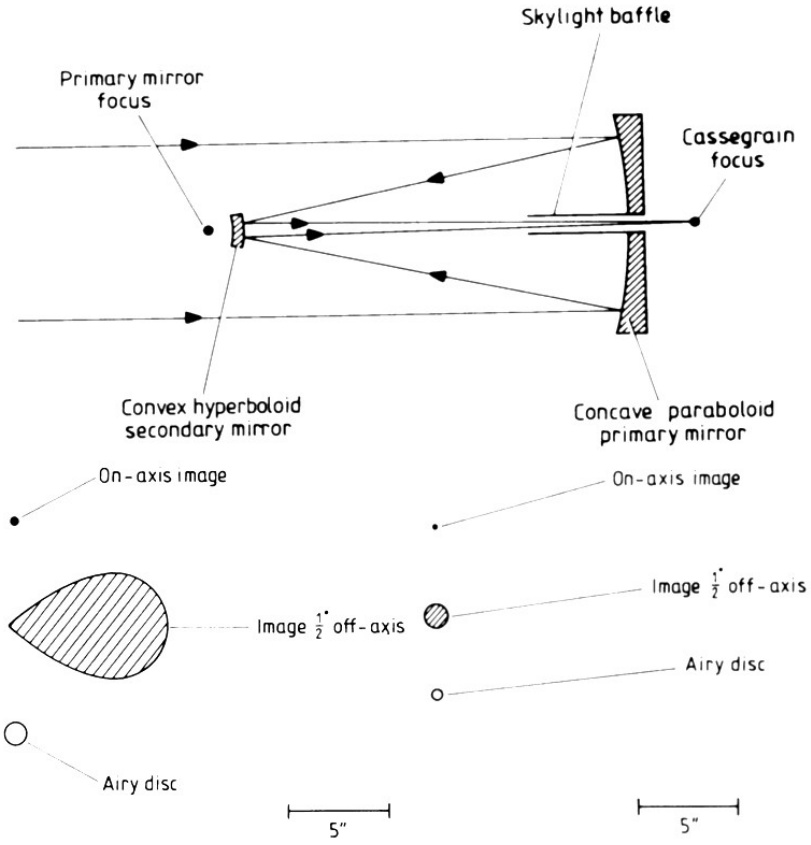

Figure 7.8: *Upper panel: Cassegrain configuration with parabolic primary and hyperbolic secondary mirror. Lower left: comparison between the on-axis Airy-disk and the coma-dominated image at an off-axis angle of 0.5 degrees. Lower right: improved off-axis performance for a two-hyperboloid Ritchey-Chretien configuration. Credit Kitchin (1987).*

age quality is also displayed in figure 7.8 for a 50 cm Ritchey-Chretien telescope with the same effective focal length as the 25 cm Cassegrain. In fact, the improvement relative to the Cassegrain system is larger than the comparison of the images displayed in figure 7.8 suggests, since a *50 cm Cassegrain* would have its off-axis image twice the size (i.e. four times the area) and the on-axis Airy disk half the size (i.e. a quarter times the area) shown in the figure. The optics employed in the Hubble Space Telescope (2.4 m primary mirror) is a Ritchey-Chretien design.
A Cassegrain system can however be improved considerably by the addition of *corrective optics* just before the focus. This corrective optics comprises lens assemblies whose aberrations oppose those of the main Cassegrain system, they involve aspheric surfaces and/or the use of exotic materials like fused quartz. Hence, images can be reduced to less than the size of the *seeing disk* (see next paragraph) up to fields of view of the order of one degree. For a more extensive discussion of telescope designs we refer here to Kitchen (1998), pages 62-80.

7.2.2 Atmospheric degradation: speckle images

The intrinsic quality of modern optical telescopes in terms of their imaging performance can be made very close to the diffraction limit, certainly when taking into account recently developed sophisticated control systems for optimizing the *figure* of the mirror surface by employing

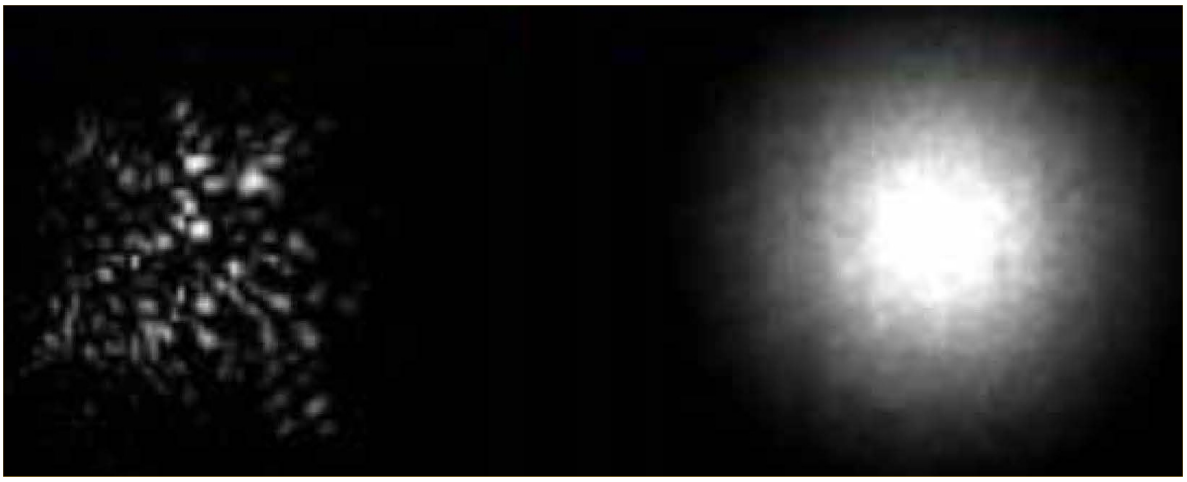

Figure 7.9: *Left panel: short exposure speckle image. Right panel: long exposure showing the smoothed "seeing" disk of the observed point source.*

active corrections for bending under gravity of the mirror mass and temperature gradients over the area, the so called *active optics*. However, as was already pointed out in Chapter 2, in ground-based telescope systems the image quality is limited by turbulent motions in the atmosphere, giving rise to a randomly varying value of the refractive index $n(\vec{r}, t)$ in the air columns over the pupil area. Horizontal scales for these fluctuations range from several *centimeters* to several *meters*. If an undistorted flat wave front enters the atmosphere, three main effects caused by atmospheric turbulence can be identified in the pupil plane of the telescope:

- Variations in amplitude of the wavefront (i.e. lighter and darker brightness patches to the "eye") corresponding to concentration or spreading of the wavefront energy (*scintillation*).
- Variation in the angle of the mean tangent plane to the wavefront causing *angular motion* of the image. Characteristic wavefront slopes are of the order of a few μm's/meter.
- Reduction of spatial coherence of the wavefront across the pupil plane due to random fluctuation of the phase, that leads to *smearing* of the image, resulting in image sizes much larger than from diffraction alone.

These effects can be described by introducing a new, *instantaneous*, pupil function which is random and complex:

$$\tilde{P}(\vec{r}, t) \;=\; P(\vec{r})\psi(\vec{r}, t) \tag{7.30}$$

in which $P(\vec{r})$ represents the simple *geometrical* pupil function introduced in equation (7.4) and $\psi(\vec{r}, t)$ represents a wavefront that randomly varies in amplitude and phase. During a very short exposure, of the order of a few milliseconds, one may consider the wavefront frozen in its instantaneous shape. If we neglect for the moment the amplitude fluctuations (i.e. scintillation), we can write:

$$\psi(\vec{r}, t) \;=\; e^{-i\phi(\vec{r}, t)} \tag{7.31}$$

in which the phase of the wave, $\phi(\vec{r}, t)$, is a random variable whose spatial statistical distribution is determined by the properties of the randomly varying value of the refractive index in the turbulent cells of the overlaying atmosphere. If we consider an atmospheric layer of

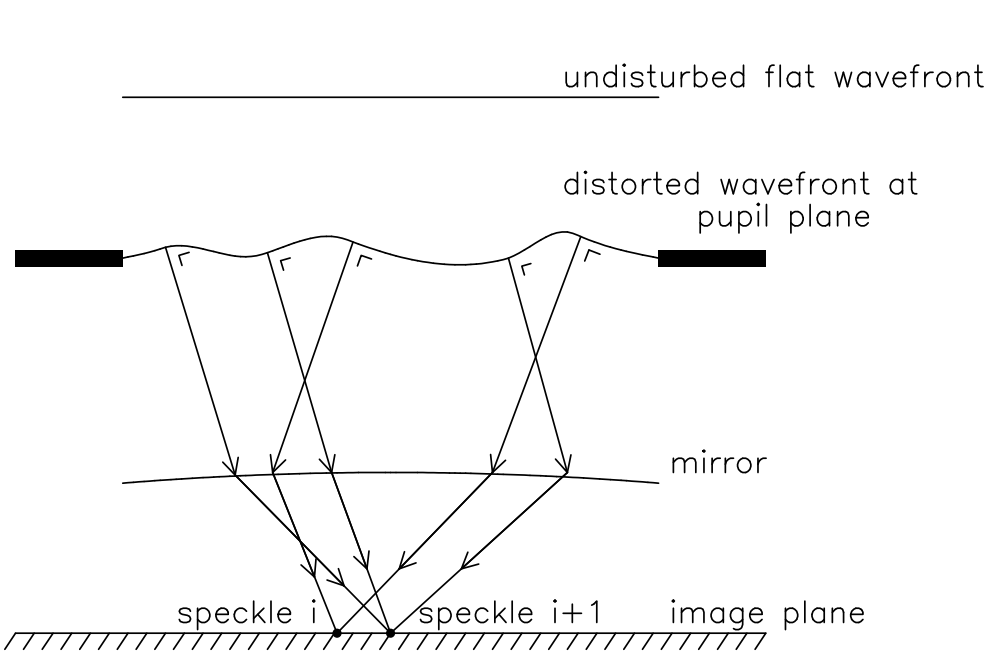

Figure 7.10: *Speckle formation resulting from rays leaving perpendicular "equal-slope" areas on the wavefront in the direction of a specific speckle.*

thickness Δh that is large compared to the scale size of the turbulent cells, so that Gaussian statistics apply (i.e. the central limit theorem), the phase shift produced by the refractive index fluctuations is:

$$\phi(\vec{r},t) \;=\; k \int_{h}^{h+\Delta h} n(\vec{r},t,z)dz \tag{7.32}$$

with $n(\vec{r},t,z)$ the refractive index random variable, z the vertical coordinate and $k = 2\pi/\lambda$ the wave number. This randomly varying phase shift describes the effects of angular motion and smearing of the image, the amplitude variations may often be neglected if the turbulence is not very severe.
Hence we have now an instantaneous, random, pupil function:

$$\tilde{P}(\vec{r},t) \;=\; P(\vec{r})e^{-i\phi(\vec{r},t)} \tag{7.33}$$

which can be used to derive the point source response of the telescope due to atmospheric turbulence. The *instantaneous image* of a point source is obtained from the Fourier transform of the *autocorrelation of the instantaneous pupil function*. Consequently, the image will be an intensity distribution in the focal plane of the telescope, that randomly changes shape with a frequency of 200 to 300 times per second, determined by the coherence time τ_c of the atmosphere. For exposures shorter than this coherence time, the wavefront is considered frozen in its momentary shape, the associated momentary intensity distribution comprises an image with a "speckle" structure as shown in figure 7.9. Every speckle has a diffraction limited PSF of λ/D, e.g. 0.1 arcseconds for a telescope diameter of 2 meters at $\lambda = 1\mu$m. In good approximation one may consider each speckle to be the image resulting from rays leaving perpendicular "equal-slope" areas on the wavefront in the direction of that specific speckle (see sketch of ray paths in figure 7.10). The speckle pattern randomly fluctuates on the same time scale as the wavefront due to the random phase fluctuation across the pupil plane, moreover the speckle pattern as a whole jitters as well following the variations of the mean tangent plane to the wavefront (the angular motion).

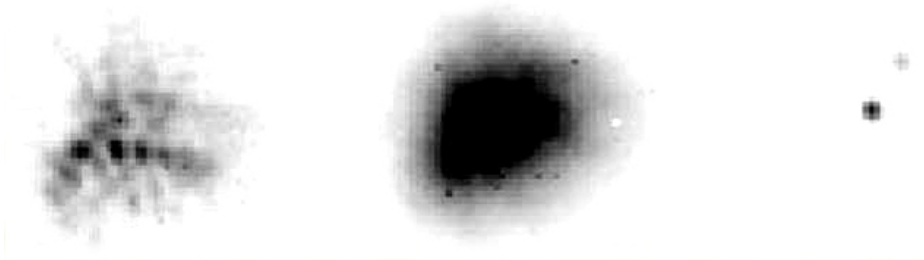

Figure 7.11: *Left frame: a 100 millisecond exposure on the bright T Tauri star V807 Tau, the speckle structure is clearly seen. Middle frame: a 40 second exposure on the same source, the speckles have averaged to a smooth fuzzy source. Right panel: Speckle-processed image revealing the binary nature of the source.*

The *technique of speckle imaging* requires taking many short exposures, which "freeze-out" the effects of the atmosphere. All short exposures are Fourier transformed and averaged in Fourier space to preserve the high-resolution (i.e. diffraction limited) information present in the individual speckle images. The averaged spatial frequency spectrum is then subjected to an inverse Fourier transform, resulting in the final image. In the picture shown in figure 7.11, the left frame shows a 100 millisecond exposure on the bright T-Tauri star V807 Tau, the speckle structure caused by the atmosphere is clearly evident. The central frame displays a 40 seconds exposure on the same source, the speckle structure has averaged out to a smooth fuzzy source image. The right panel shows the result of Fourier-processing of the series of speckle images, demonstrating that this star is actually a binary!

7.2.3 Seeing: the Fried parameter

As is evident from figures 7.9 and 7.11, long exposures combine speckle images into a severely broadened image, this broadening is called *seeing*. The resulting smoothed PSF, the so-called *seeing disk*, is slightly broader than a single speckle pattern and amounts to $\approx$ one arcsecond. This seeing-value of one arcsecond corresponds to the diffraction limit of a 10 cm diameter telescope at $\lambda = 0.5\,\mu$m. The merit of using larger optical telescopes is, therefore, not primarily sharper images but sensitivity owing to their much larger light collecting power!
The observed intensity at each point of a long-exposure image is simply the *time-averaged* instantaneous intensity $\bar{I}(\vec{\Omega}) = \mathbf{E}\left\{I(\vec{\Omega}\,,\,t)\right\}$:

$$\bar{I}(\vec{\Omega}) \;=\; \mathbf{E}\left\{s(\vec{\Omega}) * h(\vec{\Omega},t)\right\} \;=\; s(\vec{\Omega}) * \mathbf{E}\left\{h(\vec{\Omega},t)\right\} \tag{7.34}$$

with $s(\vec{\Omega})$ the intensity of a constant quasi-monochromatic source and $h(\vec{\Omega},t)$ the randomly variable PSF.
The spatial frequency spectrum of the seeing disk in long exposure images follows from the computation of the normalised mean OTF $\bar{H}(\vec{\zeta}) = \mathbf{E}\left\{H(\vec{\zeta}\,,\,t)\right\}$ which, according to equation (7.19), equals the normalised mean autocorrelation of the pupil function in the case of centrally symmetric pupils:

$$\begin{aligned}\bar{H}(\vec{\zeta}) \;&=\; \mathbf{E}\left\{\frac{1}{\int\int_{\text{pupil plane}} P^2(\vec{\zeta}\,')d\vec{\zeta}\,'}\int\int_{\text{pupil plane}} P(\vec{\zeta}\,')e^{-i\phi(\vec{\zeta}\,',t)}P(\vec{\zeta}\,'-\vec{\zeta})e^{i\phi(\vec{\zeta}\,'-\vec{\zeta},t)}d\vec{\zeta}\,'\right\}\\ &=\; \frac{1}{\int\int_{\text{pupil plane}} P^2(\vec{\zeta}\,')d\vec{\zeta}\,'}\int\int_{\text{pupil plane}} P(\vec{\zeta}\,')P(\vec{\zeta}\,'-\vec{\zeta})\mathbf{E}\left\{e^{-i[\phi(\vec{\zeta}\,',t)-\phi(\vec{\zeta}\,'-\vec{\zeta},t)]}\right\}d\vec{\zeta}\,'\end{aligned}$$

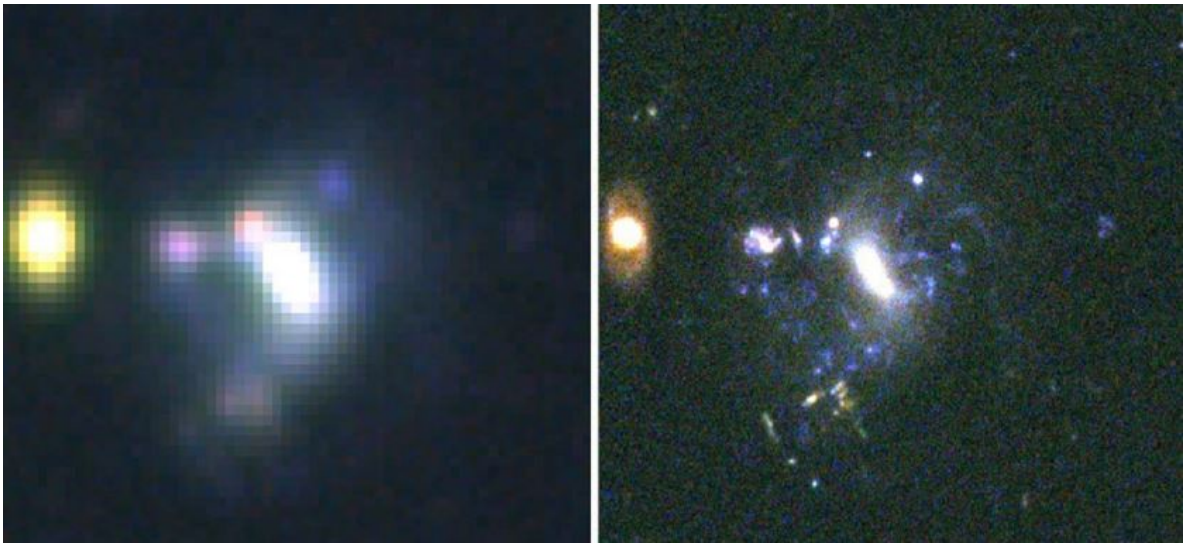

Figure 7.12: *Influence of atmospheric seeing on a sky image. Left: image obtained by a ground-based telescope, resolution 1.1 arcseconds dominated by atmospheric turbulence. Right: the same sky field imaged by the 2.4 meter Hubble Space Telescope, resolution diffraction limited to 0.05 arcseconds. Credit Space Telescope Science Institute.*

(7.35)

with $\vec{\zeta}' \equiv \vec{r}'/\lambda$, $\vec{\zeta} \equiv \vec{r}/\lambda$ and $d\vec{\zeta}' \equiv d\vec{r}'/\lambda^2$ the *scaled* pupil position vectors and differential area, normalised to the wavelength λ. The phase fluctuations $\phi(\vec{\zeta}, t)$ over the wavefront in the pupil plane can be regarded as resulting from a large number of perturbations in the overlaying atmosphere, which are mutually phase independent. According to the central limit theorem the distribution of the random variable $\phi(\vec{\zeta}, t)$ will be *Gaussian with zero mean* over both time and space. If x is a real Gaussian random variable, it is straightforward to show (verify this yourself!) that:

$$\mathbf{E}\left\{\exp(ix)\right\} \;=\; \exp\left[-\frac{1}{2}\,\mathbf{E}\left\{x^2\right\}\right] \tag{7.36}$$

and consequently we have for the expectation value in the integrand of equation (7.35):

$$\begin{aligned}\mathbf{E}\left\{\exp\left[-i[\phi(\vec{\zeta}',t) \,-\, \phi(\vec{\zeta}'-\vec{\zeta},t)]\right]\right\} \;&=\; \exp\left[-\frac{1}{2}\,\mathbf{E}\left\{\left[\phi(\vec{\zeta}',t) \,-\, \phi(\vec{\zeta}' \,-\, \vec{\zeta},t)\right]^2\right\}\right] \\ &=\; \exp\left[-\frac{1}{2}\,Q_\phi(\vec{\zeta})\right]\end{aligned} \tag{7.37}$$

where we have introduced a *structure function for the phase*:

$$\begin{aligned}Q_\phi(\vec{\zeta}) \;&=\; \mathbf{E}\left\{\left[\phi(\vec{\zeta}',t) \,-\, \phi(\vec{\zeta}' \,-\, \vec{\zeta},t)\right]^2\right\} \\ &=\; 2\left[\mathbf{E}\left\{\phi^2(\vec{\zeta}',t)\right\} \,-\, \mathbf{E}\left\{\phi(\vec{\zeta}',t)\phi(\vec{\zeta}'-\vec{\zeta},t)\right\}\right]\end{aligned} \tag{7.38}$$

This structure function for the phase distribution over the wavefront can be derived from the structure function of the refractive index for homogeneous and isotropic turbulence. We shall forego this calculation here and refer to the treatment by F. Roddier: The Effects of

Atmospheric Turbulence in Optical Astronomy (Progress in Optics XIX,281,1981). The phase correlation on the perturbed wavefront expressed by equation (7.38) can be characterised by a *wavelength dependent correlation length* $r_c = \lambda\zeta_c$. A detailed computation involving the afore mentioned structure function of the refractive index yields:

$$Q_\phi(\vec{r}) \;=\; 2\left(\frac{|\vec{r}|}{r_c}\right)^{5/3} \qquad \Longrightarrow \qquad Q_\phi(\vec{\zeta}) \;=\; 2\left(\frac{\lambda|\vec{\zeta}|}{r_c}\right)^{5/3} \tag{7.39}$$

with:

$$r_c \;=\; \left[1.45\,k^2 \int_0^\infty C_n^2(z)\,dz\right]^{-3/5} \tag{7.40}$$

in which the wave number $k = 2\pi/\lambda$ and where $C_n^2(z)$ represents the *refractive index structure constant*, that strongly depends on the altitude z, typical values range from $10^{-14}\,\mathrm{m}^{-2/3}$ near the ground decreasing to $10^{-17}\,\mathrm{m}^{-2/3}$ at an altitude of 10 km.
The common case of a *circular pupil* with a diameter $D \gg r_c$ yields for the mean value of the normalised OTF:

$$\bar{H}(p) \;=\; \exp -\left(\frac{\lambda p}{r_c}\right)^{5/3} \tag{7.41}$$

where we have again used the *scalar* spatial frequency variable p following the limitation to circular symmetry. The point source response is the Fourier Transform of $\bar{H}(p)$.
It is customary to express the degraded resolution in terms of the diameter D_F of a diffraction limited circular pupil which would give an image of the same angular extent as the seeing disk. D_F is the so-called *Fried parameter*, which can be computed from:

$$\int_0^\infty \bar{H}(p)p\,dp \;=\; \int_0^{D_F/\lambda} \frac{2}{\pi}\left[\arccos\left(\frac{\lambda p}{D_F}\right) - \left(\frac{\lambda p}{D_F}\right)\left(1 - \left(\frac{\lambda p}{D_F}\right)^2\right)^{\frac{1}{2}}\right] p\,dp \tag{7.42}$$

For the lefthand integral in equation (7.42):

$$\int_0^\infty p\left[\exp -\left(\frac{\lambda p}{r_c}\right)^{5/3}\right] dp \tag{7.43}$$

we can introduce the variable $x = [(\lambda p)/r_c]^{5/3}$ and rewrite this as:

$$\frac{3}{5}\,\frac{r_c^2}{\lambda^2}\int_0^\infty x^{1/5}\,e^{-x}\,dx \;=\; \frac{3}{5}\,\frac{r_c^2}{\lambda^2}\,\Gamma\left(\frac{6}{5}\right) \;=\; 0.55\,\frac{r_c^2}{\lambda^2} \tag{7.44}$$

Introducing a change of variable $x = (\lambda p)/D_F$, we can rewrite the righthand integral of equation (7.42) as:

$$\left(\frac{2}{\pi}\,\frac{D_F^2}{\lambda^2}\right)\left[\int_0^1 \left(x\arccos x - x^2\sqrt{(1-x^2)}\right)dx\right] \;=\; \left(\frac{2}{\pi}\,\frac{D_F^2}{\lambda^2}\right)\left(\frac{\pi}{16}\right) \;=\; \frac{D_F^2}{8\,\lambda^2} \tag{7.45}$$

Hence, the Fried parameter relates to the phase correlation length r_c on the perturbed wavefront as:

$$D_F^2 \;=\; 4.4\,r_c^2 \qquad \Longrightarrow \qquad D_F \;=\; 2.1\,r_c \tag{7.46}$$

and, implementing expression (7.40), we find:

$$D_F \;=\; \left[0.423\,k^2 \int_0^\infty C_n^2(z)\,dz\right]^{-3/5} \;=\; 0.185\,\lambda^{6/5}\left[\int_0^\infty C_n^2(z)\,dz\right]^{-3/5} \tag{7.47}$$

Subsequently, expressing the phase structure function $Q_\phi(\vec{r})$ and the mean OTF $\bar{H}(p)$ for a *circular aperture* in terms of the Fried parameter D_F, we can rewrite equations (7.39) and (7.41) as:

$$Q_\phi(\vec{r}) \;=\; 6.88\left(\frac{|\vec{r}|}{D_F}\right)^{5/3} \qquad\qquad \bar{H}(p) \;=\; \exp\left[-\,3.44\left(\frac{\lambda p}{D_F}\right)^{5/3}\right] \tag{7.48}$$

From this we see that the spatial frequency cut-off $p \approx D_F/\lambda$ ($\bar{H}(p) \approx 0.03$), consequently the angular resolution $\Delta\theta \approx \lambda/D_F$. This value is often called the *seeing angle* or simply the *seeing*. A typical value for D_F in the visible range of the spectrum ranges between 10 and 20 cm. So if for instance the seeing at the Keck 10-m telescope is 10 cm, the image quality is no better than that provided by a 10-cm amateur telescope. From expression (7.47) it is clear that the *Fried parameter is highly chromatic*: $\sim \lambda^{6/5}$. This means that the coherence area rapidly increases towards the infrared: a D_F of 20 cm at 0.5 μm increases to almost 1.2 meters at 2.2 μm.

7.2.4 Real time correction: principle of adaptive optics

Under certain conditions, it is possible to restore spatial frequencies, filtered by the atmosphere, in real time. This is the aim of *adaptive optics*, which has developed very rapidly since 1985.
An atmospheric compensation system employing active optics contains three main components: a sampling system, a wavefront sensor and a correction system. The sampling system provides the sensor with the distorted wavefront, in astronomy this normally entails a partly reflecting mirror, which typically diverts ≈ 10 percent of the radiation to the sensor, allowing the bulk of the radiation to proceed to form the main image. Many adaptive optics systems use a *guide star* rather than the object of interest to determine the distorsions of the wavefront. Inevitably, the guide star must be very close in the sky to the object of interest, or its wavefront will have undergone a different atmospheric distorsion. The region of the sky over which the images have been similarly affected by the turbulent atmosphere is called the *isoplanatic area or patch*. This can in practise be as small as a few arcseconds. The notion of the isoplanatic area is displayed in the left panel of figure 7.13. This small angular size of the isoplanatic area means that only very few objects have suitable guide stars, therefore artificial guide stars have been produced. This is being accomplished by the production of a so-called *optical echo*: a laser is tuned to one of the sodium D-line frequencies and excites the free sodium atoms in the atmosphere at a typical height of 80 - 90 km. The glowing atoms appear like a star-like point close to the object of interest. Laser-produced guide stars possess two inherent problems. Due to the relatively low height of the laser-produced guide star, the light path is slightly conical and may still differ substantially from the light path traversed by the radiation from the object of interest. Secondly, the outgoing laser beam is affected by atmospheric turbulence as well, i.e. the guide star moves with respect to the object of interest, again resulting in a blurred image during long exposures.
A wavefront sensor detects the distorsions in the incoming wavefront provided by the beam splitter. Figure 7.13 shows the so-called Hartmann sensor, frequently used in astronomical

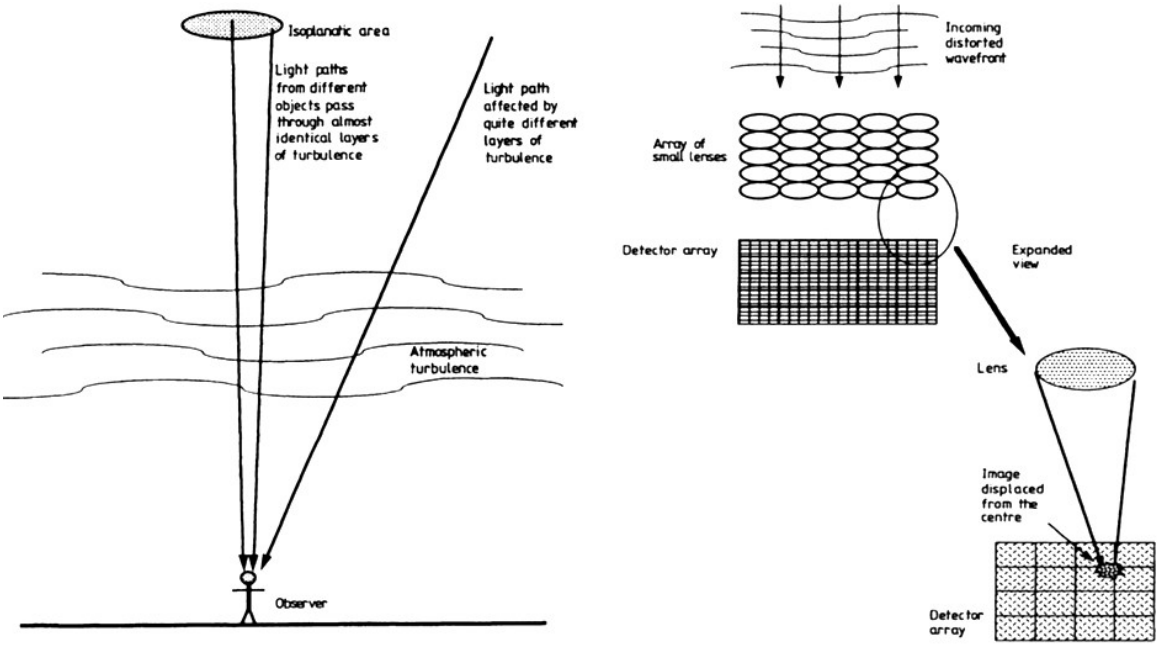

Figure 7.13: *Left: the isoplanatic area. Right: The Hartman array sensor for generation of the error signals caused by turbulence induced "folds" in the flat wavefronts arriving from a distant point source. Credit Kitchin (1987).*

adaptive optics systems. It employs a two-dimensional array of small focussing lenses, each of which providing an image onto an array-detector. In the absence of wavefront distorsions, each image is *centered* on an array-element. Distorsions in the wavefront will displace the images from the detector centres, the degree of displacement and its direction is used to generate error signals which are fed to a correction mirror. Since the atmosphere changes on a timescale of the order of ten milliseconds, the sampling, sensing and correction has to occur in a millisecond or less. The simplest systems only correct for the overall tilt of the wavefront, i.e. the mean tangent plane change of the wavefront that causes angular motion of the image. This is accomplished by suitably tilting a plane or segmented mirror placed in the light beam of the telescope in the direction opposite to the angular motion. A similar technique is the so-called *shift and add* methodology, in that case multiple short exposure images are shifted until their brightest points are aligned and then added together. More sophisticated techniques also involve fine scale displacement corrections by employing a thin mirror capable of being distorted by piezo- electric or other actuators placed undernearth the deformable mirror surface. The error signals of the sensor elements are then used to distort the mirror in the opposite manner relative to the distorsions of the incoming wavefront. Currently operating systems using this approach can achieve diffraction-limited performance in the near-infrared for telescopes of 3 to 4 meter diameter, i.e. ≈ 0.2 arcseconds at 2 μm.
The efficiency of an adaptive optics system is measured by the so-called *Strehl ratio*, which is the ratio of the intensity at the centre of the corrected image to that at the centre of a perfect diffraction-limited image of the same source. Strehl ratios of 0.6 to 0.8 are currently being achieved.

7.3 High energy imaging

7.3.1 Grazing incidence telescopes

Wavelengths shortward of ≈ 50 nanometer and longer than ≈ 0.1 nanometer, i.e. the regime of extreme-ultraviolet (EUV) and X-radiation, are absorbed by metallic surfaces at normal incidence, the only way to reflect and focus this radiation is to employ *total reflection*, since the refractive index of metals at these wavelenghts is slightly less than one. We can write the refractive index as:

$$n \;=\; 1 - \delta - i\beta \quad \text{with} \quad \delta,\, \beta \ll 1 \tag{7.49}$$

δ being a measure for the reflection and β a measure for the absorption. If we only consider the real part of n, referring to reflection, we have $n \;=\; 1 - \delta$. Employing Snell's law, the critical angle for total reflection follows from:

$$\cos\theta_{cr} \;=\; 1 - \delta \qquad \Longrightarrow \qquad \theta_{cr} \;=\; \sqrt{2\delta} \tag{7.50}$$

where the cosine term can been approximated by the first terms of the Taylor series, since $\delta \ll 1$. Typical values for the critical angle, depending on wavelength and specific metal(coating), range from 1 to 3 degrees. These small angles imply that focussing optics for this wavelength range requires very high incidence angles. It is therefore commonly referred to as *grazing incidence optics*, the grazing angle constitutes the angle between the incoming ray and the metal reflecting surface (i.e. the complement of the angle of incidence). Figure 7.14 shows the reflection efficiencies ϵ, for several grazing angles, as a function of wavelength in Å-units for gold as the reflection coating deposited on the mirror substrate.

Several grazing incidence telescope configurations have been devised, the most practical use has been a design by Wolter comprising adjacent annular sections of a paraboloidal and a hyperboloidal surface irradiated at grazing incidence. This so-called Wolter-I telescope is displayed in figure 7.15, the focus of the paraboloid coincides with the focus of the "virtual" part of the hyperboloid and the telescope focus is the focal point of the actual hyperboloidal annulus. Obviously, like in the case of the Cassegrain system, the hyperboloidal surface acts as a correction element for the large coma error of a single paraboloid for off-axis radiation. In practise one can obtain resolutions of the order of 1-10 arcseconds over fields of view (FOVs) of several arcminutes. Another design, also due to Wolter, is shown in figure 7.16. In this case the grazing incidence rays reflect from the inner surface of the paraboloidal mirror and, consecutively, from the outer surface of the hyperboloid. This so-called Wolter-II configuration is occasionally used for soft X-ray and Extreme Ultraviolet imaging, the typical grazing angles are larger than in the case of the Wolter-I configuration, however the design can be much more compact. The location of the foci of both the individual annuli and of the full telescope is indicated in figure 7.16. A drawback of grazing incidence optics is the fact that the aperture of such telescopes is only a thin ring in projection, since only the radiation incident onto the paraboloidal annulus is transmitted to the focus. In order to increase the effective area, and hence the sensitivity of the telescope system, several systems with different radii are nested inside each other in a confocal fashion. This is schematically shown in figure 7.17.

It is important to realise that at these short wavelengths it is normally no longer the diffraction that limits the resolution of the telescope (λ/D very small), but rather the accuracy of the surface *figure* such as *roundness* and *profile*. Moreover, the micro-finish of the reflecting surface (i.e. the microscopic surface roughness) plays a dominant role in the potential quality of the image: a surface with irregularities scatters rather than reflects the incoming beam, this will show up as *"wings"* in the PSF that might contain a substantial fraction of the beam

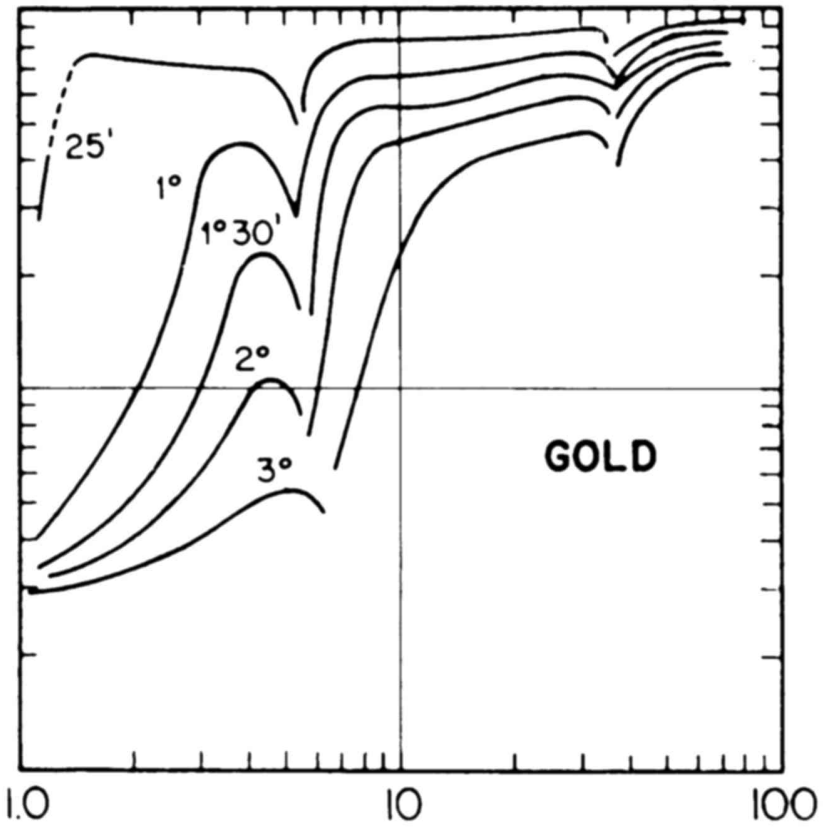

Figure 7.14: *Reflection efficiencies of gold for several grazing angles as a function of wavelength (in Å) of the incoming radiation beam. The ordinate scale for the efficiency ϵ ranges from 0.01 to 1. Credit Giacconi & Gursky (1974).*

energy. Surface smoothness of the order of 0.1 nanometer has be achieved, providing very high quality X-ray mirrors.
Grazing incidence mirrors can be produced in a variety of ways, either by direct machining and polishing or by a so-called replication technique. In the latter case a thin metal reflective layer is deposited on a highly polished (i.e. X-ray quality) mandrel of the inverse shape to that required for the mirror. Subsequently electro-deposition of e.g. nickel onto the mandrel is applied to built up a self-supporting mirror shell. When the appropriate thickness for the required mechanical integrity of the shell has been reached, the shell can be separated from the mandrel by thermal shock (cooling).
Grazing incidence mirrors with intrinsically much lower, but nevertheless still very useful, angular resolution of the order of 1-3 arcminutes can be fabricated from nesting foil mirrors that approximate the paraboloidal and hyperboloidal surfaces by truncated conical surfaces. Thin aluminum foil with a lacquer coating to provide the required smoothness and reflection efficiency has been successfully employed for this purpose, the conical approximation much reduces the complexity of the fabrication process and therefore the costs. Obviously, given the mandatory short length of the mirror cones to retain, at least geometrically, the required resolution, many hundreds of foil shells need to be nested to reach a sufficiently large effective aperture!

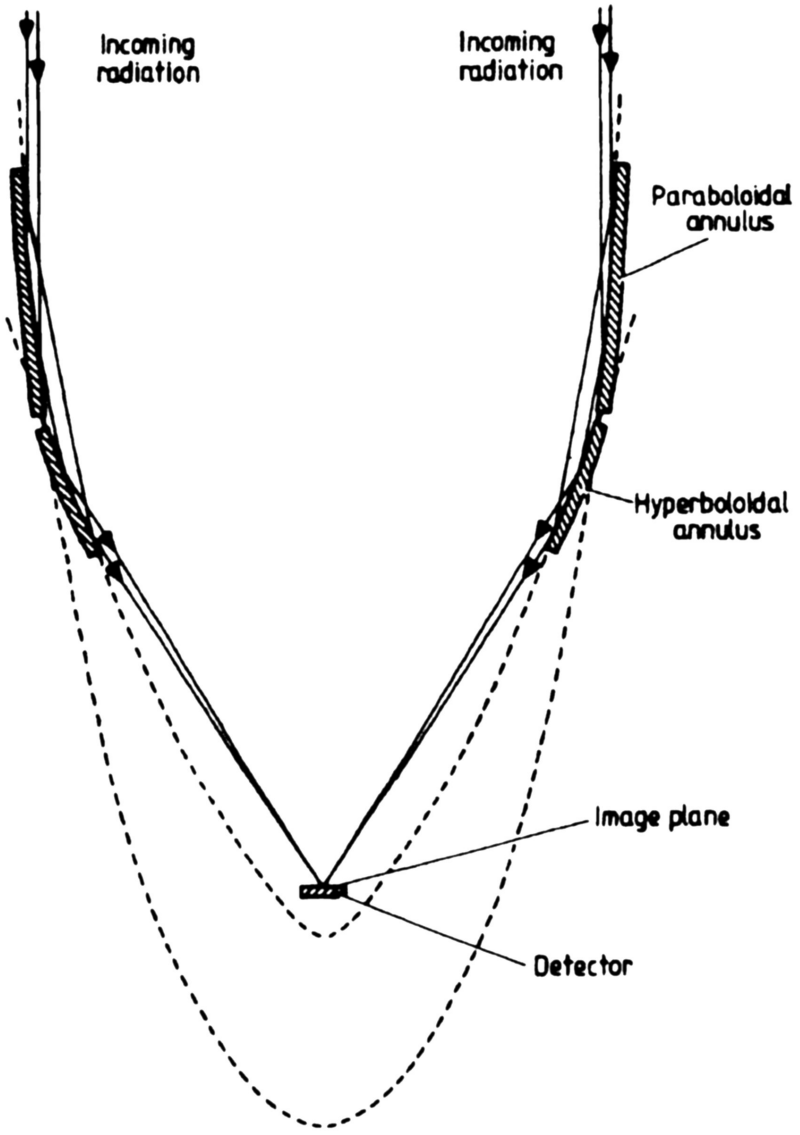

Figure 7.15: *Grazing incidence optics: Wolter-I configuration. Credit Kitchin (1998).*

7.3.2 Non-focussing optics: beam modulation

If the wavelength of the incident radiation beam becomes smaller than ≈ 0.1 nanometer, it becomes increasingly difficult to use reflection optics. Employing multi-layer coated mirrors still allows focussing of radiation in selected wavebands down to wavelengths as short as 0.02 nanometer, but not much further. Therefore, images will have to be obtained by other means. In the photon energy range where the photo-electric effect is still dominant, imaging can be accomplished by applying the *coded mask* technique. In the photon energy range where Compton scattering and pair creation are the dominant interaction processes, the *kinematics* of the interaction processes can be used to extract directional information to built up images. In that case telescope and detecting device have become one. We shall treat these latter two techniques under Gamma-ray imaging, and shall first briefly describe the principle of coded mask imaging.

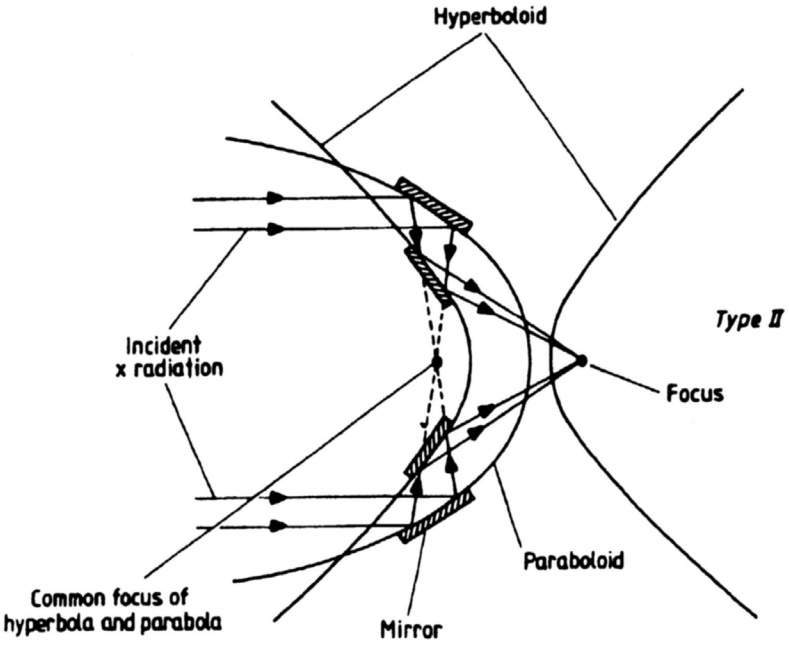

Figure 7.16: *Grazing incidence optics: Wolter-II configuration. Credit Kitchin (1998).*

Coded mask imaging is based on an old principle, the *Camera Obscura*, where a hole in a mask allows an image to form on a screen. The smaller the hole , the better the angular resolution, but unavoidably at the expense of the irradiance. Moreover, if the hole becomes too small, diffraction effects will degrade the resolution. In the X-ray domain diffraction effects become negligible considering the small wavelengths involved, and the irradiance level can be enhanced by employing a large number of holes, so that the transmission of the mask may reach a value of ≈ 50 percent. The resulting image from such a multi-hole mask is a linear superposition of the images produced by each individual hole. The distribution of the holes needs to be done in such a way that the brightness distribution of the illuminating celestial source can be reconstructed in an unambiguous fashion from the measured intensity distribution in the registered image. The appropriate pattern of *holes and stops* constitutes a so-called coded mask, this surface is described by a two-dimensional transmission function $\mathbf{M}(x, y)$. If we assume an extended radiation source $\mathbf{S}(x, y)$, the intensity distribution $\mathbf{D}(x, y)$ on the detector can be written as a convolution:

$$\mathbf{D}(x, y) \; = \; \mathbf{M}(x, y) * \mathbf{S}(x, y) + \mathbf{N} \tag{7.51}$$

with $\mathbf{N}$ representing the detector noise.
The working principle of the coded mask camera is displayed in figure 7.18. To reconstruct the brightness distribution of the extended celestial radiation source, the image $\mathbf{D}(x, y)$ needs to be deconvolved with the transmission function $\mathbf{M}(x, y)$ of the mask. The simplest operation to perform this deconvolution is a *two-dimensional cross-correlation* of the mask transmission function with the detector image. Formally, an estimate of the source distribution, $\mathbf{\Sigma}(x, y)$, can be obtained by applying a decoding function $\mathbf{A}(x, y)$:

$$\mathbf{\Sigma}(x, y) \; = \; \mathbf{A}(x, y) * \mathbf{D}(x, y) \; = \; \mathbf{A}(x, y) * \mathbf{M}(x, y) * \mathbf{S}(x, y) + \mathbf{A}(x, y) * \mathbf{N} \tag{7.52}$$

If the image detector were to be *noise free*, there should exist a one-to-one correspondence between $\mathbf{S}$ and $\mathbf{\Sigma}$, hence we require $\mathbf{A} * \mathbf{M} = \delta$ (Kronecker delta). Secondly, the noise

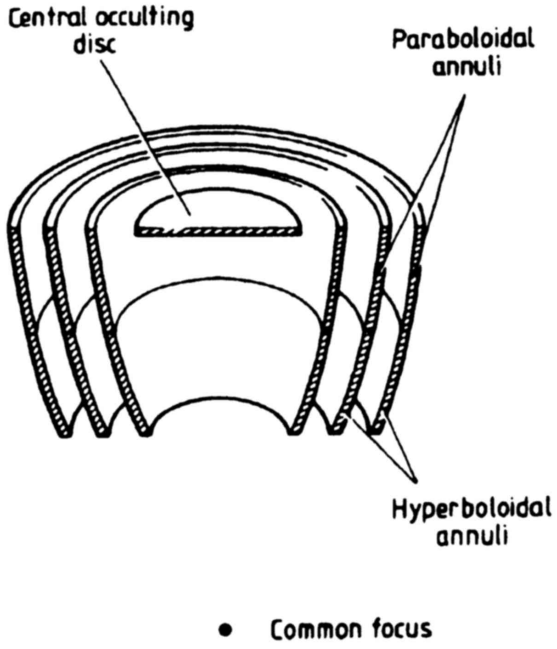

Figure 7.17: *Confocal nesting of Wolter-I telescopes to enlarge the aperture effective area. Credit Kitchin (1998).*

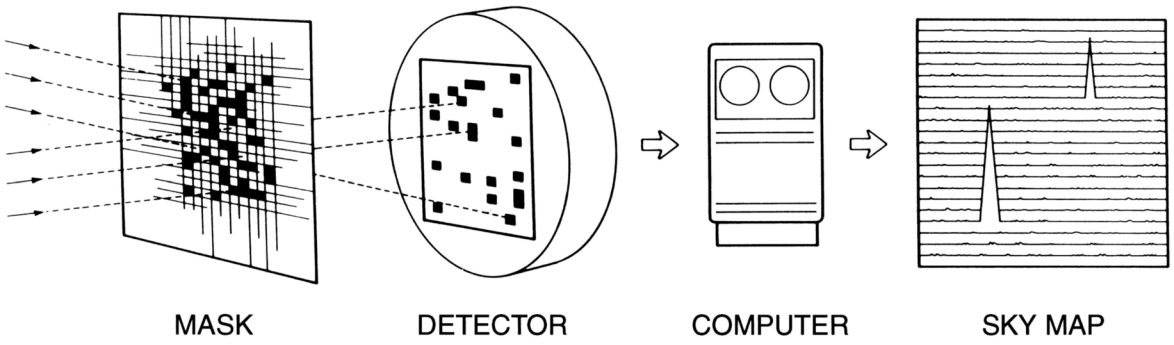

Figure 7.18: *Elements of a coded mask telescope. Credit Bleeker (2003).*

distribution should preferably be uniform over the deconvolved image. Mask patterns $\mathbf{M}(x, y)$ that satisfy these two requirements are designated *optimal*.
Note: *It is important to realize that the noise level and distribution in the detector image depends on the brightness distribution of the sky within the field of view of the coded mask telescope. Each source in the sky field observed does not only contribute to its specific location (i.e. pixel) in the detector image but also to all the other image pixels. This means that all the radiation sources in the observed sky field contribute to the noise level of the detector image.*
The angular resolution of a coded mask telescope is directly related to the size m_e of an individual mask element and the distance l between the mask plane and the detector plane:

$$\delta\theta_{res} \;=\; \arctan(m_e/l) \tag{7.53}$$

This resolution implies a proper sampling by the image detector of the mask element m_e, the Nyquist criterion is amply satisfied for a spatial resolution of the detector $d_e \approx m_e/3$. Usually

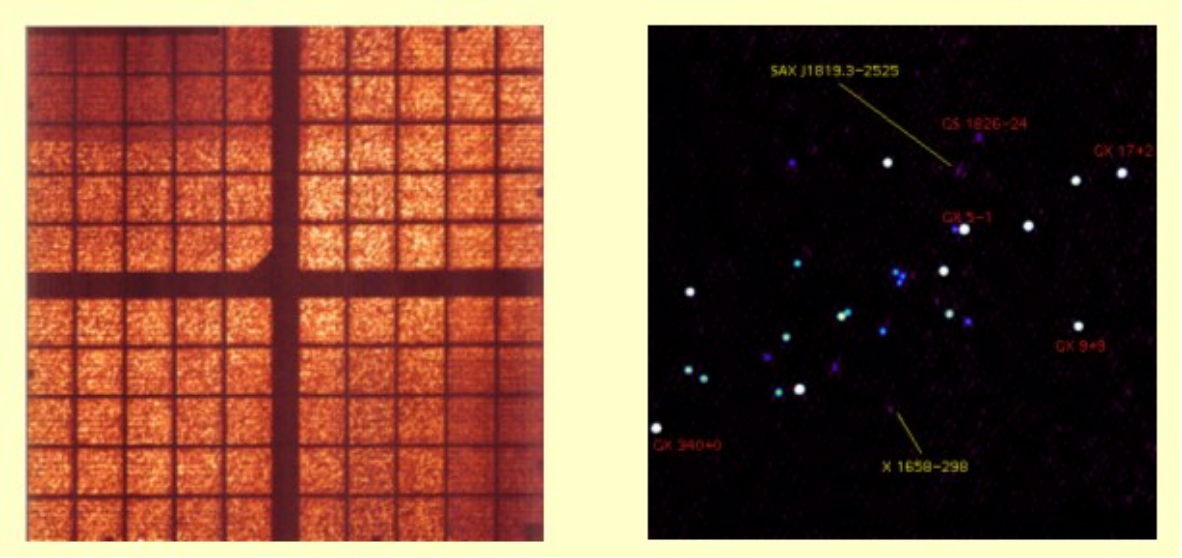

Figure 7.19: *Left: A BeppoSAX WFC coded mask picture of a sky region near the Galactic Centre in terms of a raw photon intensity map. The dark bars and stripes reflect the detector window support structure. Right: the deconvolved detector image showing the wealth of compact X-ray sources in the Galactic Bulge area. Credit Bleeker (2003).*

the size of the mask pattern covers the same area as the image detector and the *sensitivity is not uniform across the whole field of view*, being dependent on the coded fraction of the detector that is illuminated by the mask pattern. Hence, the characterisation of the field of view of a coded mask telescope can be done along three coding limits: the fully coded limit, the semi-coded limit and the zero-coded limit. If the mask has the same size as the image detector and does not comprise repetition of a (smaller size) basic coding pattern, the field that is fully coded equals zero. The field of view at half the sensitivity will be equal to the solid angle subtended by the mask as seen from the image detector. Several coded mask telescopes have been developed and built for hard X-ray and low-energy gamma-ray detection, e.g. the Dutch-Soviet coded mask X-ray camera on the Soviet MIR Space Station, the French coded mask telescope SIGMA onboard the Soviet GRANAT spacecraft, the Dutch-Italian Wide Field coded mask Cameras on the BeppoSAX satellite and the low-energy Gamma-ray Imager on the European INTEGRAL Space Observatory. The Wide-Field coded mask Cameras (WFC) onboard BeppoSAX have been particularly successful during the six year mission life time of the satellite and have made a crucial contribution to unveiling the origin of gamma-ray burst sources. The two, anti-parallel, WFCs in BeppoSAX had a 40×40 degrees^2 field of view (FWZR) and an angular resolution $\delta\theta_{res} = 5$ arcminutes with location accuracy (i.e. position resolution, see Chapter 5) of 0.7 arcminutes. The coded mask comprised a matrix of 256×256 elements with m_e =1 mm. The open fraction of the mask was chosen from numerous sky simulations to be 0.33 for optimum signal to noise ratio. The resolution of the position sensitive X-ray image detector was ≈ 0.4 mm, i.e. commensurate with the Nyquist requirement on proper sampling.
Figure 7.19 shows raw image data (left panel) from a sky region close to the Galactic Centre in terms of a photon intensity map. It is evident from this raw image that the sky field observed contains two bright point sources, which are directly visible as two light rectangles in the image arising from mechanical collimation by the tube connecting the mask with the image detector.

No other sources can yet be discerned. The right-hand panel shows the deconvolved detector image, displaying a host of point sources in a wide brightness range. All these sources can be simultaneously monitored regarding their time variability (e.g. transients, bursts, flashes, periodicities) and their spectral morphology and variability.

7.3.3 Gamma-ray imaging

Compton imaging

In the energy range from several hundred keV to several MeV, the interaction of γ-ray photons with matter is dominated by Compton scattering. The cross-section for this process is governed by the Klein-Nishina equation given in Chapter 2, equation (2.20). The atomic cross section for a target material with atomic number Z simply follows from multiplication of the KN-cross section with the atomic charge Z, where the atomic electrons are considered to be essentially free. The Compton process is therefore proportional to Z, see also Chapter 4, expression (4.17). The energy of the photon can only be measured after a cascade process of consecutive scattering interactions until the down-scattered, i.e. in energy degraded, photon is eventually absorbed by photoelectric absorption. This requires a thick absorber, that suffers from a great deal of noise due to the interaction of cosmic particle radiation with the detector material. This noise can be effectively eliminated by splitting the absorber in two separate parts, located at a certain distance l from each other. In this way directional sensitivity can be introduced by employing the kinematics of the Compton effect. The upper part of this so-called *Compton telescope* then comprises a position sensitive sensor array of a suitable low-Z material with a thickness maximised for a single Compton scattering to occur. In contrast, the lower detector in the telescope entails a position sensitive array of high-Z material of sufficient thickness to ensure total absorption of the scattered photon energy. The sky location of the incident photon can now be traced back to a circular sky contour by measuring the scattering angle and the direction of the scattered photon leaving the upper telescope sensor. This is schematically shown in figure 7.20. By measuring many source photons, the intersecting sky contours will indicate the most probable sky position of the gamma-ray source.
The scattering angle θ_{sc} between the incident photon and the scattered photon, leaving the upper telescope element, follows from the kinematics of the Compton effect:

$$\cos\theta_{sc} \;=\; 1 \;-\; mc^2 \left(\frac{1}{\epsilon_{\gamma\,'}} \;-\; \frac{1}{\epsilon_\gamma} \right) \quad \text{with} \quad \epsilon_\gamma \;=\; \epsilon_{\gamma\,'} \;+\; E_e \tag{7.54}$$

in which ϵ_γ represents the energy of the incoming photon, $\epsilon_{\gamma\,'}$ the energy of the first scattered photon and E_e the energy of the scattered Compton electron. The direction of the first Compton scattered photon, the line element AB in figure 7.20, can be reconstructed from measuring the interaction positions in the upper and lower telescope elements respectively.
Figure 7.21 depicts such a telescope configuration for the case of the Comptel instrument, launched in 1991 aboard the Compton Gamma-Ray Observatory (Compton GRO) by NASA.
The energy and position of the scattered Compton electron is measured in the upper detector, comprising a liquid scintillator array in which each element is viewed by a number of photomultipliers to obtain position resolution within a single array module. The energy and position of the first scattered photon is measured in the lower detector, constituting an array of optically thick NaI(Tl) scintillator crystals for total absorption of the scattered gamma-ray photon, again a cluster of photomultipliers is used to determine the position of the absorbed scattered photon inside a single NaI-module. By requiring simultaneous triggers from the upper and lower detector arrays within a small time window commensurate with the

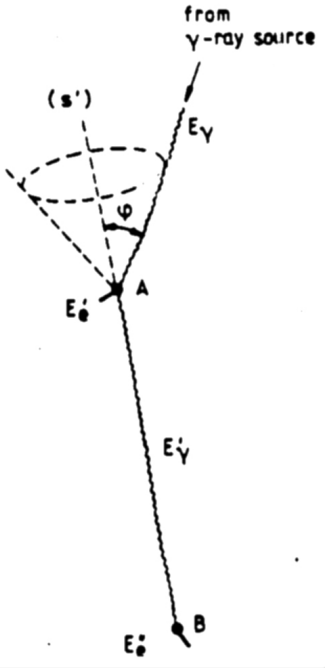

Figure 7.20: *Kinematics of the Compton effect. The sky location of the incident photon can be traced back to a circular contour by measuring the scattering angle $\phi = \theta_{sc}$ and the orientation of the line element AB.*

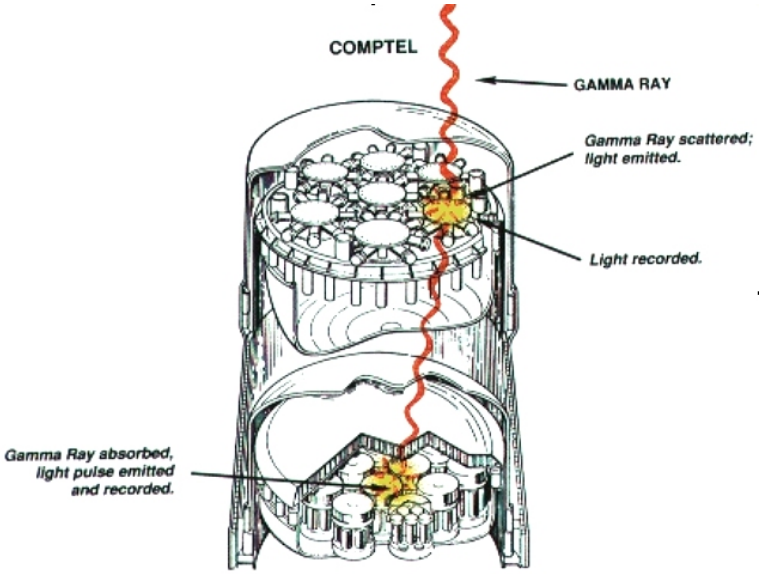

Figure 7.21: *Configuration of the Compton telescope as flown on the NASA Compton Gamma-Ray Observatory (Compton-GRO). The upper detector array (the scatterer) consists of 7 cylindrical modules filled with liquid scintillator (NE 213A, geometric area ≈ 0.42 m^2), each viewed by several photomultiplier tubes to obtain position resolution. The lower detector (the absorber) consists of 14 cylindrical modules of an anorganic scintillator (NaI(Tl), geometric area ≈ 0.86 m^2, each of them also viewed by a multitude of photomultipliers. The distance between both detector assemblies is 1.5 meter. Credit NASA/Comptel Consortium.*

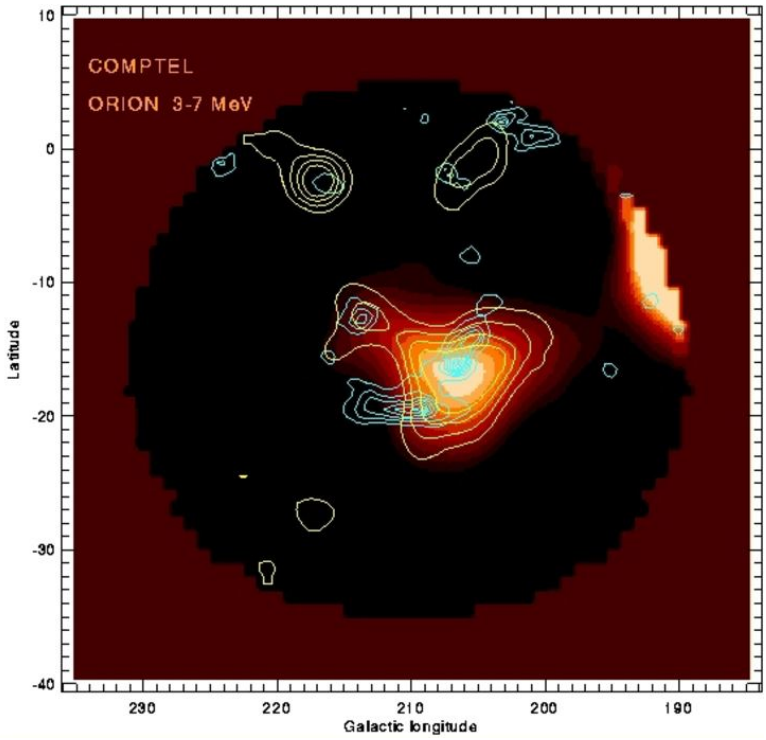

Figure 7.22: *Gamma-ray map of the Orion region in the 3-7 MeV energy range as measured by Comptel. The orange-white contours indicate the locations of gamma-ray enhancements, the blue contours represent the locations of the densest interstellar gas clouds. Credit NASA/Comptel Consortium.*

time-of-flight $t_{TOF} \approx l/c$ of the first scattered photon from the upper to the lower detector array, almost all background events can be eliminated. This can be understood by remembering that these background events either trigger only one detector array or they produce the wrong time sequence (practically all background events are produced in the high-mass high-Z absorber array). This particular Compton telescope is the most sensitive instrument in the medium-energy gamma-ray range (0.5-30 MeV) developed and operated thus far. The angular resolution depends on the measurement accuracy of the orientation of the line element AB and the scattering angle θ_{sc} and ranges from 1.7 to 4.4 degrees (FWHM) depending on the gamma-ray energy. The accuracy of source position determination, i.e. the position resolution, is 5-30 arcminutes dependent on photon energy. The field of view (FOV) of such an instrument can be quite large, depending on l and the typical diameter of the upper and lower detector-arrays, the FOV of the Comptel instrument subtends $\sim$ one steradian on the sky, similar to that of a coded mask telescope.
Figure 7.22 shows a gamma-ray map of the Orion region, the nearest birthplace of massive stars in our Galaxy. The orange-white contours depict the areas of enhancement of the measured gamma-ray flux in the 3-7 MeV region. Most of this flux appears to be concentrated near specific energies and, although the energy resolution of Comptel is rather limited (5-8 percent FWHM), this is strongly suggestive for the presence of gamma-ray line radiation at 4.4 and 6.1 MeV respectivily. The blue contours display the areas of high-density interstellar clouds. The spatial coincidence of the detected gamma-ray enhancements with these dense clouds points to interaction between energetic cosmic-ray nuclei and the gas nuclei constituting the dense interstellar clouds. The lines could then originate from the radioactive decay of

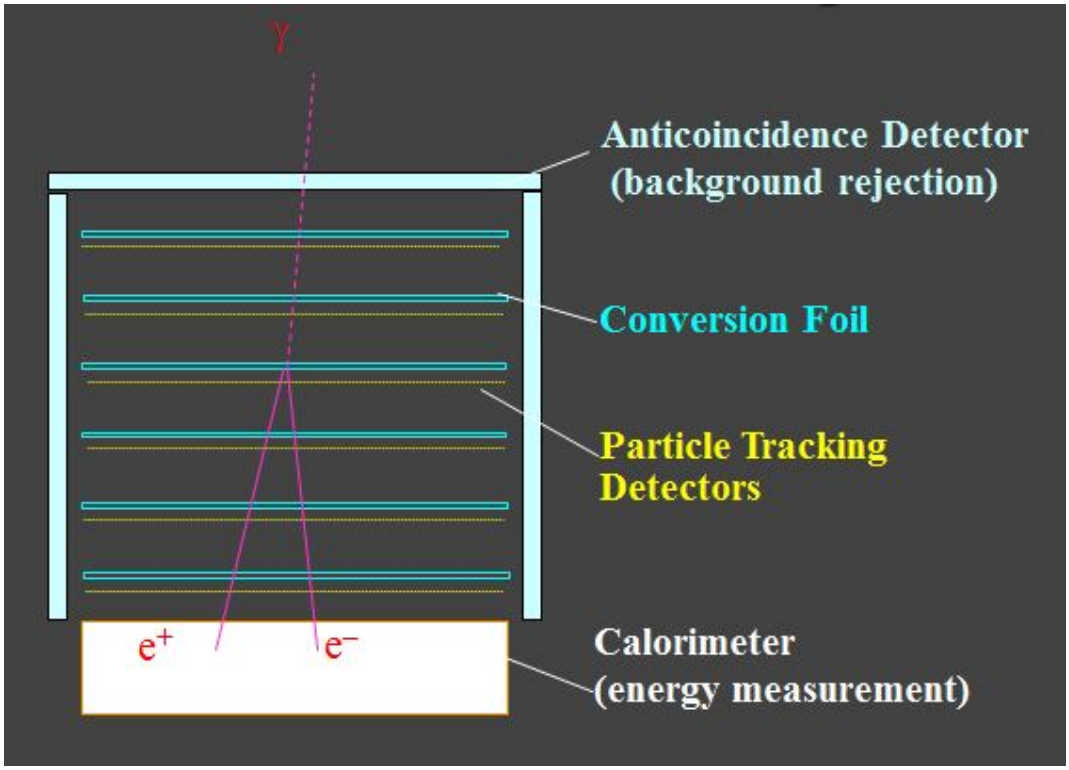

Figure 7.23: *Principle of a pair conversion telescope. Thin metal converter plates are interleaved with tracking layers, comprising gas layers or thin 2D-position-sensitive semiconductor detector planes. Credit NASA/EGRET website.*

energetic cosmic-ray nuclei of carbon and oxygen.

Imaging through pair formation

At gamma-ray energies $\geq$ 20 MeV the main interaction process with matter is pair formation, causing the disappearance of the gamma-ray photon (destructive interaction) which is converted into an electron-positron pair, both having positive kinetic energy. The interaction can only occur in the presence of a strong electric field, as encountered in the vicinity of an atomic nucleus or near an orbital electron. The nucleus takes care of conserving the momentum balance (*recoil-nucleus*), but gains negligible energy. Consequently, the energy of the incident gamma-ray photon is practically entirely converted to electron/positron mass and kinetic energy, see Chapter 4, expression (4.18). In the *centre-of-mass system*, the positron and the electron are emitted in opposite directions, however in the *laboratory-frame* they are emitted in the direction of the initiating photon, and the tracks of the electron and positron reveal the direction of the incident gamma-ray photon. *Directionality* can thus be obtained by measuring ("visualising") the 3D-orientations of the electron and positron trajectories that originate at the location of the recoil-nucleus. From these orientations the sky position of the incident gamma-ray photon can be reconstructed.

The angular distribution $N(\phi)d\phi$ of the electron(positron) relative to the direction of the incident photon is, in good approximation, given by:

$$N(\phi)\,d\,\phi \;\approx\; \frac{\phi\,d\,\phi}{(\phi_{\pm}^2 \,+\, \phi^2)^2} \quad \text{with} \quad \phi_{\pm} \,=\, \frac{mc^2}{E_{\pm}} \tag{7.55}$$

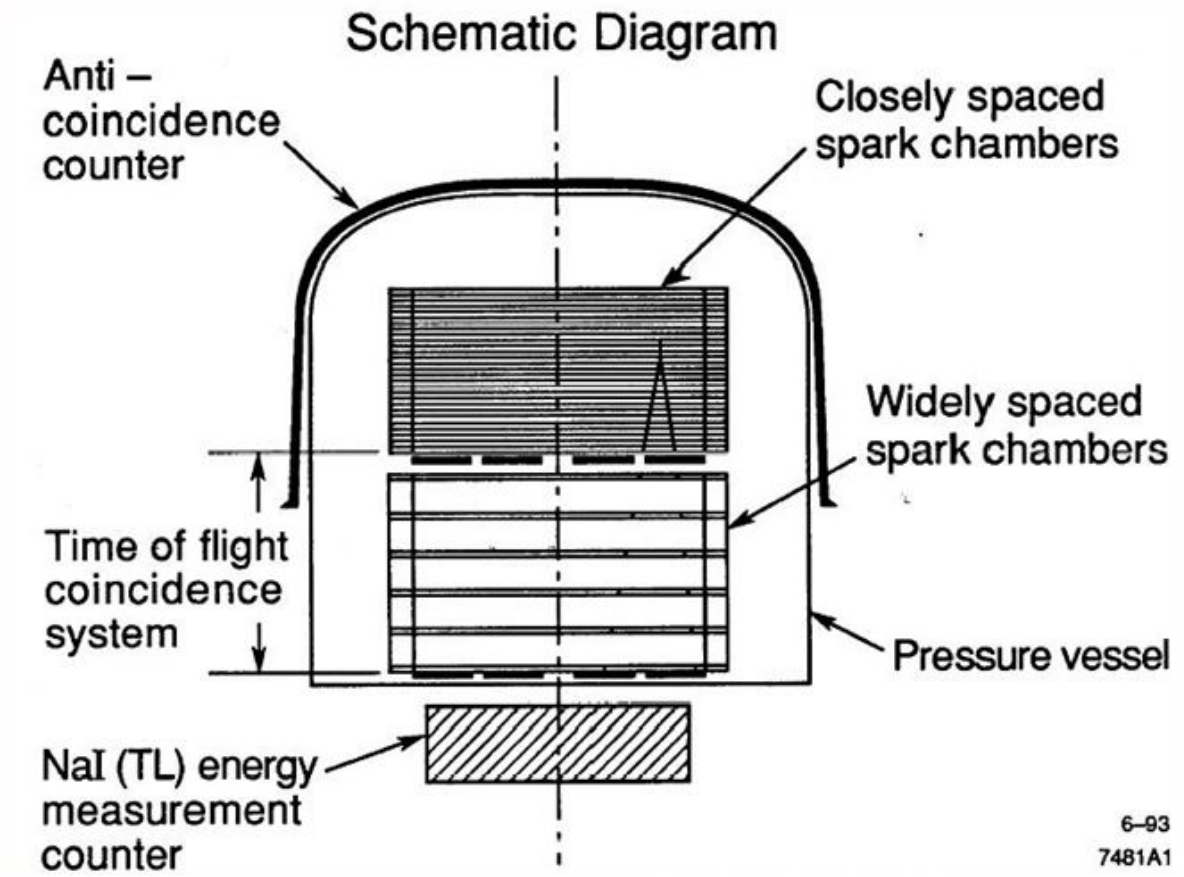

Figure 7.24: *Schematic of the EGRET pair telescope aboard the Compton Gamma Ray Observatory. The principal telescope elements are indicated, for explanation see text. Credit NASA/EGRET website.*

where $E_{\pm}$ represents the total energy of the pair-electron(positron). The most probable angle ϕ_p for electron(positron) emission follows from differentiation of expression (7.55), this results in $\phi_p = \phi_{\pm}/\sqrt{3}$.
The *angle of bipartition* is given in close approximation by:

$$\phi_b \approx \phi_{\pm} = \frac{mc^2}{E_{\pm}} \tag{7.56}$$

and is thus *inversely proportional* to the total energy of the pair-electron(positron). The angle ψ between the partners of a pair is geometrically fixed for a given combination of ϕ_-, ϕ_+ and the *dihedral* angle Φ between the photon-electron and the photon-positron planes. To a first approximation, if $\Phi = \pi$ (radian), and the positron and electron are emitted symmetrically with respect to the initiating photon, we may put $\phi_+ \approx \phi_- \approx \phi$, consequently $\psi = 2\phi$. Hence, the opening angle of the pair also diminishes inversely proportional to the energy of the initiating gamma-ray photon.

The characteristic interaction length for pair formation is given by the *radiation length* (expressed in mass per unit area), which was introduced in Chapter 4, formula (4.21). This interaction length is proportional to $[Z(Z+1)]^{-1}$, i.e. $\approx Z^{-2}$ for the higher Z-elements, furthermore it depends on the material properties under consideration but is *independent* of the energy of the incident photon.

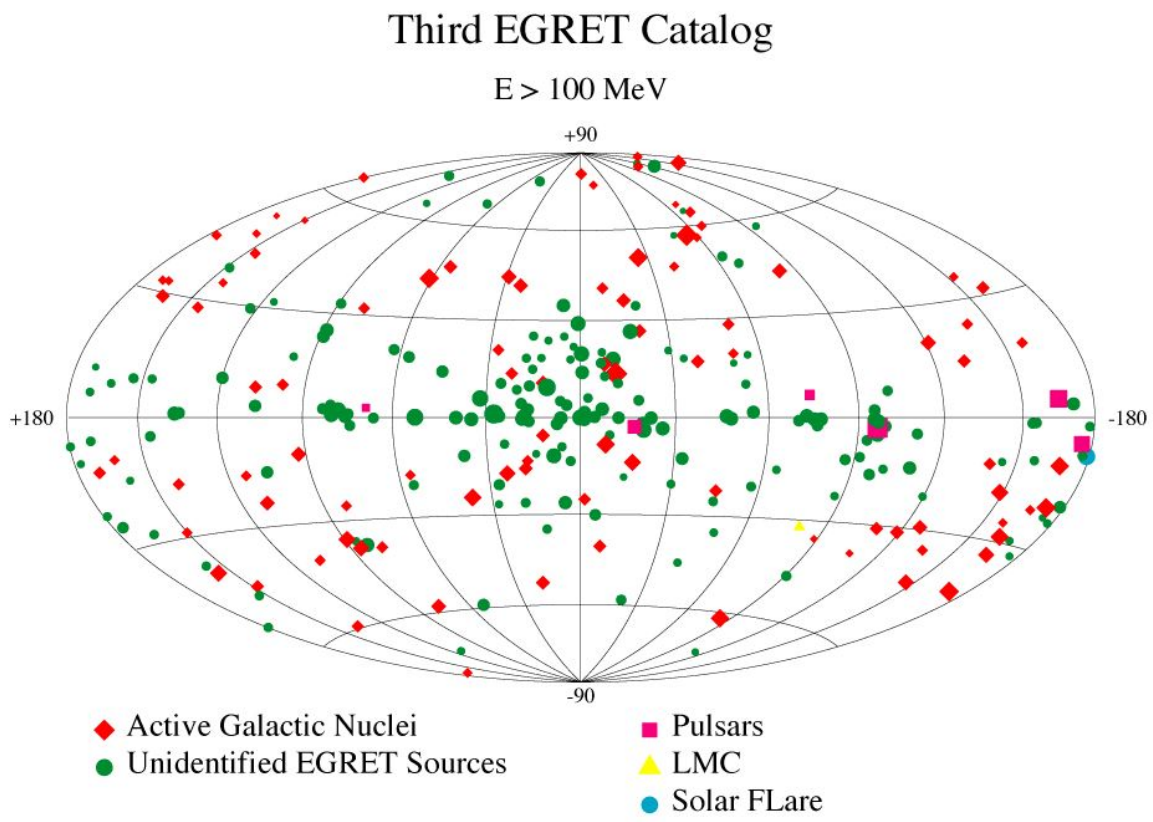

Figure 7.25: *The third EGRET all sky map of gamma-ray point sources above 100 MeV. The majority of these sources remains as yet unidentified. Credit NASA/EGRET Consortium.*

A pair forming telescope can now be constructed by stacking several thin high-Z-metal converter plates at an appropriate mutual distance, each with a thickness of a fraction of a radiation length. The full stack is built up to a total thickness of a few radiation lengths, suitable high-Z converters comprise lead or tungsten plates. The gaps between the plates in the stack, the so-called *tracking layers*, are either filled with gas or do contain thin, position sensitive, semiconductor strip detectors, this is schematically shown in figure 7.23. Once the pair has formed, the electron/positron either ionizes the gas filling along their tracks or produce an electric charge in the semiconductor strips at the particular spots of their passage.

In the case of a gas filled chamber, the registered presence of a particle-pair triggers a high voltage pulse that discharges along the particle tracks between the plates, delineating the orientation of their trajectories. Such a detector is called a *spark chamber*, the principle of which was already developed during the late 1950's and the 1960's for diagnostics in high-energy physics at particle accelerators and in cosmic ray physics. This technique was also used in the first space-borne gamma-ray telescopes on SAS-2 (NASA) and COS-B (ESA), that resulted in the first (partial) maps of the high-energy gamma-ray sky. Although more sophisticated read-out techniques, employing thin-wire grids for detection of the charges produced along the ionisation tracks, were utilized in the second generation EGRET gamma-ray telecope on the Compton Gamma-Ray-Observatory, the basic detection principle remained unaltered. Figure 7.24 shows the main constitutive elements of this pair telescope, that was designed to cover the energy range from 20 MeV to 30 GeV.

The instrument uses a multiple-layer spark chamber with thin metal pair-conversion plates.

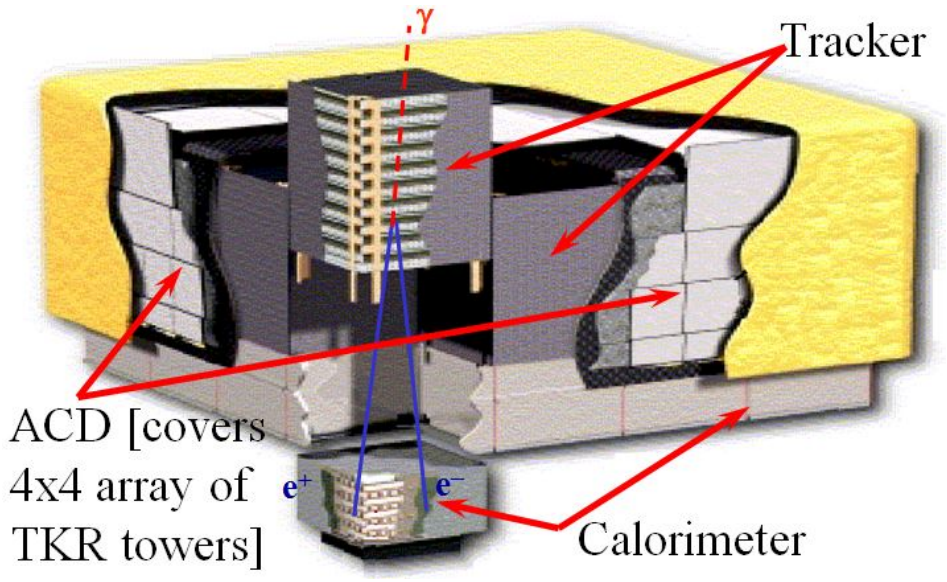

Figure 7.26: *GLAST: concept of the tracker modules. Credit NASA/GLAST Consortium.*

The total energy of the gamma-ray photon is measured by a NaI(Tl) scintillation counter beneath the spark chambers to provide good energy resolution over a wide dynamic range in energy. The absorption proces involves a cascade of non-thermal Bremsstrahlung losses by the pair-particles and renewed pair formation by the Bremsstrahlung photons, followed by Compton scattering and finally photo-electric absorption until all the initial photon energy has been depleted. The instrument is covered by a plastic scintillator anticoincidence dome to discriminate against charged particle radiation incident on the telescope. Moreover, to further separate background events from true celestial gamma-rays, a time-of-flight system is incorporated similar to the one incorporated in the Compton telescope, to ensure that the radiation is arriving in the proper time sequence.

The EGRET telescope instantaneously covers a wide field of view of ~ 0.6 steradians, the position resolution is dependent on photon energy and source strength. For a strong, hard spectrum, gamma-ray source this position resolution amounts to ~ 5 - 10 arcminutes. As outlined above, at lower photon energies the pair-angle is large, however the kinetic energy of the pair particles is relatively low and they suffer from scattering in the metal converter plates of the spark chamber. This introduces stochastic fluctuations in the particle-track determination due to the straggling behaviour of the electron/positron pairs. At high photon energies, the statistical fluctuations due to straggling are less severe, since the pair particles possess a much higher kinetic energy. However, as we have seen, the separation angle ψ diminishes with $1/E_{\pm}$, which makes accurate determination of the bipartition angle less straightforward. Figure 7.25 shows the third catalogue of EGRET detected gamma-ray point sources above 100 MeV, the large majority of these sources has not yet been identified. This is either due to the limited positional resolution of the EGRET instrument or to an intrinsic lack of counterparts at other wavelengths.

The next generation gamma-ray telescope GLAST (Gamma-ray Large Area Space Telescope), to be launced by NASA in 2006, exploits a new technology in track detection: the gas-filling of the chamber has been replaced by solid state detectors as the tracking material. This allows for improved energy and spatial resolution. An energy resolution as good as 5

percent(FWHM) is aimed for and a position resolution as good as a few arcminutes for a single gamma-ray photon and of the order of ≤ 30 arcseconds for a strong gamma-ray source. In addition, a major advantage is the fact that a replenishable supply of chamber gas is no longer needed, which will make a much longer mission life time potentially feasible.
The baseline design for the GLAST pair forming telescope involves a modular tracker array comprising four-by-four *tower modules* (total of 16), of which each module consists of interleaved planes of thin lead converter sheets and silicon-strip solid state detectors. The silicon strips are arranged in a stack of 19 pairs-of-planes, one plane of each pair for read-out in the x-direction, the other plane of the pair for read-out in the perpendicular y-direction. When the electron/positron interacts with such a plane-pair, an accurate position can be determined in two dimensions. The third dimension of the track is derived by analysing the signals from consecutive adjacent planes as the particle travels downward through the stack towards the energy calorimeter. A multi-fold (at least three) coincidence between adjacent plane-pairs triggers the read-out sequence of the particle tracks. Figure 7.26 shows the concept of the tower modules and the stack of tracking detectors. The energy bandwidth of GLAST ranges from $\sim$ 15 MeV to $\geq$ 100 GeV, with a field of view in excess of 2 steradians. The sensitivity of GLAST for point source detection will be $\sim$ 50 times that of EGRET at 100 MeV, with an enhanced positional resolving power of 0.5 - 5 arcminutes.

Observational Astrophysics

Lecture notes part 2

Contributions by Frank Verbunt: chapters 13 and 14
Astronomical Institute Utrecht

Chapter 8

Radiation Fields

8.1 Stochastic processes: distribution functions, mean and variance

A stochastic process is defined as an infinite series of stochastic variables, one for each value of the time t. For a specific value of t, the *stochastic variable* $X(t)$ possesses a certain probability density distribution. The numerical value of the stochastic variable $X(t)$ at time t corresponds to a particular draw (outcome) from this probability distribution at time t. The time series of draws represents a single time function and is commonly referred to as a *realisation* of the stochastic process. The full set of all realisations is called the *ensemble of time functions* (see Fig. 8.1).

At each time t, the stochastic variable $X(t)$ describing the stochastic process, is distributed

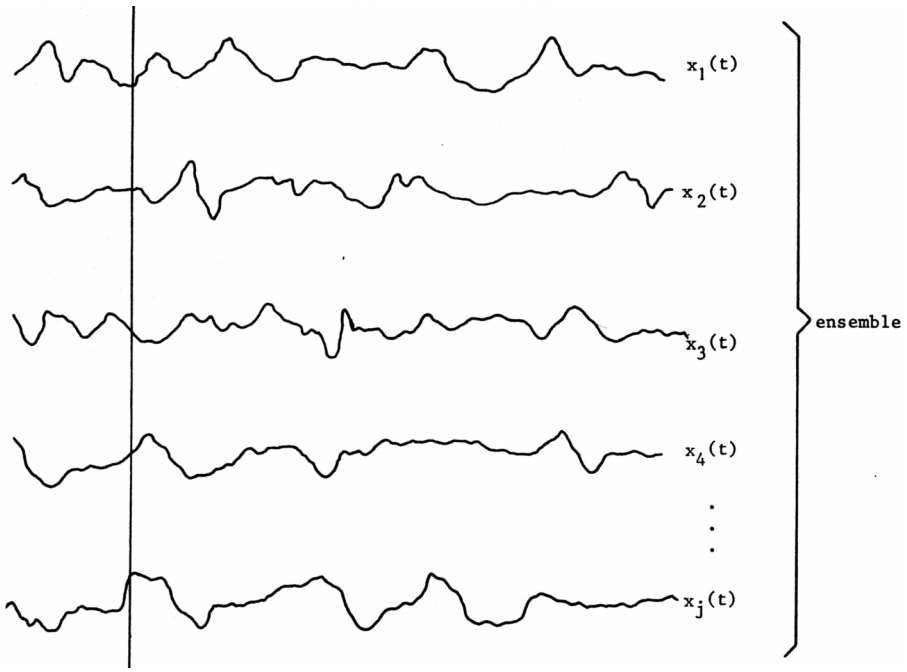

Figure 8.1: *The ensemble of time functions of a stochastic process.*

by a *momentary* cumulative distribution, called the first-order distribution:

$$F(x;t) = \mathbf{P}\{X(t) \leq x\} \tag{8.1}$$

which gives the probability that the outcome at time t will not exceed the numerical value x. The probability density function, or first-order density, of $X(t)$ follows from the derivative of $F(x;t)$:

$$f(x;t) \equiv \frac{\partial F(x;t)}{\partial x} \tag{8.2}$$

This probability function may be a binomial, Poisson or normal (Gaussian) distribution.

For the determination of the statistical properties of a stochastic process it suffices in many applications to consider only certain averages, in particular the expected values of $X(t)$ and of $X^2(t)$.

The *mean* or *average* $\mu(t)$ of $X(t)$ is the expected value of $X(t)$ and is defined as

$$\mu(t) = \mathbf{E}\{X(t)\} = \int_{-\infty}^{+\infty} x\, f(x;t)\, dx \tag{8.3}$$

The variance of $X(t)$ is the expected value of the square of the difference of $X(t)$ and $\mu(t)$ and is, by definition, equal to the square of the standard deviation:

$$\sigma^2(t) = \mathbf{E}\{(X(t) - \mu(t))^2\} = \mathbf{E}\{X^2(t)\} - \mu^2(t) \tag{8.4}$$

(in case of real functions $X(t)$ and $\mu(t)$).

8.2 Autocorrelation and autocovariance

This distribution can be generalized to higher-order distributions, for example the second order distribution of the process $X(t)$ is the joint distribution

$$G(x_1, x_2; t_1, t_2) = \mathbf{P}\{X(t_1) \leq x_1, X(t_2) \leq x_2\} \tag{8.5}$$

The corresponding second derivative follows from

$$g(x_1, x_2; t_1, t_2) \equiv \frac{\partial^2 G(x_1, x_2; t_1, t_2)}{\partial x_1\, \partial x_2} \tag{8.6}$$

The *autocorrelation* $R(t_1, t_2)$ of $X(t)$ is the expected value of the product $X(t_1) \cdot X(t_2)$ or $X(t_1) \cdot X^*(t_2)$ if we deal with complex quantities:

$$R(t_1, t_2) = \mathbf{E}\{X(t_1) \cdot X^*(t_2)\} = \int_{-\infty}^{+\infty}\int_{-\infty}^{+\infty} x_1\, x_2^*\, g(x_1, x_2^*; t_1, t_2)\, dx_1 dx_2 \tag{8.7}$$

with the asterisk (*) indicating the complex conjugate in case of complex variables (see Fig. 8.2).

The value of $R(t_1, t_2)$ on the diagonal $t_1 = t_2 = t$ represents the average power of the signal at time t:

$$R(t) = R(t,t) = \mathbf{E}\{X^2(t)\} = \mathbf{E}\{\,|\,X(t)\,|^2\,\} \tag{8.8}$$

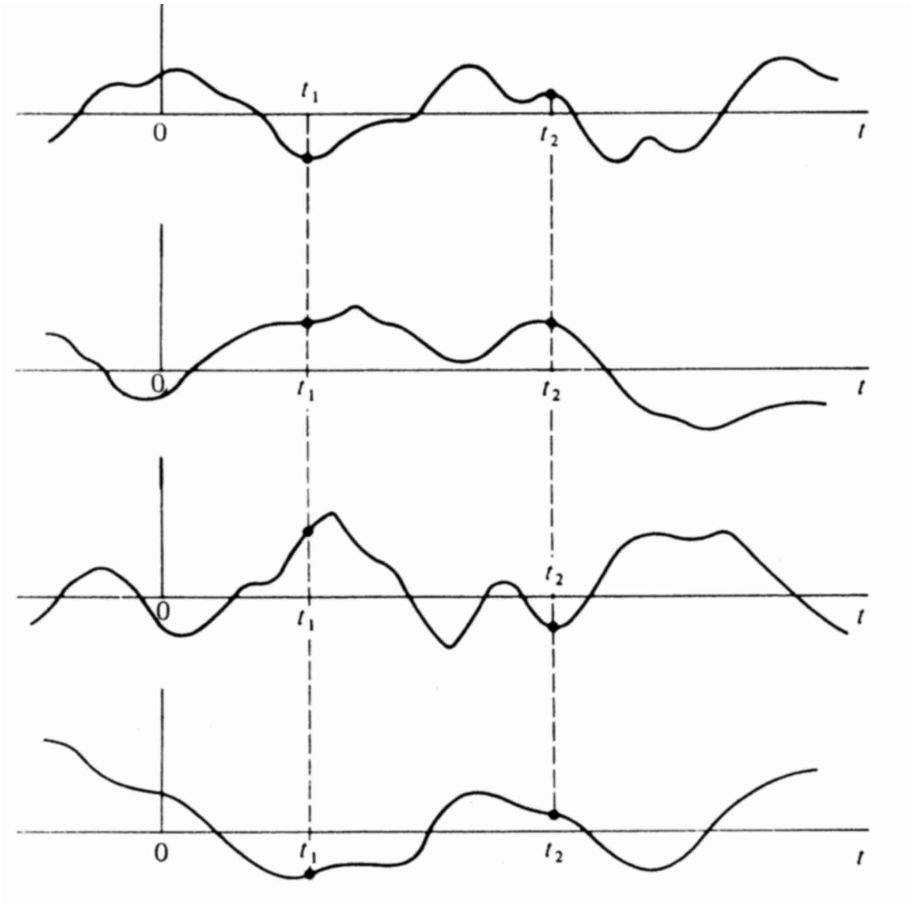

Figure 8.2: *The autocorrelation of a stochastic process.*

Since the average of $X(t)$ is in general not zero, another quantity is introduced, the *autocovariance* $C(t_1, t_2)$, which is centered around the averages $\mu(t_1)$ and $\mu(t_2)$:

$$C(t_1, t_2) = \mathbf{E}\{(X(t_1) - \mu(t_1)) \cdot (X(t_2) - \mu(t_2))^*\} \tag{8.9}$$

For $t_1 = t_2 = t$ (verify yourself)

$$C(t) = C(t, t) = R(t, t) - |\mu(t)|^2 = \sigma^2(t) \tag{8.10}$$

$C(t)$ represents the average power contained in the fluctuations of the signal around its mean value at time t.

8.3 Wide-sense stationary and ergodic signals

Next, consider a signal for which the average does not depend on time, and for which the autocorrelation only depends on the time difference $\tau \equiv t_2 - t_1$. This is called a wide-sense stationary (wss) signal. The following relations hold:

$$\text{signal average} \qquad \mu(t) = \mu = \text{constant} \tag{8.11}$$

$$\text{autocorrelation} \qquad R(t_1, t_2) = R(\tau) \tag{8.12}$$

$$\text{autocovariance} \qquad C(t_1, t_2) = C(\tau) = R(\tau) - \mu^2 \tag{8.13}$$

For $\tau = 0$:

$$R(0) = \mu^2 + C(0) = \mu^2 + \sigma^2 \tag{8.14}$$

which expresses that the total power in the signal equals the power in the average signal plus the power in its fluctuations around the average value. Note that both the autocorrelation and the autocovariance are even functions, i.e. $R(-\tau) = R(\tau)$ and $C(-\tau) = C(\tau)$.

Finally, a wss-stochastic process $X(t)$ is considered *ergodic* when the *momentaneous average* over $X(t)$ can be interchanged with its *time average*, i.e. when

$$\mu = \lim_{T\to\infty} \frac{1}{T} \int_{-\frac{1}{2}T}^{+\frac{1}{2}T} X(t)\, dt = \mathbf{E}\{X(t)\} \tag{8.15}$$

$$\text{and} \quad R(\tau) = \lim_{T\to\infty} \frac{1}{T} \int_{-\frac{1}{2}T}^{+\frac{1}{2}T} X^*(t)\cdot X(t+\tau)\, dt = \mathbf{E}\{X^*(t)\cdot X(t+\tau)\} \tag{8.16}$$

8.4 Power spectral density

The autocorrelation function $R(\tau)$ defined in equations 11.52 and 8.16, has a Fourier transform

$$S_d(s) = \int_{-\infty}^{+\infty} R(\tau)\cdot e^{-2\pi i s\tau}\, d\tau \tag{8.17}$$

Since $R(\tau)$ has the dimension of a signal power (e.g. Watt), the dimension of $S_d(s)$ is [power $\times$ time], which corresponds to power per unit frequency, e.g. Watt·Hz^{-1}. The quantity $S_d(s)$ is called the *power spectral density* (PSD), which represents the *double-sided* (meaning: frequency $-\infty \to +\infty$) power density of a stochastic variable $X(t)$. The Fourier pair $R(\tau) \Leftrightarrow S_d(s)$ is commonly referred to as the *Wiener-Khinchin relation*. For $\tau = 0$ this relation becomes:

$$R(0) = \mathbf{E}\left\{|\, X(t)\,|^2\right\} = \int_{-\infty}^{+\infty} S_d(s)\, ds \tag{8.18}$$

and if the signal average $\mu = 0$:

$$R(0) = C(0) = \sigma^2 = \int_{-\infty}^{+\infty} S_d(s)\, ds \tag{8.19}$$

i.e. the power contained in the fluctuations of a signal centered around zero mean follows from the integration of the spectral power density over the entire frequency band.

Since physical frequencies run from zero (i.e. DC) to $+\infty$, the one-sided power spectral density $S_o(s) = 2S_d(s)$ is commonly used. The total signal power follows from integration of this entity over the physical frequency domain (see also figure 8.3):

$$R(0) = \int_{0}^{\infty} S_o(s)\, ds \tag{8.20}$$

Figure 8.4 shows two examples of $S_o(s)$, displaying the PSDs which relate to the characteristic light curves of certain compact X-ray binary systems, the so-called Low Mass X-Ray Binaries

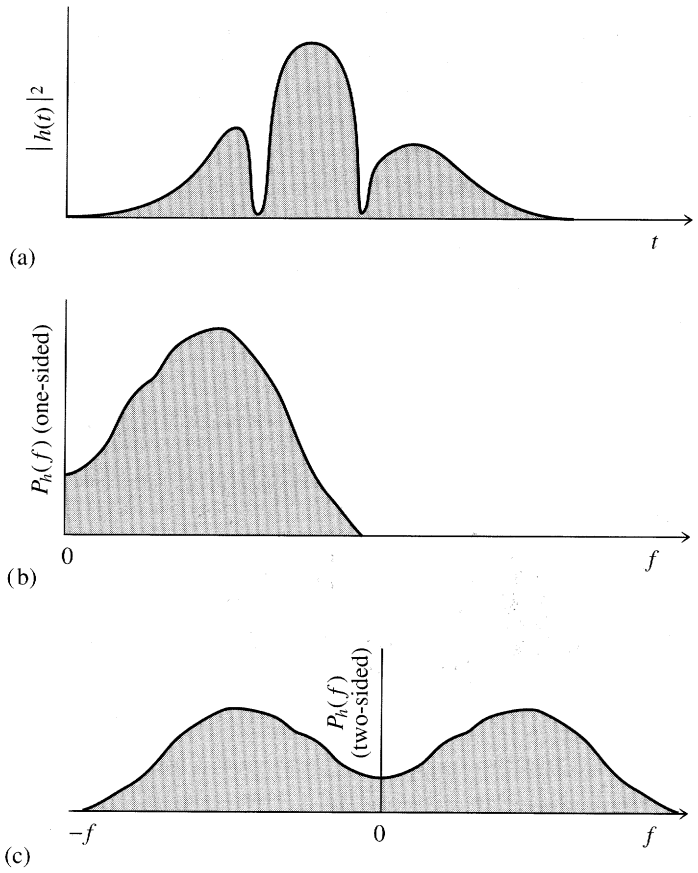

Figure 8.3: *Power spectra: the area under the square of the function $h(t)$ (panel a) equals the area under its one-sided power spectrum at positive frequencies (panel b) and also equals the area under its double-sided spectrum (panel c). Note the factor 2 in amplitude between the one-sided and double-sided spectrum. Credit Press et al. (1992).*

(LMXBs). The binary source GX5-1 shows a "red-noise" excess, i.e. the power increases at low frequencies, roughly following a power law dependence proportional to $s^{-\beta}$, on which a broad peak around a central frequency s_0 is superimposed. This peak refers to so-called quasi-periodic oscillations (QPOs), indicating that the X-ray source produces temporarily coherent oscillations in luminosity. The other source Sco X-1, shows a similar behaviour, the red-noise referring to stochastic (i.e. non-coherent) variability in X-ray luminosity is largely absent in this case.

Note: relation 8.16 defines the autocorrelation function of a stochastic process as a time average. If the stochastic variable $X(t)$ is replaced by a general function $f(u)$, the autocorrelation is defined as (provided that $\int_{-\infty}^{\infty} |f(u)|\ du$ is finite):

$$R(x) = \int_{-\infty}^{+\infty} f^*(u) \cdot f(u+x)\ du = \int_{-\infty}^{+\infty} f^*(u) \cdot f(u-x)\ du \tag{8.21}$$

where no averaging takes place. The Fourier transform $\Phi(s)$ of $R(x)$ is now given by

$$\Phi(s) = \int_{-\infty}^{+\infty} R(x) \cdot e^{-2\pi i s x}\ dx = F(s) \cdot F^*(s) = |F(s)|^2 \tag{8.22}$$

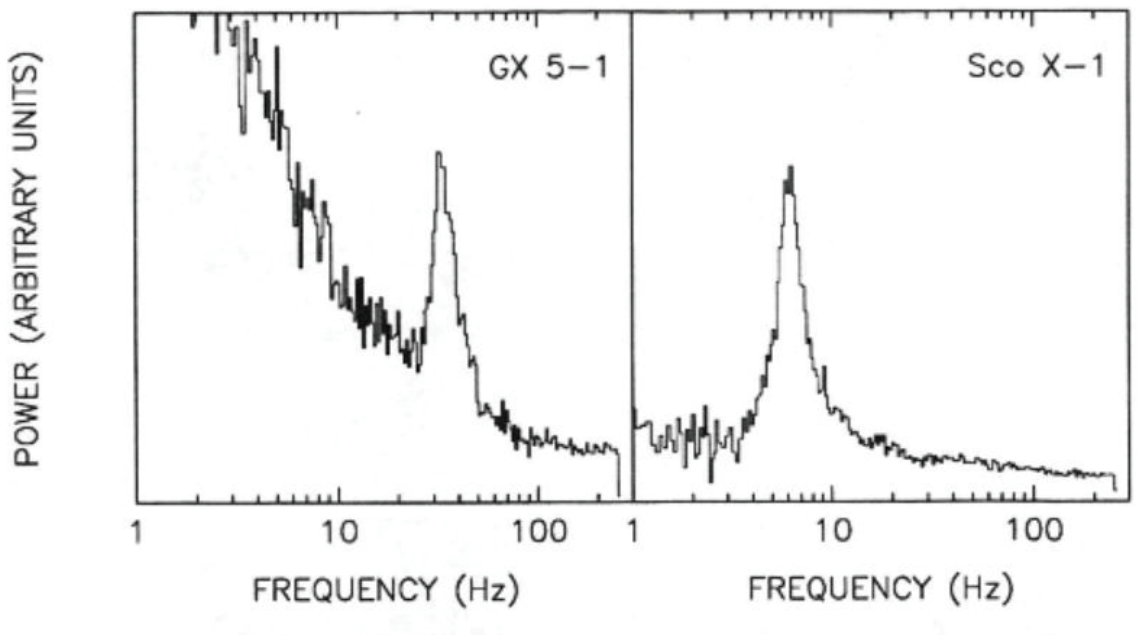

Figure 8.4: *One-sided power spectra of the X-ray sources GX 5-1 and Sco X-1. Credit van der Klis (1989).*

in which $f(u) \Leftrightarrow F(s)$. This is the *Wiener-Khinchin theorem for a finite function* $f(u)$, which is only non-zero over a limited interval of the coordinate u.

For $x = 0$ this results in:

$$R(0) = \int_{-\infty}^{+\infty} |f(u)|^2 \ du = \int_{-\infty}^{+\infty} \Phi(s)\, ds = \int_{-\infty}^{+\infty} |F(s)|^2 \ ds \tag{8.23}$$

The relation:

$$\int_{-\infty}^{+\infty} |f(u)|^2 \ du = \int_{-\infty}^{+\infty} |F(s)|^2 \ ds \tag{8.24}$$

is referred to as Parseval's theorem, each integral represents the amount of "energy" in a system, one integral being taken over all values of a coordinate (e.g. angular coordinate, wavelength, time), the other over all spectral components in the Fourier domain, see also figure 8.3. The function $\Phi(s)$, therefore, has the dimension of a *energy density*, quite confusingly (and erroneously) in the literature this is also often referred to as a power density, although no averaging process has taken place.

8.5 Intrinsic stochastic nature of a radiation beam: Application of Bose-Einstein statistics

Irrespective of the type of information carrier, e.g. electromagnetic or particle radiation, the incoming radiation beam in astronomical measurements is subject to fluctuations which derive from the incoherent nature of the emission process in the information (=radiation) source. For a particle beam this is immediately obvious from the corpuscular character of the radiation, however for electromagnetic radiation the magnitude of the fluctuations depends on

whether the wave character or the quantum character (i.e. photons) dominates. By employing Bose-Einstein statistics, the magnitude of these intrinsic fluctuations can be computed for the specific case of a blackbody radiation source which is incoherent or "chaotic" with respect to time. Photons are *bosons*, which are not subject to the Pauli exclusion principle, consequently many bosons may occupy the same quantum state.

Intermezzo: Bose-Einstein and Fermi Dirac statistics

The world is quantum-mechanical. One way of describing this, is to note that particles in a unit volume of space ('a cubic centimeter') are distributed in momentum-space in boxes with a size proportional to h^3, where h is Planck's constant. At each energy, there is a finite number Z of boxes (where $Z \propto 4\pi p^2 dp$ with p the particle momentum). Consider n_i particles, each with energy ϵ_i, and call the number of boxes available at that energy Z_i. Bosons can share a box. The number of ways $W(n_i)$ in which the n_i bosons can be distributed over the Z_i boxes is given by

$$W(n_i) = \frac{(n_i + Z_i - 1)!}{n_i!(Z_i - 1)!} \tag{8.25}$$

(To understand this: the problem is equivalent to laying n_i particles and $Z_i - 1$ boundaries in a row. The number of permutations is $(n_i + Z_i - 1)!$; then note that the particles and boundaries can be interchanged.) Similarly, we put n_j bosons in Z_j boxes, etc. The number of ways in which $N = \sum_{i=1}^{\infty} n_i$ bosons can be distributed over the boxes in momentum space thus is: $W = \Pi_{i=1}^{\infty} W(n_i)$. *The basic assumption of statistical physics is that the probability of a distribution is proportional to the number of ways in which this distribution can be obtained, i.e. to W.* The physics behind this assumption is that collisions between the particles will continuously re-distribute the particles over the boxes. The most likely particle distribution is thus the one which can be reached in most different ways. We find this maximum in W by determining the maximum of $\ln W$, by setting its derivative to zero:

$$\ln W = \sum_{i=1}^{\infty} \ln W(n_i) \Rightarrow \Delta \ln W = \sum_{i=1}^{\infty} \frac{\partial \ln W(n_i)}{\partial n_i} \Delta n_i = 0 \tag{8.26}$$

We consider one term from the sum on the right-hand side. With Stirlings approximation $\ln x! \simeq x \ln x - x$ for large x we get

$$\begin{aligned} \ln W(n_i) &= (n_i + Z_i - 1)\ln(n_i + Z_i - 1) - (n_i + Z_i - 1) - n_i \ln n_i + n_i - (Z_i - 1)\ln(Z_i - 1) \\ &\quad + (Z_i - 1) = (n_i + Z_i - 1)\ln(n_i + Z_i - 1) - n_i \ln n_i - (Z_i - 1)\ln(Z_i - 1) \end{aligned} \tag{8.27}$$

For a nearby number $n_i + \Delta n_i$, we have

$$\begin{aligned} \Delta \ln W(n_i) &\equiv \ln W(n_i + \Delta n_i) - \ln W(n_i) \simeq \Delta n_i \frac{\partial \ln W(n_i)}{\partial n_i} \\ &= \Delta n_i \left[\ln(n_i + Z_i - 1) - \ln n_i\right] \end{aligned} \tag{8.28}$$

to first order in Δn_i.
For equilibrium, i.e. the most likely particle distribution, we now have to set:

$$\Delta \ln W = \sum_{i=1}^{\infty} \Delta n_i \left[\ln(n_i + Z_i - 1) - \ln n_i\right] = 0 \tag{8.29}$$

Since we consider a system in thermodynamic equilibrium, i.e. for which the number of particles $N = \sum n_i$ per unit volume and the energy $E = \sum n_i \epsilon_i$ per unit volume are constant, the variations in n_i must be such as to conserve N and E i.e.

$$\Delta N = \sum_{i=1}^{\infty} \Delta n_i = 0 \tag{8.30}$$

and

$$\Delta E = \sum_{i=1}^{\infty} \epsilon_i \Delta n_i = 0 \tag{8.31}$$

These restrictions imply that we also have:

$$\Delta \ln W - \alpha \Delta N - \beta \Delta E \; = \; \sum_{i=1}^{\infty} \Delta n_i \left[\ln(n_i + Z_i - 1) - \ln n_i - \alpha - \beta \epsilon_i \right] \; = \; 0 \tag{8.32}$$

The sum in 8.32 is zero for arbitrary variations Δn_i, provided that for each i

$$\ln(\overline{n}_i + Z_i - 1) - \ln \overline{n}_i - \alpha - \beta \epsilon_i = 0 \Rightarrow \frac{\overline{n}_i}{Z_i - 1} = \frac{1}{e^{\alpha + \beta \epsilon_i} - 1} \tag{8.33}$$

which is the Bose Einstein distribution.
Since $Z_i \gg 1$, $\overline{n}_i/(Z_i - 1)$ can be replaced by $\overline{n}_i/Z_i$, which represents the average occupation at energy level ϵ_i (occupation number). The values of α and β depend on the total number of particles and the total energy, and can be determined from these by substituting n_i in $N = \sum_{i=1}^{\infty} n_i$ and in $E = \sum_{i=1}^{\infty} n_i \epsilon_i$. For the Planck function, the number of photons need not be conserved: e.g. an atom can absorb a photon and jump from orbit 1 to orbit 3, and then emit 2 photons by returning via orbit 2. Thus, the Lagrange condition 8.30 does not apply to photons, and we obtain the Planck function by dropping α in 8.33:

$$\frac{\overline{n}_i}{Z_i - 1} = \frac{1}{e^{\beta \epsilon_i} - 1} = \overline{n}_{\nu_k} \tag{8.34}$$

$\overline{n}_{\nu_k}$ is the average occupation number of photons at frequency ν_k. Note that photons do not collide directly with one another, but reach equilibrium only via interaction with atoms. We can make the connection to thermodynamics by taking

$$S \equiv k \ln W \Rightarrow \Delta S = k \Delta \ln W \tag{8.35}$$

With Eqs. 8.32 we get

$$\Delta S = k\alpha \Delta N + k\beta \Delta E \tag{8.36}$$

and with $T\Delta S = -\zeta \Delta N + \Delta E$ we find that $\beta = 1/(kT)$; here $\zeta \equiv -\alpha/\beta$ is the thermodynamical potential per particle.

Fluctuations around equilibrium

To investigate the fluctuations we look at the number of ways in which $n_i + \Delta n_i$ particles can be distributed, as compared to that for n_i particles:

$$\ln W(n_i + \Delta n_i) = \ln W(n_i) + \Delta n_i \frac{\partial \ln W(n_i)}{\partial n_i} + \frac{\Delta n_i^2}{2} \frac{\partial^2 \ln W(n_i)}{\partial n_i^2} \tag{8.37}$$

where we now include the 2nd order term.
In equilibrium the term in 8.37 proportional to Δn_i is zero. Consequently, we can rewrite 8.37 as

$$W(n_i + \Delta n_i) = W(n_i) \mathrm{e}^{-\frac{W''(n_i)}{2}\Delta n_i^2} \qquad \text{where} \qquad W''(n_i) \equiv -\frac{\partial^2 \ln W(n_i)}{\partial n_i^2} \tag{8.38}$$

In other words, the probability of a deviation Δn_i drops exponentially with the square of Δn_i, i.e. the probability of Δn_i is given by a Gaussian! The average value for Δn_i^2 is found by integrating over all values of Δn_i:

$$\overline{\Delta n_i^2} = \frac{\int_{-\infty}^{\infty} \Delta n_i^2 W(n_i) e^{-\frac{W''(n_i)}{2}\Delta n_i^2} d\Delta n_i}{\int_{-\infty}^{\infty} W(n_i) e^{-\frac{W''(n_i)}{2}\Delta n_i^2} d\Delta n_i} = \frac{1}{W''(n_i)} \tag{8.39}$$

(Note that $W(n_i)$ and $W''(n_i)$ do not depend on Δn_i, so that they can be considered as constants in the integrations. Note also that the maximum negative deviation has $\Delta n_i = -n_i$, and the maximum positive deviation $\Delta n_i = N - n_i$; the integrals should therefore formally be evaluated between these values; however, for large Δn_i the integrand drops rapidly to zero, and so we can extend the integrals to the full range $-\infty$ to $+\infty$)without compromising the result. Computing the second derivative of $\ln W(n_i)$ and changing sign we find for the variance:

$$\overline{\Delta n_i^2} = \left[W''(n_i)\right]^{-1} = \frac{\overline{n}_i(\overline{n}_i + Z_i - 1)}{Z_i - 1} = \overline{n}_i \left[1 + \frac{1}{e^{\alpha+\beta\epsilon_i} - 1}\right] \tag{8.40}$$

For the Planck function we must drop the α. Thus, for photons:

$$\overline{\Delta n_i^2} = \overline{n}_i \left[1 + \frac{1}{e^{\beta\epsilon_i} - 1}\right] = \overline{n_i}(1 + \overline{n}_{\nu_k}) \tag{8.41}$$

The fluctuation in the average occupation number $\overline{\Delta n_{\nu_k}{}^2}$ follows from

$$\overline{\Delta n_{\nu_k}{}^2} = \frac{\overline{\Delta n_i^2}}{Z_i} = \overline{n}_{\nu_k}(1 + \overline{n}_{\nu_k}) \tag{8.42}$$

We can repeat the same exercise for fermions. In this case the particles are not allowed to share a box, and the number of ways $W(n_i)$ in which n_i particles can be distributed over Z_i boxes with energies ϵ_i is given by

$$W(n_i) = \frac{Z_i!}{n_i!(Z_i - n_i)!} \tag{8.43}$$

The difference in $\ln W(n_i)$ between nearby numbers is

$$\ln W(n_i + \Delta n_i) - \ln W(n_i) = -\Delta n_i \left[\ln n_i - \ln(Z_i - n_i)\right] \tag{8.44}$$

to first order in Δn_i. This leads to the equilibrium, Fermi Dirac distribution:

$$\frac{\overline{n}_i}{Z_i} = \frac{1}{e^{\alpha+\beta\epsilon_i} + 1} = \overline{n}_k \tag{8.45}$$

and to an average value of the square of a deviation

$$\overline{\Delta n_i^2} = \frac{\overline{n}_i(Z_i - \overline{n}_i)}{Z_i} = \overline{n}_i \left[1 - \frac{1}{e^{\alpha+\beta\epsilon_i} + 1}\right] = \overline{n}_i(1 - \overline{n}_k) \tag{8.46}$$

The fluctuation in the average occupation number $\overline{\Delta {n_k}^2}$ follows from

$$\overline{\Delta {n_k}^2} = \frac{\overline{\Delta n_i^2}}{Z_i} = \overline{n}_k(1-\overline{n}_k) \tag{8.47}$$

End Intermezzo Bose Einstein and Fermi Dirac statistics

The volume density of photons in a blackbody Bose gas with frequencies between ν_k and $\nu_k + d\nu_k$ follows from $\bar{N}(\nu_k)d\nu_k = g(\nu_k)\bar{n}_{\nu_k}d\nu_k$, in which $g(\nu_k)$ represents the volume density of quantum states per unit frequency at ν_k. Since the stochastic variables n_{ν_k} are independent, the Bose-fluctuations $\overline{\Delta N^2}(\nu_k)$ in photon density per unit frequency can be written as (omitting the suffix k):

$$\overline{\Delta N^2}(\nu) = \bar{N}(\nu)\left(1 + \frac{1}{\exp(h\nu/kT)-1}\right) \tag{8.48}$$

where $\bar{N}(\nu)$ follows from the specific energy density $\bar{\rho}(\nu) = \rho(\nu)^{equilibrium}$ given by (see OAF1, Chapter 2):

$$\overline{\rho}(\nu)d\nu = \frac{8\pi h}{c^3}\frac{\nu^3}{\exp\left(\frac{h\nu}{kT}\right)-1}d\nu \tag{8.49}$$

through the relation $\bar{N}(\nu) = \bar{\rho}(\nu)/h\nu$. If a detection element, e.g. an antenna, is placed within a blackbody radiation field, for example inside a vacuum enclosure at temperature T, the incident photon flux is given by $\bar{n}(\nu) = \frac{1}{2}\frac{c}{4\pi}\bar{N}(\nu)A_e\Omega$. The factor $\frac{1}{2}$ refers to one component of polarisation, A_e is the effective area of the detection element and Ω constitutes the solid angle subtended by the detector beam viewing the radiation field. If radiation illuminates an extended surface (A_e) with various directions of the wave vector, i.e. an omnidirectional blackbody radiation field, coherence theory states that spatial coherence is limited to $A_e\Omega \approx \lambda^2$, the so-called *extent (etendue) of coherence*.[1] Substituting $\bar{N}(\nu)$, the expression for the specific photon flux $\bar{n}(\nu)$ (in photons s^{-1} Hz^{-1}) becomes:

$$\bar{n}(\nu) = \frac{1}{\exp(h\nu/kT)-1} \tag{8.50}$$

$$\overline{\Delta n^2}(\nu) = \bar{n}_\nu\left(1 + \frac{1}{\exp(h\nu/kT)-1}\right) \tag{8.51}$$

In the extreme case that $h\nu \gg kT$, the second term becomes much smaller than 1, hence:

$$\overline{\Delta n^2}(\nu) = \bar{n}(\nu) \tag{8.52}$$

This is the well-known expression for Poissonian noise in a sample containing $\bar{n}(\nu)$ photons. This condition is called the quantum limit of the fluctuations and it represents the minimum value of intrinsic noise present in any radiation beam. Obviously, this always holds for corpuscular radiation (cosmic-rays) and neutrinos, since the wave character is not an issue.

[1] This relation is the same as that governing the size $\theta = \lambda/D$ of a diffraction limited beam ($\Omega \approx \theta^2$) for an aperture with diameter D: $A_e \approx D^2$.

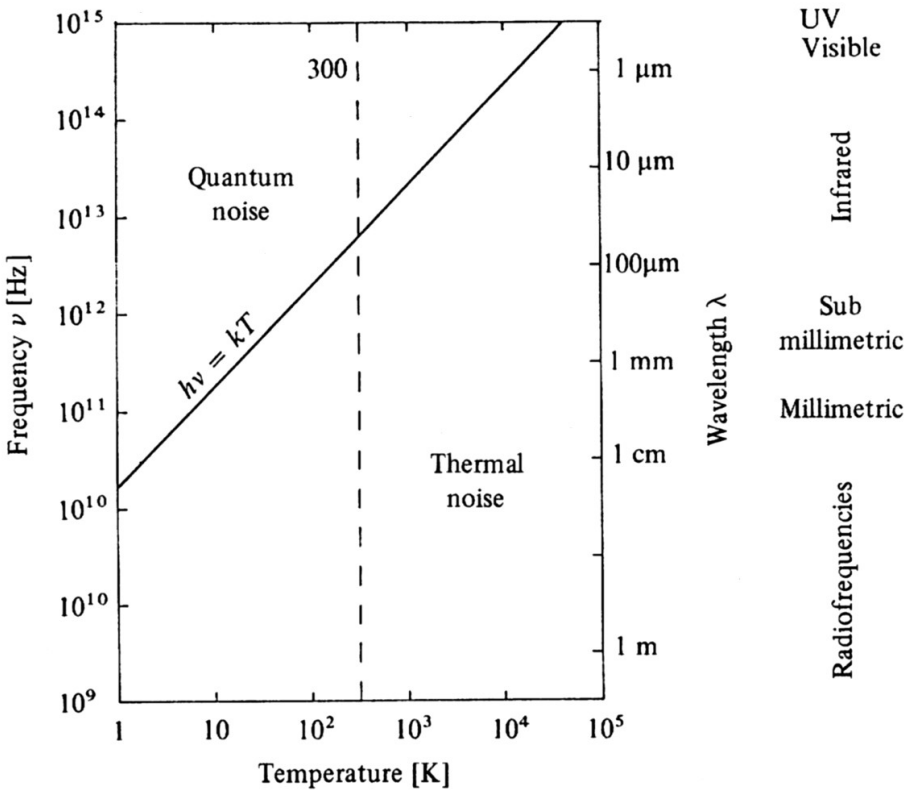

Figure 8.5: *Frequency as a function of temperature: division between thermal and quantum noise. Credit Lena et al. (1988).*

For a photon energy $h\nu \ll kT$, the noise is normally expressed in terms of the average radiation power $\bar{P}(\nu)$ (e.g. in Watt Hz^{-1}) by writing $\bar{P}(\nu) = (h\nu)\bar{n}(\nu)$ and $\overline{\Delta P^2}(\nu) = (h\nu)^2\overline{\Delta n^2}(\nu)$:

$$\overline{\Delta P^2}(\nu) = \bar{P}(\nu)\left(h\nu + \frac{h\nu}{\exp(h\nu/kT) - 1}\right) = \bar{P}(\nu)(h\nu + \bar{P}(\nu)) \tag{8.53}$$

Taking the limit $h\nu \ll kT$:

$$\overline{\Delta P^2}(\nu) = \bar{P}^2(\nu) \tag{8.54}$$

$$\text{and} \qquad \bar{P}(\nu) = kT \tag{8.55}$$

which is the expression for the classical thermal noise power per unit frequency bandwidth. This limit is called the thermal limit.

The transition between noise in the quantum limit to the thermal limit occurs at $h\nu \approx kT$. At room temperature, $T \approx 300$ K, this corresponds to a frequency $\nu \approx 6$ THz, or a wavelength $\lambda \approx 50$ μm. The relation $\nu = kT/h$ as a function of temperature T is displayed in figure 8.5. It is clear from this diagram that radio observations are always dominated by the wave character of the incoming beam and are therefore performed in the thermal limit. As a result, the treatment of noise in radio observations differs drastically from that of measurements at shorter wavelengths. Specifically at submillimetric and infrared wavelengths quantum limited observation is vigorously pursued but this remains still difficult.

The fluctuations in average power $\bar{P}(\nu)$, given in equation 8.54, for the thermal limit can be interpreted in such a way that whenever wave packet interference becomes important, the

interference will cause the fluctuations to become of the same magnitude as the signal. The low frequency fluctuations can be thought of as caused by the random phase differences and beats of the wavefields, as described in the following paragraph.

Note of Caution: The above expression for the fluctuations in a blackbody photon gas applies only to the interior of a blackbody in which the receiving element is submerged, i.e. a blackbody cavity or a thermal bath, where the condition $\lambda^2 = c^2/\nu^2 = A_e\Omega$ *is satisfied. If this condition is not fulfilled, then even in the limit* $h\nu \ll kT$ *quantum noise may dominate. For example, if a star, whose spectrum resembles a blackbody at temperature* T*, is observed at frequency* ν*, such that* $h\nu \ll kT$*, thermal noise ought to dominate. The star may however be so distant that the radiation is effectively unidirectional and hence,* $A_e\Omega \ll \lambda^2$*. The photons will consequently arrive well separated in time and quantum noise evidently dominates.*

8.6 Stochastic description of a radiation field in the wave limit

8.6.1 Wave packets, random superposition

In astrophysics, many sources of electromagnetic (EM) radiation have a thermal origin. A beam of thermal radiation will ordinarily comprise a myriad of randomly overlapping wave groups or *wave packets*. Examples of such wave packets are shown in figure (8.6). They arise from two different types of quasi-monochromatic sources:
- Gaussian shaped spectral lines which emerge when several line broadening mechanisms contribute to the line formation (*viz.* the central limit theorem).
- Spectral lines with a Lorentz profile, characteristic for the natural line broadening associated with the intrinsic time spread of the radiative atomic transitions involved that are governed by the uncertainty relation of Heisenberg $\sigma_\epsilon\sigma_t = \hbar/2$.

The characteristic length, τ_c, of these wave packets in the time domain follows from the Fourier transform of the spectral frequency distribution. A Gaussian spectral line, centered at frequency ν_0 with a full-width half-maximum (FWHM) $\Delta\nu$, corresponds to a Gaussian shaped wave packet with a characteristic width $\tau_c \simeq (1.5\Delta\nu)^{-1}$. A Lorentzian profile ($\nu_0$, FWHM $\Delta\nu$) derives from an exponentially damped harmonic oscillator with a $1/e$-value $\tau_c = (\pi\Delta\nu)^{-1}$. The characteristic time τ_c is commonly referred to as the *coherence time*, it represents the typical time scale over which the phase of the EM-wave can be predicted with reasonable accuracy at a *given location in space*. For atomic transitions in the optical $\tau_c \simeq 10^{-9}$s. Figure (8.7) shows a linearly polarised quasi-monochromatic signal comprising a random superposition of individual wavepackets.
This wave signal fluctuates both in amplitude and in frequency, the latter characterised by a typical bandwidth $\Delta\nu$ around an average frequency $\bar{\nu}$. The frequency stability of such a quasi-monochromatic wave is defined by $\bar{\nu}/\Delta\nu$.

The linearly polarised signal displayed in figure (8.7) can mathematically be expressed by the real function:

$$E(t) = E_0(t)\cos(2\pi\bar{\nu}t + \phi(t)) \tag{8.56}$$

The amplitude $E_0(t)$ of the quasi-monochromatic wave is a *wide-sense stationary* Gaussian random time function of zero mean. Moreover the stochastic process is assumed to be *mean- and correlation-ergodic*, i.e. for an arbitrary real stochastic variable $X(t)$ its *expectation value*

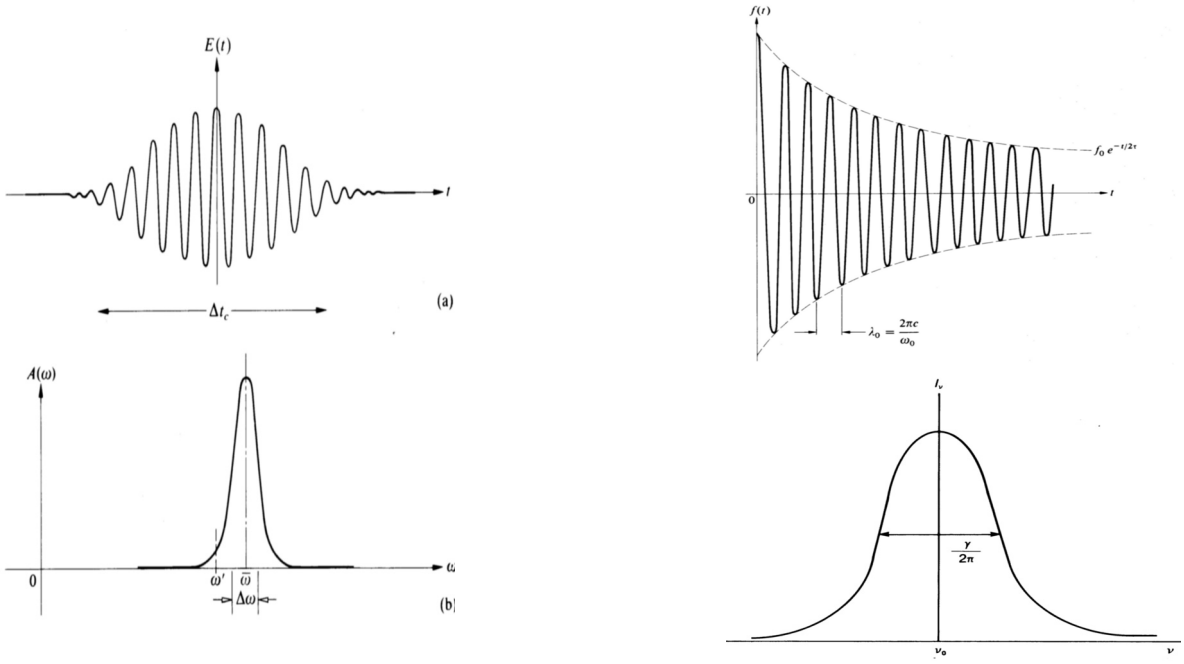

Figure 8.6: *Examples of wave packets and their Fourier (⇔) transforms. Left: Gaussian shaped wave packet ⇔ Gaussian spectral line. Right: Exponentially damped harmonic oscillator ⇔ Lorentzian spectral line. Credit Hecht (1987).*

at time t, $\mathbf{E}\{\mathbf{X(t)}\}$, can be interchanged with its time average:

$$\bar{X} \;=\; \lim_{T\to\infty}\frac{1}{T}\int_{-\frac{1}{2}T}^{+\frac{1}{2}T} X(t)\,dt = \mathbf{E}\{X(t)\} \tag{8.57}$$

Furthermore, the expectation value at time t of the autocorrelation $R_X(\tau)$ of $X(t)$ can be interchanged with its time average:

$$R_X(\tau) \;=\; \overline{X(t)\cdot X(t+\tau)} \;=\; \lim_{T\to\infty}\frac{1}{T}\int_{-\frac{1}{2}T}^{+\frac{1}{2}T} X(t)\cdot X(t+\tau)\,dt = \mathbf{E}\{X(t)\cdot X(t+\tau)\} \tag{8.58}$$

The frequency is randomly varying around an average frequency $\bar{\nu}$, the instantaneous frequency $\nu(t)$ follows from the time derivative of the argument of the cosine term according to:

$$\nu(t) \;=\; \frac{1}{2\pi}\frac{d}{dt}\left(2\pi\bar{\nu}t \;+\; \phi(t)\right) \;=\; \bar{\nu} \;+\; \frac{1}{2\pi}\frac{d\phi(t)}{dt} \tag{8.59}$$

As can be seen from equation (8.59), the time variable phase factor $\phi(t)$ fully accomodates the frequency bandwidth $\Delta\nu$ of the stochastic wave signal.

The above mathematical description suffices for a linearly polarised signal, however in case of a thermal radiator a particular *polarisation direction is only very short-lived*, i.e. only during the *coherence time τ_c of an emitted wave packet*. This can be understood by considering the emission process involved.
Thermal emission consists of an extremely large number of radiative transitions, generated

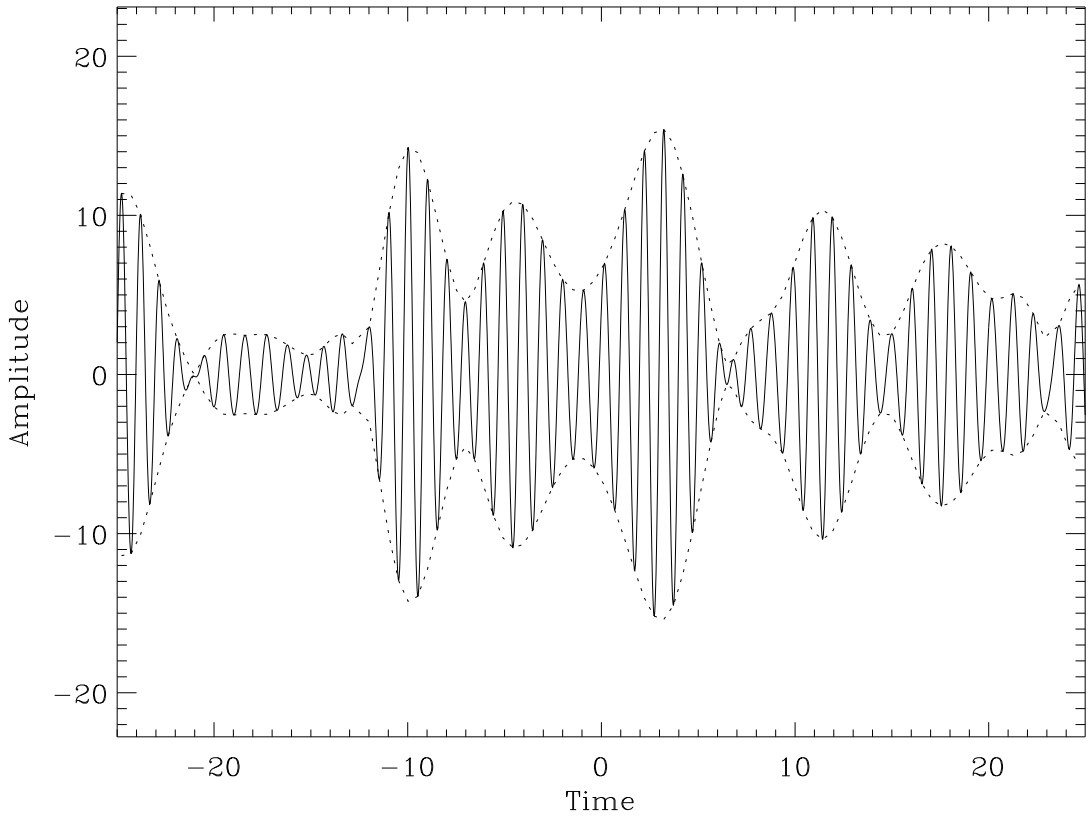

Figure 8.7: *A linearly polarised quasi-monochromatic wave.*

by randomly oriented atomic emitters. Each atom radiates a polarised wave train for roughly 10^{-8} or 10^{-9} seconds in the case of optical light depending on the natural line width $\Delta\nu$ of the transition. In the case of molecular vibrational or rotational transitions (radio and far infrared) the timescales are substantially longer. Considering a certain wave propagation direction $\vec{k}$, individual atomic (molecular) emissions along that direction will combine to generate a polarised wave, which however will not persist for more than the typical coherence time τ_c of a wave packet, i.e. in the optical $10^{-8} - 10^{-9}$ seconds. New wave trains are continually emitted and as a result the magnitude and the polarisation direction of the electric vector $\vec{E}(t)$ changes in a completely random manner on a typical time scale equal to the coherence time τ_c. If these changes occur at a rate of 10^8 to 10^9 per second, any persistent polarisation state is undiscernable. Thermal radiation is therefore designated as *natural or unpolarised light*, although the latter qualification is somewhat confusing since in actuality the light comprises a rapid succession of different polarisation states.

8.6.2 The analytic signal

The *rapid random fluctuations* in the electric vector $\vec{E}(t)$ of a thermal radiation field can be handled mathematically in a *scalar approach* by using a *complex analytic representation* of the quasi-monochromatic wave field.

Consider the time-varying electric field $E(t)$ of equation (8.56). Along with $E(t)$ one may consider a complex function:

$$\tilde{E}(t) = E(t) + iF_{Hi}(t) \tag{8.60}$$

in which:

$$F_{Hi}(t) \;=\; -\frac{1}{\pi}\int_{-\infty}^{\infty}\frac{E(t')dt'}{t'-t} \tag{8.61}$$

is the Hilbert transform of $E(t)$. This integral can be interpreted as a convolution of $E(t)$ with $(\pi t)^{-1}$:

$$F_{Hi}(t) \;=\; E(t) \,*\, \frac{1}{\pi t} \tag{8.62}$$

Applying the convolution theorem and considering the Fourier transform of $(\pi t)^{-1} \;\Leftrightarrow\; i\,\mathrm{sgn}(\nu)$, the Hilbert transform can be regarded as a *special filter* that leaves the amplitude of the spectral components unimpaired, but alters their phases by $\pi/2$, positively or negatively depending on the sign of ν. A consequence of this is, that Hilbert transforms of even functions are odd and those of odd functions even.
The complex function $\tilde{E}(t)$ of equation (8.60) is known as the *analytic signal*, the Hilbert transform is referred to as the *quadrature function* of $E(t)$. For example, the quadrature function of $\cos t$ is $\sin t$, the analytic signal is therefore $\exp(it)$.
Analytic functions are useful to describe quasi-monochromatic wave phenomena, where one deals with *modulated carrier* signals. The analytic signal contains *no negative frequency* components, it is obtainable from $E(t)$ by suppressing the negative frequencies and doubling the result.
For example $\cos 2\pi\nu_0 t$ contains frequency components at ν_0 and $-\nu_0$:

$$\cos 2\pi\nu_0 t = \frac{e^{2\pi i\nu_0 t} + e^{-2\pi i\nu_0 t}}{2}, \tag{8.63}$$

the analytic signal follows from suppression of $e^{-2\pi i\nu_0 t}$ and multiplication by 2.

Problem 1: Show with the aid of a Fourier transform that applying the above operation to $E(t)$ results in the analytic signal $\tilde{E}(t)$!

If $E(t)$ is a Gaussian process, its Hilbert transform (linear) is also a Gaussian process, moreover the autocorrelation functions are equal and the values of $E(t)$ and its Hilbert transform are *uncorrelated* at the same instant t. The analytic signal comprises a harmonic oscillation at an average frequency $\bar{\nu}$ modulated by a slowly varying envelope:

$$\tilde{E}(t) = \tilde{E}_0(t)\cdot e^{i(2\pi\bar{\nu}t)} \tag{8.64}$$

The complex amplitude (envelope function) $\tilde{E}_0(t)$ can be expressed as:

$$\tilde{E}_0(t) = |\tilde{E}_0(t)|\cdot e^{i\phi(t)} \tag{8.65}$$

This envelope function is also referred to as the *phasor* of the analytic signal, $|\tilde{E}_0(t)|$ represents the instantaneous amplitude of $\tilde{E}(t)$ and $\phi(t)$ the time variable phase. The time rate of change of $\phi(t)$, i.e. $\left(\frac{1}{2\pi}\right)\frac{d\phi(t)}{dt}$, represents the instantaneous frequency shift $\Delta\nu(t)$ of the analytic signal relative to the average carrier frequency $\bar{\nu}$.

In the next section, a quantitative fluctuation analysis of a thermal wave field will now be deployed with the aid of the expression for the analytic signal:

$$\tilde{E}(t) = |\tilde{E}_0(t)|\cdot e^{i[2\pi\bar{\nu}t+\phi(t)]} \tag{8.66}$$

8.6.3 Fluctuation analysis of a thermal wave field

The ideal monochromatic plane wave

Let's first consider the phasor expression for a, hypothetical, perfectly monochromatic plane wave and its physical interpretation.
The frequency bandwidth $\Delta\nu$ then reduces to a delta function: $\delta(\nu - \bar{\nu})$. In the time domain this is represented as an infinitely long wave train (i.e. the Fourier transform of a δ-function). If this wave train were to be resolved in two orthogonal polarisation components perpendicular to the direction of propagation, they in turn must have the same frequency, be infinite in extent and are therefore *mutually coherent*. In other words *an idealised monochromatic plane wave is always polarised*. Expressing this in terms of the phasor $\tilde{E}_0(t)$ of a linearly polarised plane wave, this results in:

$$\tilde{E}_0(t) = |\tilde{E}_0(t)| \cdot e^{i\phi(t)} = |\tilde{E}_0| \cdot e^{i\phi_0} \tag{8.67}$$

i.e. both the amplitude $|\,\tilde{E}_0\,|$ and phase ϕ_0 of the phasor are constant in time.

Polarized thermal light

Consider a radiation field emitted by a thermal source, that is subsequently passed by a polarization analyzer with its polarization direction along the X-axis in a plane perpendicular to the wave propagation vector $\vec{k}$. The time wave form in the *X - t plane* can now be regarded as the sum of a great many independent contributions of the x-components of the fields generated by the individual atoms (molecules). The random fluctuations of $\vec{E}(t)$ along the x-axis, $\vec{E}_X(t)$, can now be described by a fluctuation analysis of the phasor $\tilde{E}_{X0}(t)$, i.e. of its magnitude $|\,\tilde{E}_{X0}(t)\,|$ and its phase $\phi(t)$. For time scales short compared to the coherence time (τ_c), $\tilde{E}_{X0}(t)$ will remain almost constant in time, in the case of optical light for $\tau_c \approx 10^{-8}$ s this still comprises several million harmonic oscillations of the electric vector $\vec{E}(t)$ ($\bar{\nu} \approx$ few 10^{14} Hz). For time scales $\tau \gg \tau_c$, $|\,\tilde{E}_{X0}(t)\,|$ and $\phi(t)$ will vary randomly, this is pictorially shown in figure 8.8. The coloured phasors signify the built up of $\tilde{E}_{X0}(t)$ by a great many independent atomic contributions that are fully uncorrelated. Mathematically these fluctuations can be described by regarding the real and imaginary parts of $\tilde{E}_{X0}(t)$, $\mathrm{Re}(\tilde{E}_{X0}(t))$ and $\mathrm{Im}(\tilde{E}_{X0}(t))$, as uncorrelated Gaussian stochastic variables with equal standard deviation that vary rapidly and randomly and are mutually incoherent.

The joint (bivariate) probability density distribution is then given by:

$$\begin{aligned} &\mathbf{p}_{biv}\left(Re\tilde{E}_{X0}(t), Im\tilde{E}_{X0}(t)\right)\; dRe\tilde{E}_{X0}(t)\; dIm\tilde{E}_{X0}(t) \;= \\ &= \frac{1}{2\pi\sigma^2}\, e^{-\frac{Re^2\vec{E}_{X0}(t)+Im^2\vec{E}_{X0}(t)}{2\sigma^2}}\; dRe\tilde{E}_{X0}(t)\; dIm\tilde{E}_{X0}(t) \end{aligned} \tag{8.68}$$

Furthermore, the following relations hold:

$$|\,\tilde{E}_{X0}(t)\,|^2 \;=\; |\,\tilde{E}_X(t)\,|^2 = Re^2\tilde{E}_{X0}(t) + Im^2\tilde{E}_{X0}(t) \tag{8.69}$$

$$\phi(t) \;=\; \arg(\tilde{E}_{X0}(t)) = \arg(\tilde{E}_X(t)) - 2\pi\bar{\nu}t = \arctan\frac{Im\tilde{E}_{X0}(t)}{Re\tilde{E}_{X0}(t)} \tag{8.70}$$

Changing to polar coordinates the bivariate probability density distribution for $|\,\tilde{E}_{X0}(t)\,|$ and $\phi(t)$ can be obtained:

$$\mathbf{p}_{biv}\left(|\,\tilde{E}_{X0}(t)\,|, \phi(t)\right)\; d\,|\,\tilde{E}_{X0}(t)\,|\; d\phi(t) = \frac{|\,\tilde{E}_{X0}(t)\,|}{2\pi\sigma^2}\, e^{-\frac{|\tilde{E}_{X0}(t)|^2}{2\sigma^2}}\; d\,|\,\tilde{E}_{X0}(t)\,|\; d\phi(t) \tag{8.71}$$

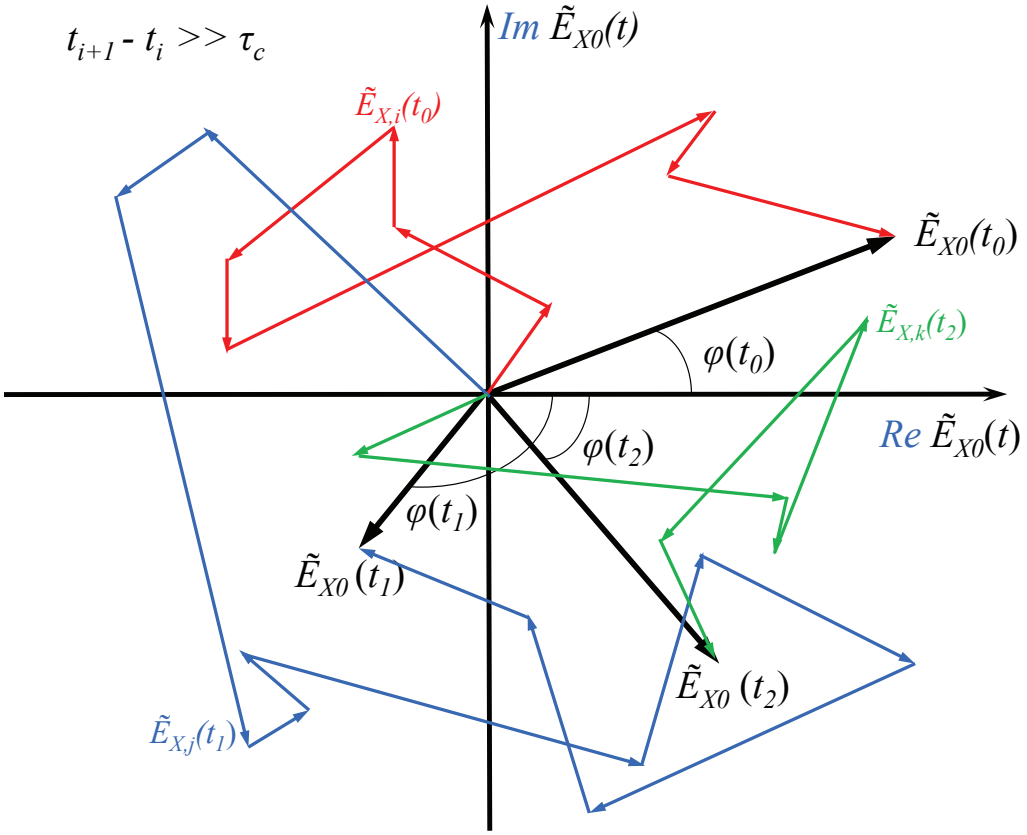

Figure 8.8: *Black: Random orientation of the complex envelopes (phasors) of polarized thermal light at a fixed point in space at three different times t_0, t_1 and t_2 separated by time intervals larger than the coherence time τ_c. Colors: signifying the great many independent complex atomic (molecular) phasors.*

Integration over $|\tilde{E}_{X0}(t)|$ yields:

$$\mathbf{p}\left(\phi(t)\right) = \frac{1}{2\pi} \tag{8.72}$$

i.e. all phase angles $\phi(t)$ are equally probable, which is obviously to be expected for randomly fluctuating phase angles.

Integration over all phase angles $\phi(t)$ yields the amplitude distribution $|\tilde{E}_{X0}(t)|$ for the X-component of the electric field vector of the thermal source:

$$\mathbf{p}_R\left(|\tilde{E}_{X0}(t)|\right) = \frac{|\tilde{E}_{X0}(t)|}{\sigma^2} \cdot e^{-\frac{|\tilde{E}_{X0}(t)|^2}{2\sigma^2}} \tag{8.73}$$

This is a so-called *Rayleigh distribution*. $\mathbf{p}_R\left(|\tilde{E}_{X0}(t)|\right)$ and $\mathbf{p}\left(\phi(t)\right)$ are displayed in figure 8.9.

Problem: 2 Show that the most probable value of $|\tilde{E}_{X0}(t)|$ equals σ and the average value for the amplitude equals $\sigma\sqrt{(\pi/2)}$. ◁

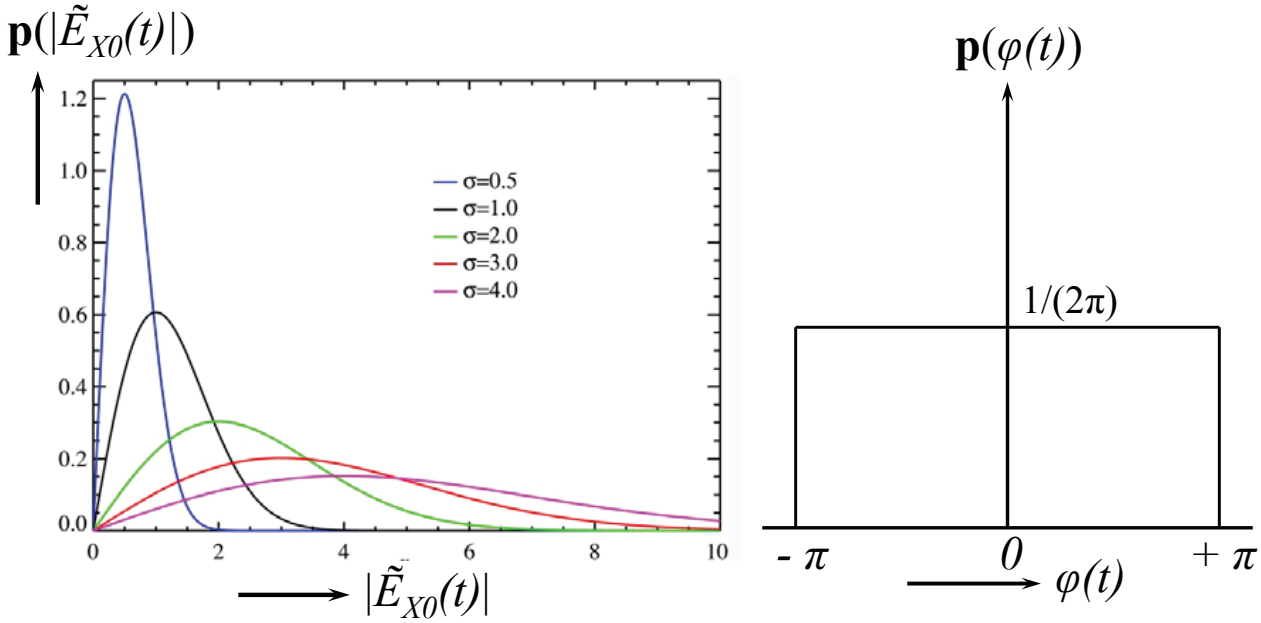

Figure 8.9: *The distribution functions* $\mathbf{p}\left(|\tilde{E}_{X0}(t)|\right)$ *and* $\mathbf{p}\left(\phi(t)\right)$.

The intensity (irradiance) of a traveling plane EM-wave

The energy streaming through space in the form of an electromagnetic wave is shared between the constituent electric and magnetic fields.
The energy density of an electrostatic field (e.g. between plates of a capacitor) $\rho_{\vec{E}} = \epsilon_r \epsilon_0 |\vec{E}|^2/2$ (dimension Joule/m^3), with $|\vec{E}|$ the magnitude of the electric vector (dimension V/m) and ϵ_0 the vacuum permittivity ($8.8543 \cdot 10^{-12}$ Asec/Vm). Similarly, the energy density of a magnetic field (e.g. within a toroid) equals $\rho_{\vec{B}} = |\vec{B}|^2/(2\mu_r\mu_0)$ (dimension Joule/m^3), with $|\vec{B}|$ the magnitude of the magnetic vector (dimension Tesla = Vsec/m^2) and μ_0 the vacuum permeability ($4\pi \cdot 10^{-7}$ Vsec/Am).
The wave equation for a **plane electromagnetic wave** traveling along the x-direction in vacuum is given by:

$$\frac{\partial^2 E(x,t)}{\partial x^2} = \frac{1}{c^2}\frac{\partial^2 E(x,t)}{\partial t^2} \quad \text{and} \quad \frac{\partial^2 B(x,t)}{\partial x^2} = \frac{1}{c^2}\frac{\partial^2 B(x,t)}{\partial t^2} \tag{8.74}$$

for the electric field wave and the magnetic field wave respectively. The magnetic field wave travels in a plane perpendicular to the electric field, both the electric field and the magnetic field directions are perpendicular to the direction of propagation (x). The plane wave solution can be expressed by a harmonic function, using a complex scalar representation:

$$\tilde{E}(x,t) \;=\; E_0 \cdot e^{i\cdot 2\pi(\nu t - x/\lambda)} \quad \text{and} \quad \tilde{B}(x,t) \;=\; B_0 \cdot e^{i\cdot 2\pi(\nu t - x/\lambda)} \tag{8.75}$$

Consistency with Maxwell's equations requires that for the EM-wave holds $\rho_{\vec{E}} = \rho_{\vec{B}}$. Hence, from the above, we have $B_0 \;=\; E_0/c$.
The flow of electromagnetic energy through space associated with the traveling EM-wave is represented by the Poynting vector $\vec{S} \;=\; (1/\mu_0)\vec{E}\,\mathbf{x}\,\vec{B}$, a vector product that symbolizes the direction and magnitude of the energy transport per unit time across a unit area (e.g. in units Watt m^{-2}). The vector magnitude $|\vec{S}| \;=\; |\tilde{E}||\tilde{B}|(\sin\phi)/\mu_0$ equals $|\tilde{E}||\tilde{B}|/\mu_0$, since the magnetic field is perpendicular to the electric field ($\phi \;=\; \pi/2$). Representing the *actual* wave signal by taking the real part of expressions (8.75) we get:

$$|\vec{S}| \;=\; E_0 B_0 \cos^2 2\pi(\nu t - x/\lambda) \;=\; \epsilon_0 c E_0^2 \cos^2 2\pi(\nu t - x/\lambda) \;=\; (\epsilon_0/\mu_0)^{\frac{1}{2}} E_0^2 \cos^2 2\pi(\nu t - x/\lambda) \tag{8.76}$$

The *average* power flux density for an *ideal monochromatic* plane wave, $\overline{I(t)}$ equals $\overline{|\vec{S}(t)|}$:

$$\overline{I(t)} \;=\; (\epsilon_0/\mu_0)^{\frac{1}{2}} E_0^2 \overline{\cos^2 2\pi(\nu t - x/\lambda)} \;=\; (\epsilon_0/\mu_0)^{\frac{1}{2}} \frac{E_0^2}{2} \;=\; 2.6544 \cdot 10^{-3} \frac{E_0^2}{2} \tag{8.77}$$

expressed in Watt/m^2 for E_0 in Volts/meter.
A perfectly monochromatic plane wave is represented in the time domain by an infinitely long wave train and is by definition *fully polarised*. A *quasi-monochromatic* radiation field from a thermal source can be described by a complex expression for the electric field $\tilde{E}(t)$, comprising a harmonic oscillation at an average frequency $\bar{\nu}$ modulated by a slowly varying envelope, accomodated by the phasor $\tilde{E}_0(t)$, i.e. $\tilde{E}(t) \;=\; \tilde{E}_0(t) \cdot e^{i(2\pi\bar{\nu}t)}$. The average power flux density for this wave then follows from the expectation value of the product $\tilde{E}(t) \cdot \tilde{E}^*(t)$:

$$\overline{I(t)} \;=\; \mathbf{E}\left\{I(t)\right\} \;=\; (\epsilon_0/\mu_0)^{\frac{1}{2}} \mathbf{E}\left\{\tilde{E}(t) \cdot \tilde{E}^*(t)\right\} \;=\; 2.6544 \cdot 10^{-3}\, \mathbf{E}\left\{|\tilde{E}_0(t)|^2\right\} \tag{8.78}$$

Since we are primarily concerned with *relative power flux densities generated by these traveling waves within the same medium*, we can disregard in what follows multiplication with the numerical constant in expression (8.78), since this (deterministic) quantity is only of relevance for assessing the *absolute numerical value* of the power flux density and bears no influence on the description of the stochastic nature of the signals. In practical computations, this constant should of course be applied!

The probability density distribution of the instanteneous intensity of polarized thermal light

From the distribution derived for $|\tilde{E}_{X0}(t)|$ in a previous paragraph, the probability density of the instantaneous intensity (or irradiance) $I_X(t)$ for a linearly polarized (along the X-axis) thermal radiation field can be readily derived.
We can now set the following equalities:

$$I_X(t) = \tilde{E}_X(t) \cdot \tilde{E}_X^*(t) \;=\; |\tilde{E}_X(t)|^2 \;=\; |\tilde{E}_{X0}(t)|^2 \tag{8.79}$$

Transformation of variables in equation (8.73) yields:

$$\mathbf{p}\,(I_X)\;dI_X = (\bar{I}_X)^{-1} \cdot e^{-I_X/\bar{I}_X}\;dI_X \tag{8.80}$$

with $\bar{I}_X = \mathbf{E}\left\{|\tilde{E}_{X0}(t)|^2\right\} = 2\sigma^2$.
This is an exponential probability density distribution that has the important property that its standard deviation σ_{I_X} is equal to its mean $\bar{I}_X$ $(= 2\sigma^2)$.

Problem 3: Prove that the variance of this intensity probability distribution is given by:

$$\overline{(\Delta I_X)^2} = \bar{I}_X^2 \tag{8.81}$$

◁

This result, which is now obtained formally from the bivariate Gaussian distributed stochastic process with zero-mean for the harmonic wave components, is the same as the fluctuation in the average radiation power per unit frequency bandwidth (Watt Hz^{-1}) for *one component of polarization* that was derived earlier for a blackbody radiation field, i.e. $\overline{(\Delta P)^2}(\nu) = \bar{P}^{\,2}(\nu)$. This should evidently hold.

Unpolarized thermal light

Light from a thermal source can be designated as unpolarized if it fullfils two conditions. First: if passed by a polarization analyzer in a plane perpendicular to the propagation vector $\vec{k}$, the intensity should be independent of the rotational orientation of the analyzer. Second: two orthogonal field components $\tilde{E}_X(t)$ and $\tilde{E}_Y(t)$ should have the property that $\tilde{E}_X(t)\tilde{E}_Y^*(t+\tau)| = 0$ for all rotational orientations of the X-Y coordinate axes and for all delays τ.
As demonstrated in the previous paragraphs, $\tilde{E}_X(t)$ and $\tilde{E}_Y(t)$ can be handled as complex Guassian random processes and since they are uncorrelated for all relative time delays τ they are statistically independent. The instanteneous intensity of the unpolarized wave field is then defined by:

$$\begin{aligned} I(t) &= |\tilde{E}_X(t)|^2 + |\tilde{E}_Y(t)|^2 \\ &= |\tilde{E}_{X0}(t)|^2 + |\tilde{E}_{Y0}(t)|^2 \\ &= I_X(t) + I_Y(t) \end{aligned} \tag{8.82}$$

From the definition of unpolarized light $I_X(t)$ and $I_X(t)$ have equal means $\bar{I}_X = \bar{I}_Y = \frac{1}{2}\bar{I}$ and are independent statistical processes.
The probability density function of the total instanteneous intensity $I(t)$ follows from the density function of the sum of $\mathbf{p}\,(I_X)$ and $\mathbf{p}\,(I_Y)$:

$$\mathbf{p}\,(I_X) = 2(\bar{I})^{-1} \cdot e^{-2I_X/\bar{I}} \tag{8.83}$$

$$\mathbf{p}\,(I_Y) = 2(\bar{I})^{-1} \cdot e^{-2I_Y/\bar{I}} \tag{8.84}$$

The probability density function of this sum is the convolution of $\mathbf{p}\,(I_X)$ and $\mathbf{p}\,(I_Y)$:

$$\mathbf{p}\,(I) = \mathbf{p}\,(I_X) * \mathbf{p}\,(I_Y) \tag{8.85}$$

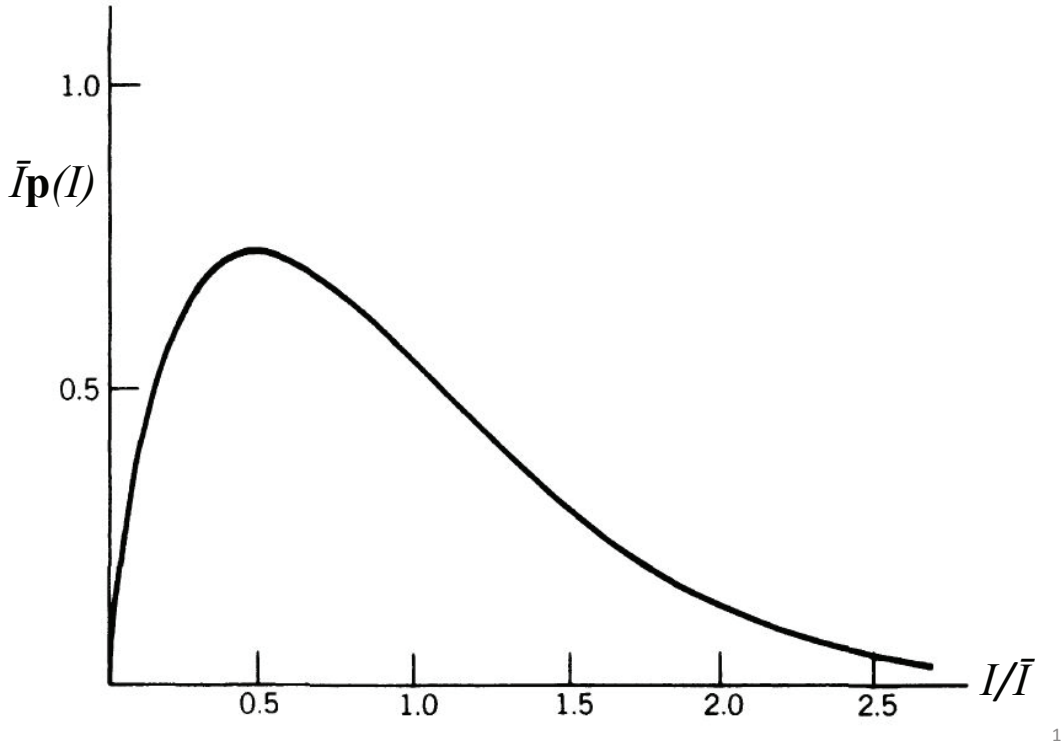

Figure 8.10: *Probability density function of the instantaneous intensity of an unpolarized thermal wave field. Credit Goodman (2000).*

Hence:

$$\mathbf{p}\,(I) \;=\; 4(\bar{I})^{-2}\int_0^I e^{-2I'/\bar{I}}e^{-2(I-I')/\bar{I}}dI' \;=\; 4(\bar{I})^{-2}Ie^{-2I/\bar{I}} \tag{8.86}$$

This density function is plotted in figure 8.10.
From this distribution it is clear that unpolarized thermal light has considerably less probability of having very small values of the instantaneous intensity than polarized thermal light. Moreover, the ratio of standard deviation σ to mean value $\bar{I}$ has reduced from unity in the case of a polarized thermal wave to $\sqrt{1/2}$ for an unpolarized thermal wave field.
In practice a radiation beam is generally neither completely polarised nor completely unpolarised, both cases are extremes. More often the electric vector $\vec{E}(t)$ varies in a way that is neither totally regular nor totally irregular, the radiation should be regarded as partially polarised. An useful way to describe this behaviour is to envision it as the result of the superposition of specific amounts of natural and polarised light. If a quantitative assessment of the degree of polarisation is required, a measurement of all four Stokes parameters is required. In radio astronomy this is often done due to the intrinsic sensitivity of the receiver front-end for a particular direction of polarisation.

8.7 Stochastic description of a radiation field in the quantum limit

8.7.1 The unfiltered Poisson process

In the quantum limit no coherence effects occur and the radiation field fluctuations can be described by photon statistics only. Consider an incident radiation beam (wide-sense stationary, ergodic) with an average flux of λ photons (or particles or neutrinos) per second. The generation of photons at random times t_i can be described by a staircase function, with discontinuities at time locations t_i (see figure 8.11):

$$\begin{aligned} Z(t) &= \sum_i U(t-t_i),\ U(t) = \text{unit-step function} \\ U(t) &= \begin{cases} 1 & \text{for } t \geq 0 \\ 0 & \text{for } t < 0 \end{cases} \end{aligned} \tag{8.87}$$

The photon *flow rate* [number of photons per second] follows from time differentiation of the

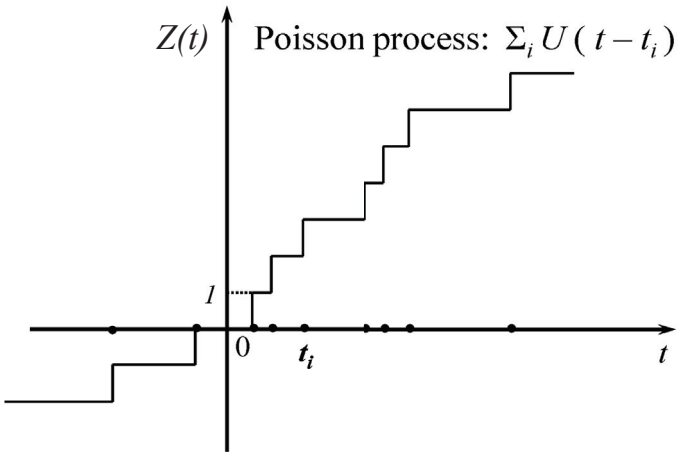

Figure 8.11: *Staircase function describing a Poisson process.*

stochastic variable $Z(t)$:

$$X(t) = \frac{dZ(t)}{dt} = \sum_i \delta(t-t_i) \tag{8.88}$$

and represents a train of Dirac impulses at random time locations t_i.
At a constant photon rate, $X(t)$ is a wide sense stationary (WSS) stochastic signal with a *time independent* average $\overline{X(t)} = \lambda$ photons per second, λ is the *rate parameter* characteristic for the process under consideration.
We can now express the stochastic process $Z(t)$, displayed in figure (8.11), in the following way:

$$Z(t) = \int_0^t X(t')dt' = \int_0^t \sum_i \delta(t'-t_i)dt' = k(0,t) \tag{8.89}$$

in which $k(t_1, t_2)$ represents the *number* of photons in a time period (t_1, t_2) of length $t = t_2 - t_1$. This number $k(t_1, t_2)$ is a Poisson distributed random variable (RV) with parameter λt, i.e. $Z(t)$ expresses an unfiltered Poisson process:

$$\mathbf{p}\{k, \lambda t\} = \frac{(\lambda t)^k}{k!} e^{-\lambda t}, \quad \text{with } \lambda \text{ the rate parameter (see above)} \tag{8.90}$$

Note: For Poisson distributed RVs hold that if two time periods (t_1, t_2) and (t_3, t_4) are considered that are non-overlapping, then the RVs $k(t_1, t_2)$ and $k(t_3, t_4)$ are independent.
From expression (8.90) we can construct a Poissonian probability density function featuring a continuous random variable (κ):

$$\mathbf{p}(\kappa, \lambda t) = \sum_{k=0}^{\infty} \mathbf{p}(k, \lambda t)\delta(\kappa - k) \tag{8.91}$$

The average value of κ and of κ^2 for assessment of the fluctuation magnitude follow from:

$$\mathbf{E}\{\kappa\} = \int_{-\infty}^{+\infty} \kappa \; \mathbf{p}(\kappa, \lambda t) d\kappa = \lambda t \tag{8.92}$$

$$\mathbf{E}\{\kappa^2\} = \int_{-\infty}^{+\infty} \kappa^2 \; \mathbf{p}(\kappa, \lambda t) d\kappa = (\lambda t)^2 + \lambda t \tag{8.93}$$

The average value for $\kappa = \lambda t$ in equation (8.92) is of course as expected; the first term of equation (8.93) is the square of the average and its second term represents the variance. Since the variance of the fluctuations associated with the flow of the photons equals λt, the standard deviation becomes $\sqrt{\lambda t}$, i.e. the 'strength' of the noise in the photon flow. The relative fluctuation or signal to noise ratio (SNR) is then:

$$SNR = \frac{\lambda t}{\sqrt{\lambda t}} = \sqrt{\lambda t} \tag{8.94}$$

Consequently, the larger λt, the smaller the relative shot noise in the photon flow. With very small λ we apparently need a long filter time to suppress this shot noise.
To determine the autocorrelation function $R_Z(t_1, t_2)$ of the Poisson process $Z(t)$ let us first consider $t_2 \geq t_1$. The variables $k(0, t_1)$ and $k(t_1, t_2)$, referring to adjacent but non-overlapping time periods, are then independent Poisson variables with parameters λt_1 and $\lambda(t_2 - t_1)$ respectively. Thus we have:

$$\mathbf{E}\{k(0, t_1)k(t_1, t_2)\} = \mathbf{E}\{k(0, t_1)\}\mathbf{E}\{k(t_1, t_2)\} = \lambda^2 t_1(t_2 - t_1), \text{ also } \Rightarrow \tag{8.95}$$

$$k(t_1, t_2) = k(0, t_2) - k(0, t_1) = Z(t_2) - Z(t_1), \Rightarrow \text{ in (8.95)} \Rightarrow$$

$$\mathbf{E}\left\{Z(t_1)\left[Z(t_2) - Z(t_1)\right]\right\} = R_Z(t_1, t_2) - \mathbf{E}\{Z^2(t_1)\} \Rightarrow$$

$$R_Z(t_1, t_2) = \lambda^2 t_1(t_2 - t_1) + \lambda^2 t_1^2 + \lambda t_1 = \lambda^2 t_1 t_2 + \lambda t_1 \tag{8.96}$$

$$\text{If } t_2 < t_1 \Rightarrow R_Z(t_1, t_2) = \lambda^2 t_1 t_2 + \lambda t_2 \tag{8.97}$$

Introducing the autocovariance $C_Z(t_1, t_2)$ of $Z(t)$ we can write:

$$R_Z(t_1, t_2) = \lambda^2 t_1 t_2 + C_Z(t_1, t_2) = \lambda^2 t_1 t_2 + \lambda t_1 U(t_2 - t_1) + \lambda t_2 U(t_1 - t_2) \tag{8.98}$$

Regarding the stochastic variable $X(t)$, the time derivative of $Z(t)$ and representing the train of Dirac impulses at random time locations, we have the time independent average value

$\mathbf{E}\{X(t)\} = \lambda =$ the rate parameter.
The autocorrelation function follows from successive partial differentiation of the autocorrelation of $Z(t)$ with respect to t_1 and t_2, thus:

$$R_X(t_1, t_2) = \frac{\partial^2 R_Z(t_1, t_2)}{\partial t_1 \partial t_2} = \lambda + \delta(t_2 - t_1) \tag{8.99}$$

Designating the time difference $(t_2 - t_1) = \tau$, we arrive at the general expression for the autocorrelation of a train of unit-value Dirac impulses at random time positions (WSS ergodic signal):

$$R_X(\tau) = \lambda^2 + \lambda\delta(\tau) \tag{8.100}$$

The second term in equation (11.52) represents the covariance $C(\tau)$ of $X(t)$, which equals in this case the variance $C(0)$ since it is zero for every value of τ except for $\tau = 0$. This is of course evident, since the Dirac impulses are randomly distributed in time and are thus mutually completely uncorrelated.

Chapter 9

Astronomical measuring process: information transfer

9.1 Integral response function for astronomical measurements

In observational astrophysics, the system response to an incoming radiation field can be characterised by a filtering process, arising from the individual elements making up the telescope configuration, of a stochastic process described by the monochromatic intensity $I(\nu, \vec{\Omega}, t)$. Generally, the time dependent output of the telescope is described by

$$X(t) = S(t) + N(t) \tag{9.1}$$

in which $S(t)$ represents the outcome of the filtering of the signal source and $N(t)$ represents the sum of all (filtered) noise components like background radiation, disturbances arising from the operational environment and intrinsic noise in the detection system, like dark current. The measuring process of the source signal $S(t)$ can be symbolically written as a series of consecutive convolutions, defined by the angular and the spectral response functions of the observational instrument:

$$S(t) = \int_{\Delta\nu} \left[R(\nu) * \int_{\Delta\vec{\Omega}_{FOV}} \left[I(\vec{\Omega}, \nu, t) * P(\vec{\Omega}, \nu) \right] d\vec{\Omega} \right] d\nu \tag{9.2}$$

$P(\vec{\Omega}, \nu)$ represents the collecting power of the telescope. which depends in general on the frequency (or wavelength, or energy). It is a function of the telescope off-axis angle in the field of view $\vec{\Omega}_{FOV}$ and contains the point spread function $H(\vec{\Omega}, \nu)$, which quantitatively describes the angular resolution (field position dependent). $\Delta\vec{\Omega}_{FOV}$ gives the solid angle over which the convolution $I(\vec{\Omega}, \nu, t) * P(\vec{\Omega}, \nu)$ is to be integrated. The choice of $\Delta\vec{\Omega}_{FOV}$ entirely depends on the number of image elements in the field of view, which may be as large as 10^8 in modern systems, and on the objective of the particular observation (e.g. ultimate angular resolution or high quality spectrum over a relatively large part of the field of view). Accordingly the integral can be done over the whole field of view $\vec{\Omega}_{FOV}$, which may cover a large part of the sky in the case of wide-field cameras, or it may be done over just one image pixel.

The integration of the signal after the second convolution with $R(\nu)$ covers the spectral range of interest $\Delta\nu$, which is part of the total bandwidth ν. Again, this may vary from a very narrow range (e.g. measuring the line profile of a single spectral line) to a very broad range (in case of photometry). The number of frequency elements can therefore range from 1 (e.g. in the case of a bolometric detector) to approximately 10^6 in a high-resolution spectrograph.

It is important to remember continually that the term *frequency* covers here three types of Fourier pairs.

- The pair $I(\vec{\Omega}) \Leftrightarrow I(\vec{\zeta})$ refers to spatial resolution, the frequency $\vec{\zeta}$ in the Fourier domain has to be interpreted as *spatial frequency*. This refers to structures in the image contrast.
- The pair $I(\nu) \Leftrightarrow I(s)$ refers to spectral resolution, in this case s is a Fourier frequency which relates to a *spectral frequency*. A spectrum containing a large number of sharp features, like narrow emission and absorption lines, possesses much power in high spectral frequencies; a featureless continuum contains only low spectral frequencies.
- The pair $I(t) \Leftrightarrow I(f)$ refers to time resolution, the frequency f relates to *temporal frequency*.

Every measurement or observation implies bandwidth limitations on each of these frequencies.

The normalised value of the Fourier transform of a particular instrument response function, e.g. $R(s)$ or $H(\vec{\zeta})$, is called the *Modulation Transfer Function* (MTF) and describes the frequency dependent filtering of the source signal in the Fourier domain. The MTF refers either to the amplitude/phase transfer function of the signal or to the power transfer function, in practice this will be explicitly clear from the specific context in which the MTF is employed.

9.2 Time filtering

9.2.1 Finite exposure and time resolution

In practice, the measurement or registration of a stochastic process always takes place over a finite period T and with a certain resolution ΔT, i.e. the minimum time bin for a data point. The limitation in measuring time T corresponds to a *multiplication in the time domain* of a stochastic variable $X(t)$ with a window (block) function $\Pi(t/T)$. This function is described as follows,

$$\Pi\left(\frac{t}{T}\right) \equiv 1 \qquad \text{for} \qquad |t| \leq \frac{1}{2}T \tag{9.3}$$

$$\Pi\left(\frac{t}{T}\right) \equiv 0 \qquad \text{for} \qquad |t| > \frac{1}{2}T \tag{9.4}$$

$$\tag{9.5}$$

Consequently a new, time filtered, stochastic variable $Y(t)$ is introduced:

$$Y(t) = \Pi\left(\frac{t}{T}\right) X(t) \tag{9.6}$$

The limitation in time resolution always arises in practice due to the frequency-limited transmission characteristic of any physical measuring device.

Suppose, as an example, the measurement is taken at time t within the measuring period T with a temporal resolution ΔT. This corresponds to an integration of the stochastic variable $Y(t)$ between $t - \Delta T/2$ and $t + \Delta T/2$, divided by ΔT (a so called running average). It follows that

$$Z(t) \equiv Y_{\Delta T}(t) = \frac{1}{\Delta T} \int_{t-\Delta T/2}^{t+\Delta T/2} Y(t')dt' = \frac{1}{\Delta T} \int_{-\infty}^{+\infty} \Pi\left(\frac{t-t'}{\Delta T}\right) Y(t')dt' \tag{9.7}$$

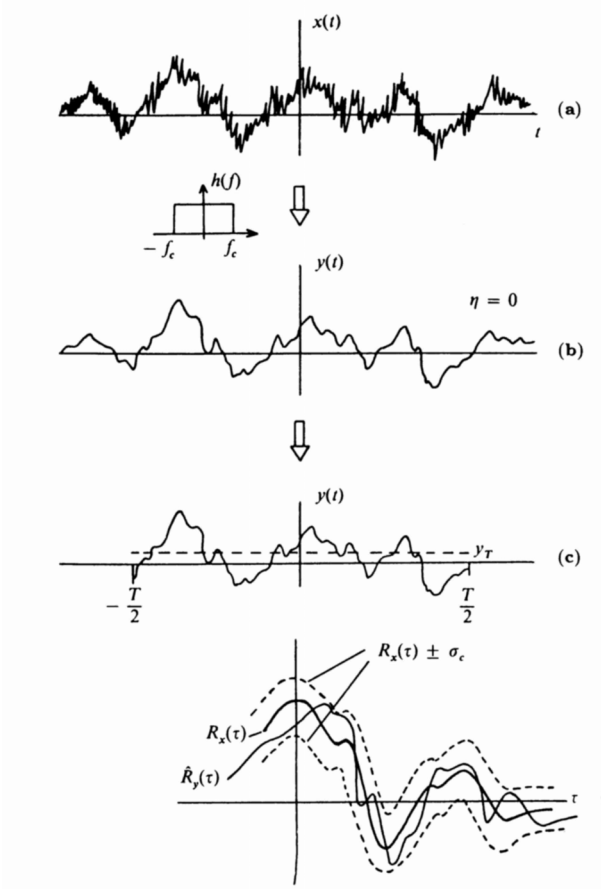

Figure 9.1: *Illustration of the errors in average and power spectrum of a stochastic process $x(t)$. a) a realization of the process b) filtered with a low-pass filter (high frequencies are removed): $y(t)$ c) measurement during finite time interval T, and the average during this interval (dashed line, value y_T) d) the autocorrelation functions of the process $R_x(\tau)$ and of the measurment $R_y(\tau)$. Credit Lena et al. (1988).*

This equation can also be expressed in terms of a convolution in the time domain:

$$Z(t) = \frac{1}{\Delta T}\Pi\left(\frac{t}{\Delta T}\right) * Y(t) = \frac{1}{\Delta T}\Pi\left(\frac{t}{\Delta T}\right) * \Pi\left(\frac{t}{T}\right) X(t) \tag{9.8}$$

which represents a low-frequency (or 'low-pass') filtering of the stochastic variable $Y(t)$. The values μ_T and $R_T(\tau)$ for an ergodic process obtained from a finite measuring period T will therefore slightly differ from the true values μ and $R(\tau)$. The error introduced by measuring the sample average μ_T rather than the true average μ is the subject of the next paragraph.

9.2.2 Error assessment in sample average μ_T

We wish to determine the accuracy with which the approximate value μ_T approaches the real value μ. An illustration of this is given in Figure 9.1. To do so we start by noting that determining the average corresponds to convolution in the time domain with a block function. We denote this

$$X(t) \rightarrow \boxed{\tfrac{1}{T}\Pi\left(\tfrac{t}{T}\right)} \rightarrow X_T \tag{9.9}$$

In terms of the Fourier transforms, the averaging corresponds to a multiplication with a sinc-function. In general, we write the effect of the measuring apparatus on the signal in the Fourier domain as $Y(f) = X(f)H(f)$ and hence $Y^*(f) = X^*(f)H^*(f)$, and with $H(f)$ the *transfer function*. We can thus also write $|Y(f)|^2 = |X(f)|^2|H(f)|^2$.

Note: in the literature the term transfer function is used both for $H(f)$, i.e. the signal transfer function, but also for $|H(f)|^2$, i.e. the power transfer function. So be prepared for the correct interpretation whenever you encounter the term transfer function in the literature!

With this we take the Fourier transform of the autocorrelation, to find:

$$S_{X_T}(f) = |H(f)|^2 S_{X(t)}(f) = \mathrm{sinc}^2(Tf) \cdot S_{X(t)}(f) \tag{9.10}$$

Transforming back to the time domain, we write this as

$$R_{X_T}(\tau) = h(\tau) * h(\tau) * R_{X(t)} \tag{9.11}$$

and note that $h \equiv (1/T)\Pi(t/T)$ is a real function. We note that the convolution of a block with itself is a triangle, and introduce the notation:

$$h(\tau) * h(\tau) \equiv \rho(\tau) \equiv \frac{1}{T}\Lambda\left(\frac{\tau}{T}\right)$$

to rewrite 9.11 as

$$R_{X_T}(\tau) = \frac{1}{T}\Lambda\left(\frac{\tau}{T}\right) * R_{X(t)} \equiv \frac{1}{T}\int_{-\infty}^{+\infty} \Lambda\left(\frac{\tau'}{T}\right) R_{X(t)}(\tau - \tau')d\tau' \tag{9.12}$$

For convenience we consider the case where $\mu = 0$, i.e. $R = C$, and find

$$C_{X_T}(\tau) = \frac{1}{T}\int_{-\infty}^{+\infty} \Lambda\left(\frac{\tau'}{T}\right) C_{X(t)}(\tau - \tau')d\tau' \tag{9.13}$$

To compute the variance we set $\tau = 0$ and find

$$C_{X_T}(0) \equiv [\sigma_{X_T}]^2 = \frac{1}{T}\int_{-\infty}^{+\infty} \Lambda\left(\frac{\tau'}{T}\right) C_{X(t)}(-\tau')d\tau' = \frac{1}{T}\int_{-\infty}^{+\infty} \Lambda\left(\frac{\tau'}{T}\right) C_{X(t)}(\tau')d\tau' \tag{9.14}$$

where we have used the fact that C is even. Explicitly writing Λ we finally obtain

$$[\sigma_{X_T}]^2 = \frac{1}{T}\int_{-T}^{+T} \left(1 - \frac{|\tau'|}{T}\right) C_{X(t)}(\tau')d\tau' \tag{9.15}$$

Two things are to be noted in this equation. First: the integral ranges from $-T$ to $+T$, i.e. over a range with length $2T$, but nonetheless the normalization factor is $1/T$. Second, the autocovariance is *always* limited in the frequency domain. As an example we consider a specific form for the transfer function, viz.:

$$H(f) = \frac{1}{1 + 2\pi i f \tau_o} \tag{9.16}$$

At small frequencies $f \ll 1/(2\pi\tau_o) \equiv f_o$ the transfer is complete, i.e. $|H(f)| = 1$, and at high frequencies $f \gg f_o$ the transfer is inversely proportional to the temporal frequency, i.e. $|H(f)| = f_o/f$. The frequency f_o is the 'cut-off' frequency of the transfer function $H(f)$. We will forego the full mathematics here, and merely conclude that the autocovariance with such a system drops exponentially with (the absolute value of) the time difference τ:

$$C_{X(t)}(\tau) = C_{X(t)}(0)e^{-|\tau|/\tau_o} \qquad \text{where} \qquad \tau_o \equiv \frac{1}{2\pi f_o} \tag{9.17}$$

This means that at times $\tau \gg \tau_o$ the correlation is virtually zero. By entering 9.17 into 9.15 and performing the integration, we get

$$[\sigma_{X_T}]^2 = 2\left[\sigma_{X(t)}\right]^2 \frac{\tau_o}{T}\left[1 - \frac{\tau_o}{T}\left(1 - e^{-T/\tau_o}\right)\right] \tag{9.18}$$

To get a feeling for the meaning of this equation we consider two limiting cases. First the one in which the duration of the measurement largely exceeds the correlation time, $T \gg \tau_o$. Eq. 9.18 then becomes

$$[\sigma_{X_T}]^2 = 2\left[\sigma_{X(t)}\right]^2 \frac{\tau_o}{T} = \frac{\left[\sigma_{X(t)}\right]^2}{\pi f_o T} \tag{9.19}$$

and we see that the variance of the measured signal is proportional to the variance of the incoming signal, and approximates zero when the duration of the measurement goes to infinity, and also when the number of frequencies over which one measures goes to infinity. The measured signal is then said to be *ergodic in the mean*. The last limit can be understood by noting that $f_o T$ is the number of cycles during T with a frequency f_o, i.e. it gives the number of measurements; 9.19 thus is analogous to the equation which gives the variance of the average $\sigma_\mu^2 = \sigma^2/N$.

The other limit we consider is the one for which the duration of the measurement equals the correlation time, $T = \tau_o$. Eq. 9.18 in this limit becomes

$$\sigma_{X_T}{}^2 = 2\sigma_{X(t)}{}^2 e^{-1} \simeq \sigma_{X(t)}{}^2 \tag{9.20}$$

This is also understandable in terms of determining the average, in the case where just one measurement is taken: $N = 1$.

The moral we can draw from this example is that one must take good care that the duration of the measurement is much longer than the correlation time, $T \gg \tau_o$, if one wishes to avoid *large* errors in the estimates of the average and of the variance. Another moral is that we must take into account the errors in the average and in the variance whenever we are looking for really *small* effects.

9.3 Data sampling in a bandlimited measuring system: Critical or Nyquist frequency

Let us consider the general case of a signal $S(x)$ which has been subject to the instrument response $R(x)$, so that the resulting measurement $M(x)$ follows from

$$M(x) = S(x) * R(x) \tag{9.21}$$

Because of the finite frequency response of the instrument, $M(x)$ is always limited in bandwidth, i.e. the Fourier transform $M(s) \Leftrightarrow M(x)$ is a bandwidth-limited function. This function is characterised by a maximum cut-off frequency s_{max}, also called the critical or Nyquist frequency (s_c). In the case of a gaussian response the frequencies will never be distributed purely gaussian, since no physical system can transmit the tail frequencies up to ∞. Shannon (and Nyquist) established a theorem for optimum sampling of band limited observations. This theorem states that no information is lost if sampling occurs at intervals $\tau = 1/(2s_c)$.

Let $M(x)$ subsequently be sampled at regular intervals, $M(x) \rightarrow M(n\tau)$ with n an integer and τ the sampling interval. To describe the sampling process quantitatively we introduce

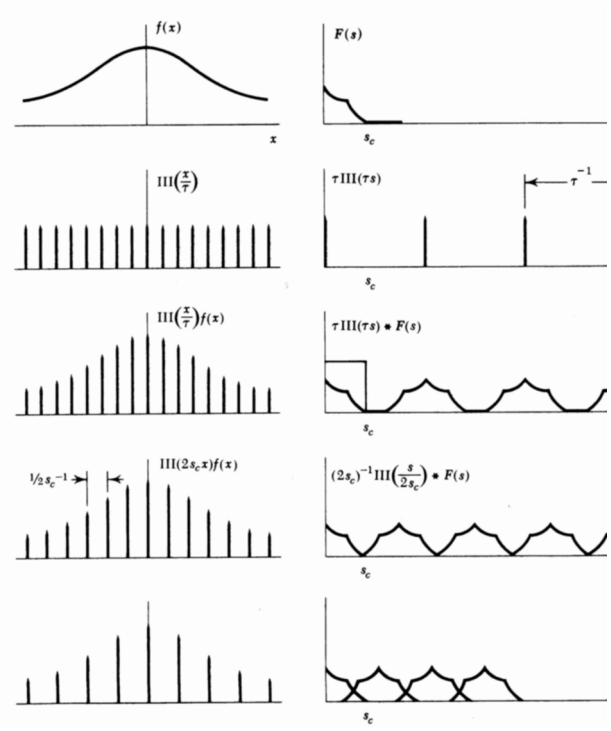

Figure 9.2: *Illustration of sampling optimally, compared with undersampling and oversampling. Left in the time domain, right in the Fourier domain. Credit Bracewell (1986).*

the *shah* function, also called the comb of Dirac, which constitutes a series of δ functions at regular distances equal to 1:

$$\perp\!\!\!\perp\!\!\!\perp(x) \equiv \sum_{n=-\infty}^{\infty} \delta(x-n) \tag{9.22}$$

This shah function can be extended to arbitrary distances by noting $a\perp\!\!\!\perp\!\!\!\perp(ax) = \sum_n \delta(x - n/a)$.

The sampled signal $M_s(x)$ can now be expressed as

$$M_s(x) = \sum_n M(n\tau)\delta(x-n\tau) = \frac{1}{\tau}\perp\!\!\!\perp\!\!\!\perp\left(\frac{x}{\tau}\right) M(x) \tag{9.23}$$

The Fourier transform $M_s(s) \Leftrightarrow M_s(x)$ equals

$$M_s(s) = \perp\!\!\!\perp\!\!\!\perp(\tau s) * M(s) = \frac{1}{\tau}\sum_n M\left(s - \frac{n}{\tau}\right) \tag{9.24}$$

This expression shows that, except for a proportionality factor $1/\tau$, $M_s(s)$ represents a series of replications of $M(s)$ at intervals $1/\tau$. Because $M(s)$ is a bandwidth-limited function with a cut-off frequency of say $s = s_c$, we can recover fully the single (i.e. not repeated) function $M(s)$ from this series by multiplication with τ and by filtering with the gate function $\Pi(s/2s_c)$:

$$\Pi\left(\frac{s}{2s_c}\right)\tau\perp\!\!\!\perp\!\!\!\perp(\tau s) * M(s) \Leftrightarrow 2s_c\mathrm{sinc}2s_c x * \perp\!\!\!\perp\!\!\!\perp\left(\frac{x}{\tau}\right) M(x) \tag{9.25}$$

$M(x)$ can be reconstructed exactly if the series of $M(s)$ functions in the frequency domain touch without overlap. This is the case if we sample at $\tau = 1/(2s_c)$, which therefore is the optimum sample interval. Performing the convolution we fully reconstruct $M(x)$, i.e.:

$$M(x) = \int_{-\infty}^{+\infty} \mathrm{sinc}\left(\frac{x-x'}{\tau}\right)\sum_n M(n\tau)\delta(x'-n\tau)dx' = \sum_n \mathrm{sinc}\left(\frac{x-n\tau}{\tau}\right) M(n\tau) \tag{9.26}$$

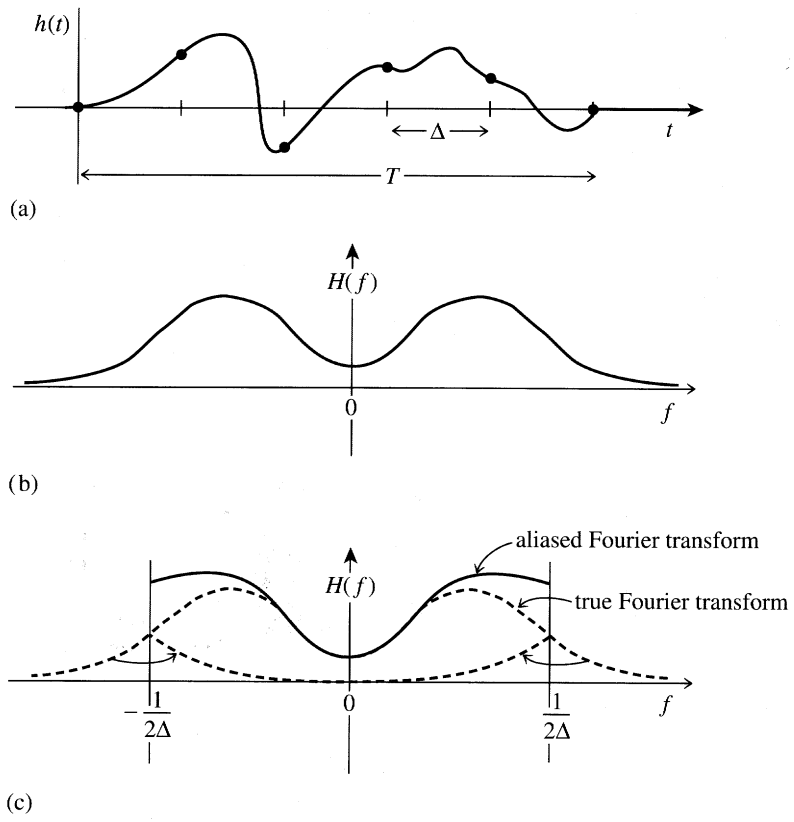

Figure 9.3: *The function $h(t)$ shown in the top panel is undersampled. This means that the sampling interval Δ is larger than $\frac{1}{2f_{max}}$. The lower panel shows that in this case the power in the frequencies above $\frac{1}{2\Delta}$ is 'mirrored' with respect to this frequency and produces an aliased transform which deviates from the true Fourier transform. Credit Press et al (1992).*

We can check this result easily at a sampling point $x = j\tau$, with $\mathrm{sinc}(j-n) = 1$ for $j = n$ and $= 0$ for $j \neq n$:

$$M(x) = M(j\tau) \tag{9.27}$$

Note: 9.25 shows that the calculation of intermediate points from samples does not of course depend on calculating Fourier transforms. The equivalent operation in the x-domain entails the convolution of $2s_c\mathrm{sinc}2s_c x$ directly with $\perp\!\!\!\perp\!\!\!\perp(x/\tau)M(x)$. Notice that the omission of the $1/\tau$ factor in 9.23 ensures the proper normalization in the s-domain!

Expression 9.26 shows that a superposition of a series of sinc-functions with weight factors $M(n\tau)$, i.e. the sample values, at intervals τ exactly reconstruct the continuous function $M(x)$. In fact the sinc-functions provide the proper interpolation between the consecutive sample points, this is the reason why the sinc-function is sometimes referred to as the *interpolation function.*

Thus, the use of a discrete Fourier transform causes no loss of information, provided that the sampling frequency $\frac{1}{\tau}$ is twice the highest frequency in the continuous input function (i.e. the source function convolved with the response function). The maximum frequency s_{max} that can be determined for a given sampling interval equals therefore $\frac{1}{2\tau}$. If the input signal is sampled too slowly, i.e. if the signal contains frequencies higher than $\frac{1}{2\tau}$, then these cannot be determined after the sampling process and the finer details will be lost (see Fig. 9.2).

More seriously however, the higher frequencies which are not resolved will beat with the measured frequencies and produce spurious components in the frequency domain below the Nyquist frequency. This effect is known as *aliasing* and may give rise to major problems and uncertainties in the determination of the source function, see figure 9.3 in the case of a time function.

Chapter 10

Indirect Imaging and Spectroscopy

10.1 Coherence

10.1.1 The Visibility function

The coherence phenomenon is directly coupled to correlation, and the degree of coherence of an EM-wave field $\tilde{E}(\vec{r},t)$ can be quantitativily described by employing the auto- and cross-correlation technique for the analysis of a stochastic process.
The electric vector of the wave field at a position $\vec{r}$ at time t, $\tilde{E}(\vec{r},t)$, is a complex quantity, denoting the amplitude and phase of the field. To assess the coherence phenomenon, the question to be answered is: how do the nature of the source and the geometrical configuration of the situation relate to the resulting phase correlation between two laterally spaced points in the wave field?
This brings to mind Young's interference experiment in which a primary monochromatic source S illuminates two pinholes in an opaque screen, see figure 10.1. The pinholes S_1 and S_2 act as secondary sources, generating a fringe pattern on a distant observation plane Σ_O. If S is an idealized monochromatic point source, the wavelets issuing from any set of apertures S_1 and S_2 will maintain a constant relative phase; they are precisely correlated and therefore mutually fully coherent. On the observation plane Σ_O a well-defined array of stable fringes will result and the radiation field is spatially coherent. At the other extreme, if the pinholes S_1 and S_2 are illuminated by separate thermal sources (even with narrow frequency bandwidths), no correlation exists; no fringes will be observable in the observation plane Σ_O and the fields at S_1 and S_2 are said to be incoherent. The generation of interference fringes is seemingly a convenient measure of the degree of coherence of a radiation field. The quality of the fringes produced by an interferometric system can be described quantitativily using the *Visibility function* V:

$$V = \frac{I_{max} - I_{min}}{I_{max} + I_{min}} \tag{10.1}$$

here I_{max} and I_{min} are the irradiances corresponding to the maximum and adjacent minimum in the fringe system.

10.1.2 Young's dual beam interference experiment

To assess the mutual coherence between two positions in a radiation field in a quantitative fashion, consider the situation displayed in figure 10.1, with an extended narrow bandwidth radiation source S, which generates fields $\tilde{E}(\vec{r}_1,t) \equiv \tilde{E}_1(t)$ at S_1 and $\tilde{E}(\vec{r}_2,t) \equiv \tilde{E}_2(t)$ at S_2,

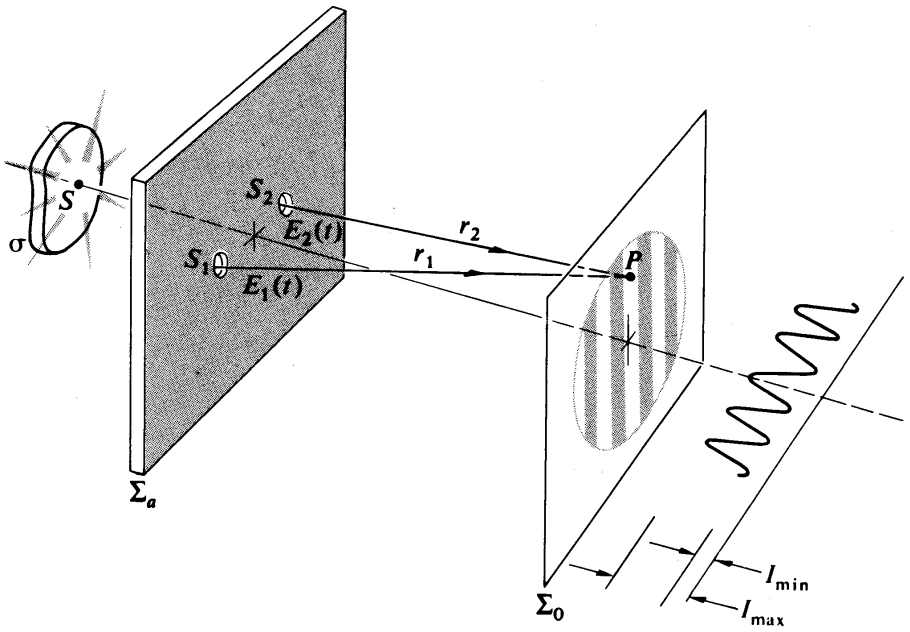

Figure 10.1: *Young's experiment using a quasi-monochromatic source S illuminating two pinholes S_1 and S_2. Credit Hecht (1987).*

respectively. *Interalia: no polarization effects are considered, and therefore a scalar treatment using $\tilde{E}(\vec{r},t)$ will suffice.*

If these two positions in the radiation field are isolated using an opaque screen with two small apertures, we are back to Young's experimental set-up. The two apertures serve as sources of secondary wavelets, which propagate out to some point P on the observation plane Σ_O. The resultant field at P is:

$$\tilde{E}_P(t) \;=\; \tilde{C}_1\tilde{E}_1(t-t_1) + \tilde{C}_2\tilde{E}_2(t-t_2) \tag{10.2}$$

with $t_1 = r_1/c$ and $t_2 = r_2/c$, r_1 and r_2 representing the pathlengths to P as measured from S_1 and S_2, respectively. This expression tells us that the field at the space-time point (P,t) can be determined from the field that existed at S_1 and S_2 at $(t-t_1)$ and $(t-t_2)$, respectively, these being the the instants when the light, which is now overlapping at P, first emerged from the apertures. The quantities $\tilde{C}_1$ and $\tilde{C}_2$ are so-called *propagators*, they mathematically reflect the alterations in the field resulting from it having transversed either of the apertures. For example, the secondary wavelets issuing from the pinholes in the Young set-up are out of phase by $\pi/2$ radians with the primary wave incident on the aperture screen. In that case, $\tilde{C}_1$ and $\tilde{C}_2$ are purely imaginary numbers equal to $e^{i\pi/2}$.

10.1.3 The mutual coherence function

The resultant irradiance at P, averaged over some time interval which is long compared to the coherence time, is:

$$I \;=\; \mathbf{E}\left\{\tilde{E}_P(t)\tilde{E}_P^*(t)\right\} \tag{10.3}$$

Employing equation (10.2) this can be written as:

$$\begin{aligned} I &= \tilde{C}_1\tilde{C}_1^*\mathbf{E}\left\{\tilde{E}_1(t-t_1)\tilde{E}_1^*(t-t_1)\right\} \\ &+ \tilde{C}_2\tilde{C}_2^*\mathbf{E}\left\{\tilde{E}_2(t-t_2)\tilde{E}_2^*(t-t_2)\right\} \\ &+ \tilde{C}_1\tilde{C}_2^*\mathbf{E}\left\{\tilde{E}_1(t-t_1)\tilde{E}_2^*(t-t_2)\right\} \\ &+ \tilde{C}_1^*\tilde{C}_2\mathbf{E}\left\{\tilde{E}_1^*(t-t_1)\tilde{E}_2(t-t_2)\right\} \end{aligned} \tag{10.4}$$

It is now assumed that the wave field is *stationary*, as is almost universally the case, i.e. the statistical nature of the wave field does not alter with time and the time average is independent of whatever time origin we select (the Wide Sense Stationary situation as described in Chapter 1). Accordingly, the first two expectation values in equation (10.4) can be rewritten as:

$$I_{S_1} = \mathbf{E}\left\{\tilde{E}_1(t)\tilde{E}_1^*(t)\right\} \text{ and } I_{S_2} = \mathbf{E}\left\{\tilde{E}_2(t)\tilde{E}_2^*(t)\right\} \tag{10.5}$$

where the time origin was displaced by amounts t_1 and t_2, respectively. The subscripts for the irradiances used here underscore the fact that they refer to the values at points S_1 and S_2. Furthermore, if we introduce the time difference $\tau = t_2 - t_1$, the time origin of the last two terms can be shifted by an amount t_2 yielding:

$$\tilde{C}_1\tilde{C}_2^*\mathbf{E}\left\{\tilde{E}_1(t+\tau)\tilde{E}_2^*(t)\right\} + \tilde{C}_1^*\tilde{C}_2\mathbf{E}\left\{\tilde{E}_1^*(t+\tau)\tilde{E}_2(t)\right\} \tag{10.6}$$

This expression comprises a complex quantity plus its own complex conjugate and is therefore equal to twice its *Real* part:

$$2\ Re\left[\tilde{C}_1\tilde{C}_2^*\mathbf{E}\left\{\tilde{E}_1(t+\tau)\tilde{E}_2^*(t)\right\}\right] \tag{10.7}$$

As noted before, the $\tilde{C}$-coefficients are purely imaginary, i.e. $\tilde{C}_1\tilde{C}_2^* = \tilde{C}_1^*\tilde{C}_2 = |\tilde{C}_1||\tilde{C}_2|$. The expectation value contained in expression (10.7) is a cross-correlation function, which is denoted by:

$$\tilde{\Gamma}_{12}(\tau) = \mathbf{E}\left\{\tilde{E}_1(t+\tau)\tilde{E}_2^*(t)\right\} \tag{10.8}$$

This equation is referred to as the **mutual coherence function** of the wave field at positions S_1 and S_2. Making use of the definitions above, equation (10.4) now takes the form:

$$I = |\tilde{C}_1|^2 I_{S_1} + |\tilde{C}_2|^2 I_{S_2} + 2|\tilde{C}_1||\tilde{C}_2|\ Re\,\tilde{\Gamma}_{12}(\tau) \tag{10.9}$$

The terms $|\tilde{C}_1|^2 I_{S_1}$ and $|\tilde{C}_2|^2 I_{S_2}$ are the irradiance at P, arising when one or the other of the apertures is open alone: either $\tilde{C}_1 = 0$ or $\tilde{C}_2 = 0$. Denoting these irradiances as I_1 and I_2 we have:

$$I = I_1 + I_2 + 2|\tilde{C}_1||\tilde{C}_2|\ Re\,\tilde{\Gamma}_{12}(\tau) \tag{10.10}$$

If S_1 and S_2 are made to coincide, the mutual coherence function becomes the autocorrelation function:

$$\tilde{\Gamma}_{11}(\tau) = \tilde{R}_1(\tau) = \mathbf{E}\left\{\tilde{E}_1(t+\tau)\tilde{E}_1^*(t)\right\} \tag{10.11}$$

or:

$$\tilde{\Gamma}_{22}(\tau) = \tilde{R}_2(\tau) = \mathbf{E}\left\{\tilde{E}_2(t+\tau)\tilde{E}_2^*(t)\right\} \tag{10.12}$$

One can imagine that two wavetrains emerge from these coalesced pinholes and somehow pick up a relative phase delay τ. In the situation at hand $\tau = 0$, since the optical path difference (*shorthand: OPD*) goes to zero. Hence:

$$\begin{aligned} I_{S_1} &= \mathbf{E}\left\{\tilde{E}_1(t)\tilde{E}_1^*(t)\right\} = \Gamma_{11}(0) = \mathbf{E}\left\{|\tilde{E}_1(t)|^2\right\} \text{ and} \\ I_{S_2} &= \mathbf{E}\left\{\tilde{E}_2(t)\tilde{E}_2^*(t)\right\} = \Gamma_{22}(0) = \mathbf{E}\left\{|\tilde{E}_2(t)|^2\right\} \end{aligned} \tag{10.13}$$

These autocorrelation functions are also called *self-coherence functions*. For $\tau = 0$ they represent the (average) irradiance (power) of the radiation field at positions S_1 and S_2 respectively.

10.1.4 Interference law for a partially coherent radiation field: the complex degree of coherence

From equation (10.10) and the selfcoherence functions we can now write:

$$|\tilde{C}_1||\tilde{C}_2| = \frac{\sqrt{I_1}\sqrt{I_2}}{\sqrt{\Gamma_{11}(0)}\sqrt{\Gamma_{22}(0)}} \tag{10.14}$$

Hence, the normalized expression for the mutual coherence function can now be defined as:

$$\tilde{\gamma}_{12}(\tau) \equiv \frac{\tilde{\Gamma}_{12}(\tau)}{\sqrt{\Gamma_{11}(0)\Gamma_{22}(0)}} = \frac{\mathbf{E}\left\{\tilde{E}_1(t+\tau)\tilde{E}_2^*(t)\right\}}{\sqrt{\mathbf{E}\left\{|\tilde{E}_1(t)|^2\right\}\mathbf{E}\left\{|\tilde{E}_2(t)|^2\right\}}} \tag{10.15}$$

This quantity is referred to as the **complex degree of coherence**, equation (10.10) can now be recast into its final form:

$$I = I_1 + I_2 + 2\sqrt{I_1 I_2}\; Re\; \tilde{\gamma}_{12}(\tau) \tag{10.16}$$

which is the *general interference law for a partially coherent radiation field.*
The quantity $\tilde{\gamma}_{12}(\tau)$ *simultaneously* gives a measure of the *spatial coherence* by comparison of two locations in space (S_1 and S_2 in the above case) and the *coherence in the time domain* by accounting for a time lag τ between both signals.
$\tilde{\gamma}_{12}(\tau)$ is a complex variable and can be written as:

$$\tilde{\gamma}_{12}(\tau) = |\tilde{\gamma}_{12}(\tau)|e^{i\psi_{12}(\tau)} \tag{10.17}$$

From equation (10.15) and the Schwarz inequality it is clear that $0 \leq |\tilde{\gamma}_{12}(\tau)| \leq 1$. The phase angle $\psi_{12}(\tau)$ of $\tilde{\gamma}_{12}(\tau)$ relates to the phase angle between the fields at S_1 and S_2 and the phase angle difference concomitant with the OPD in P resulting in the time lag τ, as shown in equation (10.8). For quasi-monochromatic radiation at a mean wavelength $\overline{\lambda}$ and frequency $\overline{\nu}$, the phase difference ϕ due to the OPD can be expressed as:

$$\phi = \frac{2\pi}{\overline{\lambda}}(r_2 - r_1) = 2\pi\overline{\nu}\tau \tag{10.18}$$

If we designate a phase angle $\alpha_{12}(\tau)$ between the fields at S_1 and S_2, we have
$\psi_{12}(\tau) = [\alpha_{12}(\tau) - \phi)]$.
Hence:

$$Re\; \tilde{\gamma}_{12}(\tau) = |\tilde{\gamma}_{12}(\tau)| \cos\left[\alpha_{12}(\tau) - \phi\right] \tag{10.19}$$

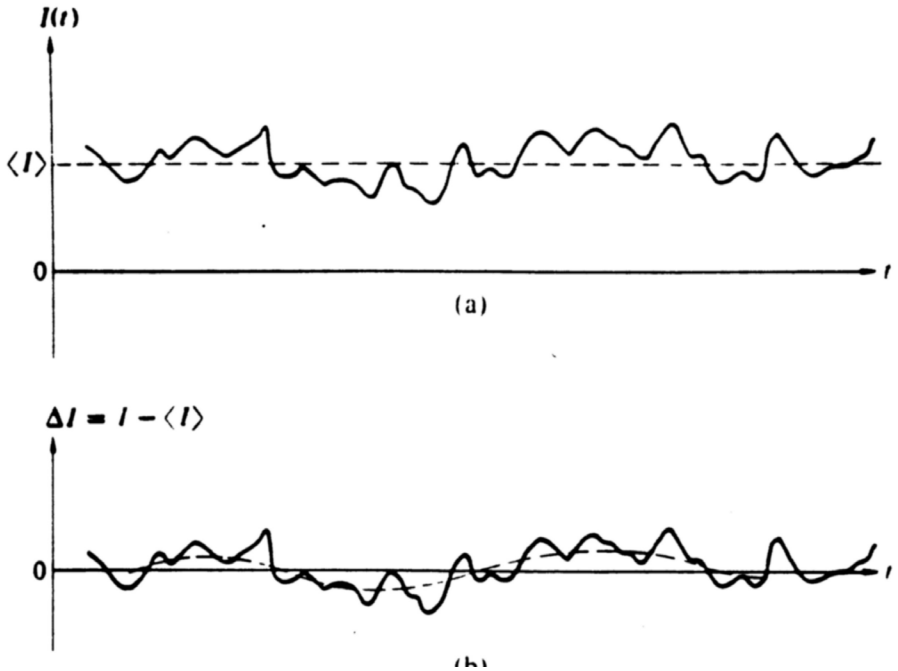

Figure 10.2: *Partially coherent intensity fluctuations in a thermal radiation source. Both absolute values* $\overline{I}$ *and relative values* $\triangle I = I - \overline{I}$ *are shown. Credit Hecht (1987).*

Substitution of this expression in the interference law for partially coherent radiation given in equation (10.16) yields for the intensity observed at point P on the observation plane Σ_O:

$$I \;=\; I_1 \;+\; I_2 \;+\; 2\sqrt{I_1 I_2}\;|\tilde{\gamma}_{12}(\tau)|\cos\left[\alpha_{12}(\tau) - \phi\right] \tag{10.20}$$

The maximum and minimum values of I occur if the cosine term in equation (10.20) equals $+1$ and -1, respectively. The Visibility V (see definition (10.1)) at position P can therefore be expressed as:

$$V = \frac{2\sqrt{I_1}\sqrt{I_2}}{I_1 + I_2}|\tilde{\gamma}_{12}(\tau)| \tag{10.21}$$

In practice, frequently things are (or can be) adjusted in such a way that $I_1 = I_2$, giving rise to the following simplified expressions for the total irradiance I and Visibility V:

$$I \;=\; 2I_0\left\{1 + |\tilde{\gamma}_{12}(\tau)|\cos\left[\alpha_{12}(\tau) - \phi\right]\right\} \text{ and } V \;=\; |\tilde{\gamma}_{12}(\tau)| \tag{10.22}$$

We note that in this case *the modulus of the complex degree of coherence is identical to the visibility of the fringes* ! This then provides an experimental means of obtaining $|\tilde{\gamma}_{12}(\tau)|$ from the resultant fringe pattern. Moreover, the off-axis shift in the location of the central fringe (no OPD $\rightarrow \phi = 0$) is a measure of $\alpha_{12}(\tau)$, the relative retardation in phase of the fields at S_1 and S_2. Thus, measurements of the visibility and the fringe position yield both the amplitude and phase of the complex degree of coherence.

Note: Dealing with the definition of the complex degree of coherence, it was noted that the intensity fluctuations are also expected to be partially coherent, since the amplitude and phase

fluctuations in a thermal signal tend to track each other. An impression of such a fluctuating wave signal is given in figure 10.2, both in absolute value and centered around the avarage value $\overline{I}$: $\triangle I = I - \overline{I}$. The random superposition of wave packets results in a Gaussian distribution of the amplitude fluctuations for one direction of polarisation and, consequently, is sometimes referred to as *Gaussian light*. This fact directly follows from the *central limit theorem*. Taking the cross-correlation $\mathbf{E}\{\triangle I_1(t+\tau)\triangle I_2(t)\}$ between two different parts of the incoming radiation beam yields now in principle an interferometric tool, which does not involve the usage of phase information. This technique, labelled as *correlation* or *intensity*-interferometry, can indeed be succesfully applied for very bright stellar sources to obtain accurate estimations of stellar angular diameters. It was first tried in radio astronomy in the middle 1950's, and later on (1956) also succesfully used in an optical stellar interferometer by Hanbury Brown and Twiss. They employed search-light mirrors to collect starlight onto two apertures, which was then focussed on two photomultiplier devices. Although photomultipliers operate on the photo-electric effect, which is keyed to the quantum nature of the optical light, laboratory experiments showed that the correlation effect was indeed preserved in the process of photo-electric emission.
The star Sirius was the first to be examined, and it was found to possess an angular diameter of 6.9 milliseconds of arc. For certain stars angular diameters of as little as 0.5 milliseconds of arc can be measured in this way.

10.2 Indirect spectroscopy

10.2.1 Temporal coherence

Temporal coherence is characterised by the coherence time τ_c . The value of τ_c follows from the finite bandwidth of the radiation source under consideration. If we assume a quasi-monochromatic (QM) source, then we have $\tau_c \approx \frac{1}{\triangle\nu}$ with $\triangle\nu$ the line width (in radiation frequency) of the QM-source.
These effects can be assessed with the aid of the Wiener-Khinchine theorem:

$$S(\nu) = \int_{-\infty}^{+\infty} R(\tau) e^{-2\pi i\nu\tau} d\tau \tag{10.23}$$

$$R(\tau) = \int_{-\infty}^{+\infty} S(\nu) e^{2\pi i\nu\tau} d\nu \tag{10.24}$$

Take as an example a Gaussian shaped spectral line profile, i.e.

$$S(\nu) \sim e^{-\left(\frac{\nu}{\triangle\nu}\right)^2} \Longleftrightarrow R(\tau) \sim e^{-\left(\frac{\tau}{\tau_c}\right)^2} \tag{10.25}$$

As can be seen from the FT (indicated by $\Longleftrightarrow$ in expression(10.25), the wave packet corresponding to this line profile has an autocorrelation function that is also Gaussian with a characteristic width τ_c, moreover the *autocorrelation* $R(\tau)$ equals the *autocovariance* $C(\tau)$. This corresponds to a wave train with a Gaussian shaped envelope for the wave amplitude (see figure 10.3).
Try to memorize the following notions:

- A first order system shows an exponential autocorrelation function $R(\tau)$ (*see Chapter 2, section 2.2.2*).

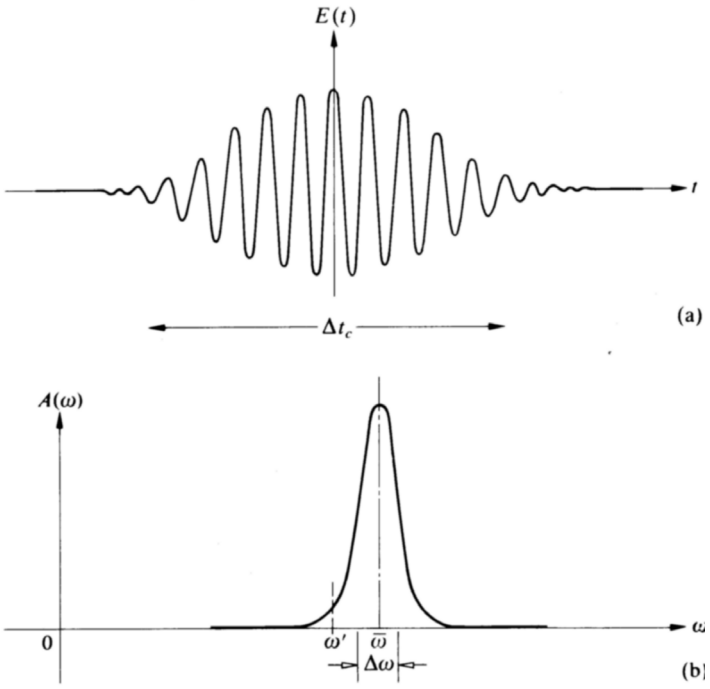

Figure 10.3: *A Gaussian shaped line profile of a quasi-monochromatic radiation source and the shape of the associated wavepacket. Credit Hecht (1987).*

- A Gaussian line profile in the frequency domain shows an amplitude modulated wave train with a Gaussian envelope in the time domain (*see discussion above*).
- A Lorentz line profile in the frequency domain shows an exponentially damped oscillator profile in the time domain (*try this yourself*).

For spectroscopic measurements at infrared and shorter wavelengths one can directly disperse the incoming radiation beam with the aid of a wavelength dispersive device, like for instance a transmission or a reflection grating, and measure the resulting intensity distribution (i.e. the spectrum). However for spectroscopy at radio and submillimeter wavelengths one employs an indirect method. The incoming wave signal is fed into a *correlator* that produces the temporal coherence function $R(\tau)$, a subsequent FT of this function yields the spectral distribution $S(\nu)$ by virtue of the Wiener-Khinchine relation.

10.2.2 Longitudinal correlation

Associated with the coherence time τ_c is the so-called coherence length $l_c = c\tau_c$.

Problem: Show that the coherence length can also be expressed as $l_c = \frac{\lambda^2}{\triangle\lambda}$ in which $\triangle\lambda$ refers to the equivalent of $\triangle\nu$ in the wavelength domain.

Now consider an EM-wave that propagates along a vector $\vec{r}$, and mark two positions P_1 and P_2 on this line of propagation at a mutual distance R_{12}. If $R_{12} \ll l_c$, there will be a strong correlation between the EM-fields at P_1 and P_2 and as a consequence interference effects will be possible. In the case of $R_{12} \gg l_c$, no interference effects are possible. This effect (i.e. potential interference *yes* or *no*) relates to the so-called *longitudinal correlation* or

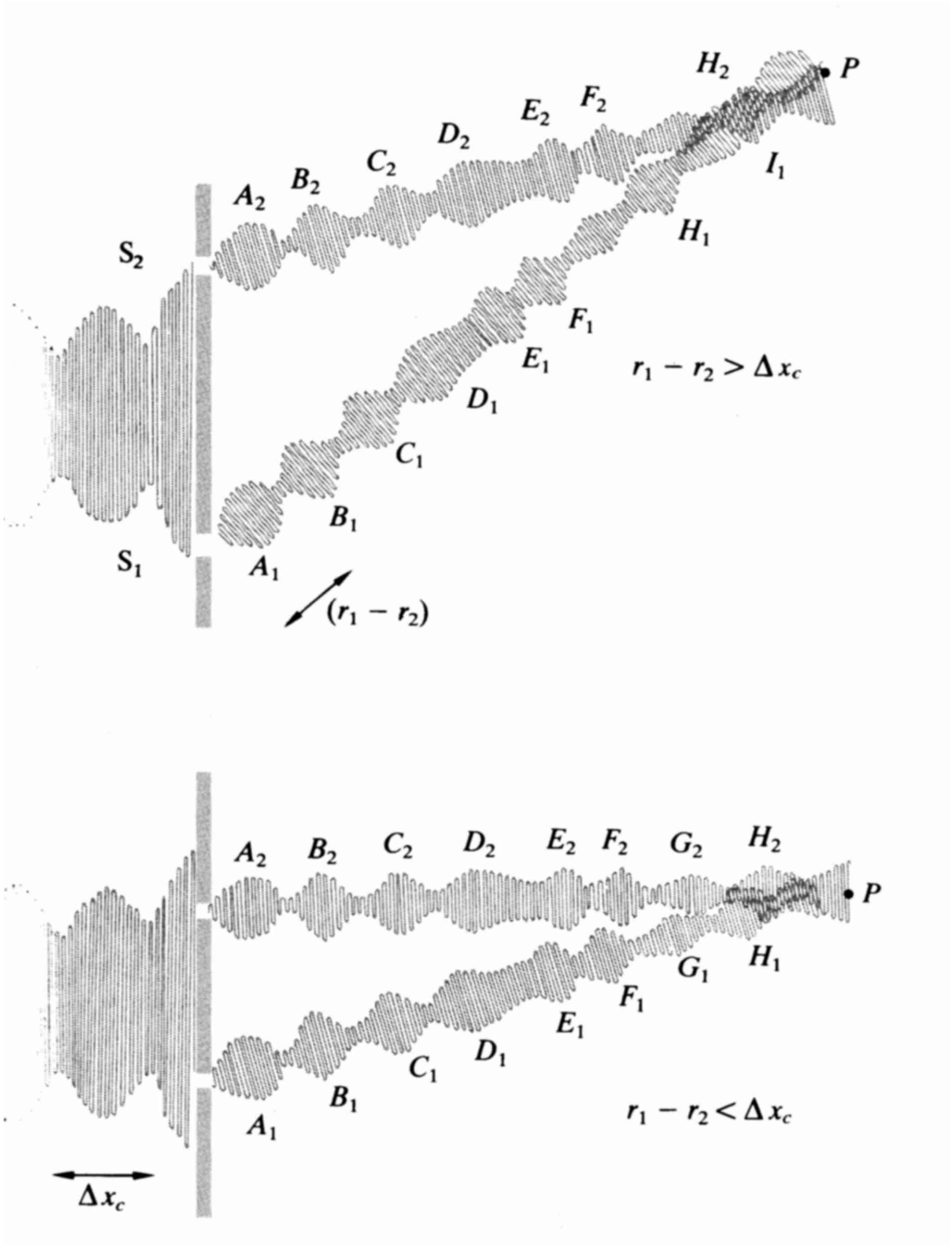

Figure 10.4: *The influence of the coherence length on the interference pattern of two diffracted coherent thermal radiation sources S_1 and S_2. Credit Hecht (1987).*

longitudinal spatial coherence.
This effect can be clearly demonstrated by considering the wave trains in Young's interference experiment (see figure 10.4). The diffracted beams emanating from S_1 and S_2, which are coherent radiation sources, cause an interference pattern. However, in the case of large path differences the interference contrast will diminish, since corresponding wave packets in the

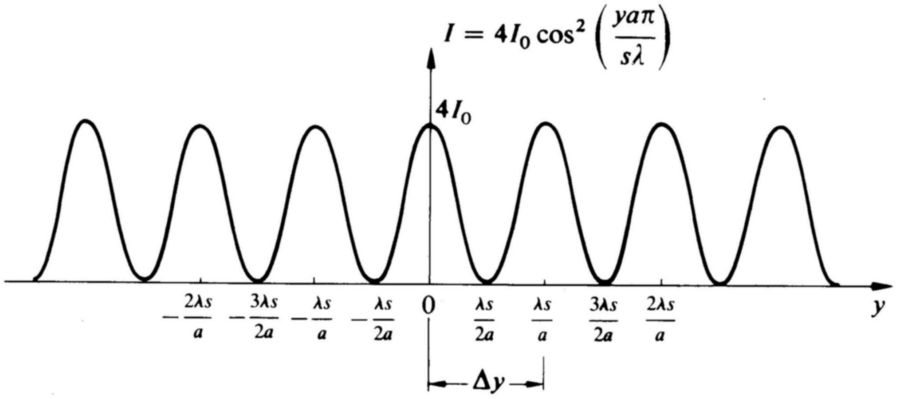

Figure 10.5: *Interferogram displaying the idealized irradiance as a function of the y-coordinate of the fringes in the observation plane Σ_O. Credit Hecht (1987).*

stochastic signal no longer overlap (see figure 10.4: packet H_1 and $H_2 \Longrightarrow$ packet I_1 and H_2).

10.3 Indirect Imaging

10.3.1 Quasi-monochromatic point source: spatial response function of a two-element interferometer

If we apply equation (10.22) to the situation of a quasi-monochromatic point source S, located on the central axis, the wavelets emanating from two infinitesimal pinholes S_1 and S_2 (fictitious case!) will be fully coherent and exactly in phase ($\alpha_{12}(\tau) = 0$) and constitute two coherent secondary sources. Interference will occur, provided the OPD between the interfering beams is less than the coherence length $l = c\tau_c$. With $V = |\tilde{\gamma}_{12}(\tau)| = 1$, the equation for the total irradiance in (10.22) reduces to:

$$I \;=\; 2I_0(1+\cos\phi) \;=\; 4I_0\cos^2\frac{\phi}{2} \tag{10.26}$$

Taking a distance a between the pinholes and assuming that the distance s to the observation plane Σ_O is very much larger than a, we can express the path difference $(r_2 - r_1)$ in equation (10.18) for ϕ in good approximation by:

$$r_2 - r_1 \;=\; a\theta \;=\; \frac{a}{s}\,y \tag{10.27}$$

Here y is the linear coordinate in the observation plane Σ_O, starting from the intersection of the central axis with this plane and running perpendicular to the fringes. Substituting ϕ in equation (10.26) by combining (10.18) and (10.27) we get an analytical expression for the interferogram in Σ_O:

$$I \;=\; 4I_0\cos^2\frac{\pi a y}{s\lambda} \tag{10.28}$$

This (idealized) irradiance versus distance distribution is displayed in figure 10.5 and constitutes basically the response of an ideal two-element interferometer to a monochromatic point source, i.e. the PSF of an ideal two-element interferometer.

The derivation of the actual PSF for a non-ideal two-element interferometer, that also accounts for the finite size of the apertures, can be accomplished by utilizing the concept of the *pupil function* which was treated for single apertures in Chapter 7 (on Imaging in Astronomy) of the OAF1 course. This concept will now first be applied to a two-element interferometer, starting with the assumption of infinitesimal apertures (the ideal case discussed above) and subsequently by implementing the practical case with finite aperture sizes. Later on in this chapter, with the introduction of aperture synthesis, this will be extended to the derivation of the point source response function (PSF) and the optical transfer function (OTF) for *multi-aperture arrays.*

Consider two circular apertures with diameter d separated by a baseline direction vector $\vec{s}$. Take the origin of the pupil function $P(\vec{r})$ on the baseline vector $\vec{s}$ symmetrically positioned between the two apertures. The pupil function $P(\vec{r})$ can now be expressed as:

$$P(\vec{r}) \;=\; \Pi\left(\frac{\vec{r}-\vec{s}/2}{d}\right) \;+\; \Pi\left(\frac{\vec{r}+\vec{s}/2}{d}\right) \tag{10.29}$$

with Π the 2-dimensional circular window function.
Introducing the ***spatial frequency variable*** $\vec{\zeta} = \vec{r}/\lambda$, the pupil function can be rewritten as:

$$P(\vec{\zeta}) \;=\; \Pi\left(\frac{\vec{\zeta}-\vec{s}/2\lambda}{d/\lambda}\right) \;+\; \Pi\left(\frac{\vec{\zeta}+\vec{s}/2\lambda}{d/\lambda}\right) \tag{10.30}$$

Now if the diameter d of the apertures is assumed to be very much smaller than the length $|\vec{s}| = D$ of the baseline vector, i.e. $d \ll D$, the pupil function can be approximated by:

$$P(\vec{\zeta}) \;=\; \delta\left(\vec{\zeta}-\vec{s}/2\lambda\right) \;+\; \delta\left(\vec{\zeta}+\vec{s}/2\lambda\right) \tag{10.31}$$

The optical tranfer function (OTF) for this limiting case of infinitesimal apertures, follows from the *self-convolution* of the the function $(\lambda/R)P(\vec{\zeta})$. Since we have a symmetrical pupil function in this case, the self-convolution is identical to the *autocorrelation* of $(\lambda/R)P(\vec{\zeta})$:

$$\begin{aligned} OTF \;=\; H_\lambda(\vec{\zeta}) \;&=\; \left(\frac{\lambda}{R}\right)^2 \int\int_{\text{pupil plane}} P(\vec{\zeta}\,')P(\vec{\zeta}\,'-\vec{\zeta})d\vec{\zeta}\,' \\ &=\; \left(\frac{\lambda}{R}\right)^2 \int\int_{\text{pupil plane}} \left[\delta\left(\vec{\zeta}\,'-\vec{s}/2\lambda\right) \;+\; \delta\left(\vec{\zeta}\,'+\vec{s}/2\lambda\right)\right]\cdot \\ &\qquad \cdot\left[\delta\left(\vec{\zeta}\,'-\vec{\zeta}-\vec{s}/2\lambda\right) \;+\; \delta\left(\vec{\zeta}\,'-\vec{\zeta}+\vec{s}/2\lambda\right)\right] d\vec{\zeta}\,' \\ &=\; 2\left(\frac{\lambda}{R}\right)^2 \left[\delta(\vec{\zeta}) + \frac{1}{2}\delta\left(\vec{\zeta}-\vec{s}/\lambda\right) \;+\; \frac{1}{2}\delta\left(\vec{\zeta}+\vec{s}/\lambda\right)\right] \end{aligned} \tag{10.32}$$

This OTF shows that the pair of pinholes transmits three principal spatial frequencies: a DC-component $\delta(\vec{0})$ and two high frequencies related to the length of the baseline vector $\vec{s}$ at $\pm\vec{s}/\lambda$. These three spatial frequencies represent a three-point sampling of the so-called uv-plane in 2-dimensional frequency(Fourier) space. **Note:** Full frequency sampling of the uv-plane will allow complete reconstruction of the brightness distribution of the celestial source being observed!
The PSF follows from $\mathrm{FT}\{H_\lambda(\vec{\zeta})\}$:

$$\delta(\vec{\zeta}) \quad\Leftrightarrow\quad \mathbf{1} \;\text{(2-dimensional sheet!)}$$

$$\delta\left(\vec{\zeta}-\vec{s}/\lambda\right) \quad \Leftrightarrow \quad e^{i2\pi\vec{\theta}\cdot\vec{s}/\lambda}$$
$$\delta\left(\vec{\zeta}+\vec{s}/\lambda\right) \quad \Leftrightarrow \quad e^{-i2\pi\vec{\theta}\cdot\vec{s}/\lambda}$$
$$\Longrightarrow PSF \;=\; \left(\frac{\lambda}{R}\right)^2\left[2(1+\cos 2\pi\vec{\theta}\cdot\vec{s}/\lambda)\right] \;=\; 4\left(\frac{\lambda}{R}\right)^2\cos^2\pi\vec{\theta}\cdot\vec{s}/\lambda \tag{10.33}$$

in which $\vec{\theta}$ ***represents the 2-dimensional angular coordinate vector*** used to describe the angular distribution of the diffracted image. The attenuation factor $(\lambda/R)^2$ results from the spherical expansion of the diffracted field in the Fraunhofer limit.
If we assume a light flux I_0 emanating from each pinhole, we can express the brightness distribution for the diffracted beam as:

$$I \;=\; 4I_0\cos^2\pi\vec{\theta}\cdot\vec{s}/\lambda \tag{10.34}$$

This is the same equation we derived before with the aid of the interference law for partially coherent light, but now in a two-dimensional setting with $\vec{\theta}$ replacing y/s and $\vec{s}$ replacing the pinhole distance a in equation (10.28). We have full constructive interference:

$$I \;=\; 4I_0 \text{ for } \frac{\vec{\theta}\cdot\vec{s}}{\lambda} \;=\; n\,(=\,0,\pm1,\pm2,\ldots) \;\;\rightarrow\;\; |\vec{\theta}| \;=\frac{n\lambda}{|\vec{s}|\cos\phi} \tag{10.35}$$

and full destructive interference:

$$I \;=\; 0 \text{ for } \frac{\vec{\theta}\cdot\vec{s}}{\lambda} \;=\; (n+\frac{1}{2})\,(=\,\pm\frac{1}{2},\pm\frac{3}{2},\pm\frac{5}{2},\ldots) \;\;\rightarrow\;\; |\vec{\theta}| \;=\frac{(n+\frac{1}{2})\lambda}{|\vec{s}|\cos\phi} \tag{10.36}$$

with $\cos\phi$ the angle between $\vec{\theta}$ and the baseline vector $\vec{s}$.
The PSF represents a *corrugated sheet* with its modulation along the direction of the baseline vector $\vec{s}$ and a periodicity $(\Delta\theta)_s = \lambda/|\vec{s}|$, i.e. a pattern of alternating bright and dark *stripes* orthogonal to the direction of the baseline vector $\vec{s}$.
In actuality, the apertures have a finite size and the diffracted light by the apertures is localized, so we have $d < S$ but the approximation by δ-functions for infinitesimal apertures no longer holds! The PSF has now to be derived from the amplitude of the diffracted field by FT of the pupil function given in expression 10.30:

$$\tilde{a}(\vec{\theta}) \;\Leftrightarrow\; \frac{\lambda}{R}\left[\Pi\left\{\frac{\lambda}{d}\left(\vec{\zeta}-\frac{\vec{s}}{2\lambda}\right)\right\} \;+\; \Pi\left\{\frac{\lambda}{d}\left(\vec{\zeta}+\frac{\vec{s}}{2\lambda}\right)\right\}\right] \tag{10.37}$$

Applying the shift and scaling theorems from Fourier theory, i.e. if $f(x) \Leftrightarrow F(s)$ then $f[a(x-b)] \Leftrightarrow \left(e^{-2\pi ibs}/a\right)F(s/a)$, we find for the amplitude of the diffracted field:

$$\begin{aligned}\tilde{a}(|\,\vec{\theta}\,|) \;&=\; \left(\frac{\lambda}{R}\right)\left[\frac{1}{4}\pi\,(d/\lambda)^2\right]\left[\frac{2J_1(\pi|\,\vec{\theta}\,|d/\lambda)}{\pi|\,\vec{\theta}\,|d/\lambda}\right]\left(e^{-2\pi i\vec{\theta}\cdot\vec{s}/2\lambda} \;+\; e^{2\pi i\vec{\theta}\cdot\vec{s}/2\lambda}\right)\\ &=\; 2\left(\frac{\lambda}{R}\right)\left[\frac{1}{4}\pi\,(d/\lambda)^2\right]\left[\frac{2J_1(|\vec{u}\,|)}{|\vec{u}\,|}\right]\cos\vec{u}\cdot\;\vec{s}/d \quad \text{with} \quad \vec{u}=\pi\,\vec{\theta}\,d/\lambda\\ \text{PSF}=|\tilde{a}(|\vec{\theta}|)|^2 \;&=\; 4\left(\frac{\lambda}{R}\right)^2\left[\frac{1}{4}\pi\,(d/\lambda)^2\right]^2\left[\frac{2J_1(|\vec{u}\,|)}{|\vec{u}\,|}\right]^2\cos^2\vec{u}\cdot\vec{s}/d\end{aligned} \tag{10.38}$$

Again we have full constructive interference for:

$$\frac{\vec{\theta}\cdot\vec{s}}{\lambda} \;=\; n\,(=\,0,\pm1,\pm2,\ldots) \;\;\rightarrow\;\; |\vec{\theta}| \;=\frac{n\lambda}{|\vec{s}|\cos\phi} \tag{10.39}$$

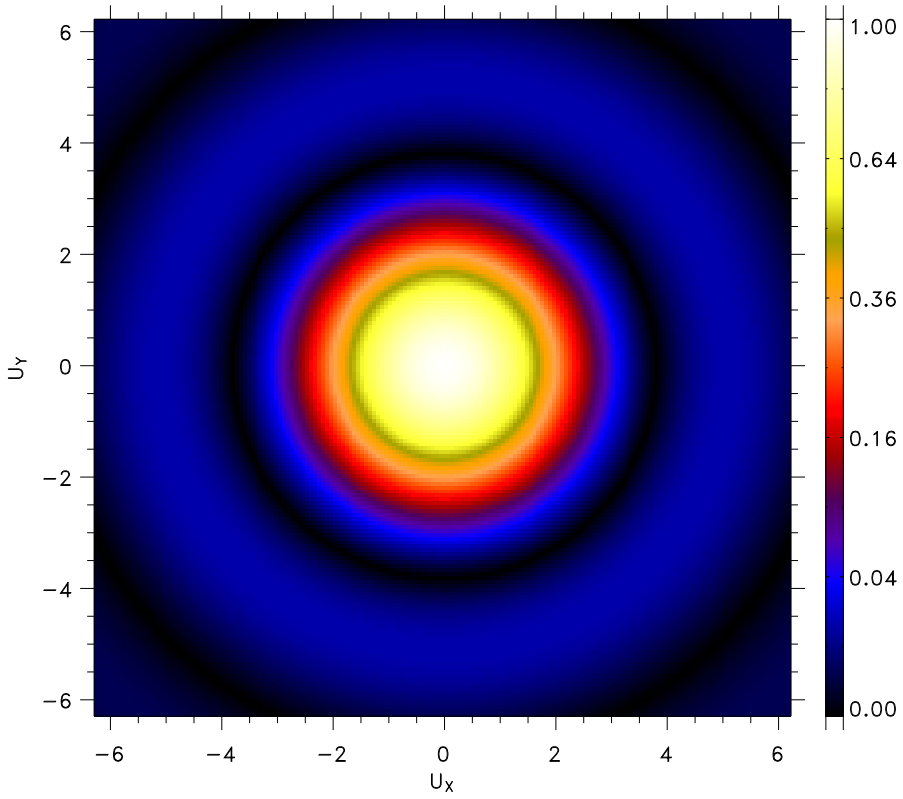

Figure 10.6: *PSF of a single circular aperture in pseudo-color as a function of the 2D-position vector $\vec{u}$ (λ-invariant display).*

and full destructive interference for:

$$\frac{\vec{\theta}\cdot\vec{s}}{\lambda} = (n+\frac{1}{2})\,(= \pm\frac{1}{2}, \pm\frac{3}{2}, \pm\frac{5}{2}, \ldots) \quad \rightarrow \quad |\vec{\theta}| = \frac{(n+\frac{1}{2})\lambda}{|\vec{s}|\cos\phi} \tag{10.40}$$

with $\cos\phi$ the angle between $\vec{\theta}$ and the baseline vector $\vec{s}$.
The first two terms in the expression for the PSF give the normalisation for $|\vec{\theta}| = 0$. The other terms represent a corrugated 2-dimensional Airy brightness distribution, intensity-modulated along the direction of the baseline vector $\vec{s}$ with periodicity $(\Delta\theta)_s = \lambda/|\vec{s}|$, i.e. a pattern of alternating bright and dark *annuli at a pitch determined by* $(\Delta\theta)_d = 1.220\lambda/d,\ 2.233\lambda/d,\ 3.238\lambda/d, \ldots$ *of the individual telescope mirrors as shown in figure 10.6 in pseudo-color* superimposed by periodic drop-outs in brightness orthogonal to the direction of the baseline vector $\vec{s}$ *at a pitch determined by* $(\Delta\theta)_s = \lambda/|\vec{s}|$. This corrugated 2-dimensional Airy brightness distribution is also displayed (λ-invariant) in pseudo-color code as a function of the 2-D position vector $\vec{u}$ in figure 10.7

A typical one-dimensional cross-section along $u_y = 0$ of the central part of the interferogram 10.7 is sketched in figure 10.8. Note that the visibilities in both figure 10.5 and in figure 10.8 are equal to one, because $I_{min} = 0$.
It can be shown that $|\tilde{\gamma}_{12}(\tau)|$ equals one for all values of τ and any pair of spatial points, if and

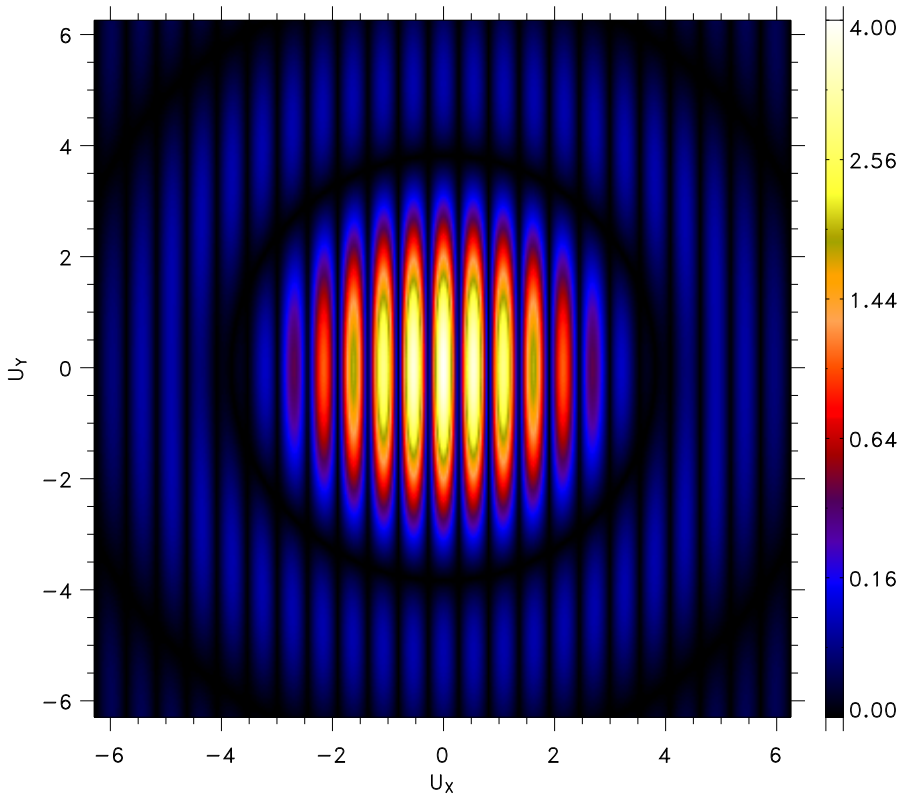

Figure 10.7: *PSF of a two-element interferometer in pseudo-color as a function of the 2D-position vector $\vec{u}$ (λ-invariant display). The aperture diameter d equals 25 meters, the length of the baseline vector $|\vec{s}|$ is chosen to be 144 meter.*

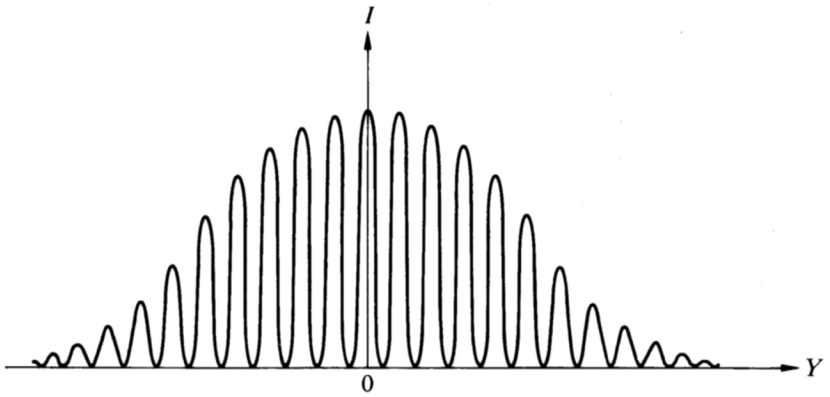

Figure 10.8: *Double beam interference fringes showing the modulation effect of diffraction by the aperture of a single pinhole. Credit Hecht (1987).*

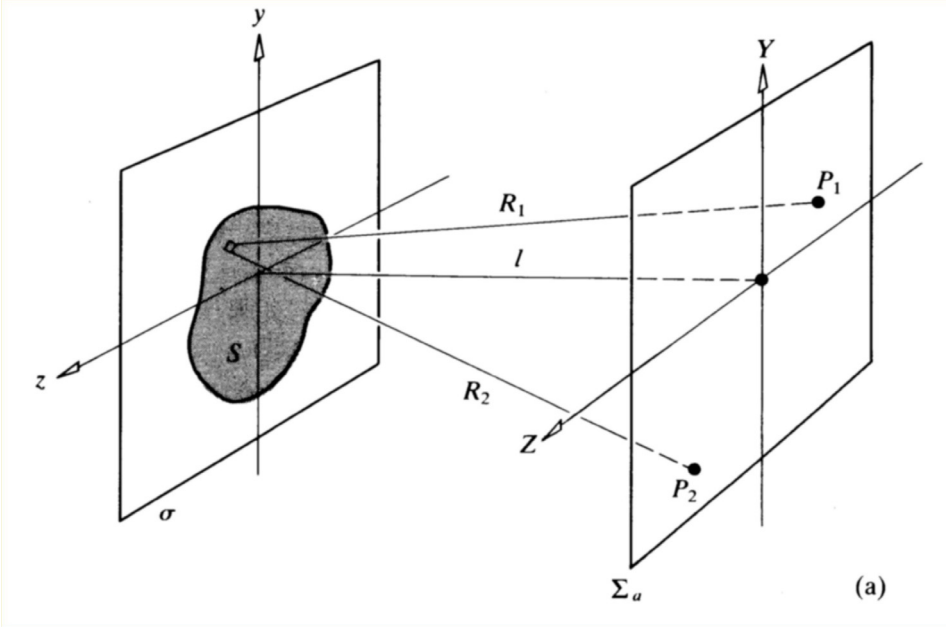

Figure 10.9: *Relating $\tilde{\gamma}_{12}(0)$ to the brightness distribution of an extended radiation source S: configuration for demonstrating the Van Cittert-Zernike theorem. Credit Hecht (1987).*

only if the radiation field is *strictly monochromatic*, in practice such a situation is obviously *unattainable* ! Furthermore, a non-zero radiation field for which $|\tilde{\gamma}_{12}(\tau)| = 0$ for all values of τ and any pair of spatial points cannot exist in free space either.

10.3.2 Quasi-monochromatic extended source: spatial or lateral coherence

Spatial coherence (also: lateral coherence or lateral correlation) has to do with the spatial extent of the radiation source.

Problem: Prove that for $\tau \ll \tau_c$:

$$\tilde{\gamma}_{12}(\tau) = \tilde{\gamma}_{12}(0)e^{2\pi i\nu_0\tau} \tag{10.41}$$

with $|\tilde{\gamma}_{12}(\tau)| = |\tilde{\gamma}_{12}(0)|$ and a *fixed phase difference* $\alpha_{12}(\tau) = 2\pi\nu_0\tau$, ν_0 represents the average frequency of the wave carrier.

In the following treatment of spatial coherence, it is implicitly assumed that the frequency bandwidth of the radiation source is suffiently narrow that the comparison between two points with respect to spatial coherence occurs at times differing by $\triangle t \ll \tau_c$

Query What is the quantitative relation between the *brightness distribution* of the spatially extended radiation source and the resulting *phase correlation* between two positions in the radiation field?

Approach Consider again Young's experiment for the case that the radiation source S is extended and illuminates the pinholes S_1 and S_2 (actually shown in figure 10.1). In the observers plane Σ, the interference is given by the expectation value of the product $\tilde{E}_1(t)\tilde{E}_2^*(t) = \mathbf{E}\{\tilde{E}_1(t)\tilde{E}_2^*(t)\} = \tilde{\Gamma}_{12}(0)$ with the subscripts 1 and 2 referring to the positions P_1 and P_2 in the Σ-plane. If $\tilde{E}_1$ and $\tilde{E}_2$ are uncorrelated, then $|\tilde{\Gamma}_{12}(0)| = 0$. In the case

of full correlation $|\tilde{\gamma}_{12}|$ $\left(= \frac{|\tilde{\Gamma}_{12}(0)|}{\sqrt{I_1 I_2}}\right) = 1$, for partial correlation we have $0 < |\tilde{\gamma}_{12}(0)| < 1$.
The extended source in Young's experiment is a collection of non-coherent infinitesimal radiators, this obviously reduces the contrast in the interferogram. This contrast can be observed and is described by the afore mentioned *Visibility function V*:

$$V = \frac{I_{max} - I_{min}}{I_{max} + I_{min}} = |\tilde{\gamma}_{12}(0)| \tag{10.42}$$

10.3.3 The Van Cittert-Zernike theorem

So how can we now relate $\gamma_{12}(0)$ (or $\Gamma_{12}(0)$) to the brightness distribution of the extended radiation source S?
This can be done in the following way (see figure 10.9). Locate S, a QM-incoherent source, in a plane σ, with an intensity distribution $I(y, z)$. Consider next the observation plane Σ parallel to σ, l is perpendicular to both planes (coincident with the X-axis) connecting the centre of the extended source $(y = 0, z = 0)$ to the zero reference in Σ $(Y = 0, Z = 0)$. Select two positions P_1 and P_2. The objective is to describe the value of $\gamma_{12}(0)$ in this plane, i.e. the coherence of the radiation field in Σ. Consider furthermore a small (infinitesimal) radiation element dS in the source at distances R_1 and R_2 from P_1 and P_2 respectivily. Suppose now that S is *not a source* but *an aperture* of identical size and shape, and suppose that $I(y, z)$ is not a description of the irradiance (or intensity distribution) but, instead, its functional form corresponds to the *field distribution* across that aperture. In other words imagine that there is a transparancy at the aperture with amplitude transmission characteristics that correspond functionally to the irradiance distribution $I(y, z)$. Furthermore, imagine that the aperture is illuminated by a spherical wave converging towards the fixed point P_2, so that a diffraction pattern will result centered at P_2. This diffracted field distribution, normalised to unity at P_2, is everywhere (e.g. at P_1) equal to the value of $\gamma_{12}(0)$ at that point. This is the *Van Cittert-Zernike theorem.*
In the limit that R_1 and R_2 are much larger than the source diameter and the relevant part of the Σ-plane we have the equivalent of Fraunhofer diffraction, this condition is practically always satisfied for astronomical observations. In that case, the van Cittert-Zernike theorem can be expressed mathematically as:

$$\tilde{\Gamma}(\vec{r}) = \int\int_{\text{source}} I(\vec{\Omega}) e^{\frac{2\pi i \vec{\Omega}.\vec{r}}{\lambda}} d\vec{\Omega} \tag{10.43}$$

$$I(\vec{\Omega}) = \lambda^{-2} \int\int_{\Sigma\text{-plane}} \tilde{\Gamma}(\vec{r}) e^{-\frac{2\pi i \vec{\Omega}.\vec{r}}{\lambda}} d\vec{r} \tag{10.44}$$

$I(\vec{\Omega})$ is the intensity distribution of the extended radiation source as a function of a unit direction vector $\vec{\Omega}$ as seen from the observation plane Σ. Taking the centre of the extended radiation source S as the zero-reference for $\vec{\Omega}$ (coincident with the central axis l in figure (10.9)) and assuming a relativily small angular extent of the source we can write $I(\vec{\Omega}) = I(\theta_y, \theta_z)$ and $d\vec{\Omega} = d\theta_y d\theta_z$, where θ_y and θ_z represent two orthogonal angular coordinate axes across the source starting from the zero-reference of $\vec{\Omega}$.
$\tilde{\Gamma}(\vec{r})$ is the coherence function in the Σ-plane, the vector $\vec{r}$ represents an arbitrary baseline $\vec{r}(X, Y)$ in this plane with $d\vec{r} = dY dZ$ (in the above example $\overline{P_1 P_2} = \vec{r}_{P_1} - \vec{r}_{P_2}$).
Expressions (10.43) and (10.44) for $\tilde{\Gamma}(\vec{r})$ and $I(\vec{\Omega})$ show that they are linked through a Fourier transform, except for the scaling with the wavelength λ. This scaling might be perceived as a "true" Fourier transform with the *conjugate variables* $\vec{\Omega}$ and $\vec{r}/\lambda$, i.e. by expressing $\vec{r}$ in units

of the wavelength λ, *writing the van Cittert-Zernike theorem as the Fourier pair*:

$$I(\vec{\Omega}) \quad \Leftrightarrow \quad \tilde{\Gamma}(\vec{r}/\lambda) \tag{10.45}$$

The complex *spatial* degree of coherence, $\tilde{\gamma}(\vec{r})$, follows from:

$$\tilde{\gamma}(\vec{r}) = \frac{\tilde{\Gamma}(\vec{r})}{\int\int_{\text{source}} I(\vec{\Omega}) d\vec{\Omega}} \tag{10.46}$$

i.e. by normalising on the total source intensity.
Note: Although the extended source S is spatially incoherent, there still exists a partially correlated radiation field at e.g. positions P_1 and P_2, since all individual source elements contribute to a specific location P in the Σ-plane.

For a derivation of the Van Cittert-Zernike relations, consider the geometry given in figure 10.10.
The observation plane Σ contains the baseline vector $\vec{r}(Y, Z)$ and is perpendicular to the vector pointing at the centre of the radiation source. The angular coordinates θ_y and θ_z across the source (see above) correspond to the linear coordinates of the unit direction vector $\vec{\Omega}(\Omega_X, \Omega_Y, \Omega_Z)$, i.e. the direction cosines of $\vec{\Omega}$ relative to the X, Y, Z coordinate system $(\Omega_X^2 + \Omega_Y^2 + \Omega_Z^2 = 1)$. The spatial coherence of the EM-field between the two positions 1 (for convenience chosen in the origin) and 2 is the outcome of a correlator device that produces the output $\mathbf{E}\left\{\tilde{E}_1(t)\tilde{E}_2^*(t)\right\}$.
In reality positions 1 and 2 are not point like, they represent *radio antennae* or *optical reflectors*, we shall come back to this later. From the geometry displayed in figure 10.10, regarding the Van Cittert-Zernike relations, we can note the following:
$\Rightarrow$ If $I(\vec{\Omega}) = I_0\delta(\vec{\Omega})$, i.e. a point source on the X-axis, the Van Cittert-Zernike relation yields $|\tilde{\Gamma}(\vec{r})| = I_0$ and $|\tilde{\gamma}(\vec{r})| = 1$: a plane wave hits the full YZ-plane everywhere at the same time, full coherence is preserved (by definition) on a plane wave front.
$\Rightarrow$ Next, let us consider an infinitesimal source element in the direction $\vec{\Omega}_0 \Longrightarrow I_0\delta(\vec{\Omega} - \vec{\Omega}_0)$. The projection of $\vec{\Omega}_0$ on the $\Sigma-$plane is $\vec{\Omega}_0'(\Omega_Y, \Omega_Z)$. There will now be a difference in path length between positions 1 and 2 given by the projection of $\vec{r}$ on $\vec{\Omega}_0$, i.e. $\vec{r}.\vec{\Omega}_0' = \Omega_Y Y + \Omega_Z Z$. Then:

$$\tilde{E}_1(t) = \tilde{E}_0(t)e^{2\pi i\nu_0\left(t + \frac{\vec{\Omega}_0.\vec{r}}{c}\right)} = \tilde{E}_0(t)e^{\left(2\pi i\nu_0 t + \frac{2\pi i\vec{\Omega}_0.\vec{r}}{\lambda}\right)} \tag{10.47}$$

$$\tilde{E}_2^*(t) = \tilde{E}_0(t)e^{-2\pi i\nu_0 t} \tag{10.48}$$

Therefore:

$$\mathbf{E}\left\{\tilde{E}_1(t)\tilde{E}_2^*(t)\right\} = \mathbf{E}\left\{|\tilde{E}_0(t)|^2\right\} e^{\frac{2\pi i\vec{\Omega}_0.\vec{r}}{\lambda}} = I_0(\vec{\Omega}_0)e^{\frac{2\pi i\vec{\Omega}_0.\vec{r}}{\lambda}} \tag{10.49}$$

Integration over the full source extent(straight forward integration, since all source elements are spatially uncorrelated) yields:

$$\tilde{\Gamma}(\vec{r}) = \int\int_{\text{source}} I_0(\vec{\Omega})e^{2\pi i\vec{\Omega}.\vec{r}/\lambda} d\vec{\Omega} \tag{10.50}$$

$$\tilde{\gamma}(\vec{r}) = \frac{\int\int_{\text{source}} I_0(\vec{\Omega})e^{2\pi i\vec{\Omega}.\vec{r}/\lambda} d\vec{\Omega}}{\int\int_{\text{source}} I_0(\vec{\Omega}) d\vec{\Omega}} \tag{10.51}$$

The meaning of this relationship is, in physical terms, that $\tilde{\Gamma}(\vec{r})$ at a certain point represents a *single* Fourier component (with baseline $\vec{r}$) of the intensity distribution of the source with

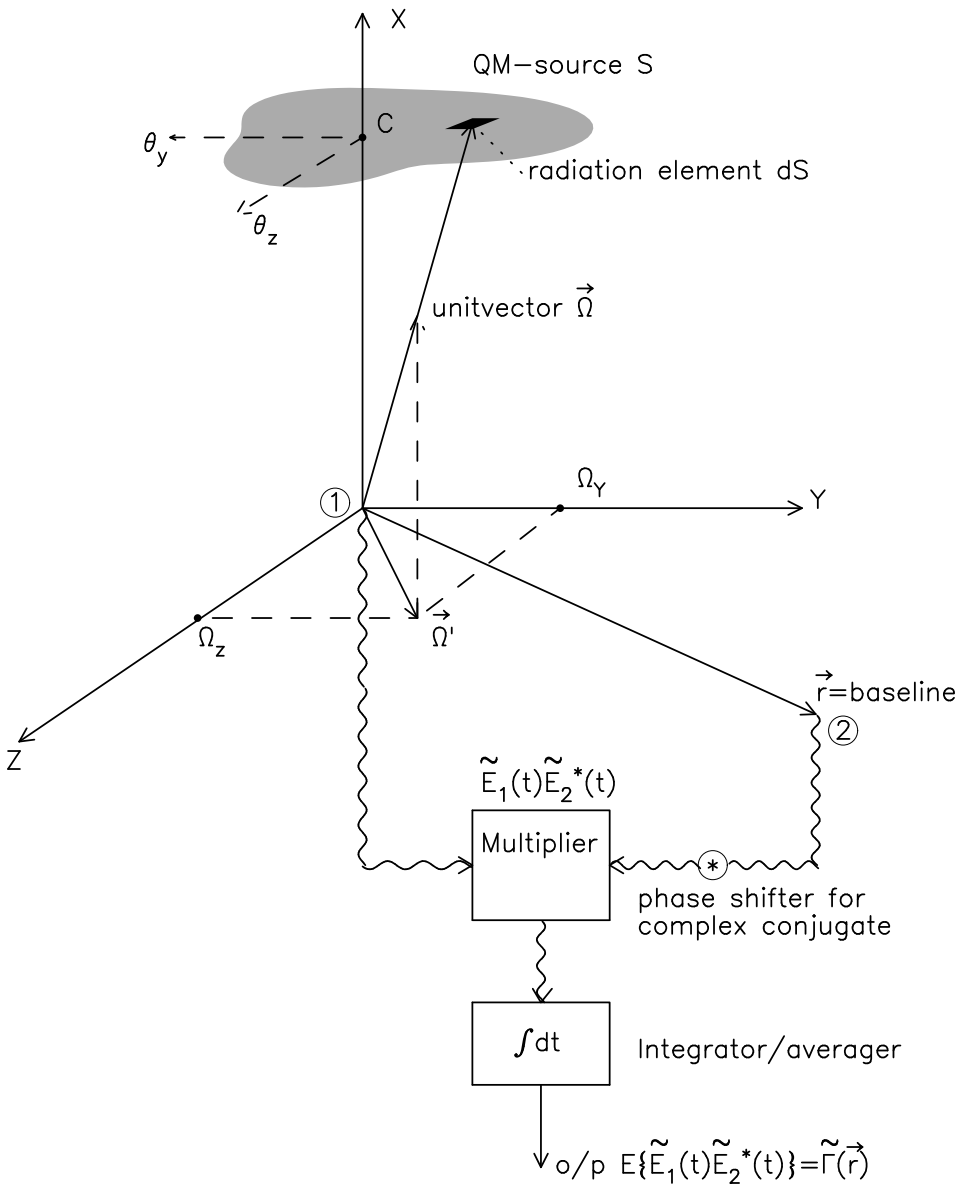

Figure 10.10: *Van Cittert Zernike relation: reference geometry.*

strength $\tilde{\Gamma}(\vec{r})d\vec{r}$. A short baseline (small $|\vec{r}|$) corresponds to a low frequency (*spatial frequency!*) component in the brightness distribution $I(\theta_y, \theta_z)$, i.e. *coarse* structure, large values of $|\vec{r}|$ correspond to *fine* structure in $I(\theta_y, \theta_z)$. The *diffraction limited* resolution in *aperture synthesis* corresponds to:

$$|\vec{r}_{max}| = L_{max} \Longrightarrow \theta_{min} = \frac{\lambda}{2L_{max}} \tag{10.52}$$

The factor 2 in the denominator of the expression for θ_{min} follows from the rotation symmetry in aperture synthesis.

Example Consider a one dimensional case. This can be done by taking the slit source of uniform intensity shown in figure 10.11 , slit width b and running coordinate ξ, the observation plane Σ, running coordinate y, is located at large distance l from the slit source (i.e. the Fraunhofer limit is applicable). The source function can be expressed as the window function

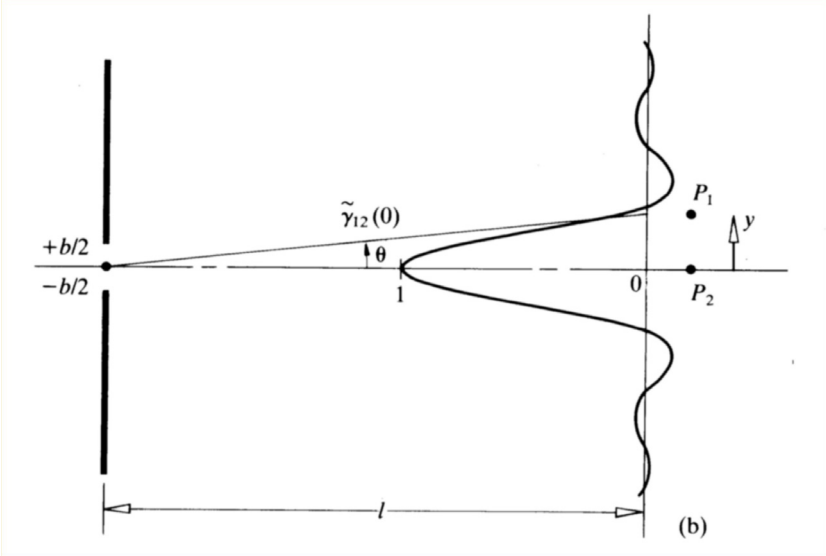

Figure 10.11: *The coherence function $\tilde{\gamma}_{12}(0)$ for a uniform slit source. Credit Hecht (1987).*

$\Pi\left(\frac{\xi}{b}\right)$, in angular equivalent $\Pi\left(\frac{\beta}{\beta_0}\right)$, with $\beta_0 = b/l$.
Application of the Van Cittert-Zernike theorem $I(\vec{\Omega}) \Leftrightarrow \tilde{\Gamma}(\vec{r}/\lambda)$ yields:

$$\Pi\left(\frac{\beta}{\beta_0}\right) \Leftrightarrow \beta_0 \text{sinc}\left(\frac{y\beta_0}{\lambda}\right) = \beta_0 \text{sinc}\left(\frac{yb}{\lambda l}\right) \tag{10.53}$$

with $\text{sinc}(x) = \left(\frac{\sin \pi x}{\pi x}\right)$. The modulus of the normalised complex coherence function becomes:

$$|\tilde{\gamma}(y)| = \left|\frac{\beta_0 \text{sinc}\frac{yb}{\lambda l}}{\beta_0}\right| = \left|\text{sinc}\frac{yb}{\lambda l}\right| = V \Rightarrow \text{Visibility} \tag{10.54}$$

Note that:

- *Enlarging* b with a factor 2, *shrinks* the coherence function with the same factor. This is of course a direct consequence of the scaling law under Fourier transform.

- The width of the coherence function follows from: $\left(\frac{y\beta_0}{\lambda}\right) \approx 1 \Rightarrow y = \left(\frac{\lambda}{\beta_0}\right)$. If the radiation source exhibitis a smooth brightness distribution over the angle $\beta_0 = \Delta$ radians, as is the case with the slit source, then $\gamma(y)$ also displays a smooth distribution over a distance of λ/Δ meters.

- If the brightness structure of a radiation source covers a wide range of angular scales, say from a largest angular scale Δ to a smallest angular scale δ (in radians), then the spatial coherence function shows a finest detail of λ/Δ and a maximum extent of $\approx \lambda/\delta$ in meters.

10.3.4 Etendue of coherence

Consider the two-dimensional case of a circular source of uniform intensity with an angular diameter θ_s, the source brightness distribution can then be described as a circular two-dimensional window function: $I(\vec{\Omega}) = \Pi\left(\frac{\theta}{\theta_s}\right)$. To compute the complex degree of coherence

in the observation plane Σ take again two positions, position 1 in the centre (origin, as before) and position 2 at a distance ρ from this centre point. Applying the van Cittert-Zernike theorem, we find for $\tilde{\Gamma}(\rho)$:

$$\Pi\left(\frac{\theta}{\theta_s}\right) \Leftrightarrow \tilde{\Gamma}(\rho/\lambda) \;=\; \frac{(\theta_s/2)J_1(\pi\theta_s\rho/\lambda)}{\rho/\lambda} \tag{10.55}$$

where J_1 represents the Bessel function of the first kind. Normalisation to the source brightness, through division by $(\pi\theta_s^2)/4$, yields the expression for the complex degree of coherence:

$$\tilde{\gamma}(\rho) \;=\; \frac{2J_1(\pi\theta_s\rho/\lambda)}{\pi\theta_s\rho/\lambda} \tag{10.56}$$

The modulus of the complex degree of coherence is therefore:

$$|\tilde{\gamma}(\rho)| = \left|\frac{2J_1(u)}{u}\right| \tag{10.57}$$

with the argument of the Bessel function $u = \pi\theta_s\rho/\lambda$. We can derive the extent of the coherence in the observation plane Σ by evaluating $J_1(u)$. If we take $u = 2$, $|\tilde{\gamma}(\rho)| = J_1(2) = 0.577$, i.e. the coherence in Σ remains significant for $u \leq 2$, or $\rho \leq 2\lambda/(\pi\theta_s)$. The area S in Σ over which the coherence remains significant equals $\pi\rho^2 = 4\lambda^2/(\pi\theta_s^2)$. In this expression, $\pi\theta_s^2/4$ equals the solid angle Ω_{source} subtended by the radiation source. Significant coherence will thus exist if the following condition is satisfied:

$$\epsilon = S\Omega_{\text{source}} \leq \lambda^2 \tag{10.58}$$

The condition $\epsilon = S\Omega_{\text{source}} = \lambda^2$ is called the *Etendue of Coherence*, to be fulfilled if coherent detection is required!

Example Consider a red giant star, of radius $r_0 = 1.5$ x 10^{11} meter, at a distance of 10 parsec. For this object $\theta_s = 10^{-6}$ radians. If this object is observed at $\lambda = 0.5\mu$m, the value of the coherence radius ρ, on earth, on a screen normal to the incident beam is $\rho = 2\lambda/(\pi\theta_s) = 32$ cm. In the infrared, at $\lambda = 25\mu$m, the radius ρ is increased fifty fold to ≈ 15 meter. In the radio domain, say at $\lambda = 6$ cm, $\rho \approx 35$ km.

In general, *good coherence* means a Visibility of 0.88 or better. For a uniform circular source this occurs for $u = 1$, that is when $\rho = 0.32\lambda/\theta$. If we consider a narrow-bandwidth uniform radiation source at a distance R away, we have

$$\rho = 0.32(\lambda R)/D \tag{10.59}$$

This expression is very convenient to quickly estimate the required physical parameters in an interference or diffraction experiment. For example, if we put a red filter over a 1-mm-diameter disk-shaped flashlight source and stand back 20 meters from it, then $\rho = 3.8$ mm, where the mean wavelength is taken at 600 nm. This means that a set of apertures spaced at about 4 mm or less should produce clear fringes. Evidently the area of coherence increases with the distance R, this is why one can always find a distant bright street light to use as a convenient source.

Important: Remember, as stated in section 1.3.1, that throughout the treatment of spatial coherence it was assumed that the comparison between the two points occurs at times differing by a $\triangle t \ll \tau_c$. If this condition is not fulfilled, for example because the frequency bandwidth of the radiation source is too large, interferometric measurements will not be possible (see section on temporal coherence). Frequency filtering will then be required to reduce the bandwidth of the source signal, i.e. make it more quasi-monochromatic.

10.4 Aperture synthesis

As already elaborated in the section on indirect imaging, the positions 1 and 2 in the observation plane Σ are in practise not pointlike, but encompass a finite aperture in the form of a telescope element of finite size, say a radio dish with diameter D. This dish has then a diffraction sized beam of λ/D. In that case the Van Cittert-Zernike relation needs to be "weighted" with the telescope element (single dish) transfer function $H(\vec{\Omega})$. For a circular dish antenna $H(\vec{\Omega})$ is the *Airy brightness function*, well known from the diffraction of a circular aperture and detailed in a previous section. The Van Cittert-Zernike relations now become:

$$\tilde{\Gamma}'(\vec{r}) = \int\int_{\text{source}} I(\vec{\Omega})H(\vec{\Omega})e^{\frac{2\pi i\vec{\Omega}.\vec{r}}{\lambda}}d\vec{\Omega} \tag{10.60}$$

$$I(\vec{\Omega})H(\vec{\Omega}) = \lambda^{-2}\int\int_{\Sigma\text{-plane}} \tilde{\Gamma}'(\vec{r})e^{-\frac{2\pi i\vec{\Omega}.\vec{r}}{\lambda}}d\vec{r} \tag{10.61}$$

The field of view scales with λ/D, e.g. if λ decreases the synthesis resolution improves but the field of view reduces proportionally!
So, in aperture synthesis the incoming beams from antenna dish 1 and antenna dish 2 are fed into a *correlator (multiplier)* that produces as output the product $\tilde{E}_1(t)\tilde{E}_2^*(t)$. This output is subsequently fed into an *integrator/averager* that produces the expectation value $\mathbf{E}\left\{\tilde{E}_1(t)\tilde{E}_2^*(t)\right\} = \tilde{\Gamma}'(\vec{r})$. By applying the Fourier transform given in (10.61), and correcting for the beam profile of the single dish $H(\vec{\Omega})$, the source brightness distribution $I(\vec{\Omega})$ can be reconstructed.
Important: Indirect imaging with an aperture synthesis system is limited to measuring image details within the *single pixel* defined by the beam profile of an individual telescope element, i.e. a single dish!

10.4.1 Quasi-monochromatic point source: spatial response function (PSF) and optical tranfer function (OTF) of a multi-element interferometer

The pupil function of a linear array comprising N circular apertures with diameter d, aligned along a baseline direction $\vec{b}$ (unit vector) and equally spaced at a distance $|\vec{s}| = \vec{b}\cdot\vec{s}$ can be written as:

$$\begin{aligned} P(\vec{\zeta}) \;=\; & \left[\Pi\left(\frac{\lambda\vec{\zeta}}{d}\right) + \Pi\left\{\frac{\lambda}{d}\left(\vec{\zeta}-\frac{\vec{s}}{\lambda}\right)\right\} + \Pi\left\{\frac{\lambda}{d}\left(\vec{\zeta}-2\cdot\frac{\vec{s}}{\lambda}\right)\right\} + \ldots \right. \\ & \left. \ldots + \Pi\left\{\frac{\lambda}{d}\left(\vec{\zeta}-(N-1)\cdot\frac{\vec{s}}{\lambda}\right)\right\} \;=\; \sum_{n=0}^{N-1}\Pi\left\{\frac{\lambda}{d}\left(\vec{\zeta}-n\cdot\frac{\vec{s}}{\lambda}\right)\right\}\right] \end{aligned} \tag{10.62}$$

Applying the shift and scaling theorems from Fourier theory, i.e. if $f(x) \Leftrightarrow F(s)$ then $f[a(x-b)] \Leftrightarrow \left(e^{-2\pi ibs}/a\right)F(s/a)$, we find for the amplitude of the diffracted field:

$$\tilde{a}(|\,\vec{\theta}\,|) \;=\; \left(\frac{\lambda}{R}\right)\left[\frac{1}{4}\pi(d/\lambda)^2\right]\left[\frac{2J_1(\pi|\,\vec{\theta}\,|d/\lambda)}{\pi|\,\vec{\theta}\,|d/\lambda}\right]\cdot\left[1 + e^{-i(2\pi\vec{\theta}\cdot\vec{s}/\lambda)} + \left(e^{-i(2\pi\vec{\theta}\cdot\vec{s}/\lambda)}\right)^2 + \ldots\right.$$

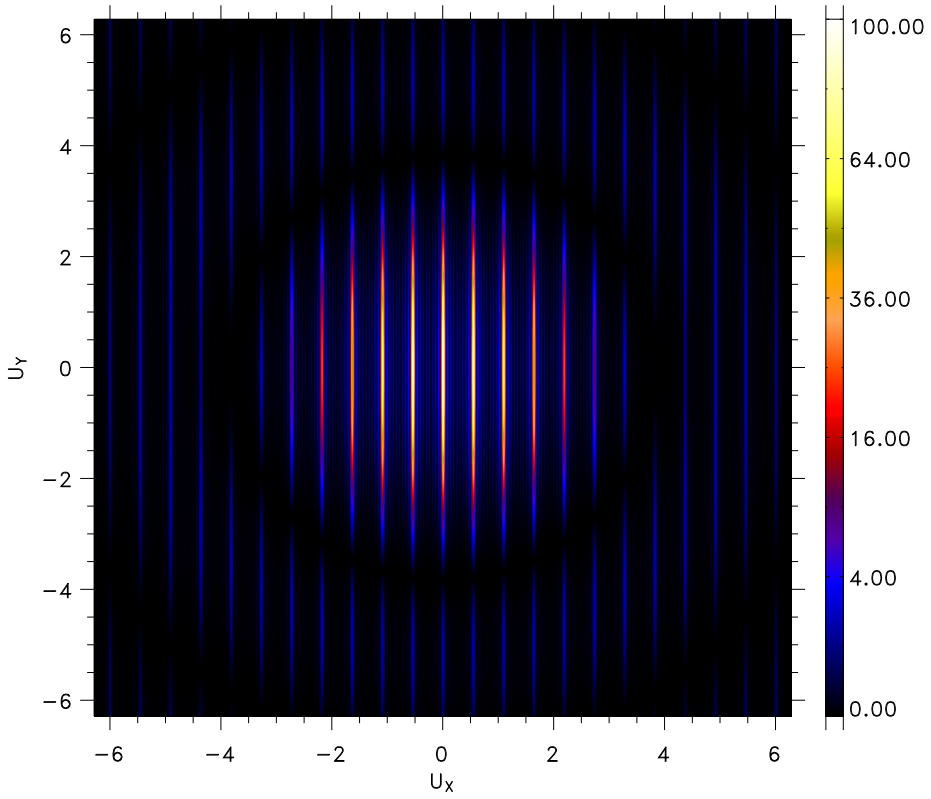

Figure 10.12: *PSF of a 10-element interferometer with circular apertures in pseudo-color as a function of the 2D-position vector $\vec{u}$ (λ-invariant display).*

$$\ldots + \left(e^{-i(2\pi\vec{\theta}\cdot\vec{s}/\lambda)}\right)^{N-1}\Big]$$

$$= \left(\frac{\lambda}{R}\right)\left[\frac{1}{4}\pi(d/\lambda)^2\right]\left[\frac{2J_1(\pi|\,\vec{\theta}\,|d/\lambda)}{\pi|\,\vec{\theta}\,|d/\lambda}\right]\sum_{n=0}^{N-1}\left(e^{-i(2\pi\vec{\theta}\cdot\vec{s}/\lambda)}\right)^n \qquad (10.63)$$

The sum of the *geometric series* of N complex exponentials, accomodating the accumulating phase shifts introduced by the addition of each subsequent telescope element equals:

$$\sum_{n=0}^{N-1}\left(e^{-i(2\pi\vec{\theta}\cdot\vec{s}/\lambda)}\right)^n = \frac{e^{-iN(2\pi\vec{\theta}\cdot\vec{s}/\lambda)}-1}{e^{-i(2\pi\vec{\theta}\cdot\vec{s}/\lambda)}-1}$$

$$= \frac{e^{-iN(2\pi\vec{\theta}\cdot\vec{s}/2\lambda)}}{e^{-i(2\pi\vec{\theta}\cdot\vec{s}/2\lambda)}}\frac{\left(e^{-iN(2\pi\vec{\theta}\cdot\vec{s}/2\lambda)} - e^{iN(2\pi\vec{\theta}\cdot\vec{s}/2\lambda)}\right)}{\left(e^{-i(2\pi\vec{\theta}\cdot\vec{s}/2\lambda)} - e^{i(2\pi\vec{\theta}\cdot\vec{s}/2\lambda)}\right)} = e^{-i(N-1)\pi\vec{\theta}\cdot\vec{s}/\lambda}\left[\frac{\sin N(\pi\vec{\theta}\cdot\vec{s}/\lambda)}{\sin(\pi\vec{\theta}\cdot\vec{s}/\lambda)}\right] \qquad (10.64)$$

The PSF for the diffracted intensity distribution follows from the relation
$\text{PSF} = \tilde{a}(|\vec{\theta}|)\cdot\tilde{a}^*(|\vec{\theta}|)$:

$$\text{PSF} = \left(\frac{\lambda}{R}\right)^2\left[\frac{1}{4}\pi\,(d/\lambda)^2\right]^2\left[\frac{2J_1(|\vec{u}\,|)}{|\vec{u}\,|}\right]^2\frac{\sin^2 N(\vec{u}\cdot\vec{s}/d)}{\sin^2(\vec{u}\cdot\vec{s}/d)} \quad \text{with} \quad \vec{u} = \pi\vec{\theta}\,d/\lambda \qquad (10.65)$$

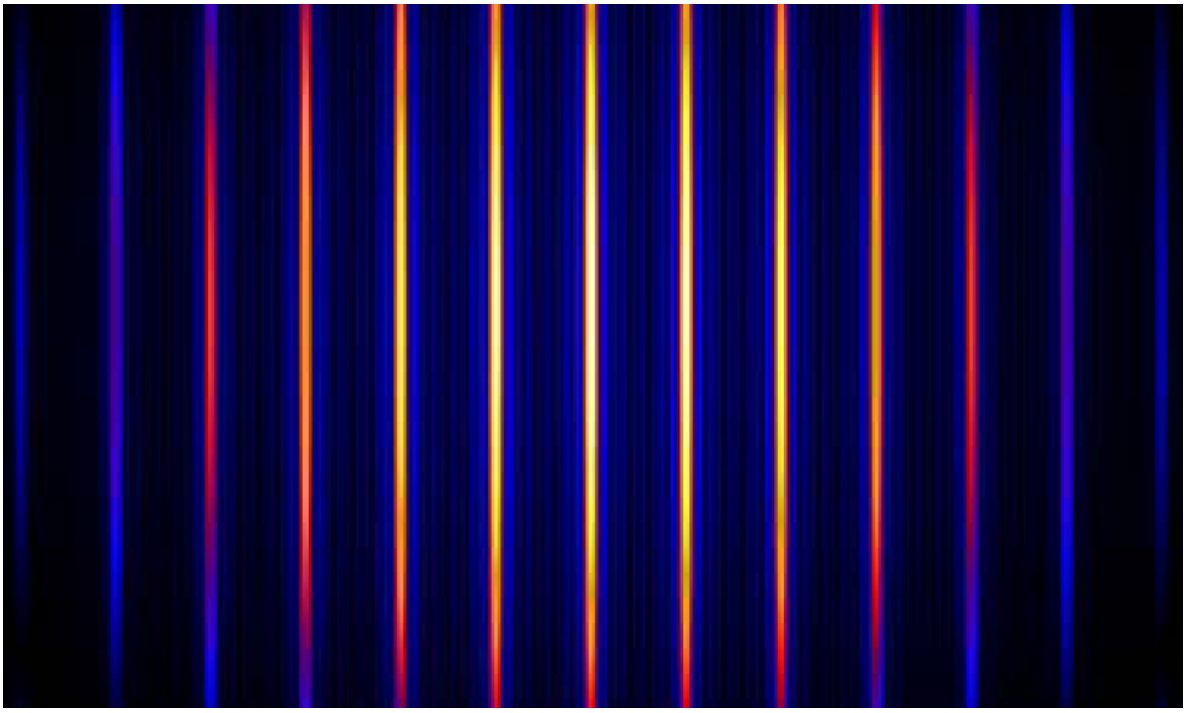

Figure 10.13: *Magnification of the central part of figure 10.12, clearly showing the locations of the subsidiary maxima and minima.*

For $N = \mathbf{1}$, we recover the Airy brightness function for a single circular aperture, for $N = \mathbf{2}$ (Michelson) we have $\sin^2 N(\vec{u}\cdot\vec{s}/d)/\sin^2(\vec{u}\cdot\vec{s}/d) = [2\sin(\vec{u}\cdot\vec{s}/d)\cos(\vec{u}\cdot\vec{s}/d)]^2 / \sin^2(\vec{u}\cdot\vec{s}/d) = 4\cos^2(\vec{u}\cdot\vec{s}/d)$, commensurate with expression (10.38).
For N apertures, **maximum** constructive interference occurs for $\sin N(\pi\vec{\theta}\cdot\vec{s}/\lambda)/\sin(\pi\vec{\theta}\cdot\vec{s}/\lambda) = N$, that is when:

$$\frac{\vec{\theta}\cdot\vec{s}}{\lambda} = n\,(= 0, \pm1, \pm2, \ldots) \quad \rightarrow \quad |\vec{\theta}| = \frac{n\lambda}{|\vec{s}|\cos\phi} \tag{10.66}$$

These so-called *principal maxima* are apparently found at the same $|\vec{\theta}|$-locations, regardless of the value of $N \geq 2$.
Minima, of **zero** flux density, exist whenever $\sin N(\pi\vec{\theta}\cdot\vec{s}/\lambda)/\sin(\pi\vec{\theta}\cdot\vec{s}/\lambda) = 0$, i.e. for:

$$\begin{aligned} \frac{\vec{\theta}\cdot\vec{s}}{\lambda} &= \pm\frac{1}{N}, \pm\frac{2}{N}, \pm\frac{3}{N}, \ldots, \pm\frac{N-1}{N}, \pm\frac{N+1}{N}, \ldots \\ \Rightarrow \quad |\vec{\theta}| &= \frac{n\lambda}{N|\vec{s}|\cos\phi}, \quad \text{for} \quad n = \pm1, \pm2, \ldots \quad \text{but} \quad n \neq kN \;\; (k = 0, \pm1, \pm2, \ldots \end{aligned} \tag{10.67}$$

with $\cos\phi$ the angle between $\vec{\theta}$ and the baseline vector $\vec{s}$.
Between consecutive principal maxima there will therefore be **N-1 minima**. Since between each pair of minima there will have to be a **subsidiary maximum**, i.e. a total of **N-2 subsidiary maxima** between consecutive principal maxima. The first two terms in the expression for the PSF give the normalisation for $|\vec{\theta}| = 0$. The other terms represent a corrugated 2-dimensional Airy brightness distribution, intensity-modulated along the direction of the baseline vector $\vec{s}$ with a periodicity $(\Delta\theta)_s = \lambda/|\vec{s}|$ of narrow bright principal maxima

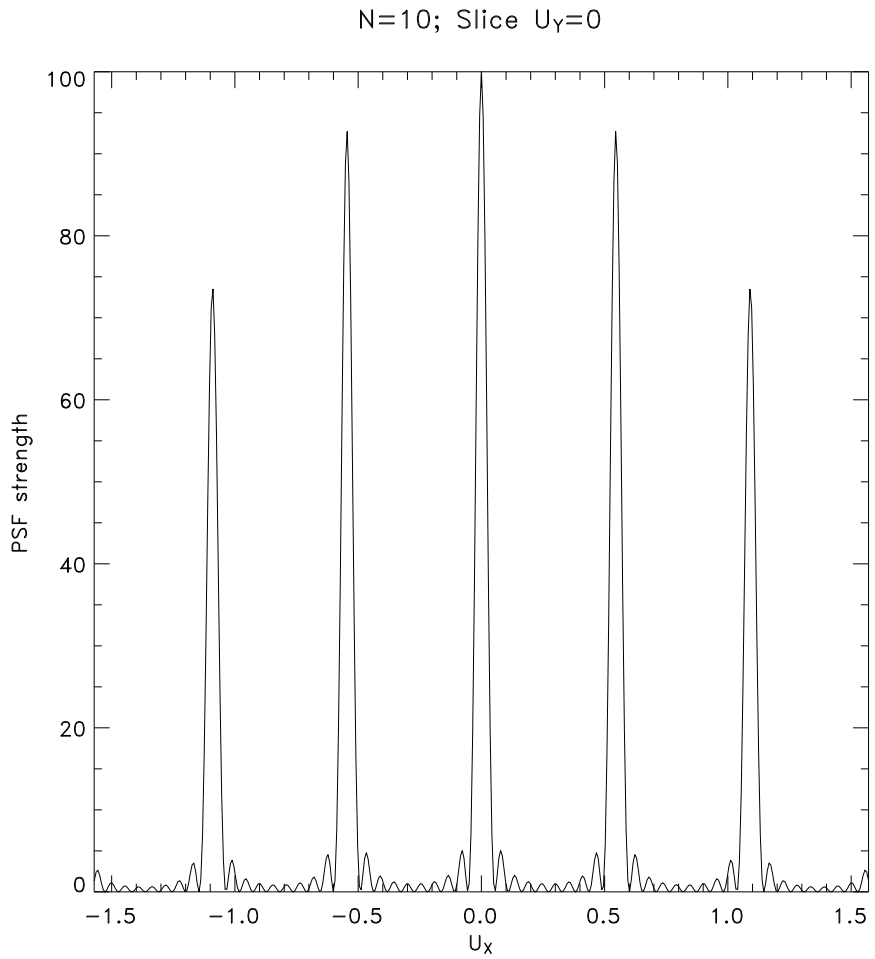

Figure 10.14: *Cross-section of the central part of the PSF for a 10-element interferometer, delineating the brightness profiles of the principal maxima and the subsidiary maxima and minima.*

and with a periodicity $(\Delta\theta)_{Ns} = \lambda/(N|\vec{s}|)$ of narrow weak subsidiary maxima, interleaved with zero-intensity minima.
The corrugated 2-dimensional Airy brightness distribution for $N = 10$, yet again for $d = 25$ meters and $|\vec{s}| = 144$ meters, is displayed (λ-invariant) in pseudo-color code as a function of the 2D-position vector $\vec{u}$ in figure 10.12. Also shown, in figure 10.13, is a magnification of the central part of the PSF that more clearly shows the interleaved subsidiary maxima and minima. A cross-section for $u_y = 0$ of the central part of the interferogram, delineating the profiles of the sharply peaked principal maxima and the adjacent series of subsidiary maxima and minima, is presented in figure 10.14.

The OTF for an array of N circular apertures can be obtained from the autocorrelation of the pupil function given in expression (10.62):

$$H_\lambda(\vec{\zeta}, N\vec{s}/\lambda) \;=\; \left(\frac{\lambda}{R}\right)^2 \left[\sum_{n=0}^{N-1} \Pi\left\{\frac{\lambda}{d}\left(\vec{\zeta} - n\cdot\frac{\vec{s}}{\lambda}\right)\right\}\right] * \left[\sum_{m=0}^{N-1} \Pi\left\{\frac{\lambda}{d}\left(\vec{\zeta} - m\cdot\frac{\vec{s}}{\lambda}\right)\right\}\right]$$

$$= \left(\frac{\lambda}{R}\right)^2 \sum_{n=0}^{N-1}\sum_{m=0}^{N-1} A_{nm}(\vec{\zeta},\, \vec{s}/\lambda) \tag{10.68}$$

in which A_{nm} represents an element of the Nx N autocorrelation matrix $\mathbf{A}$, that is given by:

$$A_{nm}(\vec{\zeta}\,, \vec{s}/\lambda) \,=\, \int\int_{pupil\,plane} \Pi\left\{\frac{\lambda}{d}\left(\vec{\zeta}' - n\cdot\frac{\vec{s}}{\lambda}\right)\right\} \Pi\left\{\frac{\lambda}{d}\left(\vec{\zeta}' - \vec{\zeta} - m\cdot\frac{\vec{s}}{\lambda}\right)\right\} d\vec{\zeta}' \tag{10.69}$$

Values $A_{nm} \neq 0$ are given by Chinese-hat functions as derived for a single circular aperture in Chapter **7** of the OAF1 course. However in the multi aperture case here, we have a series of **principal maxima** in the $H_\lambda(\vec{\zeta}\,, \vec{s}/\lambda)$ plane (= the uv-plane representing 2-dimensional frequency(Fourier) space) at spatial frequency values:

$$\vec{\zeta}_{max} \,=\, \vec{\zeta} - k\cdot\frac{\vec{s}}{\lambda} \;\text{ with }\; k = n - m = 0, \pm1, \pm2, \ldots, \pm(N-2), \pm(N-1) \tag{10.70}$$

Hence we can replace A_{nm} by A_k, where the single index k refers to the *diagonals* of the autocorrelation matrix $\mathbf{A}$: $k = 0$ refers to the main diagonal, $k = \pm1$ to the two diagonals contiguous to the main diagonal and so on. The analytical expression for the diagonal terms A_k can now be computed in the same way as for a single circular aperture, however in this case we need vector notation:

$$A_k \,=\, \frac{1}{2}\left(\frac{d}{\lambda}\right)^2 \cdot$$
$$\cdot \left[\arccos\left(\frac{\lambda}{d}\left|\vec{\zeta} - k\cdot\frac{\vec{s}}{\lambda}\right|\right) - \left(\frac{\lambda}{d}\left|\vec{\zeta} - k\cdot\frac{\vec{s}}{\lambda}\right|\right)\left(1 - \left(\frac{\lambda}{d}\left|\vec{\zeta} - k\cdot\frac{\vec{s}}{\lambda}\right|\right)^2\right)^{\frac{1}{2}}\right] \Pi\left(\frac{\lambda}{2d}\left|\vec{\zeta} - k\cdot\frac{\vec{s}}{\lambda}\right|\right) \tag{10.71}$$

which we rewrite in terms of Chinese-hat functions $\hat{C}_k(\vec{\zeta} - k\cdot\vec{s}/\lambda)$ normalised to unit aperture area:

$$A_k \,=\, \frac{1}{4}\pi\left(\frac{d}{\lambda}\right)^2 \hat{C}_k(\vec{\zeta} - k\cdot\vec{s}/\lambda) \tag{10.72}$$

The sum over all elements of matrix $\mathbf{A}$ can now be obtained from:

$$\sum_{n=0}^{N-1}\sum_{m=0}^{N-1} A_{nm} \,\equiv\, A_{sa} \sum_{k=-(N-1)}^{N-1} (N - |k|)\hat{C}_k(\vec{\zeta} - k\cdot\vec{s}/\lambda) \tag{10.73}$$

$$\text{Sum check:} \quad \sum_{k=-(N-1)}^{N-1} (N - |k|) = N + 2\sum_{k=1}^{N-1}(N-k)$$

$$= N + \frac{1}{2}(N-1)\,[2(2N-2) - 2(N-2)] = N + N^2 - N = N^2,$$

compliant with the required total number of matrix elements! The quantity $A_{sa} = \frac{1}{4}\pi(d/\lambda)^2$ represents the geometrical area of a single telescope element.
Hence, we arrive at the following expression for the OTF of the array:

$$H_\lambda(\vec{\zeta}\,, N\vec{s}/\lambda) \,=\, \left(\frac{\lambda}{R}\right)^2 N A_{sa} \sum_{k=-(N-1)}^{N-1} \frac{(N - |k|)}{N}\, \hat{C}_k(\vec{\zeta} - k\cdot\vec{s}/\lambda) \quad \text{with} \tag{10.74}$$

$$\hat{C}_k(\vec{\zeta} - k\cdot\vec{s}/\lambda) =$$
$$= \frac{2}{\pi}\left[\arccos\left(\frac{\lambda}{d}\left|\vec{\zeta} - k\cdot\frac{\vec{s}}{\lambda}\right|\right) - \left(\frac{\lambda}{d}\left|\vec{\zeta} - k\cdot\frac{\vec{s}}{\lambda}\right|\right)\left(1 - \left(\frac{\lambda}{d}\left|\vec{\zeta} - k\cdot\frac{\vec{s}}{\lambda}\right|\right)^2\right)^{\frac{1}{2}}\right] \Pi\left(\frac{\lambda}{2d}\left|\vec{\zeta} - k\cdot\frac{\vec{s}}{\lambda}\right|\right) \tag{10.75}$$

The geometrical term NA_{sa} reflects the total geometrical collecting area of the telescope array (N times the area of a single aperture A_{sa}) and the term $(\lambda/R)^2$ accomodates the attenuation due to the spherical expansion of the wave field.
The OTF for the spatial frequency throughput of the aperture array is described by a linear array of discrete spatial frequency domains in the uv-plane, characterised by Chinese-hat functions centered at zero frequency and at multiples of the baseline vector $\vec{s}/\lambda$, that specifies the equidistance (magnitude and direction) between adjacent apertures. The peak transfer declines linearly with increasing mutual separation between aperture elements relative to the zero-frequency response, i.e. proportional to $(N - |k|)/N$ for spatial frequencies centered around $k \cdot \vec{s}/\lambda$. This can be easily explained by considering the monotonously decreasing number of aperture elements, and hence the associated array collecting power, involved at larger baseline values. For the maximum available baseline $(N-1)\vec{s}/\lambda$ this throughput reduction amounts to $1/N$.

Intermezzo: Verify that $H_\lambda(\vec{\zeta}, N\vec{s}/\lambda) \Leftrightarrow$ PSF(N-apertures)**!!**

Proof: Application of the *shift theorem* yields for the Fourier transform of the single-aperture-weighted ($A_{sa} = \frac{1}{4}\pi\,(d/\lambda)^2$) Chinese-hat function at baseline position $k \cdot \vec{s}/\lambda$ the following expression for its FT:

$$\frac{1}{4}\pi\,(d/\lambda)^2\,C_k(\vec{\zeta} - k \cdot \vec{s}/\lambda) \;\Leftrightarrow\; \left[\frac{1}{4}\pi\,(d/\lambda)^2\right]^2 \left[\frac{2J_1(|\vec{u}\,|)}{|\vec{u}\,|}\right]^2 e^{-ik(2\pi\vec{\theta}\cdot\vec{s}/\lambda)} \tag{10.76}$$

Putting $x \equiv 2\pi\vec{\theta}\cdot\vec{s}/\lambda$, the Fourier transform of (10.74) can be expressed as:

$$\begin{aligned}\mathrm{FT}\left[H_\lambda(\vec{\zeta}, N\vec{s}/\lambda)\right] \;&=\; \left(\frac{\lambda}{R}\right)^2 \left[\frac{1}{4}\pi\,(d/\lambda)^2\right]^2 \left[\frac{2J_1(|\vec{u}\,|)}{|\vec{u}\,|}\right]^2 \cdot \\ \cdot \left[N\left(1 + \sum_{k=1}^{N-1} e^{ikx} + \sum_{k=1}^{N-1} e^{-ikx}\right) - \left(\sum_{k=0}^{N-1} ke^{ikx} + \sum_{k=0}^{N-1} ke^{-ikx}\right)\right]\end{aligned} \tag{10.77}$$

The first two sums of (10.77)involve simple *geometric* series and can be easily calculated, i.e.:

$$\sum_{k=1}^{N-1} e^{ikx} \;=\; \frac{e^{ix}\left(e^{i(N-1)x} - 1\right)}{e^{ix} - 1} = \frac{e^{i(N-\frac{1}{2})x} - e^{ix/2}}{2i\sin(x/2)} \qquad \text{and:}$$

$$\sum_{k=1}^{N-1} e^{-ikx} \;=\; \frac{e^{-ix}\left(e^{-i(N-1)x} - 1\right)}{e^{-ix} - 1} = -\left(\frac{e^{-i(N-\frac{1}{2})x} - e^{-ix/2}}{2i\sin(x/2)}\right)$$

Hence, after some rearrangement of the complex exponentials, this results in a real function:

$$N\left(1 + \sum_{k=1}^{N-1} e^{ikx} + \sum_{k=1}^{N-1} e^{-ikx}\right) = N\,\frac{\sin\left[(2N-1)(x/2)\right]}{\sin(x/2)} \tag{10.78}$$

The third and the fourth sum in equation (10.77) involve a combination of an *arithmetic* and a *geometric* series (a so-called *arithmetico-geometric* series). These sums can be simply derived by differentation of the expression for the sum of the geometric series, resulting in:

$$\sum_{k=0}^{N-1} ke^{ikx} \;=\; \frac{Ne^{\,i(N-1)x} - (N-1)\,e^{\,iNx} - 1}{4\sin^2(x/2)} \qquad \text{and:}$$

$$\sum_{k=0}^{N-1} ke^{-ikx} \;=\; \frac{Ne^{\,-i(N-1)x} - (N-1)\,e^{\,-iNx} - 1}{4\sin^2(x/2)}$$

Straightforward recombination of the complex exponentials again results in a (trigonometric) real function:

$$\sum_{k=0}^{N-1} ke^{ikx} + \sum_{k=0}^{N-1} ke^{-ikx} = \frac{N\cos(N-1)x - (N-1)\cos Nx - 1}{2\sin^2(x/2)} \tag{10.79}$$

Combining expressions (10.78) and (10.79), we arrive at :

$$\begin{aligned}
&\left[N\left(1 + \sum_{k=1}^{N-1} e^{ikx} + \sum_{k=1}^{N-1} e^{-ikx}\right) - \left(\sum_{k=0}^{N-1} ke^{ikx} + \sum_{k=0}^{N-1} ke^{-ikx}\right)\right] = \\
&= \frac{2N\sin(x/2)\sin(N-\frac{1}{2})x - N\cos(N-1)x + (N-1)\cos Nx + 1}{2\sin^2(x/2)} = \\
&= \frac{N\sin x\sin Nx + N\cos x\cos Nx - \cos Nx - N\cos x\cos Nx - N\sin x\sin Nx + 1}{2\sin^2(x/2)} = \\
&= \frac{1-\cos Nx}{2\sin^2(x/2)} = \frac{2\sin^2(Nx/2)}{2\sin^2(x/2)}
\end{aligned} \tag{10.80}$$

Substituting $x \equiv 2\pi\vec{\theta}\cdot\vec{s}/\lambda \equiv 2(\vec{u}\cdot\vec{s}/d)$, yields:

$$\mathrm{FT}\left[H_\lambda(\vec{\zeta}, N\vec{s}/\lambda)\right] = \left(\frac{\lambda}{R}\right)^2 \left[\frac{1}{4}\pi\,(d/\lambda)^2\right]^2 \left[\frac{2J_1(|\vec{u}\,|)}{|\vec{u}\,|}\right]^2 \frac{\sin^2 N(\vec{u}\cdot\vec{s}/d)}{\sin^2(\vec{u}\cdot\vec{s}/d)} \quad \text{Q.E.D.} \tag{10.81}$$

Note: The modulation term $\sin^2 N(\vec{u}\cdot\vec{s}/d)/\sin^2(\vec{u}\cdot\vec{s}/d)$ can be simplified for low N-values:

$$\begin{aligned}
&= 1 && \text{for N=1} \\
&= 4\cos^2(\vec{u}\cdot\vec{s}/d) && \text{for N=2} \\
&= [2\cos 2(\vec{u}\cdot\vec{s}/d) + 1]^2 && \text{for N=3} \\
&= 8\cos^2 2(\vec{u}\cdot\vec{s}/d)\cdot[1 + \cos 2(\vec{u}\cdot\vec{s}/d)] && \text{for N=4}
\end{aligned} \tag{10.82}$$

End Intermezzo

10.4.2 Earth Rotation Aperture Synthesis (ERAS)

By employing the rotation of the earth, the baseline vectors $k\cdot\vec{s}/\lambda$ of the linear N-element interferometer array, as defined in the previous section, will scan the YZ-plane displayed in figure (10.10) in case the X-axis is lined up with the North polar axis, i.e. in this particular geometry the X-coordinate of the baseline vectors is zero. The principal maxima or 'grating lobes' in the PSF of a multiple aperture array, as computed in the preceding section, will now manifest themselves as concentric annuli around a central source peak at angular distances $k\cdot\lambda/|\vec{s}\,|$. If the circular scans in the YZ-plane are too widely spaced, i.e. if $|\vec{s}\,|$ is larger than the single dish diameter, the (2-dimensional) Nyquist criterion is not respected and undersampling of the spatial frequency uv-plane (=YZ-plane) occurs. Consequently, the grating lobes will show up within the field of view defined by the single-dish beam profile. This can be avoided by decreasing the sampling distance $|\vec{s}\,|$. In the following section we shall now demonstrate these notions with the concrete configuration of the Westerbork Synthesis Radio Telescope.

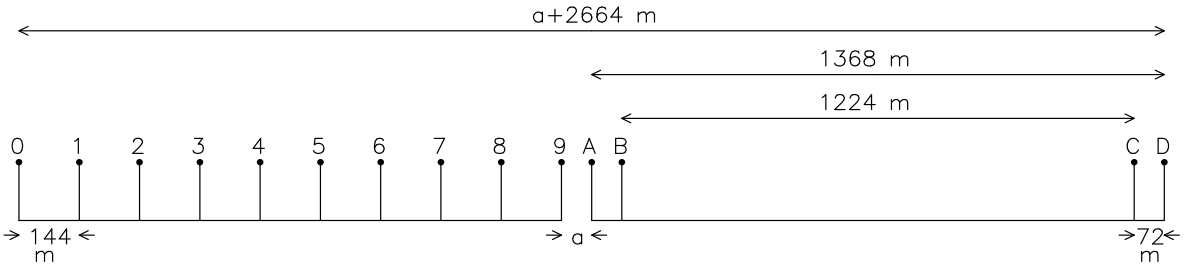

Figure 10.15: *Configuration of the Westerbork Synthesis Radio Telescope.*

10.4.3 The Westerbork Synthesis Radio Telescope (WSRT)

The WSRT consists of 14 parabolic antenna's, with single dish diameters D of 25 meter. They are accurately lined up along the East-West direction with an overall length of ≈ 2750 meter. Ten antenna's (numbers 0 thru 9) are fixed with a mutual distance of 144 meter. The other four antenna's (A thru D) can be moved collectively with respect to the fixed array, without altering their mutual distance, i.e. the variable distance between antenna's 9 and A can be preselected as a suitable baseline increment $|\vec{s}| = \triangle L$ (Figure 10.15). These 14 antenna's comprise 40 simultaneously operating interferometers. Employing the rotation of the earth, the full antenna array is rotated in a plane containing Westerbork perpendicular to the rotation axis of the earth. With reference to figure (10.10) this implies that in this geometry we are limited to sources near the North polar axis, all single dishes are thus pointed in that direction. In practise, the standard distance between antenna's 9 and A equals 72 meters. Consequently, after half a rotation of the earth the YZ-plane is covered with 38 concentric semi-circles with radii ranging from $L_{min} = 72$ meters to $L_{max} = 2736$ meters, with increments of $\triangle L = 72$ meters. The *WSRT-correlators* integrate and average over 10 seconds, this implies sampling of the concentric semi-circles every 1/24 degrees. After 12 hours, half the YZ-plane has been covered. The other half need not be covered, it can be found by mirroring the first half since $I(\vec{\Omega})$ is a real function.
The brightness distribution $I(\vec{\Omega})$ can now be reconstructed by Fourier inversion according to expression (10.44). Since we have only obtained samples of the spatial coherence function $\tilde{\Gamma}(\vec{r})$, the integral of expression (10.44) is replaced by a sum. Moreover, one normally applies in addition a *weighting function* to get a considerable reduction of the side lobes, this goes slightly at the expense of the ultimate angular resolution. This is expressed in terms of a degradation factor $\alpha \geq 1$. The simplest form of such a weighting function is a triangular shaped, circular symmetric, function (i.e. a cone), the attenuation effect on the side lobes is called *apodisation*. Leaving any constants aside for the moment , we obtain $\hat{I}(\vec{\Omega})$:

$$\hat{I}(\vec{\Omega}) = \sum_k w(\vec{r}_k)\tilde{\Gamma}(\vec{r}_k)e^{-\frac{2\pi i \vec{\Omega}.\vec{r}_k}{\lambda}} \tag{10.83}$$

with $w(\vec{r}_k)$ the weighting (apodisation) function.
Expression (10.83) yields a radio map on a discrete grid in $\vec{\Omega}$-space. The cell size of this grid (pitch) is chosen in such a way that oversampling of the spatial resolution of the array is achieved, so that *contour plots* can be constructed.
Note: The reconstructed $\hat{I}(\vec{\Omega})$ needs to be corrected for the single dish response function $H(\vec{\Omega})$, see equation (10.61).
If we consider half an earth rotation, the sum in (10.83) involves ≈ 165.000 numbers (i.e. 38 semi-circles, 12x60x6 correlator samples/semi-circle). This sum will have to be taken for

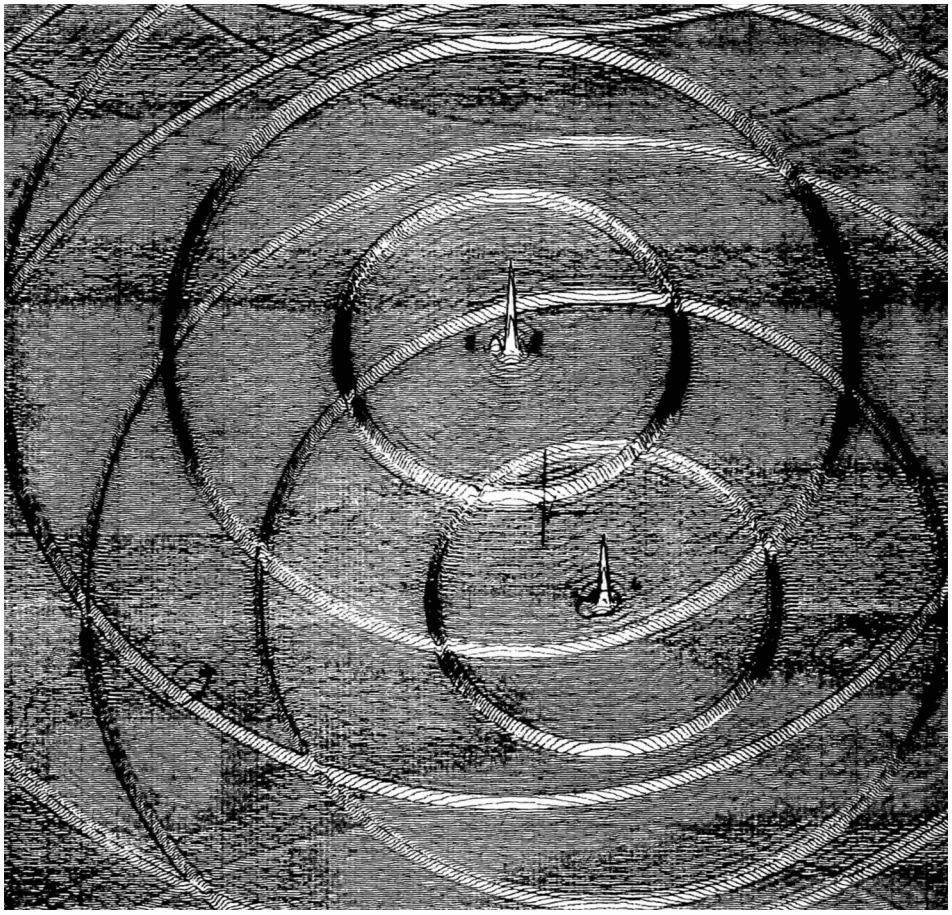

Figure 10.16: *A reconstructed "dirty" radio map showing central source peaks and grating lobes of increasing order. Credit Westerbork Radio Observatory.*

roughly the same number of image points in $\vec{\Omega}$-space. This task is accomplished by using the Fast Fourier Transform algorithm.

The Point Spread Function (PSF):

Taking a point source S as the quasi monochromatic radiation source, the spatial frequency response function of the rotated interferometer array in the uv-plane can be obtained explicitly from expression (10.74) for the OTF by implementing the geometry of concentric scans. In that case, owing to the circular symmetry, the vectorial expression $H_\lambda(\vec{\zeta}, N\vec{s}/\lambda)$ can be replaced by a, radially symmetric, scalar expression $H_\lambda(p, N\triangle L/\lambda)$, with the scalar p the (λ-normalised) spatial frequency variable ($= |\vec{\zeta}|$) and $\triangle L$ the baseline increment of the array ($= |\vec{s}|$). Although an exact expression for the scalar function $H_\lambda(p, N\triangle L/\lambda)$ would involve integration along one coordinate of the two-dimensional Chinese-hat function, a straightforward one-dimensional cross-section constitutes an adequate approximation. Hence we can write:

$$H_\lambda(p, N\triangle L/\lambda) = \left(\frac{\lambda}{R}\right)^2 NA_{sa} \sum_{k=-(N-1)}^{N-1} \frac{(N-|k|)}{N}\, \hat{C}_k(p - k\cdot\triangle L/\lambda) \qquad (10.84)$$

The PSF derives from the Fourier transform of $H_\lambda(p\,, N\triangle L/\lambda)$. Following the approach outlined in the *intermezzo* above, we arrive at:

$$PSF_{ERAS} \;=\; \left(\frac{\lambda}{R}\right)^2 \left[\frac{1}{4}\pi\,(d/\lambda)^2\right]^2 \left[\frac{2J_1(u)}{u}\right]^2 \frac{\sin^2 N(u\triangle L/D)}{\sin^2(u\triangle L/D)} \tag{10.85}$$

where we have again utilised the reduced angular variable $u = \pi\theta D/\lambda$, θ represents the, radially symmetric, diffraction angle.
Evaluation of expression (10.85) reveals two main image components:
A Central Peak:
This distribution is rather similar to the *Airy brightness pattern*, with a typical breadth, i.e. spatial resolution:

$$\triangle\theta = \frac{\lambda}{2L_{max}} radians \tag{10.86}$$

with $2L_{max}$ the maximum diameter of the array in the YZ-plane. In the derivation of (10.85), no weighting function was applied. If a weighting function is applied for efficient apodisation, expression (10.86) needs to be multiplied by a degradation factor $\alpha = 1 - 1.5$ to accomodate the loss in ultimate angular resolution. Moreover, moving outward, the sidelobes in (10.85) will progressively be reduced depending on the particular choice of the weighting function.
Concentric Grating Lobes:
The angular distances of these annuli from the central peak follow from the location of the *principal maxima* given by the modulation term $\sin^2 N(u\triangle L/D)/\sin^2(u\triangle L/D)$ in expression (10.85). For an N-element array with increment $\triangle L$, these angular positions are given by:

$$\theta_{grating} = \frac{\lambda}{\triangle L}, 2\frac{\lambda}{\triangle L}, ..., (N-1)\frac{\lambda}{\triangle L} \tag{10.87}$$

A typical source field containing these grating lobes is shown in figure (10.16).

It is clear from this figure that severe undersampling of the YZ-plane has occurred since the grating lobes are well within the field of view. For the WSRT, one way to remedy these imperfections in the PSF is by decreasing the distance between antenna's 9 and A during the second half rotation of the earth. Combined with the first half rotation, a 36 meter increment coverage is achieved at the expense of doubling the observation time from 12 to 24 hours. In the same way, combining four half rotations in 48 hours, we can increase the coverage to 18 meter increments. Since the single dish diameter D equals 25 meter, no empty space is now left in the YZ-plane, the undersampling is corrected and the grating lobes have been moved outside the field of view defined by the single dish beam profile. This is summarized in the following tables that show exposure times, maximum baselines and increments, and at four different radio wavelengths single dish fields of view, central peak angular resolutions for $\alpha = 1.5$, and angular distances of the grating lobes.

Exposure(hours)	a (meter)	L_{min} (meter)	$\triangle L$ (meter)	L_{max} (meter)
1x12	72	72	72	2736
2x12	36,72	36	36	2736
4x12	36,54,72,90	36	18	2754

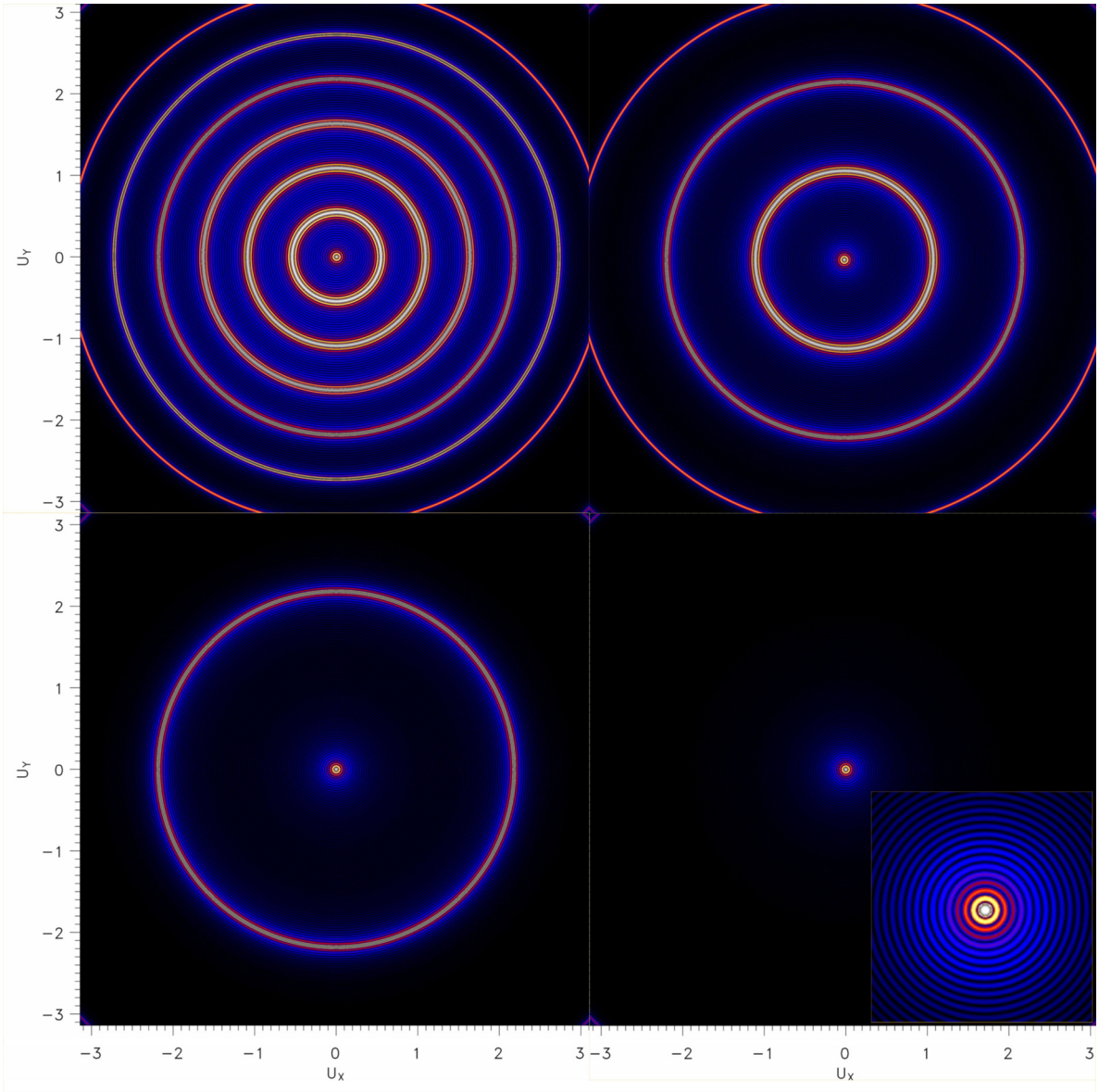

Figure 10.17: *Position of the concentric grating rings in the PSF for various sampling densities of the uv-plane. FOV:* $-\lambda/D \leq \theta_{x,y} \leq \lambda/D$ $(-\pi \leq u_{x,y} \leq \pi)$. *Upper left:* $\triangle L/D = 144/25$, *upper right:* $\triangle L/D = 72/25$, *lower left:* $\triangle L/D = 36/25$, *lower right:* $\triangle L/D = 18/25$. *The insert in the lower right panel shows a blow-up of the central peak image, displaying the circular subsidiary maxima and minima.*

λ (cm)	6	21	49	92
f (MHz)	5000	1420	612	326
Single dish pixel λ/D (arcsec)	500	1800	4200	7600
Resolution $\alpha\lambda/(2L_{max})$ (arcsec)	3	11.5	27	50
Grating lobes $\lambda/(\triangle L = 72$ m) (arcsec)	172	7600	1405	2640
Grating lobes $\lambda/(\triangle L = 36$ m) (arcsec)	344	1205	2810	5270
Grating lobes $\lambda/(\triangle L = 18$ m) (arcsec)	688	2410	5620	10540

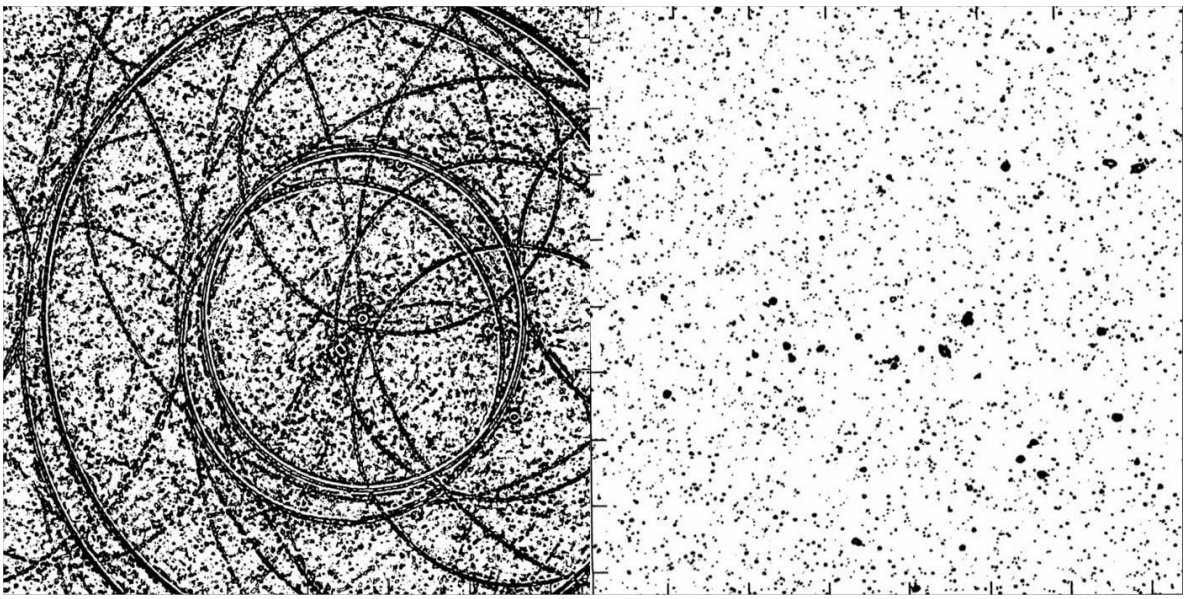

Figure 10.18: *Applying the CLEAN method for improving dirty radio maps. This is a radio map taken at* $\lambda = 50$ *cm, with a* $\triangle L = 36$ *meter increment. Left panel before CLEAN, right panel after CLEAN. Credit Westerbork Radio Observatory.*

As is clear from these tables, the grating lobes can only be moved outside the single dish pixel if the empty spaces between the samplings are filled in, the table shows that this is obviously the case for $\triangle L = 18$ m: for example the first order grating lobe at 6 centimeters is situated at an angular distance of 688 arcseconds from the centre, whereas a single dish pixel λ/D equals 500 arcseconds.
Figure (10.17) stipulates the outward movement of the grating lobes for a WSRT-type configuration by taking $D = 25$ meter and by reducing the baseline increment values from $\triangle L$=144 to 72, 36 and 18 meters respectively.
The problem of incomplete coverage of the YZ-plane is that the values of the coherence function $\tilde{\Gamma}(\vec{r})$ are set to zero in the empty spaces, which will certainly give an erroneous result. This can be circumvented by employing *interpolation* between the sampling circles based on certain assumptions regarding the complexity (or rather simplicity) of the brightness distribution of the sky region observed. Requirement is that the reconstructed (contour) map always remains consistent with the measurements at the grid points! Two mathematical techniques are often applied to get rid of the grating lobes: the CLEAN and MEM (Maximum Entropy Method) techniques. Obviously this is potentially much more efficient than elongating the observation times by a factor two or four, as was done in the above table. We shall not discuss these particular algorithms in any detail here, however the MEM technique will, in a more general fashion, be treated later on in this course. The improvement that can be achieved by applying the CLEAN method to a dirty radio map is displayed in figure (10.18), the left panel shows a dirty radio map at a wavelength of 50 cm, the right panel shows the "cleaned" map after applying the CLEAN process.

10.4.4 Maximum allowable bandwidth of a quasi-monochromatic source

As was already stated, the coherence length of the radiation source needs to be larger than the maximum path length difference at the longest baseline present in the interferometer array.

This imposes a maximum frequency bandwidth for the observation of the radiation source, which is disadvantageous since the noise in the image decreases with $\sqrt{\triangle\nu T_{obs}}$. The largest angle of incidence equals half the field of view, i.e. $\lambda/2D$, with D the single dish diameter. At this angle, the coherence length compliant with the largest baseline needs to obey:

$$L_{coh} \gg \frac{\lambda}{2D} L_{max} \tag{10.88}$$

This translates in the following condition for the allowable frequency bandwidth:

$$\frac{\triangle\nu}{\nu_0} \ll \frac{2D}{L_{max}} \tag{10.89}$$

In the case of the WSRT5 the ratio $2D/L_{max} \approx 1/50$. At a wavelength of 21 centimeters ($\approx$ 1400 MHz), this yields $\triangle\nu \ll 28$ MHz. This corresponds to a coherence length of more than 10 meters. In practise a value of $\triangle\nu \approx 10$ MHz is chosen, which corresponds to a coherence length of about 30 meters.
If one wishes to increase the bandwidth in order to improve sensitivity, than division in frequency subbands is required. For instance, if one observes at 21 centimeters and $\triangle\nu = 80$ MHz is required, this bandwidth is subdivided into eight 10 MHz subbands by filters. The individual subband maps are subsequently scaled (with λ) and added. This then yields the required signal to noise ratio.

10.4.5 The general case: arbitrary baselines and a field of view in arbitrary direction

In deriving the Van Cittert-Zernike relations, we took the baseline vector $\vec{r}(Y,Z)$ in a plane perpendicular to the vector pointing at the centre of the radiation source. In the WSRT case we were, therefore, limited to consider a field of view near the north polar direction.
Consider now an extended source in a plane σ in an arbitrary direction, an observation plane Σ parallel to σ, the centre of the radiation source is located on the X-axis, which is perpendicular to both planes. We designate the intersection point of the X-axis with the Σ-plane as the position of antenna 1 (for convenience, as we did before) and position antenna 2 at arbitrary coordinates (X,Y,Z). This defines an arbitrary baseline vector $\vec{r}(X,Y,Z)$. During the earth rotation the antenna beams are kept pointed at the source direction $\vec{\Omega}$, i.e. this vector does not move, however the tip of the baseline vector $\vec{r}(X,Y,Z)$ describes a trajectory $X(t), Y(t), Z(t)$ in space. Consider again radiation incident on the Σ-plane parallel to the X-axis, like in the case of the original Van Cittert-Zernike derivation. In that case the path difference at positions 1 and 2 was zero, since the baseline was located in the Y,Z-plane, now the path difference is given by $X(t)$. To restore maximum coherence between positions 1 and 2, this path difference can be compensated by delaying the signal of antenna 2 by $X(t)/c$, in other words radiation from direction X arrives at the same time at both inputs of the correlator. Taking the centre of the source as the zero reference point for the source direction vector in the X,Y,Z reference frame, we can select an infinitesimal source element in the direction $\vec{\Omega}_0(\Omega_{X0},\Omega_{Y0},\Omega_{Z0})$ (unit vector) $\Longrightarrow I_0\delta(\vec{\Omega}-\vec{\Omega}_0)$. The path difference at the input of the correlator is the projection of the baseline on that unit vector under subtraction of the compensation $X(t)$:

$$\vec{r}.\vec{\Omega}_0 - X = [\Omega_{Y0}Y + \Omega_{Z0}Z + (\Omega_{X0}-1)X] \tag{10.90}$$

If the extent of the radiation source (or the field of view defined by a single antenna beam) is sufficiently small, the value of the direction cosine $\Omega_{X0} \approx 1$, i.e. $(\Omega_{X0}-1)X \ll \lambda$. In

that case the difference in path length, like in the case of the original VanCittert-Zernike derivation, equals the scalar product of two vectors in the YZ-plane: the path difference equals $\approx \vec{r}_p.\vec{\Omega}'_0 = \Omega_{Y0}Y + \Omega_{Z0}Z$, with $\vec{r}_p$ the projection of the baseline vector on the YZ-plane and $\vec{\Omega}'_0$ the projection of the unit direction vector on the YZ-plane. If $I(\vec{\Omega})$ represents the brightness distribution over the sky, the VanCittert-Zernike relation for obtaining the coherence function is now given by:

$$\tilde{\Gamma}(\vec{r}_p) = \int\int_{\text{source}} I_0(\vec{\Omega}) e^{2\pi i \vec{\Omega}.\vec{r}_p/\lambda} d\vec{\Omega} \tag{10.91}$$

with $\vec{r}_p$ the *projected* baseline!
Conclusion: Arbitrary baselines do not change the aperture synthesis technique, except that the 3D baselines are projected on the observation plane Σ and become 2D.
Note: the pathlength difference $X(t)$ changes continually during the rotation of the earth and, hence, needs continues electronic compensation with an accuracy of a small fraction of the wavelength λ. In practise, for the WSRT, this is accomplished in two steps: *coarse compensation* with a delay line and subsequent *fine tuning* with the aid of an electronic phase rotator.
At the beginning of the description of earth rotation aperture synthesis, we considered the radiation source to be located in the direction of the rotation axis. Suppose now that the extended radiation source (or the single telescope field of view) is located along a direction vector that makes an angle ϕ_0 with the rotation axis of the earth. This is then the direction of the X-axis, perpendicular to this axis is the YZ-plane. The East-West oriented WSRT baselines physically rotate in a plane perpendicular to the earth axis, producing concentric circles as described earlier. These concentric circles now need to be projected on the YZ-plane, i.e. the observation plane Σ perpendicular to the viewing direction of the centre of the source (or the centre of the field of view). The circles change into ellipses and the coherence function is now sampled on ellipses, rather then on circles. The major axes of these ellipses remain equal to the physical length of the WSRT baselines, the minor axes are shortened by $\cos\phi_0$. This causes the *point spread function (PSF)* to become elliptical as well, the angular resolution therefore reduces with the lowering of the declination $[(\pi/2) - \phi_0]$. As a result, celestial directions along the declination are subject to a broadening of the central peak of the PSF according to:

$$PSF = \frac{\alpha\lambda}{2L_{max}\cos\phi_0} \tag{10.92}$$

Apart from the central peak, the *grating lobes* are scaled accordingly, this can be clearly seen in figures (10.16) and (10.18). For the WSRT the most extreme case of baseline shortening would occur with a source in the equatorial plane (declination 0), no resolution would be left in one direction. To circumvent this problem, baselines need to contain always North-South components. This is for example the case with the US VLA (Very Large Array) aperture synthesis telescope.

Chapter 11

Radiation sensing: a selection

11.1 General

In modern astrophysics a host of radiation sensors is employed to cover the full extent of the electromagnetic spectrum, the different species in cosmic-ray particle beams and the interaction products of cosmic neutrino capture. In this course it is not possible, nor desirable, to strive for any degree of completeness on this subject. Rather, a few specific sensor types have been selected since they feature very prominently in state of the art telescope systems used in present day astrophysical research. No attempt is made to describe these sensor types in any technical depth, nor will the, often very complex, electronic processing and data management chain be described. The focus will be entirely on a basic understanding of their working principle and physical characteristics, so as to allow a proper insight in their applicability and limitations. In the following sections, a treatment is given of three generically largely different sensor types:

- heterodyne receivers for coherent detection in the radio, microwave and far-infrared domain
- photoconductors for sensing primarily in the visible and infrared bands
- charge coupled devices (CCD) for sensing in the optical, UV and X-ray domain.

11.2 Heterodyne detection

In radio and microwave astronomy, the signal power is often a very small fraction of the system noise. Hence, large values of the product $T_{obs} \cdot \Delta\nu$ are required to obtain the proper value of the limiting sensitivity for the detection of a weak source. As a consequence, the receivers employed must be very stable and well calibrated. Stable amplifiers are available at relatively low radio frequencies (i.e. up to 10 GHz), but large amplification factors and stability do become a problem at high frequencies. In order to overcome this problem, extensive use is made in radio and sub-millimeter applications of *heterodyne techniques*.
In this technique, the incoming radio signal is mixed with a reference signal at a frequency relatively close to the average signal frequency $\bar{\nu}_s$. This reference signal at frequency ν_l is produced by a so-called local oscillator with high frequency stability, i.e. $\Delta\nu_l$ is almost a δ-function. In that case the reference signal has a very large coherence time and may therefore be regarded as coherent in the mixing process. Both signals are combined and fed to a non-linear detection element, the mixer element, which has the effect to produce signal power at

both sum $\nu_s + \nu_l$ and difference $|\nu_s - \nu_l|$ frequencies (recall: $\nu_s = \frac{1}{2\pi}\frac{d}{dt}(2\pi\bar{\nu}_s t + \phi(t))$). This can be quantitatively described by considering the following processing sequence. The wave

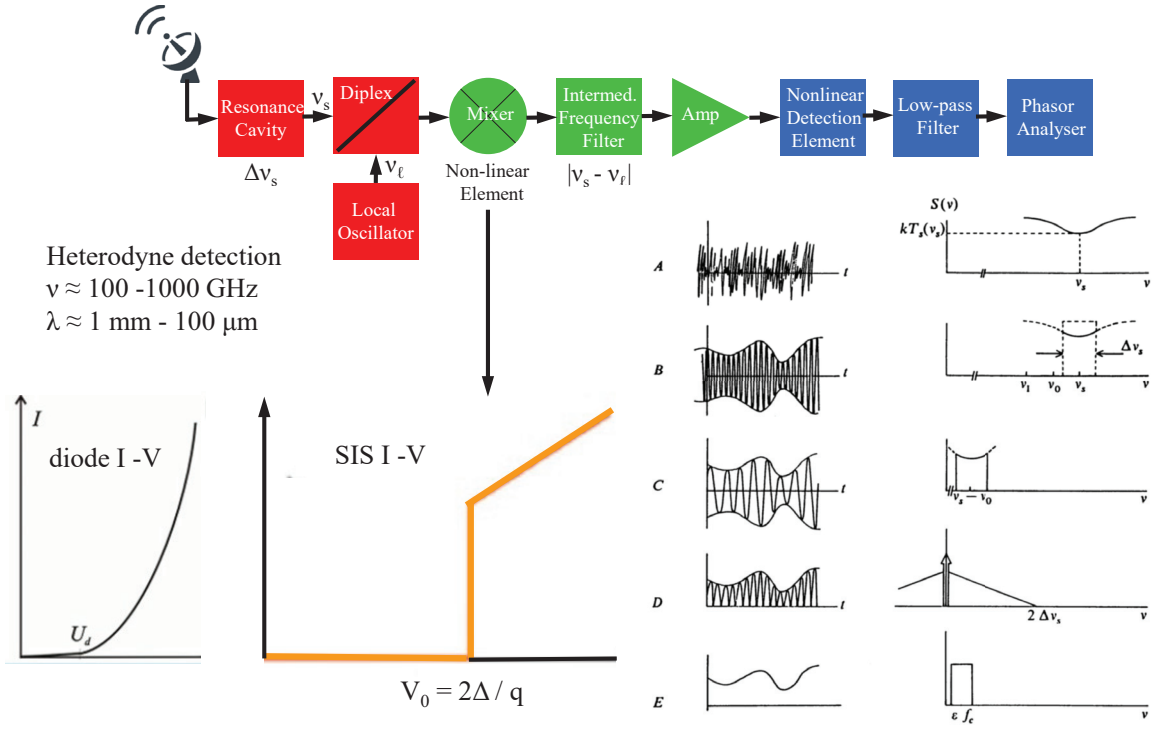

Figure 11.1: *Super heterodyne processing chain.*

signal received at the focus of the telescope is first passed through a horn and a resonance cavity, which select the polarisation direction and the frequency bandwidth $\Delta\nu$. Subsequently the signal of the (tunable) local oscillator, at frequency ν_l, is coupled (superimposed) to the high frequency source signal ν_s through a so-called diplexer (or coupler) and funneled onto the non-linear mixer element. As discussed previously, a thermal source signal can be expressed as

$$\tilde{E}_s(t) = |\,\tilde{E}_{s,0}(t)\,| \cdot e^{i(2\pi\bar{\nu}_s t + \phi(t))} \tag{11.1}$$

Similarly, the signal of the local oscillator can be expressed as

$$\tilde{E}_l(t) = \tilde{E}_{l,0}(t) \cdot e^{i(2\pi\nu_l t)} \tag{11.2}$$

in which $\tilde{E}_{l,0}(t)$ represents the phasor of the local oscillator signal. Regarding the local oscillator as a coherent signal source, this phasor can be written as

$$\tilde{E}_{l,0}(t) = |\,\tilde{E}_{l,0}\,| \cdot e^{i\psi_l} \tag{11.3}$$

Hence:

$$\tilde{E}_l(t) = |\,\tilde{E}_{l,0}\,| \cdot e^{i(2\pi\nu_l t + \psi_l)} \tag{11.4}$$

Since the source signal concerns one component of polarization, the wave signal at the non-linear mixer element can be written as

$$E_M(t) = |\,\tilde{E}_{s,0}(t)\,| \cdot \cos(2\pi\bar{\nu}_s t + \phi(t)) + |\,\tilde{E}_{l,0}\,| \cdot \cos(2\pi\nu_l t + \psi_l) \tag{11.5}$$

Detection by the mixer element causes a *frequency conversion* through the occurrence of a product component arising from the non-linear response. Assuming a non-linear mixer response **proportional to** $E_M^2(t)$, a product component $2 \mid \tilde{E}_{s,0}(t) \mid \cdot \mid \tilde{E}_{l,0} \mid \cdot \cos(2\pi\bar{\nu}_s t + \phi(t)) \cdot \cos(2\pi\nu_l t + \psi_l)$ is formed. Applying the trigonometric relation $\cos\alpha \ \cos\beta = \frac{1}{2}[\cos(\alpha + \beta) + \cos(\alpha - \beta)]$ two frequency components can be distinguished:

- one centered at $\bar{\nu}_s + \nu_l$: $\mid \tilde{E}_{s,0}(t) \mid \cdot \mid \tilde{E}_{l,0} \mid \cdot \cos(2\pi(\bar{\nu}_s + \nu_l)t + \phi(t) + \psi_l)$
- one centered at $\mid \bar{\nu}_s - \nu_l \mid$: $\mid \tilde{E}_{s,0}(t) \mid \cdot \mid \tilde{E}_{l,0} \mid \cdot \cos(2\pi(\bar{\nu}_s - \nu_l)t + \phi(t) + \psi_l)$

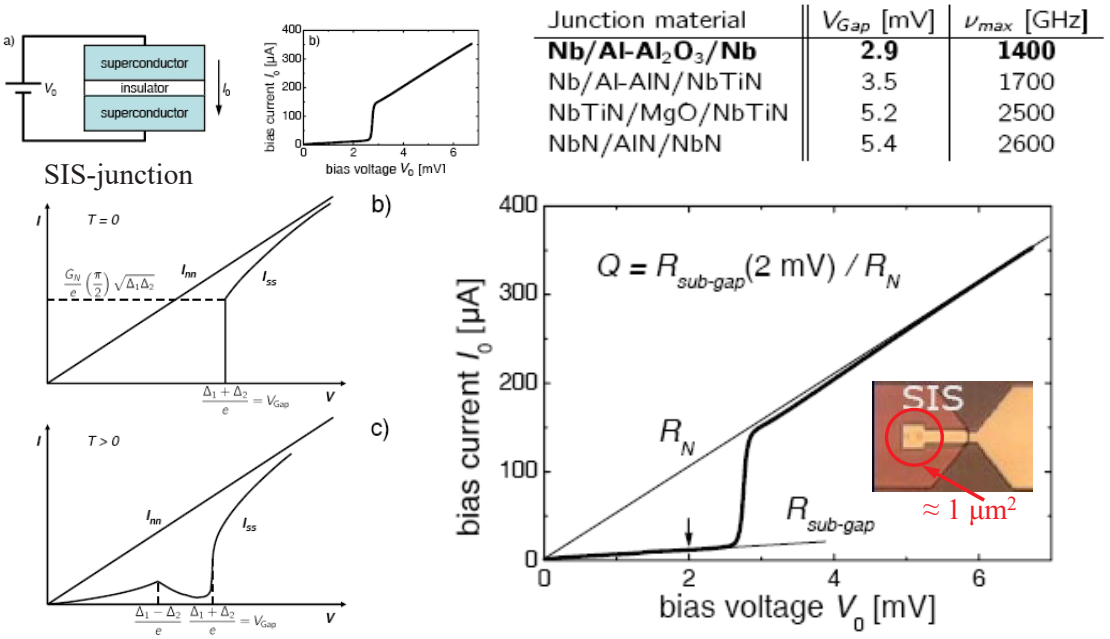

Junction material	V_{Gap} [mV]	ν_{max} [GHz]
Nb/Al-Al$_2$O$_3$/Nb	**2.9**	**1400**
Nb/Al-AlN/NbTiN	3.5	1700
NbTiN/MgO/NbTiN	5.2	2500
NbN/AlN/NbN	5.4	2600

Figure 11.2: Characteristics of SIS junctions.

The latter expression is linearly proportional to the amplitude of the source signal $\mid \tilde{E}_{s,0}(t) \mid$ and possesses all the characteristics of the original signal, but now centers at a much lower difference frequency $\mid \bar{\nu}_s - \nu_l \mid$ (except for the phase shift ψ_l). In the sub-millimeter application with $\bar{\nu}_s \approx 1$ THz, $\mid \bar{\nu}_s - \nu_l \mid$ is of the order 10 GHz. Remember that the bandwidth of the source signal $\Delta\nu_s$ is contained in the time dependent phase factor $\phi(t)$ and, consequently, the *mixer element should have adequate wide frequency response* to cover the complete bandwidth.
The converted signal at the difference or intermediate frequency (IF) can be selected by employing an intermediate frequency filter (IFF) and can subsequently be amplified by a stable low noise IF amplifier (A). Obviously the mixer element should have the lowest possible noise temperature, near-quantum limited operation near 1000 GHz has been achieved (see further).

By employing a tunable local oscillator the average frequency $\bar{\nu}_s$ of the source signal can be shifted while maintaining a fixed $\bar{\nu}_{IF}$ and associated filter circuitry, i.e.:

$$\bar{\nu}_s = \bar{\nu}_l \ (\text{tunable}) \ + \bar{\nu}_{IF} \ (\text{fixed}) \tag{11.6}$$

The IF signal is finally fed into a non-linear detection element (D) which, after low-pass filtering (LPF), generates the frequency spectrum associated with the signal phasor for one component of polarization $\mid \tilde{E}_{s,0}(t) \mid \ \cos\phi(t)$, i.e. the envelope function of the high frequency source signal $\tilde{E}_s(t)$. This frequency spectrum represents the spectral distribution of the

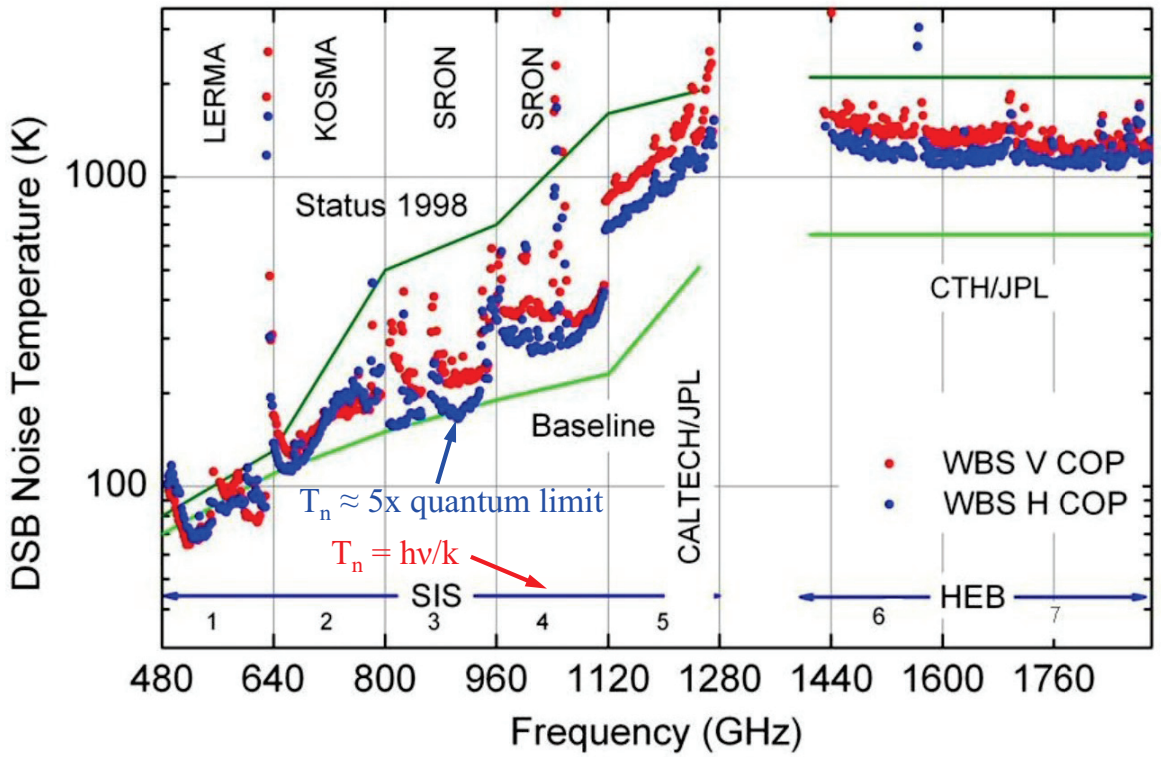

Figure 11.3: *In-flight noise temperatures achieved in several frequency channels of the HIFI-Wide Band Spectrometer on board the Herschel Space Observatory.*

radio signal centered at $\bar{\nu}_s$ over the bandwidth $\Delta\nu_s$. This signal can be fed into a frequency analyser (spectrometer) for spectral analysis. Figure (11.1) shows the signal processing chain and various stages in the detection process. Panel A displays the high frequency thermal signal incident on the telescope (antenna). Panel B shows the output of the resonance cavity into the diplexer, limited to the bandwidth $\Delta\nu_s$. Panel C shows the envelope function superimposed on the IF-carrier signal $\bar{\nu}_{IF} = |\,\bar{\nu}_s - \nu_l\,|$, after frequency conversion by the non-linear mixing element. In panel D this signal is fed through the non-linear detection element (normally a quadratic response) after which the low frequency phasor signal can be filtered out (panel E). Heterodyne detection at sub-millimeter and infrared wavelengths is a powerful spectroscopic technique. In this case the mixer element consists of a *superconductive tunnel junction*, comprising two superconducting electrodes separated by a thin oxide barrier (see figure (11.2). Because of an energy gap 2Δ in the material of the superconducting electrodes, the current-voltage characteristics (the so-called I-V diagram) of this Superconductor Insulator Superconductor (SIS) junction is highly non-linear. SIS-mixers are the most sensitive heterodyne mixers in the 0.2–1.2 THz frequency range, where the upper frequency is determined by the energy gap 2Δ of practical superconducting materials (e.g. Niobium (Nb) and Niobium-Titanium (NbTi)). The frequency down-conversion process can be achieved with near quantum-limited noise performance. An example is shown in figure (11.3) that shows the noise temperatures which were obtained in a number of high frequency channels of the Wide Band Spectrograph (WBS) in the HIFI-instrument on board the Herschel Space Observatory. Up to 700 GHz a noise temperature of a few times (≈ 5) the quantum limit has been obtained, the mixer operates near the quantum limit, but input losses and IF amplifier noise decreases the overall performance. Above 1.2 THz hot-electron bolometer mixers (HEBM)

are used which are not limited by the energy bandgap of the superconductor, since they do not operate on the individual photon energy but on the total absorbed power. The physical foundation of bolometer operation will be treated in a later section.
Note: The factor $|\tilde{E}_{l,0}|$ in the product component can be made large so that the signal to noise ratio can be largely improved with respect to the internal noise sources in the receiver chain. This assumes of course that $|\tilde{E}_{l,0}|$ is ultra stable and, also, that the quantum noise of the local oscillator is still negligible.

11.3 Frequency limited noise in the thermal limit: signal to noise ratio and limiting sensitivity

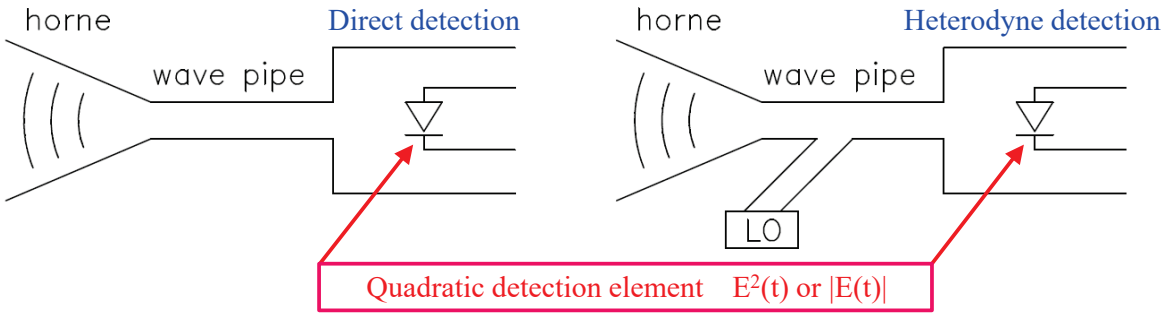

Figure 11.4: *Schematic view of a radio receiver with the receiving horne, which selects the frequency ν_s and the frequency bandwidth $\Delta\nu_s$, the wave pipe, and the 'quadratic' detection element (left). By mixing the radio signal with that of a local oscillator (LO), the carrier frequency can be shifted to much lower frequencies without any information loss (heterodyne detection), suitable for electronic processing (right).*

The average spectral noise power in the thermal limit ($h\nu \ll kT$) for one degree of polarization, equals kT. This is the situation which prevails in radio-, microwave- and submillimeter receivers and hence gives rise to a description of signals and noise with the aid of characteristic temperatures, e.g. source temperature T_s and noise temperature T_n. The one-sided power spectral density $S(\nu) \equiv \overline{P}(\nu) = kT$ Watt Hz^{-1} is constant as a function of frequency and, as a consequence, is termed white noise.
In practice, due to the finite frequency response of any receiver system, this will be frequency limited. Hence we can express the double-sided power spectral density for a thermal source for one degree of polarization as:

$$S_d(\nu) = \frac{1}{2}kT\Pi\left(\frac{\nu}{2\nu_c}\right) \quad \text{with} \quad \nu_c \ll \frac{kT}{h} \tag{11.7}$$

where ν_c constitutes the cut-off frequency of the receiver system under consideration, i.e. the total energy contained in the power spectrum remains finite, as it should be for any physical system.
Continuing now with the detection of radio signals, we wish to consider the signal-to-noise ratio. As discussed previously,the linearly polarized signal displayed in figure (8.7) can mathematically be expressed by the real function:

$$E(t) = E_0(t)\cos(2\pi\bar{\nu}t + \phi(t)) \tag{11.8}$$

The amplitude $w(t) \equiv E_0(t)$ of the quasi-monochromatic wave is a *wide-sense stationary Gaussian* random time function of zero mean. Moreover the stochastic process is assumed to be *mean- and correlation-ergodic*, i.e. for an arbitrary real stochastic variable $w(t)$ its *expectation value* at time t, $\mathbf{E}\{\mathbf{w(t)}\}$, can be interchanged with its time average.
Detection of such a radio signal requires, like in the case of *mixing*, a non-linear operation like $\psi(t) \equiv |w(t)|$ or $\psi(t) = w^2(t)$, to extract the power present in the signal. We shall consider here the case of quadratic detection, i.e. $\psi(t) = w^2(t)$, since this is mathematically straightforward in contrast to absolute-value transformations.

If $w(t)$ can be described as a stationary random process with a normally distributed amplitude around zero mean, the probability density function is given by:

$$f(w) = \frac{1}{\sigma_w\sqrt{2\pi}} e^{-w^2/2\sigma_w^2} \qquad (\mu_w = 0) \tag{11.9}$$

and the measuring process is schematically indicated by

$$w(t) \rightarrow \text{transformation} \rightarrow \psi(t) \equiv w^2(t) \tag{11.10}$$

For the transformation $\psi(t) = w^2(t)$, with $\sigma_w^2 = R_w(0)$, we can write the probability density of ψ as

$$f(\psi) = \frac{1}{2[2\pi R_w(0)\psi]^{1/2}} \exp\left[\frac{-\psi}{2R_w(0)}\right] U(\psi) \tag{11.11}$$

with $U(\psi)$ the Heaviside step function. (In understanding expression (11.11), don't forget the transformation $dw \Rightarrow d\psi$!). Thus, the stochastic process $\psi(t)$ is apparently *not* normally distributed, and of course also $\mu_\psi \neq 0$.

To derive the power spectral density of $\psi(t)$ we need to find an expression for the autocorrelation function $R_\psi(\tau)$ of $\psi(t)$. One can show that for a normally distributed $w(t)$ the autocorrelation of $\psi(t) \equiv w^2(t)$ follows from:

$$\begin{aligned} R_\psi(\tau) &= \mathbf{E}\{\psi(t)\psi(t+\tau)\} = \mathbf{E}\left\{w^2(t)w^2(t+\tau)\right\} = \\ &= \mathbf{E}\left\{w^2(t)\right\}\mathbf{E}\left\{w^2(t+\tau)\right\} + 2\mathbf{E}^2\{w(t)w(t+\tau)\} \end{aligned} \tag{11.12}$$

The derivation of this relation applying the theory of stochastic processes makes use of the so-called moment-generating functions of $w(t)$. Hence:

$$R_\psi(\tau) = R_w^2(0) + 2R_w^2(\tau) = \mu_\psi^2 + C_\psi(\tau) \tag{11.13}$$

The average μ_ψ of $\psi(t)$ equals the variance of $w(t)$, the autocovariance of $\psi(t)$ equals twice the square of the autocovariance of $w(t)$, and the variance of $\psi(t)$ is $\sigma_\psi^2 = 2\sigma_w^4$. The *double-sided* power spectral density of $\psi(t)$ follows from the Wiener-Khinchin theorem:

$$S_{d_\psi}(\nu) = R_w^2(0)\delta(\nu) + 2S_{d_w}(\nu) * S_{d_w}(\nu) \tag{11.14}$$

It is important to realize that in the case of quadratic detection a number of frequency components is introduced in the case of an amplitude-modulated signal like $w(t)$. We shall demonstrate this, as an example, for a deterministic signal, i.e. an amplitude-modulated high frequency carrier of the form:

$$x(t) = A(1 + m\cos\eta t)\cos\omega t \tag{11.15}$$

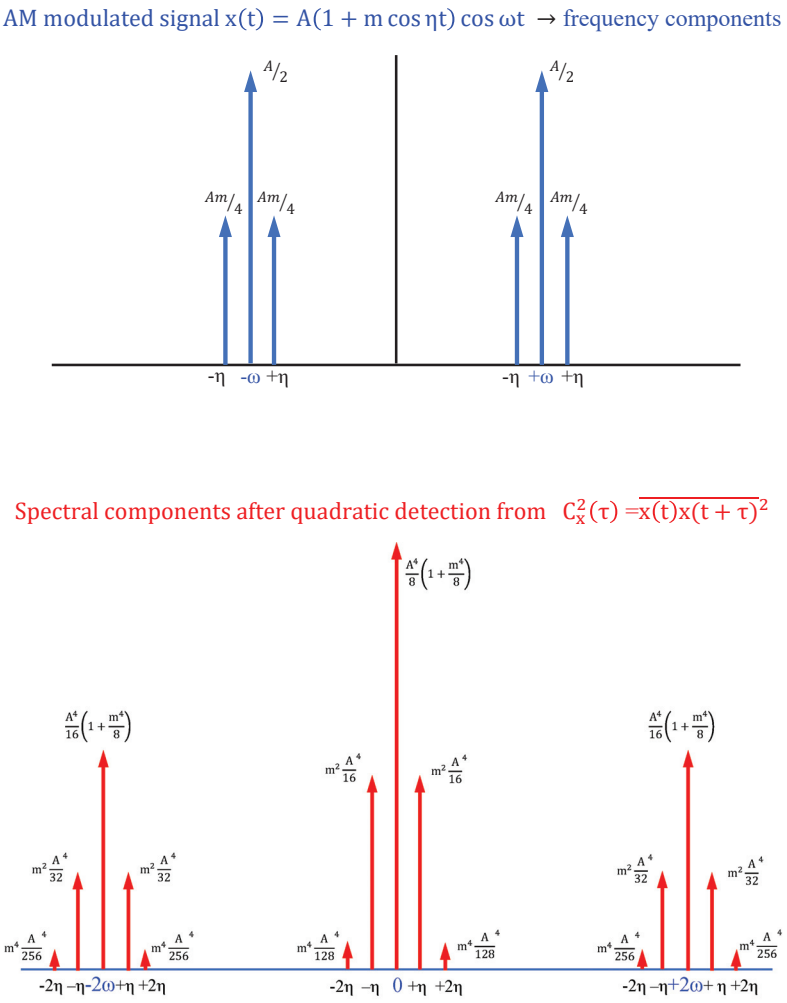

Figure 11.5: *Frequency components of an amplitude modulated (frequency η) carrier (frequency ω) with modulation index m (upper panel). The spectral components that emerge after quadratic detection present in the autocovariance function are shown in the lower panel. Evidently the sidebands appear at twice the carrier frequency ω, moreover the signal bandwidth 4η amounts to twice the original bandwidth 2η.*

This represents a high frequency carrier (ω) the amplitude (A) of which is modulated by a much lower frequency (η). m is called the modulation index.
The signal $x(t)$ contains three discrete frequencies, $\omega - \eta$, ω, and $\omega + \eta$. This is easily seen by using $\cos\alpha \cos\beta = \frac{1}{2}[\cos(\alpha + \beta) + \cos(\alpha - \beta)]$.

The instantaneous intensity of this signal can be expressed as $I = x^2(t)$, and for the average intensity we get

$$\overline{I} = \overline{x^2(t)} = \frac{1}{2}A^2(1 + \frac{1}{2}m^2) \tag{11.16}$$

The equivalent of the term $\mathbf{E}\{a^2(t)\}\,\mathbf{E}\{a^2(t+\tau)\}$ in expression (11.12) amounts in this case

to a DC-term representing the square of the average intensity:

$$\overline{I}^2 = \frac{1}{4}A^4\left(1+\frac{1}{2}m^2\right)^2 \tag{11.17}$$

To arrive at the equivalent of the autocovariance term $2\mathbf{E}^2\{a(t)a(t+\tau)\}$ in equation (11.12), we first have to compute the autocovariance $C_x(\tau)$ of $x(t)$:

$$C_x(\tau) = \overline{x(t)x(t+\tau)} = \frac{1}{2}A^2[\cos\omega\tau + \frac{1}{4}m^2\cos(\omega+\eta)\tau + \frac{1}{4}m^2\cos(\omega-\eta)\tau] \tag{11.18}$$

Subsequently:

$$\overline{x(t)x(t+\tau)}^2 = \frac{1}{4}A^4(1+\frac{1}{2}m^2\cos\eta\tau)^2\cos^2\omega\tau \tag{11.19}$$

Using the relation $\cos^2\alpha = \frac{1}{2}(\cos 2\alpha + 1)$ this can be disentangled in various components:

$$\begin{aligned}\overline{x(t)x(t+\tau)}^2 &= \frac{A^4}{8}(1+\cos 2\omega\tau) + \frac{m^2A^4}{8}[\cos\eta\tau + \frac{1}{2}\cos(2\omega-\eta)\tau + \\ &+ \frac{1}{2}\cos(2\omega+\eta)\tau] + \frac{m^4A^4}{64}[1+\cos 2\eta\tau + \frac{1}{2}\cos(2\omega-2\eta)\tau + \\ &+ \cos 2\omega\tau + \frac{1}{2}\cos(2\omega+2\eta)\tau]\end{aligned} \tag{11.20}$$

This expression shows that the original frequencies in the power spectral density of $x(t)$, ω and $\omega\pm\eta$ have been transformed in the squaring process to frequency components at DC, η, 2η, 2ω, $2\omega\pm\eta$ and $2\omega\pm 2\eta$. Displayed on a double-sided frequency diagram this shows twice the original frequency bandwidth centered at DC and $\pm 2\omega$ (see figure 11.6). In the case of the stochastic signal $w(t)$ we shall see the same characteristics in the power spectral density of the autocovariance $C_\psi(\tau)$.

Consider now the front-end of a receiver behind a radio antenna (telescope), see (Figure (8.7). This front-end generally contains a resonance cavity tuned at a central frequency $\overline{\nu} = \nu_s$ with a bandwidth $\Delta\nu_s$. If the noise entering the receiver can be characterized by a noise temperature T_n the double-sided power spectral density of $w(t)$ for one degree of polarization is given by:

$$S_{d_w}(\nu) = \frac{1}{2}kT_n\left[\Pi\left(\frac{\nu-\nu_s}{\Delta\nu_s}\right) + \Pi\left(\frac{\nu+\nu_s}{\Delta\nu_s}\right)\right] \tag{11.21}$$

This signal is then fed to a non-linear detection element, like a Schottky-diode or an induction coil, which introduces the transformation $\psi(t) = w^2(t)$. Consequently, we have:

$$R_w^2(0) = (\sigma_w^2)^2 = \left(\frac{1}{2}kT_n\int_{-\infty}^{+\infty}\left[\Pi\left(\frac{\nu-\nu_s}{\Delta\nu_s}\right) + \Pi\left(\frac{\nu+\nu_s}{\Delta\nu_s}\right)\right]d\nu\right)^2 = (kT_n\Delta\nu_s)^2 \tag{11.22}$$

and

$$\begin{aligned}2\left[S_{d_w}(\nu) * S_{d_w}(\nu)\right] &= \frac{1}{2}(kT_n)^2\left[\Pi\left(\frac{\nu-\nu_s}{\Delta\nu_s}\right) + \Pi\left(\frac{\nu+\nu_s}{\Delta\nu_s}\right)\right] * \left[\Pi\left(\frac{\nu-\nu_s}{\Delta\nu_s}\right) + \Pi\left(\frac{\nu+\nu_s}{\Delta\nu_s}\right)\right] \\ &= (kT_n)^2\Delta\nu_s\left[\Lambda\left(\frac{\nu}{\Delta\nu_s}\right) + \frac{1}{2}\Lambda\left(\frac{\nu-2\nu_s}{\Delta\nu_s}\right) + \frac{1}{2}\Lambda\left(\frac{\nu+2\nu_s}{\Delta\nu_s}\right)\right]\end{aligned} \tag{11.23}$$

$S_{d_\psi}(\nu)$ consists therefore of a component $(kT_n\Delta\nu_s)^2\delta(\nu)$, a *time independent average value at zero frequency* (stationary Gaussian random amplitudes) and three 'triangle-functions'

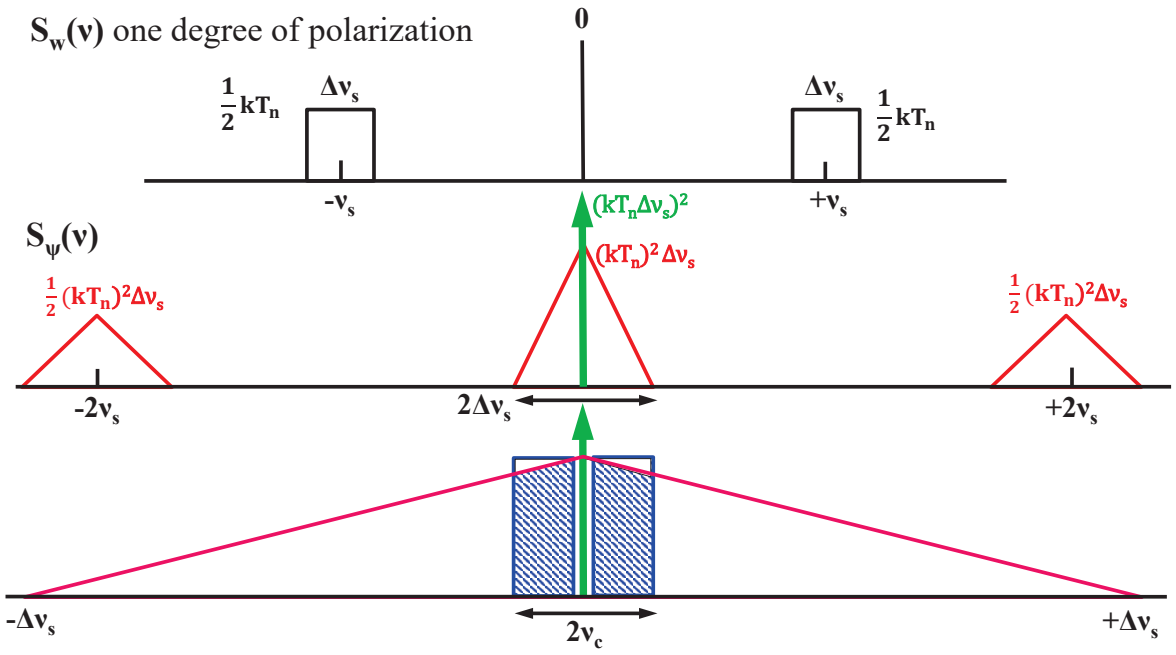

Figure 11.6: *Upper panel: Double-sided power spectral density of thermal radiation for one degree of polarization ($\bar{P} = kT$ Watt Hz^{-1}), over a channel bandwidth $\Delta\nu_s$ centered at frequency ν_s, incident on a non-linear detection element. Middle panel: double-sided power spectral density at the output of the detection element. Lower panel: low frequency filtering (cut-off ν_c) providing signal averaging over a time interval $\Delta T_{av} = 1/2\nu_c$. This time averaging process obviously does not influence the DC-component, this is schematically indicated in the figure by showing an exclusion of the green arrow.*

centered at zero frequency and at frequencies $-2\nu_s$ and $+2\nu_s$ with a basewidth of $2\Delta\nu_s$, as illustrated in figure 11.6. Note the correspondence in frequency shift and bandwidth with the example involving the deterministic amplitude modulated signal above! In practice one always has $\nu_s \gg \Delta\nu_s$, in the centimeter range for example one typically has $\nu_s \simeq 10^{10}$ Hz and $\Delta\nu_s \simeq 10^7$ Hz. The detection of a *potential radio source signal* will then have to be assessed in the context of the *autocovariance of the noise signal*, i.e. we need an expression for $C_\psi(\tau)$. This follows from the Fourier transform of the term $2\,[S_{d_w}(\nu) * S_{d_w}(\nu)]$ in equation (11.23). Applying the shift theorem and the $\Lambda \Leftrightarrow \mathrm{sinc}^2$ transform from Fourier analysis, we get:

$$\begin{aligned} C_\psi(\tau) &= (kT_n\Delta\nu_s)^2 \left[\frac{e^{-2\pi i(2\nu_s\tau)} + e^{2\pi i(2\nu_s\tau)}}{2}\right] \mathrm{sinc}^2\tau\Delta\nu_s + (kT_n\Delta\nu_s)^2\mathrm{sinc}^2\tau\Delta\nu_s \\ &= (kT_n\Delta\nu_s)^2(1+\cos 2\pi(2\nu_s\tau))\mathrm{sinc}^2\tau\Delta\nu_s \end{aligned} \tag{11.24}$$

The $\cos 2\pi(2\nu_s\tau)$ term refers to the high frequency carrier which will be filtered off in any low frequency averaging process. This averaging process can be taken over an arbitrary time intervalΔT_{av}. This is equivalent to filtering in the frequency domain with a filter $\Pi(\nu/2\nu_c)$ with $\nu_c = 1/(2\Delta T_{av})$ commensurate with the Nyquist sampling theorem.
The averaged value of the autocovariance is then obtained in the τ domain by convolution of $C_\psi(\tau)$ with the Fourier transform $\Pi(\nu/2\nu_c) \Leftrightarrow 2\nu_c\mathrm{sinc}2\nu_c\tau$.
Assuming $\nu_c \ll \Delta\nu_s \ll \nu_s$, the $\cos 2\pi(2\nu_s\tau)$ term in expression (11.24) averages to zero.

Consequently we have:

$$\begin{aligned}[C_\psi(\tau)]_{\Delta T} &= (kT_n\Delta\nu_s)^2\mathrm{sinc}^2\tau\Delta\nu_s * 2\nu_c\mathrm{sinc}2\nu_c\tau \\ &= (kT_n\Delta\nu_s)^2\cdot 2\nu_c\int_{-\infty}^{+\infty}\mathrm{sinc}^2\tau'\Delta\nu_s\mathrm{sinc}2\nu_c(\tau-\tau')d\tau' \end{aligned} \tag{11.25}$$

and with a change of variables $u' \equiv \tau'\Delta\nu_s$ this becomes:

$$[C_\psi(u)]_{\Delta T} = (kT_n)^2\Delta\nu_s\cdot 2\nu_c\int_{-\infty}^{+\infty}\mathrm{sinc}^2u'\mathrm{sinc}\frac{2\nu_c}{\Delta\nu_s}(u-u')du' \tag{11.26}$$

Since $\nu_c/\Delta\nu_s \ll 1$, $\mathrm{sinc}(2\nu_c/\Delta\nu_s)u'$ varies very slowly compared to sinc^2u'. We may therefore regard sinc^2u' as a δ-function in comparison to $\mathrm{sinc}(2\nu_c/\Delta\nu_s)u'$. Moreover we also have the proper normalization, since $\int_{-\infty}^{\infty}\mathrm{sinc}^2u'du' = \int_{-\infty}^{+\infty}\delta(u')du' = 1$. Applying this approximation we get:

$$\begin{aligned}[C_\psi(u)]_{\Delta T} &= (kT_n)^2\Delta\nu_s\cdot 2\nu_c\int_{-\infty}^{+\infty}\delta(u')\mathrm{sinc}\frac{2\nu_c}{\Delta\nu_s}(u-u')du' \\ &= (kT_n)^2\Delta\nu_s\cdot 2\nu_c\mathrm{sinc}\frac{2\nu_c}{\Delta\nu_s}u \end{aligned} \tag{11.27}$$

Substituting $\tau = u/\Delta\nu_s$ we arrive at the final expression for the ΔT-averaged value of the noise autocovariance:

$$[C_\psi(\tau)]_{\Delta T} = (kT_n)^2\Delta\nu_s\cdot 2\nu_c\mathrm{sinc}2\nu_c\tau \tag{11.28}$$

The noise variance $[C_\psi(0)]_{\Delta T} = (kT_n)^2\Delta\nu_s\cdot(2\nu_c)$ should be compared to the strength of a radio source signal characterized by a source temperature T_s. The average value of this source signal after quadratic detection follows from:

$$(\mu_\psi)_s = R_{w_s}(0) = \sigma^2_{w_s} = kT_s\Delta\nu_s \tag{11.29}$$

and the signal-to-noise ratio thus becomes:

$$\mathrm{S/N} = \frac{(\mu_\psi)_s}{[C_\psi(0)]^{1/2}_{\Delta T}} = \frac{T_s}{T_n}\left(\frac{\Delta\nu_s}{2\nu_c}\right)^{1/2} \tag{11.30}$$

i.e. the signal to noise is proportional to the square root of the receiver bandwidth $\Delta\nu_s$ and inversely proportional to the double-sided bandwidth of the integrating (averaging) low-pass filter ν_c. Introducing $\Delta T_{av} = 1/(2\nu_c)$ (Nyquist sampling) we get:

$$\mathrm{S/N} = \frac{T_s}{T_n}\left(\Delta\nu_s\Delta T_{av}\right)^{1/2} \tag{11.31}$$

i.e. the S/N ratio improves with the square root of the product of the radio-channel bandwidth and the integration time ΔT_{av}. In practice the noise temperature of a radio-wave receiving system is designated as the system or operational temperature that includes the contributions to the noise of the sky, the antenna and the receiver system. The S/N =1 sensitivity for

detecting a radio source against the system thermal noise temperature is sometimes referred to as the *radiometer equation*:

$$\mathrm{S/N} = \frac{T_{source}}{T_{system}} \left(\Delta\nu_s \Delta T_{av}\right)^{1/2} \quad \text{radiometer equation!} \tag{11.32}$$

The minimum detectable *source power for one degree of polarization* with a signal to noise ratio of one is given by:

$$(P_s)_{min} = kT_n \left(\Delta\nu_s \Delta T_{av}\right)^{-1/2} \tag{11.33}$$

11.4 Photoconductor

11.4.1 Operation principle and Responsivity

A photoconductor exhibits a change in conductance (resistance) when radiant energy (photons) is incident upon it. The radiant energy increases the conductance (σ_0) by producing *excess charge carriers* in the photoconductor, which is fabricated from a semiconductor material. The charge carriers comprise electron-hole pairs in the case of an intrinsic semiconductor. In extrinsic semiconductors the excess charge carriers comprise either electrons (n-type) or holes (p-type). The spectral responsivity of a particular photoconductor is determined by its energy gap: only photons that have energies greater than the gap energy will be absorbed and cause an excess current flow. The photoconductor is operated in a mode that involves the application of an external electric field (voltage bias) that gives rise to a bias current. This bias current becomes modulated by the excess charge carriers that are produced by photon-excitation. Hence a photoconductor belongs to the category of modulation transducers (see figure (11.7). To put the above discussion about the operation principle on a proper physi-

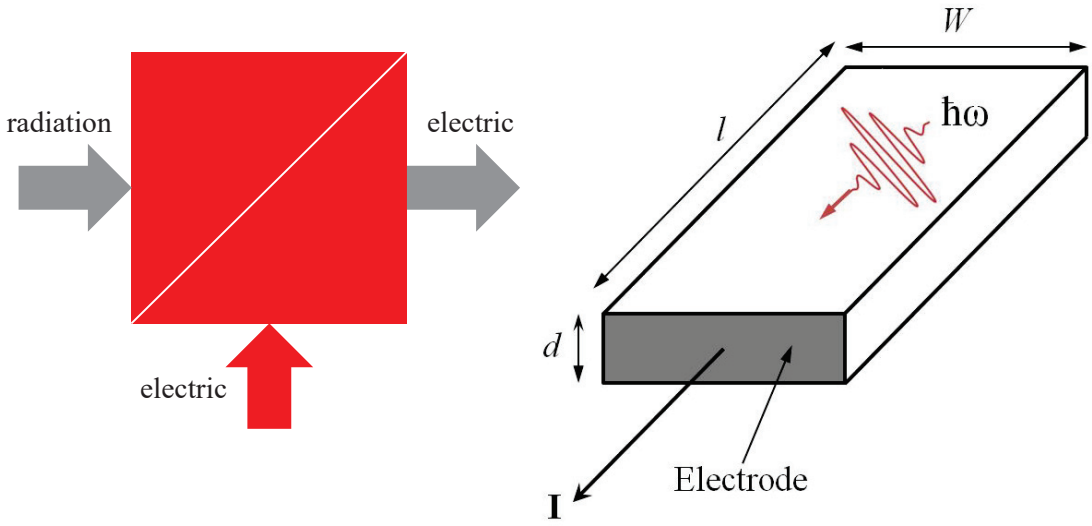

Figure 11.7: *(Left): Photoconductors belong to the category of modulation transducers. (Right): Sketch of the geometry of a photoconductive element.*

cal basis, the response to a radiative signal will be derived in this section. A material with conductivity σ_0 produces a current density $\vec{j}$ given by:

$$\vec{j} = \sigma_0 \vec{E} \tag{11.34}$$

in which $\vec{E}$ represents the electric field strength generated by the bias voltage V_B accross the photoconductor ($|\vec{E}|$ in Volt$\cdot$m^{-1} and σ_0 in Ohm$^{-1}\cdot$m^{-1}). Microscopically the current density $\vec{j}$ can also be expressed as

$$\vec{j} = Nq\vec{v} \tag{11.35}$$

in which N represents the volume density of the free charge carriers, q the elementary charge and $\vec{v}$ the drift velocity of these charges in the applied electric field. This drift velocity $\vec{v}$ can also be written as $\vec{v} = \mu_c \vec{E}$, with μ the so-called mobility of the charge carrier. For an intrinsic semiconductor a distinction needs to be made between electron conduction and hole conduction: the mobilities μ_n for electrons and μ_p for holes are quite different ($\mu_n \approx 3\mu_p$):

$$\vec{j} = -nq\vec{v_n} + pq\vec{v_p} \tag{11.36}$$

with n/p the electron/hole densities and $\vec{v_n}/\vec{v_p}$ the electron/hole drift velocities (opposite directions). Note that q is the elementary charge and has a positive sign. Combining equations (11.34) and (11.36), an expression for the conductivity σ_0 follows:

$$\sigma_0 = q(n\mu_n + p\mu_p) \tag{11.37}$$

which reduces to $\sigma_0 = qn\mu_n$ and $\sigma_0 = qp\mu_p$ in the case of a heavily doped n-type, respectively p-type extrinsic semiconductor.
Consider now a n-type semiconductor, which is irradiated by a beam of radiant energy with a spectral photon irradiance (= monochromatic photon flux density) $F(\lambda)$. In the equilibrium situation the number of excess conduction electrons follows from the fact that the generation rate should match the recombination rate:

$$\frac{d\Delta n}{dt} = g - \frac{\Delta n}{\tau_l} = 0 \tag{11.38}$$

with Δn the equilibrium number of excess electrons per unit volume (= excess carrier concentration), τ_l the life time of these electrons against recombination and g the generation rate:

$$g = \frac{\eta(\lambda)F(\lambda)}{d} \tag{11.39}$$

with $\eta(\lambda)$ the photon detection efficiency and d the thickness of the photoconductor material. The increase in conductivity $\Delta\sigma = \sigma - \sigma_0$ follows from:

$$\Delta\sigma = q\mu_n \Delta n = \frac{q\mu_n \eta(\lambda)F(\lambda)\tau_l}{d} = \frac{q\mu_n \eta(\lambda)\tau_l}{Ad}\,\frac{\lambda}{hc}\,\Phi(\lambda) \tag{11.40}$$

in which $\Phi(\lambda)$ the monochromatic radiation flux in Watt, A the illuminated area of the photoconductor and λ the wavelength under consideration. Given a fixed bias voltage V_B across the photoconductors, the relative change in conductivity $\Delta\sigma/\sigma$ can be related to a relative change in current $\Delta I/I_0$ and resistance $\Delta R/R_0$ as:

$$\frac{\Delta\sigma_0}{\sigma_0} = -\frac{\Delta R}{R_0} = \frac{\Delta I}{I_0} = \frac{I_{pc}}{I_0} \tag{11.41}$$

in which I_0, R_0 represent the photoconductor DC-current/resistance in the absence of radiation and $\Delta I = I_{pc}$ the photon-generated current (*photo-current*).
Introducing the detector width W and length l ($A = lW$, see figure (11.7), I_0 can be expressed as

$$I_0 = Wd\,|\vec{j}\,| \tag{11.42}$$

and hence:

$$I_{pc} = I_0\,\frac{\Delta\sigma_0}{\sigma_0} = \frac{\eta(\lambda)q\lambda}{hc}\cdot\frac{\tau_\ell\mu_n V_B}{l^2}\cdot\Phi(\lambda) \tag{11.43}$$

The term $\tau_\ell\mu_n V_B/l^2$ is commonly referred to as the photoconductive gain G. Introducing the transition time τ_{tr} of the free charge carriers accross the photoconductor length l, i.e. $\tau_{tr} = \frac{l^2}{\mu_n V_B}$, G gives the ratio between the carrier life time against recombination in the photoconductor and its transition time, i.e. $G = \tau_\ell/\tau_{tr}$.
The *current responsivity* $R^I_{pc}(\lambda,\nu)$, assuming a modulation of the photon flux density $\Phi(\lambda)$ with frequency ν follows from:

$$R^I_{pc}(\lambda,\nu) = \frac{I_{pc}}{\Phi(\lambda)} = G\eta(\lambda)q\,\frac{\lambda}{hc} \tag{11.44}$$

in Ampere/Watt.
In practice the photocurrent I_{pc} is measured over a load resistance R_L in series with the photoconductor resistance R_0, translating I_{pc} in an equivalent voltage V_0, see figure (11.8).

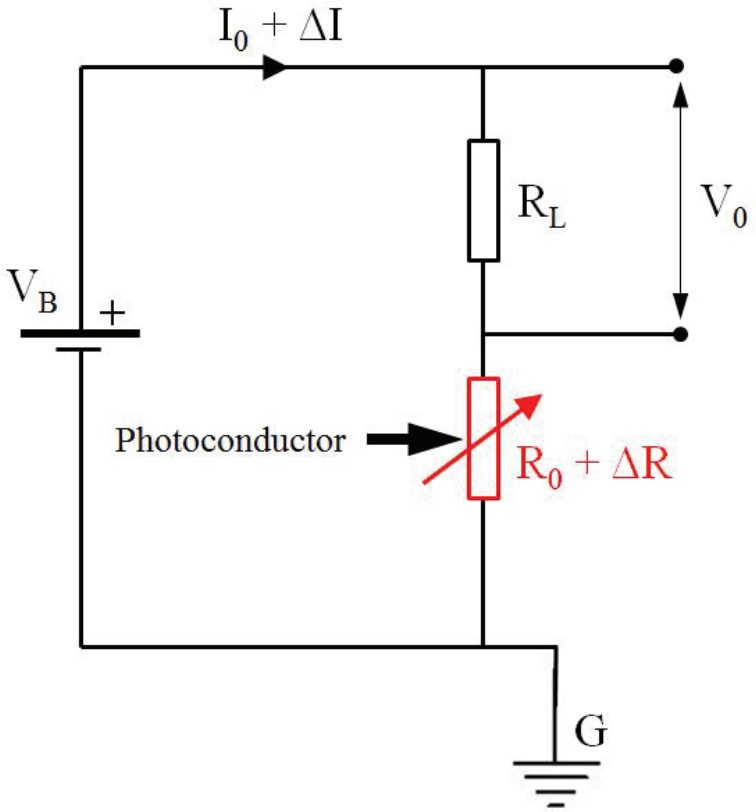

Figure 11.8: *Photoconductor: bias circuit.*

In this case the *spectral voltage responsivity* is given by:

$$R_{pc}^{V}(\lambda,\nu) = \frac{R_L R_0}{R_L + R_0}\, G\eta(\lambda) q\, \frac{\lambda}{hc} \tag{11.45}$$

in Volt/Watt. ◁

The above expressions are only valid for low-frequency operation of the photoconductor, where dielectric relaxation or recombination life-time effects are not of concern. In the next section, the frequency response of photoconductors will be addressed.
In order to raise the responsivity of a photoconductor, one should

- enlarge the quantum efficiency $\eta(\lambda)$ by minimizing reflection effects at the entrance plane through application of anti-reflection coatings and by creating a larger cross-section for the internal photo-electric effect.
- increase the carrier life time, which raises the photoconductive gain G.
- enlarge the carrier mobility μ_c (recall that n-type charge carriers have substantially higher mobility than p-type charge carriers).
- increase the operational bias voltage V_B, which lowers the value of the transition time τ_{tr} in the expression for the photoconductive gain G.

11.4.2 Temporal frequency response

Consider a step-function in charge carrier generation due to a switch-on of the photoconductor exposure to a radiation source. The response of the photoconductor is now obtained from solving the time dependent continuity equation:

$$\frac{d\Delta n(t)}{dt} = g - \frac{\Delta n(t)}{\tau_\ell} \tag{11.46}$$

with boundary condition $\Delta n = 0$ at $t = 0$. The solution of this differential equation is straightforward:

$$\Delta n(t) = g\tau_\ell(1 - e^{-\frac{t}{\tau_\ell}}) = \Delta n_{eq}(1 - e^{-\frac{t}{\tau_\ell}}), \tag{11.47}$$

with $\Delta n_{eq} = g\tau_\ell$ the *equilibrium* excess free carrier density [m^{-3}] The time dependent excess carrier concentration (density) can also be expressed as the convolution of a charge generation step-function, $\Delta n_{eq} U(t)$ with the photoconductor impulse response function $h_{pc}(t)$:

$$\Delta n(t) = \Delta n_{eq} U(t) * h_{pc}(t) \tag{11.48}$$

Fourier (Laplace) transform for $t \geq 0$ to the temporal frequency domain yields:

$$\Delta n(2\pi j\nu) = \frac{\Delta n_{eq}}{2\pi j\nu}\, H_{pc}(2\pi j\nu) \tag{11.49}$$

Substituting expression (11.47) in $\Delta n(t) \Leftrightarrow \Delta n(2\pi j\nu)$ yields the photoconductor response function for a dynamical input signal:

$$\frac{\Delta n_{eq}}{2\pi j\nu}\, \frac{1}{1 + 2\pi j\nu\tau_\ell} = \frac{\Delta n_{eq}}{2\pi j\nu}\, H_{pc}(2\pi j\nu) \qquad \Rightarrow \qquad H_{pc}(2\pi j\nu) = \frac{1}{1 + 2\pi j\nu\tau_\ell} \tag{11.50}$$

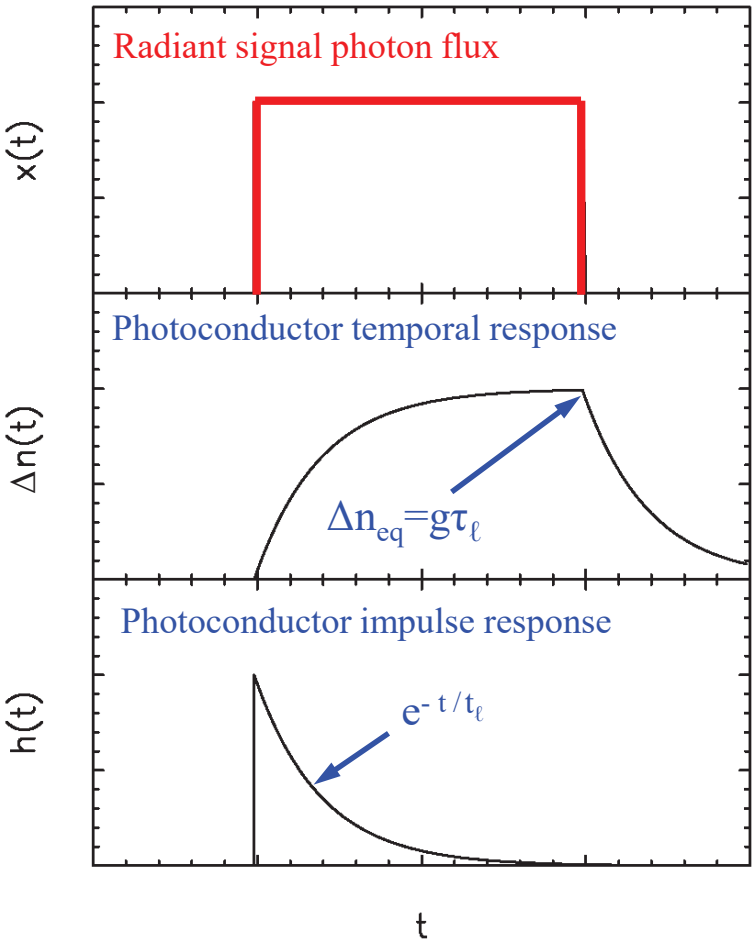

Figure 11.9: *For a block function $x(t)$ of illuminating photons (top), the number of excess charges per unit volume $[m^{-3}]$ $\Delta n(t)$ in a photoconductor increases on a finite time scale towards the equilibrium value, and drops exponentially once the illumination ceases (middle). The impulse response function $h_{pc}(t)$ is an exponential (below).*

and hence the frequency dependent amplitude transfer:

$$|H_{pc}(2\pi j\nu)| = \frac{1}{\sqrt{1+4\pi^2\nu^2\tau_\ell^2}} \tag{11.51}$$

This expression shows that the photoconductor acts as a frequency filter that takes the form of a first order system (see figure 11.9). At a frequency $\nu = 1/(2\pi\tau_\ell)$, the responsivity reduces with 3 dB ($= 1/\sqrt{2}$). For $2\pi\nu\tau_\ell \gg 1$, the responsivity rolls off with 6 dB per octave; i.e. a reduction of a factor 2 by each doubling of the frequency. The cut-off frequency $\nu_c = 1/(2\pi\tau_\ell)$ determines the characteristic bandwidth of a photoconductor with a charge carrier life time τ_l. This breakpoint in the frequency domain is typically around 1 MHz, which of course varies for various detector types. Typical response times of photoconductive radiation sensors are, therefore, intrinsically limited to microsecond time scales.

Intermezzo: frequency filtering of a Poisson process

In chapter 8 we derived a general expression for the autocorrelation of a train of unit-value Dirac impulses at random time positions, an unfiltered Poisson process (WSS and ergodic):

$$R_X(\tau) = \lambda^2 + \lambda\delta(\tau) \tag{11.52}$$

From this, by applying the Wiener Khinchin theorem to $R_X(\tau)$ we can now compute the power spectral density:

$$R_X(\tau) \Leftrightarrow S_{d_X}(\nu) = \int_{-\infty}^{+\infty} R_X(\tau) e^{-2\pi j\nu\tau} d\tau = \lambda^2\delta(\nu) + \lambda \tag{11.53}$$

which is inconsistent with physical reality since it implies an infinitely high power signal. In practice there is always a frequency cut-off at say ν_c, owing to some (high frequency) filtering process. We might perceive this as follows. The photon detection process involves conversion to charge carriers that are subsequently fed into a filter network, e.g. a first order RC filter. The RC-network acts on each individual charge impuls q (δ-function) with a current response function $h(t)$. If we now assume for convenience that each single photon generates a charge carrier (detection efficiency=1), implying also an average charge carrier rate λ, the resulting photo-current follows from a convolution of the Dirac δ-function train $X(t)$ with $h(t)$:

$$\frac{I(t)}{q} \;=\; X(t) \rightarrow h(t) \rightarrow Y(t) \tag{11.54}$$

with $h(t)$ the filter circuit *impulse* current response function (*Note*: $h(t) = 0$ for $t < 0$ and is a normalized function: $\int_0^\infty h(t)dt = 1$).
Hence we have:

$$Y(t) = h(t) * X(t) = \int_0^\infty \sum_k \delta(t' - t_k) h(t - t') dt' = \sum_k h(t - t_k) = \overline{Y} + \Delta Y(t) \tag{11.55}$$

Owing to the high carrier density in the charge flow, there will be a large degree of overlap between subsequent responses. This will result in a total current $I(t)$ that shows a Gaussian (normal) distribution around a mean value $\overline{I}$. For the expectation value of $Y(t)$ we thus find

$$\begin{aligned} \overline{Y} &= \mathbf{E}\{Y(t)\} = \mathbf{E}\{\int_0^\infty X(t - t')h(t')dt'\} \\ &= \int_0^\infty \mathbf{E}\{X(t - t')\}\, h(t')dt' = \lambda \int_0^\infty h(t')dt' = \lambda\, H(0) \end{aligned} \tag{11.56}$$

where for the last transition we have used:

$$H(2\pi j\nu) \equiv \int_0^\infty h(t') e^{-2\pi j\nu t'} dt' \Rightarrow H(0) = \int_0^\infty h(t')dt' \tag{11.57}$$

In the Fourier domain we write for the *current* power spectral density:

$$\begin{aligned} S_{d_Y}(\nu) &= |H(2\pi j\nu)|^2\; S_{d_X}(\nu) \\ &= \lambda^2\, |H(2\pi j\nu)|^2\, \delta(\nu) + \lambda\, |H(2\pi j\nu)|^2 = \lambda^2\; H^2(0) + \lambda\, |H(2\pi j\nu)|^2 \end{aligned} \tag{11.58}$$

Evidently the power is now finite, as it should be. We obtain the autocorrelation by taking the Fourier transform of the *current* power spectral density $S_{d_Y}(\nu)$:

$$R_Y(\tau) = \lambda^2 \, H^2(0) + \lambda \, [h(\tau) * h(\tau)] \tag{11.59}$$

where the first term on the right hand side gives the *mean* charge response of the linear dynamic system, and the second term represents the noise. Taking the autocovariance at $\tau = 0$ we obtain the variance of the noise signal:

$$C_Y(0) = \lambda \int_{-\infty}^{+\infty} h^2(t) dt = \lambda \int_{-\infty}^{+\infty} |H(2\pi j\nu)|^2 d\nu = 2\lambda \int_{0}^{+\infty} |H(2\pi j\nu)|^2 d\nu \tag{11.60}$$

in taking the last steps we have applied Parseval's theorem and changed from a double sided $S_{d_I}(-\infty < \nu < +\infty)$ to a one-sided S_I: twice the integral from $0 < \nu < \infty$ to accommodate physically real frequencies.

End intermezzo: frequency filtering of a Poisson process

We shall now apply the above analysis to the specific case of a photoconductive semiconductor device, where the shot noise Poisson process is associated with the random generation (G) and recombination (R) of charge carriers and where the frequency filtering arises intrinsically from the finite life time τ_ℓ of the generated charge carriers.

11.4.3 Photoconductor shot noise limited sensitivity

Generation/Recombination(GR) shot noise in semiconductors

Generation-Recombination noise (GR noise) originates in thermally or optically-stimulated electronic transitions between valance and conduction band or transitions between impurity levels, traps, or recombination centers and one of these bands. Associated with these transitions are fluctuations in the numbers of free carriers and in their lifetimes, thus giving rise to the GR noise. The detailed mathematical treatment of GR noise depends on many specific parameters like the number of energy levels, the energies corresponding to these levels, the electron population, and the occupancy of states.
As a simple example, the common case of an extrinsic semiconductor such as Germanium or Silicon containing both donors and acceptors, one being predominant and exceeding in number the number of free carriers, will be treated here.
For a simple GR two-level system we assume a generation rate (number per unit time) $g(N)$ and a recombination rate $r(N)$ which describe the transition from the impurity level to the conduction band and the reverse (recombination) process. N is a random variable that represents the number of free carriers (predominantly electrons) in the conduction band at time t. We further assume that both rates g and r depend explicitly *only* on the momentaneous number of free carriers in the conduction band, $N(t)$. In general g is a decreasing function of N (i.e. negative slope), whereas r is an increasing function of N (i.e. positive slope). In the equilibrium (steady state) situation we have balance between the generation and recombination rates, say at a free carrier average number value $\overline{N} = N_e$ at time t. Hence, for $g_e = g(N_e)$

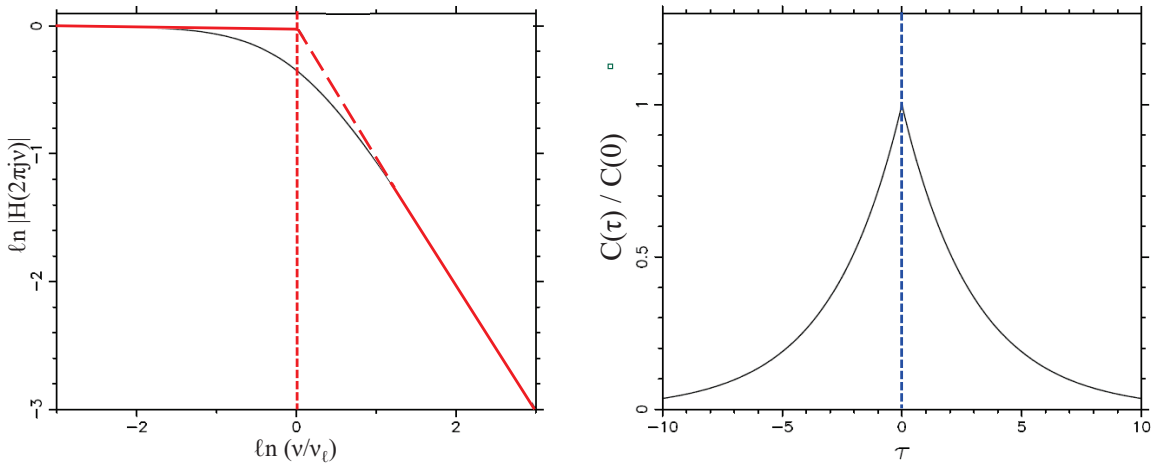

Figure 11.10: *For a first order transfer function with tipping point $\nu = \nu_\ell$ (left), the autocovariance drops exponentially with $|\tau|$ (right).*

and $r_e = r(N_e)$ we have

$$g_e = r_e \quad \text{and } N \text{ normally distributed around } N_e \quad \Rightarrow \tag{11.61}$$

$$\mathbf{p(N)} = p(N_e)\exp -\frac{1}{2}\left[\frac{(N-N_e)^2}{\overline{\Delta N^2}}\right] \text{ with variance } \overline{\Delta N^2} = N_e \tag{11.62}$$

Taking the derivatives $g'_e = (dg/dN)_{N=N_e}$ and $r'_e = (dr/dN)_{N=N_e}$ as the generation rate and the recombination rate at the equilibrium number value N_e respectively (dimension $[\sec^{-1}]$), we can assign specific time scales to the GR process by defining $1/\tau_g = -g'_e$ and $1/\tau_r = r'_e$ leading to a free carrier life time:

$$\frac{1}{\tau_\ell} = -\frac{d}{dN}(g-r)_{N=N_e} \quad \Rightarrow \quad \frac{1}{\tau_\ell} = -(g'_e - r'_e) = \frac{1}{\tau_g} + \frac{1}{\tau_r} \text{ and:} \tag{11.63}$$

$$\overline{\Delta N^2} = N_e = g_e \cdot \tau_\ell \tag{11.64}$$

The carrier life time τ_ℓ dictates the dynamical response of the semiconductor on changes in free carrier generation, this response can be quantified by solving the time dependent continuity equation for change $dN(t)/dt$:

$$\frac{dN(t)}{dt} = g - \frac{N(t)}{\tau_\ell} \quad \Rightarrow \quad N(t) = g\tau_\ell\left(1 - e^{\frac{-t}{\tau_\ell}}\right) \tag{11.65}$$

The dynamical behavior expressed in equation (11.65) is characterized by a first order system with transfer function $H(2\pi j\nu) = 1/(1 + 2\pi j\nu\tau_\ell)$, its frequency response $|H(2\pi j\nu)|$ trails off at high frequencies with a tipping point at $\nu_\ell = 1/(2\pi\tau_\ell)$. This is shown, one-sided, in the left

panel of figure (11.10). The associated autocovariance function is shown in the right panel of figure (11.10). It constitutes a double-sided exponential function centered on $\tau = 0$ with a decay constant τ_ℓ that follows from the Fourier transform of the *double sided* transfer function:

$$\begin{aligned} H(2\pi j\nu) + H(-2\pi j\nu) &= \left(\frac{1}{(1+2\pi j\nu\tau_\ell)} + \frac{1}{(1-2\pi j\nu\tau_\ell)}\right) \Rightarrow \text{FT} \Rightarrow \\ &\Leftrightarrow \quad \frac{e^{-\frac{\tau}{\tau_\ell}}}{2\tau_\ell}U(\tau) + \frac{e^{\frac{\tau}{\tau_\ell}}}{2\tau_\ell}U(-\tau) = \\ &= \quad \frac{e^{-\frac{|\tau|}{\tau_\ell}}}{2\tau_\ell} \;=\; C(\tau) \end{aligned} \tag{11.66}$$

where $U(\tau)$ is the Heaviside step function: $U(\tau) = 0$, $\tau < 0$; $U(\tau) = 1$, $\tau \geq 0$. Hence we have:

$$C(\tau) = C(0)\, e^{-\frac{|\tau|}{\tau_\ell}} \quad \text{with} \quad \tau_\ell = \frac{1}{2\pi\nu_\ell} \tag{11.67}$$

For the GR-process, featuring the random count variable N, we can thus express the variance $\overline{\Delta N^2}$ for some time delay τ following excitation *or* decay as an exponential autocovariance according to:

$$C_N(\tau) = \overline{\Delta N^2}\, e^{-\frac{|\tau|}{\tau_\ell}} \tag{11.68}$$

The associated power spectral density $S_N(\nu)$ can now be obtained by applying the Wiener-Khinchin theorem. Since we are dealing here with two *independent* random processes, i.e. an excitation process followed by a decay process, in computing the spectral noise power we incorporate a factor 2 in taking the integral of the autocovariance over all physical delays τ. Subsequently we need to convert this *one-sided* spectral density to a *double-sided* spectral density (S_{d_N}) to accomodate the *negative* frequencies and time delays used in Wiener-Khinchin theorem. Thus we have:

$$S_N(\nu) = 2\int_0^\infty \overline{\Delta N^2}\, e^{-\frac{|\tau|}{\tau_\ell}}\, e^{-2\pi j\nu\tau} d\tau \quad \Rightarrow \quad S_{d_N}(\nu) = \int_{-\infty}^{\infty} \overline{\Delta N^2}\, e^{-\frac{|\tau|}{\tau_\ell}}\, e^{-2\pi j\nu\tau} d\tau \tag{11.69}$$

Performing the Fourier transform in equation (11.69) results in:

$$S_{d_N}(\nu) = \frac{2\tau_\ell \overline{\Delta N^2}}{1+(2\pi\nu\tau_\ell)^2} = \frac{2g_e\tau_\ell^2}{1+(2\pi\nu\tau_\ell)^2} \tag{11.70}$$

As shown before, the value of the average current density $|\vec{j}|$ in the semiconductor equals $nq|\vec{v}_d|$ with $n = N/V$ the charge carrier volume density, q the elementary charge and $\vec{v}_d$ the drift velocity in the applied electric field. With a cross sectional area A we have a total average current $I_e = A \cdot |\vec{j}| = A \cdot (N_e/V)q(d/\tau_{tr}) = qN_e/\tau_{tr} = qg_e(\tau_\ell/\tau_{tr})$ in which d represents the distance between the electrodes of the semiconductor and $\tau_{tr} = d^2/(\mu V)$ the charge carrier transit time between the electrodes (with μ the carrier mobility and V the bias voltage). Substituting in (11.70) and multiplying $S_{d_N}(\nu)$ by $(q/\tau_{tr})^2$ yields an expression for the current spectral density of the GR noise:

$$S_{d_I} = \left(\frac{q}{\tau_{tr}}\right)^2 S_{d_N}(\nu) = 2qI_e\left(\frac{\tau_\ell}{\tau_{tr}}\right)\left(\frac{1}{1+(2\pi\nu\tau_\ell)^2}\right) \tag{11.71}$$

The mean square GR current noise $\overline{\Delta I^2}$ follows from integration of S_{d_I} over all frequencies:

$$\overline{\Delta I^2} = 2qI_e\left(\frac{\tau_\ell}{\tau_{tr}}\right)\int_{-\infty}^{+\infty}\frac{d\nu}{1+(2\pi\nu\tau_\ell)^2} \Rightarrow \quad \overline{\Delta I^2} = 4qI_e\left(\frac{\tau_\ell}{\tau_{tr}}\right)\Delta\nu_c \text{ with} \tag{11.72}$$

$$\Delta\nu_c = \int_0^{+\infty}\frac{d\nu}{1+(2\pi\nu\tau_\ell)^2} \text{ the noise equivalent bandwidth within } 0<\nu<\infty$$

For low frequencies the (*one-sided*) current spectral power can be expressed as:

$$S_I(0) = \frac{\overline{\Delta I^2}}{\Delta\nu_c} = 4qG_nI_e \quad [\text{Ampere}^{\,2}\ \text{Hz}^{\,-1}] \quad \text{with} \quad G_n = \left(\frac{\tau_\ell}{\tau_{tr}}\right) = \frac{\tau_\ell\mu E}{d} \tag{11.73}$$

G_n is the so-called *noise gain*. In case the semiconductor has uniform resistance and an uniform electric field, the noise gain is proportional to this applied electric field. The GR-current noise can then be expressed as $\left(\sqrt{\overline{\Delta I^2}}\right)_{GRn} = \sqrt{4qG_nI_e\Delta\nu_c}$, with $\left(\sqrt{\overline{\Delta I^2}}\right)_{GRn}$ the rms-noise current, I_e the average total current and $\Delta\nu_c$ the noise equivalent bandwidth.

Photoconductor shot noise in the signal-photon limit

The average number of charge carriers generated by a radiation beam with an average monochromatic photon flux density $F(\lambda)$ (average spectral photon irradiance) at wavelength λ equals $G\eta(\lambda)F(\lambda)A_{pc}$, in which A_{pc} represents the active area of the photoconductor, $\eta(\lambda)$ the quantum efficiency for photo-absorption and G the photoconductive gain. The average photocurrent $\mathbf{E}\{I_{ph}(t)\}$ can therefore be expressed as:

$$\mathbf{E}\{I_{ph}(t)\} = \overline{I_{ph}(t)} = qG\eta(\lambda)F(\lambda)A_{pc} \tag{11.74}$$

with q the elementary charge. The frequency response can be expressed as (see equation (11.65)):

$$H_{pc}(2\pi j\nu) = \frac{1}{1+2\pi j\nu\tau_\ell} \tag{11.75}$$

where τ_ℓ is the charge carrier life time.

$$\left(\sqrt{\overline{\Delta I^2}}\right)_{GR_{ph}} = \sqrt{4qG\overline{I_{ph}(t)}\Delta\nu_c} = 2qG\sqrt{\eta(\lambda)F(\lambda)A_{pc}\Delta\nu_c} \tag{11.76}$$

with $\left(\sqrt{\overline{\Delta I^2}}\right)_{GR_{ph}}$ the rms-noise current, $\overline{I_{ph}(t)}$ the average total photo-current, $F(\lambda)$ the average radiant signal photon flux and $\Delta\nu_c = \int_0^{+\infty} d\nu/(1+[2\pi\nu\tau_\ell]^2)$ the one-sided noise equivalent bandwidth within the frequency range $0<\nu<\infty$. Substituting $\Delta\nu_c$ by performing the integration over frequency we get:

$$\left(\sqrt{\overline{\Delta I^2}}\right)_{GR_{ph}} = qG\left(\frac{\eta(\lambda)F(\lambda)A_{pc}}{\tau_\ell}\right)^{\frac{1}{2}} \tag{11.77}$$

Finally, for the signal to noise ratio *in the signal photon limit* we obtain

$$\text{SNR} = \left(\frac{\overline{I_{ph}(t)}}{(\sqrt{\overline{\Delta I^2}})_{GR_{ph}}}\right) = (\eta(\lambda)F(\lambda)A_{pc}\tau_\ell)^{1/2} \tag{11.78}$$

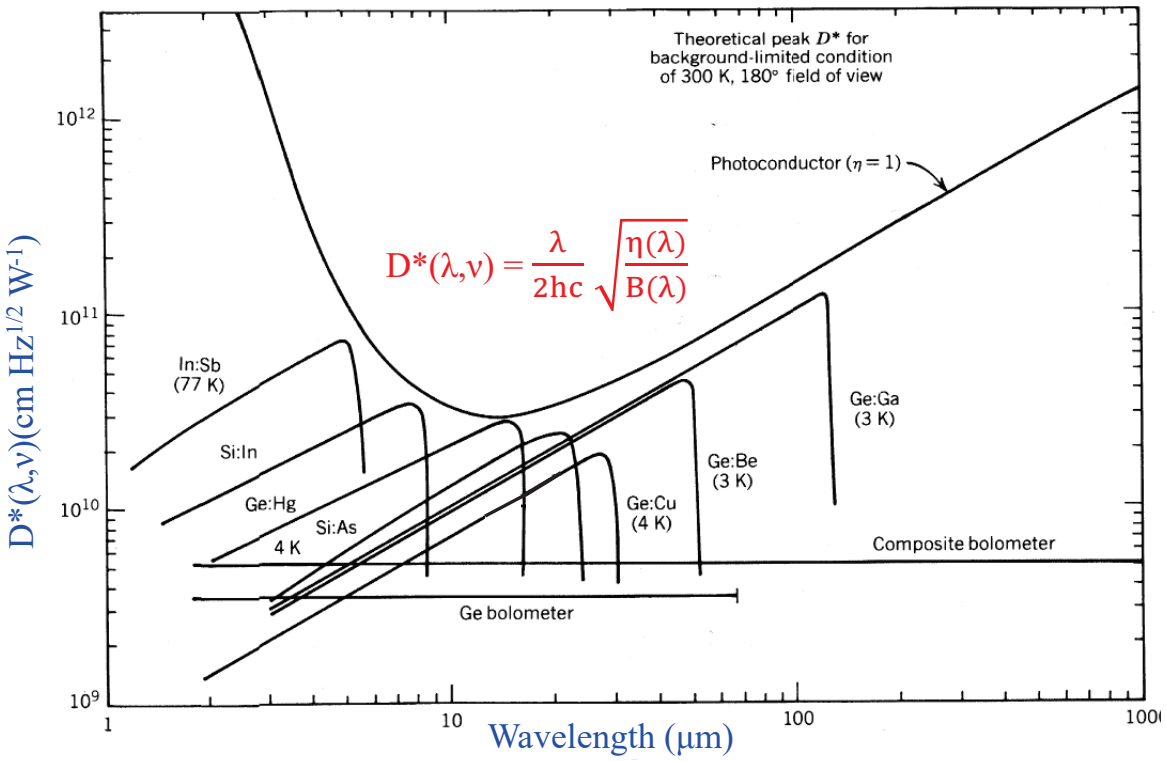

Figure 11.11: *Typical detectivities for several photo-conductors. Figure taken from Dereniak and Crowe 1984.*

This last equation tells us that a high value for the frequency cutoff $\nu_\ell = 1/(2\pi\tau_\ell)$ leads to a lower signal to noise for the photo-current; the reason for this is that the intrinsic system noise is less filtered.

Photoconductor shot noise in the background-photon limit

The rms-noise in the photocurrent, derived in the previous paragraph, dominates over thermal noise if the photoconductor is sufficiently cooled.
From expression (11.77) for the rms-noise in the photocurrent $\left(\sqrt{\overline{\Delta I^2}}\right)_{GR_{ph}}$ we can also assess the spectral Noise Equivalent Power ($NEP(\lambda,\nu)$) if we assume that this photocurrent arises from an *average monochromatic background-photon flux density* $B(\lambda)$ instead of the average signal-photon flux density $F(\lambda)$ considered above. This $NEP(\lambda,\nu)$ represents the so-called *radiation Background Limited Performance (BLIP)*. Let us use the relations:

$$NEP(\lambda,\nu) = \frac{\left(\sqrt{\overline{\Delta I^2}}\right)_{GR_{ph}}}{R^I_{pc}(\lambda,\nu)} = \frac{hc}{\lambda}\left(\frac{B(\lambda)A_{pc}}{\eta(\lambda)\tau_\ell}\right)^{\frac{1}{2}} \tag{11.79}$$

and the BLIP normalised detectivity $D^*(\lambda,\nu)$:

$$D^*(\lambda,\nu) = \frac{\sqrt{A_{pc}\Delta\nu_c}}{NEP(\lambda,\nu)} = \frac{\lambda}{2hc}\left(\frac{\eta(\lambda)}{B(\lambda)}\right)^{\frac{1}{2}} \quad \text{by substituting } \Delta\nu_c = 1/(4\tau_\ell) \tag{11.80}$$

Figure 11.11 shows the theoretical *peak detectivity* for $\eta(\lambda) = 1$ as a function of wavelength, assuming radiation Background Limited Performance(BLIP) arising from an omnidirectional blackbody radiation field at 300 K integrated over the upper hemisphere of 180°. Also included in figure (11.11) are a number of common extrinsic photoconductors and their corresponding operating temperatures. Detectivities of two types of thermal detectors (bolometers) are displayed for comparison. The thermal detectors lack the cut-off feature in wavelength due to the different detection principle, they show a considerably lower value of $D^*(\lambda, \nu)$ but cover a wider spectral band than the photo-conductive devices.

11.4.4 Photoconductor noise limited performance

So far we have only considered the generation of GR-noise in photoconductive devices as a consequence of irradiation by an external photon source, both as a signal source or as an omnidirectional background source. However, if the photo-conductor is not exposed to external radiation, there still remain intrinsic noise contributions owing to the presence of a resistive bias circuit, the thermal environment of the device and imperfections in the homogeneity of the conducting material and the electrical contacts. These noise components are often labelled as 'dark noise' contributions since they do not relate to photoconductor irradiance. The imperfections in materials and contacts cause a 1/f noise component and since photoconductors require a bias current there will always be 1/f noise present. The mean square current noise is obtained from integrating the 1/f current power spectral density over the equivalent noise bandwidth $\Delta\nu_{1/f}$:

$$\overline{\Delta I^2_{1/f}} = \int\limits_{\Delta\nu_{1/f}} S_I(\nu) d\nu \;=\; a\, I_b^2 \int\limits_{\Delta\nu_{1/f}} \frac{d\nu}{\nu} \tag{11.81}$$

with a a proportionality constant and I_b the bias current through the photoconductor. For a photoconductor it is an observational fact that at low frequencies the dominant noise exhibits a 1/f dependence incorporated in the expression for its current power spectral density. As the frequency increases this component drops below the GR-noise or the thermal noise in case of a low photon flux, see figure (11.12). The 1/f noise component does not constitute a fundamental limit to sensitivity, careful surface preparation and contact technology can potentially reduce the integral contribution of this noise to negligible levels. In addition to the GR-noise generated by an external radiation source, we also have a GR-noise contribution to the dark noise owing to thermal agitation of charge carriers:

$$\left(\sqrt{\overline{\Delta I^2}}\right)_{GR_{th}} = \sqrt{4q^2G^2 g_{th}\Delta\nu_c} = qG\sqrt{\frac{g_{th}}{\tau_\ell}} \quad \text{with } \Delta\nu_c = 1/(4\tau_\ell) \tag{11.82}$$

in which g_{th} represents the thermal generation rate. If the device is sufficiently cooled, the thermal generation will decrease so that it can be neglected compared to the other noise contributions.
Thermal noise occurs in all resistive materials. If we assume that the photo-conductive device has a resistence R_{pc} and is part of a a bias circuit as displayed in figure (11.8), the mean square thermal noise current can be expressed as:

$$\overline{\Delta I^2_{th}} = 4k\left(\frac{T_{pc}}{R_{pc}} + \frac{T_L}{R_L}\right)\Delta\nu_c = \frac{k}{\tau_n}\left(\frac{T_{pc}}{R_{pc}} + \frac{T_L}{R_L}\right), \text{ substituting } \Delta\nu_c = 1/(4\tau_n) \tag{11.83}$$

where T_{pc} and T_L are the temperatures of the photo-conductive sensor and the load resistor (R_L) respectively, τ_n represents the high frequecy cut-off parameter of the electronic processing filter. For simplicity we shall assume that this electronic filter comprises a single

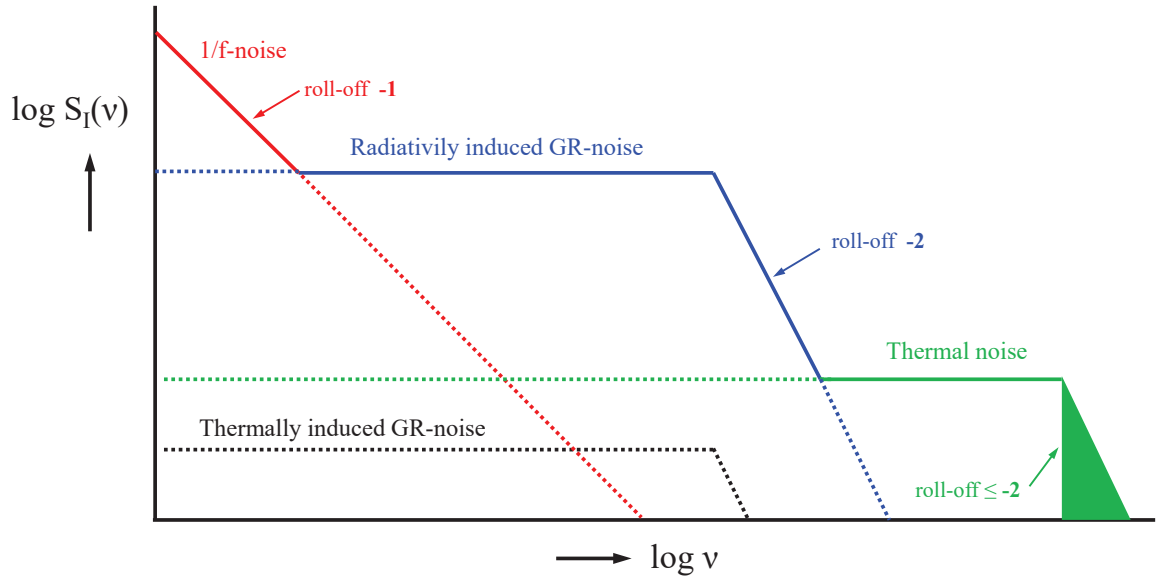

Figure 11.12: *Bode diagram of the current power spectral densities $S_I(\nu)$ for noise components encountered in photo-conductive devices as a function of temporal frequency. At low frequency the 1/f component dominates with a roll-off slope of -1 ($\propto \nu^{-1}$), however between 100 Hz and 1 MHz the GR-noise due to external irradiance should dominate if the temperature is kept low enough to suppress the thermally generated GR-noise (black dotted) and the thermal noise. Above the roll-off point due to the life time τ_ℓ of the radiation generated charge carriers (slope -2), the thermal noise will gradually take over at the higher frequencies up to a high frequency cut-off determined by the chosen filter pass band in the processing electronics (roll-off slope ≤ -2).*

integration with time constant τ_n and transfer function $H(2\pi j\nu) = 1/(1 + 2\pi j\nu\tau_n)$. If the load resistor is mounted on the heat sink of the photoconductor, we have $T_{pc} = T_L = T$, which is advantageous for the thermal noise of the load resistor, since photoconductors are often cryogenically cooled. We can then substitute R_{pc} and R_L by a single parallel equivalent resistor $R_{par} = R_{pc}R_L/(R_{pc} + R_L)$.
All noise components add in quadrature (summation of noise variances), hence for the total mean square noise current, including both BLIP noise and 'dark' noise, we can now write:

$$\overline{\Delta I^2_{tot}} = \left(\frac{a\, I_b^2 \Delta\nu_{1/f}}{\nu} + \frac{kT}{R_{par}\tau_n} + \frac{q^2G^2}{\tau_\ell}[\eta(\lambda)B(\lambda)A_{pc} + g_{th}] \right) \tag{11.84}$$

The current power spectral densities of these various noise components are displayed in figure (**??**). As already mentioned, the total contribution of the $1/f$ noise can be made negligible by proper component manufacturing technologies and cooling will significantly suppress the thermally generated GR-noise. Therefore, in practice, the thermal resistor noise in the bias circuit will be the main factor in determining to which irradiance level background-photon GR-noise will dominate the photoconductor's performance, i.e we have the condition:

$$\frac{T}{R_{par}} \ll \frac{q^2G^2}{k}\left(\frac{\tau_n}{\tau_\ell}\right)[\eta(\lambda)B(\lambda)A_{pc}] \tag{11.85}$$

In practice the ratio $\tau_n/\tau_\ell \approx 1$ so as to arrive at an optimum match between the electronic filter and the photoconductor response that is governed by the charge carrier lifetime.
In order to remain background-photon-noise(BLIP)-limited, the ratio of temperature to resistance must go down as $B(\lambda)$ decreases, so this sets certain limits to the load resistor and the operational temperature of the photo-conductive element. For high performance extrinsic IR sensors, the load resistor is much smaller than the sensor resistance, so $R_{par} \approx R_L$ allowing for external tuning. However for intrinsic photo-conductors like HgCdTe $R_{par} \approx R_{pc}$, in that case resistance tuning in the bias circuit is no option.
Equation (11.80) shows that the BLIP spectral D^* gets better if the level of the background irradiance goes down. If it is reduced to zero no further improvement in the value of D^* can be achieved since the condition given in equation (11.85) is no longer fulfilled. This is the case where the thermal noise becomes the dominant noise contribution. Hence, we can write the following expression for the spectral noise equivalent power $NEP(\lambda, \nu)$:

$$NEP(\lambda, \nu) = \frac{hc}{\lambda q G \eta(\lambda)} \left(\frac{kT}{R_{par}\tau_n} \right)^{\frac{1}{2}} \tag{11.86}$$

From this we can now derive the D^* for the thermal-noise-limited case of a photo-conductive element:

$$D^*(\lambda, \nu) = \frac{\sqrt{A_s \Delta\nu_c}}{NEP(\lambda, \nu)} = \frac{\lambda}{2hc}[qG\eta(\lambda)] \left(\frac{A_s R_{par}}{kT} \right)^{\frac{1}{2}}, \quad \text{with } \Delta\nu_c = 1/(4\tau_n) \tag{11.87}$$

From this expression for the normalized detectivity in case of thermal-noise-limited performance, it can be seen that the maximum achievable D^* is governed by the resistance-area ($A_s R_{par}$) product, i.e. high performance photoconductors require a high RA-product. Moreover the performance is also linearly related to the photoconductive gain, so sensors with an intrinsically low RA-product, like HgCdTe, can still attain a relatively high D^* value owing to a high photoconductive gain factor. For sensors with an $R_s \gg R_L$ operating in the thermal noise limit, the theoretically achievable maximum D^* is determined by the value of the load resistor R_L and is described by the same equation as the one for a photovoltaic sensor in which the equivalent R_{par} is in the junction resistance (viz. the next paragraph on photovoltaic sensor elements). As an example: for the low-background case, in order for a photoconductive sensor with a $G = 0.5$ to have equivalent performance as the photovoltaic sensor, the load resistance R_L should be four times higher than the junction resistance of the photovoltaic sensor.

11.5 Charge Coupled Devices

11.5.1 Operation principle

A charge-coupled device (CCD) in its simplest form constitutes a closely spaced array of metal-insulator-semiconductor (MIS) capacitors. The most important among the MIS elements is the metal-oxide-semiconductor (MOS) capacitor, made from silicon (Si) and employing silicon dioxide (SiO_2) as the insulator. The charge position in the MOS-array of capacitors is electrostatically controlled by voltage levels. Dynamical application of these voltage levels and their relative phases serves a dual purpose: injected charges (e.g. due to radiation generated electron-hole pairs) can be stored in the MOS capacitor and the built-up charge (i.e. charge packet) can subsequently be transferred across the semiconductor substrate in a controlled

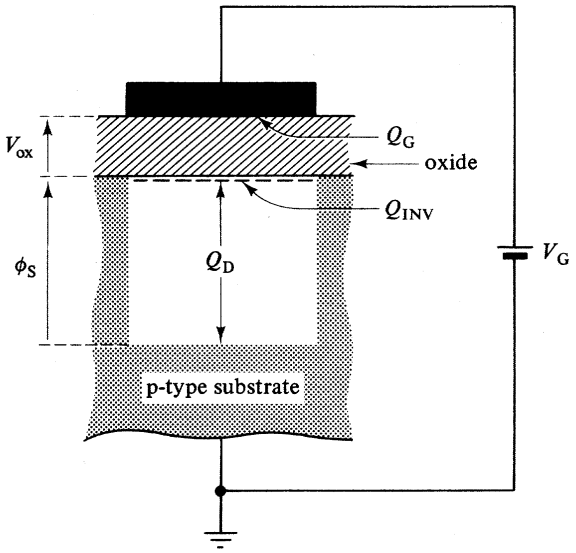

Figure 11.13: *Single CCD-electrode. V_G is positive, Q_{Inv} and Q_D are negative.*

manner. Monolithic CCD arrays are available for imaging in the near-infrared, the visible and the X-ray range, for the mid-infrared (up to 20 μm), hybrid fabrication is employed in which the infrared-sensitive detector material is sandwiched to a CCD array of cells for read-out.

In the following sections a short description is given of the storage and transfer mechanisms and of a few focal-plane CCD-architectures.

11.5.2 Charge storage in a CCD

Two basic types of charge coupled structures exist. In the one type, charge packets are stored very close to the interface between the semi-conductor (Si) and the overlaying insulator (SiO_2). Since the charges reside virtually at the surface of the semiconductor layer, these devices have become known as surface channel CCDs (SCCDs). In the other type, charge packets are stored at some distance away from the surface of the semiconductor, such devices have become known as bulk or buried channel CCDs (BCCDs). From the user point of view both devices are very similar, therefore the discussion here is mostly limited to SCCDs since their concept is easier to understand.

Figure 11.13 shows a single CCD-electrode comprising a metal gate, separated by a thin oxide layer (few times 0.1 μm) from a p-type semiconductor (hole-conduction). Prior to the application of a voltage bias to the gate electrode, there will be a uniform distribution of holes (majority free charge carriers) in the p-type semiconductor. As the gate electrode is made positive however, the holes are repelled immediately beneath the gate and a so-called depletion layer (devoid of free charge) is created. Increasing the gate voltage causes the depletion region to extend further into the semiconductor and the potential at the semiconductor/insulator interface (ϕ_S) becomes increasingly positive. Eventually, a gate voltage bias is reached at which the surface potential ϕ_S becomes so positive that electrons (i.e. the minority charge carriers in the p-type material !) are attracted to the surface where they form an extremely thin(≈ 0.01 μm thick), but very dense (in terms of charge density) layer, a so-called *inversion layer*. Basically the electrons reside in the deep potential well at the semiconductor surface and do not recombine with holes, since the latter are immediately repelled from the depletion layer upon creation. Therefore, if radiation is incident on a single CCD electrode, the electrons

from the produced electron-hole pairs will be stored in the inversion layer, the holes will be repelled from the depletion region. An analytical expression for the variation of the surface potential ϕ_S with the gate voltage V_G and the surface-charge density Q_{Inv} in the inversion layer can be derived as follows. From figure 11.13 it can be seen, since the p-type substrate is grounded, that

$$V_G = V_{ox} + \phi_S \tag{11.88}$$

Charge neutrality prescribes:

$$Q_G = -(Q_{Inv} + Q_D) \tag{11.89}$$

in which $Q_D = -qN_a x_D$ represents the surface charge density in the depletion later (i.e. the volume charge density $-qN_a$ integrated over the thickness of the depletion layer x_D). N_a is the density of the acceptor doping in the p-type semiconductor, q is the elementary charge. From the theory of depletion penetration, which basically involves integration of the Poisson equation in electrostatics, $x_D = 2\epsilon\phi_s/qN_a$, with ϵ the dielectric constant ($\epsilon = \epsilon_0\epsilon_r$). Substituting this in Q_D and writing $Q_G = V_{ox}C_{ox}$ (C_{ox} represents the oxide capacitance per unit area ($C_{ox} = \epsilon/t_{ox}$ with t_{ox} the oxide thickness)), the expression for the surface potential ϕ_S becomes after some manipulation:

$$\phi_S = V_G + V_0 + \frac{Q_{Inv}}{C_{ox}} - \sqrt{2\left(V_G + \frac{Q_{Inv}}{C_{ox}}\right)V_0 + V_0^2} \tag{11.90}$$

V_0 is a constant ($q\epsilon N_a/C_{ox}^2$), with the dimension Volt. The value of ϕ_S as a function of V_G (with $Q_{Inv} = 0$) and as a function of Q_{Inv} (with $V_G = 10$ and 15 V respectively) is displayed in figure 11.14 and figure 11.15 for a few thicknesses of the insulating oxide layer.

The surface potential ϕ_S can be interpreted as a *potential well*, the depth of which is determined by the magnitude of the inversion charge packet Q_{Inv} (in analogy with a bucket partially filled with fluid). From the figures it can be seen that ϕ_s is practically a linear function of Q_{Inv} and V_G, this arises from the fact that the constant V_0 is relatively small compared to typical values for V_G; i.e. $V_0 = 0.14$ Volt for a 0.1 μm thick oxide layer. Since $V_G = 10$ - 15 Volt:

$$\phi_S = V_G + \frac{Q_{Inv}}{C_{ox}} \qquad \text{in good approximation} \tag{11.91}$$

Note: in the above computation the difference in workfunction between the metal and the semiconductor has been neglected, i.e. the so-called *flat-band condition* has been assumed. In practice this can always be achieved by adaptation of the potential V_G. Moreover ϕ_S has a minimum value related to the Fermi-level in the semi-conductor, this boundary condition has been omitted from the above formulae, since it is of no direct relevance to the storage principle.

As will be seen in the next section, storage of charge at the Si-SiO_2 interface introduces potential losses of accumulated charge during charge transport, owing to charge trapping in the atomic surface states. To prevent such losses the charge packet should preferably be kept at a potential minimum separate from the Si-SiO_2 interface, i.e. a minimum in the bulk-silicon has to be generated. This can be achieved by adding an n-type layer on top of the p-type silicon. The ionised positive ions of the n-type top layer raise the positive gate voltage to an ever higher channel potential inside the silicon. Figure 11.16 shows the comparison with the original situation (electron-potential minimum at the interface). As illustrate, the potential well in the n-type Si has now a minimum (for electrons) deeper in the bulk Si. This is the principle of the BCCD, charge is now stored and transported in a channel embedded in the bulk silicon and is not anymore subject to charge loss at surface states. Figure 11.16 shows

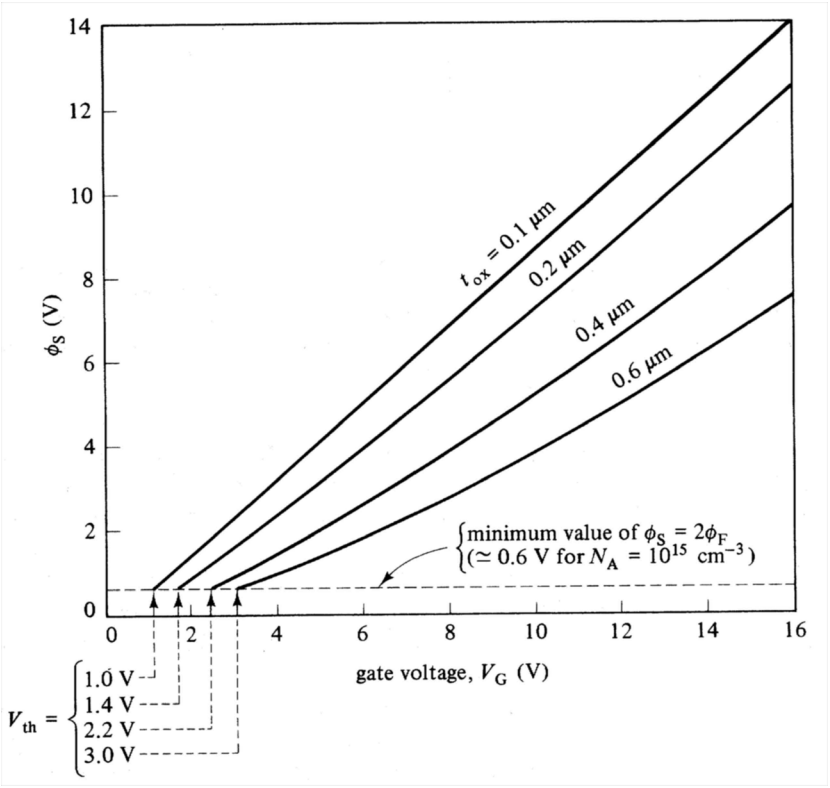

Figure 11.14: *Variations of the surface potential ϕ_S with the gate voltage V_G for different values of the oxide thickness t_{ox}. The charge in the inversion layer Q_{Inv} is zero in all cases. Figure taken from Beynon & Lamb (1980).*

also the comparison between an empty and partly filled SCCD, (a) and (b), and an empty and partly filled BCCD, (c) and (d). In the latter case the charge packet flattens the minimum of the potential well, this can be regarded as a "neutral layer" which increases in width if it becomes filled with charge.

11.5.3 Charge transport in a CCD

The way in which a charge packet is transported through a CCD structure (charge-coupling) is illustrated in figure 11.17. Assume the charge packet is stored initially in the potential well under the second electrode (from the left in the figure) which is biased to say 10 V. All CCD electrodes need to be kept at a certain minimum bias (≈ 2 V) to ensure that each MOS capacitor operates in the inversion-mode. The potential well under the 10 V electrode is much deeper than those under the 2V electrodes and, provided it is not "overfilled" with charge, it is only in this well that charge will be stored. Suppose that the bias on the third electrode is now increased to 10 V. If the second and third electrode are sufficiently close, both wells will merge. The equations that govern the charge transfer process comprise the current density and the continuity equation. For an n-type channel (electron charge) these equations are:

$$j(x,t) = q\mu_n n(x,t)\frac{\partial\phi(x,t)}{\partial x} + qD_n\frac{\partial n(x,t)}{\partial x} \tag{11.92}$$

$$\frac{\partial n(x,t)}{\partial t} = \frac{1}{q}\frac{\partial j(x,t)}{\partial x} \tag{11.93}$$

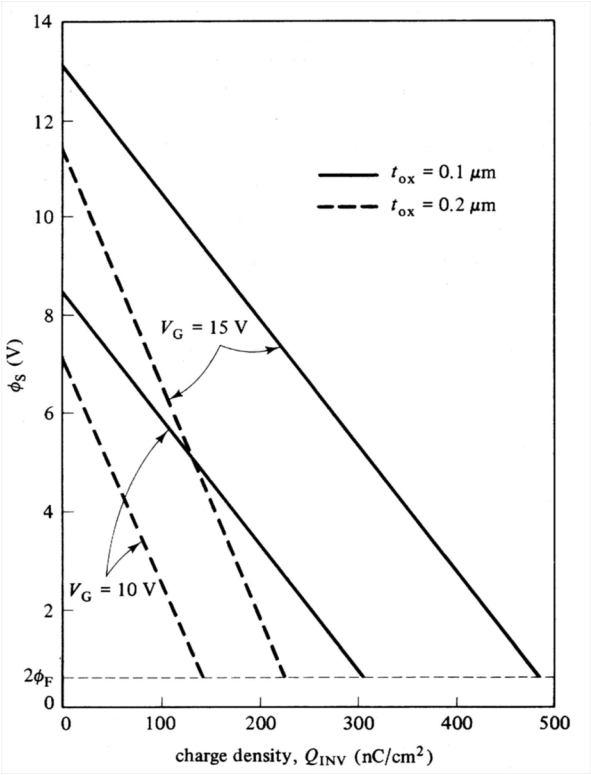

Figure 11.15: *Variations of the surface potential ϕ_S as a function of the inversion charge Q_{Inv} for two values of the gate voltage V_G and of the oxide thickness t_{ox}. Figure taken from Beynon & Lamb (1980).*

where charge propagation is in the x direction (no vector treatment), $n(x,t)$ is the electron density, μ_n the electron mobility and D_n the electron diffusion coefficient. This diffusion coefficient is related to the mobility of the charge carriers μ_n through

$$\frac{D_n}{\mu_n} = \frac{kT}{q} \tag{11.94}$$

(the so-called Einstein relation). The first right-hand term in equation 11.92 refers to drift of the charge packet under a gradient in electric potential, the second term refers to thermal diffusion under the presence of an density gradient. The drift component arises from two causes. The first cause derives from *self-induced fields* in the presence of a gradient in charge concentration, charges of the same type will mutually repel and reshuffle the concentration of charge carriers in such a way that this gradient becomes zero. Secondly, due to so-called *fringing fields*, in which charges are forced to move due to the existence of electric fields generated by the various voltage levels on the gates.

The equalizing of charge concentration under electrodes two and three described above is hence governed by the drift speed due to self-induced fields and by thermal diffusion. In practice these two processes are frequently described by introducing an effective diffusion coefficient $D_{n,eff}$, since both arise from the existence of a gradient in carrier concentration. For large charge packets (large concentration difference), the process is mainly determined by the self-induced drift, for small charge packets (e.g. $< 1\%$ of the well charge capacity) thermal diffusion dominates and slows the transfer process down.

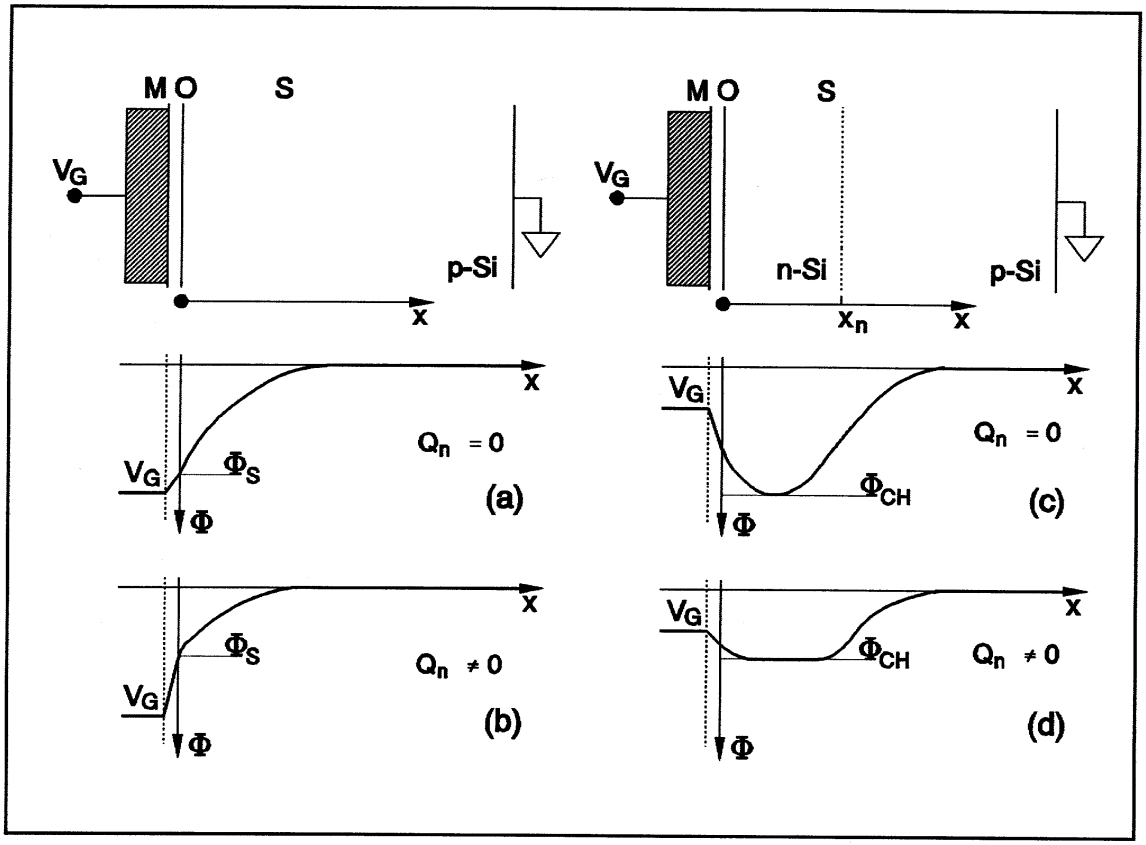

Figure 11.16: *Surface and channel potential for a SCCD ((a) and (b)) and a BCCD ((c) and (d)), with empty ((a) and (c)) and filled ((b) and (d)) wells. Figure taken from Theuwissen (1995).*

Returning now to figure 11.17, if the charge is evenly distributed under electrodes 2 and 3 (situation c), reducing the potential on the second electrode to 2 V will introduce a fringe field and the remaining content of this well will drift into the third well owing to the fringe field. The final situation shown in (e) is a deep potential well and its associated charge packet moved one position to the right. By applying a succession of varying voltages to the gate electrodes, the charge packet can be transported through the CCD structure in a controlled manner. The gate electrodes can be grouped together with each group or *phase* connected to a different voltage clock. Various CCD structures and electrode systems are employed, the one described above requires a three-phase clocking system and is therefore referred to as a *three phase CCD*. Each image pixel requires in this case three gate electrodes to store and transport the charge packet.

It is obvious that the transfer mechanisms described are not perfect, i.e. not all of the charge is transferred and some signal charge is left behind. The charge transfer efficiency (CTE) is the ratio of charge transferred to the initial charge present. A complementary term often used in the literature on these devices is the transfer inefficiency (CTI), i.e. the charge lost to the initial charge packet: CTI = 1 - CTE. Typical values of CTE are of the order 0.99999 for a good device or CTI = 10^{-5}. As already mentioned before the CTE of a SCCD is, without special measures not discussed here, considerably worse compared to the BCCD due to the interface trapping states. Moreover, due to the relaxation of charges from the

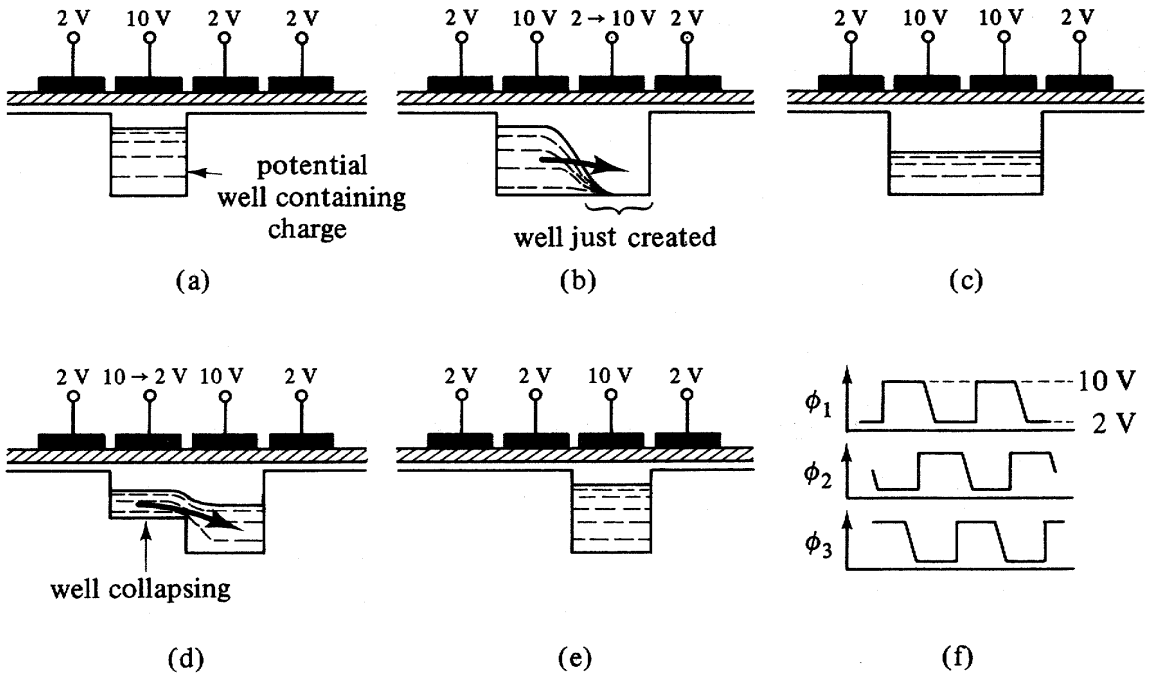

Figure 11.17: *(a)-(e) Transport of a charge packet in a CCD. (f) clocking waveforms for a three phase CCD. Figure taken from Beynon & Lamb (1980).*

traps, the so-called trapping noise in a SCCD is at least an order of magnitude larger than in BCCDs, which explains the preference for BCCDs in certain applications.

Till now, only charge transport along the gate electrodes in one direction had been discussed. It is of course necessary to limit the extent of the potential well in the orthogonal direction. This *lateral confinement* of the charge packet is achieved by a so-called *channel-stop diffusion*, which comprises a heavily doped region of the semiconductor relative to its neighboring regions. This region exhibits a large conductivity σ relative to the surrounding material and quenches the surfaces potential ϕ_S so that no depletion region can be formed. In this way one dimensional columns (or rows) are implemented in the CCD structure along which the charge transfer occurs, isolated from its neighboring columns (rows). At the positions of the channel stop diffusion (p^+ or n^+ material), the field oxide separating it from the gate structure is much thicker as to prevent break-down of the p^+ (n^+) contact to the conducting gate electrodes. A three dimensional display of a BCCD structure is shown in figure 11.18.

11.5.4 Charge capacity and transfer speed in CCD structures

The amount of charge that can be stored in a CCD pixel depends mainly on two variables: the clock voltages and the electrode area in combination with a SCCD or a BCCD structure.

Regarding a SCCD, the full-well storage capacity is in good approximation given by the oxide capacity under the gate electrode ($A_{elec}C_{ox}$) and the gate voltage V_G:

$$A_{elec}C_{ox} = \frac{Q_{Inv}}{V_G} \qquad \Longrightarrow \qquad Q_{Inv} = A_{elec}C_{ox}V_G \tag{11.95}$$

(Remember: C_{ox} is the oxide capacitance per unit area, A_{elec} is the electrode geometric area).

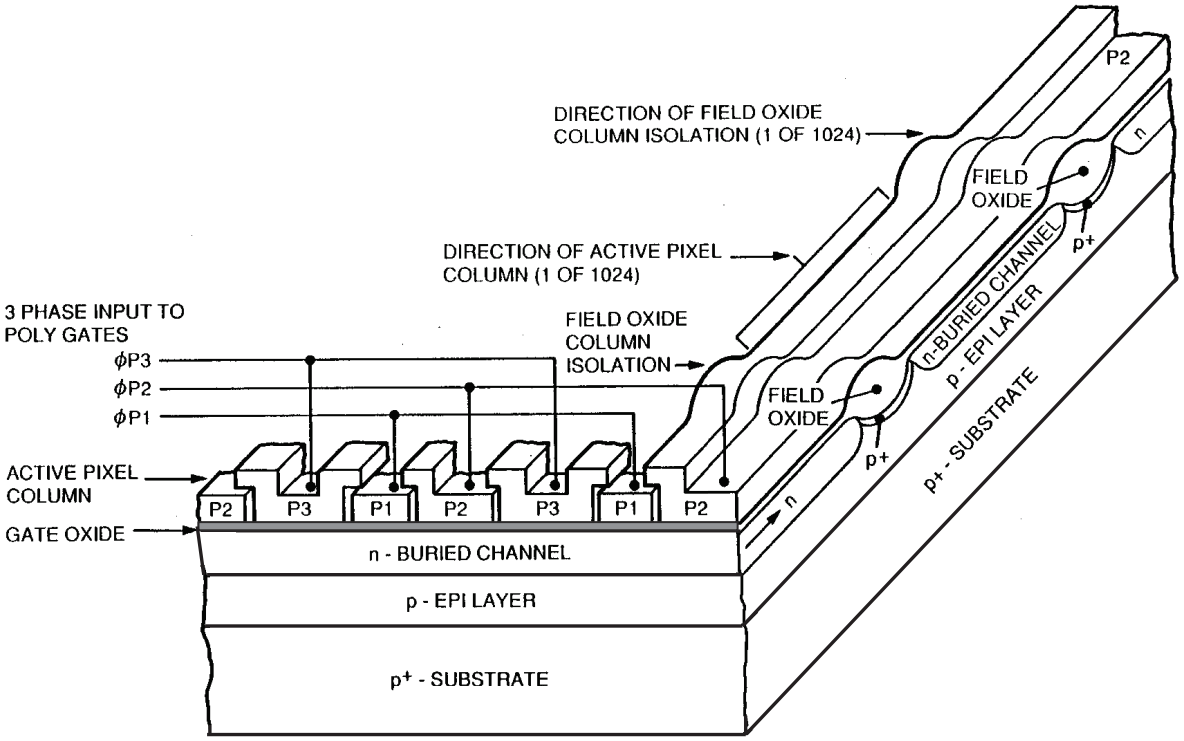

Figure 11.18: *Three dimensional display of a BCCD structure.*

As an example, take $A_{elec} = 10 \times 20$ μm^2, $t_{ox} = 0.1$ μm ($C_{ox} = \epsilon_{ox}/t_{ox}$) and $V_G = 10$ V: in that case $Q_{Inv} = 0.6$ pC $\approx 3.6{\cdot}10^6$ electrons.

In case of a BCCD, the expression is somewhat more complicated due to the finite depth of the charge storage and transport in the Si. However the ratio in charge handling capacity between SCCD and BCCD structures can be shown to approximate:

$$\frac{Q_{SCCD}}{Q_{BCCD}} = 1 + \frac{\epsilon_{ox} x_n}{3\epsilon_{Si} t_{ox}} \tag{11.96}$$

in which x_n represents the width of the neutral layer in the BCCD when the full storage capacity is reached. For typical values $x_n = 2$ μm and $t_{ox} = 0.1$ μm, this ratio amounts to about 3. Consequently, creation of an embedded channel lowers the charge handling capacity by a substantial factor.

The intrinsic speed of charge transport in a CCD structure is governed by transport equation 11.36, depending on the time constants for self-induced drift, thermal diffusion and fringe field drift.

In a SCCD the time constant for self-induced drift is a function of charge density, C_{ox} and the interelectrode spacing. For $C_{ox} = 1$ pF, $Q_{Inv} = 10^{12}$ cm^2 and spacing 25 μm, the time constant $\tau_{Si} = 0.14$ μs. The time constant for thermal diffusion of an electron packet ($D_n \approx 10$ cm$^2{\cdot}$s^{-1}) amounts to 0.25 μs. On this basis the high frequency limit would appear to be a few MHz, however the fringing field of the neighboring gate electrodes aid the transfer considerably, especially when thermal diffusion is dominant and clocking frequencies up to 15 MHz can be used for SCCDs

In the case of the BCCD the speed is potentially dominated by the fringing field of the neighboring gate due to the depth of the charge channel. The potential levels do not exhibit the

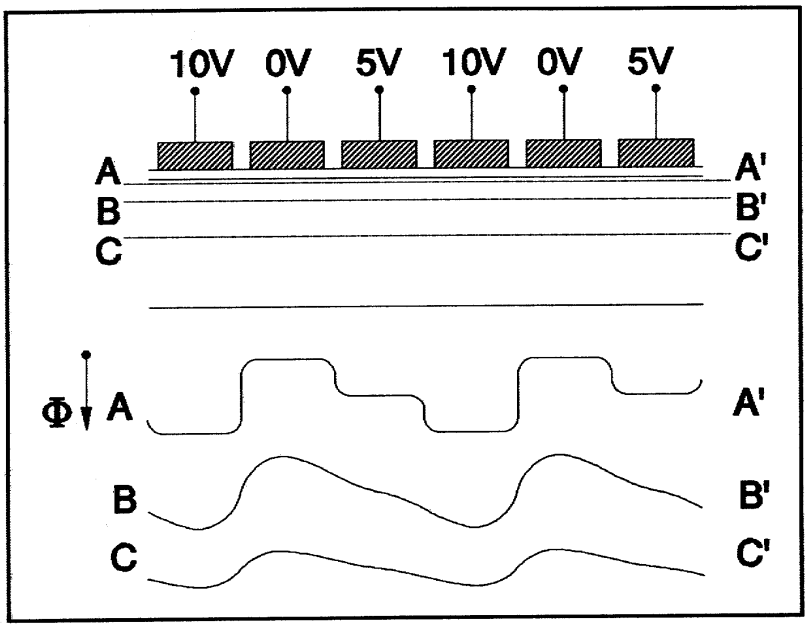

Figure 11.19: *Fringing fields at the Si-SiO_2 interface at several depths. Figure taken from Beynon & Lamb (1980).*

flat structures encountered at the Si-SiO_2 interface as displayed in figure 11.17 but possess a continuous gradient along which charge can drift swiftly to a potential minimum. The situation is schematically shown in figure 11.19 for a few depths of the charge channel. BCCDs, with usually smaller charge packets, can therefor be read out at much higher frequencies, up to 300 MHz, while still retaining acceptable values of the CTE for several imaging applications.

11.5.5 Focal plane architectures

The two-dimensional CCD imaging arrays can be subdivided into *frame-transfer* (FT) imagers, *interline-transfer* (IL) imagers and *frame-interline-transfer* (FIT) devices. The FT and IL architectures are briefly described below.

Figure 11.20 shows the device architecture of a frame-transfer image sensor, the operation is shown in figure 11.21. The CCD comprises a photosensitive array and a memory array coupled to a linear output register. The light sensitive top part of the device, or image section, integrates the charges produced by the impinging photons over a predefined integration time. At the end of this period the charge packets are transferred along the columns into the memory array (figure 11.21(b)). This transfer needs to be done quickly to prevent disturbance by light falling on the image section during read-out. Subsequently each row in the memory section is clocked into the linear output register from which it is shifted to the output stage amplifier (video signal). During transport of all video information from the storage area to the output stage, all CCD cells in the image array are again biased in the integration mode, allowing the build-up of the next image.

A simpler version of the frame-transfer imager is the *full-frame* device, which lacks the storage section. During read-out the incoming light should be interrupted to avoid disturbances. This can be done by using a shutter which cuts out the light path to the imager.

The typical architecture of the interline-transfer imager is displayed in figure 11.22. In

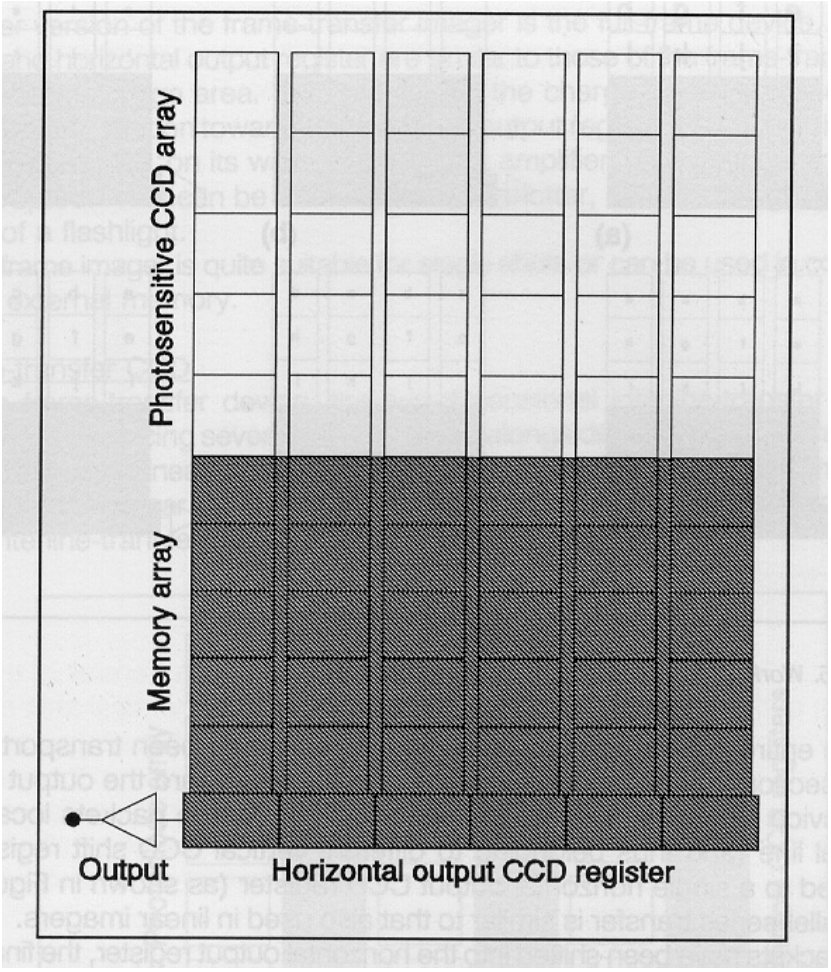

Figure 11.20: *Architecture of a frame-transfer image sensor. Figure taken from Theuwissen (1995).*

this case the photo-sensitive pixels are located near the shielded CCD transport register. The integration of charge takes place in the photo-sensitive pixels during exposure to the radiation source, at the end of the integration time the charge packets from the photo-sensitive columns are transferred in parallel to the vertical registers alongside them, see figure 11.23(b). The vertical shift registers are emptied into the horizontal-output register row by row which are read-out serially at the output. The advantage of this architecture is the very short transfer time to the parallel storage column as compared to the serial shift to the storage section in the case of the frame-transfer CCD. On the other hand, the presence of periodic storage columns in the image area may introduce severe aliasing effects close to the spatial Nyquist frequency of the CCD-array.

If a pixel has a characteristic size Δx, the sampling of an image can be described with an array of normalized window functions: $\frac{1}{\Delta x}\Pi\left(\frac{x}{\Delta x}\right)$. The spatial frequencies (s) associated with this window function is obtained from its Fourier transform: $\mathrm{sinc} s\Delta x$.

If the pitch of the pixels in the image plane is given by x_0, the Nyquist frequency follows from $s_N = \frac{1}{2x_0}$. Normalizing the spatial frequency s on s_N yields the geometrical MTF for a

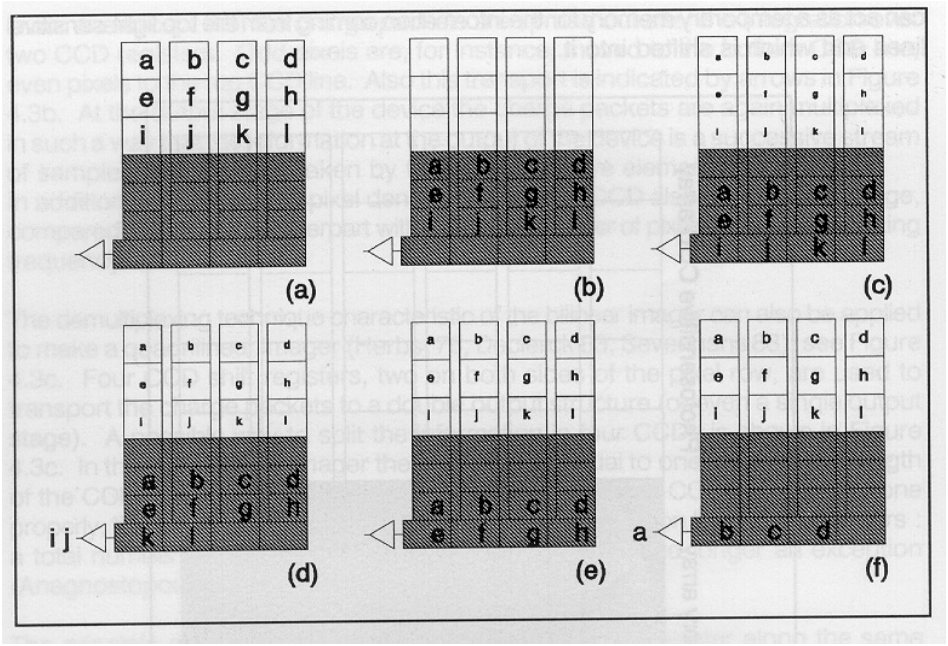

Figure 11.21: *Working principle of a frame-transfer image sensor. Figure taken from Theuwissen (1995).*

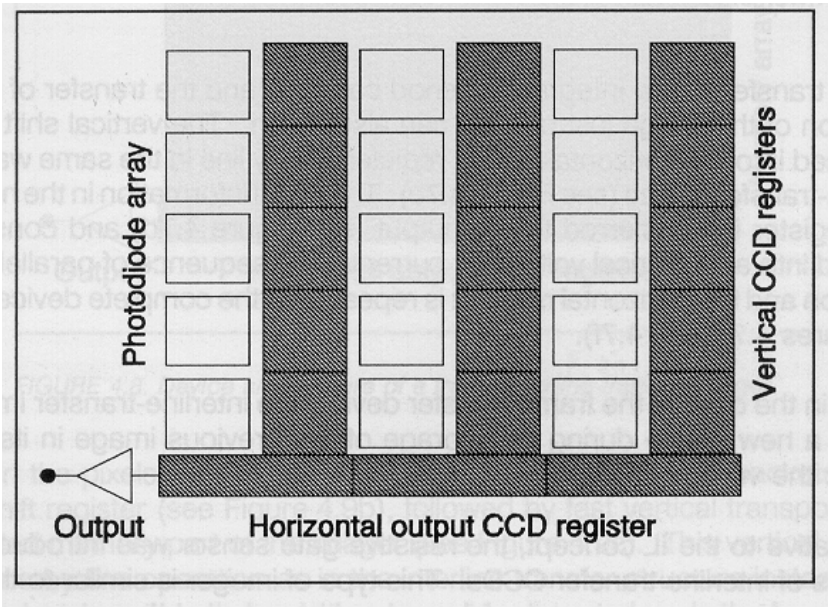

Figure 11.22: *Architecture of an interline-transfer image sensor. Figure taken from Theuwissen (1995).*

linear array of pixels Δx with pitch x_0 ($s_0 = s/s_N$):

$$MTF_{geo} = \mathrm{sinc}\frac{s_0 \Delta x}{2x_0} \tag{11.97}$$

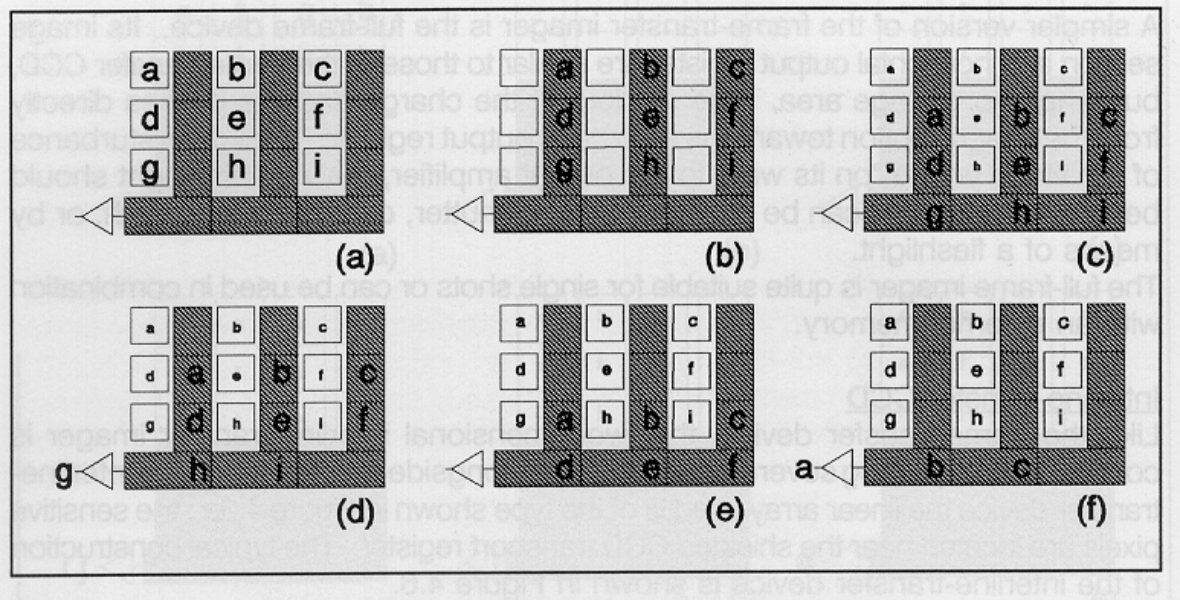

Figure 11.23: *Working principle of an interline-transfer image sensor. Figure taken from Theuwissen (1995).*

For contiguous pixels, like in a frame-transfer CCD array, $\Delta x \approx x_0$ yielding:

$$MTF_{FT} = \text{sinc}\frac{s_0}{2} \tag{11.98}$$

with $MTF_{FT} = 0$ for $s_0 = 2$, i.e. $s = 2s_N$.

For non-contiguous pixels, like an interline transfer CCD array,$\Delta x \approx \frac{x_0}{2}$ yielding:

$$MTF_{IL} = \text{sinc}\frac{s_0}{4} \tag{11.99}$$

with $MTF_{IL} = 0$ for $s_0 = 4$, i.e. $s = 4s_N$.

This analysis indeed shows that the MTF of the interline-transfer CCD extends twice as high above the Nyquist frequency as compared to the frame-transfer CCD, giving rise to potential Moiré fringes due to aliasing. This effect can only be avoided by limiting the spatial frequencies of the input-image signal to s_N.

11.5.6 Wavelength response of CCDs

For visual light applications, two possibilities can be considered to irradiate the CCD, i.e. irradiation through the front surface and irradiation through the back-surface, so-called back-illumination. Illumination through the front surface, i.e. the side which contains the gate structure, requires the usage of poly-silicon gate electrodes which transmit light. A problem encountered in this case entails the strongly wavelength dependent absorption and interference effects occurring in the thin poly-silicon gate layer (≈ 0.5 μm) and the thin oxide layer ($\approx 0.1 - 0.2$ μm). The current responsivity and the interference effects are shown in figure 11.24. Also, the blue-responsivity is strongly suppressed by absorption in the poly-silicon gate material.

Back-illumination requires thinning of the Si-substrate to ensure that the photon-generated charge reaches the potential wells. The charge transport can be aided by building an electric field gradient into the semi-conductor, this electric field gradient can be provided by increasing

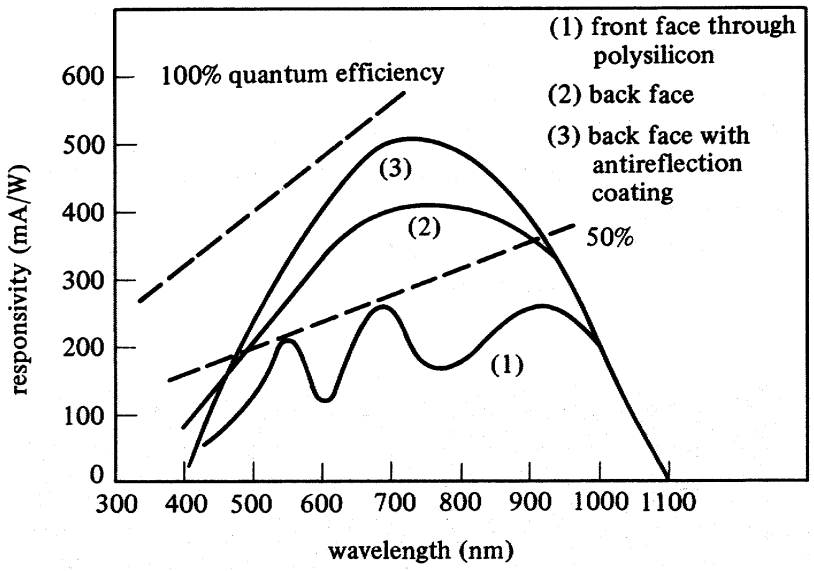

Figure 11.24: *CCD spectral response. Figure taken from Beynon & Lamb (1980).*

the substrate doping concentration in the regions close to the silicon surface. This increased doping has the effect of *bending* the energy bands at the back of the surface so as to accelerate the photon-generated carriers towards the front surface and the potential wells. This technique is particularly useful for increasing the blue-responsivity where the charge carriers are generated close to the rear silicon surface. This back-face response can be further improved by minimizing the reflection of light from the back surface employing a $\lambda/4$ thick layer of silicon monoxide at the wavelength of interest. Figure 11.24 shows a quantum efficiency of about 50 % with back-illumination, which can be raised to a peak efficiency of about 90% by using the proper antireflection coating. Figure 11.25 shows a complete family of CCDs for optical light with different architectures and array sizes.

Non-visible imaging with CCDs is normally divided into three wavelength ranges:

Wavelengths longer than 1 μm, for which the photo-electric absorption coefficient in silicon is too low ($h\nu_{IR} <$ bandgap) and all photons pass through the structure without being absorbed. For this reason infrared photons need to be converted first into electrons, e.g. by means of so-called Schottky-barrier structures in which pixels are used made out of platinum-silicide (PtSi). An array of these detectors is then coupled to a CCD read-out system.

The responsivity in the thermal IR can theoretically be extended in this way to approximately 5.6 μm.

For wavelengths shorter that 0.4 μm and longer than 10 nm the opposite is the case as compared to the IR range: the absorption is very high since not only silicon, but also the silicon oxide layer has a very high absorption coefficient in this wavelength regime. In figure 11.26 the penetration depth in silicon is displayed over a wide wavelength range, it is clear that the UV photon will be stopped in the top layers above the CCD. To avoid this problem several solutions are possible:

Deposition of an UV-sensitive phosphor on top of the active area of the imager which down-converts the energy of the UV-photons to longer wavelengths. An example is Coronene, which fluoresces in the green portion of the visible spectrum under UV exposure.

Also, as in the visible regime, back-illumination is an option. However, due to the high

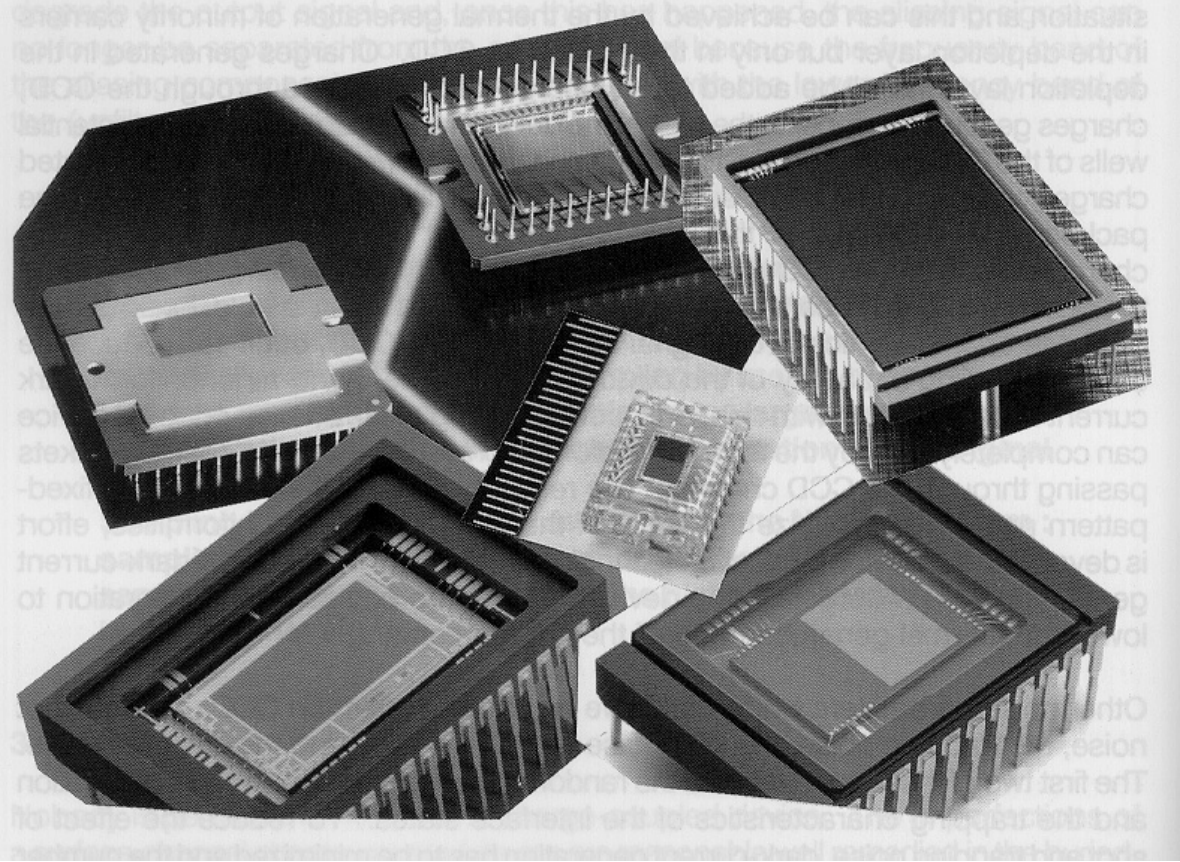

Figure 11.25: *Photo of several CCDs. Top left: back-side illuminated FT imager with 1260 × 1152 pixels. Top right: a full frame CCD with 3k × 2k pixels, each of 9 μm × 9 μm. Middle: a low-cost FT sensor with 270,000 pixels, total diameter of the image section is 3.2 mm. Bottom left: HDTV IT image sensor with 2M pixels, 11 mm diagonal. Bottom right: FT CCD for broadcast applications with 500,000 pixels.*

absorption, the substrate of the CCD has to be thinned to typically 10 μm, which is a very expensive process and requires subsequently very delicate handling of the device. An alternative is deep depletion of a lightly-doped, high-resistivity substrate, such that the depletion region under the CCD gates extends to the back of the siliconwafer. The charge carriers generated by the UV illumination are swept to the front side into the potential wells by the electric field of the deep depletion layer. This approach does not require the extreme thinning mentioned above for conventional high-doped material, a thickness of 50 μm still allows adequate collection of charge owing to the deep depletion field.

Application of CCDs in X-ray imaging has made a substantial development over the recent years, in particular for X-ray astronomy where the X-ray photon flux is sufficiently low to register the (small) charge packet associated with a single X-ray photon. In contrast to the optical application, exposures yielding no more than one X-ray photon per 100 pixels is pursued before read-out, since in this case both spectral an spatial information can be obtained simultaneously, i.e. the magnitude of the charge packet represents in this case the energy of the impinging X-ray photon. Moreover, apart from the simultaneous spatial and spectral resolution, deep depletion CCDs (30 – 50 μm) provide a high quantum efficiency (> 90%) over a wide X-ray range (0.2 – 10 nm) and are therefore ideally suited as an imaging

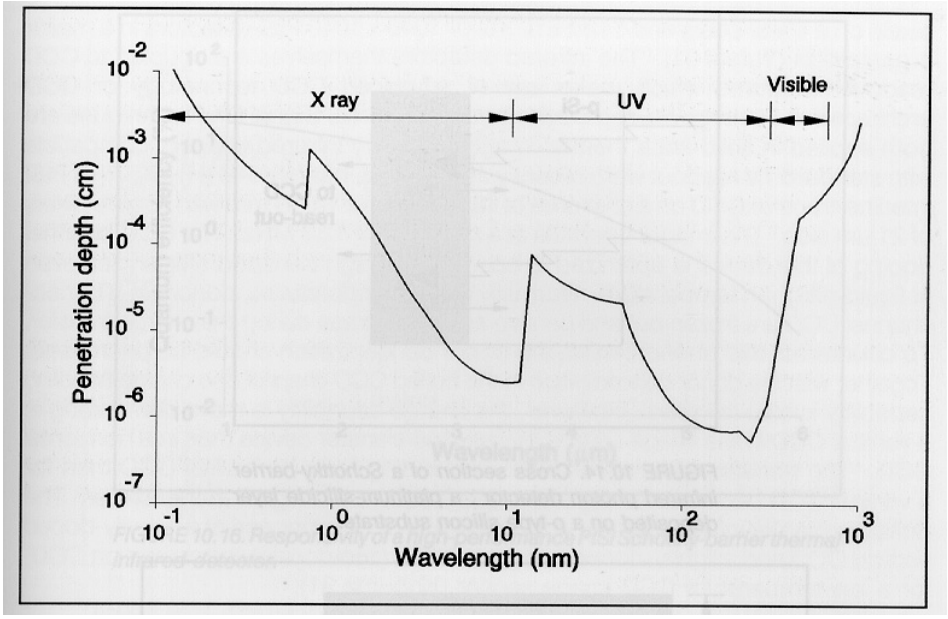

Figure 11.26: *Penetration depth of silicon as a function of wavelength. Figure taken from Theuwissen (1995).*

spectrometer behind a grazing incidence X-ray telescope. Back-illumination, which again avoids the problem of penetrating the gate structure and the oxide layer, gives quite superior response to low-energy X-rays (2 – 10 nm). Moreover, as importantly, a deep depletion layer minimizes the effect of charge diffusion of the X-ray-generated charge cloud, since the electric field causes this cloud to quickly drift into the potential well. In this way degradation of spatial and spectral resolution is minimized. A second cause of degradation of spatial and spectral resolution is charge loss when X-ray photons are absorbed at the boundary of two or more pixels, since charge splitting between these pixels will occur. This problem can be dealt with later in the image processing, provided no charge loss occurs due to a recombination process (e.g. near a highly-doped stop-diffusion).

X-ray CCDs require a very high CTE value (CTI = 10^{-5} – 10^{-6}) to retain the intrinsic, quantum noise dominated, spectral resolution. Moreover, the CCD needs to be cooled to an operating temperature of about 200 K to reduce the influence of several noise sources (thermal noise, read-out noise).

Chapter 12

Fitting observed data

In this chapter we discuss how one can describe observations, and how one can compare measurements with model predictions.
We first introduce discrimination between systematic and random errors, and show how the most common distribution functions for random errors are most effectively computed, followed by a discussion of error propagation. Next, we discuss the criteria that should be used to decide which fit of a data set is considered to be best, for the case where the errors are distributed according to a Gaussian distribution, and for the case where they are Poissonian. We describe fitting procedures specific for the least squares criterion, both for the linear and the non-linear case. Finally, we discuss fitting procedures which are more generic, that may be applied both to least squares and to the case where the errors follow a Poissonian distribution.

12.1 Errors

12.1.1 Accuracy versus precision

We may discriminate between the accuracy and the precision of an experiment. The *accuracy* of an experiment is a measure of how close the result of an experiment comes to the true value. Therefore, it is a measure of the correctness of the result. The *precision* of an experiment is a measure of how exactly the result is determined, without reference to what that result means. It is also a measure of how reproducible the result is. The *absolute precision* indicates the magnitude of the uncertainty in the result in the same units as the result. The *relative precision* indicates the uncertainty in terms of a fraction of the value of the result.
It is obvious that accuracy and precision need to be considered simultaneously for any experiment. It would be a waste of time to determine a result with high precision if we knew the result would be highly inaccurate. Conversely, a result cannot be considered to be accurate if the precision is low. The accuracy of an experiment as defined here generally depends on how well one can control or compensate for *systematic errors*. These are the errors which will make a result differ from the true value *with reproducible discrepancy*. The precision of an experiment is dependent on how well one can overcome or analyse *random errors*. These are the fluctuations in observations which yield results that differ from experiment to experiment and that require repeated trials to yield precise results. A given accuracy implies a precision at least as good and, consequently, depends to some extent on the random errors also. So we discriminate between:

- *A systematic error*: reproducible inaccuracy introduced by faulty equipment, calibration, or technique.

- *A random error*: Indefiniteness of result due to the *a priori* finite precision of an experiment. Also: measure of the fluctuation in a result after repeated experimentation.

In Chapter 3, section 2, of the OAF1 lecture series we have introduced the subject of random phenomena and variables that constitutes the mathematical basis for handling random errors. If an infinite number of measurements could be taken, the result would give the way in which the observed data points are distributed, i.e. the *true* probability distribution. This distribution is referred to as the *parent distribution*, any practical measurement can be perceived as a *sample* of an infinite number of possible measurements. Consequently the experimental data only allow an *estimate* of the parameters that describe the parent distribution. For a description of the most common probability distributions we refer here to OAF1-section 3.2. For convenience we only repeat here the definition of the sample parameters which can be derived from a limited number of available measurements to approximate the parameter values describing the underlying parent distribution.

For the average we have:

$$\mu \simeq \overline{x} \equiv \frac{1}{N}\sum_{i=1}^{N} x_i \tag{12.1}$$

and for the variance:

$$\sigma^2 \simeq s^2 \equiv \frac{1}{N-1}\sum_{i=1}^{N}(x_i - \overline{x})^2 = \frac{1}{N-1}\left(\sum_{i=1}^{N} {x_i}^2 - N\overline{x}^2\right) \tag{12.2}$$

In estimating the average with Eq. 12.1 we assume that all measurements x_i are independent. In estimating the variance with Eq. 12.2 we note that we already have used the x_i values to estimate the average, which implies that we have $N-1$ independent measurements left. (If we know $N-1$ values of x_i and $\overline{x}$, we can determine the one remaining x_i.) This is the reason that the sum of $(x_i - \overline{x})^2$ is divided by $N-1$ (instead of by N). Indeed, if we only have one measurement, i.e. $N = 1$, then the best value for the average is given by this one measurement, but we have no measure for the variance.

Take $\overline{x}$ as a variable in Eq. 12.2; to find the value of $\overline{x}$ for which s^2 is minimal, we set the derivative of s^2 with respect to $\overline{x}$ to zero:

$$\frac{\partial s^2}{\partial \overline{x}} = \frac{-2}{N-1}\sum_{i=1}^{N}(x_i - \overline{x}) = \frac{-2}{N-1}\left(\sum_{i=1}^{N} x_i - N\overline{x}\right) = 0 \tag{12.3}$$

From the last two terms we obtain once more Eq. 12.1. This shows that the definition Eq. 12.1 for the sample average minimizes the sample variance given by Eq. 12.2.

When the measurements are binned, as is always the case if we have digital measurements but also often in other cases, we find the average and its variance from the binned data. We write the number of bins as B, and denote the value of x in bin b as x_b and the number of measurements in that bin as N_b, where $b = 1, \ldots, B$. We normalize the number of measurements in each bin on the total number of measurements, to find the probability that a measurement from the sample falls in bin b as $P_b \equiv N_b / \sum_{b=1}^{B} N_b$, and rewrite Eqs. 12.1,12.2 as

$$\overline{x} = \sum_{b=1}^{B} P_b x_b \tag{12.4}$$

and

$$s^2 = \frac{N}{N-1}\left(\sum_{b=1}^{B} P_b {x_b}^2 - \overline{x}^2\right) \tag{12.5}$$

Higher order moments of distributions with points far from the average ('outliers') are very sensitive to outliers: a large $x_i - \overline{x}$ value dominates much more in the distribution of the $(x_i - \overline{x})^2$'s than in the distribution of $|x_i - \overline{x}|$'s.

For an analogous reason, it is strongly recommended never to use even higher moments, such as the third order moment or *skewness* and the fourth order moment or *kurtosis*. For completeness, here are the definitions of these moments:

$$\text{Skewness} \equiv \frac{1}{N\sigma^3}\sum (x_i - \overline{x})^3 \tag{12.6}$$

and

$$\text{Kurtosis} \equiv \frac{1}{N\sigma^4}\sum (x_i - \overline{x})^4 - 3 \tag{12.7}$$

where σ is the standard deviation. The subtraction of 3 in the kurtosis is made so that the kurtosis of a Gauss distribution is zero.
In this course we shall stick to the common practice of mainly using the variance.
First of all, we shall show now how the various probability distributions can be computed most effectively.

12.1.2 Computing the various distributions

In the bad old days, one was forced to use tables in thick, heavy books whenever one used the distributions described above. Nowadays, fast computers allow us to compute the quantities we need, with relative ease. Chapter 6 of *Numerical recipes* (2nd edition) contains everything we need, and more...

We start with the factorials, necessary in calculations with binomial and Poisson function. We first define the *gamma function*

$$\Gamma(z) = \int_0^\infty t^{z-1} e^{-t} dt \tag{12.8}$$

and then note that for integer z, the gamma function equals the factorial, with an offset of one in the argument:

$$n! = \Gamma(n+1) \tag{12.9}$$

For small values of n, the factorial can be computed directly as $n \times (n-1) \times (n-2) \ldots$; for large values we can use the gamma-function. For large n there is the danger that the factorial is larger than the largest number allowed by the computer. In that case it is better to calculate the logarithm of the factorial (or equivalently, the logarithm of the gamma function).

These considerations are taken into account in the following useful function routines from Numerical Recipes:

- `function gammln(x)` returns $\ln\Gamma(x)$ for input x
- `function factrl(n)` returns real $n!$ for input integer n
- `function factln(n)` returns real $\ln n!$ for input integer n
- `function bico(n,k)` returns real $\begin{pmatrix} n \\ k \end{pmatrix}$ for integer inputs n, k

These routines enable us to compute binomial and Poisson probabilities.

A useful quantity is the cumulative Poisson probability, the probability that a Poisson process will lead to a result between 0 and $k-1$ inclusive:

$$P_x(< k) \equiv \sum_{n=0}^{k-1} P_P(k,x)$$

For its computation we use the *incomplete gamma function*:

$$P(a,x) \equiv \frac{1}{\Gamma(a)} \int_0^x t^{a-1} e^{-t} dt \tag{12.10}$$

Its complement is also called the incomplete gamma function (which is somewhat confusing...):

$$Q(a,x) \equiv 1 - P(a,x) \equiv \frac{1}{\Gamma(a)} \int_x^\infty t^{a-1} e^{-t} dt \tag{12.11}$$

It is easily shown that the cumulative Poisson probability is given by (the second type of) the incomplete gamma function:

$$P_x(< k) = Q(k,x)$$

The corresponding routines in Numerical Recipes are:

- `function gammp(a,x)` returns $P(a,x)$ for input a, x
- `function gammq(a,x)` returns $Q(a,x)$ for input a, x

Finally, we look at the integral probability of the Gauss function, which can be computed from the *error function*:

$$\mathrm{erf}(x) = \frac{2}{\sqrt{\pi}} \int_0^x e^{-t^2} dt \tag{12.12}$$

Equally useful is the *complementary error function*

$$\mathrm{erfc}(x) = \frac{2}{\sqrt{\pi}} \int_x^\infty e^{-t^2} dt \tag{12.13}$$

The wonderfull fact is that we don't have to write a new routine to compute the error functions, because they are given by the incomplete gamma functions:

$$\mathrm{erf}(x) = P(1/2, x^2) \qquad (x \geq 0)$$

$$\mathrm{erfc}(x) = Q(1/2, x^2) \qquad (x \geq 0)$$

The corresponding routines in Numerical Recipes are:

- `function erf(x)` returns $\mathrm{erf}(x)$ for input x, using `gammp`
- `function erfc(x)` returns $\mathrm{erfc}(x)$ for input x, using `gammq`
- `function erfcc(x)` which returns $\mathrm{erfc}(x)$ based on a direct series development of 12.13.

12.2 Error propagation

Suppose we have a function f of a number of variables $u, v, \ldots$:

$$f \equiv f(u, v, \ldots) \tag{12.14}$$

We want to know how we can estimate the variance of f,

$$\sigma_f{}^2 \equiv \lim_{N\to\infty} \frac{1}{N} \sum_{i=1}^{N} (f_i - \overline{f})^2 \tag{12.15}$$

from the variances $\sigma_u, \sigma_v, \ldots$ of the variables $u, v, \ldots$. To derive this we will make the assumption, which is usually only approximately correct, that the average of f is well approximated by the value of f for the averages of the variables:

$$\overline{f} = f(\overline{u}, \overline{v}, \ldots) \tag{12.16}$$

We make a Rayleigh-Taylor expansion of f around the average:

$$f_i - \overline{f} \simeq (u_i - \overline{u}) \frac{\partial f}{\partial u} + (v_i - \overline{v}) \frac{\partial f}{\partial v} + \ldots \tag{12.17}$$

to write the variance in f as

$$\sigma_f{}^2 \simeq \lim_{N\to\infty} \frac{1}{N} \sum_{i=1}^{N} \left[(u_i - \overline{u}) \frac{\partial f}{\partial u} + (v_i - \overline{v}) \frac{\partial f}{\partial v} + \ldots \right]^2$$

$$= \lim_{N\to\infty} \frac{1}{N} \sum_{i=1}^{N} \left[(u_i - \overline{u})^2 \left(\frac{\partial f}{\partial u} \right)^2 + (v_i - \overline{v})^2 \left(\frac{\partial f}{\partial v} \right)^2 + 2(u_i - \overline{u})(v_i - \overline{v}) \frac{\partial f}{\partial u} \frac{\partial f}{\partial v} + \ldots \right] \tag{12.18}$$

We rewrite this by using the definitions for the variances of u and v,

$$\sigma_u{}^2 \equiv \lim_{N\to\infty} \frac{1}{N} \sum_{i=1}^{N} (u_i - \overline{u})^2; \qquad \sigma_v{}^2 \equiv \lim_{N\to\infty} \frac{1}{N} \sum_{i=1}^{N} (v_i - \overline{v})^2 \tag{12.19}$$

and defining the covariance of u and v as

$$\sigma_{uv}{}^2 \equiv \lim_{N\to\infty} \frac{1}{N} \sum_{i=1}^{N} (u_i - \overline{u})(v_i - \overline{v}) \tag{12.20}$$

to obtain:

$$\sigma_f{}^2 = \sigma_u{}^2 \left(\frac{\partial f}{\partial u} \right)^2 + \sigma_v{}^2 \left(\frac{\partial f}{\partial v} \right)^2 + 2\sigma_{uv}{}^2 \frac{\partial f}{\partial u} \frac{\partial f}{\partial v} + \ldots \tag{12.21}$$

If the differences $u_i - \overline{u}$ and $v_i - \overline{v}$ are not correlated, the sign of their product is as often positive as negative, and the sum in eq. 12.20 will be small as subsequent terms (almost) cancel. On the other hand, if the differences are correlated, most products $(u_i - \overline{u})(v_i - \overline{v})$ will be positive, and the cross-correlation term in Eq. 12.21 can be large as subsequent terms add up.

12.2.1 Examples of error propagation

weighted sum: $f = au + bv$

For the partial derivatives we have

$$\frac{\partial f}{\partial u} = a, \qquad \frac{\partial f}{\partial v} = b \tag{12.22}$$

and substituting these in eq. 12.21 we obtain

$${\sigma_f}^2 = a^2 {\sigma_u}^2 + b^2 {\sigma_v}^2 + 2ab{\sigma_{uv}}^2 \tag{12.23}$$

Note that a and b can each have positive or negative sign. Their signs only have an effect on the cross-correlation term, which as a consequence can be negative, and *make the variance smaller*! For example, if each u_i is accompanied by a v_i such that $v_i - \overline{v} = -(b/a)(u_u - \overline{u})$, then $f = a\overline{u} + b\overline{v}$ for all u_i, v_i pairs, and ${\sigma_f}^2 = 0$.

product: $f = auv$

With

$$\frac{\partial f}{\partial u} = av, \qquad \frac{\partial f}{\partial v} = au \tag{12.24}$$

we obtain

$$\frac{{\sigma_f}^2}{f^2} = \frac{{\sigma_u}^2}{u^2} + \frac{{\sigma_v}^2}{v^2} + \frac{2{\sigma_{uv}}^2}{uv} \tag{12.25}$$

division: $f = au/v$

$$\frac{\partial f}{\partial u} = \frac{a}{v}, \qquad \frac{\partial f}{\partial v} = -\frac{au}{v^2} \tag{12.26}$$

hence

$$\frac{{\sigma_f}^2}{f^2} = \frac{{\sigma_u}^2}{u^2} + \frac{{\sigma_v}^2}{v^2} - \frac{2{\sigma_{uv}}^2}{uv} \tag{12.27}$$

exponent: $f = ae^{bu}$

$$\frac{\partial f}{\partial u} = bf \tag{12.28}$$

hence

$$\frac{\sigma_f}{f} = b\sigma_u \tag{12.29}$$

power: $f = au^b$

$$\frac{\partial f}{\partial u} = \frac{bf}{u} \tag{12.30}$$

hence

$$\frac{\sigma_f}{f} = b\frac{\sigma_u}{u} \tag{12.31}$$

12.3 Errors distributed as a Gaussian and the least squares method

Suppose we have a series of measurements y_i with associated errors distributed according to a Gaussian with width σ_i, i.e. each measurement is drawn from a Gaussian with width σ_i around a model value y_m. For one measurement, the probability $P(y_i) \equiv P_i$ of obtaining a measurement y_i, in an interval Δy, is then given by

$$P_i \Delta y = \frac{1}{\sqrt{2\pi}\sigma_i} e^{\frac{-(y_i - y_m)^2}{2{\sigma_i}^2}} \Delta y \tag{12.32}$$

where we allow that different measurements have different associated errors σ_i. If we have a series of N measurements the overall probability of obtaining such a series is:

$$P(\Delta y)^N \equiv \prod_{i=1}^{N} (P_i \Delta y) = \frac{1}{(2\pi)^{N/2} \prod_i \sigma_i} \exp\left[-\frac{1}{2} \sum_{i=1}^{N} \frac{(y_i - y_m)^2}{{\sigma_i}^2} \right] \Delta y^N \tag{12.33}$$

The highest probability P is that for which

$$\chi^2 \equiv \sum_{i=1}^{N} {\chi_i}^2 \equiv \sum_{i=1}^{N} \frac{(y_i - y_m)^2}{{\sigma_i}^2} \tag{12.34}$$

is smallest. If we wish to determine the most probable model value for y_m for a series of measurements y_i, we thus must find the value(s) for y_m for which the sum of the squares $(y_i - y_m)^2/{\sigma_i}^2$ is minimal. This is called the method of least squares and was described first in 1804 by Gauss, following earlier work by Lagrange and Laplace.

According to the assumption that the errors are gaussian, as stipulated above, each χ_i is a random draw from a normal distribution; the sum of the ${\chi_i}^2$ is called chi-square. If we have N measurements, and we fit M parameters, we have $N - M$ independent measurements left. The probability distribution for χ^2 is called the chi-square distribution for $N - M$ degrees of freedom. This distribution is what we get if would draw $N - M$ random samples from a normal distribution, square them, and add the squares, and repeat this many times, each time producing one χ^2. The probability of a given χ^2 can be computed with the `gammq`-function, as follows: the probability that an observed χ^2_{obs} or greater is reached for $N - M$ degrees of freedom is $P(\chi^2_{obs}) = \texttt{gammq}(0.5(N-M), 0.5\chi^2_{obs})$. If the probability that we get is very small, then something is wrong. The most obvious possibility is that the model is wrong. Another possibility is that the errors have been under-estimated, so that we demand a better agreement with the model than the measurement accuracy warrants. A third possibility is that the errors are not distributed as Gaussians. This latter possibility tends to increase the observed χ^2; and often causes us to accept probabilities somewhat lower than one would superficially expect. Thus in many cases, a probability of 0.05 is considered quite acceptable. The reason one can do this, is that really wrong models easily produce much smaller probabilities, less than 0.000001, say. Also, even in a perfect statistical process, a probability of 5% arises on average once every 20 trials, so that finding such a probability due to chance is quite common. If one finds in a certain experiment that one always produces low probabilities, one must look into it and try to determine the cause.

It is worth noting that apparently significant results can arise from ignoring negative results. The most obvious case is the winning of a lottery. Suppose the winner is the person who has guessed the correct six-digit number. The probability for one person to have the

winning number is one in a million, but if several million people participate we expect several to have guessed the correct number. A less obvious case is an experiment which is repeated many times. A well-known case here is the stock-broker. Suppose that one starts with ten million people, who predict how stocks change in value. After a year, select the people who are among the ten best predictors; repeat this five times (so that six rounds have been made), then there will be (on average) ten stock brokers who have predicted among the best 10% for six years in a row, if the prediction process is purely random! It is thus by no means obvious that a stock-broker who has predicted correctly for many years in a row is better than random – one can only find out if one knows how many stock-brokers there are.... (Indeed, in experiments in which a gorilla selects the stocks, the gorilla often doesn't do bad at all.)

When we make a fit of a model to a dataset, the result should always consist of three parts:

1. the best values of the parameters $a_1, a_2, \ldots$
2. the errors on these parameter values
3. the probability that the measured χ^2 is obtained by chance; i.e. the probability that the model adequately describes the measurements

It is very important always to provide all these three desiderata.

We will discuss three cases for y_m, viz. i) a constant, in which y_m is the same for all i; ii) a straight line $y_m = a + bx$ where y_m depends on the variable x and the model parameters a and b; and iii) the general case in which y_m depends on a variable x and a set of parameters $a_1, a_2, \ldots$, which we write as $y_m = y_m(x; \vec{a})$.

12.3.1 Weighted averages

If the model for $y_m = a$ is the same for all measurements, then the constant a is the (best estimate for the) average $\overline{y}$ of the y_i's. The least squares method tells us that we find the most probable value for a by minimizing eq. 12.34 with respect to a, i.e.

$$\frac{\partial}{\partial a}\left[\sum_{i=1}^{N}\frac{(y_i-a)^2}{{\sigma_i}^2}\right] = 0 \Rightarrow \sum_{i=1}^{N}\frac{y_i-a}{{\sigma_i}^2} = 0 \tag{12.35}$$

Thus the least squares are found for

$$\overline{y} \equiv a_{min} = \frac{\sum_{i=1}^{N}\frac{y_i}{{\sigma_i}^2}}{\sum_{i=1}^{N}\frac{1}{{\sigma_i}^2}} \tag{12.36}$$

To obtain an estimate of the error in $\overline{y}$, we note that $\overline{y}$ is a function of the variables $y_1, y_2, \ldots$. *If the measurements y_i are not correlated*, we find the variance for $\overline{y}$ from (see eq. 12.21):

$${\sigma_{\overline{y}}}^2 = \sum_{i=1}^{N}\left[{\sigma_i}^2\left(\frac{\partial\overline{y}}{\partial y_i}\right)^2\right] = \sum_{i=1}^{N}\left[{\sigma_i}^2\left(\frac{1/{\sigma_i}^2}{\sum_{k=1}^{N}(1/{\sigma_k}^2)}\right)^2\right] \tag{12.37}$$

which gives

$${\sigma_{\overline{y}}}^2 = \frac{1}{\sum_{i=1}^{N}(1/{\sigma_i}^2)} \tag{12.38}$$

In the case where all measurement errors are identical, $\sigma_i \equiv \sigma$, eqs. 12.36,12.38 can be further simplified to

$$\overline{y} = \frac{(1/\sigma^2)\sum_{i=1}^{N} y_i}{(1/\sigma^2)\sum_{i=1}^{N}(1)} = \frac{1}{N}\sum_{i=1}^{N} y_i \tag{12.39}$$

and

$$\sigma_{\overline{y}}{}^2 = \frac{\sigma^2}{N} \tag{12.40}$$

12.3.2 Fitting a straight line

We write the model of a straight line as

$$y_m(x,a,b) = a + bx \Rightarrow y_m(x_i,a,b) = a + bx_i \tag{12.41}$$

where the parameters to be fitted are a and b. We now wish to minimize the χ^2, according to Eq. 12.34, with respect to a and b, and do this by looking for the values for which the derivative of χ^2 is zero:

$$\frac{\partial \sum_{i=1}^{N}[(y_i - a - bx_i)/\sigma_i]^2}{\partial a} = 0 \Rightarrow \sum_{i=1}^{N}\left(\frac{y_i - a - bx_i}{\sigma_i{}^2}\right) = 0 \Rightarrow \sum_{i=1}^{N}\frac{y_i}{\sigma_i{}^2} - a\sum_{i=1}^{N}\frac{1}{\sigma_i{}^2} - b\sum_{i=1}^{N}\frac{x_i}{\sigma_i{}^2} = 0 \tag{12.42}$$

$$\frac{\partial \sum_{i=1}^{N}[(y_i - a - bx_i)/\sigma_i]^2}{\partial b} = 0 \Rightarrow \sum_{i=1}^{N}\frac{x_i(y_i - a - bx_i)}{\sigma_i{}^2} = 0 \Rightarrow \sum_{i=1}^{N}\frac{x_i y_i}{\sigma_i{}^2} - a\sum_{i=1}^{N}\frac{x_i}{\sigma_i{}^2} - b\sum_{i=1}^{N}\frac{x_i{}^2}{\sigma_i{}^2} = 0 \tag{12.43}$$

The important thing to note now is that all the sums can be evaluated without knowledge of a or b. To make the equations easier to interpret we define the sums as

$$\sum_{i=1}^{N}\frac{1}{\sigma_i{}^2} \equiv S; \qquad \sum_{i=1}^{N}\frac{x_i}{\sigma_i{}^2} \equiv S_x; \qquad \sum_{i=1}^{N}\frac{x_i{}^2}{\sigma_i{}^2} \equiv S_{xx}$$

$$\sum_{i=1}^{N}\frac{y_i}{\sigma_i{}^2} \equiv S_y; \qquad \sum_{i=1}^{N}\frac{x_i y_i}{\sigma_i{}^2} \equiv S_{xy}; \qquad \Delta \equiv SS_{xx} - (S_x)^2$$

and rewrite the above two equations as two equations for two unknowns a and b:

$$aS + bS_x - S_y = 0$$

$$aS_x + bS_{xx} - S_{xy} = 0$$

with the solutions

$$a = \frac{S_{xx}S_y - S_x S_{xy}}{\Delta} \tag{12.44}$$

$$b = \frac{SS_{xy} - S_x S_y}{\Delta} \tag{12.45}$$

To find the errors in a and b, we note that a and b depend on the independent parameters y_i, such that

$$\frac{\partial a}{\partial y_i} = \frac{S_{xx} - x_i S_x}{\sigma_i{}^2\Delta}; \qquad \frac{\partial b}{\partial y_i} = \frac{x_i S - S}{\sigma_i{}^2\Delta} \tag{12.46}$$

and use Eq. 12.21 to obtain (after some rewriting)

$$\sigma_a{}^2 = \frac{S_{xx}}{\Delta}; \qquad \sigma_b{}^2 = \frac{S}{\Delta} \tag{12.47}$$

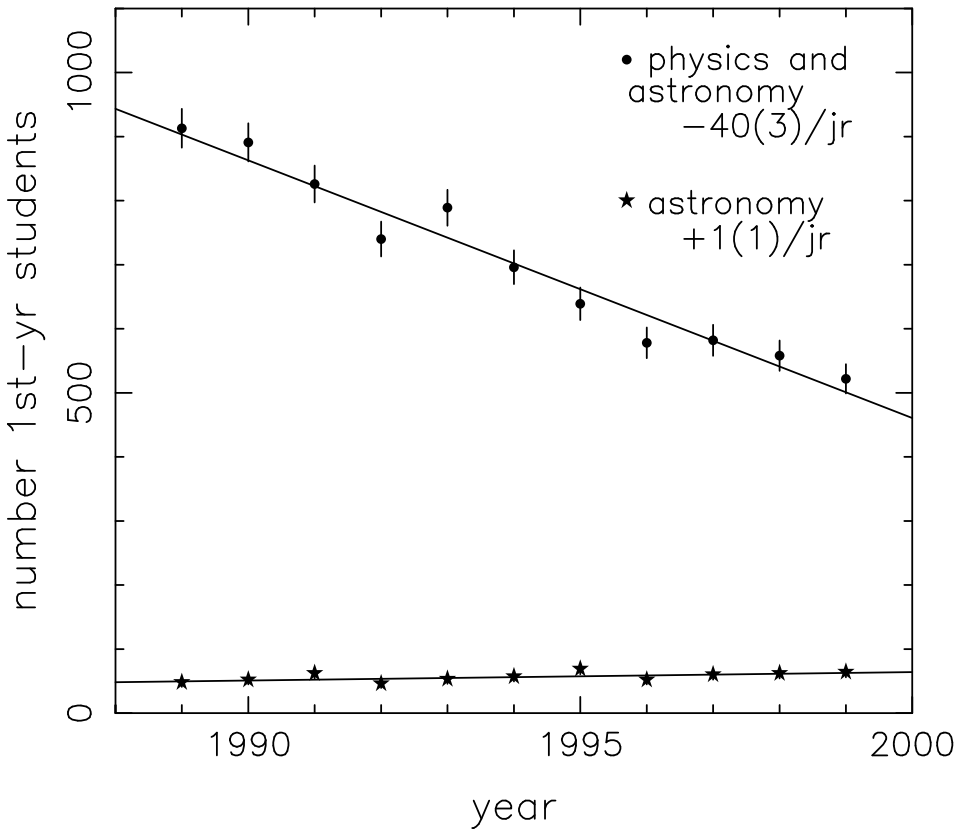

Figure 12.1: *Total number of 1st-year students in the Netherlands in physics and astronomy (above) and in astronomy only (below) between 1990 and 2000. Assumed poissonian errors are indicated. Data taken from the* Nederlands Tijdschrift voor Natuuurkunde*, which stopped publishing these numbers in 2000...*

As the third ingredient of our fit we determine the probability that a good fit would produce the observed ${\chi^2}_{obs}$ or bigger as

$$Q = \texttt{gammq}\left(\frac{N-2}{2}, \frac{{\chi^2}_{obs}}{2}\right) \tag{12.48}$$

As an illustration of some more subtleties we have a look at Figure 12.1, where the number of new physics and astronomy students in the Netherlands are plotted for the last decade of the 20st century. The first point concerns the errors in measured integer numbers. It is assumed in the figure that the error on the number of students is given by the square root of the number, and these errors are shown. The reader may be surprised now, and say: 'Why is there an error? After all, we know exactly how many students there are in a given year!'. The answer is that *for the purpose of fitting a model* the numbers of students can vary due to chance, and that the actual number in a year is drawn from a distribution (poissonian in this case) around the expected value. Similarly, if an X-ray experiment detects N photons in a given time interval, in a given energy range, then the error that we assign to this number when we fit it in a model is *not* zero – even though we know exactly how many photons were measured!

The second point concerns a good choice of a and b. If we fit the number of students as $N(t) = a + bt$ where t is the year, then a gives the number of students for the year 0.

Apart from the fact that this number is meaningless in the current context, there are two other problems associated with this choice. The first one is that the sums involving x_i-values in Eqs. 12.44–12.47 are very large numbers, so that subtracting them from one another (as in computing Δ) easily leads to roundoff errors, and thus to wrong results. The second one is that in this choice of a and b there will be a very strong correlation between the errors: if we change b a little, a changes dramatically in one direction. Both these problems can be circumvented by centering the time interval around the point of fitting, i.e. by effectively fitting $N = a + b(t - 1994)$. Now, the sums involve smaller numbers, and the pivot point around which a and b vary is such that the correlation of their variations are minimized.

Also for non-linear fits, it is good practice in astronomy to define the time with respect to some fiducial point somewhere near the middle of the measurements.

12.3.3 Non-linear models: Levenberg-Marquardt

When our model involves a parameter a which enters the y_m, and through this the χ_i, non-linearly, we cannot execute a summation without having (an estimate for) the value of a. As an example, consider the function $y = \sin(ax)$, which has (see Eq. 12.34)

$$\frac{\partial \chi^2}{\partial a} = -2 \sum_{i=1}^{N} \frac{[y_i - \sin(ax_i)] x_i \cos(ax_i)}{{\sigma_i}^2} \tag{12.49}$$

and we see that the summation cannot be executed without a value for a.

In general, this means that a model $y(x, \vec{a})$ which is non-linear in $\vec{a}$ can be fitted to a set of data only iteratively, in the sense that one needs a first set of values for $\vec{a}$, and then finds successive improvements of these values.

To understand how this is done, we discuss first a one-dimensional case where there is one parameter a that is fitted, so that $\chi^2 = \chi^2(a)$. We are then looking for the value of a for which $\chi^2(a)$ is minimized.

When one is far from the minimum, we can use the derivative $\partial\chi^2/\partial a$ to decide in which direction to look for the improved value:

$$a_{n+1} = a_n - K \frac{\partial \chi^2}{\partial a} \tag{12.50}$$

where K is a constant (the value of which we discuss below).

Once we get close to the minimum of χ^2, this way of stepping towards a better solution becomes less efficient, since near the minimum the first derivative approaches zero. Close to the minimum we approximate χ^2 as a quadratic function of a: $\chi^2(a) = p + q(a - a_{min})^2$, where p is the minimum value of χ^2, reached at $a = a_{min}$. We combine the derivatives $\partial\chi^2/\partial a = 2q(a - a_{min})$ and $\partial^2\chi^2\partial a^2 = 2q$, to write:

$$a - a_{min} = \frac{\partial\chi^2/\partial a}{\partial^2\chi^2/\partial a^2} \Rightarrow a_{n+1} = a_n - \frac{\partial\chi^2/\partial a}{\partial^2\chi^2/\partial a^2} \tag{12.51}$$

Now make the step to a more-dimensional case, i.e. with more than one parameter, and write

$$\chi^2(\vec{a}) \simeq p - \vec{q} \cdot \vec{a} + \frac{1}{2} \vec{a} \cdot \vec{\vec{D}} \cdot \vec{a} \tag{12.52}$$

where for model $y_m = y_m(x, \vec{a})$ we have:

$$q_k \equiv \frac{\partial \chi^2}{\partial a_k} = -2 \sum_{i=1}^{N} \frac{[y_i - y_m]}{{\sigma_i}^2} \frac{\partial y_m}{\partial a_k} \equiv -2\beta_k \tag{12.53}$$

and

$$D_{kl} \equiv \frac{\partial \chi^2}{\partial a_k \partial a_l} = 2 \sum_{i=1}^{N} \frac{1}{{\sigma_i}^2} \left[\frac{\partial y_m}{\partial a_k} \frac{\partial y_m}{\partial a_l} - [y_i - y_m] \frac{\partial^2 y_m}{\partial a_k \partial a_l} \right] \equiv 2\alpha_{kl} \tag{12.54}$$

The second term on the right hand side is expected to be small with respect to the first one, because $y_i - y_m$ will almost equally often be positive as negative, and subsequent terms in the summation will almost cancel. To save computing time, one can drop the second term. It often turns out that the iteration to the best solution becomes more stable by doing this.

For the more dimensional case we can write for Eqs. 12.50,12.51:

$$\beta_k = \lambda \alpha_{kk} \delta a_k \tag{12.55}$$

$$\beta_k = \sum_{l=1}^{M} \alpha_{kl} \delta a_l \tag{12.56}$$

Here we have chosen to scale the proportionality constant K in Eq. 12.50 with the second derivative, where λ is a constant.

The Levenberg-Marquardt method now continues by adding the two last equations:

$$\beta_k = \sum_{l=1}^{M} \alpha'_{kl} \delta a_l \qquad \text{where} \qquad \alpha'_{kl} = \alpha_{kl} \quad (\text{if } k \neq l); \quad \alpha'_{kl} = \alpha_{kl}(1+\lambda) \quad (\text{if } k = l) \tag{12.57}$$

For large λ Eq. 12.57 approaches Eq. 12.55, and for small λ it approaches Eq. 12.56.

The solution of the equation then proceeds as follows. One picks an initial solution, and a small value for λ (i.e. one hopes that the solution is already close enough for the quadratic approximation). Compute the χ^2 for the initial solution, and compute a new value for $\vec{a}$ with Eq. 12.57. If the χ^2 for the new solution is smaller (larger) than for the old one, then the quadratic approach does (doesn't) work, and one should decrease (increase) λ to get closer to the purely quadratic (linear) method of Eq. 12.56 (12.55). This process is iterated until the minimum χ^2 is found.

We also need the errors on the best parameters $\vec{a}$. For this we use the general relation (near minimum)

$$\delta\chi^2 = \delta\vec{a} \cdot \vec{\vec{\alpha}} \cdot \delta\vec{a} \tag{12.58}$$

If the best values of the parameters are not correlated, then the matrix α is close to diagonal, i.e. the off-diagonal elements α_{kl} are much smaller than the elements α_{kk} on the diagonal. In that case the inverse matrix C is almost given by $C_{kk} = 1/\alpha_{kk}$, and the distance δa_k to the best value a_k has

$${\delta a_k}^2 = \frac{\Delta\chi^2}{\alpha_{kk}} \tag{12.59}$$

Thus to estimate a 1-*sigma* error in a_k we enter $\Delta\chi^2 = 1$ in Eq. 12.59.

When the errors are correlated, the situation is more complex, and the matrix C gives the correlation between the deviations of the parameters from their best values. For details we refer to Numerical Recipes, Press et al. (1992).

12.3.4 Optimal extraction of a spectrum

For this topic we refer to the article by Horne (1985).

12.4 Errors distributed according to a Poisson distribution and Maximum likelihood

In measurements in which a small number of events is counted, we are often dealing with a distribution of the measurements which is given by the Poisson distribution. In this case, the least-squares methods do not apply. We will discuss the maximum-likelihood method for errors with a Poissonian distribution. In the literature, this method is often referred to as *the maximum-likelihood method*, where the Poissonian error distribution is implied. We will follow this practice, but only after noting that this abbreviated name is misleading, in that the least-squares method is also a maximum-likelihood method, viz. the maximum-likelihood method for errors distributed as Gaussians!

To illustrate the maximum-likelihood method we consider the number of counts on a photon-counting detector. We write the number of counts detected in location i as n_i, and the number of counts predicted for that location by the model as m_i. The probability at one location to obtain n_i photons when m_i are predicted is

$$P_i = \frac{{m_i}^{n_i} e^{-m_i}}{n_i!} \tag{12.60}$$

If the values of m_i (and n_i) are large, this probability may be approximated with a Gaussian, and one may use a least-squares method. Typically, a value of 20 is used. This value is based on the assumption that the difference between the Poisson and Gaussian distributions for large μ is less important than the uncertainties due to systematic effects in the measurements. In principle, this assumption should be verified in each case.

For small values of m_i (and n_i) we proceed to use the Possion distribution. To maximize the overall probability we thus have to maximize

$$L' \equiv \prod_i P_i \tag{12.61}$$

and for computational ease we maximize the logarithm of this quantity

$$\ln L' \equiv \sum_i \ln P_i = \sum_i n_i \ln m_i - \sum_i m_i - \sum_i \ln n_i! \tag{12.62}$$

The last term in this equation doesn't depend on the assumed model, and thus – in terms of selecting the best model – may be considered as a constant. Thus maximizing L' is equivalent to minimizing L, where

$$\ln L \equiv -2 \left(\sum_i n_i \ln m_i - \sum_i m_i \right) \tag{12.63}$$

If one compares two models A and B, with number of fitted parameters n_A and n_B and with likelihoods of $\ln L_A$ and $\ln L_B$, respectively, the difference $\Delta L \equiv \ln L_A - \ln L_B$ is a χ^2 distribution with $n_A - n_B$ degrees of freedom, for a sufficient number of photons [Cash (1979); Mattox et al. (1996)].

12.4.1 A constant background

As a first example we model a constant background: $m_i = A$. With Z pixels we thus have a total number of photons in the model $N_m = ZA$; write the total observed number of photons as N_o Inserting this in eq. 12.63 we have

$$-0.5 \ln L = \sum n_i \ln A - \sum A = N_o \ln A - ZA = N_o \ln(N_m/Z) - N_m \tag{12.64}$$

and we have to minimize this with respect to N_m. Thus

$$\frac{\partial \ln L}{\partial N_m} = 0 \Rightarrow \frac{N_o}{N_m} - 1 = 0 \Rightarrow N_o = N_m \tag{12.65}$$

and we see that the best solution, as expected, is the one in which the number of photons in the model equals that in the observation.

12.4.2 Constant background plus one source

Let us now assume that we have a source with strength B, and that a fraction f_i of this lands on pixel i. Eq. 12.63 now becomes

$$-0.5 \ln L = \sum_i n_i \ln(A + Bf_i) - \sum_i (A + Bf_i) \tag{12.66}$$

We search the minimum of L for variations in A and B:

$$\frac{\partial \ln L}{\partial A} = 0 \Rightarrow \sum_i \frac{n_i}{A + Bf_i} - \sum_i (1) = \sum_i \frac{n_i}{A + Bf_i} - Z = 0 \tag{12.67}$$

$$\frac{\partial \ln L}{\partial B} = 0 \Rightarrow \sum_i \frac{n_i f_i}{A + Bf_i} - \sum_i f_i = \sum_i \frac{n_i f_i}{A + Bf_i} - 1 = 0 \tag{12.68}$$

We thus have two equations for the two unknowns A and B. Multiply the first equation with A, the second with B, and add the two equations to find

$$\sum_i n_i = AZ + B \tag{12.69}$$

i.e. the total number of counts in the best model is equal to the total number of observed counts. This condition may be used so that one only has to fit one, rather than two parameters.

12.5 General Methods

To produce the best fit for the case of Poissonian errors, several methods are available, of which we discuss a few. The methods are distinct from the methods discussed above for the least-squares cases, in that they do not use the derivative of the function, but only the function value itself, together with the criterion of best fit. These methods are equally suited for least-squares problems, with Eq. 12.34 as the criterion, and for maximum-likelihood problems with Poisson statistics, where Eq. 12.63 must be minimized. For simple problems, these methods tend to be slower in converging on a good solution than the Levenberg-Marquardt method. For problems with many variables, where the matrix α (Eq. 12.54) becomes very big, and for problems in which the χ^2 distribution has many local minima, the methods discussed below are actually more efficient than the Levenberg-Marquardt method. An example is the fit to the lightcurves (in U,B,V) and radial velocities of a binary: this problem has many variables, and can have many local minima.

12.5.1 Amoebe

See Numerical Recipes, Press et al. (1992), chapter 10.4.

12.5.2 Genetic algorithms

For an explanation of the principle of genetic algorithms we refer to Charbonneau (1995).

An interesting extension is the use of *black sheep*, i.e. bad descendents from good parents, in the genetic algorithm scheme. This is treated by Bobinger (2000).

12.6 Exercises

Problem 1. Calculate the average and the variance of the Gauss function.

Problem 2. Show that $\mathrm{erf}(x) = P(1/2, x^2)$.

Problem 3. $x = a\ln(\pm bu)$. Give the relation between σ_x and σ_u.

Computer Problem 1. Write a fortran program which computes

a. the binomial probability for given k, n, p.

b. the Poisson probability for given k, μ.

c. the Gauss function for given x, μ, σ.

To check your program, verify the following statements:

a. if one throws 10 dice, the probability that precisely 7 three's are up is 2.48×10^{-4}.

b. if the expected number of arriving counts is 15, the probability of measuring 30 counts is 2.21×10^{-4}, the probability of measuring 0 counts is 3.06×10^{-7}.

c. if one estimates the probabilities calculated in b) by approximating the Poisson function with a Gaussian, one finds 5.70×10^{-5} for both.

Computer Problem 2. Compute $\mathrm{erf}(x)$ for $x = 1, 3, 5, 10$.

Computer Problem 3. Reproduce (the dots in) Figure **??**.

Reading task 1. Read chapters 6.1 and 6.2 of Numerical Recipes with care, and have a look at the fortran functions described in there.

Problem 4. Radiopulsar PSR J 1713 + 0747 has an observed period $P = 4.5701 \times 10^{-3}\,\mathrm{s}$ and period derivative $\dot{P} = 8.52 \times 10^{-21}$, both with (for the purpose of this problem) negligible errors. Two components of its proper motion μ have been measured as $\mu_\alpha = 4.9 \pm 0.3\,\mathrm{mas/yr}$ and $\mu_\delta = -4.1 \pm 1.0\,\mathrm{mas/yr}$; its distance is estimated from the dispersion measure as $d = 1.1 \pm 0.3\,\mathrm{kpc}$.

As noted by Shklovskii, the ratio $\dot{P}/P$ must be corrected for the apparent acceleration due to the proper motion, so that the intrinsic ratio is:

$$\left(\frac{\dot{P}}{P}\right)_i = \frac{\dot{P}}{P} + \frac{\mu^2 d}{c} \tag{12.70}$$

The (intrinsic) spindown age of a radio pulsar is

$$\tau_{c,i} = \left(\frac{P}{2\dot{P}}\right)_i \tag{12.71}$$

Calculate the intrinsic spindown age and its error.

Computer Problem 4. Via computer you obtain a list of dates and logarithms of bolometric fluxes for supernova SN1987A. The errors in $\log L_b$ due to uncertainty in photometry are 0.003 until day 455, 0.005 until day 526, 0.02 until day 635, and 0.03 thereafter. Write a computer code which reads the file, and fits a straight line to the data between a first and a last day. Calculate $d\log L_{bol}/dt$ and convert the result to a half-life time, for all data after day 150; and for data between day 150 and 300. Compute the differences between the fit and the measurements, and plot these for both fits as a funcion of time. What do you learn from these plots?

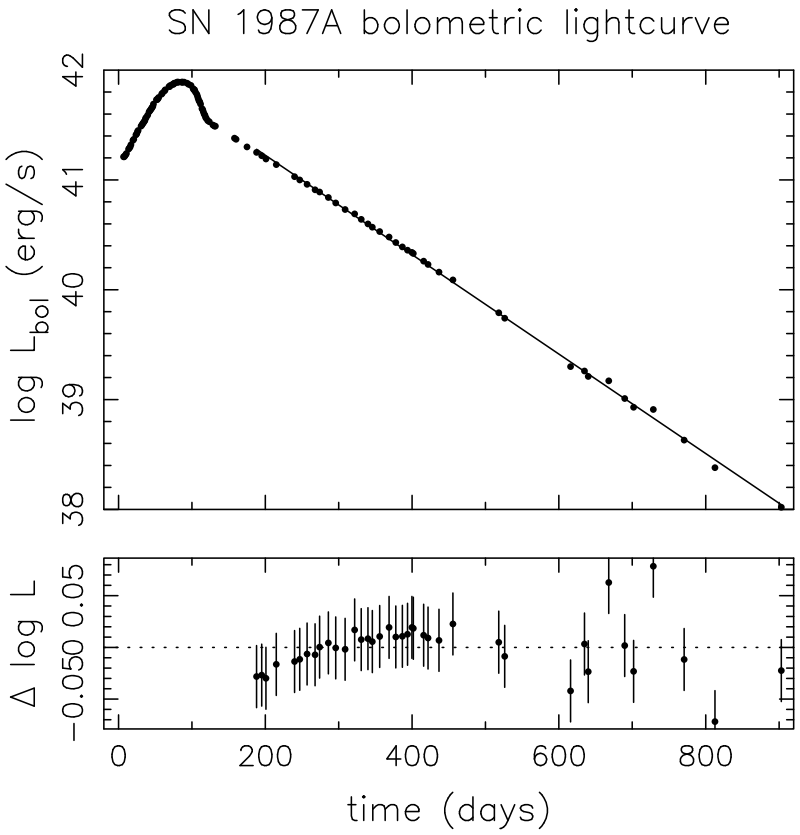

Figure 12.2: *Lightcurve and fit of the bolometric magnitude of SN 1987A.*

Computer Problem 5. Via computer you obtain a list with the ratios of $^{87}Rb(t)/^{86}Sr$ and $^{87}Sr(t)/^{86}Sr$, and associated errors, for 26 meteorites. Here t is the time since solidification of the parent asteroid from which the meteorites originate. The relation between the two ratios is given by

$$\frac{^{87}Sr(t)}{^{86}Sr} = \frac{^{87}Sr(0)}{^{86}Sr} + \left(e^{\lambda t} - 1\right) \frac{^{87}Rb(t)}{^{86}Sr} \tag{12.72}$$

From the obervations we can determine t by inference the age of the solar system. There are some subtleties, however:

a. Which of the two quantities has the smallest errors? Rewrite Eq. 12.72 in a form suitable for fitting a straight line.

b. Fit a straight line to all points, and make a plot of the fit, and of the differences between fit and observations, in terms of $\chi \equiv (y_i - y_m)/\sigma_i$ Where i refers to the observation number, and m to the model fit.

c. Why are some points far from the fit? Remove the worst points one by one, until you get an acceptable probability.

Computer Problem 6. Via computer you obtain a list with fluxes as a function of wavelength for the Mg II 2800 line in a cataclysmic variable.
a. Read the file, make a plot of flux as a function of wavelength, and fit a straight line to all the data.
b. Now write a subroutine for use in `MRQMIN` which computes the function values and their derivatives, for a straight line plus a Gaussian line.
c. Estimate initial values for the best parameters, and apply the routine from b) to make a fit of the data.
d. Compare the χ^2 from a) and c) to decide whether the addition of the line improves the fit significantly.

Chapter 13

Looking for variability and periodicity

This chapter provides a brief first guide on how one decides whether a time series of N measurements y_i with errors σ_i at times t_i shows significant variability, and how one searches for periodicity in the variation. This chapter is mainly descriptive, and many results are given without proof (but with appropriate references).

A first indication may be found by testing the hypothesis that the source is constant. The best guess for this constant is (in the case of Gaussian errors) given by Eq. 12.36. Compute the chi-squared for this average with Eq. 12.34, and the probability that this chi-squared is obtained by chance, from $P(\chi^2_{obs} = \texttt{gammq}((N-1)/2, \chi^2_{obs}/2)$. If this probability is high, it depends on the quality and length of the time series whether one stops here. To understand this, we do a thought experiment with a series of N measurements y_i, all drawn from a Gaussian distribution around a constant value, all with the same error σ. Thus, the observed chi-squared is due to chance. Now, order the measurements, so that $y_N \geq y_{N-1} \geq \ldots y_2 \geq y_1$. The time series thus obtained has the same chi-squared, but clearly cannot be obtained by chance: however, its significant increase of y_i with time is not uncovered by the chi-squared test. As a second example, take the same series y_i for the case that the measurements are made at equidistant time intervals: $t_i = i \times \Delta t$. Now order the y_i so that the higher values are assigned to t_i with even i and the lower values to t_i with odd i. Again, the significant periodicity present in the re-ordered data is not uncovered by the chi-squared test. If the time series is long enough, we can uncover the significant variability from other tests. In our thought experiments, on could for example try a Kolmogorov-Smirnov test for the first case (see Sect. 13.3), and a Fourier transform for the second case (see Sect. 13.4).

In general, the level of sophistication that is appropriate increases when the measurement series is larger and of higher quality.

13.1 Fitting sine-functions: Lomb-Scargle

As a first example, we look at the data obtained by the Hipparcos satellite on the pulsational variable W UMa (Fig. 13.1). It is clear from the range of variation as compared to the size of the error bars that this source is significantly variable. Due to the observing method of the satellite, the data are taken at irregular intervals. For such data, one method to search for periodicity is to fit a (co)sine curve:

$$V_h = a\cos(\omega t - \phi_o) = A\cos\omega t + B\sin\omega t \tag{13.1}$$

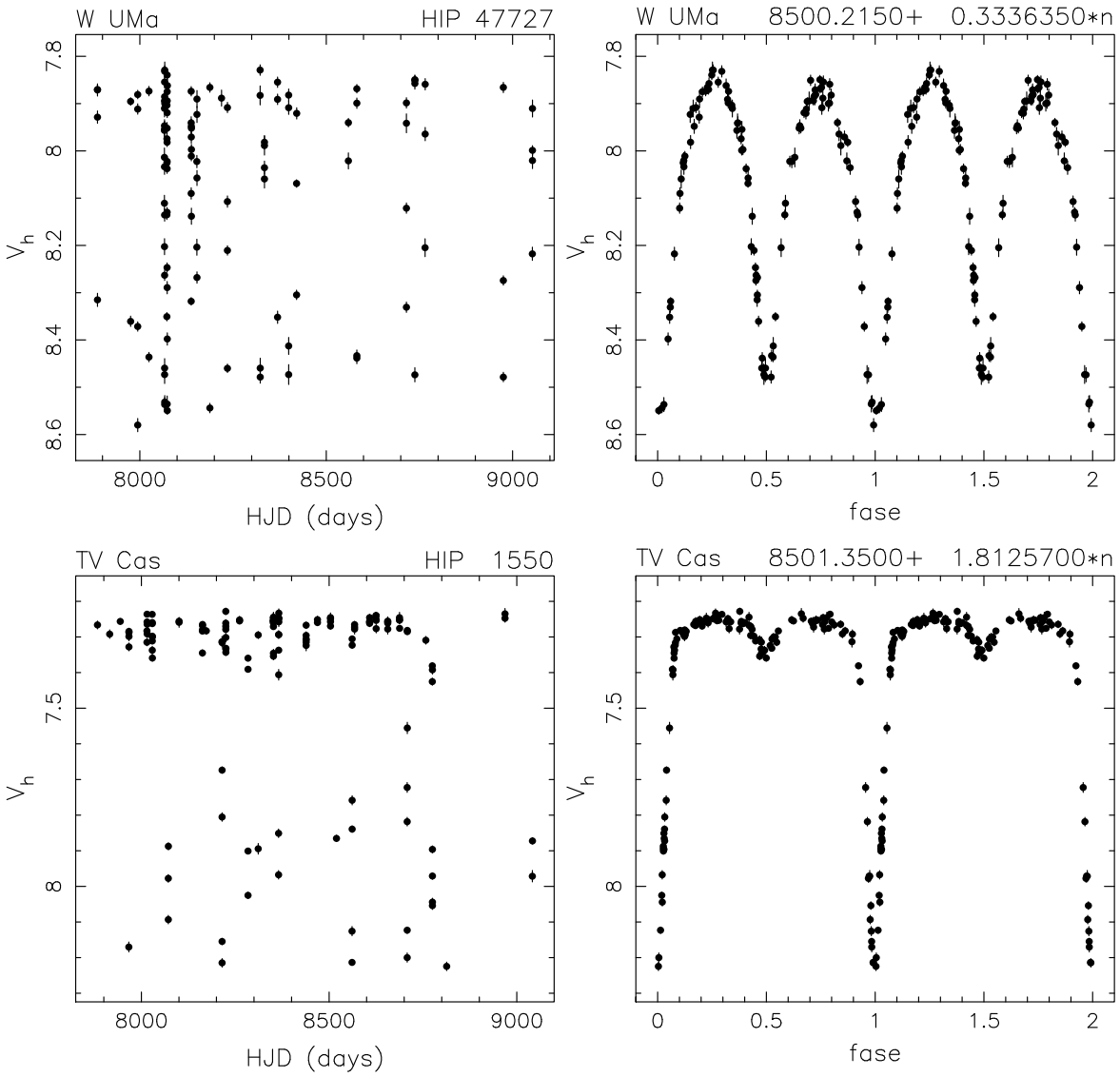

Figure 13.1: *Magnitudes of eclipsing binaries W UMa (above; 117 points) and TV Cas (below, 133 points) as measured with Hipparcos, in order of observation date (left) and after folding on the orbital period (right; the zero-phase and orbital period are indicated in days).*

where A and B are related to a and ϕ_o as

$$a^2 = A^2 + B^2; \qquad \tan\phi_o = \frac{B}{A} \tag{13.2}$$

One can look for the best values for a, ϕ_o and $\omega \equiv 2\pi/P$ by minimizing the sum of the chi-squares. In principle, one could use one of the methods we discussed in the previous chapter, but a more specialized method, developed for this specific problem, is more efficient. First suggested by Lomb (1976), it was successively improved by Scargle (1982), Horne & Baliunas (1986), and Press & Rybicki (1989), and is described in Numerical Recipes, Press et al. (1992), Ch. 13.8.

In the case of W UMa, the folded lightcurve is roughly sinusoidal, and the Lomb-Scargle method (as it is commonly called) may be expected to work well.

In some cases, the lightcurve is (close to) a sine function with two maxima and two minima at each orbital period. In such a case, it is sometimes difficult to decide whether the real period is the one found, or twice as long. For example, contact binaries (also called W UMa variables) often have two almost equal minima per orbital period (Fig. 13.1). Depending on the quality of the data one may or may not find a significant difference between the two minima. In such a case, additional knowledge ('W UMa systems have two minima and two maxima in each orbit') must decide whether the period coming out of the Lomb-Scargle test is the actual period, or half of it.

13.2 Period-folding: Stellingwerf

In the case of TV Cas, the folded light curve is very different from a sine. One therefore expects that the Lomb-Scargle method may not be optimally efficient in finding the period. Stellingwerf (1978) has developed a method which works for lightcurves of arbitrary forms. The basic idea is as follows. Fold the data on a trial period to produce a folded lightcurve. Divide the folded lightcurve, in M bins. If the period is (almost) correct, the variance ${s_j}^2$ inside each bin $j \in 1, M$is small; if the period is wrong, the variance in each bin is almost the same as the total variance. The best period has the lowest value for $\sum_{j=1}^{M} {s_j}^2$.

Stellingwerf discusses how many periods one should take, in which interval, and how many bins, etc., as derived from the data set itself. In other cases, one may have other information which may help in selecting a period range, for example when one knows that the star is a δ Cepheid variable with a known approximate absolute magnitude.

In general, both with the Lomb-Scargle and with the Stellingwerf method, one must ask the question what the probability is that the result obtained is due to chance. Analytic derivation of this probability is fraught with difficulties, and often the safest estimate is obtained by simulations. For example, if one has N measurements y_i at t_i, one can scramble the data and apply the Lomb-Scargle or Stellingwerf method. The scrambled data should not have a periodicity. Therefore, by perfoming many scrambles, one can find out what the distribution of significances is that arises due to chance, and thereby what the probability is that the period obtained from the actual data is due to chance. This probability is often referred to as the *false-alarm probability*.

13.3 Variability through Kolmogorov-Smirnov tests

Data may be variable without strict periodicity. Consider a detector which is open for T seconds and in this period detects N photons. If the interval is divided in M bins of equal length $T/(M-1)$, then for a constant source, each bin should contain $n = N/(M-1)$ photons, and one can do chi-squared or maximum-likelihood test that the observed numbers $n_j, (j \in 1, M)$ differ significantly from this. The problem with this approach is that the number of bins that one loses information by binning, and that the result depends on the number of bins chosen.

The Kolmogorov-Smirnov test (shorthand: KS-test) test avoids these problems. The KS-test in general computes the probability that two distributions are the same; or phrased differently, the probability that two distributions have been drawn from the same parent distribution. The one-sided KS-test compares a theoretical distribution (which has no errors associated to it) with the observed distribution. The two-sided KS-test compared two observed distributions, each of which has errors.

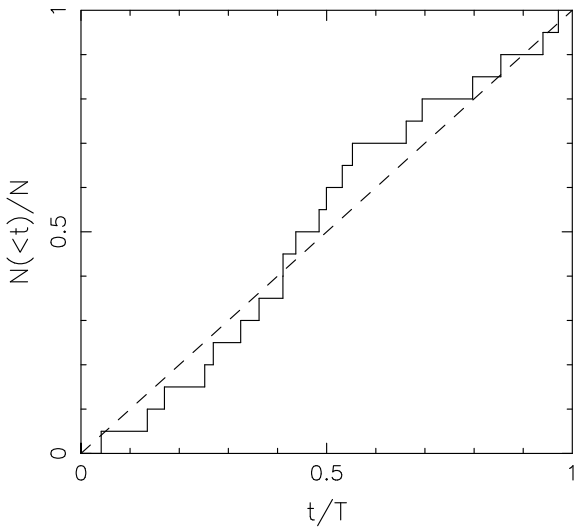

Figure 13.2: *Illustration of the Kolmogorov-Smirnov test for variability of an assumed constant source. The largest difference d between the theoretical straight line and the actually observed histogram is a measure of the probability that the variability is due to chance.*

In a search for variability, the assumption for a constant source is that the expected number of photons detected (or the integrated flux received) increases linearly with time. Normalize the total number N of detected photons to 1. The theoretical expectation is that the normalized number of photons $N(< t)$ that arrive before time t increases linearly with t from 0 at $t = 0$ to 1 at $t = T$. The observed distribution is a histogram which starts at 0 for $t = 0$, and increases with $1/N$ at each time $t_i, i \in 1, N$ that a photon arrives. This is illustrated in Figure 13.2. Now determine the largest difference d between the theoretical curve and the observed curve. The KS-test gives the probability that a difference d or larger arises in a sample of N photons due to chance. It takes into account that for large N one expects any d arising due to chance to be smaller than in a small sample.

The Kolmogorov-Smirnov test is described in Numerical Recipes, Press et al. (1992), Chapter 14.3.

13.4 Fourier transforms

The Fourier transform uses the fact that a periodic signal builds up with time to discover a periodic signal in a long time series, even if the signal is small with respect to the noise level. It works best in data taken in an un-interrupted series of equidistant intervals, and this is the case we will discuss here. Our discussion is based on a tutorial by Michiel van der Klis. Interruptions in the time series, i.e. data gaps, lead to spurious periodicities, and techniques have been developed to remove these successively, for example 'cleaning'. This is not dicussed here.

Mathematically, we can discriminate between the continuous and the discrete Fourier transforms. In observations, only the discrete transform occurs. To understand some of the properties of the discrete transform it is useful to compare with the continuous transform. With $i \equiv \sqrt{-1}$, the continuous transform $a(\nu)$ of signal $x(t)$ is given by

$$a(\nu) = \int_{-\infty}^{\infty} x(t) e^{i2\pi\nu t} dt \qquad \text{for } -\infty < \nu < \infty \tag{13.3}$$

and the reverse transform

$$x(t) = \int_{-\infty}^{\infty} a(\nu) e^{-i2\pi\nu t} d\nu \qquad \text{for } -\infty < t < \infty \tag{13.4}$$

From this it can be derived that

$$\int_{-\infty}^{\infty} x(t)^2 dt = \int_{-\infty}^{\infty} a(\nu)^2 d\nu \tag{13.5}$$

The above equations are occasionally written with the cyclic frequency $\omega \equiv 2\pi\nu$.

If we write $e^{i2\pi\nu t}$ as $\cos(2\pi\nu t) + i\sin(2\pi\nu t)$ in Eq. 13.3, we see that the Fourier transform gives the correlation between the time series $x(t)$ and a sine (or cosine, see Eq. 13.1) function, in terms of amplitude and phase at each frequency ν.

13.4.1 The discrete Fourier transform

Now consider a series of measurements $x(t_k) \equiv x_k$ taken at times t_k where $t_k \equiv kT/N$ with T the total time during which the N measurements are made. The time step for the x_k is $\delta t = T/N$. The discrete Fourier transform is defined at N frequencies ν_j, for $j = -N/2, \ldots, N/2-1$, with a frequency step for the a_j of $\delta\nu = 1/T$.

The discrete equivalents of the above equations 13.3, 13.4 and 13.5 are

$$a_j = \sum_{k=0}^{N-1} x_k e^{i2\pi jk/N} \qquad j = -\frac{N}{2}, -\frac{N}{2}+1, \ldots \frac{N}{2}-2, \frac{N}{2}-1 \tag{13.6}$$

$$x_k = \frac{1}{N} \sum_{j=-N/2}^{N/2-1} a_j e^{-i2\pi jk/N} \qquad k = 0, 1, 2, \ldots, N-1 \tag{13.7}$$

and

$$\sum_{k=0}^{N-1} |x_k|^2 = \frac{1}{N} \sum_{j=-N/2}^{N/2-1} |a_j|^2 \tag{13.8}$$

The last equation is called Parseval's theorem. These equations are occasionally also written in terms of cyclic frequencies $\omega_j \equiv 2\pi\nu_j$.

The $1/N$-term is located here on the right-hand side of Eq. 13.7. This is a matter of convention, and other conventions can be used, and in fact are used in the literature, e.g. putting the $1/N$-term on the right hand side of Eq. 13.6, or putting a $1/\sqrt{N}$-term in both Eqs. 13.6 and 13.7. When reading an article, first find out which convention is used!

In the general definition of the Fourier transforms, both x and a are complex numbers. In the application we discuss here, the x_j are the numbers of photons detected at times t_k, and are therefore real. This implies that the amplitude at frequency $-j$ is the complex conjugate of the amplitude at frequency j, i.e. $a_{-j} = a_j{}^*$, ensuring that the x_k found from the complex a_j through Eq. 13.7 are real again. The highest frequency that occurs is $\nu_{N/2} = 0.5N/T$; it is called the Nyquist frequency. . Since $a_{-N/2} = a_{N/2}$:

$$a_{-N/2} = \sum_{k=0}^{N-1} x_k e^{-i\pi k} = \sum_{k=0}^{N-1} x_k (-1)^k = a_{N/2} \tag{13.9}$$

we may list the amplitude at the Nyquist frequency either at the positive or negative end of the series of a_j. Again, it is a matter of convention. The amplitude at zero frequency is the total number of photons:

$$a_o = \sum_{k=0}^{N-1} x_k \equiv N_{tot} \tag{13.10}$$

Parseval's theorem Eq. 13.8 allows us to express the variance of the signal in terms of the Fourier amplitudes a_j:

$$\sum_{k=0}^{N-1}(x_k-\overline{x})^2=\sum_{k=0}^{N-1}{x_k}^2-\frac{1}{N}\left(\sum_{k=0}^{N-1}x_k\right)^2=\frac{1}{N}\sum_{j=-N/2}^{N/2-1}|a_j|^2-\frac{1}{N}{a_o}^2 \tag{13.11}$$

The discrete Fourier transform converts N measurements x_k into $N/2$ complex Fourier amplitudes $a_j = {a_{-j}}^*$. Each Fourier amplitude has two numbers associated with it, an amplitude and a phase, $a_j = |a_j|e^{i\phi_j}$. If the N measurements are uncorrelated, the N numbers (amplitudes and phases) associated with the $N/2$ Fourier amplitudes are uncorrelated as well. Mathematically, this follows from the following Equations (the derivation of which can be checked with Problem 6.1):

$$\sum_{k=0}^{N-1}\sin\omega_j k=0,\qquad \sum_{k=0}^{N-1}\cos\omega_j k=0\quad(j\neq 0) \tag{13.12}$$

$$\sum_{k=0}^{N-1}\cos\omega_j k\cos\omega_m k=\begin{cases}N/2, & j=m\neq 0\quad\text{or}\quad N/2\\ N, & j=m=0\quad\text{or}N/2\\ 0, & j\neq m\end{cases} \tag{13.13}$$

$$\sum_{k=0}^{N-1}\cos\omega_j k\sin\omega_m k=0 \tag{13.14}$$

$$\sum_{k=0}^{N-1}\sin\omega_j k\sin\omega_m k=\begin{cases}N/2, & j=m\neq 0\quad\text{or}\quad N/2\\ 0, & \text{otherwise}\end{cases} \tag{13.15}$$

In searching for a periodic variation, the phase of the variation often is less important than the period. For this reason, a period search is often based on the power of the Fourier amplitudes, defined as a series of $N/2$ numbers, each number being given by

$$P_j\equiv\frac{2}{a_o}|a_j|^2=\frac{2}{N_{tot}}|a_j|^2\qquad j=0,1,2,\ldots,\frac{N}{2} \tag{13.16}$$

where we have used Eq. 13.10. The series P_j is called the *power spectrum*. By using the power spectrum, we do not use all available information, in particular we do not use the information on phases. The normalization of the power spectrum is by convention, and different authors may use different conventions. In deciding whether a periodicity that one find from the power spectrum is significant, one should know which convention is used. The convention of Eq. 13.16 is called the *Leahy normalization*.

Whereas the Fourier amplitudes a_j follow the super-position theorem, the Fourier power spectrum P_j does not. Specifically, if a_j is the Fourier amplitude of x_k and b_j the Fourier amplitude of y_k, then the Fourier amplitude c_j of $z_k = x_k + y_k$ is given by $c_j = a_j + b_j$; but the power spectrum of z_k is $|c_j|^2 = |a_j + b_j|^2 \neq |a_j|^2 + |b_j|^2$, the difference being due to the correlation term $a_j b_j$. Only if the two signals x_k and y_k are not correlated, then the power of the combined signal may be approximated with the sum of the powers of the separate signals.

The variance given by Eq. 13.11 may be expressed in terms of the powers as

$$\sum_{k=0}^{N-1}(x_k-\overline{x})^2=\frac{N_{tot}}{N}\left(\sum_{j=1}^{N/2-1}P_j+\frac{1}{2}P_{N/2}\right) \tag{13.17}$$

In characterizing the variation of a signal one also uses the *fractional root-mean-square variation*,

$$r \equiv \frac{\sqrt{\frac{1}{N}\sum_k (x_k - \overline{x})^2}}{\overline{x}} = \sqrt{\frac{\sum_{j=1}^{N/2-1} P_j + 0.5 P_{N/2}}{N_{tot}}} \tag{13.18}$$

13.4.2 From continuous to discrete

Consider a series of measurements x_k taken in the time interval between $t = 0$ and $t = T$, at equidistant times t_k.
Mathematically, this series can be described in terms of a continuous time series $x(t)$, multiplied first with a window function

$$w(t) = \begin{cases} 1, & 0 \leq t < T \\ 0, & \text{otherwise} \end{cases} \tag{13.19}$$

and then with a sampling function ('Dirac comb')

$$s(t) = \sum_{k=-\infty}^{\infty} \delta(t - \frac{kT}{N}) \tag{13.20}$$

Let $a(\nu)$ be the continuous Fourier transform of $x(t)$, and let $W(\nu)$ and $S(\nu)$ be the Fourier transforms of $w(t)$ and $s(t)$, respectively:

$$|W(\nu)|^2 \equiv \left| \int_{-\infty}^{\infty} w(t) e^{-i2\pi\nu t} dt \right|^2 = \left| \frac{sin(\pi\nu T)}{\pi\nu} \right|^2 = |T \mathrm{sinc}(\pi\nu T)|^2 \tag{13.21}$$

i.e. the Fourier transform of a window function is (the absolute value of) a sinc-function, and

$$S(\nu) = \int_{-\infty}^{\infty} s(t) e^{-i2\pi\nu t} dt = \frac{N}{T} \sum_{m=-\infty}^{\infty} \delta\left(\nu - m\frac{N}{T}\right) \tag{13.22}$$

i.e. the Fourier Transform of the Dirac comb is also a Dirac comb. Al these transforms are symmetric around $\nu = 0$ by definition.

Now we note that *'The Fourier Transform of a product is the convolution of the Fourier Transforms'* to understand how the discrete transform derives from the continuous one. Remember, the convolution of $a(\nu)$ and $b(\nu)$ is

$$a(\nu) * b(\nu) \equiv \int_{-\infty}^{\infty} a(\nu') b(\nu - \nu') d\nu' \tag{13.23}$$

First consider the product $x(t)w(t)$. The effect of the window function $w(t)$ on the Fourier transform $a(\nu)$ of $x(t)$ is to convolve each component in it with a sinc-function. For example, a δ function is turned into a sinc-function. The widening $d\nu$ is inversely proportional to the length of the time series: $d\nu = 1/T$.

Next consider the product $[x(t)w(t)]s(t)$. The multiplication of the signal by a Dirac comb corresponds to a convolution of its transform with a Dirac comb, i.e. by an infinite repeat of the convolution.
Mathematically, the conversion from the continuous $a(\nu)$ to the discontinuous $a_d(\nu)$ is as follows:

$$\begin{aligned} a_d(\nu) \equiv & \quad a(\nu) * W(\nu) * S(\nu) = \textstyle\int_{-\infty}^{\infty} x(t) w(t) s(t) dt \\ = & \quad \textstyle\int_{-\infty}^{\infty} x(t) \sum_{k=0}^{N-1} \delta\left(t - \frac{kT}{N}\right) e^{i2\pi\nu t} dt = \sum_{k=0}^{N-1} x\left(\frac{kT}{N}\right) e^{i2\pi\nu kT/N} \end{aligned} \tag{13.24}$$

Thus, the finite length of the time series (windowing) causes a broadening of the Fourier transform with a width $d\nu = 1/T$ with sidelobes, and the discreteness of the sampling causes the aliasing, a reflection of periods beyond the Nyquist frequency into the range $0, \nu_{N/2}$.

In the above we have assumed that each sample is obtained instantaneously. In practice, the smaple is often an integration over a finite exposure time. This can be described mathematically by convolving the time series $x(t)$ with a window function with the width of the exposure time:

$$b(t) = \begin{cases} N/T, & -\frac{T}{2N} < t < \frac{T}{2N} \\ 0, & \text{otherwise} \end{cases} \tag{13.25}$$

Since 'The Fourier transform of a convolution is the product of the Fourier transforms', this implies that the Fourier transform $a_d(\nu)$ is multiplied with the Fourier transform of $b(t)$:

$$B(\nu) = \frac{\sin \pi\nu T/N}{\pi\nu T/N} \tag{13.26}$$

At frequency zero, $B(0) = 1$, at the Nyquist frequency $B(\nu_{N/2} = T/(2N)) = 2/\pi$, and at double the Nyquist frequency $B(\nu = N/T) = 0$. Therefore, the frequencies beyond the Nyquist frequency that are aliased into the window $(0, \nu_{N/2})$ have a reduced amplitude. We can understand this: the integration of the exposure time corresponds to an averaging over a time interval T/N, and this reduces the variations at frequencies near N/T.

13.4.3 The statistics of power spectra

Now that we have the power spectrum, we want to know how to extract a signal from it. We assume in out discussion that the time series $x(t)$ consists of noise and a signal, and that noise and signal are not correlated. We can then write:

$$P_j = P_{j,\text{noise}} + P_{j,\text{signal}} \tag{13.27}$$

For many types of noise, the power $P_{j,\text{noise}}$ approximately follows the chi-squared distribution with 2 degrees of freedom. The normalization of the powers given by Eq. 13.16 ensures the power of Poissonian noise is exactly distributed as the chi-squares with two degrees of freedom. Thus, the probability of finding a power $P_{j,\text{noise}}$ larger than an observed value P_j is given by

$$Q(P_j) = \texttt{gammq}(0.5 * 2, 0.5P_j) \tag{13.28}$$

(see the discussion following Eq. 12.34).

The standard deviation of the noise powers is equal to their mean value: $\sigma_P = \overline{P_j} = 2$. In other words, fairly high values of P_j are possible du to chance.

In order to reduce the noise of the power spectrum, one may choose to average it. The are two ways to do this. The first is to bin the power spectrum, i.e. take the average of every W consecutive powers. The second is to divide the time series into M subseries, determine the power spectrum for each subseries, and then average the power spectra. In both cases, the price that one pays is a loss of frequency resolution. The gain is that the power spectrum is now much less noisy. The chi-squared distribution of a power spectrum of a time series which has been divided into M interval, and in which W successive powers in each spectrum are averaged, is given by the chi-squared distribution with $2MW$ degrees of freedom, scaled by $1/(MW)$. The average of the distribution is 2, its variance $4/(MW)$ and its standard deviation $2/\sqrt{MW}$. In other words, the probability that a binned, averaged power is higher than the observed power $P_{j,\text{b}}$ is given by

$$Q(P_{j,\text{b}} = \texttt{gammq}(0.5[2MW], 0.5[MWP_{j,\text{b}}]) \tag{13.29}$$

For sufficiently large MW this approaches the Gauss function.

13.4.4 Detecting and quantifying a signal

From Eq. 13.28 and 13.29 we can decide whether at a given frequency the observed signal exceeds the noise level significantly, for any significance level we want to set. Thus, if we wish 90% significance, we first compute the P_j for which $Q = 0.1$, i.e. the probability which is exceeded by chance in only 10% of the cases. Then we check whether the observed power is bigger than this P_j.

The above reasoning is true is we decide on the frequency *before* we do the statistics, i.e. if we first select *one single frequency* ν_j. Such is the case if we wish to know whether a source is significantly variable on a known period, for example the orbital period of a binary, or the pulse period for a pulsar.

In general, we are searching for a period, i.e. we do not know which frequency is important, and thus we apply Eq. 13.28 and 13.29 many times, viz. once for each frequency. This corresponds to many trials, and thus our probability level has te be set accordingly. To see how, first consider one frequency. Suppose that the a value $P_{\rm detect}$ has a probability $1 - \epsilon'$ *not* to be due to chance. Now try $N_{\rm trials}$ frequencies. The probability that the value $P_{\rm detect}$ is not due to chance *at any of these frequencies* is given by $(1 - \epsilon')^{N_{\rm trials}}$, which for small ϵ' equals $1 - N_{\rm trials}\epsilon'$. Thus, the probability that the value $P_{\rm detect}$ *is* due to chance *at any of these frequencies* is given by $\epsilon = N_{\rm trials}\epsilon'$. In conclusion, if we wish to set an overall chance of ϵ, we must take the chance per trial as $\epsilon' = \epsilon/N_{\rm trials}$, i.e.

$$\epsilon' = \frac{\epsilon}{N_{\rm trials}} = \texttt{gammq}(0.5[2MW], 0.5[MWP_{\rm detect}]) \tag{13.30}$$

Suppose we have an observed power $P_{j,\rm b}$ which is higher than the detection power $P_{\rm detect}$ for given chance ϵ'. Because the observed power is the sum of the noise power and the signal power (Eq. 13.27), this implies

$$P_{j,\rm signal} > P_{j,\rm b} - P_{j,\rm noise} \qquad (1 - \epsilon') \quad \text{confidence} \tag{13.31}$$

Suppose on the other hand that we find no observed power at any frequency to exceed the detection level. We may then be interested in setting an upper limit to the signal power. To do this, we proceed as follows. First we determine the level $P_{\rm exceed}$ which is exceeded by the noise alone with a high probability $(1 - \delta)$, from

$$1 - \delta = \texttt{gammq}(0.5[2MW], 0.5[MWP_{\rm exceed}]) \tag{13.32}$$

If the highest actually observed power in the range of interest is $P_{\rm max}$, then the upper limit $P_{\rm UL}$ to the power is

$$P_{\rm UL} = P_{\rm max} - P_{\rm exceed} \tag{13.33}$$

in the sense that, if there were a signal power higher than $P_{\rm UL}$, the highest observed power would be higher than $P_{\rm max}$ with a $(1 - \delta)$ probability.

13.5 Exercises

Problem 4. Derive Eq. 13.12 to 13.15 we use the following intermediate steps.
a. Show that

$$\sum_{k=0}^{N-1} e^{i\lambda k} = \frac{e^{i\lambda N} - 1}{e^{i\lambda} - 1} = e^{i\lambda(N-1)/2} \quad \frac{e^{i\lambda N/2} - e^{-i\lambda N/2}}{e^{i\lambda/2} - e^{i\lambda/2}} \tag{13.34}$$

b. Now use Euler's equation $e^{i\lambda} = \sin\lambda + i\cos\lambda$ and its inverse relations

$$\cos\lambda = \frac{1}{2}\left(e^{i\lambda} + e^{-i\lambda}\right), \qquad \sin\lambda = \frac{1}{2i}\left(e^{i\lambda} + e^{-i\lambda}\right) \tag{13.35}$$

to show

$$\sum_{k=0}^{N-1}\cos(\lambda k) = \cos[\lambda(N-1)/2]\frac{\sin(\lambda N/2)}{\sin(\lambda/2)}, \qquad \sum_{k=0}^{N-1}\sin(\lambda k) = \sin[\lambda(N-1)/2]\frac{\sin(\lambda N/2)}{\sin(\lambda/2)} \tag{13.36}$$

c. From Euler's equations we also have

$$\sin(\lambda+\mu) = \sin\lambda\cos\mu + \cos\lambda\sin\mu \qquad \cos(\lambda+\mu) = \cos\lambda\cos\mu - \sin\lambda\sin\mu \tag{13.37}$$

and the inverse relations

$$\cos\lambda\cos\mu = \frac{1}{2}\left[\cos(\lambda+\mu) + \cos(\lambda-\mu)\right] \tag{13.38}$$

$$\cos\lambda\sin\mu = \frac{1}{2}\left[\sin(\lambda+\mu) - \sin(\lambda-\mu)\right] \tag{13.39}$$

$$\sin\lambda\sin\mu = \frac{1}{2}\left[\cos(\lambda-\mu) - \cos(\lambda+\mu)\right] \tag{13.40}$$

Problem 5. Consider a symmetric window function $w(t)$ which has values $w(t) = 1$ for $-T/2 < t < T/2$ and $w(t) = 0$ otherwise, and show that its Fouriertransform is a sinc function.

Computer problem 6. Via computer you obtain a list of 65536 points (16 per line) with simulated X-ray data from a low-mass X-ray binary. Each number gives the number of photons detected during one millisecond. There are no gaps in the data.

a. write a little computer program which reads the first 8 numbers from this list, and calculates the Fourier transform.

b. now use the routine `realft`$(data, n, isign)$ from Numerical Recipes to compute the Fourier transform of the same 8 points, and show that you obtain the same result. As input, the routine `realft` requires an array $data$ with the data points, the integer n which gives the number of data points, and the integer $isign$ which tells it whether to perform a forward or a backward Fourier transformation. As output it gives $data(1)$ as the total number of photons, which equals a_0, $data(2)$ is $a_{n/2}$, and for the remaining components of the transform we have $data(2j+1) = Re\{a_j\}$ and $data(2j+2) = Im\{a_i\}$. Show that you obtain the same result as with your own code of a.

c. Now compute the Fourier transform of the whole data set, and compute and plot the power spectrum.

d. We want to see whether the highest peak observed in the power spectrum is significant. To do this, determine the detection level of 90% and 99% probability. Take account of the number of trials!

e. Reduce the noise in the power spectrum by averaging in bins of 16 powers. Do you note new features?

Chapter 14

References

- M. Harwit, ***Cosmic Discovery***, 1984, MIT press, Cambridge.
- R. Bowers and T. Deeming, ***Astrophysics***, 1984, Jones and Bartlett Publishers, Inc.
- M.S. Longair, ***High Energy Astrophysics***, 1992, Cambridge University Press.
- G.B. Rybicky and A.P. Lightman, ***Radiative Processes in Astrophysics***, 1979, John Wiley and Sons, Inc.
- P. Lena, F. Lebrun and F. Mignard, ***Observational Astrophysics***, 1998, Springer-Verlag.
- C.R. Kitchin, ***Astrophysical Techniques***, 1998, Institute of Physics Publishing.
- R. Giacconi and H. Gursky, ***X-ray Astronomy***, 1974, Reidel Publishing Company.
- J.D. Kraus, ***Radio Astronomy***, 1966, McGraw-Hill Book Company.
- E.L. Dereniak and D.G. Crowe, ***Optical Radiation Detectors***, 1984, John Wiley and Sons, Inc.
- E.L. Dereniak and G.D. Boreman, ***Infrared Detectors and Systems***, 1996, John Wiley and Sons,Inc.
- R.A. Greiner, ***Semiconductor Devices and Applications***, 1961, McGraw-Hill, Inc.
- S. Middelhoek and S.A. Audet, ***Silicon Sensors***, 1989, Academic Press Limited.

- E. Hecht, ***Optics***, 1987, Addison-Wesley Publishing Company Inc.

- J.W. Goodman, ***Statistical Optics***, 2000, Wiley Classics Library, John Wiley and Sons, Inc.

- A. Papoulis, ***Probability, Random Variables, and Stochastic Processes***, 1991, McGraw-Hill Book Company International Editions.

- P.R. Bevington, ***Data Reduction and Analysis for the Physical Sciences***, 1969, McGraw-Hill, Inc.

- P.Z. Peebles, Jr., ***Probability, Random Variables and Random Signal Principles***, 2001, McGraw-Hill International Edition.

- J.R. Taylor, ***An Introduction to Error Analysis***, 1982, University Science Books, Oxford University Press.

- W.H. Press et al, ***Numerical Recipes***, 1992, Cambridge University Press.

- R.N. Bracewell, ***The Fourier Transform and its Applications***, 1986, McGraw-Hill Book Company International Editions.

- J.D.E. Beynon & D.R. Lamb, ***Charge-Coupled Devices and their applications***, 1980, McGraw-Hill, London.

- A.J.P. Theuwissen, ***Solid State Imaging with Charge-Coupled Devices***, 1995, Kluwer Academic Publishers, Dordrecht.

- J.M. Weisberg and J.H. Taylor, ***The Relativistic Binary Pulsar B1913+16: Thirty Years of Observations and Analysis***, 2005, ASP Conference Series, Vol **328**, 25.

- M. van der Klis, ***Quasi-Periodic Oscillations and Noise in Low-Mass X-ray Binaries***, 1989, Annual Rev. Astron.& Astrophys., **27**, 517.

- J.A.M. Bleeker, ***BeppoSAX: the Wide Field Camera prospect***, in BeppoSAX (Eds: E. van den Heuvel, R. Wijers and J. in 't Zand), 2004, Nuclear Physics B, Proc. Supplements.

- K.D. Horne, ***An Optimal Extraction Algorithm for CCD Spectroscopy***, 1985, PASP, **98**, 609.

- W. Cash, ***Parameter Estimation in Astronomy through Application of the Likelihood Ratio***, 1979, Ap.J., **228**, 939.

- J.R. Mattox *et al*, ***The Likelihood Analysis of EGRET Data***, 1996, Ap.J., **461**, 396.

- P. Charbonneau, ***Genetic Algorithms in Astronomy and Astrophysics***, 1995, Ap.J. Suppl. Series, **101**, 309.

- A. Bobinger, ***Genetic Eclipse Mapping and the Advantage of Black Sheep***, 2000, Astron. & Astrophys., **357**, 1170.

- N.R. Lomb, ***Least-Squares Frequency Analysis of Unequally Spaced Data***, 1976, Astrophysics & Space Science, **39**, 447.

- R.F. Stellingwerf, ***Period Determination Using Phase Dispersion Minimization***, 1978, Ap.J., **224**, 953.

- J.D. Scargle, ***Studies in Astronomical Time Series Analysis.II.***, 1982, Ap.J., **263**, 835.

- J.H. Horne and S.L. Baliunas, ***Prescription for Period Analysis of Unevenly Sampled Time Series***, 1986, Ap.J., **302**, 757.

- W.H. Press and G.B. Rybicki, ***Fast Algorithm for Spectral Analysis of Unevenly Sampled Data***, 1989, Ap.J., **338**, 277.